SAES2018

THE 6th INTERNATIONAL SYMPOSIUM ON APPLIED ENGINEERING AND SCIENCES

Abstracts List

Kyutech
Kyushu Institute of Technology

UPM
UNIVERSITI PUTRA MALAYSIA
BERILMU BERBAKTI

Contents

Oral Presentation

Poster Presentation

Kyutech
Kyushu Institute of Technology

UPM
UNIVERSITI PUTRA MALAYSIA
BERILMU BERBAKTI

Oral


Kyutech
Kyushu Institute of Technology


UPM
UPM
UNIVERSITI PUTRA MALAYSIA
BERILMU BERBAKTI

Please choose: Oral/ Poster/ Either
Presentation session: Material Science and Technology
Presenter name: Meng-Jiy Wang

Copolymerization of Sulfobetaine Methacrylate and Acrylic Acid by Using Atmospheric Pressure Plasma Jet

Yueh-Han Huang, Meng-Jiy Wang*

Department of Engineering, National Taiwan University of Science and Technology, 106, Taipei, Taiwan

Email: mjwang@mail.ntust.edu.tw

Keywords: Atmospheric Pressure Plasma Jet (APPJ); Copolymerization; Sulfobetaine Methacrylate; Acrylic Acid; Plasma reactions

Free radical polymerization is one of the most common used method to synthesized polymers industrially. Atmospheric pressure plasma jet (APPJ) in contact with liquid can generate several reactive oxygen and nitrogen species (RONS) such as OH radical, NO_2 radical, H_2O_2, and NO_3^-. In this work, sulfobetaine methacrylate (SBMA) and acrylic acid (AA) were copolymerized in deionized water by using 13.56 MHz radio-frequency (RF) APPJ to scan monomer solution. Different applied power and scan numbers were used to understand the effects on polymer structure and composition. On the other hand, to know the difference between APPJ and conventional free radical polymerization method, ammonium persulfate (APS) was also used to initiate the copolymerization. The chemical functionality, composition, and molecular weight were analyzed by fourier transform infrared spectroscopy (FTIR), ^{1}H-neclear magnetic resonance spectroscopy (^{1}H-NMR), and gel permeation chromatography (GPC), respectively. It was observed that APPJ can successfully synthesize copolymers with high molecular weight in a short manner. Moreover, APPJ-assisted polymerization can also provide copolymer with different composition by simply adjust the parameters of plasma. After the characterization, poly(SBMA-co-AA) synthesized by APPJ or free radical polymerization methods were then modified on glass slides via hydrogen bond and electrostatic force to evaluate the ability of anti-fouling. The preliminary anti-fouling test regarding protein fouling showed that APPJ-assisted copolymerization at low applied power and short treatment time can provide poly(SBMA-co-AA) with excellent anti-fouling ability and suggest the potential of this technique for the application to synthesize different polymers in a most cost-effective and solvent free manner.

Please choose: Either
Presentation session: Applied Chemistry
Presenter name: Safarul Mustapha

Effect of Acid Treatment on Nanocellulose as Reinforcing Agent in Silicone Elastomers

Safarul MUSTAPHA, Yoshito ANDOU and Hideo NISHINO

Department of Biological Functions Engineering, Graduate School of Life Science and Systems Engineering, Kyushu Institute of Technology, 2-4 Hibikino, Wakamatsu, Kitakyushu 808-0196, Japan

Email: safarul.bin-mustapha533@mail.kyutech.jp

Keywords: Nanocellulose, composite polymer, acid hydrolysis, regenerated cellulose, Sylgard; Composite; Elastomer

[Introduction]

Silicones are synthetic polymers with organic groups attached to an inorganic backbone giving a combination of unique properties such as a high flexibility, low surface energy, high thermal stability, high gas permeability, and low biological activity. With this unique properties, silicones or mostly used is polydimethylsiloxanes (PDMS) have been used in large range of applications including coatings, painting, building industry, medical applications, cosmetics, sensors, and optical materials. Nanocellulose (NC) derived from renewable nature, eco-friendly, excellent mechanical properties, good biocompatibility, and tailorable surface chemistry. The addition of NC into the polymers can enhance mechanical strength and making a light weight compare to other Fibre-reinforced plastic (FRP). Mechanical properties of the composite polymer are dependent on the distribution of particles in the matrix microstructure. The size and distribution of nanofiller is important because of the defect due to an agglomeration that reduce the mechanical properties of the composite. In this study, Nanocellulose (NC) is treated with different acid solution and used as nanofiller in silicone to improve tensile strength of the composite polymer. The Silicone/NC composites was mixed using conditioning mixer and poured in the glass petri dish as a mould and were characterized according to the tensile properties including tensile strength and elongation.

[Experiment]

1. Acid hydrolysis

Commercial nanocellulose (5% w/v) (average particle size: 20 µm) was hydrolysed by acid solution and mixed acid as listed in Table 1. NC with acid solution were treated under ultrasonic 40 Hz for 3 hours and continued stirred for 4 hours at room temperature. After hydrolysis, the product was washed and centrifuged for acid and alkali removal. This process was repeated until the product reached pH 6−7 followed by buffer exchange with ethanol prior to preparation silicone polymer.

2. Preparation of NC/silicone composite

0.6 % of Nanocellulose was added into of Sylgard 184 (DOW CORNING TORAY CO., LTD) using a mixing ratio of 10:1 between base polymer and curing agent as listed in Table 1. The blend was mixed using conditioning mixer for 2.5 minute successively. Then, the mixture was slowly poured into a glass petri dish (9 cm diameter) and degassed under vacuum for 2 hours to eliminate air bubbles and finally, the mixture was cured at 80 °C for 2h and demoulded to cast a silicone/NC composite with average 0.8 mm thickness for mechanical testing. Silicone and silicone/NC non-treatment were used as a control.

3. Mechanical Properties

The tensile strength and elongation were determined by an IMC-18E0 model machine (Imoto Machinery Co. Ltd, Kyoto, Japan) at a rate of 10 mm min^{-1} at 23°C.

[Result and Discussion]

The NC reinforcements enhanced the tensile properties of the silicone composite (Figure 1). The silicone/NC composites were characterized according to the tensile strength and elongation. The highest tensile values were recorded at 3.4 MPa with the treatment of phosphoric acid and almost similar value was obtained for the NC that was treated with sulphuric acid/hydrochloric acid/NaOH. There was an improvement of 78.0 % and 17.0 % in the tensile strength of the silicone/NC polymer with acid treatment and silicone/NC polymer with acid non treatment upon comparing to silicone respectively. Pertaining the elongation, the improvement was found to be 35.75 % for NC without treatment, followed by silicone/NC sulphuric acid/Hydrochloric acid/NaOH at 32.57 % with treatment upon comparing with silicone. Based on the Figure 2b, the NC were well dispersed in the transparent silicone matrix as depicted in Figure 2a. Thus, treated NC has improved tensile properties due to the addition of nanofiller in the silicone composite when compared to the silicone polymer.

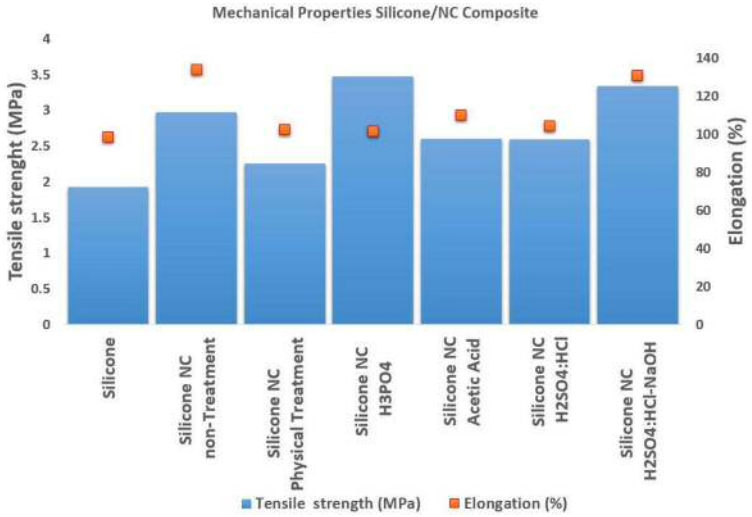

Figure 1: Mechanical properties silicone/NC composite

Table 1: List of Acid Treatment on NC

Sample Code Name	Cellulose (5% w/v)	Acid	Acid Vol. (Total 100ml)	Silicone	
				Pre-polymer	Curing agent
Silicone	-	-	-	7.45g	0.725g
Silicone NC non-Treatment	10g	-	-	7.45g	0.725g
Silicone NC Physical Treatment	10g	-	-	7.45g	0.725g
Silicone NC H3PO4	10g	Phosphoric acid (98% w/w)	30 ml	7.45g	0.725g
Silicone NC Acetic Acid	10g	Acetic acid (98% w/w)	30 ml	7.45g	0.725g
Silicone NC H2SO4:HCl	10g	Sulphuric acid (98% w/w), and Hydrochloric acid (37% w/w),	30ml and 10ml	7.45g	0.725g
Silicone NC H2SO4:HCl-NaOH	10g	Sulphuric acid (98% w/w), Hydrochloric acid (37% w/w) and Sodium hydroxide (10% w/v)	30ml,10ml and 10g	7.45g	0.725g

Figure 2: A) Silicone, B) Silicone/NC Composite (2.0mm Thickness)

Please choose: Oral/ ~~Poster~~
Presentation session:
Presenter name: Haslina Jaafar

Characterization of Latex-Graphene Composite for Flexible Electronic Applications

Nadia Amalyna, Ramly[1], Nur Haziqah, Abd Aziz[1], Suhaidi, Shafie[1,2], Mohd Nizar, Hamidon[1,2], Mohd Amrallah, Mustaffa[1,2], Haslina, Jaafar*[1,2]

[1]Faculty of Engineering, University Putra Malaysia, 43400 UPM Serdang, Selangor, Malaysia
[2]Institute of Advanced Technology, University Putra Malaysia, 43400 UPM Serdang, Selangor, Malaysia

*Email: jhaslina@upm.edu.my

Abstract
Flexible electronics is one of the growing technologies and will become more important in the future. Graphene is recognized as the best carbon material and widely used for electronic applications other than carbon nanotube (CNT). In this study, the characterization of latex composites through two different preparation methods such as dip and casting methods were studied. Some characterization tests were carried out on latex composites such as electrical and mechanical properties. Physical characterization using FESEM, EDX and Raman Spectroscopy tools was carried out to study the structure of the layers and compositions of elements in composites for both methods of preparation. Result shows the graphene dispersion into the latex for cast film is better than the dipped film. Thus, the cast film samples with graphene is conductive while dipped film sample is not conductive. Results also show the higher percentage of graphene (4phr) in the composite has high conductivity than the 3phr samples. In this project, sample-five (S5) shows the best performance than other samples. The conductivity of this sample is the highest compared to other samples which is 1.1051m $(\Omega m)^{-1}$. This composite has almost 90% of strechability. Thus, this latex-graphene material is a good sensing material for flexible and wearable electronic application for human motion detection, personal health monitoring, sports performance monitoring and other applications.

Keywords (maximum 5 words) – Graphene, Latex, Conductive Composite, Flexible

Introduction
Graphene is one of the best carbon material due to graphene has an excellent electrical conductivity. Introduction of graphene fillers into latex could improve the polymer composite properties such as mechanical properties, thermal conductivity, electrical conductivity and optical properties. Thus, we use graphene as nanofiller in natural latex to produce latex-graphene nanocomposite. The study compared the two preparation of latex-graphene composite using dip and casting processes.

Methodology
The latex and latex-graphene samples for dip and casting preparation process are characterized using Raman spectroscopy, Field Emission Scanning Electron Microscopy (FESEM) and Energy-dispersive X-ray Spectroscopy (EDX) tools. Raman spectroscopy is used to analyze the structural and the chemical properties of the samples. The sample is illuminated by monochromatic light like laser light in Raman spectroscopy. Raman technology is the one of advanced technology that can measure inelastic scattering of the scatter light over the samples. FESEM provides topographical and elemental information at magnifications of 10x to 300,000x, with virtually unlimited depth of field. EDX is an analytical technique used for the elemental analysis or chemical characterization of a sample. This test is used to analyze the element inside the samples and to compare with the control latex sample. For electrical properties, I-V characteristics of conductive samples are measured using probe and Keithley Measurement System tools. Only two of the sample were characterized as only two are conductive. Four point probe and I-V analyzer meter is used to measure the I-V characteristics of the sample.

Results and Discussion

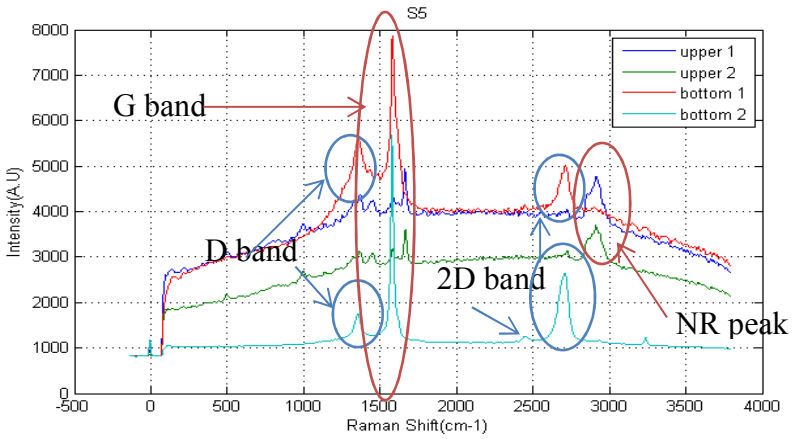

Fig.1. Raman full spectra with all four points for sample S5.

Fig. 1 shows the Raman spectra of sample S5. This sample is a sample of NR-Latex with more than 4phr of graphene. The G band appeared at 1550 cm-1 and the D band is appeared at 1350 cm-1. Only at the bottom of this sample has clearly D band, while the upper part cannot clearly seen the D band.

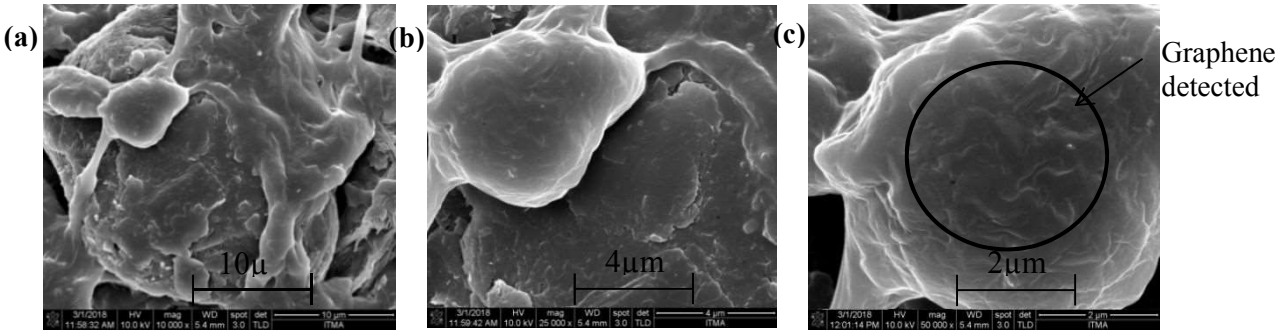

Fig. 2. FESEM results of bottom part sample S5 with three different of magnification.

Fig.2 shows FESEM for bottom part of sample S5. This sample is sample with more than 4 phr of graphene by using casting process. The figure (a) are 10000 mag, (b) 25000 mag and (c) 50000 mag. Wrinkling graphene layer clearly can be seen in (c) and it seen many of graphene layers as in circle above.

Table 1. Conductivity and resistivity of the samples.

Samples		Average		
		Resistance (kΩ)	Resistivity (kΩm)	Conductivity (m(Ωm)$^{-1}$)
S5	No 1	56.738	1.4260	0.7013
	No 2	27.647	0.6949	1.4392
	No 3	33.972	0.8538	1.1712
	No 4	35.882	0.9018	1.1089

The average of resistivity and conductivity for sample S5 is 0.96911kΩm and 1.1051m (Ωm) $^{-1}$.

Conclusion

Physical, electrical and mechanical properties of latex-graphene composite were successfully characterized. Latex-graphene composite with higher number of graphene shows higher conductivity. Only samples prepared with casting method are conductive. However the bottom side of samples are more conductive compared to the upper side.

Please choose: Oral
Presentation session: Biological Sciences
Presenter name: Mohd Shukuri Mohamad Ali

Isolation, Characterization and Potential Application of Cold Adapted Lipase from an Antarctic *Pseudomonas* sp

Mohd Shukuri Mohamad Ali[1, 2*], Norhayati Yaacob[1], Nor Hafizah Ahmad Kamarudin[1], Adam Thean Chor Leow[1,4], Abu Bakar Salleh[1], Raja Noor Zaliha Raja Abd Rahman[1, 3]

[1]Enzyme and Microbial Technology Research Centre (EMTech), [2]Department of Biochemistry, [3]Department of Microbiology, [4]Department of Cell and Molecular Biology, Faculty of Biotechnology and Biomolecular Sciences, Universiti Putra Malaysia, 43400 Serdang, Selangor Malaysia

Email: mshukuri@upm.edu.my

Abstract

Cold-active lipases have lately attracted attention as a result of their increasing use in organic synthesis and catalysis at low temperature. In this study, a lipase was isolated from an Antarctic *Pseudomonas* sp. The recombinant lipase produced in *E.coli* was characterized using biochemical approach. The lipase was found to be active in organic solvent. Computational analysis showed the stability of cold-active lipase towards exposure to organic solvents is highly dependable on surface residues as it involved the hydrophobicity profile and their interaction with organic solvent. This approach offers an alternative way to gain molecular insight of the interactions between non aqueous solvents and enzymes that to date has not been widely exploited. Activity and stability of cold-active lipase in organic solvents has been regarded as a valuable property for various biotechnological and industrial applications.

Keywords: Antarctica, AMS8 lipase, cold-adapted, *Pseudomonas* sp, organic solvent tolerant lipase

Introduction

Psychrophiles produces cold active enzymes, which are more active at low and moderate temperatures compared to homologous mesophilic enzymes. These enzymes are capable of maintaining the flexibility and dynamics of their active site at low temperature. It is highly useful in biotechnological application as it saves energy cost, prevents undesired chemical transformation, prevents the loss of volatile compounds and does not require expensive heating or cooling system [1]. In general, lipases are long chain fatty acid ester hydrolases, and are currently attracting an enormous attention because of their biotechnological potential. Cold-adapted lipases are largely used in the detergent industry, where cold washing reduces both energy consumption and the wear and tear of textile fibers. They are also preferred in the food industry, as these enzymes can be inactivated at reasonably low temperatures, and by that conserving the nutritional quality of the food.

Experiment

Cloning and Expression of Recombinant AMS8 Lipase

Recombinant plasmid harbouring *lipAMS8* was constructed in the cloning and expression studies Ali et al., 2013. *lipAMS8* was cloned in pET32b(+) vector and transformed into *Escherichia coli* strain BL21(De3).

Purification of AMS8 Lipase

Purification of recombinant lipase was performed using affinity chromatography and gel filtration technique. The fractions containing the protein of interest were confirmed through lipase assay and SDS-PAGE. The protein content of was determined using the Bradford method.

Characterization of the Purified AMS8 Lipase

The purified lipase was characterized by means of temperature, pH, organic solvent, and metal ions. The lipase capacity to perform synthesis reaction was conducted by esterification of alcohol and low molecular weight acid.

Molecular Modeling and Dynamic Simulation of AMS8 Lipase

The lipase structure was predicted via homology modeling. The predicted structure was simulated with and without organic solvent using molecular dynamic simulation software

Results and Discussion

Cold active lipases have huge biotechnological prospects due to their high catalytic activity at low temperature. The utilization of organic solvents as reaction media for low molecular weight ester synthesis coupled with low temperature process for enzymatic reaction provides numerous industrially attractive advantages. A gene encoding a lipase from an Antarctic *Pseudomonas* sp was expressed in *E.coli*, purified and characterized. The cold-active lipase exhibited alkaliphilic profile and was particularly active in water-immiscible solvent. Thus, it was of interest to investigate the effect of organic solvent towards the lipase structure via computational approach. Molecular dynamic simulations and protein-solvent interaction analysis showed that the interaction of organic solvent and lipase was based on hydrophobicity effect [1,2]. The synthesis of short chain flavour ester was conducted. The cold active lipase was able to synthesize ethyl haxanoate with best conversion of ester obtained at low temperature. These unique properties of this Antarctic lipase will provide considerable potential for many industrial applications and organic synthesis at low temperature in the near future.

References

[1] Margesin R, Gander S, Zacke G, Gounot AM, Schinner F. Extremophiles 2003.7: 451-458
[2] Ganasen, M.; Yaacob, N.; Rahman, R.N.Z.R.A; Basri, M.; Salleh, A.B.; Ali, M.S.M. *Int. J. Biol. Macromol*. 2016, 92, 1266-1267.
[3] Yaacob, N.; Ali, M.S.M.; Rahman, R.N.Z.R.A.; Leow, T.C.T. *Molecules* 2017, *22*, 1312

Please choose: Oral
Presentation session: Biological Science
Presenter name: MOHD ZULKHAIRI MOHD YUSOFF

Biocharcoal from oil palm biomass as a potential adsorbent for textile final discharges

Mohd Zulkhairi, MOHD YUSOFF[1,2*] , Izzudin, IBRAHIM[1] and Mohd Ali, HASSAN[1]

[1]Department of Bioprocess Technology, Faculty of Biotechnology and Biomolecular Sciences, Universiti Putra Malaysia, 43400 UPM Serdang, Selangor, Malaysia
[2]Laboratory of Biopolymer and Derivatives, Institute of Tropical Forestry and Forest Products (INTROP), Universiti Putra Malaysia, 43400 UPM Serdang, Selangor, Malaysia

Email: mzulkhairi@upm.edu.my

Keywords: Biocharcoal, oil palm biomass, adsorbent, wastewater, final discharge

Introduction

Malaysia aims to be a developed country by the year of 2020. In order to achieve the target a lot of activity related to economic growth being intensified throughout the country. One of the increasing growth is textile industries which have contributed to Malaysia's economic leverage (Subki, 2011). However, these industries have certain drawbacks which it uses a lot of water. Water consumption involved in various stages such as to do dilution, transfer, and cleaning them at the very end. This usage some time exceeding needs for the industries and have a major concern about resources availability and limitation. With the inception of stringent environmental legislation, these industries have to introduce a green or sustainable approach in order to fulfil the requirements and needs (Bertea, Butnaru, Berariu, & Florin, 2013).

Even though textiles industries is a major contribution to the color pollutant, many industries could have discharged wastewater (colour pollutant) such as chemical, refineries, plastic, and food processing plants. These effluent dyes or colour are not easily degradable and affect and alters the aquatic ecosystems by limiting light penetration. Other than that, it is harmful to human health where acute exposure to certain dyes could lead to heart attack, vomiting, jaundice and others. Therefore, to prevent such harmful effects proper treatment of wastewater needs to be introduced.

A simple solution to wastewater discolouration is using adsorption. Several methods or technique introduced towards discolouration process of wastewater for example coagulation, membrane separation process, electrochemical, chemical oxidation, reverse osmosis and aerobic and anaerobic microbial degradation; however, these methods have not successfully washed out the colour completely. Using adsorbent from activated carbon have been widely used and currently, most researchers have to consider renewable resources such agricultural waste as an alternative carbon resource (Jibril et al., 2013; Mahmoud et al., 2012). The aim of this study is to perform chemical free treatment in the textile industry for colour removal in their final discharge. The oil palm mesocarp fibre (OPMF) was used as an adsorbent for colour removal in the final discharge.

Experiment

Textile wastewater final discharge characterization

Textile wastewater final discharges from the textile industry were examined for the COD, Total solid, suspended solids, pH, turbidity, colour and elemental analysis. The samples were stored in a fridge to prevent any biological activity.

Absorption process

The main purpose of the adsorption process is to absorb colour from the wastewater using biomass activated carbon. Adsorption is the adhesion of molecules onto the surface of an adsorbent solid using various processes of differing intensity (using Van der Waals forces of attraction = physical adsorption).

Two stages of an experiment to be carried out

Jar test approach in lab scale was done in lab scale using jar test equipment with 100 ml capacity to observe the feasibility study using different types of activated carbon to obtain higher efficiency and dosage for the colour removal from the sample. A river water was used as a control for the final treatment.

Raw oil palm mesocr

Impregnation process

Carbonization ar activation

Activated OPMF

Result and Discussion

Results: A three different coloured dye wastewater samples labelled as yellow, red and blue was used in this study (Fig.1). Characterization of the raw and treated samples was then performed. Treatment was performed using oil palm mesocarp fibre activated carbon and jar test experiment.

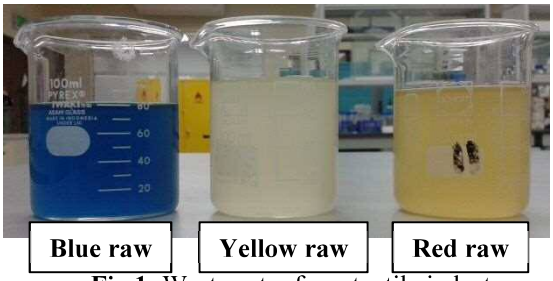

Fig 1: Wastewater from textile industry

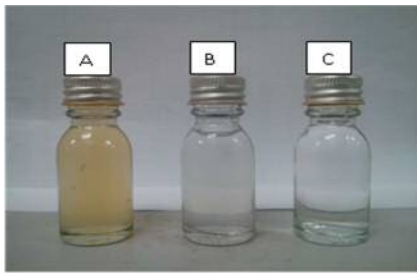

Fig 2: Indicates raw wastewater, B: Treated

The coloured wastewaters have undergone treatment process using activated carbon of OPMF as describe in methodology. Each experiment was carried out in triplicate to make sure the reproducible of the colour removal. The contact time has increased from 30 min to 1 hr due to the colour characteristic of the wastewater was different from the previous sample. The increment contact time required to provide ample time for the absorption process. OPMF was used as activated carbon for the absorption process due to its surface area was 545 m^2/g and comparable with market activated carbon. From the colour removal process, physically almost all coloured wastewater were absorbed by the activated carbon form all samples. Clear wastewater observed from the treated sample after the treatment process. The settled solids and suspended colloidal obtained after treatment were from the activated sludge introduced in the

Conclusion and future work: More than 90% colour removal obtained during the lab-scale study and more than 80% colour removal proven during the pilot-scale study, respectively. However, lower colour removal obtained during pilot scale study was due to reaction parameters and activated carbon regime dosage strategy. The reduction can be improved by altering the parameters such as mixing speed, detention time and dosage strategy and amount of wastewater. The solid and suspended colloidal is the organic material which originally from OPMF it is safe to be discarded in the effluent.

Reference

1. Ibrahim, I., Hassan, M.A., Abd-Aziz, S., Shirai, Y., Andou, Y., Othman, M.R., Ali, A.A.M., (...), Zakaria, M.R.Reduction of residual pollutants from biologically treated palm oil mill effluent final discharge by steam-activated bioadsorbent from oil palm biomass (2017) *Journal of Cleaner Production*, 141, pp. 122-127.
2. Othman, M.R., Hassan, M.A., Shirai, Y., Baharuddin, A.S., Ali, A.A.M., Idris, J.Treatment of effluents from palm oil mill process to achieve river water quality for reuse as recycled water in a zero emission system (2014) *Journal of Cleaner Production*, 67, pp. 58-61.

Please choose: Oral/ Poster/ Either
Presentation session: Applied Chemistry
Presenter name: Kubra Eksiler

Innovative surface modification of hydrophilic biomass to hydrophobic via Vapor-phase assisted surface polymerization

Kubra Eksiler[1], Yoshito Andou[1]

[1]Graduate School of Life Science and Systems Engineering, Kyushu Institute of Technology, 2-4 Hibikino, Wakamatsu-ku, Kitakyushu, Fukuoka 808-0196, Japan

Email: keksiler@life.kyutech.ac.jp

Keywords: Fibrillation, vapor-phase assisted surface polymerization, oil palm mesocarp fiber, polycaprolactone, surface modification

[Introduction]

In the field of materials, biomass has commercial importance and is regarded as a value-added additive. The interest in nanofibers from biomass has been gradually increasing worldwide due to their large specific surface areas. The nanofibers act as a fortification substance by increasing the strength and stiffness, as well as decreasing the weight of the resulting composites. Until biomass turns into nanofiller for the composite, the basic methodology followed by researchers consists of the production of nanofibers from biomass first and then the surface modification of the fibers to avoid agglomeration in a nonpolar polymer matrix. Although one of the main reasons to utilize nanofibers as filler is to manufacture eco-friendly composites, the methods commonly used to produce nanofibers are not eco-friendly and require harmful chemicals and a high amount of solvents and time. On the other hand, functionalization of nanofibers also suffers many problems, such as the need for multiple steps, the use of large volumes of organic solvents. The vapor-phase-assisted surface polymerization (VASP) method has been developed to coat many substrate surfaces with polymers, resulting in the conspicuous achievements of control over hydrophobic/hydrophilic properties and surface grafting. The VASP process is an excellent method for preserving the delicate surfaces of materials. The polymerization is a solvent-free method, takes place by gas–solid interface interaction, and provides higher grafting rate when compared with the commonly used liquid processes.

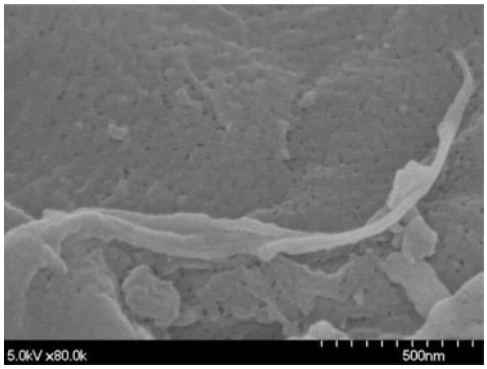

Figure 1. FE-SEM image of the nanolignocellulose from OPMF

In our previous studies, we reported an easy and eco-friendly production of nanoscale lignocellulosic fiber from waste oil palm mesocarp fiber (OPMF) through the combination method of mortar grinder mill and ionic liquid (M-IL) [1] (Figure 1). When ionic liquid acts solvent role for the removal of some substances from the fiber, the magnetic pestle ball pulverized the fiber in the range of nanoscale. In our another study, we developed an effective method for the production of surface-modified nano-lignocellulose fibers [2]. As opposed to the conventional methodology order used to produce functionalized nanofibers, for the first time, it was shown by our research group that the fibrillation can be done easily using surface-modified micro-size lignocellulose via VASP. Herein, it was aimed to graft PCL from the surface of the nanofiber [M-IL-OPMF] via VASP of ε-caprolactone to develop an environmentally friendly and efficient surface modification approach.

[Experimental]

OPMF (1 g) was treated with the combined method to produce nanofibers as descripted in our previous study (Eksiler et al., 2017). The obtained sample, which is the substrate of the polymerization, was named as [M-IL-OPMF]. 0.32 mmol $Sn(Oct)_2$ was dissolved in 5 mL of acetone. The solution was then mixed with [M-IL-OPMF] (0.2 g) at room temperature to be absorbed the catalyst on the surface. After it was dried under ambient atmosphere, the remaining solvent was removed under vacuum at room temperature. A typical procedure of VASP was done in a H-shaped glass tube reactor with a vacuum cock. The catalyst-supported

[M-IL-OPMF] was put into a Petri dish, having 4.40 cm^2 bottom surface area, and then the Petri dish was settled onto the bottom of one of the legs of H-shaped glass tube reactor. Purified ε-caprolactone (13.5 mmol) was introduced onto the bottom of the other leg. The reactor was then degassed by three freeze-pump-thaw cycles and lastly sealed. Polymerization was carried out at 70°C for 24h and 72h in a thermostatic oven. After VASP, the obtained sample was dried to remove unreactants in vacuo.

[Results and Discussion]

VASP of ε-caprolactone was carried out in an H-shaped glass tube reactor on M-IL-OPMF fibers as a substrate, on which surfaces Sn(II) 2-ethylhexanoate ($Sn(Oct)_2$) as a catalyst for the anionic ring opening polymerization of ε-caprolactone was supported. During the polymerization in the H-shaped glass tube reactor, vaporized monomer molecules are diffused to active sites on the substrate surface, after that, the absorbed molecules undergo polymerization. In the end of 24h, the product, which is named as [M-IL-OPMF]-VASP, was appeared as a solid layer. On the basis of the increased weight of the products over 24h period, its compositions were estimated to be: 35.7% fiber/64.3% polymer. The changes in the UV/RI intensity ratio of each fraction in SEC profiles of the synthesized PCL (Mw 12,000) and the samples, [M-IL-OPMF]-VASP for 24h, were shown in Figure 2. It is known that when polymer chains graft from lignocellulosic materials which have different UV/RI ratio values, the new UV/RI ratio value will show an alteration in accordance with the grafting ratio whereby the solubility of the graft polymers in chloroform might be also differed. The result can be explained by the higher grafting efficiency on lignocellulosic materials, the higher UV/RI ratio. This increase also signifies that PCL grafted successfully from the fiber components by which covalent bonding occurred during VASP. The sample exhibited a 4.1-fold increase in the UV/RI ratio, proofing the removal of some PCL grafted components from the lignocellulose material by washing.

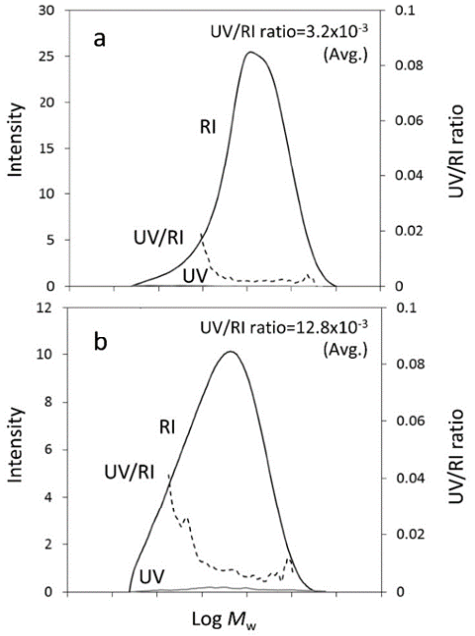

Figure 2. SEC profiles of UV/RI intensity ratios of synthesized PCL (a), [M-IL-OPMF]-VASP for 24h (b)

Another evidence for the grafting of PCL is the FT-IR results of the residues after washing. When FTIR spectra of [M-IL-OPMF]-VASP and [M-IL-OPMF]-VASP after washing samples were compared, both samples showed the same characteristic peaks as commercial PCL at 1722 cm^{-1} assignable to carbonyl peak of PCL (C=O). This finding indicates the presence of PCL grafted from lignocellulosic materials, such as hemicellulose, cellulose and lignin, after the removal of accumulated PCL from the fiber.

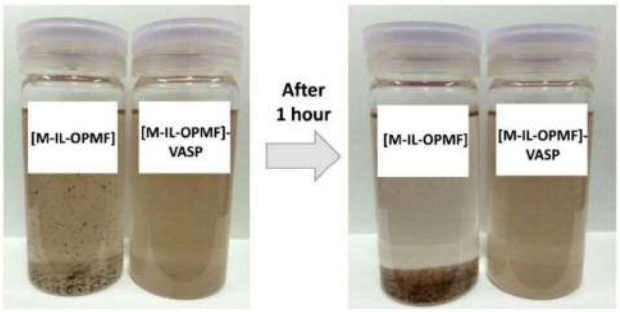

Figure 3. Appearances of [M-IL-OPMF] and [M-IL-OPMF]-VASP solutions in chloroform after standing for 1h

Photographs showing the dispersion of [M-IL-OPMF] before and after VASP in chloroform support the findings of FT-IR and SEC (Figure 3). As a result of the hydrophilic nature of [M-IL-OPMF], the fibers were precipitated in the solvent. [M-IL-OPMF]-VASP fibers dispersed homogenously and remained as it is after 1h, implying the VASP was proceeded successfully.

[References]

[1] Eksiler K, Andou Y, Yilmaz F, Shirai Y, Ariffin H, Hassan MA (2017) Dynamically controlled fibrillation under combination of ionic liquid with mechanical grinding. J Appl Polym Sci 134(7):44469

[2] Eksiler K, Andou Y, Shirai Y (2018) Simple manufacture of surface-modified nanolignocellulose fiber via Vapor-Phase-Assisted Surface Polymerization. ACS Omega 3(4):4545–4550

Please choose: Oral/ Poster
Presentation session:
Presenter name:

Co-precipitation of Tamoxifen and magnetic nanoparticles with biodegradable polymer using Supercritical Anti Solvent Process

[Dalila,Alias][1], [Robiah,Yunus][2], [Che Azurahanim, Che Abdullah][3], [Gun Hean,Chong][4]

[1]Institute of Advanced Technology, University Putra Malaysia, 43400 UPM Serdang, Selangor, Malaysia
[2]Faculty of Engineering, University Putra Malaysia, 43400 UPM Serdang, Selangor, Malaysia
[3]Faculty of Science University Putra Malaysia, 43400 UPM Serdang, Selangor, Malaysia
[4]Faculty of Food Science and Technology, University Putra Malaysia, 43400 UPM Serdang, Selangor, Malaysia

Email: dalilaalias@gmail.com, robiah@upm.edu.my

Abstract
Magnetic nanoparticle (MNP) is small in size but has a vast potential usage is various field such as biomedicine, magnetic resonance imaging, and magnetic particle imaging. In targeted drug delivery, MNP can be conjugated with drug or co-precipitated with drugs or polymers. This work is aiming to assess the potential of using supercritical antisolvent (SAS) process in encapsulating Tamoxifen and magnetic nanoparticle in a biodegradable polymer. Carbon dioxide CO_2 is being used as supercritical fluid.CO_2 is attractive in SAS process because it has low critical pressure and critical temperature value, thus allowing the process to be operated at much lower pressure and temperature as compared to other type of supercritical fluid. In this particular work, Tamoxifen; an anti-estrogen drug which has been widely used in breast cancer treatment is co-precipitated with MNP which has been coated with oleic acid (OA) and poly-L-Lactic acid (PLLA); a widely used biodegradable polymer in medicine. In SAS process, OAMNP, TAM and PLLA were dissolved in dichloromethane (DCM) and sprayed into precipitation vessel filled with $SCCO_2$. As the solution comes in contact with $SCCO_2$, high supersaturation condition is created and precipitation of OAMNP, TAM and PLLA is induced. Final product of SAS process is in powder form and readily to be used without any downstream processes. FTIR analysis and applying magnetic field using super-paramagnetic magnet have been performed to confirmed presence of OAMNP in final product. This work has proved that MNP can be co-precipitated with TAM and PLLA using SAS process.

Keywords (maximum 5 words)
Magnetic nanoparticles, supercritical antisolvent process, supercritical fluid, encapsulation, breast cancer

Introduction

Tamoxifen is an anti-estrogen drug which has been used widely in the breast cancer treatment. As it is an excellent choice especially for prevention for breast cancer and for post-operation treatment, it has been reported that Tamoxifen has caused side effects to the patients in a long term use. To reduce the side effects, research works has been carried out to apply tamoxifen in targeted-drug delivery application. Through drug targeting, negative effects of tamoxifen can be reduced by maintaining concentration level at non-targeted organs and tissues at minimal levels.
In this work, tamoxifen is attached with magnetic nanoparticle in a biodegradable polymer as magnetic nanoparticles has high targeting efficiency and considered as non-invasive effort.
Magnetic nanoparticles offer advantages that can be used in biomedical application due to many reasons such as (Mornet et al., 2004) (Lu et al., 2007) (Chomoucka et al., 2010):

1. Rapid response upon applied magnetic fields and negligible residual magnetism.
2. No risk of agglomeration at room temperature
3. Offers no harm to human body except for patients with magnetized materials in the body
4. Can be used in hyperthermia treatment; a cancer therapy treatment using heat
5. Complimentary to modern diagnostic method such as magnetic resonance imaging (MRI)

6. Ability to direct active ingredient directly to the vicinity of targeted area in the body

The potential of o-precipitation of magnetic nanoparticle and active ingredient within particulate carriers offer more opportunities and possibilities in research and development on controlled drug delivery and drug targeting.

Experiment

Tamoxifen citrate ($C_{32}H_{37}NO_8$) (98%) is an anti-estrogen drug purchased from Acros Organic, Belgium, HPLC Grade. Commercial grade poly-l-lactic acid (CH_3O $(C_6H_8O_4)_{nH}$) was purchased from Sigma Aldrich St Loius United States. HPLC grade Dichloromethane (DCM) was obtained from Fisher Scientific, Loughborough, United Kingdom. Purified grade of Carbon Dioxide was supplied by Linde Malaysia used as Supercritical Fluid (SCF). Oleic acid- coated magnetic nanoparticle were given by Department of Physics, Science Faculty, Universiti Putra Malaysia. All material were used as per supplied, without any pre-treatment.

Results and Discussion

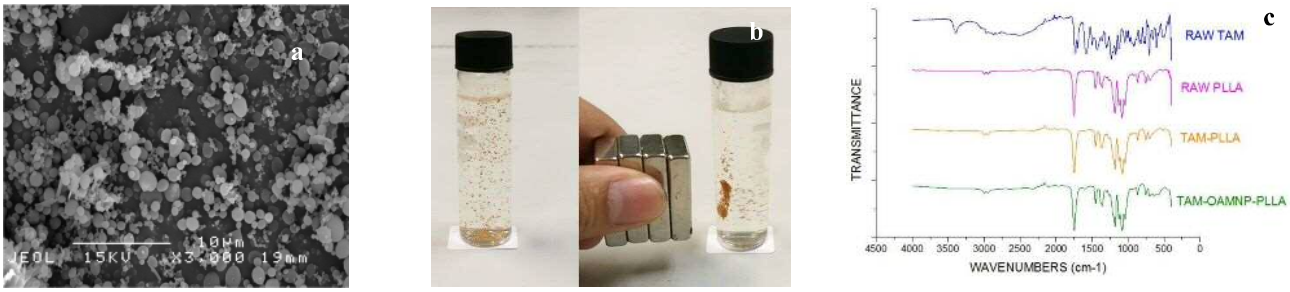

Figure 1a) SEM picture of co-precipitation product of TAM-PLLA-OAMNP, 1b) Photograph of final product attracted to magnet, 1c) FT-IR spectra of TAM-PLLA-OAMNP final product

Co-precipitation of PLLA-OAMNP-TAM was studied in this work. SEM of the particles are presented in Figure 1. These experiments were carried out at operating pressure 130 bar, operating temperature at 35°C and solution flow rate of 0.5 mL/min. Optimized particles of PLLA-OAMNP-TAM of 0.6 µm was produced. Morphology of co-precipitation product is influenced by structure of the biodegradable polymer used in SAS process. As PLLA is a semi-crystalline polymer (Kalb, B.; Pennings, 1980), morphology of final product from SAS is expected to be spherical shape (Kalani and Yunus, 2011) and has been proved in SEM microphotographs in Figure 1a. To detect presence of magnetite in the final product, a magnet was placed next to a vial consist of PLLA-OAMNP-TAM particle dispersed in Phosphate Buffered Solution pH 7.4. On application of the external magnetic field, the particles was attracted to the side of vial that was in vicinity of the magnet, resulting in a clear solution on the other side. This simple experiment confirms that the magnetism of OAMNP is retained in the synthesized product of SAS process. FT-IR analysis (Figure 1c) was carried out to confirm presence of OAMNP in the final product and to understand functional groups present in the synthesized particles. In this work, characteristic bands for OAMNP was identified. The presence of absorption bonds at around 634.5cm^{-1} and 597.3cm^{-1} are from the bond stretching between Fe-O ions of FE_3O_4. From the results, it is confirmed that TAM-OAMNP has been successfully co-precipitate with PLLA using SAS process.

[References]

Chomoucka, J., Drbohlavova, J., Huska, D., Adam, V., Kizek, R., Hubalek, J., 2010. Magnetic nanoparticles and targeted drug delivering. Pharmacol. Res. 62, 144–149. https://doi.org/10.1016/j.phrs.2010.01.014

Kalani, M., Yunus, R., 2011. Application of supercritical antisolvent method in drug encapsulation: a review. Int. J. Nanomedicine 6, 1429–1442. https://doi.org/10.2147/IJN.S19021

Kalb, B.; Pennings, A.J., 1980. General Crystallization Behaviour of Poly(L-lactic acid). Polymer (Guildf). 21, 607–612. https://doi.org/10.1016/S1474-4422(08)70216-3

Lu, A.H., Salabas, E.L., Schüth, F., 2007. Magnetic nanoparticles: Synthesis, protection, functionalization, and application. Angew. Chemie - Int. Ed. 46, 1222–1244. https://doi.org/10.1002/anie.200602866

Mornet, S., Vasseur, S., Grasset, F., Duguet, E., 2004. Magnetic nanoparticle design for medical diagnosis and therapy. Forunal Mater. Chem. 14, 2161–2175. https://doi.org/10.1039/b402025a

Please choose: Oral/ Poster/ Either
Presentation session:
Presenter name: Liana Noor Megashah

Isolation of Cellulose from Oil palm empty fruit bunch by Multi-Step, Totally Chlorine Free Treatment Method for Cellulose Nanofibril Production

Liana Noor Megashah1[1], Hidayah Ariffin[1,2*], Mohd Ali Hassan[1], Mohd Rafein Zakaria[1], Yoshito Ando[3]

[1]Faculty of Biotechnology and Biomolecular Sciences, Universiti Putra Malaysia, 43400 UPM Serdang, Selangor, Malaysia
[2]Institute of Tropical Forestry and Forest Products (INTROP), Universiti Putra Malaysia, 43400 UPM Serdang, Selangor, Malaysia
[3]Eco-Town Collaborative R&D Center for the Environment and Recycling, Kyushu Institute of Technology, 2-4 Hibikino, Wakamatsu-ku, Kitakyushu, Fukuoka 808-0196, Japan.

Email: hidayah@upm.edu.my

Keywords: oil palm fronds, totally chlorine free, cellulose isolation, cellulose nanofiber, characterization

Abstract. Effect of multi-step treatment on the characteristics of cellulose from oil palm frond (OPF) fiber was evaluated. The treatment involved several steps namely thermal treatment (superheated steam), enzymatic treatment (xylanase) and non-chlorinated chemical treatment (totally chlorine-free chemicals). The chemical structure and chemical composition of fibers greatly changed after the treatments proving the successful removal of non-cellulosic components such as lignin, hemicellulose and small amount of extractives from the OPF sample. Cellulose obtained after the multi-step treatment had purity of 83.4%, with some residue of hemicellulose. Cellulose nanofibrils (CNF) were then produced from the treated cellulose using a wet disc mill (WDM), and characterized for their morphological, crystallinity and thermal properties. It was found that CNF produced from multi-step treated cellulose had smaller diameter size in the range of 13-33 nm, compared to that of conventionally treated cellulose using soda pulping (18-52 nm). Results obtained from this study exhibited that multi-step pretreatment method is the promising and eco-friendly method for cellulose isolation from lignocellulose for CNF production.

Introduction

Nanocellulose is one of the materials which could be produced from agricultural residues. It is a cellulose-based material with one of its dimension is in nanosize. Cellulose in nature is a polysaccharide consisting anhydroglucose ($C_6H_{10}O_5$) repeating units which are linked together by β-glucosidic bond (Krässig et al., 2000). Nanocellulose has various potential applications, namely as reinforcement material in biocomposite, for biomedical applications, food rheology control and paper packaging products (Chang et al., 2012; Szczesna-Antczak et al., 2012; Iwamoto et al., 2014). Nanocellulose from plant resources can be classified into cellulose nanocrystals (CNC) and cellulose nanofibrils (CNF) (Dufresne, 2013). Cellulose isolation is an important procedure prior to nanocellulose production since most of the agricultural residues are in lignocellulosic form, which consists not only of cellulose but also of lignin and hemicellulose. These two components may interfere the fibrillation and hydrolysis process which could cause failure in CNF production.

Experiment

Multi-step pretreatment is a combined pretreatment method consisted of superheated steam (SHS) treatment, enzymatic hydrolysis and reduced concentration alkaline treatment. SHS pretreatment was conducted using a lab scale superheated steam oven (QF-5200C, Naomoto Corporation, Osaka, Japan) and with the aim to partially remove the hemicellulose (Nordin *et al.,* 2013). The pretreatment was conducted at atmospheric pressure. Subsequently, enzymatic pretreatment was conducted using xylanase at 2 wt% of SHS-treated OPEFB in sodium phosphate buffer (pH 5.5), using 10% (v/v) of enzyme loading. Afterwards, alkaline pretreatment was conducted using 5% (w/v) of sodium hydroxide. Soda pulping was conducted as reported earlier (Megashah *et al.*, 2018). Pretreated fibers from multi-step and soda pulping pretreatment methods were subjected to bleaching step using TCF chemicals. Cellulose nanofiber (CNF) was produced by using a high shear ultrafine friction grinder, or wet disc mill, WDM (Multi mill, Grow Engineering, Adachi-ku, Tokyo, Japan).

Results and Discussion

Both of the cellulose isolation methods were evaluated in term of its eco-efficiency for the production of CNF from OPF. Among the key elements of eco-efficiency are to re-engineer the process and revalorize by-products (WBCSD, 2006). To further elaborate this, five related aspects were evaluated: total unit operations involved, pretreatment conditions, energy requirement, waste production and management, and potential for by-products valorization.

Table 1. Impact of the pretreatment method on the following aspect

Aspect	Multi-step	Soda pulping
Total unit operations	×	✓
Pretreatment conditions	✓	×
Energy requirement	×	×
Waste production and management	✓	×
By-products valorization potential	✓	×

***Note:** ✓ - Good; × - Poor

Please choose: Oral
Presentation session:
Presenter name: Dr Mariatulqabtiah Abdul Razak

Self-assembling characteristic of an avian papillomavirus L1 capsid protein

Nurulhuda, Najihah[1], Chean Yeah, Yong[2], Wen Siang, Tan[1,2], Abdul Razak, Mariatulqabtiah[1,2*]

[1]Institute of Bioscience, Universiti Putra Malaysia, 43400 UPM Serdang, Selangor, Malaysia
[2]Faculty of Biotechnology and Biomolecular Sciences, Universiti Putra Malaysia, 43400 UPM Serdang, Selangor, Malaysia

Email: mariatulqabtiah@upm.edu.my

Keywords: avian, papillomavirus, L1, capsid, VLP

Introduction

All papilloma virions are non-enveloped 50-60 nm icosahedral structures which comprise of well-conserved L1 major and L2 minor capsid proteins. According to Schiller and Lowy (2012), purified recombinant L1 protein can self-assemble into a highly immunogenic structure that mimic the natural surfaces of native papillomavirus virions, without any chaperones. These assembled particles are potent immunogens, due to the innate B-cell recognition of the regular icosahedrally-displayed spacing of its surface epitopes. This has served as a basis for the development of vaccines against cancer-causing human papillomavirus (HPV) types 16 and 18.

In the current HPV vaccines, the immunogens used were from assembled L1 VLPs from the rigid mature form of the virion during its transmission from one cell to another. During the assembling process, the L1 interactions must be flexible enough to allow selective uptake of viral genomic DNA into the virion lumen. In order to achieve transmission, fragile immature virions must gain the ability to remain infectious in desiccated state for days. Through the maturation process, the flexible immature virions will achieve a more rigid state that is stabilized through disulfide crosslinks between the neighbouring L1 molecules, forming a unimolecular cage (Buck and Trus, 2012). L1 will form the exterior surface of the stabilized mature virion. Hence, it will become the mediator to provide initial attachment of the virion to a host cell and responsible on the release of viral genome into a new target cell (Buck et al., 2013).

Self-assembling characteristics of human and bovine papillomaviruses have been studied extensively. However, no comparison was made to other host species such as avian. Thus, the objective of this study is to evaluate the self-assembling characteristic of an avian papillomavirus L1 capsid protein.

Experiment

The full-length DNA coding region of avian papillomavirus from African grey parrot L1 capsid protein was amplified by polymerase chain reaction (PCR) using a pair of primer set. The PCR was carried out in 50 µl of reaction mixture containing 1µM of each primers, 0.2 mM of deoxynucleoside triphosphate mixture (dNTPs mix), 1.5 mM $MgCl_2$, 2.5 U of Taq DNA recombinant polymerase (Thermo Fisher Scientific) and 1X PCR buffer. The amplicon was separated on 1% TAE agarose gel electrophoresis and excised prior to DNA purification using the Qiaquick Gel Extraction kit (Qiagen). The purified amplicon was then ligated into the expression vector (Invitrogen) at room temperature prior to transformation into *E. coli* competent cells. Positive colonies were cultured and induced with IPTG. Expressed proteins were subjected to immobilized metal affinity chromatography (IMAC) purification technique as performed by Goh et al. (2011).

Protein separation analysis using SDS-PAGE was performed according to Sambrook et al. (2001) using a 12% (w/v) SDS-polyacrylamide gel. Upon successful viewing of the gel using Coomassie brilliant blue R-250, the gel was electro-transferred onto a nitrocellulose membrane (GE Healthcare). The membrane was incubated with an anti-His monoclonal antibody at 1:5000 dilution, prior to colour development by BCIP/NBT substrate.

For observation of self-assembled particles, purified protein sample was absorbed onto carbon coated grids for 5 min. The grids were negatively stained with a freshly prepared uranyl acetate solution, dried and viewed under a transmission electron microscope (TEM; Hitachi H7700, Japan).

Result and Discussion

Result showed successful cloning, expression (Figure 1), purification and self-assembling formation (Figure 2) of L1 VLPs, with the molecular mass of approximately 45 kD and a diameter of 30 nm. The diameter of the VLP is smaller compared to the common range of HPV type 18 VLP vaccines, which is 40-60 nm (Zhang et al., 2015). Our findings were in accordance to the expression of HPV type 6, 11, and 16 L1 proteins in *Saccharomyces cerevisiae,* which yielded irregularly shaped and broadly distributed VLPs of smaller in size (30–50 nm) (Mach et al., 2006). The analysis of these VLPs will add to the limited molecular and structural knowledge of avian papillomaviruses for future vaccine development or drug delivery studies.

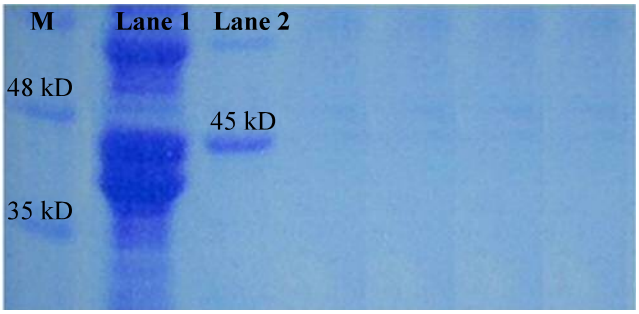

Figure 1. SDS-PAGE of the recombinant L1 capsid protein on a 12% denaturing polyacrylamide gel stained with Coomassie Brilliant Blue. Lane 1, the lysate of *E. coli* cells which served as a negative control; lane 2, the lysate of *E. coli* cells harbouring the recombinant L1 capsid protein. The arrow in the gel indicates the size of approximately 45 kDa. Lane M, molecular mass markers in kDa. Western blotting result was not shown.

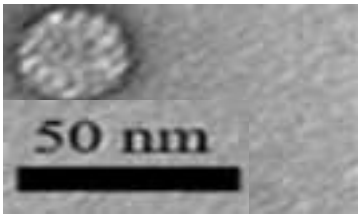

Figure 2. Transmission electron microscopic analysis of L1 VLPs produced in *E. coli.* The diameter of the spherical particles was about 30 nm.

References

Buck, C.B., Day, C.M., & Trus, B.L. (2013). The papillomavirus major capsid protein L1.Virology. 445(0), 169-174.

Buck, C.B., & Trus, B.L. (2012). The papillomavirus virion: a machine built to hide molecular Achilles' heels. Advances in Experimental Medicine and Biology. 726:403-422

Goh, Z.H., Tan, S.G., Bhassu, S., & Tan, W.S. (2011). Virus-like particles of *Macrobrachium rosenbergii* nodavirus produced in bacteria. Journal of Virological Methods. 175, 74– 79.

Mach, H., Volkin, D.B., Troutman, R.D., Wang, B., Luo, Z., Jansen, K.U., & Shi, L. (2006). Disassembly and reassembly of yeast-derived recombinant human papillomavirus virus-like particles (HPV VLPs). Journal of Pharmaceutical Sciences. 95(10), 2195-206.

Schiller, J.T., & Lowy, D.R. (2012). Understanding and learning from the success of prophylactic human papillomavirus vaccines. Nature reviews Microbiology. 10, 681–692.

Zhang, X., Xin, L., Li, S., Fang, M., Zhang, J., Xia, N., & Zhao, Q. (2015). Lessons learned from successful human vaccines: Delineating key epitopes by dissecting the capsid proteins. Human Vaccines & Immunotherapeutics. 11(5), 1277–1292.

Please choose: Oral/ Poster
Presentation session:
Presenter name: Che Azurahanim Che Abdullah

SYNTHESIS OF BIOCOMPATIBLE MARINE WASTE HYDROXYAPATITE FOR TISSUE ENGINEERING APPLICATION

Che Azurahanim Che Abdullah[1,2]. Luqman Mokhtar[1] and Mohd Eszarul Fahmi Isa[1]
[1]Biophysics Laboratory, Department of Physics, Universiti Putra Malaysia, Malaysia

[2] Material Synthesis and Characterization Laboratory, Institute of Advanced Technology, Universiti Putra Malaysia, Malaysia

Email: azurahanim@upm.edu.my

Abstract
Hydroxyapatite (HAp) is a biomaterial which is naturally found in the inorganic component of human bone and enamel. HAp can be easily attached to the hard tissue like enamel without giving any tissue rejection. Thus, it is a biomaterial of great interest with various application. Current work focusses mainly on the preparation of HAp from marine waste as the calcium precursor. The wet chemical precipitation method was the choice of interest where the HAp was formed by simply mixing the calcium hydroxide $Ca(OH)_2$ and phosphoric acid (H_3PO_4) as the phosphorus precursor. Samples were fabricated in the pellet form and sintered using microwave oven. Prepared samples were characterized by XRF for elemental analysis, X-Ray Diffraction (XRD), Fourier Transform Infrared Spectroscopy (FTIR), Scanning Electron Microscopy (SEM) and Energy Dispersive X-Ray Spectroscopy (EDX) in order to determine the chemical, structural, morphology and molecular bonding properties. The pure single phase of HAp of prepared samples were confirmed after analysing the XRD patterns by comparing with the standard HAp pattern. The functional groups that significance for HAp structure were analysed using FTIR.

Keywords (maximum 5 words)
Hydroxyapatite, marine waste, dental application, wet chemical precipitation

[Introduction]

In the last few years, the role of biomaterials has become very important field of research especially in the medical field. A biomaterial is any matter, surface, or construct that will relate with biological systems thus, it is usually exploited in contact with living tissues, organisms and microorganisms. Biomaterials can be derived either from nature or synthesized in the laboratory using a variety of chemical approaches utilizing metallic components, polymers, ceramics or composite materials. Biomedical engineering has been largely responsible for many of the recent advances in the modern medicine with one of the reasons is due to the lower material cost. Marine waste shells are one of the examples of the biomaterial that is widely used for biomedical purpose in bone regeneration. For example the substance most commonly found in the lining of mollusks such as oysters, mussels, or abalone shells. It became one of the current essential materials for tissue engineering. In 1992, Lopez *et al.* discovered that natural nacre layer from the pearl oyster *Pinctada maxima* provide both biocompatible and osteoinductive graft. Another researcher showed the use of nacre promotes osteogenic activity after implantation in the human bone environment (Silve *et al.*, 1992). Large bone defects designed from raw nacre layers were used as bone replacement bone graft in the femur of sheep to create a bone-nacre interface for repair process. The use of marine waste can be an alternative way for repairing bone fractures and influences stronger regeneration of bone since the artificial bones are very expensive. Although the raw material is cheap but there is an issue regarding methods on how to retrieve the HAp the mollusk shell. The shell consists of two layers which are the prismatic layer that is the outer shell surface and the nacreous layer that on the top of the inner part

of the shell surface. The important part for used in tissue engineering is the nacreous layer, which consists of organic material that promotes bone-regeneration process, HAp. The produced HAp successfully characterized by XRF for elemental analysis, X-Ray Diffraction (XRD), Fourier Transform Infrared Spectroscopy (FTIR), Scanning Electron Microscopy (SEM) and Energy Dispersive X-Ray Spectroscopy (EDX) in order to determine the chemical, structural, morphology and molecular bonding properties. The pure single phase of HAp of prepared samples were confirmed after analysing the XRD patterns by comparing with the standard HAp pattern. The functional groups that significance for HAp structure were analysed using FTIR.

[Experiment]

All chemicals are of analytical grade (Sigma Aldrich). The raw marine waste shells from *Modiolus philippinarum* species were collected from *Merambong Shoal* seagrass bed at Pulai River Estuary Johor, Malaysia as described by Wong. *et al*, (2013). Figure 1 shows both the inside and outside layer of the shells of *Modiolus philippinarum* species. The shells were scrubbed with a wire brush under running tap water to clean the shells and remove residual adhering organic matter in the shells. Then, the shells were left to dry on filter paper in the air. Then the waste shells were introduced to the crushing and grinding process using the grinding machine. The material was crushed and grind until powder form is obtained as smallest as possible.

Figure 1: The inside and outside of *Modiolus Philippinarum*'s shells.

[Results and Discussion]

Current study successfully retrieve HAp from the mollusk shells. In order to determine the most effective methods to retrieve HAp, the methods must produce a high yield with a good quality of HAp.The nacre obtained was characterized using characterized by XRF for elemental analysis, X-Ray Diffraction (XRD), Fourier Transform Infrared Spectroscopy (FTIR), Scanning Electron Microscopy (SEM) and Energy Dispersive X-Ray Spectroscopy (EDX) in order to determine the chemical, structural, morphology and molecular bonding properties as well as UV-Vis spectroscopy techniques. In this study, a worthwhile biomedical application of HAp from marine waste was successfully synthesized with optimal characteristics for the application of both bone and dental tissue engineering. Though the resulting HAp resembles that found naturally in terms of its composition, this continuous research efforts have produced new economic synthesis approaches and can be applied in future research.

Please choose: Oral
Presentation session: Applied Chemistry
Presenter name: Akihiko Tsuge

Organogelators and Ambidextrous Gelators

Akihiko, Tsuge

Department of Applied Chemistry, Faculty of Engineering, Kyushu Institute of Technology,
1-1 Sensui-cho, Tobata-ku, Kitakyushu-shi, Fukuoka, 804-8550, Japan

Email: [tsuge@che.kyutech.ac.jp]

Keywords: organogelator, ambidextrous gelator, cyclophane, hydrogen bonding, ferrocene

[Introduction]

Organogels based on low-molecular-weight gelators have received significant attentions as novel functional soft materials. Their attractiveness lies in bottom-up strategy inspiring the development of the next generation of functional soft matters. From these points of view various kinds of small organic molecules capable of gelation such as amides, peptides, ureas and so forth have been investigated. The process of gelation is considered to arise from the self-assembly of the gelators into networks that entangle and entrap organic solvents. These procedures generally require specific intermolecular non-covalent interactions, including hydrogen bonding, π-π stacking, van der Waals forces and charge-transfer interactions among organic gelators. The organogelators consisting of various aromatic units, including naphthalene, anthracene, pyrene, perylene, naphthalimide and other π-conjugated molecules have been studied due to their potential applications. The gels can be divided into two main categories, namely organogel and hydrogel which are swollen networks containing organic solvents and water, respectively. In the course of our research on such gelators we have been also studying ambidextrous gelators that are capable of forming both organo- and hydro-gels. From these points of view we have employed some unique units such as the cyclophane skeleton, the Eu-complex and the ferrocene moiety to develop novel functional organogelators. As a novel ambidextrous gelator some amphiphilic molecules have been designed.

[Result and Discussion]

1) Organogelators derived from [3.3]metacyclophane skeleton with the urea unit (1a-f)

Dithia[3.3]metacyclophanes with the urea unit having the long alkyl chains have been prepared. It has been found out that some of them gave stable organogels in some solvents, and their gelating ability depends on structural properties of both aromatic components in the dithia [3.3]metacyclophane.

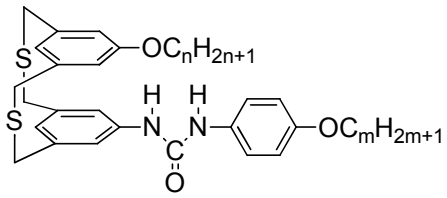

1a-f; n = 0~12, m = 6~12

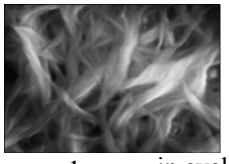

in cyclohexane

Fig. 1. Optical and SEM images of gel from **1f** (n=12, m=6).

2) Design and properties of glutamic acid based coumarin derivatives as organogelators (2a-b)

Two kinds of glutamaic acid-based coumarin derivatives show a quite different trend against gelation in organic solvents in terms of inter- or intramolecular hydrogen bonds involved. It has been found out that addition of the valinate structure into the coumarine derivative could improve its gelation ability.(**Fig. 1**)

3) Organogelators based on metacyclophane skeleton having urea units in the bridge (3)

Metacyclophanes having the urea units in their bridge have been prepared. It has been found out that some of them afford stable organogels in some solvents. It was also observed that addition of fluoride anion broke DMSO gel, and then this gel was formed again by addition of MeOH.

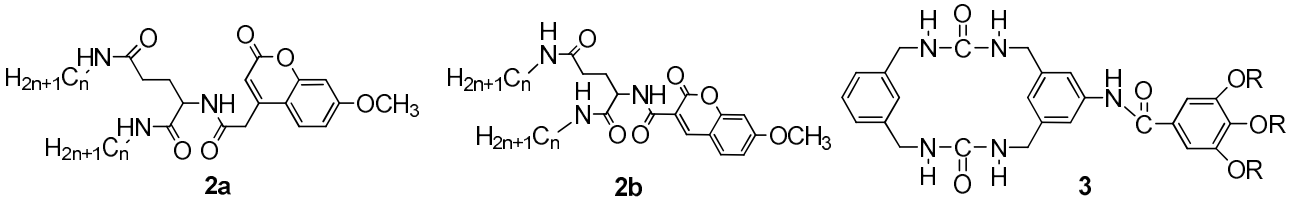

2a **2b** **3**

4) Formation of Luminescent Organogels from the Europium-based Complexes (4a-d)

Formation of organogel from the europium(III) complexes consisting of the ligands having an amide or an urea unit has been achieved, which is characterized by strong red-emission. (**Fig. 2**)

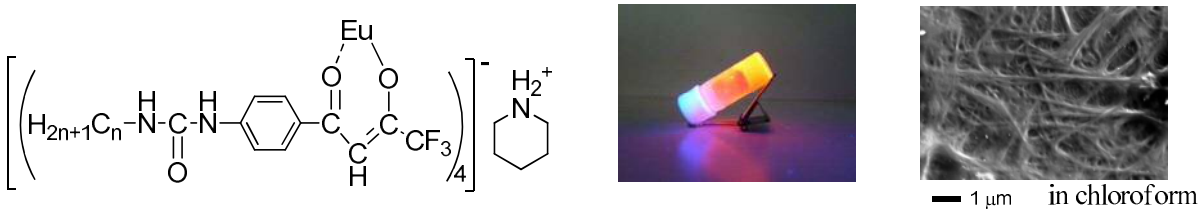

4a; n = 6 **4b**; n = 8 **4c**; n = 10 **4d**; n = 12

Fig. 2 Optical and SEM images of gel from **4c**.

5) On-off switching of gel formation by red-ox reaction (5)

Organogelator candidates which consist of the ferrocene unit have been prepared. It has been suggested that two amino acid residues in the structure are necessary to form a stable organogel. Addition of an oxidizing agent such as NaClO induces the collapse of the gel, and reproduction of the gel was observed by addition of a reducing agent such as glutathione. It has been found out that the on-off switching of gel formation can be achieved by red-ox reaction. (**Fig. 3**)

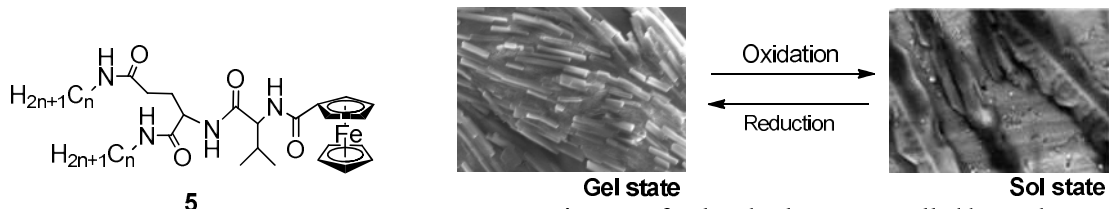

5

Fig. 3 SEM images of gel and sol state controlled by re-dox reaction.

6) Ambidextrous gelators and the cyclohexane-based gelators (6, 7)

Ambidextrous gelators should be dissolved in water and in organic solvents such as benzene and toluene. Considering this requirement the compound has to be an amphiphilic molecule, meaning that it contains a hydrophilic part and a hydrophobic part. Thus, we designed the molecule in which the hydrophobic part and the hydrophilic part are connected by the aromatic ring. All compounds describes here have the aromatic units, expecting a π-π interaction between the molecules. So we have prepared these kinds of cyclohexane-based compounds having the glutamic acid residue.

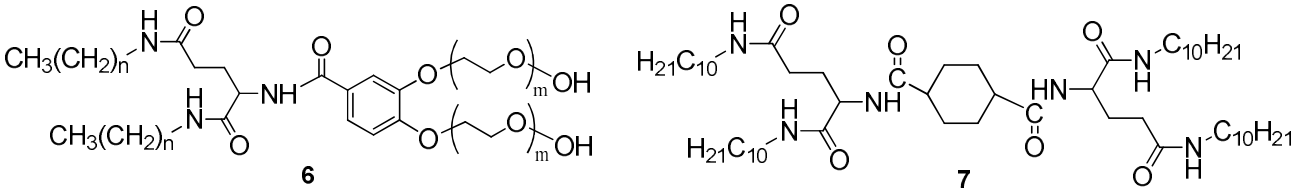

6 **7**

Please choose: Oral/ Poster/ Either
Presentation session:
Presenter name:

Struvite Recovery From Wastewater

Mohamad Amran, Mohamad Salleh[1,2], Stephen, Agudosi[1]

[1]Faculty of Engineering, University Putra Malaysia, 43400 UPM Serdang, Selangor, Malaysia
[2]Institut Teknologi Maju (ITMA), University Putra Malaysia, 43400 UPM Serdang, Selangor, Malaysia

Email: asalleh@upm.edu.my

Keywords: Struvite, wastewater, crystallization, phosphorous, recovery

Introduction

Natural phosphorous supply is naturally reducing and will definitely deplete in the future due to increasing demand in agriculture just like any other natural resources. Recovery of phosphorous by struvite crystallization is one of the ways to reduce the burden to natural P mining demand. Struvite contains an equimolar amount (1:1:1) of magnesium ammonium and phosphate ions; $MgNH_4PO_4 \cdot 6H_2O$. It is soluble in water in acidic condition but can be produced in alkaline condition (Huang et al., 2016). It is suitable to be used as fertilizer and possibly a slow release fertilizer. It has been demonstrated that generating 1 kg of MAP per day is enough to fertilize 2.6 ha of arable land (Kim et al., 2014)

Struvite can be recovered from various types of wastewater by adding Mg into the rich N and P effluents (Rahman et al., 2014). The wastewater of interest here is the animal manure effluents. Epsom salt was tested as the Mg source in this study considering that it is cheap and easily available in comparison to other Mg source.

Experiment

The cow urine was obtained from Universiti Putra Malaysia dairy farm and the ammonia nitrogen, pH, and total phosphorus were analysed immediately in accordance with APHA 1995 standard methods. 200ml urine samples were mixed with Epsom salt in stoichiometric proportion to the concentration of orthophosphate analyzed previously a mixing speed of 200 rpm for a mixing duration of 10 minutes using magnetic stirrer. The pH was adjusted by adding 0.1 M NaOH to raise the pH to 9.0. Allow the mixed solution to be settled for 30 minutes at room tempreature. The sample solution is then filtered through a 0.45 μm glass filter or blotting paper to obtain a filtrate. The precipitates were analysed to confirm the presence of struvite. The room temperature X-ray diffraction spectra of the different powders were recorded with a powder X-ray diffractometer (XRD 6000, Shimadzu, Japan) with a radiation condition of Cu Kα (λ = 0.15405 nm). The quality of the struvite recovered using different magnesium salt at optimum conditions is compared using the XRD patterns they produced by matching them with that of the standard struvite XRD pattern of International Centre for Diffraction Data (ICDD).

Result and Discussion

On average the phosphorous removal from the cow manure was recorded at 93% and the ammonia removal was at 46%. The XRD show the material recovered show similar pattern to the standard struvite XRD curve (Figure 1 and Figure 2). The slight difference may be due to impurities in the cow urine by the presence of traces of other ions. However, the XRD pattern indicated the sample as orthorhombic crystal which is the common crystal shape of struvite reported in the past.

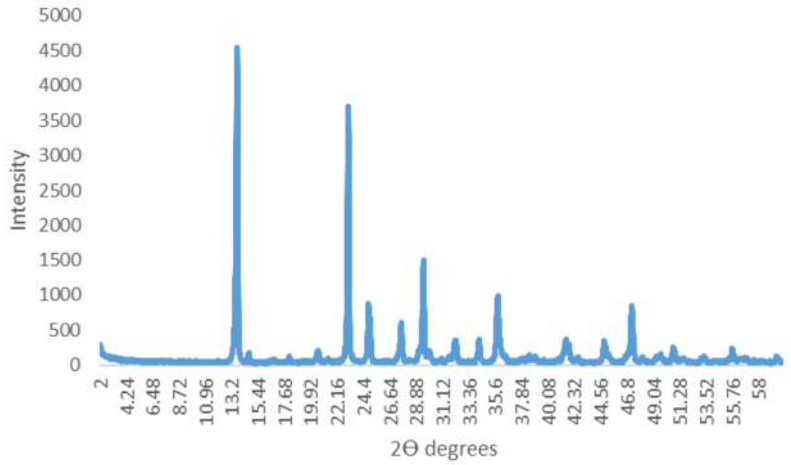

Figure 1: Powder XRD pattern for the crystallised product obtained from cow urine with mixing molar ratio of 1:1 at pH of 9.0 using Epsom salt

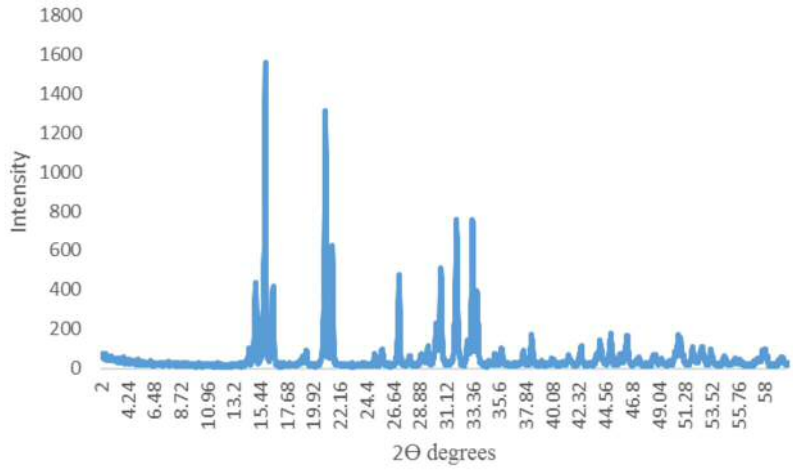

Figure 2: Powder XRD pattern a synthetic struvite

Please choose: Oral/ Poster/ Either
Presentation session:
Presenter name: Hasfalina Che Man

Email: [your email]

THE POTENTIAL USE OF CARBIDE LIME WASTE FOR AMMONIA STRIPPING

Adam Lim[1], Hasfalina Che Man[2], Nurul Hanira Mat Lazim[3], Muhammad Hazwan Hamzah[4]

[2]Tel. Num:03-89464340; Email address of corresponding author:hasfalina@upm.edu.my
[1]Tel Num:+6012-5961103; Email address of corresponding author: adamlim5575@gmail.com
[3]Tel Num:03-89464340; Email address of corresponding author: hazwanhamzah@upm.edu.my
[1,2,3,4]Institution address; Department of Biological and Agricultural Engineering,
Faculty of Engineering, 43400 UPM, Serdang, Selangor.

E-mail: hasfalina@upm.edu.my

ABSTRACT

Carbide lime is a by-product and considered as a waste from the production of acetylene gas. The characteristics of carbide lime was investigated as to confirm its suitability usage. This study used carbide lime, because it has high calcium content that can increase pH value of hazardous waste landfill leachate prior further treatment by ammonia stripping. In practice, the pH has to be raised up to 11 by the application of calcium hydroxide or sodium hydroxide, also known as lime. Jar test was used in the laboratory to investigate the capability of carbide lime in treating leachate. The optimum quantity of carbide lime obtained in treating is 6 g/L g which can increase pH value and reduces the ammonia content in leachate. The experimental results show that carbide lime has potential to be used to partly treat hazardous waste landfill leachate.

Keywords: Carbide lime waste, hazardous landfill leachate, jar test, ammonia removal, ammonia stripping

1. INTRODUCTION

Carbide lime or lime sludge is a by-product of acetylene production through the hydrolysis of calcium carbide that is generated as an aqueous slurry, mainly composed of calcium hydroxide, $Ca(OH)_2$. In a typical acetylene gas plant with a capacity of 864,000 m^3 weighing 950,400 kg, there will be about 2700 tonnes of carbide lime is produced annually. This means that there will be a huge amount of continuous supply and the study to utilize this waste is feasible to sustain. The carbide lime offers a variety of ways to reuse it due to its highly basic property at pH 12 – 13 in the raw form. Generally, the usage of the carbide lime can be compared to the properties of pure calcium hydroxide due to similar properties. One of the prospects in this study is to utilize carbide lime in the process of ammonia stripping from scheduled waste landfill leachate. Hence, the main objective of this study is to assess the potential use of the carbide lime. The specific objectives are to characterize the carbide lime and to investigate the potential use of carbide lime in ammonia stripping process of scheduled waste landfill leachate as to replace of pure calcium hydroxide.

2. METHODOLOGY

Sample Preparation and Characterization

Samples of carbide lime waste was obtained from an acetylene gas plant in Perak. The raw carbide lime sample was dried in an oven for 12 hours period at 105 °C. SEM with EDX used is SEM/EDX analysis functions to allow close observations of the elements present and also quantitative information of the compositions of the carbide lime. BET Analyzer Model used was SA-9600 Series by Horiba.

Jar test

The jar test experiments were conducted in a batch system by preparing various pH value of 200 ml leachate which were at different dosage of carbide lime. The various mixtures of carbide lime and leachate were allowed to stand with continuous stirring at 90 rpm for 30 minutes and 50 rpm for 5 hours with the constant amount of adsorbent dosage of the leachate samples. About 1.5 L of leachate sample is diluted at a ratio of 1:1 with distilled water. The desired amount of carbide lime was added at 4, 5 or 6 g/L). The mixture was then stirred thoroughly and then left for 20 minutes to completely settle the remaining grey particles. At this point, the leachate sample will appear clearer with a strong smell. The Hach ISENH4181 was used to measure the ammonia nitrogen content. Leachate flow rate was maintained at 0.1 L min^{-1}, while the air flow rate varied at 2, 4 and 8 L min^{-1}. The ranges for air-liquid ratio were 40, 60 and 80 respectively. The ranges of dosage, and air-liquid ratio were selected based on Hanira et. al. (2017). The jar was operated on a batch mode with each experiment was carried out for 8 hours with sample withdrawn from sampling point and analysed on hourly basis using the Hach ISENH4181. The result of experiment denoted as Y is the removal efficiency of ammonia nitrogen, NH_3-N from sample. Y is calculated using the equation:

$$\text{Removal efficiency of } NH_3\text{-N, } Y = \frac{\text{Initial } NH_3\text{-N} - \text{Final } NH_3\text{-N}}{\text{Initial } NH_3\text{-N}} \times 100\% \quad (3)$$

Design Expert software (Version 10) was used for the multilevel categoric design of experiments and analysis of data.

3. RESULTS AND DISCUSSIONS

Composition of Carbide Lime Waste Compared to Hydrated Lime

Carbide lime is generally calcium hydroxide ($Ca(OH)_2 \approx 85–95\%$) with traces of calcium carbonate ($CaCO_3 \approx 1–10\%$), unreacted carbon and silicates (1–3%). Since the carbide lime is highly basic with pH more than 12 in its raw solid form, it serves as a suitable replacement for industrial hydrated lime in reactions where the lime is used to increase the pH. The difference of colour in the limes where carbide lime was grey as opposed to white shown by pure hydrated lime was because of the presence of impurities. The results of the chemical analysis of the CLW determined by X-ray fluorescence technique showed that the carbide lime waste is a calcium-based lime since it contains 67.03% by weight of calcium oxide. The presence of 0.12% sulfur possibly cause its colour to be grey (Ayeche and Hamdaoui, 2012). The carbide lime and hydrated lime also has quite similar mineralogical composition as depicted in Table1.

The compositions of carbide lime waste as investigated from the EDX analysis revealed the composition of carbide lime to contain calcium oxide, carbon and silica dioxide at 75.04 %, 20.02% and 4.94 % respectively due to the process reactions chain of lime and acetylene gas productions. The powdered form of the sample as can be seen from the SEM images are not uniform with large and small particles mixed and had a BET reactions surface of 17.6336.

Table 1: Compositions of both limes determined using wet analysis. Source (Cardoso et al., 2009).

Composition	Hydrated Lime (%)	Carbide Lime (%)
CaO	70.9	71.2
MgO	0.31	0.06
SO_3	0.16	0.12
CO_2	5.29	4.54
Fe_2O_3+Al_2O_3	0.68	0.68

Effect of Carbide Lime Dosages and Air-Liquid Ratios on Ammonia Removal Efficiency

From Figure 2, it can be seen that generally higher lime dosages provide higher ammonia nitrogen removal efficiency-from the leachate. This is because of the pH adjustment by the usage of carbide lime on the leachate. Hydroxide ions (OH-) from the carbide lime will react with ammonium ions (NH_4^+) in the leachate to form ammonia gas (NH_3). The optimum pH for such reaction to occur is 10.5 to 12. As compared to Hanira

et al. study, they used 6g/L calcium hydroxide and the ammonia nitrogen removal rate was 80% for 8 hours operation while the obtained results using carbide lime was 75.5 % in the same time period.

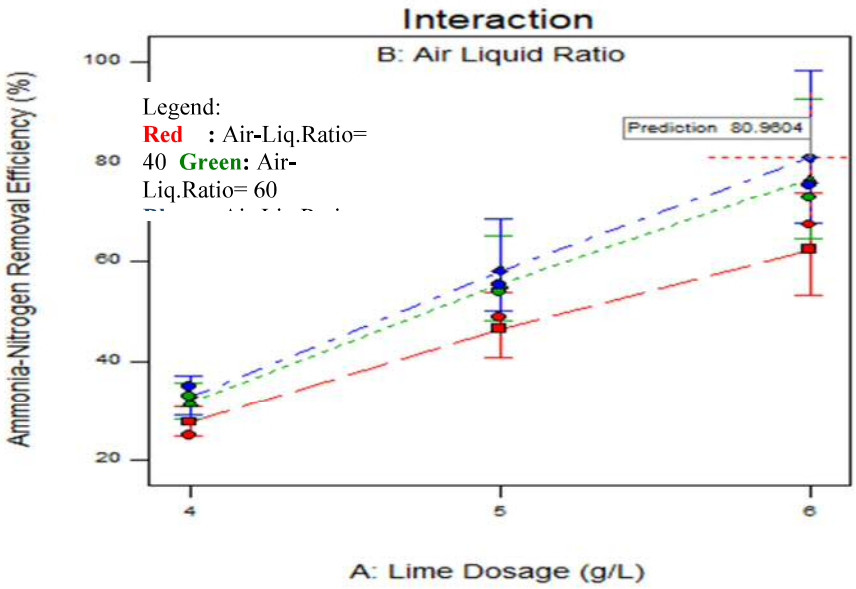

Figure 2: Design-expert plot; interactions plot for ammonia nitrogen removal efficiency at different lime dosages and air-liquid ratio

On the other hand, the disparities between the ranges of lime dosage was also observed. At an air flow of 80 mg/L, the ammonia removal efficiencies were 35 %, 55.4% and 75.5 for lime dosages 4 g/L, 5 g/L and 6 g/L respectively. It can be concluded that, the most suitable dosage of carbide lime required to remove ammonia was 6 g/L. This might be due to the pH level of the leachate required for gas removal after fixation which was 11.5 to 12 (Huang and Shang, 2006). It means that only when 6 g/L of carbide lime powder was added, the ammonia gas removal was satisfactory. Although carbide lime is not pure calcium hydroxide, it managed to achieve a result with a difference of 4.5% only. In general, the carbide lime has worked well as compared to calcium hydroxide for the ammonia removal. Thus, the use of carbide lime for pH adjustment is very promising.

Moreover, cost analysis can be made to further strengthen the feasibility of using carbide lime waste instead of commercial calcium hydroxide powder. The price of calcium hydroxide powder that was used for pH fixation costs 120 USD per metric tonne while the carbide lime is considered as waste. But still, it is certainly practicable to utilize this waste for other waste treatment purposes such as scheduled waste landfill leachate.

4. CONCLUSIONS

The ammonia removal was found to be the maximum at each factor which were at lime dosage of 6g/L and at air-liquid ratio of 80. The initial ammonia nitrogen level for the diluted leachate was 897 mg/L and it was reduced until 220 mg/L after 8 hours of operation for the optimal conditions. It can be concluded the carbide lime has a potential to be used for ammonia stripping process with the availability to provide the high pH. Thus, a systemic approach to prepare the sample at the correct sizes that provide the perfect size for reactions should be studied further. Nevertheless, in order to make the study viable for large scale use more studies must be conducted to make carbide lime waste a plausible pH fixing agent for ammonia stripping.

Please choose: Oral/ Poster/ Either
Presentation session:
Presenter name:

Polyhydroxyalkanoates – a potential substitute for single-use plastics and other non-plastic applications

Kumar, Sudesh

School of Biological Sciences, Universiti Sains Malaysia, 11800 Penang, Malaysia

Email: ksudesh@usm.my

Keywords: Polyhydroxyalkanoate, PHA, biodegradable, bioplastic, biocompatible

Introduction

Polyhydroxyalkanoates (PHAs) are a family of high molecular weight polyesters that serve as carbon and energy storage compounds for most microorganisms. PHAs are usually stored in the microbial cell cytoplasm as discrete water insoluble granules. The PHA granules upon extraction from the microbial cells can be processed into biodegradable plastics that have properties resembling polypropylene (PP) and low-density polyethylene (LDPE) that are widely used in disposable products. Therefore, much research and developmental works are ongoing in various countries to produce PHAs in an economically feasible and sustainable manner to substitute some single-use plastics. It is clear that we are unable to manage the increasing amount of plastic waste that we generate. Ironically, most plastic waste from developed countries are finding their ways to developing countries to be processed or recycled illegally at the expense of the environment.

Fig. 1. Large quantities of plastic waste from developed countries are imported by illegal companies in Malaysia to be recycled despite having no proper technologies or facilities.

Malaysia and Indonesia are the world's largest producers and exporters of palm oil. The palm oil industry generates large quantities of oil and/or fatty acid rich waste streams which can be used to produce PHAs. Some bacteria such as *Cupriavidus necator* can grow to high-cell density in culture medium containing fatty acids and/or oil. In Malaysia, efficient biosynthesis processes for PHAs were developed in order to use various derivatives and byproducts from the palm oil industry. In addition, a newly reported biological recovery process is also being developed to extract the PHA granules from the bacterial cells without using harmful solvents. The purified PHA was then used in agricultural applications for the development of controlled release of fertilizers.

Experiment

The wild-type *C. necator* was modified by replacing the native PHA synthase gene with a novel PHA synthase gene discovered from the metagenome of mangrove in Penang, Malaysia. PHA biosynthesis was carried out in shake flasks followed by 13L bioreactor. Mineral medium (MM) was used in the presence of palm oil derivatives as the sole carbon source and urea as the nitrogen source. At the end of cultivation, cells were harvested by centrifugation, washed once with distilled water and dried by either freeze-drying or spray drying. PHA was extracted from the bacterial cells by a new technique termed biological extraction whereby the dried cells were fed to mealworms as a protein source. The bacterial cells were digested by the enzymes in the mealworm gut but the PHA granules were not digested and therefore excreted in to form of fecal pellets. The partially purified PHA granules were then further purified by washing with water and some chemicals if

necessary according to its final applications. The PHA was analyzed by gas chromatography to determine its monomer composition. Gel permeation chromatography was used to determine the molecular weights. The biologically recovered PHA was then processed for various applications.

Results and Discussion

Cost is one of the major problems in the production and commercialization of PHA. The cost of producing petrochemical-based plastic resins are very cheap, partially because of the low-cost of the ingredient, which is petroleum or more recently in the U.S., natural gas liquids (NLGs). In addition, petroleum is drilled for its application as fuel for energy mainly and plastics are actually byproducts, which results in plastics production being cost effective. Likewise, the production of bio-based plastics has to be made cost-effective in order for them to be economically feasible for various application. The production of PHA is currently very costly compared to petroleum-based plastics because the feedstocks for making PHAs are renewable resources derived from agricultural products such as sugars and vegetable oils. In addition, the recovery and purification of PHA granules from the bacterial cells contribute to an additional 50% of the cost of PHA.

Recently, a broad-substrate-specificity PHA synthase was identified from mangrove metagenome in Penang, Malaysia.[1] By using this new PHA synthase the efficient biosynthesis of poly(3-hydroxybutyrate-*co*-3-hydroxyhexanoate) [P(3HB-*co*-3HHx)] was achieved. P(3HB-*co*-3HHx) copolymers with controllable 3HHx monomer compositions of up to 20 mol% were successfully synthesized from palm oil in a 13L bioreactor. The harvested cells were then dried and fed to mealworms as shown in Fig. 2 in order to recover the PHA granules.[2]

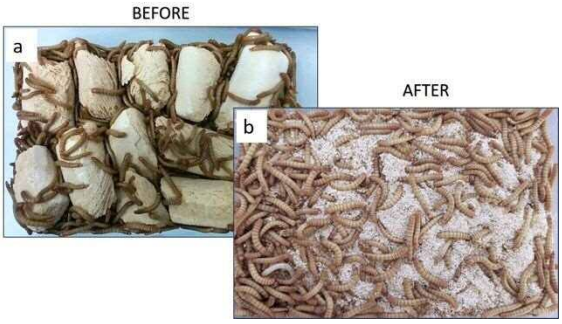

Fig. 2. Biological recovery of PHA granules from bacterial cells by feeding the cells to mealworms. The PHA granules were excreted in the form of fecal pellets because the granules cannot be digested by the mealworms. a) Freeze-dried cells at the beginning of feeding to the mealworms and b) at the end of the feeding experiment.

The resulting fecal pellets of mealworms were then washed with water to remove water soluble components and the water insoluble PHA granules were dried. The entire processes of recovery and purification of PHA granules were achieved without the use of solvents and hazardous chemicals.[3] The biologically recovered PHA was then used for the development of controlled release fertilizer for application in the oil palm nursery. The PHA could also be melt-casted into films for various agricultural applications.

Conclusion

PHAs have good potential as a biodegradable thermoplastic. By reducing the cost of production, PHAs may find a wide range of applications.[4] Non-plastic applications such as for the development of controlled release fertilizer are also attractive.

References

1. Foong, C. P., M. Lakshmanan, H. Abe, T. D. Taylor, S. Y. Foong, K. Sudesh. (2018) A novel and wide substrate specificity polyhydroxyalkanoate (PHA) synthase from unculturable bacteria found in mangrove soil. J. Polym. Res. 25(1): 23
2. Ong, S. Y., H.-P. Kho, S. L. Riedel, S.-W. Kim, C.-Y. Gan, T. D. Taylor, K. Sudesh. (2018) An integrative study on biologically recovered polyhydroxyalkanoates (PHAs) and simultaneous assessment of gut microbiome in yellow mealworm. J. Biotechnol. 265: 31-39.
3. Ong, S. Y., I. Zainab-L, S. Pyary, K. Sudesh. (2018) A novel biological recovery approach for PHA employing selective digestion of bacterial biomass in animals. Appl. Microbiol. Biotechnol. 102: 2117-2127.
4. Thinagaran, L., K. Sudesh. (2017) Evaluation of sludge palm oil as feedstock and development of efficient method for its utilization to produce polyhydroxyalkanoate. Waste Biomass. Valor. https://doi.org/10.1007/s12649-017-0078-8

Please choose: Either
Presentation session: Biological Science
Presenter name: Syafinaz, Amin Nordin

Positivity of non-organ specific autoantibodies (NOSA) among patients suspected with autoimmune liver disease (AILD) in a Malaysian hospital from 2012 to 2015

Yuhin Karina, Yusoff[1], Hasni, Mahayidin[2], Norazlah, Bahari[3], Syafinaz, Amin Nordin[1]

[1]Department of Medical Microbiology and Parasitology, Faculty of Medicine and Health Sciences, Universiti Putra Malaysia, 43400 Serdang, Selangor, Malaysia. [2]Department of Pathology, Faculty of Medicine and Health Sciences, Universiti Putra Malaysia, 43400 Serdang, Selangor, Malaysia
[3]Department of Pathology, Hospital Selayang, 68100 Batu Caves, Selangor, Malaysia.

Email: syafinaz@upm.edu.my

Keywords : non-organ specific autoantibodies, autoimmune, chronic liver, Malaysia

Introduction

Non-organ specific autoantibodies (NOSA) play a key role in the diagnosis and differentiation of the spectrum of autoimmune liver disease (AILD) comprising of autoimmune hepatitis (AIH), primary biliary cirrhosis (PBC), overlap syndromes and less often primary sclerosing cholangitis (PSC). However, the presence of these autoantibodies has also been reported in various non-autoimmune liver diseases (non-AILD) which limit the usefulness of the antibodies as diagnostic markers and reduce their specificity. This study aimed to provide the profile of NOSA positivity in the various liver diseases of autoimmune and non-autoimmune etiology that would be useful for the clinical management and diagnostic laboratory testing of suspected AILD. We also investigated the associations of NOSA with the clinical and biochemical characteristics in patients with AILD and non-AILD.

Experiment

A retrospective study in a national tertiary referral centre in Malaysia for liver diseases was conducted. This study included 380 patients from January 2012 to December 2015 with suspected autoimmune liver disease (AILD). They were subjected for complete profiling of NOSA which consists of anti-nuclear antibodies (ANA), anti-smooth muscle antibodies (ASMA), anti-mitochondrial antibodies (AMA) and anti-liver kidney microsomal antibodies (anti-LKM) by indirect immunofluorescence (IIF) method.

Results and Discussion

Table 1 illustrates the demography and clinical features of patients in the study. A total of 144 patients (37.9%) were tested positive to any autoantibodies (ANA 50.0%, ASMA 50.0%, AMA 18.8% and anti-LKM 0.6%). Majority of them, 99 (66.7%) had underlying AILD which were autoimmune hepatitis (68.8%), overlap syndromes (15.6%), primary biliary cirrhosis (14.6%) and primary sclerosing cholangitis (1%). Positive NOSA was also detected in 48 (33.3%) patients diagnosed as having non-AILD which were chronic hepatitis B (25%), NAFLD (27%), cirrhosis of unknown aetiology (14.6%), drug-induced liver injury (DILI) (16.7%), chronic hepatitis C (4.2%) and alcoholic liver disease (4.2%). In AILD, NOSA-positive were seen more in female patients (80.2%), those above 36 years old (72.0%), and of Malay ethnicity (45.8%). The most frequently detected NOSA in non-AILD were ANA and ASMA, which are also the markers for autoimmune hepatitis, the most common type of AILD. Positive NOSA was significantly associated with female gender and elevated serum IgG in AILD. However, no significant association of positive NOSA with any of the demographic and biochemical characteristics tested in non-AILD were demonstrated.

NOSA was commonly detected in patients with AILD and these serological markers are important for the diagnosis and differentiation of AILD. The prevalence of positive NOSA is low among patients in our study. We also found that positive NOSA in patients with chronic liver diseases does not conclude an autoimmune aetiology. Therefore, in view of their low specificity, a careful evaluation with combined clinical, histopathological and imaging are essential in patients with liver disease.

Table 1: Demographic and clinical features of the study patients (n=380)

Characteristic	Diagnosis				Total patients	
	AILD (n=102)		Non-AILD (n=278)		n	(%)
	n	(%)	n	(%)		
Age						
18-35	26	(6.8)	47	(12.4)	73	(19.2)
36-60	58	(15.3)	166	(43.7)	224	(59)
61 or above	18	(4.7)	65	(17.1)	83	(21.8)
Gender						
Male	23	(6.1)	156	(41.0)	179	(47.1)
Female	79	(20.8)	122	(32.1)	201	(52.9)
Race						
Malay	63	(16.6)	141	(37.1)	204	(53.7)
Chinese	27	(7.1)	77	(20.3)	104	(27.4)
Indian	11	(2.9)	59	(15.5)	70	(18.4)
Others	1	(0.25)	1	(0.25)	2	(0.5)
Clinical presentation						
Deranged liver enzymes	41	(10.8)	139	(36.6)	180	(47.4)
Jaundice	28	(7.4)	35	(9.2)	63	(16.6)
Cirrhosis	28	(7.4)	95	(25.0)	123	(32.4)
Esophageal varices	5	(1.3)	9	(2.4)	14	(3.7)

**Others are Indonesians

Please choose: Oral
Presentation session: Material Science and Technology
Presenter name: Hadiyawarman

Fabrication of Ag-Ag_2S core-shell nanoparticles for neuromorphic device

Hadiyawarman[1], Masanori Eguchi[2], Hirofumi Tanaka[1]

[1]Graduate School of Life Science and Systems Engineering, Kyushu Institute of Technology, 2-4 Hibikino, Wakamatsu, Kitakyushu, 808-0196 , Japan
[2]Fuzzy Logic System Institute, Kure National College of Technology, 2-2-11 Agaminami, Kure, Hiroshima, 737-8506 Japan

Email: tanaka@brain.kyutech.ac.jp

Keywords: Atomic switches, Memristor, Reservoir Computing, Ag-Ag_2S core-shell nanoparticles, Brust-Schriffrin synthesis

[Introduction]

Recent notable development of artificial neural networks (ANNs) were demonstrated by the performance of AlphaGo and its variants[1], which showed the capability of machine to learn and compete with human being in the game. This successful development was implemented in conventional computing which showed the limitation owing to high power consumption. Compared to conventional computing platform, such as Von Neumann computer, neuromorphic devices have a high-performance arithmetic circuit with very low power consumption, which can be efficient to support ANNs algorithm. Besides, such system mimicking human brain information processing is expected to be applied in many fields. Atomic switch is one of the promising platform material to enable mimicking human brain device due to memristive behavior resulted from device using Ag-Ag_2S materials [2]. H. O. Sillin et al., reported the functionality of Ag-Ag_2S nanowires for logic circuit [3]. In the present study, we demonstrated a fabrication of the network among the Ag-Ag_2S core-shell nanoparticles and its electrical properties for reservoir computing application.

[Experiment]

The synthesis procedure was depicted in the Figure 1. The Ag-Ag_2S core-shell nanoparticles were synthesized by modified Brust-Schiffrin procedure [4] at room temperature with Ag/S molar ratios of 0.25/1; 0.5/1; and 1/1. The fabrication of Ag-Ag_2S core-shell nanoparticles with Ag/S molar ratios of 0.25/1 is as follows: A toluene solution of allylmercaptane (0.37 ml, 4.71 mmol) is mixed with a solution of silver nitrate (200 mg, 1.18 mmol). Then, tetraoctylammonium bromide in deionized (DI) water (360 mg, 0.658 mmol) was added to the solution and followed by adding sodium borohydride solution in DI water (260 mg, 6.87 mmol). The mixture was allowed to react for 2 h at room temperature with magnetic stirring. The water phase was then removed from obtained solution and then was centrifuged at 4000 rpm for 20 min to separate the nanoparticles from the liquid phase. The nanoparticles were then measured by XRD, TEM, and XPS to investigate their structural properties. The results were depicted in figure 2.

The device was fabricated by e-beam lithography process and following by depositing Pt/Ti with thickness of 24/6 nm, respectively. After that, the nanoparticles were immersed in ethanol and drop-casted onto the device. To evaporate the ethanol, during drop-casting, the device was heated on hot plate at 50°C. The aggregated particles were then measured by applying DC bias to the electrode. Figure 3 showed the I-V characteristic of the device with trapped particles at the center of electrodes.

[Result and Discussion]

The structural properties of Ag-Ag_2S nanoparticles were investigated by XRD, XPS and TEM. Two different crystal structures were found in our nanoparticles during XRD examination, as depicted in Figure 2, indicating the existing of Ag and Ag_2S crystal. Then, to investigate the chemical bonding state at the outer shell of the particle, XPS was taken into account. As the result, three peaks were observed at S2p area after

deconvolution process was taken and were located at 161.4, 162.4, and 163.4, which correspond to the $S2p_{3/2}$ Ag_2S-like, $S2p_{1/2}$ Ag-S-R, and $S2p_{3/2}$ physisorbed AM, respectively. Those peaks indicate the existence of Ag-S bonding at the surface of Ag nanoparticles. Furthermore, the structure of nanoparticles was observed by TEM as can be seen in inset of XRD. According to those results, the existence of Ag-Ag_2S core-shell nanoparticles was confirmed.

The electrical properties was investigated by I-V characteristics. Figure 3 shows the change in the current flowing in the atomic switch when the bias voltage was continuously swept between 0 and 5 volts. At the beginning of the first sweeps, the atomic switch was in the tunneling regime, i.e., there was a gap between the two nanoparticles. The current was observed to increase continually with the history of subsequent sweeps, as evident in the evolution of the hysteresis loops. The existence of the hysteresis in the I-V graph indicates the memristive behavior, which is suitable for neuromorphic device. Besides, the device also showed gradual increase of current, indicating the learning behavior of Ag-Ag_2S core-shell nanoparticles, which is one of the characteristics of neuromorphic device.

References:

[1] D. Silver et al., Nature 550, 354 (2017)
[2] K. Terabe et al., Nature 433, 47 (2005)
[3] H. O. Sillin et al., Nanotechnology 24, 384004 (2013)
[4] C. Battocchio et al., J. Phys. Chem. C 116, 19571 (2012)

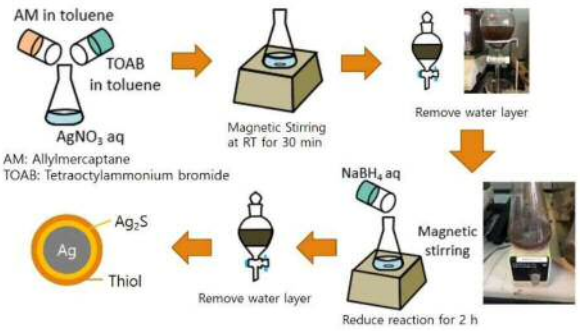

Figure 1. Synthesis of Ag-Ag2S core-shell nanopaerticles using modified Brust-Schiffrin procedure

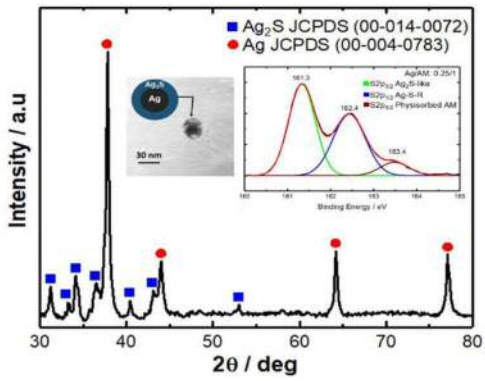

Figure 2. The structural properties of nanoparticles was examined by XRD, XPS and TEM

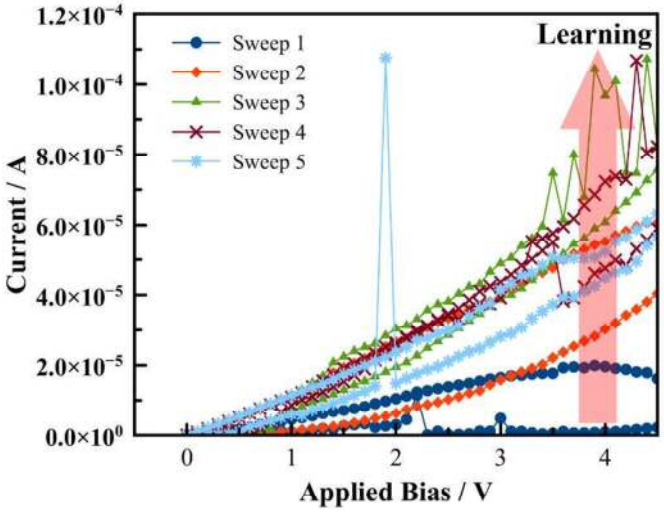

Figure 3. The I-V characteristics of neuromorphic device based Ag-Ag2S core-shell nanoparticles

Please choose: Oral
Presentation session: Applied Engineering
Presenter name: Ajendra Kumar Vats

Implication of Dye Molecular Structure on Adsorption Behavior and Anchoring Stability Using NIR Sensitive Squaraine Dyes

Ajendra Kumar Vats, Anusha Pradhan, Shuzi, Hayase and Shyam S, Pandey
[1]Graduate School of Life Science and Systems Engineering, Kyushu Institute of Technology, 2-4 Hibikino, Wakamatsu, Kitakyushu 808-0196, Japan
Email: ajendra.vatts09@gamil.com

Keywords: Squaraine dyes, Photosensitization, Anchoring group, Dye-sensitized solar cells, Adsorption rate, and Anchoring stability.

Introduction

Lower fabrication cost in combination of low cost raw materials, esthetic color and transparency make dye-sensitized solar cells (DSSCs) one of strong contenders amongst next generation solar cells. Efforts of various optimizations for different components of DSSCs in last two decades resulted in to demonstration of power conversion efficiency (PCE) surpassing amorphous silicon (12-14 %). Moreover, this PCE has been achieved for efficient photon harvesting (>90 %) by photon harvesting only in visible region (<700 nm) of the solar spectrum. This provides a good hope for further enhancement in the PCE by design and development of novel dyes having light absorption beyond far-red to NIR wavelength region. Amongst various components involved in the construction of DSSCs, dye-sensitizers play a dominant role in controlling the overall efficiency owing to actual light absorber. Apart from energetic matching, high molar absorption coefficient, tunable wavelength, presence of a suitable anchoring group at the right position of the main molecular framework is highly desired for an optimal sensitizer. These anchoring groups play a dominant role not only for attachment of dye molecules upon the mesoporous TiO_2 but also for their binding strength is associated with stability of DSSCs thus fabricated. In this work, we have designed and synthesized four new squaraine dyes having same main π-framework with varying anchoring groups. After successful synthesis, these dyes were subjected to their photophysical characterizations and investigation of their anchoring as well as stability on the mesoporous TiO_2.

Experiment

A series of unsymmetrical squaraine dyes bearing same main molecular framework but different functional groups (**-COOH, -OH, -SO_3H and -PO_3H_2**) with molecular structures shown in the Fig. 1 were synthesized in this work. All of these dyes exhibit cyan color in the ethanol solution as shown in the inset of Fig. 1. These dyes were subjected to photophysical characterization by absorption and emission spectroscopy, cyclic voltammetry, and estimation of energy band gap. Dye adsorption behaviour on the mesoporous TiO_2 was conducted for dipping the respective ethanolic solution of dyes for different time intervals. Anchoring stability of dyes after adsorption on TiO_2 was measures after placing the dye adsorbed TiO_2 in dark and in acetonitrile solution followed by monitoring the extent of adsorption for different time intervals.

Figure 1.Structure of NIR dyes synthesized and photographs of the 5 μM solution of dyes in ethanol solution.

Result and Discussion

In the photoanodes of the DSSCs, sensitizers are attached on the mesoporous TiO_2 by the chemical bond formation between the –OH groups present on the surface of TiO_2 with the functional groups present in the dye molecules. The basic idea behind the dye design was investigation of nature of different anchoring groups not only on their photophysical characteristics but also on their adsorption behavior on the mesoporous TiO_2 along with the strength of bonding to delineate the dye structure with stability of DSSCs. Optical characterization in

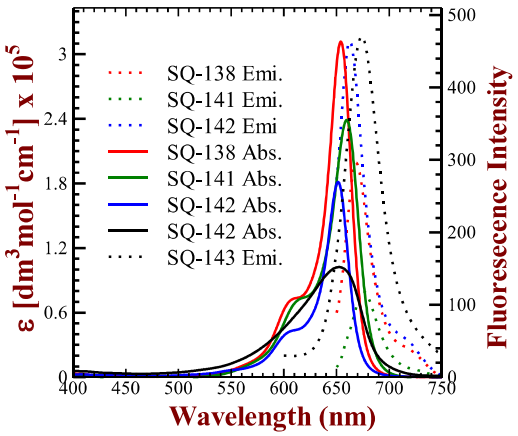

Figure 2. Absorption and emission of the 5 μM solution of dyes in ethanol.

the solution state of these dyes was conducted the measurement of their optical absorption and fluorescence emission spectra as shown in the Fig. 2. It can be clearly seen that these dyes exhibit very sharp, intense and narrow light absorption mainly in the far-red (550-700 nm) region of the solar spectrum with very high molar extinction coefficients (ε) of 1-3 $dm^3.mol^{-1}.cm^{-1}$. **ε** value shown by dyes in this work are about 10 times higher as compared to typical ruthenium complex based sensitizer like N3. High ε is beneficial for DSSCs since even in thin layers of mesoporous TiO2 sufficient photons can be easily absorbed making them suitable for semitransparent solar cells. At the same time, emission spectra reveals similar narrow spectral width with very small relatively small Stokes shift as compared to typical visible sensitizers used in the DSSC research. Small Stokes shift also represents the molecular stability of the molecules in the excited state.

Energetic matching of sensitizers with respect to the wide band gap semiconductor and redox electrolyte is one of the most important requirements for the suitability of the sensitizer. A perusal of the energy band diagram shown in the Fig. 3 clearly corroborates that LUMO energy level of all of the sensitizers under investigation are higher than that of the conduction band (CB) energy level of TiO_2. This ensures that electrons after photoexcitation can be easily injected. At the same, lower HOMO energy level of the dyes with respect to I^-/I_3^- redox energy level of iodine electrolyte ensures that oxidized dyes after the electron injection can be easily regenerated. In this respect, **SQ-141 with –OH** anchoring group seems to be a non-optimal sensitizer owing to its shallow HOMO energy level.

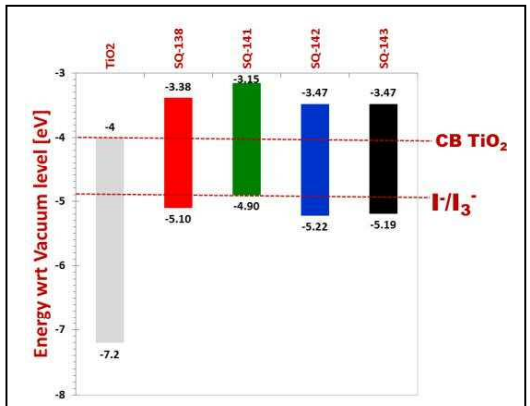

Figure 3. Energy band diagram for squaraine dyes. CB of TiO_2 and iodine electrolyte energy level are considered as per literature reports.

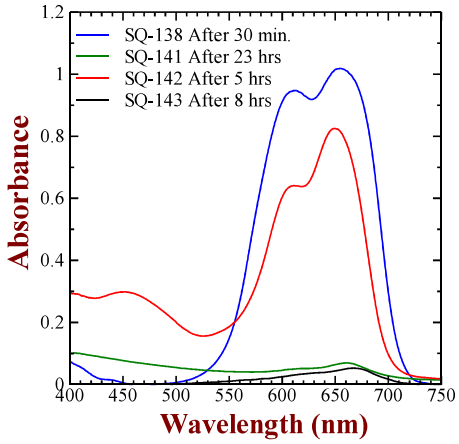

Figure 4. Adsorption behavior of dyes under investigation on the mesoporous TiO_2.

Figure 4 depicts the adsorption behavior of of squaraine dyes on TiO_2, which was conducted on 4 μm thick mesoporous TiO_2 from the 0.1 mM ethanolic solution of the respective dyes at room temperature. It can be clearly seen that SQ-138 with –COOH functional group exhibits very swift adsorption on the TiO2 while SQ-143 with Phosphonic acid anchoring group exhibited the slowest adsorption. Rate of dye adsorption on the mesoporous TiO_2 was found to be **SQ-138>>SQ-142>SQ-143>>SQ-141**. Anchoring stability of the dyes on mesoporous TiO_2 was also investigated after maximal adsorption of the sensitizers on the mesoporous TiO_2. This was conducted by storing the dye-adsorbed photoanodes in air and in acetonitrile solution under dark followed by monitoring the extent of dyes as a function of time. Details about synthesis and photophysical characterizations and dye adsorption and stability on mesoporous TiO_2 will be discussed during my presentation.

Acknowledgement: One of the authors, SSP would like to thank Japan Society for Promotion of Science for the financial support by Grant-in-Aid for scientific research (C) [**Grant No.-18K05300**] to carry out the research being presented here.

Oral/ Poster/ Either
Presentation session:
Presenter name: Sazlinda Kamaruzaman

Synthesis and Characterization of Graphene Oxide-Molecularly Imprinted Polymer for Neopterin Adsorption Study

[Sazlinda Kamaruzaman][1], [Wai Chat Khoo][1], [Siti Nurul Ain Mad Jamil][1], [Hong Ngee Lim][1,2]

[1]Faculty of Science, University Putra Malaysia, 43400 UPM Serdang, Selangor, Malaysia
[2]Institute of Advance Technology, University Putra Malaysia, 43400 UPM Serdang, Selangor, Malaysia

Email: sazlinda@upm.edu.my

Keywords: Neopterin; graphene oxide; molecularly imprinted polymer; adsorption

[Introduction]
Neopterin (NEO) is a chemical compound which belongs to a class of chemicals known as pteridines. In 1979, Wachter and his co-researchers found out that patients who suffered from malignant diseases have elevated concentrations of neopterin in their urine excretion. In the past decades, various journals have been published, reporting on the positive relation between different malignant diseases and neopterin concentration in human urine and bodily fluids, proving that neopterin is a reliable marker in malignant diseases. Molecularly imprinted polymers (MIP) is made up of cross-linked functional monomers which are polymerized under the presence of target molecules known as templates. Although MIPs show resounding performance in various applications, it often suffers from nonhomogeneous molecular cavities, slow response time, and low reproducibility of the binding performance. the imprinting effect of non-covalent MIPs are found to be generally low as the polymer complex often suffers from structural collapse and shrinking of the majority of the binding sites due to the build-up of stress in the polymer network, leading to relaxation of the polymer chains. In order to overcome the drawbacks of MIP, graphene oxide (GO) is introduced to form a graphene oxide-molecularly imprinted polymer (GO-MIP) hybrid material. multiple reports can be found utilizing GO modified MIPs for the determination of various organic compounds with great success. However, there has not been any report on the synthesis of GO-MIP using neopterin as template. Therefore, the aim of this research was to successfully synthesize GO-MIP using neopterin as template molecule via free radical polymerization method. The synthesized GO-MIP was characterized using FT-IR, CHNS, TGA, FESEM, and TEM. Neopterin adsorption was carried out and analyzed using HPLC-FLD, while the adsorption mechanisms were studied using Langmuir isotherm, Freundlich isotherm, and Lagergren kinetic models.

[Experiment]
GO-MIP was synthesized via free radical polymerization method, inspired and modified from the work of Del Sole, Shagufta Khan, and Duan. Firstly, 0.16 mmol (40 mg) of NEO, 0.40 mmol (54 µL) of MAA, and 15 mg of GO powder were added to 6.4 mL/1.6 mL v/v DMSO/ACN mixture solution in a round-bottom flask. The mixture was then left for 1 hour for pre-polymerization. Next, 2.56 mmol (482 µL) of EGDMA and 0.054 mmol (12 mg) of APS were added into the mixture, and sonication was carried out for 10 minutes in a water bath (Fisherbrand FB15150 sonicator). After that, the mixture was deoxygenated using nitrogen gas for 1 hour, followed by polymerization performed in a fume hood at 50°C for 24 hours under inert nitrogen atmosphere. The product was washed with the use of 1M HCl solution for multiple times to remove NEO and leave behind empty binding sites. 20 mL HCl 1M solution was added into a centrifuge tube containing synthesized GO-MIP. Sonication was carried out for 15 minutes followed by 30 minutes of centrifugation at 6000 rpm. The washing process was monitored by analyzing the remaining NEO concentration in the supernatant via a 1601 Shimadzu (Japan) double beam ultraviolet-visible (UV-Vis) spectrometer. Lastly, the GO-MIP was washed with deionized H_2O to remove the remaining acid, and then dried in an oven to remove the H_2O. Upon drying, the GO-MIP was grinded to fine powder using a ceramic grinder. GO-NIP was also synthesized following the same method as described above but without the addition of NEO for comparison purposes. Multiple characterizations were done on synthesized GO-MIP, GO-NIP, and the GO powder such as FT-IR, CHNS, TGA, FESEM, and TEM. For the adsorption tests, the procedures are as follow; the adsorption of NEO on

synthesized GO-MIP was carried out via batch adsorption method. 10 mg of GO-MIP was mixed with 1 mL of NEO 10 mg/L working standard solution in a 4 mL amber glass vial. The suspension was then stirred with the use of magnetic stirrer and a magnet bar at 300 rpm for 60 min. After that, the supernatant was collected and filtered using a 0.22 µm nylon syringe filter, and was submitted for HPLC-FLD analysis. These procedures were applied to determine the selectivity, static adsorption and kinetic adsorption test.

[Result and Discussion]

In this research, GO-MIP was successfully synthesized with NEO as the template molecule, using MAA as the monomer, EGDMA as the cross-linker, APS as the free radical initiator, and DMSO/ACN 8/2 v/v solution as the porogen solvent via free radical polymerization method. The formation of GO-MIP hybrid along with the presence of binding sites imprinted by NEO template were validated via FT-IR (Figure 1), CHNS, TGA (Figure 2), FESEM (Figure 3), and TEM (Figure 4) characterization methods. The adsorption test results indicated that the GO-MIP possessed high selectivity towards NEO (Figure 5), and the presence of NEO imprinted binding sites improved the adsorption performance. Static and kinetic adsorption tests concluded that the adsorption process of NEO on GO-MIP was best described using Freundlich isotherm (Figure 6) and Lagergren pseudo-second-order model (Figure 7). The adsorption occurred in a multi-layer manner and is chemisorption.

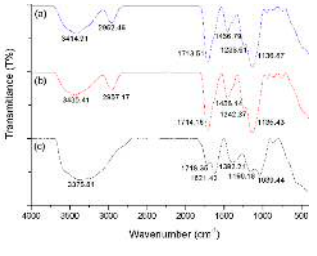

Figure 1

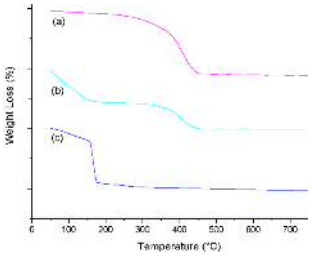

Figure 2

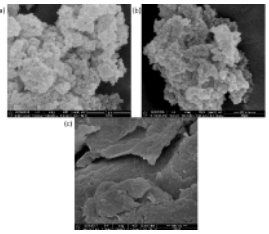
Figure 3

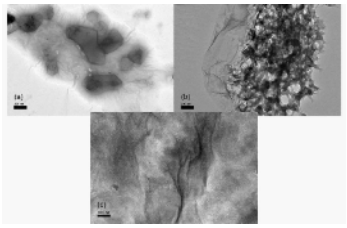
Figure 4

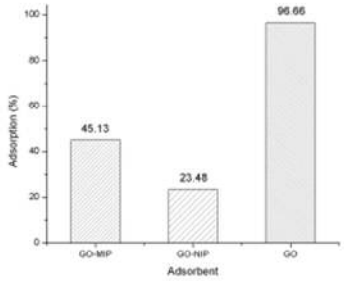

Figure 5

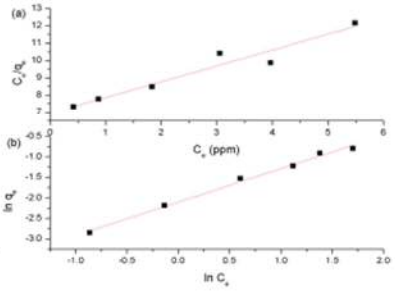

Figure 6

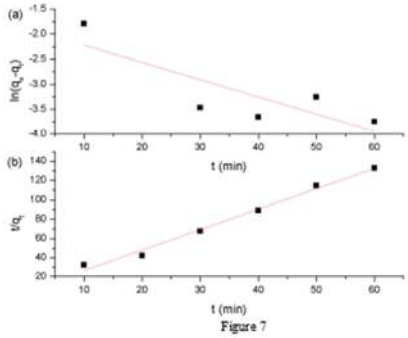

Figure 7

Figure 1: FT-IR analysis data of (a) GO-MIP, (b) GO-NIP, and (c) GO

Figure 2: TGA analysis data of (a) GO-MIP, (b) GO-NIP, and (c) GO

Figure 3: FESEM characterization of (a) GO-MIP, (b) GO-NIP, and (c) GO

Figure 4: TEM characterization result of (a) GO-MIP, (b) GO-NIP, and (c) GO

Figure 5: NEO adsorption study using different adsorbents

Figure 6: Linear regression plots of (a) Langmuir isotherm, and (b) Freundlich isotherm

Figure 7: Lagergren kinetic models linear regression plots of (a) pseudo-first-order and (b) pseudo-second-order

Please choose: Oral
Presentation session: Applied Engineering
Presenter name: Nikita Kumari

Two-Dimensional Positional Mapping of Macroscopically Oriented Thin Films of Organic Semiconducting Polymers

Nikita Kumari[1], Manish Pandey[1], Atul SM Tripathi[1], Suichi Nagamatsu[2], Shuzi Hayase[1], Shyam S. Pandey [1]

[1]Graduate School of Life Science and Systems Engineering, Kyushu Institute of Technology, 2-4 Hibikino, Wakamatsu, Kitakyushu 808-0196, Japan
[2]Department of Computer Science and Electronics, Kyushu Institute of Technology, 680-4 Kawazu, Iizuka, 820-8502, Japan

Email: nikita.jisce@gmail.com

Keywords: Self-assembly, Orientation, Thienothiophene, Anisotropic-charge transport, OFET

Introduction

Organic semiconductors play a pivotal role in flexible and wearable electronics but their performance lags behind the inorganic semiconductor counterparts due to their relatively hampered charge carrier transport. Charge transport in this class of materials occur through π–conjugated backbones, therefore, control of intermolecular π-π stacking, intermolecular and inter-domain hopping are inevitable for facile carrier transport. Although high performance organic electronic devices utilizing organic molecular semiconductor have been achieved through vacuum deposition and growing single-crystals in their thin films [1] but such thin film processing techniques are not suitable for the mass production of organic electronic devices. However, semiconducting polymers show better solubility in common organic solvents and their better solution rheology makes them a potential candidate for printed electronics [2]. Due to one-dimensional nature of semiconducting conjugated polymers (SCPs), they are prone to self-assembly in the condensed state, therefore, their film morphology and molecular orientation plays a dominant role in deciding the final device performance. Since the charge transport properties significantly varies with respect to film anisotropy, thus their uni-axial molecular orientation is highly desired. To provide the orientation in SCP films, techniques like mechanical rubbing, strain-alignment, off-center spin-coating, solution shearing etc. have been although reported but they are not suitable for the large area roll to roll printing technology, ease of fabrication and processing cost [3,4].

We have recently developed a facile and highly cost-effective technique to fabricate large area anisotropic films of SCPs known as ribbon-shaped floating film transfer method (R-FTM) [5]. This method is the recent improvisation of our previous conventional FTM [6,7] utilizing a slider, which promotes uni-directional film growth leading to cost-effective and large area anisotropic films [6.7]. Although the molecular orientation in the R-FTM films can be tuned by parametric optimizations [8] but it is very important to probe the film homogeneity in terms of thickness and extent of orientations especially in the large area of the films. Although, there are several techniques to probe orientation intensity and backbone conformation of oriented SCP films like atomic force microscopy, grazing incidence x-ray diffraction, near edge x-ray absorption fine structure spectroscopy, variable angle spectroscopic ellipsometry, polarized UV-Vis-NIR absorption spectroscopy and polarized Raman spectroscopy etc. [9,10] but in these systems, a tiny area is scanned. Since to optimize the material property, investigation on small area of the sample is adequate (at laboratory scale) but precise characterization of large area SCP films through them will be a troublesome job. Here we would like to report a new technique to map the positional distribution of thickness and molecular orientation in a large area oriented films of PBTTT-C14 as a representative SCP fabricated by R-FTM.

Experiment

Poly[2,5-bis(3-tetradecylthiophen-2-yl)thieno[3,2-b]thiophene] (PBTTT-C14), purchased from Sigma Aldrich was used as representative SCP in this work. PBTTT-C14 films were fabricated by R-FTM (with concentration 1% w/w in hot dehydrated chloroform) as per the methods reported previously [5], friction transfer (at 75 ℃ substrate temperature, constant stage speed of 50 mm/min and a fixed load of 30 Kgf/cm^2) and spin-coating (with concentration 0.25% w/w in hot dehydrated 1,2-dichlorobenzene with 0.25% w/w). These films were then subjected to characterization by the newly developed 2-D positional mapping system and UV-Vis-NIR (JASCO V-570) spectrophotometric investigations. The bottom-gated top-contact OFETs were fabricated on SiO_2 substrate utilizing the optimum film probed by the mapping technique.

Result and Discussion

The film morphology was characterized through the mapping technique and schematic representation for the 2D-Positional mapping system used is shown in the Fig.1. A white light was incident on the sample and transmitted light was received through the aligned optical fiber cable connected to photonic multichannel analyzer (PMA, 7473-36, Hamamatsu Photonics). The PMA is a Czerny-Turner type spectrograph in which received beam is collimated and dispersed in constituent wavelengths. The whole dispersed optical band is simultaneously collected through a set of 1024 back-thinned CCD image sensors. In this way, absorption spectra of whole sample film was taken by scanning array of point areas (3.14×10^{-2} mm^2). The incident beam width was 5 mm and the effective aperture of light collecting optical fiber (connected to PMA) was of 1 mm in diameter, a mask of diameter 0.2 mm was used to increase the resolution. A joy-stick controlled X-Y mobile stage was used to precisely position the sample area for scanning. A polarizer was placed between the sample and light beam in order to get the polarized optical absorption spectra for the investigation of molecular anisotropy of the film. At every point area, absorption spectrum was taken with spectral resolution of 2 nm and to improve S/N ratio five data were averaged out and further all the spectra were integrated through the interfaced computer.

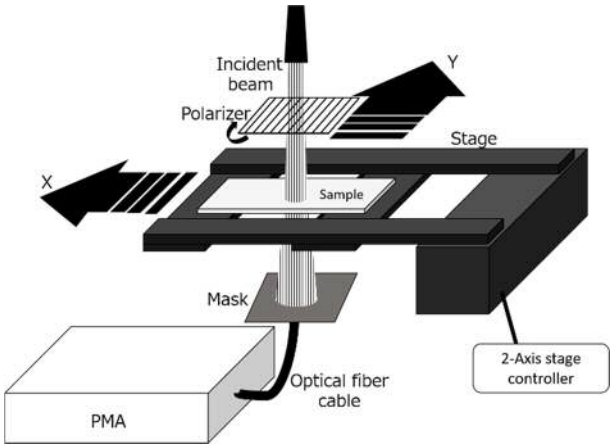

Fig. 1 Schematic illustration of developed measurement system for the 2D positional mapping of large area oriented films.

Extent of the orientation in R-FTM represented in publication coated and samples' film is having films of PBTTT-C14 was calculated and terms of dichroic ratio (DR) as per our earlier [11]. The mapped film morphology of the spin-friction-transferred films and the corresponding photograph are shown in Fig. 2. The spin-coated slightly increasing trend in thickness distribution from the spinning axis towards outward. The Friction-transferred film is having almost uniform thickness distribution with slight variation, which can be attributed to the non-uniformity of the pellet surface. From the perusal of Fig. 2 it is also visible that lower thickness of the friction-transferred-film is having higher DR because it is an interface driven phenomena. Details about the fabrication of films, their optical characterization along with the positional mapping and device fabrication and characterization will be discussed during the presentation.

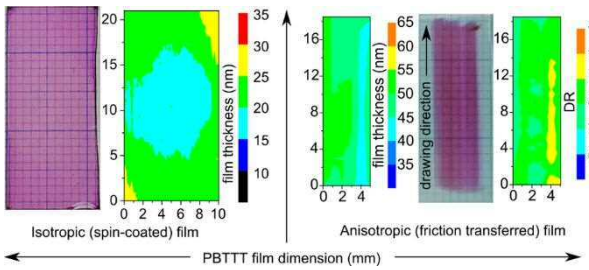

Fig. 2 Spin-coated and Friction transferred film with corresponding morphology distribution measured through 2D positional mapping technique

References

[1] A.L. Briseno, R.J. Tseng, M.M. Ling, E.H.L. Falcao, Y. Yang, F. Wudl, Z. Bao, Adv. Mater. **18** (2006) 2320.

[2] I. Mcculloch, M. Heeney, M.L. Chabinyc, D. Delongchamp, R.J. Kline, M. Cölle, W. Duffy, D. Fischer, D. Gundlach, B. Hamadani, R. Hamilton, L. Richter, A. Salleo, M. Shkunov, D. Sparrowe, S. Tierney, W. Zhang, Adv. Mater. **21** (2009) 1091.

[3] M. Brinkmann, L. Hartmann, L. Biniek, K. Tremel, N. Kayunkid, Macromol. Rapid Commun. **35** (2014) 9.

[4] D. Khim, A. Luzio, G.E. Bonacchini, G. Pace, M.-J. Lee, Y.-Y. Noh, M. Caironi, Adv. Mater. (2018) 1705463.

[5] A.S.M. Tripathi, M. Pandey, S. Sadakata, S. Nagamatsu, W. Takashima, S. Hayase, S.S. Pandey, Appl. Phys. Lett. **112** (2018) 123301.

[6] T. Morita, V. Singh, S. Nagamatsu, S. Oku, W. Takashima, K. Kaneto, Appl. Phys. Express. **2** (2009) 12–15.

[7] M. Pandey, S. Nagamatsu, S.S. Pandey, S. Hayase, W. Takashima, Org. Electron. Physics, Mater. Appl. **38** (2016) 115.

[8] M. Pandey, S.S. Pandey, S. Nagamatsu, S. Hayase, W. Takashima, J. Nanosci. Nanotechnol. **17** (2017) 1915.

[9] M.M. Nahid, E. Gann, L. Thomsen, C.R. McNeill, NEXAFS spectroscopy of conjugated polymers, Eur. Polym. J. **81** (2016) 532.

[10] X. Zhang, L.J. Richter, D.M. Delongchamp, R.J. Kline, M.R. Hammond, I. McCulloch, M. Heeney, R.S. Ashraf, J.N. Smith, T.D. Anthopoulos, B. Schroeder, Y.H. Geerts, D.A. Fischer, M.F. Toney, J. Am. Chem. Soc. **133** (2011) 15073.

[11] M. Pandey, S. Nagamatsu, S.S. Pandey, S. Hayase, W. Takashima, J. Phys. Conf. Ser. **704** (2016) 12005.

Oral/ Poster/ Either
Presentation session:
Presenter name:

Phase Equilibria Studies of Bismuth Copper Niobate Ternary System

M. P. Chon[a], *K. B. Tan[a], C. C. Khaw[b], Z. Zainal[a], Y. H. Taufiq-Yap[a], S. K. Chen[c] and P.Y. Tan[a]
[a]*Department of Chemistry, Faculty of Science, Universiti Putra Malaysia, 43400 Serdang, Selangor, Malaysia.*
[b]*Department of Mechanical and Material Engineering, Lee Kong Chian Faculty of Engineering and Science, Universiti Tunku Abdul Rahman, 43000 Bandar Sungai Long, Kajang, Selangor, Malaysia.*
[c]*Department of Physics, Faculty of Science, Universiti Putra Malaysia, 43400 Serdang, Selangor, Malaysia.*
**Corresponding author at: Tel.: +603 – 8946 7491; fax: +603 – 8943 5380.*
E-mail address: tankarban@upm.edu.my (K.B. Tan)

Keywords: Pyrochlore; Solid Solution; Ceramics; Solid-state reaction; Phase diagram

[Introduction]

Ternary Bi-pyrochlore systems have captured much research interest owing to their potential applications as high permittivity dielectrics in multilayer capacitors, electronics and devices operating at microwave frequency [1, 2]. The interesting electrical properties found in these systems are attributed to their variable stoichiometry, unique structure and defect. The pyrochlores of chemical formula, $A_2B_2O_6O'$ could generally be categorised into two different types, $A_2^{2+}B_2^{5+}O_6O'$ and $A_2^{3+}B_2^{4+}O_6O'$, respectively [2]. The ternary Bi-pyrochlores found in the Bi_2O_3-MO-N_2O_5 (M = Zn, Cu, Ni, Fe, Mg; N = Ta, Nb, Sb) systems are in fact an averaged type of the latter. The distribution of three different cations of varying ionic radii is best described as $[Bi_{1.5}M(1)_{0.5}][M(2)_{0.5}N_{1.5}]O(1)_6O(2)$; the larger A site is dominated by the eight-fold coordinated Bi cations whereas the smaller N cations would occupy the six-fold coordinated B site together with smaller divalent M cations that distributed over both A and B sites. The overall pyrochlore structure could be portrayed as two interpenetrating $A_2O(2)$ tetrahedral and $B_2O(1)_6$ octahedral frameworks.

It is worthwhile highlighting that structural stability of the complex family of pyrochlores could be controlled by a self-compensating mechanism in composition especially the occupancy of ions at different sites may adjust accordingly. The flexibility of pyrochlore structure is well recognised to allow a wide selection of dopants, defects and/or subsolidus solution formation in series or up to an extent of a broad area. By far, Zn analogues in the bismuth based ternary systems, Bi_2O_3-ZnO-N_2O_5 (N = Ta, Nb and Sb) had been well characterised for their synthesis, electrical properties and the phase compatibilities between various phases in these systems [1-4]. As seen in the Zn-analogues, Bi-pyrochlores containing Nb are preferable to those systems with pentavalent Sb and Ta. This was due to the advantages of having ease of synthesis (lower cost and moderate refractory nature of Nb) and, the resulted phases had relatively higher permittivities and lower dielectric losses. Consequently, various attempts were made to introduce a wide variety of divalent cations into Bi_2O_3-MO-Nb_2O_5 systems at which cation M could be of alkaline earth metals (Mg and Ca) and/or transition divalent metals (Cr, Mn, Fe, Co, Ni, Cu) of the late period 3d elements [3, 4]. This gave rise to numerous new phases in Bi-pyrochlore systems. Given the complicated structure and variable stoichiometry of pyrochlore, a detailed phase diagram study is highly beneficial to gain further insight into the correlation between structure-composition-property of various phases in the Cu-substituted pyrochlore system.

[Experiment]

Over 100 samples in the bismuth copper niobate (BCN) system were prepared by solid-state technique at their optimised consitions. Detailed qualitative and quantitative X-ray analyses were performed for the determination of phase compatibility and phase assemblages over a wide range of compositions in the BCN ternary system. The Gibbs' phase rule approach and disappearing phase method were applied for the construction of BCN ternary phase diagram. The routine X-ray data collection was performed using a Shimadzu X-ray diffractometer coupled with CuKα at a step size of 2° in the 2θ range of 10-70°; whilst, the structural refinements of monophasic BCN pyrochlores were based on the Zn-analogue by *Chekcell* software

using the data collected at a step size of 0.1 °/min. The elemental analyses of single-phase materials were carried out by inductively coupled plasma-optical emission spectrometry (ICP-OES) using a Perkin Elmer Optima 2000DV instrument.

[Result and Discussion]

A complete subsolidus ternary phase diagram of the Bi_2O_3-CuO-Nb_2O_5 (BCN) system was constructed. Careful firing control and phase analysis were applied to determine the phase assemblages and compatibilities over the temperature range 700°C-925°C. Phase-pure BCN pyrochlores were found to crystallise in a cubic symmetry, space group *Fd*3*m*, No. 227 with lattice constants in the range 10.4855 (5) < x < 10.5321 (3). The mechanism of this limited subsolidus series could be represented by a general formula, $Bi_{3.08-x}Cu_{1.84+2x/9}Nb_{3.08+7x/9}O_{14.16+6x/9}$ ($0 \leq x \leq 0.36$) wherein the reduction in Bi content was compensated by a proportion amount of copper and niobium together with non-stoichiometry in oxygen. The solely ternary phase appears in the BCN system is a subsolidus pyrochlore series covering three compositions, 83, 200 and 146, which are located between the two-phase assemblages of pyrochlore-CuO and pyrochlore-$BiNbO_4$, respectively (Fig.1). The locus of the BCN subsolidus pyrochlores is found to be nearly at the centre of the BCN phase diagram, illustrating the compositions with increasing Nb content, i.e. above 37.5 mole %. These values are generally higher than that of ideal pyrochlore with cationic mole % ratio of Bi : Cu : Nb = 37.5 : 25 : 37.5, respectively. The formation mechanism based on composition 83, as the origin, could be proposed with a general formula, $Bi_{3.08-x}Cu_{1.84+2x/9}Nb_{3.08+7x/9}O_{14.16+6x/9}$ ($0 \leq x \leq 0.36$) wherein the reduction of bismuth content is compensated by a proportion amount of copper and niobium together with non-stoichiometry in oxygen. Hence, the overall electroneutrality of the BCN system is prevailed through a chemical equation, $x\ Bi^{3+} \leftrightarrow 2x/9\ Cu^{2+} + 7x/9\ Nb^{5+} + 6x/9\ O^{2-}$. This mechanism is further supported by an almost linear change in the lattice constant for which the Vegard's law is obeyed. The smaller unit cell is probably due to the lower concentration of larger Bi cation by both smaller Nb and Cu cations.

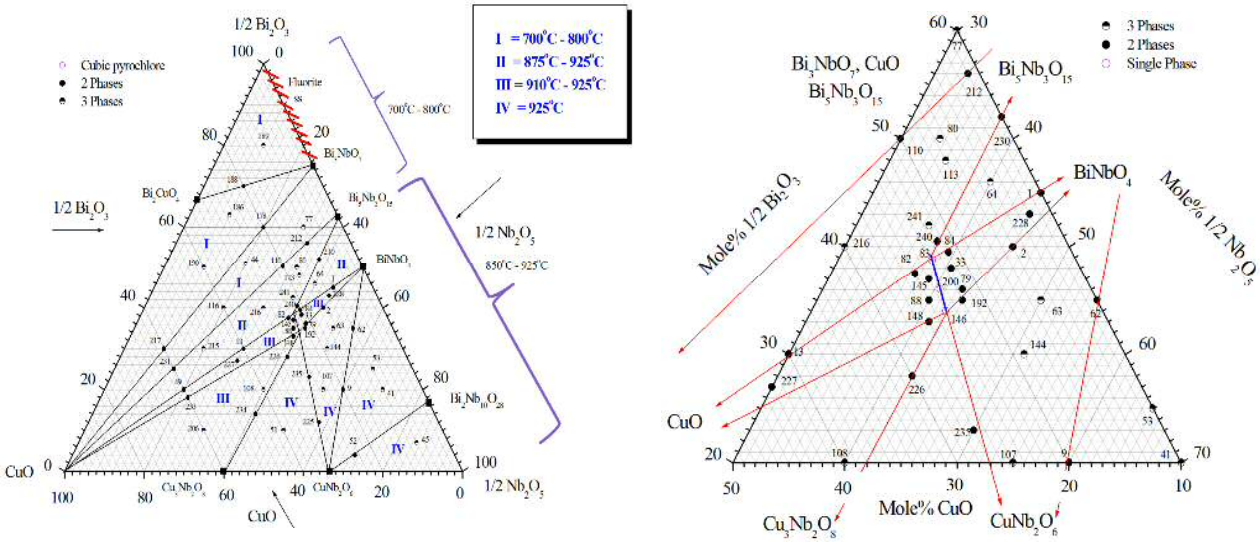

Figure 1: The overall subsolidus ternary phase diagram (left) and the expanded region (right) show the phase compatibility between BCN subsolidus pyrochlore series with other related phases in the BCN ternary system.

[References]

[1] D.P. Cann, C.A. Randall, T.R. Shrout, Investigation of the dielectric properties of bismuth pyrochlores, Solid State Commun. 100 (1996) 529-34.

[2] M.A. Subramanian, G. Aravamudan, G.V. Subba Rao, Oxide pyrochlores: a review, Prog. Solid-State Chem. 15 (1983) 55–143.

[3] M.P. Chon, K.B. Tan, C.C. Khaw Z. Zainal, Y. H. Taufiq-Yap, S.K. Chen and P. Y. Tan, Subsolidus Phase Equilibria and Electrical Properties of Pyrochlores in the Bi_2O_3-CuO-Ta_2O_5 Ternary System, J. Alloy. Compd., 2016, 675, 116-127.

[4] C.C. Khaw, K.B. Tan, C.K. Lee, A.R. West, Phase equilibria and electrical properties of pyrochlore and zirconolite phases in the Bi_2O_3-ZnO-Ta_2O_5 system, J. Eur. Ceram. Soc. 32 (2012) 671-80.

Please choose: Oral
Presentation session: Applied Engineering
Presenter name: Atul S M Tripathi

Utilization of Oriented Conjugated Polymer Film Prepared by ribbon shaped FTM Towards Its Application for Flexible Organic Field Effect Transistor

Atul S M, Tripathi[1], Nikita, Kumari[1], Shuichi, Nagamatsu[2], Shuzi, Hayase[1], Shyam S, Pandey[1]
[1]Graduate School of Life Science and Systems Engineering, Kyushu Institute of Technology, 2-4 Hibikino, Wakamatsu, Kitakyushu 808-0196, Japan
[2]Department of Computer Science and Electronics, Kyushu Institute of Technology, 680-4 Kawazu, Iizuka, 820-8502, Japan

Email: tripathi-atul@edu.life.kyutech.ac.jp

Keywords Floating Film Transfer, Conjugate polymer, Orientation, Flexible transistor, Anisotropy

Introduction:
Recent past has witnessed the rapid growth of conjugated polymers as organic semiconductor for their potential applications in low cost organic electronic devices such as organic field effect transistors (OFETs), organic light emitting diode and solar cells. Conjugated polymers having the one important feature of solution processability make them more valuable for the fabrication of electronic devices on a desired substrate such as plastics, glass, paper and cloths. Presently development of lightweight flexible transistors is in trend and efforts are being directed towards optimization of the dielectric and semiconducting interfaces for improving the charge carrier transport. For deposition of thin film of active semiconducting layer, various techniques have been used. Amongst these technique, most commonly used spin coating, drop cast etc. provide non-oriented and isotropic films. On the other hand, utilization of techniques like mechanical rubbing, friction transfer, solution sharing and roll transfer etc. provide oriented thin films leading to anisotropic charge transport. Although, oriented thin films provide the improved device performances but drawbacks such as mechanical damage, static charge accumulation, solubility inside the layer and bottleneck for multilayer thin film fabrication. To resolve such issues our group have developed the simple and quick method named as floating film transfer method [1]. In order to further solve the existing problems of non-uniformity and multi-directional film spreading, we have recently designed an assisting slider for providing the directionality. This slider based FTM achieved the large area oriented thin films due to film spreading in one direction in the shape of ribbon and this method was named as ribbon-shaped FTM [2,3]. In this work, fabrication and characterization flexible OFETs is being reported where solution processability has been utilized not only to coat the oriented organic semiconductor but also the gate dielectric gate insulator on a flexible plastic substrate.

Experiment:
In this study, we have selected the regioregular poly (3-hexylthiophene) [RR-P3HT] as a representative conjugated polymer for the fabrication of oriented thin film on liquid substrate. For that have taken the optimized thin film fabrication conditions such as casting temperature of 50°C, hydrophobic polymer solution concentration of 2% (w/w) and ethylene glycol and glycerol (3:1) as hydrophilic viscous liquid substrate. The oriented thin films of the polymer were transferred on glass substrate for the optical characterization. This was performed by polarized electronic absorption spectral measurement by utilizing Glan-Thomson polarizing prism. For the charge transport, flexible OFETs were fabricated in the bottom gate top contact (BGTC) device architecture. Oriented film of the semiconducting polymer was transferred on plastic substrate coated with ITO (gate) and Poly(methyl methacrylate) [PMMA] as a dielectric layer. Finally to top source-drain electrodes having channel length (L= 20 µm) and width (W=2 mm) were thermally evaporated using Ni shadow mask. Electrical characterization of OFETs thus fabricated was done with computer controlled two-channel source measure unit (Keithley-2612) at a pressure of 10^{-3} Torr.

Result and Discussion:
We have fabricated large area oriented thin films RR-P3HT of size [20 cm (L) × 2 cm (W)] on liquid substrate by controlling the three important controlling factors such as casting temperature, concentration of polymer solution and viscosity of the liquid substrate [2]. Oriented thin films were transferred on glass substrate for the investigation of orientation in terms of dichroic ratio (DR) calculated by maximum absorbance for parallel

oriented films ($\lambda_{max}\|$) to the absorbance for films with perpendicular orientation ($\lambda_{max}\|$) using the relation (DR= $A_{\|}/A_{\perp}$). The polarized absorption spectra is shown in Fig. 1 along with that of prepared by spin coating for comparison. From the figure it is clear that the oriented film absorption in parallel is, red shifted as compared to that prepared by spin coating and achieved the DR of 2.2 without any post heat treatment.

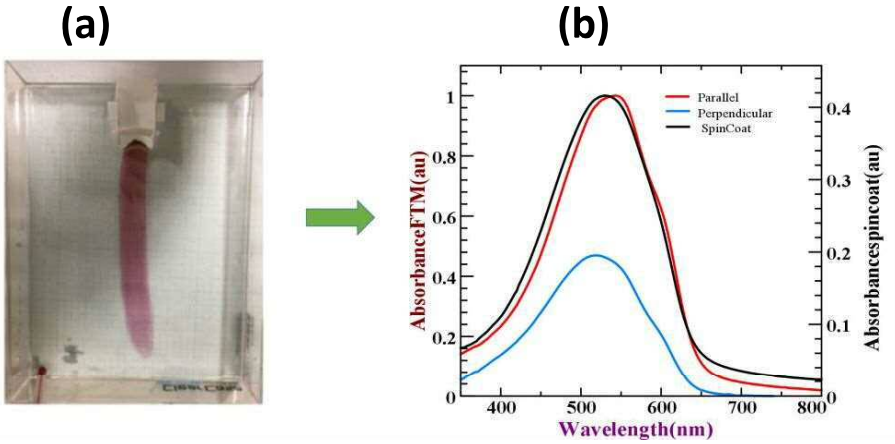

Figure 1. Large area RR-P3HT oriented thin film prepared by ribbon-shape FTM (a) and normalized absorption spectra of the parallel oriented and spin coated films (b).

Main aim of this work was to fabricate the flexible OFETs of oriented film of conjugated polymer on plastic substrate for investigation of anisotropic charge transport by controlling the dielectric layer thickness and insulation properties. In this work, we selected the BGTC device architecture for the OFET fabrication utilizing bottom ITO as a gate and top gold as source and drain electrodes. The oriented film of RR-P3HT acts as an organic semiconducting layer on the PMMA gate dielectric layer shown in the Fig. 2. The oriented films were successfully transferred on the plastic substrate and achieved the charge carrier mobility in the range of 1×10^{-2} Cm^2/Vs. Detailed discussion of optimization of oriented polymer film as well as dielectric layer along with anisotropic charge transport will be discussed.

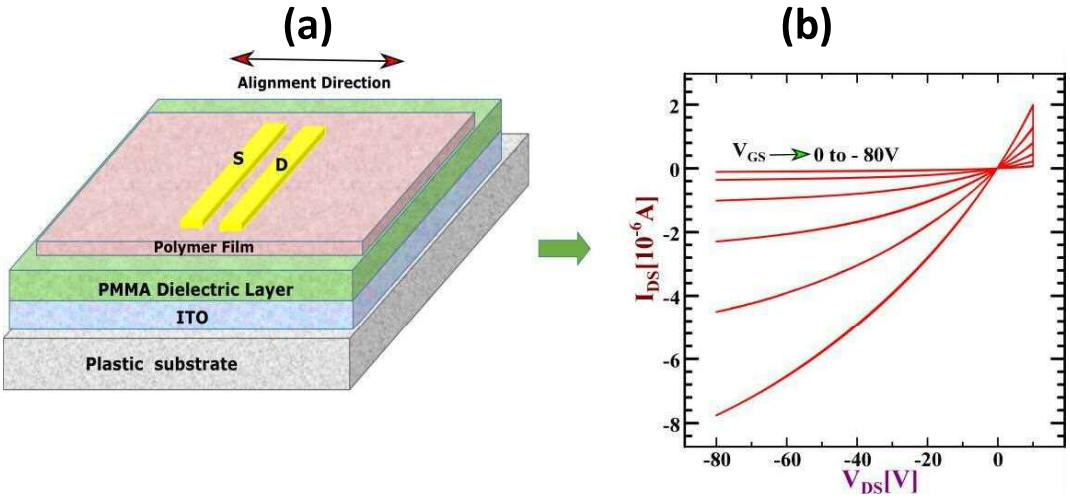

Figure 2. Device architecture (a) output characteristics of oriented film of regio-regular P3HT in parallel (b)

References:

1. T. Morita, V. Singh, S. Nagamatsu, S. Oku, W. Takashima, K. Kaneto, Appl. Phys. Express **2** (2009) 111502.
2. A. Tripathi, M Pandey, S Nagamatsu ,S.S Pandey , S. Hayase and W. Takashima, IOP Conf. Series: Journal of Physics: Conf. Series **924** (2017) 012014.
3. A.S. M. Tripathi, M. Pandey, S. Sadakata, S. Nagamatsu, W. Takashima, S. Hayase and S.S. Pandey, Appl. Phys. Lett. **112** (2018) 123301.

Synthesis of Blue Sensitizers for Cobalt Redox Shuttle based Dye Sensitized Solar Cells

Anusha Pradhan, Shuzi Hayase and Shyam S. Pandey

Graduate School of Life Science and Systems Engineering, Kyushu Institute of Technology, 2-4, Hibikino, Wakamatsu, Kitakyushu, Japan

ansupradhan9@gmail.com

Keywords: Near Infrared Dye, Cobalt electrolyte, wide wavelength photon harvesting, surface passivation, driving force.

1. Introduction: Since the pioneering work of Graetzel and O`Regan in 1991, dye sensitized solar cells (DSSCs) have attracted mammoth attention in the field of converting light into electrical energy, which mimics the natural photosynthesis. This solar cell is, not only green for the environment but also the ease of fabrication and low cost demands it highly for the next generation solar cell. Dyes play the vital role in the photon harvesting, which is in fact directly related to the current density of the device. However, still the two-decade research have only been successful in the design of the visible dye suitable for the operation of the solar cell. Maximum photon flux of the solar spectrum falls in the near infrared region (NIR), the dyes absorbing in this region will be able to furnish more current density. Although, record efficiency of the Dye Sensitized Solar Cell of ~14% has already reached with visible dyes, therefore, there are plenty of rooms to enhance the current if the designed sensitizers would be able to harvest the NIR photons. Nevertheless, on photon absorption, the dye excites to its higher energy level, which is then regenerated by the electrolyte. Therefore the electrolyte also plays a crucial role in the performance. Moreover, the open circuit voltage (Voc) is given by the difference of the fermi of electron on TiO_2 and the redox potential of the electrolyte. Therefore, the electrolyte with deeper redox potential will be furnishing more Voc. To meet this criteria, cobalt based redox shuttle have been widely used. However, the bulky nature of it and low ionic diffusion owing to mass transport credentials demand a strict need of surface passivation at the dye level as well with metal oxide compact layer to inhibit the back electron transfer. Moreover, the condition that the highest occupied molecular orbital energy level should be lower than the redox potential of the electrolyte for efficient dye regeneration, which was taken in to consideration while design of novel NIR dye in my work. In this work, we have synthesized novel blue and green dyes as sensitizers for cobalt redox shuttle of which cobalt bipyridyl complex has been the choice for DSSCs. A series of squaraine dyes with the electron donating indole moiety bearing a direct –COOH group but various alkyl substitution at the N position was synthesized and used as sensitizers for DSSCs using cobalt electrolyte.

2. Experiment:

2.1 Synthesis of intermediates: The required indole group was synthesized following the Fisher indole synthesis, which was then subjected to alkylation at the N position of it. To differ in the alkyl chain, various reagent with alkyl bromide or alkyl iodide was chosen. The alkylation was carried out taking the indole moiety, alkylating agent and a proper solvent (acetonitrile for shorter chain and propionitrile for longer chain alkyl group) and then refluxed. Once the TLC showed the completion of the reaction (around 48 hours), the solvent was evaporated completely. To it, ample amount of diethyl ether was added for precipitation. The subject was then filtered to afford brownish pink solid as the N substituted indole.

2.2 Synthesis of Semi Squaraine ester: The required N substituted indole was made to react with diethoxy squarate in trimethylamine with ethanol as the solvent under reflux condition for around 8 hours. The

solvent was then completely evaporated and the crude was subjected to flash column chromatography (hexane and ethanol system) to give a fluorescent yellow compound. The obtained yellow semi squaraine ester was hydrolyzed with 40% NaOH in ethanol for about 30 minutes. It was then neutralized with conc. HCl and then extracted in ethyl acetate to give a red solid compound. To enhance the absorption in the higher wavelength, the obtained semi squaraine ester was reacted with ethyl cyano acetate or malononitrile to substitute the oxygen of the square with the respective conjugated group.

2.3 Synthesis of Squaraine dye: The obtained red semi squaraine and the other indole moiety was made to reflux in toluene and n butanol azeotrope (1:1) for 18 hours. The solvent was then evaporated and the crude was subjected to flash column in chloroform/methanol system to afford a bright royal blue solid compound in good yield.

2.4 Fabrication of Dye sensitized solar cell: The 1 cm x 2 cm cut FTO substrate was subjected to thorough cleaning with detergent, distilled water, acetone and isopropanol. After ozone plasma treatment of them, they were dipped in 40 mM $TiCl_4$ at 70^0C for 30 minutes followed by sintering at 450^0C for 30 minutes to afford a compact layer of TiO_2. Then they were coated with the commercial TiO_2 paste via screen printing to afford the desired thickness of the mesoporous TiO_2 followed by sintering at 450^0C. They were then subjected to $TiCl_4$ treatment again as mentioned above. The substrates were then dipped in 0.2 mM squaraine dye containing 4 mM of CDCA as coadsorber for 4 hours. After fine rinsing, the dye bearing FTO and the platinum counter electrode were affixed with 25 µm surlyn spacer for the electrolyte injection and finally sealed with UV active resin.

3. Results and Discussion: The synthesized squaraine dye had a strong and sharp absorption in the far-red region around 660 nm. The dye bearing the malononitrile and ethyl cyano acetate even resulted in the red shift with absorption at 690 nm for SQ-133. In the energy level, the dye SQ-75 with a minimum energy barrier of 0.15 eV for dye regeneration was also profoundly working with cobalt electrolyte as shown in terms of its short circuit current density. As our main aim and approach was to synthesize NIR dye for cobalt electrolyte, multiple branched alkyl chain bearing squaraine dye was synthesized like in SQ-110 to promote surface passivation in the dye level. For cobalt electrolyte, it was also found that the passivation with compact titania is must to control recombination. As squaraine dyes have absorption only in the far-red region, a complementary visible dye D-35 was used in an optimum ratio with it to result in a wide wavelength photon harvest and a good photoconversion efficiency. Surface passivation with various metal oxide on the mesoporous TiO_2 for the dye cocktail not only resulted in high current density but also an enhanced Voc which is a sign of inhibition in recombination.

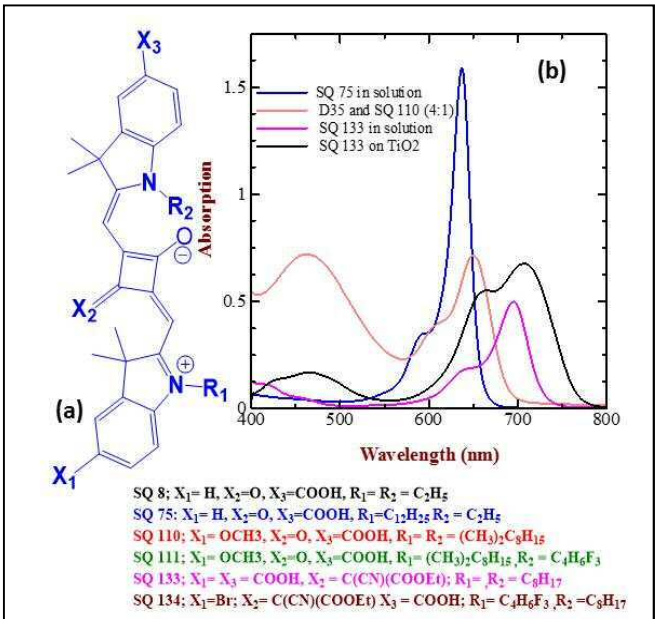

Figure 1. Structure of Squaraine dyes used in this work (a) and electronic absorption spectra dyes in the ethanol solution (b).

Please choose: Oral
Presentation session:
Presenter name:

PHYSICOCHEMICAL PROPERTIES OF DRIED POMELO WASTE (*Citrus Grandis* L. Osbeck)

Rahman, N.F.A. [1], Shamsudin R. [1,2,*], A. Ismail[3], N.N.A.K. Shah[1], J. Varith[4]

[1]Department of Process and Food Engineering, Faculty of Engineering, Universiti Putra Malaysia, 43400 UPM Serdang, Selangor, Malaysia

[2]Halal Science Research Laboratory, Halal Products Research Institutes, Universiti Putra Malaysia, 43400 UPM Serdang, Selangor, Malaysia

[3]Department of Nutrition and Dietetics, Faculty of Medicine and Health Sciences, Universiti Putra Malaysia, 43400 UPM Serdang, Selangor, Malaysia

[4] Division of Food Engineering, Faculty of Engineering and Agro-Industry, Maejo University, Chiang Mai, Thailand

*Email: rosnahs@upm.edu.my

ABSTRACT

The present study was carried out to compare the physicochemical properties of different parts of dried pomelo waste. Pomelo waste involved in this research were flavedo (exocarp), albedo (endocarp), lamella (cover pulp) and pomace (pulp waste). Physicochemical properties particularly nutritional composition can be further utilize in producing livestock feed. The samples were dried using conventional oven dryer (50°C) for 24 hours. Proximate analysis showed variation of the nutritional composition value between different parts of pomelo waste. Flavedo showed higher protein (11.64%) and fat (1.27%) content, lamella showed greater crude fibre (14.83%) content, while pulp waste showed higher ash (10.65%) composition and lastly albedo showed higher carbohydrate content (71.42%). Different parts showed significant value in particular nutritional composition which can be potential source in functional food ingredients or livestock feed.

INTRODUCTION

The largest kind of citrus fruits is known as pomelo (*Citrus grandis* (L.) osbeck). In Malaysia, pomelo also known as limau bali, limau jambua, limau abong, limau betawi, limau besar, limau bol, or Bali lemon (Toh et al., 2013). Tambun (PO51), Sha Thing (PO51), and KK2 (Melo Mas) are among the popular varieties of popular fruits in Malaysia (Shah et al., 2014). The fruits commonly consumed freshly which leads to buildup of significant waste. This is because ~50% of the fruits weight was considered as wastes (Shamsudin et al., 2015). Handling waste operation increase the cost labor, exploit extensive place and hence leads to environmental pollution. Currently, pomelo wastes were found contain a potential source of dietary fibre (Zain et al., 2014) and natural antioxidants (Rahman et al., 2018). Nevertheless, limited studies was found on physicochemical properties particularly on nutritional compound of dried pomelo wastes (flavedo, albedo, lamella and pomace). Therefore, in current study, proximate analysis was conducted to determine the nutritional content in each different parts of pomelo wastes.

MATERIALS AND METHODS

Most cultivated and consumed variety of pomelo in Malaysia known as P052 Tambun White (*Citrus grandis*) was used in this study. Selection of fruits was based on the uniformity if size, color and commercial maturity stage taken from a commercial orchard in Tambun, Perak. The fruits were washed and manually separate the peels into 4 different parts known as flavedo (green color exocarp), albedo (whitish color endocarp), lamella (peel covers the pulp) and pomace was obtained after juice extraction process. Then, the peels were subjected to the drying treatment at 50°C for 24 hour in an oven (DO6836, Memmert, Germany). The proximate composition (moisture, ash, protein, lipid and fiber) of dried pomelo residues were determined using AOAC (1995) method. Each analysis was performed in triplicate and the results were expressed as the mean ± standard deviations. Statistical analysis was performed using SPSS Statistics 21.0. Data were analyzed using one-way ANOVA followed by Duncan's test. The confidence limits are based on 95% ($p < 0.05$).

RESULTS AND DISCUSSIONS

The results of the proximate analysis of dried pomelo waste are presented in Tables 1.

Table 1. Proximate analysis of dried pomelo waste using air oven drying method at 50°C

Analysis/ Parts of byproducts	Pomelo, raw*	Flavedo	Albedo	Lamella	Pulp waste
Moisture content (%)	88.40	10.18 ± 0.59^{a}	6.53 ± 0.55^{b}	5.85 ± 0.37^{b}	10.07 ± 0.63^{a}
Ash content (%)	0.50	6.45 ± 0.21^{b}	4.60 ± 0.14^{c}	3.65 ± 0.21^{d}	**10.65** ± 0.35^{a}
Protein content (%)	0.60	**11.64** ± 0.01^{a}	6.18 ± 0.03^{d}	6.74 ± 0.08^{c}	10.47 ± 0.11^{b}
Fat content (%)	0.20	**1.27** ± 0.25^{a}	0.20 ± 0.10^{d}	0.47 ± 0.06^{c}	0.73 ± 0.06^{b}
Crude fibre content (%)	0.70	**14.10** ± 1.90^{a}	11.07 ± 0.12^{b}	**14.83** ± 1.55^{a}	8.00 ± 0.35^{c}
Carbohydrate content (%)	9.60	56.34 ± 2.43	**71.42 ± 0.49**	68.44 ±1.59	60.13 ±1.03

The values indicate mean ± standard deviation from three replications. Values within the same row with similar letters are not significantly different (p >0.05).
*Puwastien et al. (2014) - Result presented for fresh pomelo

In brief, dried pomelo waste (flavedo, albedo, lamella and pulp waste) consisted of lower moisture content (MC) (5.85 - 10.18%) compared to raw pomelo (88.40%). Evaporation of moisture occurred and simultaneously reducing the MC from the sample. In addition, dried pulp waste showed the highest percentage 10.65% of ash content, followed by dried flavedo (6.45%), dried albedo (4.60%) and dried lamella (3.65 ± 0.21%). In general, dried pulp waste shows the highest content of mineral compared to other dried pomelo residues and has a potential of functional food. The protein content of the dried flavedo (11.64 %) showed significantly highest (p <0.05) value followed by dried pulp waste (10.47%), dried lamella (6.74%) and dried albedo (6.18 %). Meanwhile, for fat content of dried flavedo shows the highest percentage (1.27%) compared to pulp waste (0.73%), lamella (0.47%) and albedo (0.20%).This is consistent with the essential oil discovered in the previous study (Chaiyana et al., 2014). Dried lamella and flavedo possesses significantly higher crude fibre content (14.83%) than other parts of pomelo waste. This could be one of the potential sources of pectin, as pectin composed various chains of polysaccharides.

CONCLUSION

Different parts of dried pomelo waste possessed significant value of particular nutritional composition. The highest protein (11.64%) and fat (1.27%) content were discovered in dried flavedo whereby these composition is highly beneficial for human growth and retains and maintaining the texture, flavor and pigments of the fruits. Dried pomace shows the highest content of minerals (10.65%) and it is highly potential to be utilized as a functional foods as food ingredient. As for crude fibre content, dried lamella and flavedo shows high crude fibre content (14.83% and 14.10% respectively) which can be potentially becoming one of the sources of pectin in food application. Lastly, greater carbohydrate (71.42%) content was found in albedo which can be used as a natural alternative source of sugars. Thus, proving the advantages of re-using pomelo wastes in various food and health application.

ACKNOWLEDGEMENT

The authors would like to gratefully acknowledge the financial and technical support from Ministry of Higher Education of Malaysia under the Fundamental Research Grant Scheme (03-01-14-1412FR) and Universiti Putra Malaysia.

REFERENCES

Puwastien, P., Burlingame, B., Raroengwichit, M., and Sungpuag, P. (2014). *ASEAN Food Composition Database*. Electronic version 1, February 2014, Thailand. Institute of Nutrition, Mahidol University http://www.inmu.mahidol.ac.th/aseanfoods/composition_data.html

Association of Official Analytical Chemists (AOAC).(1995). Official Methods of Analysis, 16th ed., AOAC: Arlington VA, USA

Chaiyana, W., Phongpradist, R., and Leelapornpisid, P. (2014). Characterization of hydrodistillated pomelo peel oil and the enhancement of biological activities using microemulsion formulations. *International Journal of Pharmacy and Pharmaceutical Sciences*, 6(9), 596-602.

Chang, S.Q., and Azrina, A. (2017). Antioxidant content and activity in different parts of Pomelo (*Citrus grandis* (L.) Osbeck) by-Products. *Acta Horticulturae* 1152, 27–34.

Rahman, N. F. A., Shamsudin, R., Ismail, A., Shah, N. N. A. K. and Varith J. (2018). Effect of drying methods on antioxidant properties of pomelo peels. *Innovative Food Science and Emerging Technologies*. 50, 217-225

Shah, N. N. A. K., Rahman, R. A., Shamsuddin, R. and Adzahan, N.M. (2014). Effects of pectinase clarification treatment on phenolic compounds of pummelo (*Citrus grandis* L. Osbeck) fruit juice. *Journal of Food Science and Technology* 52(8), 5057–65

Shamsudin, R., Buang, S., and Aziz, N. A. (2015). Effect of Different Extraction Methods on the Physico- chemical Properties of Pomelo Juice, *Chemical Engineering Transactions,* 44, 265–270.

Toh, J.J., Khoo, H.E., and Azrina, A. (2013). Comparison of antioxidant properties of Pomelo (*Citrus grandis* (L .) Osbeck) varieties. *International Food Research Journal* 20(4), 1661–68.

Zain, N.F.M., Yusop S.M. and Ahmad I. (2014). Preparation and characterization of cellulose and nanocellulose from Pomelo (*Citrus grandis*) Albedo. *Journal Nutrition Food Science.* 5, 334-337.

Please choose: ~~Oral~~/ ~~Poster~~/ Either
Presentation session:
Presenter name: Mohd Nizar Hamidon

[A quick and effective functionalization of carbon nanotubes for pressure sensing applications]

[Saman, Azhari][2], [Mohd Nizar, Hamidon][1,2], [Muhd asnawi, Kusaimi][2], [Intan Helina, Hasan][2], [Alin, Azhari][2]

[1]Faculty of Engineering, University Putra Malaysia, 43400 UPM Serdang, Selangor, Malaysia
[2]Institute of Advanced Technology (ITMA), University Putra Malaysia, 43400 UPM Serdang, Selangor, Malaysia

Email: [Samanar@gmail.com]

Keywords (CNTs, Functionalization, PDMS, H_2SO_4, H_2O_2)

[Introduction]
In recent years as a result of technological advancements, the growth rate in all fields of applied science have been extraordinary. As a result materials such as carbon nanotubes (CNTs) and graphene have been introduced. Carbon nanomaterials are increasingly getting more attention considering their properties which allows them to be exploited in various applications. In the past couple of decades the uses of CNTs in various polymeric materials have been studied by various groups for variety of applications; in fact nanocomposites are the ever growing field. Nonetheless utilizing CNTs is still a challenging task due to van der Waals forces, 1D morphology, hydrophobicity and aspect ratio that results in aggregation and agglomeration of these wonder material. To overcome such challenges researchers have proposed various methods and techniques such as, chemical functionalization, use of ionic liquids or surfactants.
Polydimethylsiloxane (PDMS) is one of the many polymers that is being extensively studied. It is of an interest to this research due to its low Young's modulus. Since pressure is the outcome of applied force over area, to devise a sensor in low pressure range with high sensitivity, PDMS is favorable. CNTs/PDMS nanocomposite is one the many approaches that is being taken to devise a low range pressure sensor. CNTs behave as Piezoresistive materials due to their high gauge factor which is why they may be an ideal material to replace the conventional strain gauges and in our case to detect smallest deformations as a result of applied pressure.
To fabricate CNTs/PDMS sensor many approaches have been taken by various groups but one of the most important factors to devise such a device is the homogeneous dispersion of CNTs in polymer without agglomeration and aggregation. To overcome these issues and improve the dispersion of CNTs in PDMS hydroxyl and carboxyl functionalization of CNTs is performed. This will enable CNTs and PDMS to form a chemical bond which in return improves the response, sensitivity and repeatability of the sensor.
[Experiment]
At first piranha solution of sulfuric acid (Sigma Aldrich) and hydrogen peroxide (Sigma Aldrich) with the ratio of 4:1 were prepared. 1 gram of CNTs (NTP) were dispersed in the solution and then sonicated for 3 hours. The slurry were then diluted with distilled water and kept for overnight; CNTs form agglomerate and sediment in this step. The solution was then filtered using vacuum filtration and PTFE membrane filters. The CNTs were then further washed and filtered with distilled water until pH 7 reached. The sample was then placed in the oven and dried at 80 ^{o}C overnight.
[Result and Discussion]
Raman data of for each sample was recorded at three different point. The results display a more consistent G band in comparison with as purchased CNTs which could mean that via this treatment defective sites are completely oxidized which in return results in more consistent G band. The I_D/I_G ratio was calculated after averaging the three recorded data for each sample; this ratio was 0.954 for prepared sample and 0.944 for as purchased CNTs. This indicates a slight increase in disordered graphitic structure as a result of functionalization although the increase in I_{2D}/I_G from 0.454 (as

purchased) to 0.471 (prepared sample) signifies improvements in crystalline honeycomb lattice of CNTs. Fourier Transfer infrared (FTIR) data suggest the formation of carbonyl (1714-1740 cm^{-1}) and hydroxyl (3442 cm^{-1}) groups on the surface of CNTs in addition to aliphatic group (2856 - 2914 cm^{-1}) and other oxygen containing functional groups. Multiple weak peaks from 1800 - 2800 cm^{-1} appear in recorded FTIR result which indicates the effect of oxidative treatment and confirms the presence of aldehyde and carboxyl groups. The Thermal gravimetric analysis (TGA) was performed to confirm the oxidative effect of treatment. Thermal oxidation under oxygen rich atmosphere was recorded from 30 – 610 °C. TG curve of the prepared sample displays multiple weight loss as a result of attachments of various functional groups. Based on TGA results we could conclude that hydroxyl (2 wt% loss below 200 °C), carboxyl (2 wt% loss 200-300 °C) and carbonyl (5 wt% loss 300-500 °C) groups are attached to the surface of the CNTs. These data suggest that via this method the OH functional groups are attached to the surface of the CNTs while oxidation of carbon structures are taking place, on another note we could conclude that this method is an effective method since the amorphous structures tend to oxidized quicker than the crystalline honeycomb lattice of CNTs which is greatly preferred. We may also conclude that this is the preferred method since the attached functional groups are necessary in order for CNTs to form chemical bonds with PDMS. The TGA result suggest that in addition to functionalization this method could purify the CNTs of catalyst particles but the purification is not as effective as other reported methods.

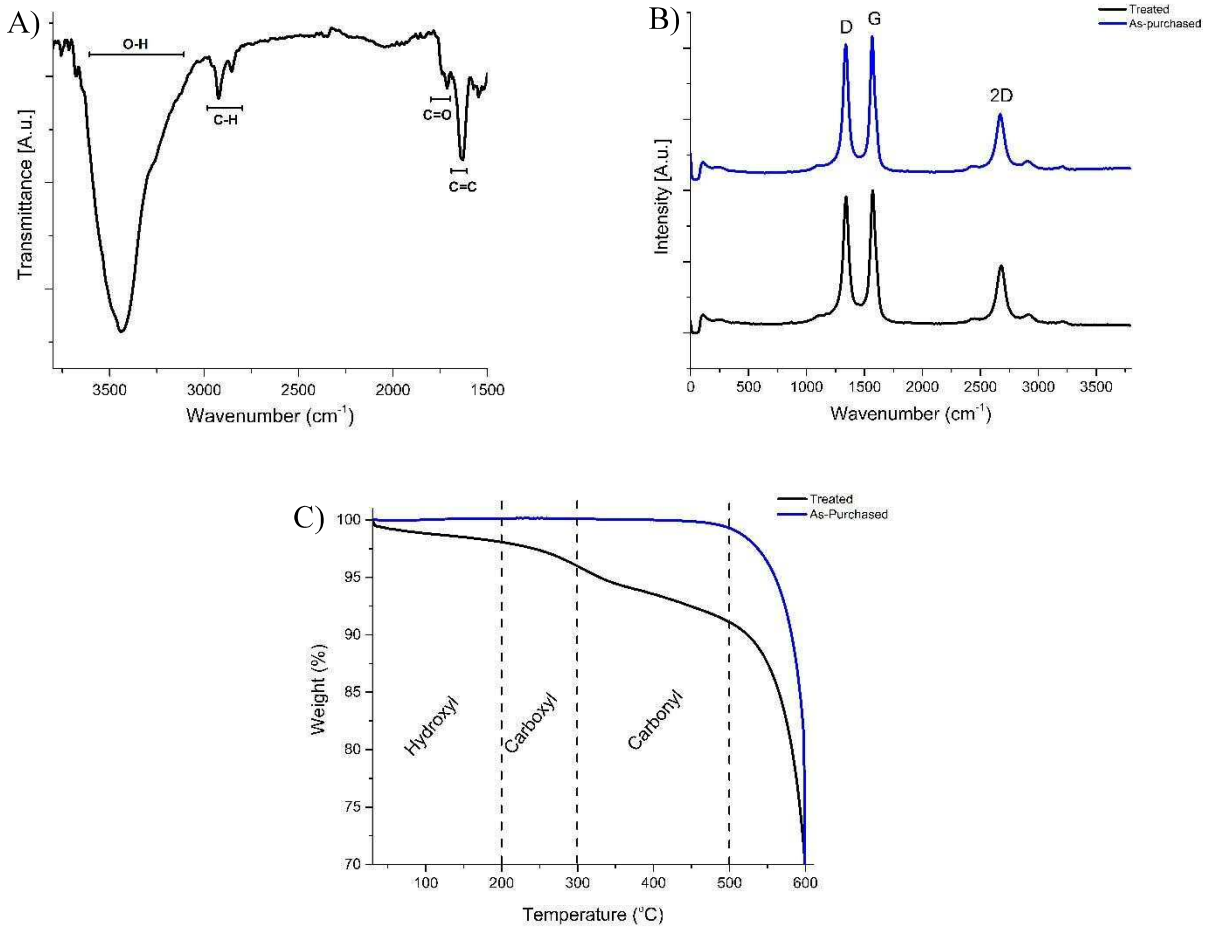

Figure A) Raman spectrum of treated and as purchased sample; B) FTIR spectrum of treated sample; C) TGA results of treated and as purchased sample

Please choose: Oral/ ~~Poster~~
Presentation session:
Presenter name: Suhaidi Shafie

[Dye Sensitized Solar Cell utilizing Nitrogen Doped Plasmonic Photo-anode for Power Conversion Efficiency Enhancement]

[Suhaidi, Shafie][1, 2],[Samaila, Buda][2], [Ali Khalifa, Abdulgalil][1], [Suraya, Abdul Rashid][1, 2], [Haslina, Jaafar][1, 2]

[1]Faculty of Engineering, University Putra Malaysia, 43400 UPM Serdang, Selangor, Malaysia
[3]Institute of Advanced Technology, University Putra Malaysia, 43400 UPM Serdang, Selangor, Malaysia

Email: suhaidi@upm.edu.my

Abstract
This paper discuss the dye-sensitized solar cell power conversion efficiency enhancement through improvement of light absorption as well as carrier transport in the photoanode. Synthesis of nitrogen-doped TiO_2 nanoparticle with a suitable band gap for improved light absorption in dye-sensitized solar cell, as well as silver nanoparticles (AgNP) with optimum particle size and percentage was carried out and utilize its surface plasmon effect for improved performance of DSSC. Mathematical models that optimize nitrogen concentration, AgNP concentration, film thickness and dye-loading for maximum charge collection efficiency and power conversion efficiency of the DSSC was developed.

Keywords
Dye Sensitized Solar Cell, Plasmonic Solar Cell, Nitrogen doped, Renewable Energy

[Introduction]
Solar energy generation become important today due to high energy demand since carbon based fuels contribute to greenhouse effect that increase the global temperature. In recent years, commercially available silicon and thin film solar cell dominate solar cell market due to its high efficiency and stability. Nevertheless the third generation solar cell namely Dye-sensitized solar cells (DSSCs) have attracted considerable attention due to its advantages such as of low production cost, non-toxic material and simple fabrication process. However, more effort is needed to enhance the DSSC overall efficiency toward commercialization. DSSC highest efficiency reported by Sharp Corporation in 2016 was 11.9% using Balck Dye as synthesizer and Cobalt electrolyte as hole transport material.Then, recently, certified 14.1% and even certified 17.9% PCE have been achieved by replacing the dye with a hybrid organic/inorganic lead halide perovskite absorber and the liquid electrolyte by a solid hole transporting material (HTM) giving birth to a new technology called perovskite solar cells, for which progresses are remarkably fast.

[Experiment]
In this session, we will discuss on how to enhance power conversion efficiency of dye-sensitized solar cell through improvement of light absorption as well as carrier transport in the photoanode.Synthesis of nitrogen-doped TiO_2 nanoparticle with a suitable band gap for improved light absorption in dye-sensitized solar cell, as well as silver nanoparticles (AgNP) with optimum particle size and percentage was carried out and utilize its surface plasmon effect for improved performance of DSSC. Mathematical models that optimize nitrogen concentration, AgNP concentration, film thickness and dye-loading for maximum charge collection efficiency and power conversion efficiency of the DSSC was developed.The nanocomposite with different amount of Ag were prepared by chemical reduction method using $AgNO_3$ as precursor.

[Results and Discussion]

The incorporation of Ag onto the TiO_2 has considerably improved the absorption in the visible region of solar spectrum due to the surface plasmon effect by silver nanoparticles. The Photoluminescence spectroscopy

showed a decrease in the electron-hole recombination in the photoanode as a result of Ag acting as an electron sink. Transmission Electron Microscopic images showed a uniform distribution of Ag nanoparticle of sizes between 6-10nm on the TiO_2 surface. Then, a reduction of TiO_2 bandgap which ensures visible light absorption of the semiconductor was realized upon doping with nitrogen. Table 1 summarized the measurement I-V results of various type of DSSC. The nitrogen doped plasmonic DSSC shows the highest current, volatge and fill factor, therefore it has the highest efficiency. The optimisation study for the charge collection efficiency and power conversion efficiency for the nitrogen doped plasmonic DSSC by using Response Surface Methodology has shown that the optimum charge collection efficiency of 61% and power conversion efficiency 8.02% was achieved at the targeted value of 15mL of Nitrogen, 5wt% of silver nanoparticles, 10µm of film thickness and 18 hours of dye loading time.

Table 1. Current-voltage characteristics of N-TiO_2/Ag based DSSC

Photoanode	**J_{sc} ($mAcm^{-2}$)**	**V_{oc} (V)**	**J_{max} ($mAcm^{-2}$)**	**V_{max} (V)**	**FF**	**η (%)**
TiO_2	9.69	0.69	8.79	0.5	0.66	4.40
N-TiO_2	13.6	0.68	12	0.52	0.67	6.24
TiO_2/Ag	13.86	0.72	11.5	0.57	0.66	6.56
N-TiO_2/Ag	14.92	0.73	13.89	0.58	0.74	8.02

Please choose: Oral/ Poster
Presentation session: Invited Speaker
Presenter name: Prof. Dr. Robiah Yunus

Graphene as rheology optimizer and filtrate reducer for ester-based drilling fluid

[Siti Zulaika, Razali][1], [Robiah, Yunus][1,2], [Suraya, Abdul Rashid][1,2], [Janet, Lim][1,3], [Badrul Hisham, Mohamad Jan][4] [Niloofar, Arsanjani][5]

[1]Institute of Advanced Technology, University Putra Malaysia, 43400 UPM Serdang, Selangor, Malaysia
[2]Faculty of Engineering, University Putra Malaysia, 43400 UPM Serdang, Selangor, Malaysia
[3]Faculty of Science, University Putra Malaysia, 43400 UPM Serdang, Selangor, Malaysia
[4]Faculty of Engineering, University of Malaya, 50603 Kuala Lumpur, Malaysia
[5]Global Research and Technology Centre of Scomi Oiltools Sdn. Bhd., 40105, Selangor, Malaysia

Email: robiah@upm.edu.my

Abstract
The idea of pushing the limits of drilling oil and gas wells in deepwater and ultra-deepwater with sensitive marine ecosystem by improving environmental properties of drilling fluids is very crucial particularly to fulfill certain functional tasks. The oil producers are currently looking for a cost efficient drilling operations. Hence, most researches on exploration and drilling are now focusing on the wonders of nanotechnology in the drilling fluids which forms the basis of the work presented here. Ester with improved properties such as reduced viscosity, low pour point, high flash point and good thermal and hydrolytic stability has been synthesized by using vacuum-assisted pulsed looped reactor. Ester-based drilling fluid (EBDF) then were prepared according to standard API 13B-2. Five different concentration of graphene have been used to investigate its effect on EBDF. Results showed that the incorporation of graphene in drilling fluid has improved the plastic viscosity by 11% while maintaining a good yield point, low-shear-stress yield point and gel strength. As for filtrate reducer, filtration loss reduced by 18% and cake thickness has been reduced by 43%.

Keywords (drilling fluid, ester, rheology modifier, graphene, deepwater)

Introduction

Changing economics and the exhaustion of some shallow offshore resources have led producers to deepwater and ultra-deepwater operations. Diesel-based drilling fluid which failed to comply with stringent environment regulations has encouraged the development of synthetic-based drilling fluid. Ester is known as the best biodegradable synthetic-based fluid. Nevertheless, some drawbacks of esters such as high kinematic viscosity, has a poor thermal stability, high pour point, and prone to hydrolysis limit its applications in ultra deepwater. Current EBDF is able to withstand temperature up to 320 °F (160 °C). This work investigates the effect of incorporation of graphene into EBDF at 360 °F and 500 psi.

Experiment

The ester was synthesized by a reaction between coconut oil-based methyl ester and 2-Ethylhexanol in a vacuum-assisted pulsed loop reactor. The mixture was then heated to the reaction temperature followed by the addition of catalyst. The reaction was carried out in 20 minutes under 10mbar. The product was collected and cooled down before filtered to remove soaps. Subsequently, purification of ester was done by vacuum distillation.

The invert-emulsion EBDF was prepared by mixing ester, emulsifiers, organophilic clay, synthetic copolymer, lime, brine (25% $CaCl^2$ in water), and barite, using Hamilton Beach Fann mixer. The mud weight was 1977 kg/m3 (16.5 lb./gal), the specific gravity was 1.98, and the oil-water ratio was 85:15. Next, various concentrations of graphene powder were added to the prepared EBDF (0.001%, 0.004%, 0.007%, 0.01% and 0.014% wt/wt respectively, i.e., 0.001% means 0.01 gm of graphene was added

into 693 gm of the mud sample). All the mud samples were aged in a hot rolling oven at 182 °C for 16 h to simulate the circulation of drilling mud through the hole under the actual drilling conditions. The properties of ester-based drilling fluids with various concentration of graphene were carried out by measuring the properties of rheology and high-pressure high-temperature (HPHT) filtration according to the API 13B-2 standard. The rheological properties such as plastic viscosity (PV), yield point (YP), gel strength and low shear rate-yield point were measured before and after hot rolling at a standard temperature of 120 °F (48.8 °C) using a rotational viscometer Fann Model 35.

Results and Discussion

The synthesized ester has some outstanding properties namely low kinematic viscosity, low pour point, high flash point, and acceptable thermal and hydrolytic stability. These properties are suitable for the formulation of ester-based drilling fluid for deepwater and ultra-deepwater drilling operations. Fig. 1 (a) shows a temperature control effect by mud samples containing graphene. The PV and YP decrease with increase of graphene concentration in the muds. PV shows a reduction by 11%. This indicates that the graphene is interacted well and dispersed homogenously in the mud, thus making the mud less viscous when compared to the base mud after 16 hrs of aging at 182 °C. The critical value of graphene concentration is 0.007 wt/wt% (Fig. a). Any value higher than this weight percent does not improve the EBDF. The magnitude of low shear stress at low shear rate (6 and 3 rpm) is more important to observe mud's suspension ability, hole cleaning capability and mud sagging. Overall, addition of graphene in EBDF has reduced the low-shear-rate yield by 10-20% (Fig. 1b). However, this reduction is still manageable and will not lead to barite sagging. Increasing gel strength of EBDF with graphene is a good indicator for better suspension of drill cuttings at static condition when drilling operation is halted. However too high of gel strength may require bigger force to break the gel (Fig. 1c). Fig. 1d depicts an improvement of HPHT filtration properties of EBDF containing graphene. The filtrates loss and cake thickness were reduced by 18% and 43% respectively. Overall, the addition of almost negligible concentration of graphene has shown improvement in the properties of EBDF in HPHT condition.

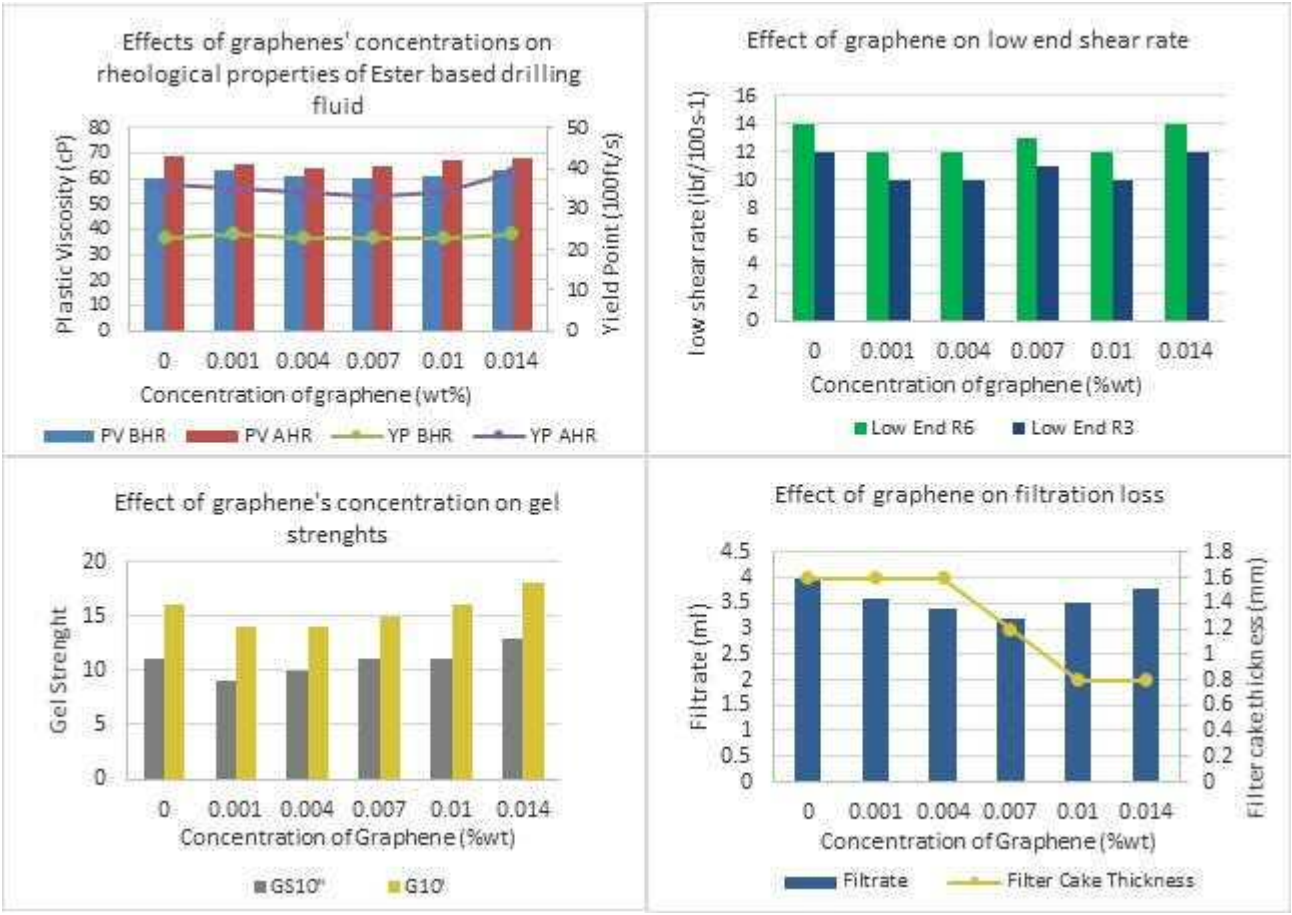

Fig. 1 Effects of graphene on ester-based drilling a) rheology b) low-shear-rate yield point c) gel strength d) filtration properties

Please choose: Oral/ ~~Poster/ Either~~
Presentation session: Biological Science
Presenter name: Norhayati Ramli

The use of bacterial indicator in biomonitoring the river water contamination due to palm oil mill effluent final discharge

Siti Suhailah Sharuddin[1], Diana Mohd-Nor[2], Mohd Ali Hassan[1], Toshinari Maeda[2], Yoshihito Shirai[2], Kenji Sakai[3], Yukihiro Tashiro[3], Norhayati Ramli[1*]

[1]Department of Bioprocess Technology, Faculty of Biotechnology and Biomolecular Sciences, Universiti Putra Malaysia, 43400 UPM Serdang, Selangor, Malaysia
[2]Department of Biological Functions Engineering, Graduate School of Life Science and Systems Engineering, Kyushu Institute of Technology, Japan
[3]Laboratory of Soil and Environmental Microbiology, Division of Systems Bioengineering, Department of Bioscience and Biotechnology, Faculty of Agriculture, Graduate School of Bioresources and Bioenvironmental Sciences, Kyushu University, 744 Motooka, Nishi-ku, Fukuoka 819-0395, Japan

Email: yatiramli@upm.edu.my

Keywords: Palm oil mill effluent; Polluted river; Wastewater; Bacterial community; Bioindicator

Introduction

Palm oil mill effluent (POME) is known as one of the high strength wastewaters generated from palm oil extraction process which could create potential hazards to the environment if it is not being handled properly. The POME undergoes several stages of treatment before it is being released into the nearby river or land. However, the generation of a huge amount of POME has become a critical issue to satisfy the increasingly stringent environmental regulations of the final discharge. Thus, the used of biological monitor using microorganisms is one of the promising approaches to determine the impact of POME to the receiving river water since they are continuously exposed to the perturbations and variations in the natural ecosystem; thus, their response reflects the ecological consequences of the environmental variability.

Experiment

A thorough outlook on the effect of POME final discharge towards the functional status and bacterial community in the receiving river is provided in this study by using nucleic acid double staining assay based on flow cytometry and high-throughput MiSeq, respectively. The bacterial community dynamics in POME final discharge was compared with the bacterial community in the unpolluted and polluted river due to final discharge. The functional status of the bacterial community at single-cell level is determined with regards to their abundance, viability and nucleic acid content to monitor the effect of POME final discharge in the affected river. The assessment of bacterial community compositions in relation to physicochemical properties in the different POME final discharges was also provided in this study to confirm the reliability of the proposed bacterial indicators.

Result and Discussion

This study showed that the POME final discharge did not only alter the natural physicochemical properties of the river water, but also changed the bacterial community dynamics in the receiving river. The shift of low nucleic acid (LNA) to high nucleic acid (HNA) bacterial cells in the affected river suggests the transformation of dormant to active cells due to POME final discharge which may serves as potential bioindicator in the screening of anthropogenic effect due to POME final discharge in the river water with originally high LNA proportions (**Fig. 1**). Based on the assessment of bacterial community compositions, the *Chromatiaceae* and *Alcaligenaceae* which were not detected in the upstream but were detected in the downstream part of the river are proposed as the indicator bacteria to indicate the river water contamination caused by POME final discharge (**Fig. 2**). The emergence of the potential indicator bacteria in the downstream part of the river was shown to be carried over by the effluent. Interestingly, the proposed bioindicators, the *Alcaligenaceae* and *Chromatiaceae* families, were found to be present in the different final discharges despite the different characteristics of the mills and the different biotreatment processes used by them. These bioindicators were also strongly and positively correlated with the biochemical oxygen demand (BOD_5) concentration. This

makes them reliable bacterial indicators to detect the presence of POME final discharge in river water. Monitoring the effluent discharge at low trophic level using flow cytometry and MiSeq sequencing is considered as an accurate pollution monitoring approach which can be used to complement the conventional POME pollution assessment method.

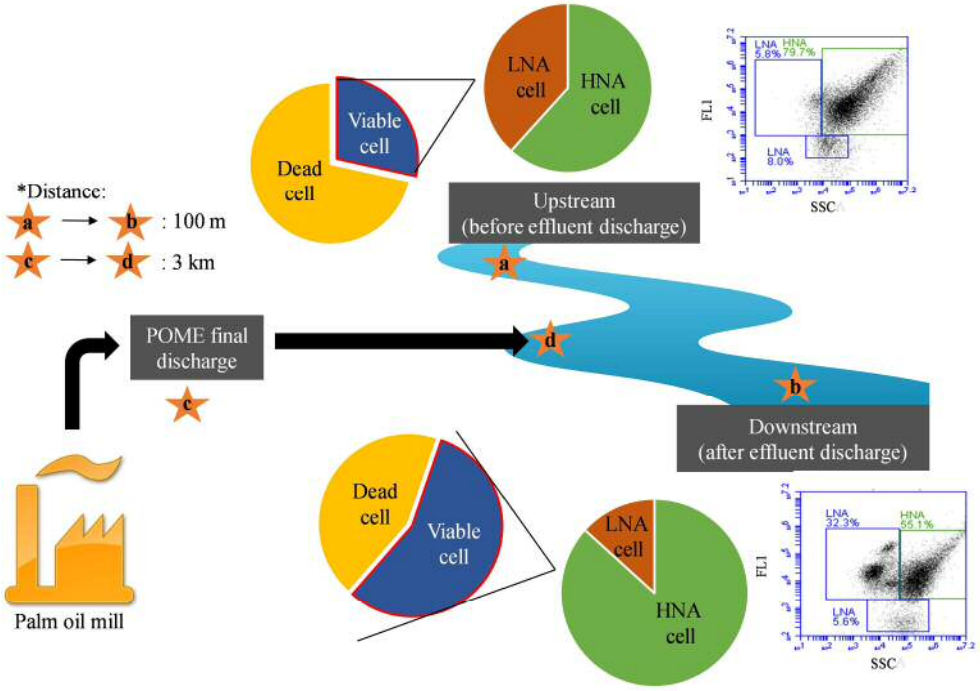

Fig. 1. The shift of low nucleic acid (LNA) to high nucleic acid (HNA) bacterial cells from the unpolluted river water (upstream) to the polluted river water (downstream) due to POME final discharge

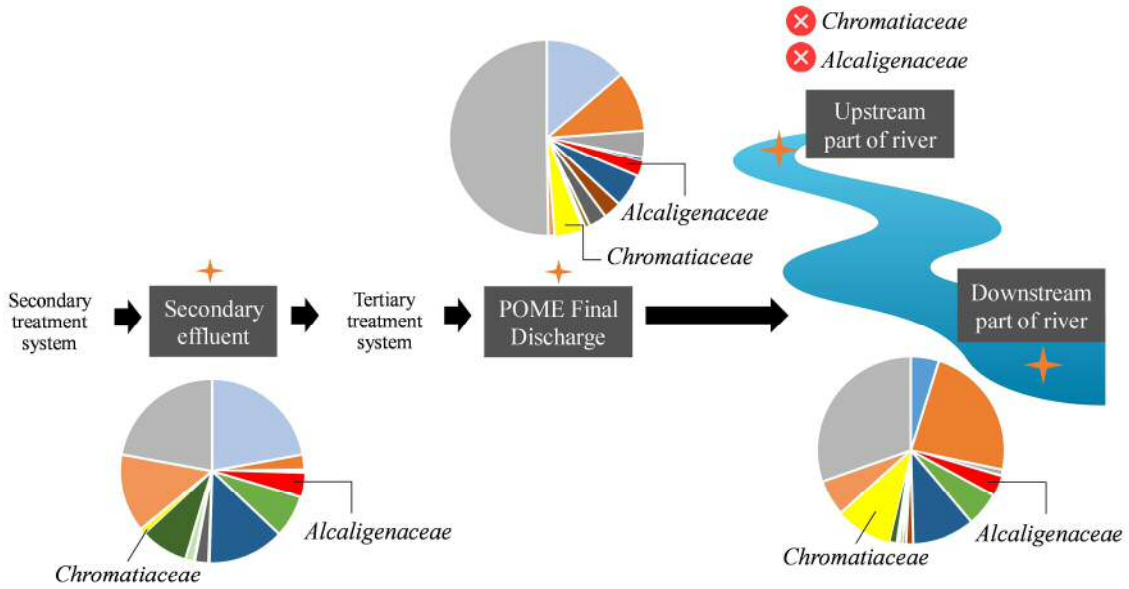

Fig. 2. The potential bioindicators, *Alcaligenaceae* and *Chromatiaceae* were shown to be carried over from the treatment of POME to the polluted river due to final discharge (downstream), but not detected in the unpolluted river due to final discharge (upstream)

Please choose: Oral
Presentation session:
Presenter name: Nor Azah Yusof

Conciliating electrochemical characterization of a newly developed sensitive electrode anchored on Gold nanoparticle-chitosan functionalized multi-walled carbon nanotube platform for the detection of secondary metabolites in oil palms *(Elaeis guineensis Jacq.)* roots

Sulayman Akanbi, Fowotade [1,2], ***Nor Azah Yusof*** [1,3*], *Jaafar Abdullah*[1] *and Yusran Sulaiman*[1]
[1] Department of Chemistry, Faculty of Science, Universiti Putra Malaysia, 43400 Serdang, Selangor, MALAYSIA
[2] Department of Science Laboratory Technology, Hussaini Adamu Federal Polytechnic, Kazaure, Jigawa, NIGERIA
[3]Institute of Advanced Technology (ITMA), Universiti Putra Malaysia, 43400 Serdang, Selangor, MALAYSIA
*e-mail: azahy@upm.edu.my Tel: +60192424072

Secondary metabolites (SMs) are low molecular organics which do not take part in the growth and development of plants but often relate the plants to their ecosystem. The detection of these metabolites is crucial to the early detection of *Ganoderma boninense*, the causative fungal of basal stem rot (BSR) disease in oil palms. These metabolites are often excreted by the oil palms as defensive soldiers whenever the pathogenic fungal launch lethargic attack on the economic trees. A new electrochemical sensor using functionalized multi-walled carbon nanotubes modified screen printed carbon electrode is developed for fast and sensitive detection of SMs in healthy and infected extracts from oil palms. Measurements were carried out on miniaturized instrument consisting of a dropsens potentiostat with an insertion pot to accommodate modified electrodes and a desk top computer with control software under cyclic voltammetric optimized conditions of 180s accumulation time, -0.52V accumulation potential and 0.60V/s scan rate. The measurement required that the developed electrode be employed in different root secondary metabolites (root-SMs) solutions. For this electrode, cyclic voltammograms of root-SMs showed oxidation peak at +0.154V (14DHRSMs), +0.114V (14DIRSMs), 0.250V (30DHRSMs) and +0.043V(30DIRSMs). Linear sweep voltammetry (LSV) is applied in this case for speedy and sensitive characterization. The newly developed electrode revealed satisfactory linear oxidative peak current (Ipa) response over the set concentration range of 0.1 – 0.5ppm with coefficient of regression(R^2) ranging from 0.9433 to 0.9996. The limit of detection, LOD (3 S/N) is between 7.87ppb and 18.54ppb for all the secondary metabolites samples analyzed. The proposed electrochemical sensor displayed good sensitivity, selectivity and reproducibility.

Keywords (5 words)

Secondary Metabolites; Oil palm Extracts; Voltammetry; Multi-Walled Carbon Nanotubes; Screen Printed Carbon Electrode

[Introduction]

Southeast Asia countries, like Malaysia and Indonesia are proud producers of oil palm (OP) products, which have no doubt assisted in eradicating poverty in these regions and means of earning foreign exchange. Despite the disease-free nature of this crop plant, it could not be speared by a fungus called *Ganoderma boninense* (*G. boninense*). This supine fungus traded two closely related categories of disease namely basal stem rot (BSR) and upper stem rot (USR). Here we present an unexplored strategy to detect the excreted SMs from both healthy and *G. boninense* post inoculated root extracts, by using modified electrode based on the gold nanoparticles mixed with chitosan nanoparticles functionalized multi-walled carbon nanotubes anchored on disposable screen-printed carbon electrode ([AuNPs-aMWCNTs/ChTSNPs-aMWCNTs]$_4$/SPCE), using ultrathin layer-by-layer self-assembly. We believed that, the main benefits of the newly developed electrode lie in its

characteristics such as large effective electroactive surface area, fine accumulation of analyte, and control over immediate microenvironment to provide better performance as electrochemical assays

[Experiment]

Briefly, the synthesized AuNPs and ChTSNPs were grafted on to the aMWCNTs by sonication and centrifugation to obtain hybrid nanomaterials, namely gold nanoparticles-activated multi-walled carbon nanotubes (AuNPs-aMWCNTs) and chitosan nanoparticles-activated multi-walled carbon nanotubes (ChTSNPs-aMWCNTs). Then, the LBL modified screen-printed carbon electrodes (BLn/SPCE, where n = number of depositional cycles) procedures approach was applied. This fabricated electrode is referred as BL1/SPCE. The deposition cycle was continued to produce the required number of nanoparticles modifier bilayers.

[Results and Discussion]

As depicted in Fig. below, the curve (i), no significant voltammetric response was observed for detection of (14 days healthy root secondary metabolite)14DHRSMs, (14 days infected root secondary metabolite)14DIRSMs, (30 days healthy root secondary metabolite)30DHRSMs, and (30 days infected root secondary metabolite)30DIRSMs, respectively, using bare/SPCE. This indicates that the electrochemical behaviors of all the root-SMs proceeded in a very slow manner at the surface of the bare electrodes in the applied potential window. However, the oxidation anodic current increase apparently at the surface of the modified electrodes (BL4/SPCE) as can be seen in Fig. below for the curves (ii). The response increments are more noticeable for all the SMs, which can be ascribed to the presence of functionalized CNTs on the surface of the electrodes.

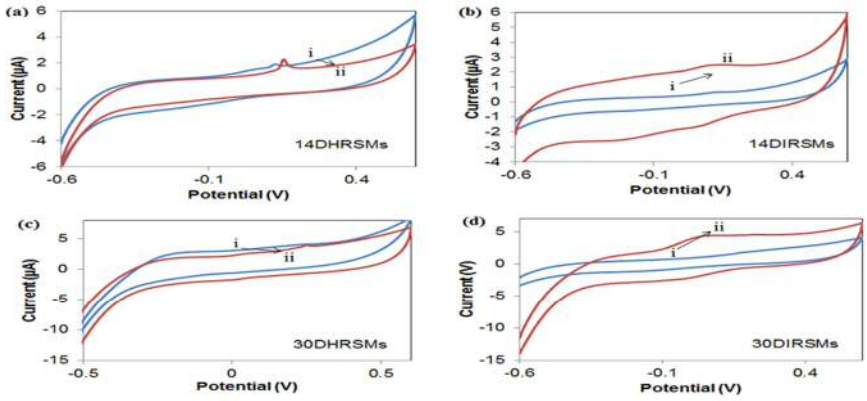

[Conclusion]

Gold nanoparticles-activated multi-walled carbon nanotubes (AuNPs-aMWCNTs) and chitosan nanoparticles-activated multi-walled carbon nanotubes (ChTSNPs-aMWCNTs) has been used to modified electrode using layer by layer technique. The modified electrode has shown potential to differentiate the infected and healthy oil palm.

Oral
Applied Engineering
Yuki Tanaka

Analysis of DNA Integral Controller by using Singular Perturbation Theory

Yuki Tanaka, Takashi Nakakuki

Department of Systems Design and Informatics, Kyushu Institute of Technology, 680-4 Kawazu, Iizuka, Fukuoka, 820-8502, Japan

Email: tanaka.yuki915@mail.kyutech.jp, nakakuki@ces.kyutech.ac.jp

Keywords (5 words)
DNA Computing, DNA strand displacement, integral controller, analysis method, singular perturbation theory

[Introduction]

In the field of molecular robotics, we aim to create a several micron scaled robot made from biomolecules such as DNAs and proteins. Since a signal processing inside the robot is realized by binding and dissociation reactions of artificial DNAs, a control theory that keeps the DNA concentrations at the target level is required. A controller modeled on a protein stabilization mechanism in an intracellular signal transduction system has been reported (DNA Integral Controller, hereinafter referred to as D.I.C) [1]. In this study, we analyze D.I.C by using singular perturbation theory.

[DNA Integral Controller (D.I.C)]

The reaction scheme of D.I.C [1] is shown in Fig. 1. In this system, a regulation is realized by a state transition of linearly increasing DNA strands and exponentially decreasing DNA strands. The reference level R is obtained by calculating the equilibrium state of the state transition. In Fig. 2, it can be seen that the output strand (x_{15}) reaches R. This system can be expressed by a mathematical model of a feedback control system with an integral control (1). The parameter α including the time variables x_{13} and x_{19} does not fluctuate much from initial densities, so it is regarded as a constant parameter.

$$\begin{cases} \dot{x}_{15}(t) = -\alpha x_{15}(t) + \beta x_p(t) \\ x_p(t) = -\int_0^t \gamma(x_{15}(t) - x_{15}^*(t))dt \end{cases} \quad (1)$$

where α, β, γ and R are given by

$$\alpha = k_{f_{12}} x_{13}(t) + k_{f_{15}} x_{19}(t), \quad (2)$$

$$\beta = k_{f_{15}} x_{19}(t), \quad (3)$$

$$\gamma = k_{f_{12}} x_{13}(t), \quad (4)$$

$$R = x_{15}^*(t) = \frac{k_{f_5}\, x_4(t) x_6(t)}{k_{f_{12}} x_{13}(t)} \quad (5)$$

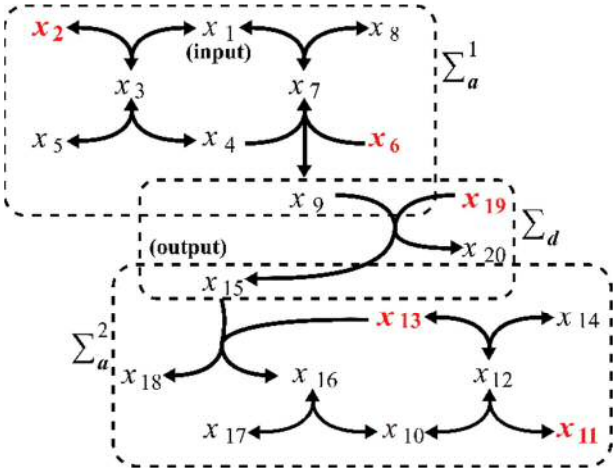

Fig. 1 Reaction scheme of D.I.C.

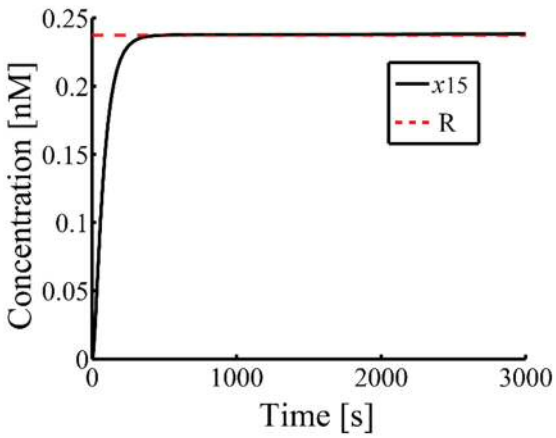

Fig. 2 Time-course plots of x_{15} (output) and R.

[Singular Perturbation Theory]

A singular perturbation is a systematic approximation method of differential equations. The following system is called a singular perturbation system.

$$\begin{cases} \dot{x} = f(x,z), x(0) = x_0, x \in Dx \subset \mathbb{R}^n \\ \varepsilon\dot{z} = g(x,z,\varepsilon), z(0) = z_0, x \in Dz \subset \mathbb{R}^n \end{cases} \quad (6)$$

f and g can be continuously differentiated with respect to $x, z,$ and ε, and then ε is assumed to be very small. In this case, x and z can be thought of as a slow system and a fast system respectively. Generally, when applying the singular perturbation theory to the system, it is necessary to make the system a non-dimensional form. Since the z-system of (6) is a very fast system, the z-system reaches a steady state before x changes from its initial value. In the case of $\varepsilon = 0$, the z-system reaches equilibrium in a moment and becomes the following equation (7).

$$0 = g(x,z,0) \quad (7)$$

This real solution is defined as $z = h(x)$. Then, by substituting (7) into (6), we obtain (8) called a quasi-stationary state system or a low-dimensional system.

$$\dot{x} = f(x, h(x)), x(0) = x_0 \quad (8)$$

[Results]

In this research, by using the method introduced in [2], we obtain the non-dimensional D.I.C (9)-(10). Here, because of $\varepsilon \ll 1$ ($T_s \ll T_f$), the system becomes a differential perturbation form of D.I.C. We obtain (12) by solving (9)-(10) with $\varepsilon = 0$. In Fig. 3, z_{11}, which is a singular perturbation form of the output strand of D.I.C, is consistent with x_{15} which is an output strand.

[Conclusions]

In this study, we analyzed D.I.C by using singular perturbation theory. As a result, it was confirmed that the output strand of D.I.C, the reference level R shown in [1], and z_{11} which is obtained by using the singular perturbation theory are consistent.

$$f(x,z) = \begin{bmatrix} -k_{f_1} z_1 x_1 + k_{r_3} z_2 \\ -k_{f_5} z_3 x_2 \\ -k_{f_8} z_8 x_3 + k_{r_9} z_9 \\ -k_{f_{11}} z_{10} x_4 - k_{f_{12}} z_{11} x_4 + k_{r_{10}} z_9 \\ -k_{f_{15}} z_7 x_5 \end{bmatrix} \quad (9)$$

$$g(x,z,\varepsilon) = \begin{bmatrix} -k_{f_1} x_1 z_1 + k_{r_2} z_2 - \varepsilon k_{f_7} z_1 z_6 + k_{r_6} z_5 \\ k_{f_1} x_1 z_1 - k_{r_2} z_2 + \varepsilon k_{f_4} z_3 z_4 - k_{r_2} z_2 \\ \vdots \\ -k_{f_{12}} x_4 z_{11} + k_{f_{15}} x_5 z_7 \\ \vdots \\ k_{f_{15}} x_5 z_7 \end{bmatrix} \quad (10)$$

where

$$\varepsilon = \frac{T_s}{T_f}, \quad (11)$$

T_s, T_f : Concentration of DNA strands

$$z = h(x) = \left\{ z_2 = \frac{k_{f_1} x_1 z_1}{k_{r_2} + k_{r_3}}, z_3 = \frac{k_{r_3} z_2}{k_{f_5} x_2}, \right.$$

$$z_5 = \frac{k_{r_3} z_2}{k_{r_6}}, z_7 = \frac{k_{r_3} z_2}{k_{f_{15}} x_5}, z_8 = \frac{k_{r_3}(k_{r_9} + k_{r_{10}}) z_2}{k_{f_8} k_{r_{10}} x_3},$$

$$\left. z_9 = \frac{k_{r_3} z_2}{k_{r_{10}}}, z_{11} = \frac{k_{r_3} z_2}{k_{f_{12}} x_4}, z_{12} = \frac{k_{r_3} z_2}{k_{r_{13}}} \right\} \quad (12)$$

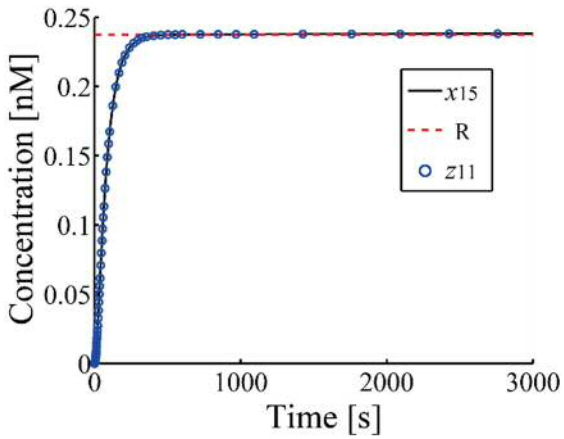

Fig. 3 Time-course plots of x_{15}, R, and z_{11}.

[References]

[1] Y. Tanaka, T. Nakakuki, and S. Nomura, DNA Integral Controller Learning from Biological System, *SICE Annual Conference (SICE2017)*, pp.781-786, Sep. 2017.

[2] T. Nakakuki, J. Imura, Analysis method of DNA feedback regulator as an artificial molecular machine, *SICE Annual Conference*, pp. 1572-1573, 2018.

Please choose: Oral/ ~~Poster/ Either~~
Presentation session:
Presenter name: Nurul Izza Ab Ghani

The genetic diversity between two populations of Malaysia endangered Southern river terrapin (*Batagur affinis*) (Cantor, 1847)

Nurul Aini, Ismail[1], Pelf-Nyok, Chen[2], Latifah, Abd Manaf[3], Ahmad, Ismail[1], Nurul Izza, Ab Ghani[1]

[1]Department of Biology, Faculty of Science, Universiti Putra Malaysia, 43400 UPM Serdang, Selangor, Malaysia
[2]Turtle Conservation Society of Malaysia, 6513, RAKR Kg. Fikri, 24000 Chukai, Kemaman, Terengganu Darul Iman, Malaysia
[3] Department of Environmental Sciences, Faculty of Environmental Studies, Universiti Putra Malaysia, 43400 UPM Serdang, Selangor, Malaysia

Email: nurul_izza@upm.edu.my

Batagur affinis is one of endemic and endangered species in Malaysia. Many conservation efforts have been conducted including building of three conservation centres, many regulations and many biological studies. However, the numbers of individuals in the wild populations are not increasing. These are due to over exploitation of natural habitats of the species, as well as because of egg and meat harvests. In addition, the current breeding and conservation programs are not including genetic information, since the genetic basis of this species has not yet well studied. It is important to understand and include genetic information when breed and conserve endemic and endangered species because the species usually have small gene pool/ low genetic diversity which usually impede the progress of any successful breeding and conservation programs. Therefore, the genetic diversity of *B. affinis* from the captive population of Bota Kanan, Perak and the wild population of Kemaman, Terengganu were studied. It was found that both populations had moderate genetic diversity (Bota Kanan: H_O = 0.29 and Kemaman: H_O = 0.40) and deviated from Hardy-Weinberg equilibrium (p = 0.05). In addition, both populations were inbred. But, Kemaman population had lower inbreeding than Bota Kanan population (Kemaman: F_{is} = 0.43 *cf.* Bota Kanan: F_{is} = 0.57). Hence, suggests that future breeding program for conserving *B. affinis* should be conducted among genetically distinct individuals to maintain the current genetic diversity and/or reduce further inbreeding, as well as minimise allelic deviation from Hardy-Weinberg equilibrium.

(241 words)

Keywords (*Batagur affinis*, Bota Kanan, endangered species, genetic diversity, Kemaman)

Introduction

Conservation of endangered species is one of principles in the Malaysia National Policy on Biological Diversity 2016 – 2025. To support and realise the principle, it is important to understand the genetic basis of the endangered species including understanding the genetic diversity, probability of inbreeding, rate of mutation and genetic distance between populations of the same species (Frankham, 1995, 2010). That genetic information is needs to better explain internal processes behind factors that influence the extinction of endangered species. There are several factors that influence the extinction of endangered species including: (i) demands of increasing human populations, (ii) killing of the species through hunting, fishing and trapping, (iii) habitat loss through habitat degradation, fragmentation, pollution and climate change (iv) introduction of non-native species (i.e. invasive species), pathogens, parasites, predators and competitors (Lindenmayer and Burgman, 2005).

In Malaysia, the Southern river terrapin (*Batagur affinis*, or locally known as "tuntong") which is one of endemic and endangered freshwater turtles in the world (Moll et al., 2015; IUCN, 2017; Figure 1) can be found only at three states: Kedah (Kedah River), Perak (Perak River) and Terengganu (Setiu, Dungun and Kemaman Rivers) (Moll et al., 2015). It is threats by over exploitation of its natural habitats by human for development purposes, as well as because of egg and meat harvests. Therefore, many conservation efforts

have been conducted including building of three conservation centres, many regulations and many biological studies. However, the current breeding and conservation programs which are practice in those three conservation centres (i.e. captive breeding, eggs incubation, raise and release head-start turtles) not include genetic information, since the genetic basis of this species has not yet well studied. Therefore, in this study the genetic diversity of *B. affinis* from the captive population of Bota Kanan, Perak and the wild population of Kemaman, Terengganu were studied. It is important to obtain genetic diversity of this species to ensure the progress of any breeding and conservation programs of this species will be sustainable.

Figure 1: A female Malaysian Southern river terrapin (*Batagur affinis*).

[Experiment]

Tissue sample collection

Two populations of *B. affinis* were used: the captive population of Bota Kanan, Perak (n = 30 pieces of tissues from the swimming web of the rear foot of randomly chosen adults) and the wild population of Kemaman, Terengganu (n = 30 pieces of tissues from the sculte of randomly chosen hatchlings) (Figure 2). All tissues were collected with the help of staffs at each conservation centre under special permits: T-00465-16-16 and NRE 600-2/2/21 Jld.4 (12). Those collected tissues were kept in individual 1.5 ml microcentrifuge tube containing 70% ethanol at room temperature.

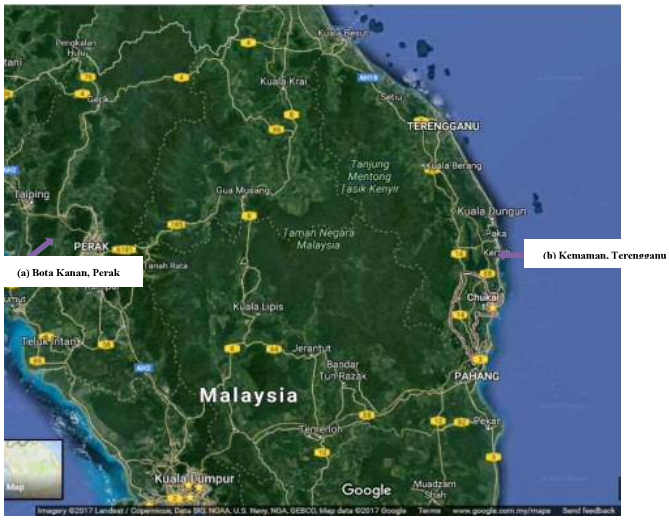

Figure 2: Two sampling populations of *B. affinis*: (a) the captive population of Bota Kanan, Perak, and (b) the wild population of Kemaman, Terengganu. (Source: Google Satellite, 2018).

Data collection and analysis

All DNA were isolated using ReliaPrep™ gDNA Tissue Miniprep System kit by following the manufacture protocol and eluted in 100 µl of Nuclease-Free water before kept at -20^{o}C. Then, Polymerase Chain Reactions (PCRs) were carried out using nine cross-species microsatellites (hereafter loci): four loci form Burmese Roofed Turtle [*B. trivittata*] (Love et al., 2013), and five loci from Yellow-headed Sideneck [*Podocnemis unifilis*] (Fantin et al., 2007) (Table 1) to obtain genotyping data. The detail of PCR protocols and volumes was stated in Ismail (2018). All PCR products were visualized on 3% agarose gel electrophoresis and run for 90 min at 78 V with 20 bp size marker as allele size reference to obtain genotyping data by manually scored.

All genotyping data were checked using MICROCHECKER (van Oosterhout et al., 2004) for null alleles or allelic dropout. Then, CREATE software (Coombs et al., 2008) was used to convert the genotyping data into a readable format for further analysis. The genetic diversity (H_O), Hardy-Weinberg equilibrium and inbreeding (F_{is} value) in the two populations were calculated using GENEPOP on the web (http://genepop.curtin.edu.au/).

[Result and Discussion]

Table 1: The genetic diversity (observed heterozygosity values (H_O)), expected heterozygosity values (H_E), Hardy-Weinberg equilibrium and inbreeding (F_{is} values) of all nine studied loci for Kemaman and Bota Kanan populations of Southern river terrapin.

Locus	Kemaman				Bota Kanan			
	Genetic diversity		Hardy-Weinberg equilibrium	Inbreeding	Genetic diversity		Hardy-Weinberg equilibrium	Inbreeding
	H_O	H_E	p-value	F_{is}	H_O	H_E	p-value	F_{is}
Batr16	0.38	0.60	0	0.89	0.40	0.65	0.01	0.51
Batr25	0.31	0.39	0	0.49	0.03	0.35	0	0.99
Batr30	0.03	0.47	0	0.98	0.45	0.53	0.01	0.28
Batr39	0.30	0.57	0	0.32	0.05	0.52	0	0.91
Puni_1A5	0.00	0.00	0	-	0.00	0.00	0	-
Puni_1E1	0.70	0.46	0	-0.52	0.00	0.45	0	1.00
Puni_1H9	0.97	0.54	0	-0.07	0.57	0.65	0	0.57
Puni_2A9	0.00	0.00	Monomorphic	-	0.60	0.43	0.03	-0.41
Puni_2C11	0.93	0.51	0	-0.87	0.50	0.58	0.27	0.28
Mean	**0.40**	**0.39**		**0.43**	**0.29**	**0.46**		**0.57**

Both Kemaman and Bota Kanan populations showed moderate level of genetic diversity (Bota Kanan: H_O = 0.29 and Kemaman: H_O = 0.40; Table 1) and deviated from Hardy-Weinberg equilibrium (p = 0.05; Table 1). In addition, both populations were inbred with Kemaman population had lower value than Bota Kanan population (Kemaman: F_{is} = 0.43 *cf.* Bota Kanan: F_{is} = 0.57; Table 1). These suggest that the two studied populations of endemic and endangered *B. affinis* are prone to become extinct in the near future if no improvement in the current conservation and breeding programs are taken. This is probably due to its small effective population size because of its low turnover (i.e. 25 years old to reach age of maturation, or earlier at 22 years old at carapace size of 510 mm, and annually reproduce and 23 to 30 of average number of eggs per clutch; Chan and Chen, 2011). Small effective population size in endemic and endangered species with low turnover is common (IŞIK, 2011).

The Bota Kanan population consists of about 200 adults *B. affinis*, but, the effective population size is unknown since no detail pedigree record is keep (personal conversation with the staffs of PERHILITAN Perak). It is likely the effective population size in this population is less than 200 because not all of those adults are fertile (personal conversation with the staffs of PERHILITAN Perak). Meanwhile, the effective population size of Kemaman population also unknown since it is a wild population and no record is keep because of difficult access. The effective population size consequently affects genetic diversity (Lindenmayer and Burgman, 2005). Preservation of genetic diversity and minimise inbreeding are important genetic factors to ensure the perseverance and evolution of endemic, endangered and small sized (i.e. small effective population size) (Brook et al., 2002; Blambert et al., 2016).

In conclusion, mating among genetically close individuals should be avoided to maintain the current genetic diversity and/or to reduce deviation from Hardy-Weinberg equilibrium in the Bota kanan and Kemaman populations of *B. affinis*. Thus, extinction of *B. affinis* can be avoided. More genetic information should be gathered to further understand internal processes behind factors that may induce the extinction of this endemic and endangered species for better breeding and conserve programs.

[Acknowledgements]
We would like to thank the staffs of Department of Wildlife and National Park (PERHILITAN) of Perak, the Turtle Conservation Society of Malaysia (TCS), the villagers of Kg. Tok Kapor, Kg. Pasir Gajah and Kg. Dadong in Kemaman, and anonymous reviewers for their supportive comments on the earlier versions of this paper. This research was supported by the Geran Putra-Insentif Putra Berkumpulan (GP-IPB/2014/9441102), and conducted under the 'Permit Khas Jabatan PERHILITAN Semenanjung Malaysia' (NRE 600-2/2/21 Jld.4 (12)).

[References]

Brook, B. W., Tonkyn, D. W., O'Grady, J. J. and Frankham, R. 2002. Contribution of Inbreeding to Extinction Risk in Threatened Species. *Conservation Ecology*. **6(1)**: 16.

Blambert, L., Mallet, B., Humeau, L. and Pailler, T. 2016. Reproductive Patterns, Genetic Diversity and Inbreeding Depression in Two Closely Related *Jumellea* species with Contrasting Patterns of Commonness and Distribution. *Annals of Botany*. **118(1)**: 93-103.

Chan, E-H. and Chen, P-N. 2011. Nesting Activity and Clutch Size of *Batagur affinis edwardmolli* from the Setiu River, Terengganu, Malaysia. *Chelonian Conservation and Biology*. **10(1)**: 129-132.

Coombs, J. A., Letcher, B. H. and Nislow, K. H. 2008. Create: A Software to Create Input Files from Diploid Genotypic Data for 52 Genetic Software Programs. *Molecular Ecology Resources*. **8(3)**: 578-580

Fantin, C., Carvalho, C. F., Hrbek, T., Sites, Jr. J. W., Monjeló, L. A. S., Astolfi-Filho, S. and Farias, I. P. 2007. Microsatellite DNA Markers for *Podocnemis Unifilis*, the Endangered Yellow-spotted Amazon River Turtle. *Molecular Ecology Notes*. **7(6)**: 1235-1238.

Frankham, R. 2003. Genetics and Conservation Biology. *Comptes Rendus Biologies*. **326(1)**: S22-S29.

Frankham, R. 1995. Inbreeding and Extinction: A Threshold Effect. *Conservation Biology*. **9(4)**: 792-799.

http://genepop.curtin.edu.au/

IUCN. 2018. *The IUCN Red List of Threatened Species*. Version 2018-1. <http://www.iucnredlist.org>. Downloaded on 05 July 2018.

IŞIK, K. 2011. Rare and endemic species: Why are they prone to extinction? *Turkish Journal of Botany*. **35(4)**:411-417.

Ismail, A. 2018. *Genetics Assessment of Endangered River Terrapin (Batagur affinisi, Cantor) in Bota Kanan and Kemaman River, Malaysia*. Master-thesis, Universiti Putra Malaysia.

Lindenmayer, D. and Burgman, M. 2005. *Practical Conservation Biology*. Collingwood: CSIRO Publishing.

Love, C. N., Hagen, C., Horne, B. D., Jones, K. L. and Lance, S. L. 2013. Development and Characterization of Thirty Novel Microsatellite Markers for the Critically Endangered Myanmar Roofed Turtle, *Batagur trivittata* and Cross-amplification in the Painted River Terrapin, *B. borneoensis*, and the Southern River Terrapin, *B. affinis*, Using Paired-end Illumina Shotgun Sequencing. *Conservation Genetics Resource*. **5(2)**: 383-387.

Moll, M. O., Platt, S. G., Chan, E. H., Horne, B. D., Platt, K., Praschag, P., Chen, P. N. and van Dijk, P. P. 2015. *Batagur affinis* (Cantor 1847) – Southern River Terrapin, Tuntong. *Conservation biology of freshwater turtles and tortoises. Chelonian Research Monographs*. **5**: 090.1-090.17.

van Oosterhout, C., Hutchinson, W. F. D., Wills, D. P. and Shipley, P. 2004. MICRO-CHECKER: Software for Identifying and Correcting Genotyping Errors in Microsatellite Data. *Molecular Ecology Notes*. **4(3)**: 535-538.

Please choose: Oral
Presentation session: Environmental Biotechnology
Presenter name: Nurul Asyifah Mustapha

Survival Game by Bacterial Soldiers in Waste Sewage Sludge-Understanding the Bacterial Natural Selection

Nurul Asyifah MUSTAPHA[1], Toshinari MAEDA[1]

[1] Department of Biological Functions Engineering, Graduate School of Life Science and Systems Engineering, Kyushu Institute of Technology, 2-4 Hibikino, Wakamatsu, Kitakyushu 808-0196, Japan

Email: nurul-asyifah@life.kyutech.ac.jp

Keywords: bacterial soldier, inoculant, bioaugmentation, bacterial interactions, natural selection

[Introduction]

A successful bioaugmentation depends on the effectiveness of an exogenous microorganism carrying a specific function in the pollutant degradation. However, it is still far from fully functions because the ability of exogenous microorganisms is often temporary and decreases shortly after the inoculation. The interaction with indigenous microorganisms is believed to be one of the factors. In this study, *Escherichia coli* with enhanced green fluorescent protein (EGFP) was inoculated in waste sewage sludge (WSS) to mimic the bioaugmentation process for evaluating its survival and the substantial bacterial dynamics at which the inoculants are going to be killed by the natural selection inside the WSS. Furthermore, a unique approach using an antibiotic, by which bacterial activity related to the natural selection should be changed in WSS, allowed us to find the main bacterial community acting as a soldier that could be responsible in killing the inoculated exogenous cells. Controlling the bacterial soldiers may have great potential to maximally enhance the success rate of bioremediation.

[Experiment]

1. Determination of survival rates of inoculant in WSS

Overnight culture of EGFP-expressing *E. coli* with tetracycline resistant gene was inoculated in WSS with or without the addition of tetracycline and in the sterilized WSS. Samples at 0, 8, 24, and 48 hours were diluted sequentially, spread on the LB-tetracycline agar, and incubated at 37°C overnight to count the number of EGFP-expressing *E. coli* cells.

2. Determination of bacterial soldiers through two approaches

a) The isolation of bacterial soldier in WSS was done using an agar plate containing only inoculant cells. Overnight culture of EGFP-expressing *E. coli* was washed with phosphate saline buffer and mixed with agar. WSS was spread on the agar and incubate at 37°C until colonies were formed. Colonies were isolated and identified by sequencing the 16S ribosomal RNA gene.

b) An antibiotic, tetracycline was used to determine all bacterial community in WSS. RNA was extracted from WSS inoculated with EGFP-expressing *E. coli* either with or without the addition of tetracycline and used as templates for the MiSeq analysis. Some of bacterial communities showing lower abundant percentage in the WSS with tetracycline when compared to WSS without tetracycline were selected as possible soldiers.

3. Indirect co-culture of bacterial soldiers and inoculant

A dual cultivation system was used to perform indirect co-culture between EGFP-expressing *E. coli* and candidates of bacterial soldiers obtained from the above two approaches. The killing effect of *E. coli* cells by each bacterial soldier was examined by counting the remaining *E. coli* cells.

[Result and Discussion]

1. Survival of EGFP-expressing *E. coli* in WSS

EGFP-expressing *E. coli* as an inoculant was unable to survive in WSS. However, as an interesting result, it was strongly able to grow in WSS in the presence of tetracycline indicating that the bacterial soldiers may be inactivated by this antibiotic or incapable to kill the escalate amount of inoculant for their growth. (Fig. 1). The inoculant cannot survive in WSS than autoclaved WSS which has relatively low stress because of no competition with indigenous community.

2. Expected bacterial soldiers

Expected bacterial soldiers were listed in Table 1. The isolated bacterial soldiers from WSS were able to grow on EGFP-expressing *E. coli* agar because they can consume it as a nutrient for their growth. Thus, there are absolutely bacteria soldiers in WSS and by adding tetracycline, the survival rate of inoculant cells increased due to the decrease of bacterial soldiers. Therefore, through MiSeq analysis, the noticeable difference in percentage of bacterial community between inoculated WSS with or without tetracycline were considered as bacterial soldiers. The species belongs to family order of bacterial soldiers were selected and purchased from NBRC.

3. Direct evidence of killing effect by bacterial soldiers

The number of EGFP-expressing *E. coli* was decreased when co-culture with all bacteria soldiers at 24 h and 48 h except for *M. virescens* and *M. xanthus* at 48 h (Fig. 2). The isolated bacterial soldiers; *K. pneumonia*, *Shigella* sp., and *S. sediminis* had highest impact on the inoculant number. Based on MiSeq analysis, *Comamonadaceae* and *Myxococcaceae* are the expected group of bacterial soldiers in WSS. The EGFP-expressing *E. coli* was killed when co-culture with representative bacteria soldiers of *Comamonadaceae* and *Myxococcaceae* even it occurred at a slow rate. *Myxococcalles* can produce Ripostatin, a toxic metabolite to inhibit *E. coli* RNA polymerase while *Comamonadaceae* is active in WSS due to a high net growth rate and can outcompete other late colonizers.

[Conclusion]

All of expected bacterial soldiers in WSS showed the ability to kill the EGFP-expressing *E. coli* except *Pseudomonas* sp. The antibiotic approach in this study is valuable to understand and improve the bioaugmentation process by avoiding the bacterial natural selection through controlling the bacterial soldiers.

Table 1: Isolated and expected bacterial soldiers in WSS

Source	Bacteria	Taxonomy level (Family)
Isolated bacteria from WSS	*Pseudomonas sp.*	*Pseudomonadaceae*
	Klebsiella pneumoniae	*Enterobacteriaceae*
	Shigella sp.	*Enterobacteriaceae*
	Shewanella sediminis	*Shewanellaceae*
	Chrysobacterium sp.	*Flavobacteriaceae*
NBRC strains	*Caldimonas manganoxidans*	*Comamonadaceae*
	Diaphorobacter sp.	*Comamonadaceae*
	Myxococcus virescens	*Myxococcaceae*
	Myxococcus xanthus	*Myxococcaceae*

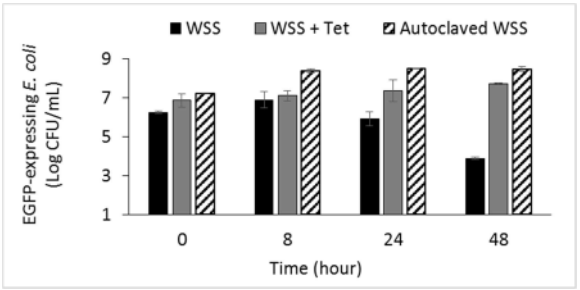

Fig. 1: Survival of EGFP-expressing *E. coli* in different conditions

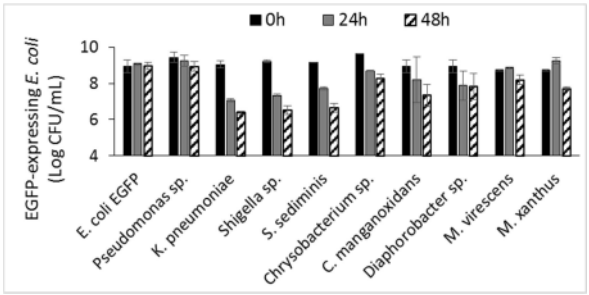

Fig. 2: Survival of EGFP-expressing *E. coli* through indirect co-culture

Please choose: Oral
Presentation session: Biological Science
Presenter name: Noor Baity Saidi

Integration of bioinformatics and intelligent video analytic for early detection of Fusarium wilt outbreak in banana farm

Noor Baity, Saidi[1,2], Zool Hilmi, Ismail[3,4], Fatin Nadiah, Jamil[2], Mohd Ibrahim, Shapiai@Abd. Razak[3,4], Mas Aisyah, Ahmad[3]

[1]Faculty of Biotechnology and Biomolecular Sciences, University Putra Malaysia, 43400 UPM Serdang, Selangor, Malaysia
[2]Institute of Biosciences, University Putra Malaysia, 43400 UPM Serdang, Selangor, Malaysia
[3]Center for Artificial Intelligence and Robotics, Universiti Teknologi Malaysia, Kuala Lumpur, Malaysia.
[4]Malaysia-Japan International Institute of Technology, Universiti Teknologi Malaysia, Kuala Lumpur, Malaysia.

Email: norbaity@upm.edu.my

Keywords : banana, Fusarium wilt, soil microbial profile, aerial imaging, deep convolutional neural network

Introduction

Banana is considered as one of the most valuable food crop and market commodity for Malaysia. However, the crop is now threatened by the deadly race of the fungus Fusarium oxysporum f. sp. Cubense (Foc), the Tropical race 4 (TR4)(1). Fusarium wilt disease seriously affects the crop's production, with serious repercussions on the livelihoods of small scale farmers and workers (2). Therefore, field monitoring is critical for early detection of Fusarium wilt outbreak. However, manual field inspection and monitoring is laborious and costly for farm resources management. Advances in agricultural technology have led to a demand for a new era of automated field monitoring using drones, assisted by deep learning-based video analysis. Simultaneously, the advent of Next-Generation Seqencing (NGS) technologies complemented with the predictive power of bioinformatics has transformed our capacity to explore the uncharted microbial world that inhabit the soil (3). Knowledge on the microbial status of soils in relation to their potential to suppress phytopathogen is the key indicator for plant health. The aim of this research is to provide actionable intelligent agriculture to banana farming community in an effort to control Fusarium wilt disease through the automation of field monitoring using drones and integration of aerial imagery analysis with microbial profile of soil within deep learning context.

Experiment

The study area was located in Puchong Farm, University Agriculture Park, Universiti Putra Malaysia which covers 5 acres of flat terrain (Figure 1, left). A mapping approach was first developed based on high spatial resolution orthophotos to delineate individual banana plants to help with plant identification. The acquired images taken using DJI Phantom 4 were imported into Pix4D mapper v3.2 (Pix4D Inc., Switzerland) for offline processing. Camera correction and calibration was applied to remove geometric distortions from images. For the purpose of detection and classification processes, deep learning framework via Faster-RCNN (4) was utilized to overcome the traditional difficulties of computer vision tasks, such as variable lighting, photos taken at day and night, different season and species exhibiting a variety of poses. To profile the soil microbes, bulk and rhizosphere soils were collected (Figure 1 [C, D]) from banana farm plot for NGS analysis, a service provided by Apical Scientific Sdn Bhd which include shotgun metagenomics and fungal and bacterial community analysis. Plant sample was also collected for confirmation Fusarium wilt disease via molecular analysis (Figure 1 [A, B]).

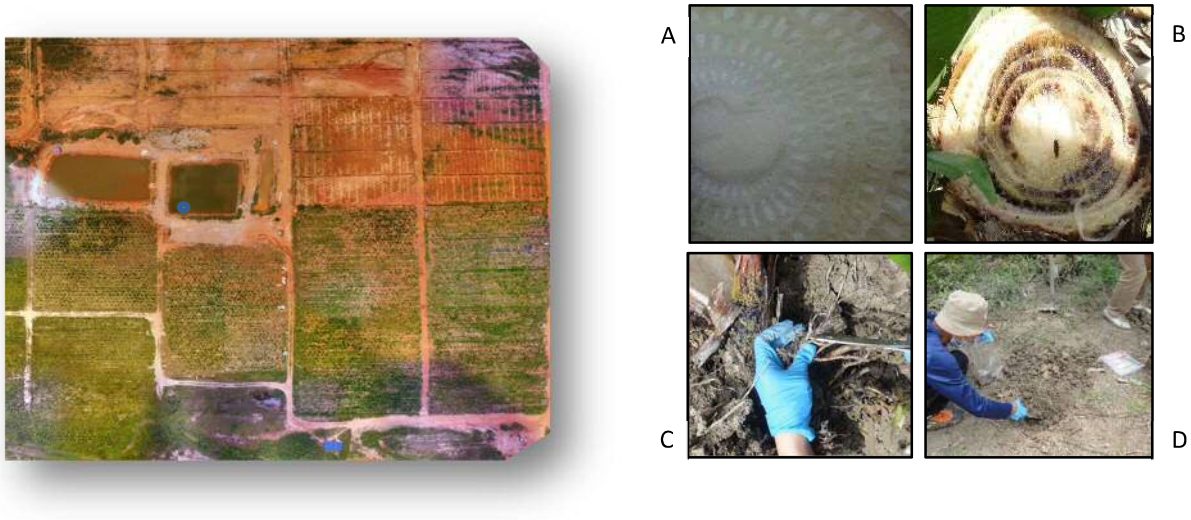

Figure 1: (Left) Banana field plots in the study area of Puchong Farm, Universiti Agriculture Park, Universiti Putra Malaysia. (Right) Sampling of tissues from healthy banana [A], symptomatic banana [B] and collection of rhizosphere soil [C] and bulk soil [D].

Result and Discussion

Soil samples were successfully collected from selected farm plot. However, only low amount of genomic DNA managed to be extracted from the rizhosphere samples. Hence, the samples have to be pooled for NGS analysis. DNA extraction from bulk soil is still on-going.

Figure 2: Auto-detection of banana tree with and without fruits for early counting

Figure 2 shows the result of automatic detection and counting of banana tree with and without fruits (Figure 2) which allows effective reporting of fruit growth status in short period of time. The aerial platform would feature on-board sensing such as cameras, and also have capability to upload data from terrestrial sensors. Once NGS analysis is completed, all the data will be integrated via an online reporting system and made available to farm owners.

References

1. Source: www.promusa.org
2. Ordonez N, Seidi MF, Waaljik C, Drenth A, Killian A, Thomma BPHJ, Ploetz RC, Kema GHJ (2015) Worse comes to worst: bananas and panama disease - when plant and pathogen clones meet. PLoS Pathog. 11: e1005197
3. Waldor MK, Tyson G, Borenstein E, Ochman H, Moeller A, Finlay BB, Kong HH, Gordon JI, Nelson KE, Dabbagh K, Smith H (2015) Where next for microbiome research. PLoS Biol. 13:e1002050

4. Badrinarayanan, V., Kendall, A., and Cipolla, R. (2015). Segnet: A deep convolutional encoder-decoder architecture for image segmentation. arXiv preprint arXiv:1511.00561.

Please choose: Oral/ ~~Poster~~
Presentation session: Day 1
Presenter name: Mashitah ShikhMaidin

Nutrition and Reproductive Performance of Small Ruminants

Mashitah, ShikhMaidin

Department of Biology, Faculty of Science, Universiti Putra Malaysia, 43400 UPM Serdang, Selangor Darul Ehsan, Malaysia

Email: mashitah@upm.edu.my

Abstract
In the concept of "focus feeding", short-term nutritional supplements are used to enhance reproduction whilst keeping costs under control. In small ruminants, nutrition appears to reproductive performance via metabolic hormones and hypothalamic-pituitary-ovarian axis. For example, supplementing sheep for 6 days just before ovulation increases multiple births. However, if supplementation continues into early pregnancy it can increase embryo mortality. The similarities between sheep and goats in their basic reproductive biology suggest that the same responses would be seen in female goats. Studied in Cashmere goats, it seems that the way the ovarian follicles respond to a nutritional supplement are different compared to sheep. Supplementation changed the metabolic hormones but had no consistent effect on progesterone secretion or embryo survival. The good news for farmers is that goats will not suffer early embryo mortality from excessive feeding. It is important to understand the differences between species in their reproductive responses to nutrition because the outcomes strongly influence the rate of production of offspring and may help avoid reproductive failure. This is particularly important in countries such as Malaysia where the goat industries contribute heavily to the domestic economy.

Keywords
Goats, supplementation, progesterone, reproduction

Introduction

In small ruminants, reproductive wastage due to early embryo mortality and single kidding are critical issues for the livestock industry because it reduces reproductive efficiency and limits livestock productivity. In addition, the rate of production of offspring is a basic factor in the economic success of the goat industry, a particularly important issue in countries such as Malaysia where the goat industries contribute heavily to the domestic economy. The potential to improve reproductive performance through nutritional supplementation has been highlighted by decades of studies on sheep, with the most refined system being 'focus feeding' and its embodiment in the concept of 'clean, green and ethical' management (Martin et al., 2004).

Nutrition and reproductive response

Similarities in basic reproductive biology suggest the link between nutrition and embryo survival that has been documented for sheep might also be seen in goats. It has been reported that short-term nutritional supplementation would induce reproductive responses in female goats that would be similar to those documented for female sheep: an increase in ovulation rate and a decrease in embryo survival, pregnancy rate and kidding rate. Compared to the massive history of research into the nutritional control of reproduction in sheep, the goat literature is sparse. In goats, there is a debate about the responses of reproductive performance and hormonal patterns to changes in nutrient intakes.

Underfed or overfed animals at certain periods directly or indirectly affect the reproductive performance of the animals. Delay in puberty and in growth and development of embryo is mostly affected by nutritional restriction due to low energy level. While overfed animals, most of the study relates with embryo mortality and progesterone clearance.

Hormonal pathways and reproduction

Changes in nutrition result in changes in the presence of nutrients and metabolic hormones in the blood stream, many of which seem to act as peripheral messages to the hypothalamus where they might act through central pathways to regulate GnRH secretion. It is well-known that female reproductive functions is controlled by series of hormonal pathways which mainly controlled by hypothalamic-pituitary-ovarian axis (Shikh Maidin et al. 2014).

Short-term supplementation of high protein and energy to female sheep able to increase ovulation rate, however significantly affect the survival of embryo. Insufficient of luteal progesterone during early pregnancy is one of the main factor occurs in overfed ewes with high protein intake. Overfed sheep with high level of nutrient intake does not necessary linked with increment of live body weight. For example, short-term supplementation with lupin grain does increase multiple ovulations but not significantly increase the live body weight of the animals (Munoz-Gutierrez et al., 2002; Vinoles et al., 2005; Scaramuzzi et al., 2006). The effect of feed intake on the hormonal-reproductive axis is mediated by metabolic hormones such as leptin and insulin (review: Scaramuzzi et al., 2011). Inhibitory effect from these metabolic factors could act directly to center of brain and change the homeostatic system. Sheep and goats fed with high energy feed intake increase in concentrations of leptin and insulin, due to changes in hypothalamic-pituitary axis. These could directly affect reproductive performance of the animals.

Conclusion

Importantly, it seems highly likely that nutritional control plays an important tool to changes or manipulates the hypothalamic-pituitary-ovarian axis that mediated by metabolic factors. With respect to the livestock industry, mainly in Malaysia, to respond to the increasing demand for goat products, better feed management strategies are required to reduce Malaysia's dependence on imported goats.

Acknowledgments

Thank you to Universiti Putra Malaysia for providing financial assistance for me to attend this conference. Also to Dr Che Azurahanim Che Abdullah to invite me to join this Kyutech-UPM conference.

References

1. Martin, G. B., Rodger, J., and Blache, D. (2004). Nutritional and environment effects on reproduction in small ruminants. *Reproduction, Fertility and Development.* 16: 491-501
2. Munoz-Gutierrez, M., Blache, D., Martin, G. B., and Scaramuzzi, R. J. (2002). Folliculogenesis and ovarian expression of mRNA encoding aromatase in anoestrous sheep after 5 days of glucose or glucosamine infusion or supplementary lupin feeding. *Reproduction.* 124: 721-731.
3. Scaramuzzi, R. J., Baird, D. T., Campbell, B. K., Driancourt, M.-A., Dupont, J., Fortune, J. E., Gilchrist, R. B., Martin, G. B., McNatty, K. P., McNeilly, A. S., Monget, P., Monniaux, D., Vinoles, C., and Webb, R. (2011). Regulation of folliculogenesis and the determination of ovulation rate in ruminants. Reproduction Nutrition Development. 23: 444–467.
4. Scaramuzzi, R. J., Campbell, B.K., Downing, J.A., Kendall, N.R., Khalid, M., Munoz-Gutierrez, M., and Somchit, A. (2006). A review of the effects of supplementary nutrition in the ewe on the concentrations of reproductive and metabolic hormones and the mechanism that regulate folliculogenesis and ovulation rate. *Reproduction Nutrition Development.* 46: 339–354
5. ShikhMaidin, M., Blackberry, M.A., Milton, J.T.B., Hawken, P.A.R., and Martin, G.B. (2014). Nutritional Supplements, Leptin, Insulin and Progesterone in Female Australian Cashmere Goats. APCBEE Procedia, 8: 299-304.
6. Vinoles, C., Forsberg, M., Martin, G.B., Cajarville, C., Repetto, J., and Meikle, A. (2005). Short-term nutritional supplementation of ewes in low body condition affects follicle development due to an increase in glucose and metabolic hormones. Reproduction. 129: 299-309.

Please choose: Oral/ ~~Poster~~
Presentation session:
Presenter name: Nurul Husna Shafie

Zebrafish embryo assay: A rapid and alternative model for *in vivo* toxicity screening

Siti Nuratiqah, Rambli[1], Nurul Husna, Shafie[1,2], Hasnah, Bahari[3]

[1]Department of Nutrition and Dietetics, Faculty of Medicine and Health Sciences, Universiti Putra Malaysia, 43400 Serdang, Selangor, Malaysia
[2]Laboratory of UPM-MAKNA Cancer Research, Institute of Bioscience, Universiti Putra Malaysia, 43400 Serdang, Selangor, Malaysia

[3]Department of Human Anatomy, Faculty of Medicine and Health Sciences, Universiti Putra Malaysia, 43400 Serdang, Selangor, Malaysia

Email: nhusnashafie@upm.edu.my

Abstract

Keywords (maximum 5 words)

Food irradiation, toxicity, plant products, zebrafish

Introduction: Fish embryo toxicity (FET) testing is used to identify acute toxicity of chemical substances or plant extracts on embryonic stages of zebrafish (*Danio rerio*), as an alternative for the other conventional *in vivo* toxicity test. Food irradiation is one of the food processing techniques that have been used to reduce the number of spoilage foods and to increase the quality of food products. The irradiation of foods can serve many purposes such as inhibit the growth of pathogenic microorganisms, increase the shelf life of the food products and help to purify the food products. *Archidendron jiringa* and *Archidendron bubalinum* are considered as underutilized tropical vegetables in Malaysia, Indonesia, and Thailand. High consumption of any plant products could lead to the toxicity which can contribute to the health problems. The objective of this study is to determine the toxicity in hot aqueous extracts of non-irradiated and irradiated (3, 6, 9 and 12 kGy) *A. jiringa* and *A. bubalinum* using FET test.

Experiment: The toxicological evaluation was carried out using the zebrafish embryo toxicity test. Briefly, the newly fertilised zebrafish eggs were exposed to test samples with different concentrations for 96 hours. Every 24 hours, several apical observations were observed and recorded to indicate the lethality of the test samples.

Results and Discussion: The main finding of this study is both non-irradiated and irradiated *A. jiringa* and *A. bubalinum* extracts showed the potential of having toxicity at the tested concentration (Fig.1). The LC50 value of non-irradiated and irradiated *A. jiringa* and *A. bubalinum* were in the ranges of 300 to 900 µg/ml, which considered as toxic. The hot aqueous extracts of non-irradiated and irradiated *A. jiringa* and *A. bubalinum* showed the potential of toxicity, therefore, it is important to monitor the amount of both *A. jiringa* and *A. bubalinum* to be consumed that could affect our health.

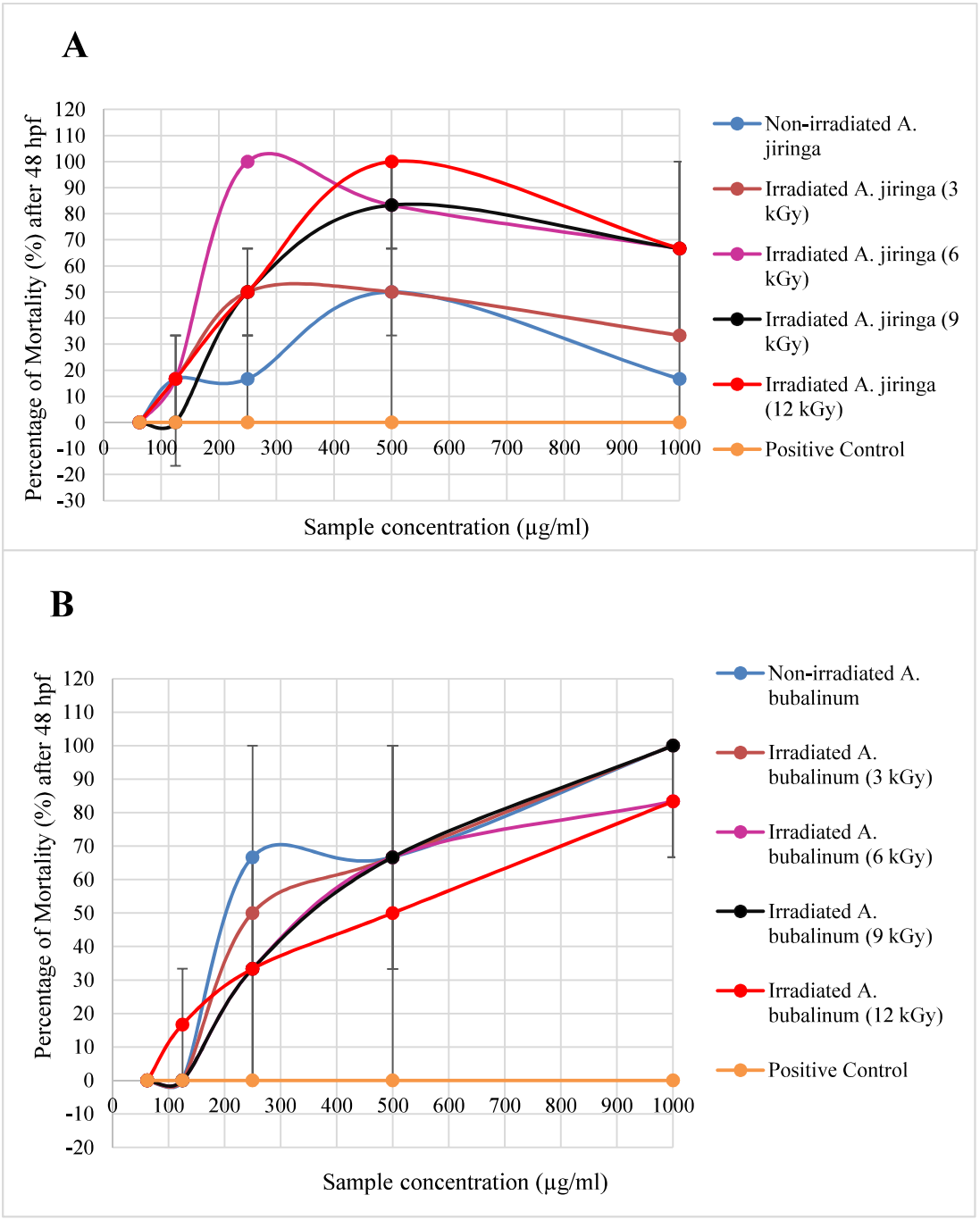

Figure 1: Non-linear regression curve of percentage of mortality (%) for zebrafish embryo toxicity test of hot aqueous extracts of non-irradiated and irradiated (3, 6, 9 and 12 kGy) *A. jiringa* and positive control (A) and *A. bubalinum* and positive control (B) after 48 hpf.

Please choose: Oral
Presentation session: Applied Chemistry
Presenter name: Zhu Jiangyu

Effect of Ferulic Acid from Rice Bran on *Haematococcus lacustris* and *Euglena gracilis*

Jiangyu ZHU[1], Minato WAKISAKA[1]

[1]Graduate School of Life Science and Systems Engineering, Kyushu Institute of Technology, 2-4 Hibikino, Wakamatsu-ku, Kitakyushu, 808-0196, Japan

Email: wakisaka@life.kyutech.ac.jp

Keywords: Ferulic acid, agro waste, growth, morphology, metabolism

[Introduction]

Microalgae are the main primary producers in aquatic ecosystems and they can produce many beneficial metabolites. Therefore, they have been widely applied in many fields, such as food, supplements, and cosmetics. In face with the increasing market demand from consumers, how to enhance the productivity of biomass and valuable metabolites has become a top priority. Introducing a growth regulator derived from agro waste is considered a cheaper and safer strategy to improve biomass productivity compared with other alternatives such as implementing genetic engineering or adding nutrients and plant hormones as growth stimulator. In consideration of cost and safety to environmental application, ferulic acid from rice bran was selected as a potential candidate of microalgae growth promotor. Effect of ferulic acid on the growth, cell morphology and metabolism of *Haematococcus lacustris* and *Euglena gracilis* were investigated.

[Experiment]

Haematococcus lacustris and *Euglena gracilis* were cultured in NIES-C and CM medium, respectively. Dimethyl Sulfoxide (DMSO) was used as an auxiliary solvent to improve the solubility and bioavailability of ferulic acid. For cell culture, 10 mL algal cells in the exponential phase were inoculated into Erlenmeyer flasks and different concentrations of ferulic acid dissolved in DMSO stock solution were then added. Finally, the DMSO concentration of experimental groups was adjusted to 1% and each flask contained 100 mL medium. A solvent control group was additionally set to evaluate the effect of the auxiliary solvent DMSO. *H. lacustris and E. gracilis* cells were continuously illuminated under the light condition of 5000 lx by cool-white fluorescent lamps (12:12h light-dark cycle). Cell growth was assessed by cell density and dry weight. Cell morphology in different conditions was observed by microscope and analyzed using Image J software. Pigments content were estimated by following Lichtenthaler's method. Astaxanthin content of *H. lacustris* and paramylon content of *E. gracilis* were also measured.

[Result and Discussion]

The effect of ferulic acid on the growth of *H. lacustris* was shown in Figure 1.

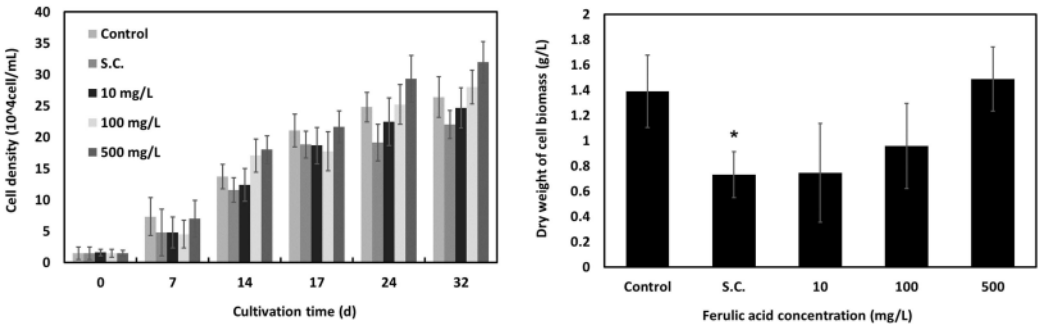

Figure 1. Growth profile of *H. lacustris* with different concentrations of ferulic acid. S.C., solvent control group.

As can be seen from the figure, the cell density of the solvent control group was lower than that of the blank control group throughout the culture. With the addition of ferulic acid, the growth of *H. lacustris* was recovered to a certain extent. When the ferulic acid concentration reached 500 mg/L, the cell density was 45.45% higher than that of the solvent control group, however, there was no significant difference compared with the blank control group. Intracellular astaxanthin content was not influenced significantly by ferulic acid. We speculated that DMSO was slowly oxidized under the catalysis of light during the cultivation, and a large amount of reactive oxygen species such as free radicals were generated and adversely affected the cells, and ferulic acid was able to alleviate the growth inhibitory effect of DMSO.

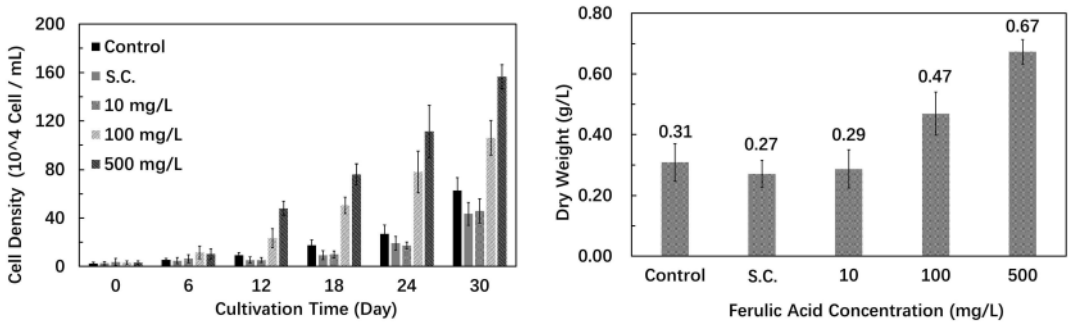

Figure 2. Growth profile of *E. gracilis* with different concentrations of ferulic acid. S.C., solvent control group.

Figure 2 shows the growth profile of *E. gracilis* with various concentrations of ferulic acid. The cell density in the solvent control group was significantly lower than that of the control group. However, at higher concentrations of ferulic acid, their growth was significantly promoted in a concentration-dependent manner. At day 30, cell density in the 500 mg/L ferulic acid treatment group showed a 2.5-fold increase compared with that of the control group and a 3.6-fold increase compared to that of the solvent control group. As for the particular mechanism of the promotion effect, on the one hand, ferulic acid and its oxidative products might serve as an exogenous organic carbon source for *E. gracilis* growth. On the other hand, products of ferulic acid might play phytohormone-like regulatory roles in cell growth.

Dry content of pigments and paramylon is shown in Figure 3. The chlorophyll a content in the solvent control group was significantly decreased. In the ferulic acid treatment groups, chlorophyll a content was restored and increased in a dose-dependent manner with increasing ferulic acid concentrations.

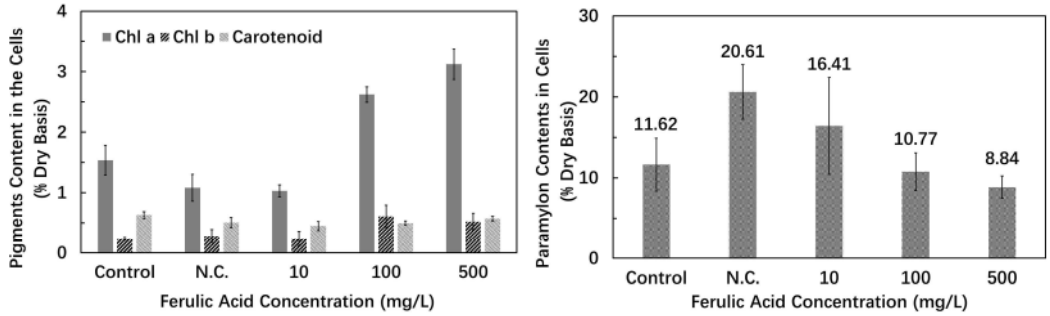

Figure 3. Content of pigments and paramylon in *E. gracilis* cells cultured with different concentrations of ferulic acid. S.C., solvent control group.

The paramylon content of *E. gracilis* cells showed opposite trend to chlorophyll a content. A higher paramylon content was obtained in the solvent control group. After the addition of ferulic acid, the paramylon content decreased and eventually reached a normal level, indicating ferulic acid does not diminish the accumulation of paramylon. Because paramylon storage would increase when *E. gracilis* cells grew slowly under unfavorable conditions, while paramylon was consumed in groups that showed rapid growth.

Effect of ferulic acid on the growth and metabolism of microalgae was different from species to species. Ferulic acid could alleviate the stress caused by DMSO both in *H. lacustris* and *E. gracilis* cultures. In addition, ferulic acid have been proven for the first time as excellent growth promoters which was able to increase the cell biomass of *E. gracilis* and production of paramylon.

Please choose: Oral/ Poster
Presentation session:
Presenter name: Mohd. Esa, Norhaizan

Sapodilla Leaf, a Potential Source of Antiproliferative Agents, Selectively Induces Apoptosis in HepG2 Cells through Downregulation of Akt1/ERK1/2

Norhaizan, Mohd. Esa[1], Bee Ling, Tan[1],

[1]Faculty of Medicine and Health Sciences, Universiti Putra Malaysia, 43400 UPM Serdang, Selangor, Malaysia

Email: nhaizan@upm.edu.my

Abstract

This paper presents a new finding of the traditional medicinal plant as an anti-liver cancer agent. Liver cancer has become the second leading cause of mortality worldwide. Despite tremendous efforts have been performed in the last few decades to improve the available therapeutic approaches, conventional therapy is not likely effective due to an adverse outcome, yet metastasis and recurrence still tend to occur. Hence, the discovery of new anti-cancer agents from natural products has drawn an intense interest among scientists. *Manilkara zapota* (L.) P. Royen, called as sapodilla, belongs to the family *Sapotaceae*. The previous finding has demonstrated that ethyl acetate extract of *Manilkara zapota* leaf inhibits the Ehrlich ascites carcinoma in mice. Nevertheless, there is no pharmacological study on anti-liver cancer properties of *Manilkara zapota* leaf water extract in the literature. Therefore, our present study is designed to investigate the ability to induce apoptosis and the underlying mechanisms of *Manilkara zapota* leaf water extract inducing cytotoxicity in human hepatocellular carcinoma (HepG2) cells. Overall analyses revealed that *Manilkara zapota* leaf water extract can increase the total percentage of apoptotic HepG2 cells, increase intracellular reactive oxygen species (ROS) level, upregulate c-Jun N-terminal kinase 1 (*JNK1*) and inducible nitric oxide synthase (*iNOS*), reduce *Akt1* and vascular endothelial growth factor A (*VEGFA*) transcriptional activities. Our data suggest that *Manilkara zapota* leaf water extract can suppress the growth of HepG2 cells via modulation of *ERK1/2*/*Akt1*/*JNK1* transcriptional expression.

Keywords

Akt1, c-Jun N-terminal kinase 1, liver cancer, reactive oxygen species, sapodilla

Introduction

Liver cancer has become the second leading cause of mortality worldwide. Despite tremendous efforts have been performed in the last few decades to improve the available therapeutic approaches, conventional therapy is not likely effective due to an adverse outcome, yet metastasis and recurrence still tend to occur. Hence, the discovery of new anti-cancer agents from natural products has drawn an intense interest among scientists. *Manilkara zapota* (L.) P. Royen, called as sapodilla, belongs to the family *Sapotaceae*. The previous finding has demonstrated that ethyl acetate extract of *Manilkara zapota* leaf inhibits the Ehrlich ascites carcinoma in mice. Nevertheless, there is no pharmacological study on anti-liver cancer properties of *Manilkara zapota* leaf water extract in the literature. Therefore, our present study is designed to investigate the ability to induce apoptosis and the underlying mechanisms of *Manilkara zapota* leaf water extract inducing cytotoxicity in human hepatocellular carcinoma (HepG2) cells.

Experiment

Manilkara zapota leaf sample was extracted using water as previously described by Tan *et al*. (2013). The apoptosis and intracellular reactive oxygen species (ROS) activities were analyzed using Annexin V-propidium iodide staining and dichlorodihydrofluorescein diacetate, respectively, by NovoCyte Flow

Cytometer. The associated molecular pathways were evaluated by quantitative real-time PCR. The statistical significance of the difference between the control and treatment groups was analyzed using a one-way analysis of variance (ANOVA). Statistical analyses were performed using the Statistical Package for Social Science (SPSS) version 19.0. A P value less than 0.05 was considered statistically significant.

Results and Discussion

Overall analyses revealed that *Manilkara zapota* leaf water extract can increase percentage of early apoptotic cells, induce the formation of ROS, upregulate c-Jun N-terminal kinase 1 (*JNK1*) and inducible nitric oxide synthase (*iNOS*), and reduce *Akt1* and vascular endothelial growth factor A (*VEGFA*) transcriptional activities. Our data suggest that *Manilkara zapota* leaf water extract can suppress the growth of HepG2 cells via modulation of *ERK1/2/Akt1/JNK1* transcriptional expression.

Conclusion

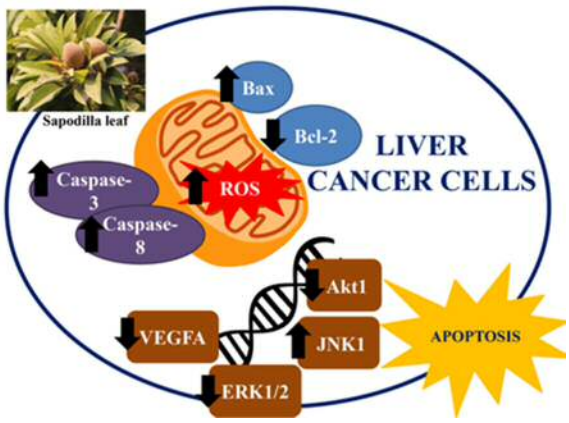

Please choose: Oral/ Poster
Presentation session:
Presenter name:

Evaluation of acute toxicity induced by supercritical carbon dioxide extract of *Canarium odontophyllum* (CO) Miq. pulp oil in SPF Sprague Dawley rats

Azrina, Azlan[1], Nurdiyana, Abdul Manap[1], Hazilawati, Hamzah[2], Sharida, Fakurazi[1]

[1]Faculty of Medicine and Health Sciences, Universiti Putra Malaysia, 43400 UPM Serdang, Selangor, Malaysia
[2]Faculty of Veterinary Medicine, Universiti Putra Malaysia, 43400 UPM Serdang, Selangor, Malaysia

Email: azrinaaz@upm.edu.my

Abstract

Keywords (Acute toxicity, supercritical extraction, *Canarium odontophyllum*)

[Introduction Dabai fruit or *Canarium odontophyllum* (CO) Miq., is a fruit-bearing tree of the genus Canarium in the family Burseraceae. It is an infamous fruit, also prized as a seasonal delicacy in Sarawak and loved by the locals. The solvent extracted fat of this fruit has been proven scientifically for their natural antioxidants with good fatty acid composition. However, to date no data was available on acute toxicity testing of the CO oil prepared using carbon dioxide supercritical fluid extraction (SCO_2) as preliminary of complete toxicity information]

[Experiment SCO_2 liquid was used to extract CO oil from CO pulp at a temperature of 40°C and pressure of 40 MPa. The extracted CO oil was stored in an airtight container to maintain the availability of crude compound in the oil. Two to three rats (total n=28, 14 male, and 14 female) were randomly housed per cages and the rats were fed and allowed to drink sterilized water *ad libitum*. An observation was carried out after a single dose of 5000 mg/kg was administered for general behavior and toxic signs. At the end of the study period (14 days), biochemical parameters and relative weights of the organs (liver, kidney, spleen, heart, stomach, and brain) were measured**.]**

[Results and Discussion No deaths of rats were recorded on the rats receiving the single dose oral gavage of the SCO_2CO oil. SCO_2CO oil extract did not affect the relative organ weights and biochemical parameters (liver, kidney, and lipid profile test) of the rats. The SCO_2CO oil extract also did not induce toxicity on biochemical parameters at the highest dose. These results show that SCO_2 CO oil has exhibited No-Observed-Adverse-Effect-Level (NOAEL) at 5000 mg/kg; where there is no statistical significance between the control and treated groups in both sexes. These corroborate the findings of a previous work using *Canarium ovatum*, Engl. that also had shown the same findings. Therefore, SCO_2 CO oil can be considered for further investigations of subchronic and chronic toxicity studies as well as for its therapeutic efficacy.]

Table 1: Weekly body weight (g) of male and female Sprague Dawley rats treated with SCO_2 CO oil for 14 days.

Treatment (mg/kg)	Weeks (g)			
	Acclimatization		Induction	
	1	2	3	4
Male rats				
Control	157.6±7.5	207.4±8.0	252.0±15.6	303.8±22.1
5000 mg/kg	153.8±11.4	204.4±18.5	204.4±18.5	315.2±19.8
Female rats				
Control	142.6±14.1	174.8±15.7	207.2±17.4	223.8±15.7
5000 mg/kg	135.0±9.8	170.4±13.6	188.0±27.4	213.2±19.0

Values are mean ± S.D. (n = 5/sex/dose). No statistical difference: control vs treated group (T-test)

Table 2: Biochemical parameters of male and female Sprague Dawley rats treated with SCO_2 CO oil for 14 days

Treatment (mg/kg)	TG[a] (mmol/L)	Chol[b] (mmol/L)	AST[c] (U/L)	ALT[d] (U/L)	ALP[e] (U/L)	TBil[f] (µmol/L)	Urea (µmol/L)	Creat[g] (µmol/L)
Male rats								
Control	1.3±0.3	2.4±0.4	119.6±47.2	60.2±22.6	191.8±12.9	1.5±0.3	7.2±0.5	41.4±5.0
5000 mg/kg	1.0±0.3	2.5±0.9	100.0±12.9	43.0±4.9	229.8±61.0	1.6±0.3	7.0±0.7	41.8±1.6
Female rats								
Control	1.1±0.4	2.9±0.4	79.0±34.1	38.0±7.9	129.0±30.7	1.5±0.6	6.9±1.1	37.4±2.1
5000 mg/kg	1.1±0.5	2.5±0.3	109.2±31.7	42.2±5.6	119.2±14.4	1.2±0.2	6.6±1.1	38.6±4.5

Values are mean ± SD (n = 5/sex/dose). No significance differences between control and treated group (t-test).
[a] Triglycerides, [b] Cholesterol, [c] Aspartate aminotransferase, [d] Alanine transaminase, [e] Alkaline phosphatase, [f] Total bilirubin, [g] Creatinine.

Please choose: Oral/ Poster/ Either
Presentation session: Biological Science
Presenter name: Barakatun-Nisak Mohd Yusof

Effect of White Rice on Blood Glucose Level: Lessons from animal model to applied science

Barakatun-Nisak, Mohd Yusof[1,2], Jeevetha, Subramaniam[1], Amin Ismail[1,2], Azrina, Azlan[1,2], Nor Azmi Kamaruddin[3]

[1]Faculty of Medicine and Health Sciences, Universiti Putra Malaysia, Serdang Selangor, Malaysia
[2]Research Centre of Excellent for Nutrition and Non-communicable Diseases, Faculty of Medicine and Health Sciences, Universiti Putra Malaysia, Serdang Selangor, Malaysia
[3]Faculty of Medicine, National University of Malaysia Kuala Lumpur, Malaysia

Email: bnisak@upm.edu.my

Keywords (5 words): Rice, glucose, diabetes, Asian and postprandial

Introduction: In most Asian countries, white rice remains the major staple diet. Despite its widespread use, white rice has been the focal point of interest because epidemiologic studies documented that higher consumption of white rice is associated with increased risk for type 2 diabetes (T2D) especially among Asian population. We present findings of our work from animal model and human studies on the effect of white rice consumption on blood glucose levels.

Experiment: We started an animal model to investigate the effect of white rice (WR) vs. Corn-based diet as a control diet (CD) on glucose and body weight of the rats. A total of 32 rats were equally distributed into four groups for 8 weeks feeding duration. The four groups were the experimental WR diet which was further divided into (1) WR-with normal carbohydrate (WRN; CHO=55%Cal) and (2) WR-high carbohydrates (WRH; CHO=65%Cal); and the CD diet which was further divided into (3) positive control (Corn-High Fat (CHF; Fat=50%Cal) and (4) negative control (AIN-93M Purified Rat Diet (PD; CHO=75%Cal; Fat= 10%Cal). Outcomes measures included fasting plasma glucose, insulin, HOMA-IR, triglycerides and body weight. In human study, we conducted the cross-sectional study to determine the white rice consumption pattern and its association with glucose control in patients with T2D. The rice consumption pattern were assessed using food frequency questionnaire (FFQ) and the glucose control were assessed using HbA1c level, a marker of overall glucose control in diabetes.

Result and Discussion: In animal model, parameters at baseline were homogenous in all groups. At the end of 8 weeks, rats in the WRH group had significantly higher fasting blood glucose (FBG 16.9 $\pm$ 2.4 mmol/L) and higher triglycerides (1.3 $\pm$ 0.1 mmol/L) than the other studied group (Table 2; $p < 0.05$) despite having comparable body weight across group. On the other hand, rats in the CHF (41.9±2.5mU/L) group had greater fasting insulin levels and this was significantly different than those rats from the WRN (36.3±1.15mU/L) and PD (33.9±1.55mU/L) groups ($p<0.05$). The insulin resistance indicator (HOMA-IR) showed that rats in WRH (537.7±95.9) had significantly highest HOMAIR value compared with WRN (373.4±50.1), HF (178.5±24.9) and PD (161.6±7.7) groups ($p<0.05$). In human study, we found that patients with T2D who were eating white rice using a smaller bowl had significantly better blood glucose control as compared to the bigger white rice-bowl rice eater (HbA1c 8.2% vs. 9.5% $p < 0.05$). Nevertheless, the type of rice did not correlates with HbA1c and other parameters. In conclusion, our study in animal model showed that eating high carbohydrate-white rice based diet may induce diabetes in rats. Although a corn-based high fat diet induced a higher insulin level, but is not as a higher degree to insulin resistance indicator as shown after eating high carbohydrate-white rice diet. In human study, better glucose control was observed among patients with T2D who were using smaller rather than bigger rice bowl. The mechanism warrants further investigation but it could be due to the high glycemic index and load of the white rice.

Please choose: Either
Presentation session: Environmental Biotechnology
Presenter name: Toshinari MAEDA

Understanding Social Cheater-like Bacteria during Methane Fermentation using Waste Sewage Sludge

Toshinari MAEDA, Vi Hoang Bao LE, Nurul Asyifah MUSTAPHA

Graduate School of Life Science and Systems Engineering, Kyushu Institute of Technology, 2-4 Hibikino, Wakamatsu-ku, Kitakyushu, Fukuoka,808-0196, Japan

Email: toshi.maeda@life.kyutech.ac.jp

Keywords (5 words)
social cheater, cheating, methane fermentation, waste sewage sludge, bacterial interaction

[Introduction]

Social cheaters have been found in an adaptive process for the inhibition of quorum sensing, in which the social cheaters that cannot digest high-molecular compounds can survive through grabbing nutrients digested by another bacteria (cooperators). Such public manners of social cheaters may be conceivable in the microbial ecosystem. Methane fermentation using waste sewage sludge (WSS) is one of the good examples to understand how social cheater-like bacteria in the microbial community influence the process of methane fermentation because the initial digestion of WSS should be conducted by a "public good" manner. In the methane fermentation using WSS, the microorganisms which play a key role in the three processes, hydrolysis, acidogenesis, and methanogenesis are reported to be responsible for methane production; however, there are no reports on the presence and the role of social cheater-like bacteria in WSS; in particular, the relationship between microorganisms related to methane production and social cheater-like bacteria. In this study, the presence of social cheater-like bacteria in WSS was examined. Furthermore, based on our previous results that the addition of antibiotic azithromycin (AZM) or chloramphenicol (CM) to WSS influences methane fermentation through the change of microbial activities in WSS, the effect of antibiotics to social cheater-like bacteria was also examined. In addition, the next generation sequencer (MiSeq) was used to analyze more detail categories of social cheater-like bacteria. The relationship between methane production and social cheater-like bacteria can be figured out more clearly to enhance methane production using WSS.

[Experiment]

1. Counting the number of social cheater-like bacteria in WSS

- Prepared WSS (10%-w/w) which has been routinely obtained from the Hiagari sewage treatment plant was diluted sequentially and spread on LB-skim milk agar plates and then incubated at 37°C for 24 hours under aerobic and anaerobic conditions to determine social cheater-like bacteria. The colonies that no haloes were observed on LB-skim milk were transferred to LB-starch, LB-CMC and LB-lipid agar plates and incubated at 37 °C for 18, 24, 36 hours. The final colonies which did not show any halo in all agar plates were identified as social cheater-like bacteria.

2. Effect of an antibiotic (azithromycin or chloramphenicol) to social cheater-like bacteria

- Anaerobic digestion was done by using 10% WSS for 4 types of samples: (1: WSS as control, 2: WSS + Ethanol (as a solvent for each antibiotic), 3: WSS + azithromycin (AZM) and 4: WSS + chloramphenicol (CM)) and incubated at 37 °C with 120 rpm. Methane production and the number of social cheater-like bacteria were determined at 0, 5, and 10 days.

3. Identification of social cheater-like bacteria using 16S ribosomal RNA gene

- Each single colony of social cheater-like bacteria was used for the colony PCR. The PCR product was purified by using a gel extraction kit and used for the DNA sequence analysis which was handled by a sequencing company.

4. Screening organic acid producers in social cheater-like bacteria

- The social cheater-like bacteria were spreading on MRS-$CaCO_3$ plate. These plates were incubated at 37°C for 2 days, and the colonies grown on with the clear halo were selected to analyze the organic acid production.

5. Identification of social cheater-like bacteria using MiSeq

- All of the social cheater-like bacteria and the supernatants were used for the DNA extraction for running MiSeq.

[Result and Discussion]

1. Social cheater-like bacteria in WSS

Social cheater-like bacteria present in WSS were detected under aerobic and anaerobic conditions. The ratio of social cheater-like bacteria to the total bacteria was 79 ± 1% indicating that social cheater-like bacteria are present in WSS at a relatively-high proportion and the number of social cheater-like bacteria in the anaerobic condition was higher than that in the aerobic one.

2. Effect of azithromycin or chloramphenicol to social cheater-like bacteria

Our previous result showed that azithromycin improves and chloramphenicol represses methane fermentation. Therefore, the relationship between social cheater-like bacteria and methane fermentation with each antibiotic was investigated. In 3 samples (WSS, WSS + Ethanol, and WSS + AZM) the number of social cheater-like bacteria decreased with time. On the other hand, in the sample of WSS + CM, a high number of social cheater-like bacteria was still detected at day 5 but finally decreased at day 10.

3. Identification of social cheater-like bacteria using 16S ribosomal RNA gene

Using each 10 colonies determined as social cheater-like bacteria under the 4 conditions, the homology analysis of 16S ribosomal RNA gene was conducted to identify each bacterial species. As a result, most of the colonies were classified as *Proteobacteria* group, and some from *Firmicutes* and *Actinobacteria* group.

4. Identification of social cheater-like bacteria using MiSeq

The microbial communities and the social cheater-like bacteria in WSS with or without the addition of each antibiotic were evaluated using Illumina MiSeq. The results of MiSeq showed that *Proteobacteria* is the most dominant phylum, followed by *Firmicutes*, *Bacteroidetes*, and *Actinobacteria.*

5. Screening organic acid producers in social cheater-like bacteria

The social cheater-like bacteria isolated were selected for their ability in producing organic acid by MRS-$CaCO_3$ medium. Among 50 colonies of social cheater-like bacteria isolated on LB medium, there are 15 social cheater-like bacteria colonies which can produce organic acids (5 colonies form WSS, 2 colonies from WSS + Ethanol, 3 colonies from AZM and 5 colonies from WSS + CM). Based on this finding, 15 social cheater-like bacteria were used to checking organic acids production in MRS medium by HPLC. The result showed that all social cheater-like bacteria isolated from LB medium produced lactic acid and acetic acid.

6. Conclusion

The use of antibiotics which has the different effect on methane fermentation shows the different pattern of social cheater-like bacteria. In fact, AZM has altered the microbial community and the social cheater-like bacteria in WSS, which the methane production was higher than the control WSS. The addition antibiotic CM inhibited the methane production from WSS and the social cheater-like bacteria, which was changed higher than three other samples.

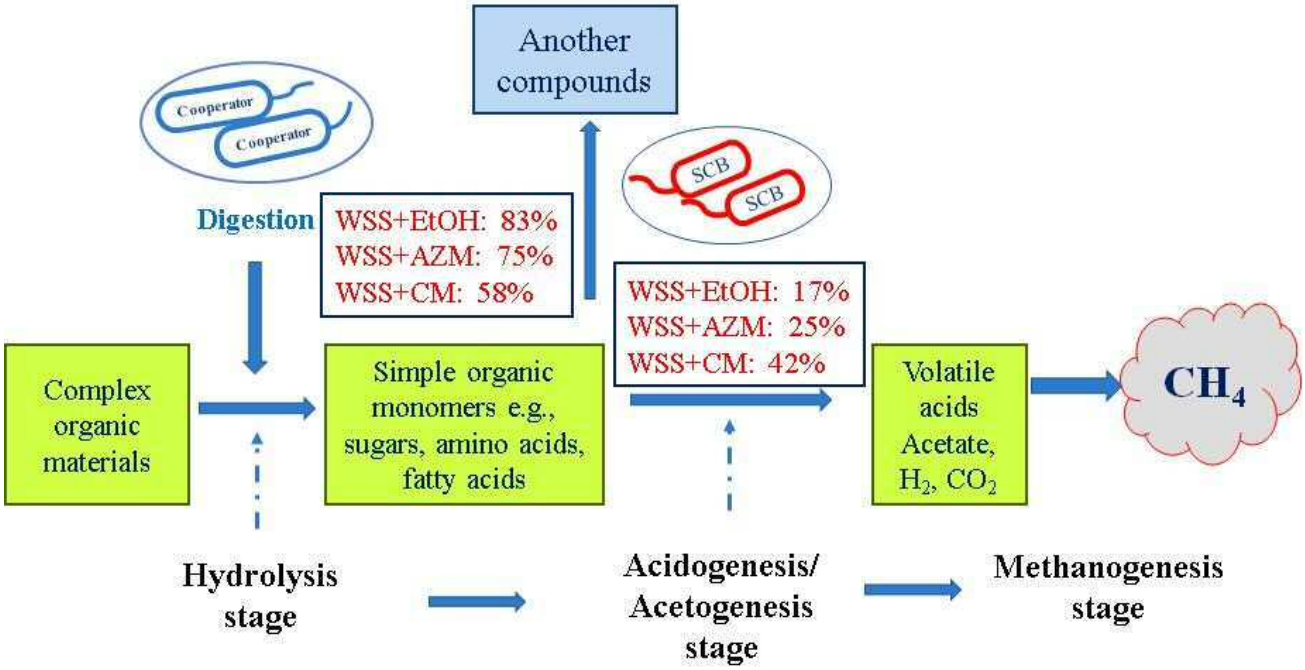

Fig. 1. Relationship of social-cheater like bacteria in the process of methane fermentation using waste sewage sludge. A large number of social-cheater like bacteria convert sludge components into another compound other than produce methane; as a result, a low amount of methane was produced.

Please choose: Oral
Presentation session: Applied Chemistry
Presenter name: Hongsuk Suh

Syntheses and Characterizations of Push-pull Types of Conjugated Polymers for Photovoltaic Solar Cells

Juae Kim, Hongsuk Suh

Department of Chemistry and Chemistry Institute for Functional Materials, Pusan National University,
63 Beon-gil 2, Busandaehag-ro, , Geumjeong-gu, Busan 46280, KOREA
Email: [hssuh@pusan.ac.kr]

Keywords (5 words): Conjugated Polymers, PSCs, electron-rich unit, electron-deficient unit, PCE.

[Introduction]

Polymer solar cells (PSCs) with reported efficiencies of over 10% in single-junction polymer solar cells have attracted significant amount of attentions attributed to their diverse advantages. Many well-planned strategies for the achievement of high efficiency ought to enhance the values of open circuit voltage (V_{OC}), short circuit current (J_{SC}) and fill factor (FF). In addition to the reduction of the HOMO energy level to increase the V_{OC} of the device, extension of the long wavelength absorption, for the better coverage of the solar spectrum, by using intra-molecular charge transfer (ICT) has been accomplished by utilizing the push-pull types of conjugated polymers containing electron-rich units and electron deficient units.

[Experiment]

Nat. Commun. **2014**, *5*, 5688.

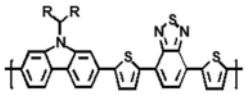

***J. Polym. Sci. Pol. Chem.* 2016, *54*, 771.**

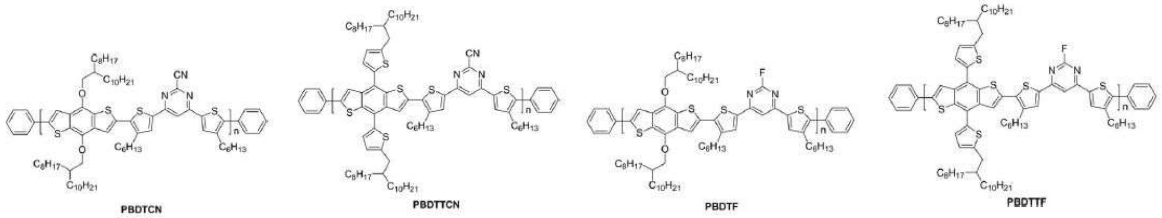

***Polymer* 2016, *83*, 50.**

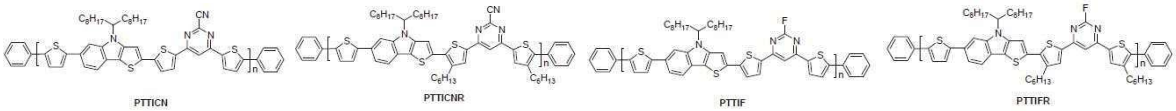

***Polym. Chem.*, 2015**, *6*, 6011.

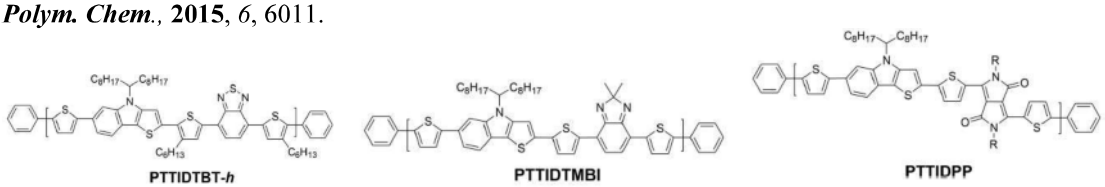

***Polymer* 2017**, *109*, 115.

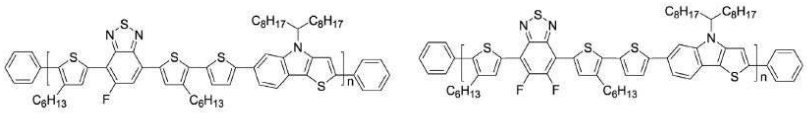

***Polymer* 2015**, *71*, 113.

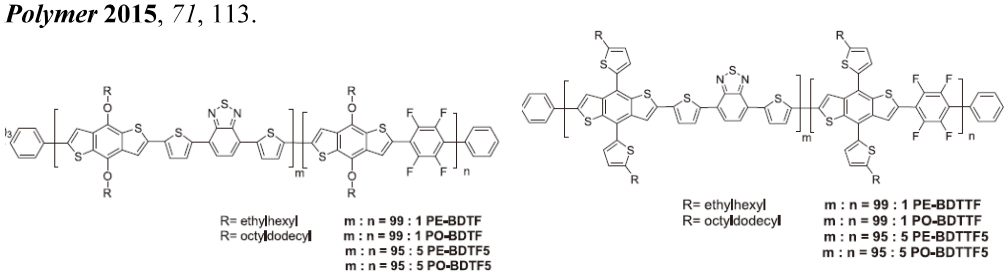

***Polymer* 2016**, *102*, 84.

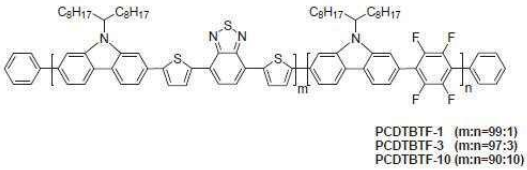

***Polymer* 2016**, *95*, 36.

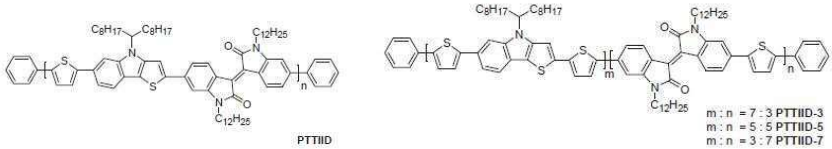

***Sol. Energ. Mat. Sol. C.* 2015**, *141*, 24.

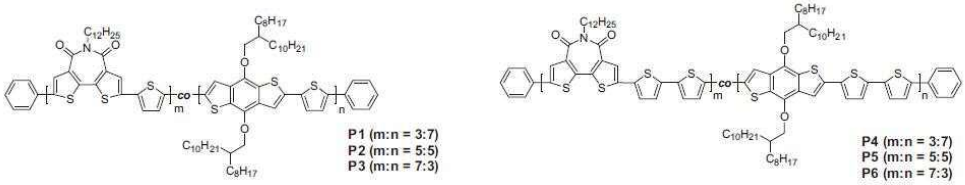

[Result and Discussion]

All of the above push-pull types of polymers with electron rich units and electron deficient units were synthesized for the generation ICT to expand the coverage of the solar spectrum. The devices with the configuration of ITO/ZnO/L-PCDTBT:$PC_{71}BM$/MoO_3/Ag were fabricated to elucidate the *Voc, Jsc,* FF and PCE values. Especially, the PCDTBT was synthesized and divided into three fraction with deferent molecular weights. L-PCDTBT showed the highest PCE and the PCE value was maintained about 80% over 20 months at room temperate under air with illumination of AM 1.5 G solar spectrum with encapsulation.

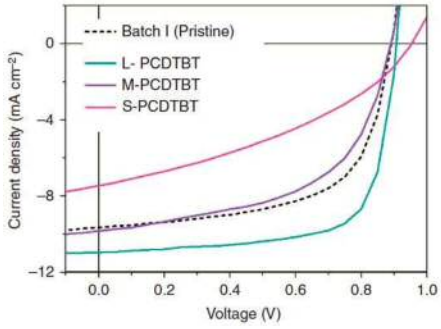

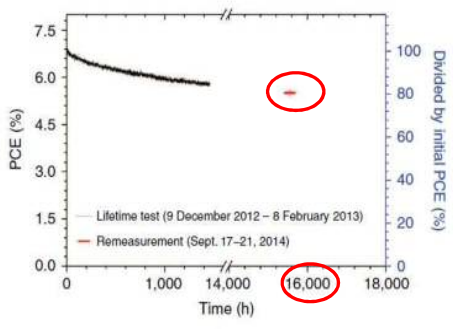

Batch		V_{OC} (V)	J_{SC} (mA cm^{-2})	FF	PCE (%)	M_n (kDa)	PDI
I	Pristine	0.90	9.63	0.60	5.15	21	3.0
	L -PCDTBT	0.91	10.9	0.71	7.04	59	1.8
	M-PCDTBT	0.88	9.83	0.59	5.10	20	2.4
	S -PCDTBT	0.95	7.46	0.37	2.62	4.6	1.9

Please choose: Oral
Presentation session: Applied Engineering
Presenter name: Shyam S. Pandey

Correlating Molecular Orientation and Device Performance in Organic Electronic Devices based on Oriented Thin Films of Conjugated Polymers

Shyam S. Pandey[1], Manish Pandey[1], Nikita Kumari [1], Atul SM Tripathi[1], Suichi Nagamatsu[2] and Shuzi Hayase[1]

[1]Graduate School of Life Science and Systems Engineering, Kyushu Institute of Technology, 2-4 Hibikino, Wakamatsu, Kitakyushu 808-0196, Japan
[2]Department of Computer Science and Electronics, Kyushu Institute of Technology, 680-4 Kawazu, Iizuka, 820-8502, Japan

Email: shyam@life.kyutech.ac.jp

Keywords: Conjugated polymers, Orientation, Anisotropy, Charge transport, OFETs

Introduction

Recent past has witnessed a fast pace development in organic semiconductors and their utilization as active components of organic electronic devices aiming towards the practical realization of low-cost flexible and printable electronics. OFETs are one of most important components of electronic devices and there is a need for reduction of the production cost with minimal or no compromise on their performance. It has been widely accepted that performance of OFETs are controlled by nature of the organic semiconductors and quality of their thin films. At the same time, cost is controlled by the methodology adopted for the fabrication of high quality thin films on gate insulators. Organic electronic devices generally bear multilayer devise architecture where, control of the morphology along with the various interfaces critically controls the overall device performance. Therefore, there is need for logical approaches towards the fabrication of large area uniform films of organic semiconductors with controllable film morphology and minimal interference to underlying layers by the over layers during formation of multilayer films. We have developed a novel method of film fabrication known as floating film transfer method (FTM), which provides not only large area uniform films but also highly oriented thin films CPs by rapid molecular self-assembly. Our recent improvisation of FTM utilizing PTFE slider lead to the fabrication of very large area and oriented uniform thin films, which was applicable to a variety of CPs. At the same time, we have also developed a fast and facile 2D positional mapping system for the efficient profiling of film uniformity as well as molecular orientation.

Experiment

A number of CPs like P3HT, PTB7, PQT, PBTTT and F8T2 have been utilized for the fabrication of thin films using different methods like spin coating, FTM and friction transfer. Thin film fabrication of CPs using FTM was conducted as per our earlier publications [1] and schematically shown in the Fig.1. Thin film of CPs by friction transfer method were fabricated by optimizing the substrate temperature, stage speed and applied load. Molecular orientation in the oriented film was estimated by polarized spectral measurement while film uniformity of the fabricated film and orientation was characterization by 2-D positional mapping system and verified by conventional and UV-Visible spectrophotometric investigations. The bottom-gate top-contact device architecture was utilized to fabricate OFETs were fabricated on Si/SiO_2 substrate using anisotropic oriented and isotropic non-oriented thin films in order to probe implication of molecular orientation on the anisotropic charge carrier transport.

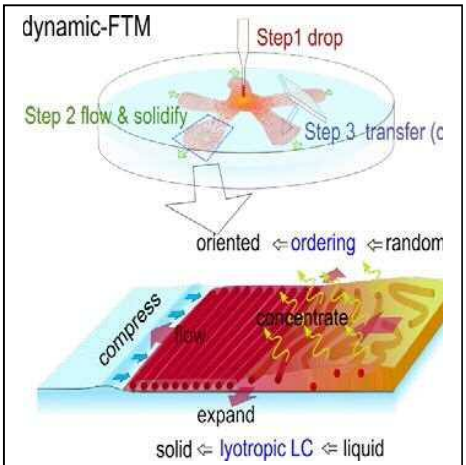

Figure 1. Schematic illustration and mechanism of oriented film fabrication by FTM.

Result and Discussion

Spin coating has been most widely used for the fabrication of thin films of CPs towards their application for organic electronic devices but existing problems like huge material wastage and dissolution of underlayer has

led to proposal of the FTM as an amicable solution. FTM offers several advantages like simplicity of the process, cost-effectiveness, optical anisotropy, minimum material wastage and multilayer fabrication without disturbing the morphology of under layers. A perusal of Fig. 2 reveals that FTM not only exhibited oriented films but also in multilayers, spectral behavior for each layer is preserved. We have recently shown that by controlling the film fabrication parameters using NR-P3HT under FTM led to not only macroscopically oriented films but also there was a remarkable enhancement in the mobility (> 10^2 times) as compared to their non-oriented spin-coated thin film counterpart based devices.

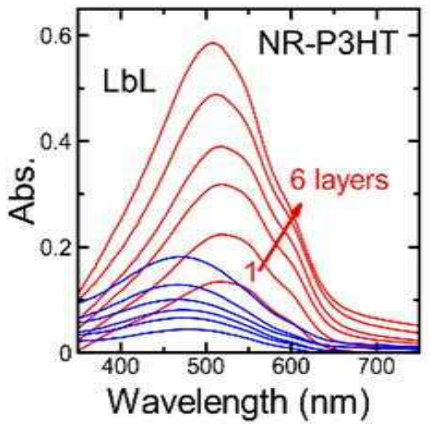

Figure 2. FTM fabricated multilayer thin films of NR-P3HT. Blue and red exhibits absorption spectrum for films with perpendicular and parallel orientation.

In order to provide large area oriented thin films, we have demonstrated that utilization of newly designed slider in FTM led the formation of large area (>2 cm x 18 cm) oriented thin films. A number of CPs as P3HT, PQT, PBTTT, F8T2 and PTB7 have been successfully oriented using this ribbon-shaped FTM. Amongst various CPs subjected to fabrication of oriented thin films exhibited ribbon-shaped films as shown in the Fig. 3, but PQT exhibited highest optical anisotropy of 5.1. Utilization of the oriented thin film of the PQT for OFETs, exhibited anisotropic charge transport with mobility anisotropy 7.1 and charge carrier mobility of 0.05 cm^2/Vs for the parallel oriented films.

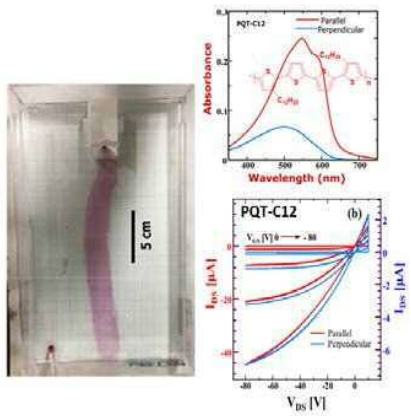

Figure 3. Large area and oriented thin films of various CPs fabricated by Ribbon-shaped FTM and its optoelectronic characterizations.

Fabrication and characterization of devices with facile solution processing, improved charge carrier transport in combination with high device reproducibility is crucial for the practical realization of the next generation and low cost flexible devices. In the case of large area solution processed thin films, film thickness and morphological variations are one of major obstacles leading to poor reproducibility of fabricated devices. We have developed 2D positional mapping system, which is capable of successful profiling of not only the film uniformity (thickness distribution) but also the molecular orientation for large area thin films. Results of 2D positional mapping of thickness and molecular orientation for 1 cm × 1 cm samples of PQT-C12 thin films prepared at two different temperatures and taken from three different locations is shown in Fig. 4. A perusal of the comparative mapping results indicates that film cast at higher temperature (50°C) exhibits relatively uniform distribution of thickness and higher molecular orientation as compared to the films cast at lower temperature (30°C). PQT-C12 ribbon-shaped FTM film cast at 50°C were thus used to fabricate OFETs in, bottom gate top contact device structure. In this case, FTM films were stamped from far-end region owing to its high uniformity and high DR as shown in the Fig. 4. Electrical parameters like μ and ON/OFF (I_{on}/I_{off}) ratio were estimated from the transfer curve shown in Figure 6(b). Extracted μ in $\parallel$ ($\mu_{\parallel}$) and in $\perp$ ($\mu_{\perp}$) direction were found to be 0.17 $cm^2/V{\cdot}s$ and 4.45 $\times 10^{-3}$ $cm^2/V{\cdot}s$, respectively.

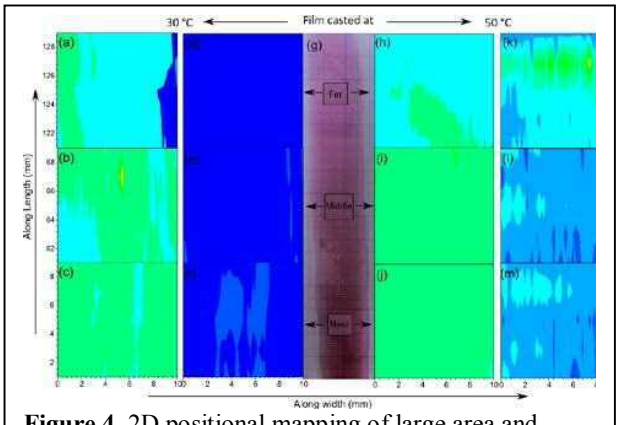

Figure 4. 2D positional mapping of large area and oriented thin films of various CPs fabricated by Ribbon-shaped FTM.

Near-infrared photoluminescence of PbS/MnS core shell quantum dots prepared by cation exchange method

Mazliana Ahmad Kamarudin[1], Muhammad Safwan Zaini[1], Josephine Liew Ying Chyi[1], Shahrul Ainliah Alang Ahmad[2], Abdul Rahman Mohmad[3]

[1]Department of Physics, Faculty of Science, Universiti Putra Malaysia, 43400, UPM Serdang, Selangor Darul Ehsan, Malaysia.
[2]Department of Chemistry, Faculty of Science, Universiti Putra Malaysia, 43400, UPM Serdang, Selangor Darul Ehsan, Malaysia.
[3]Institute of Microengineering and Nanoelectronics, Level 4, Research Complex, Universiti Kebangsaan Malaysia, 43600, Bangi, Selangor, Malaysia.

Corresponding author: mazliana_ak@upm.edu.my

Keywords: Quantum Dots, core shell, lead sulphide, photoluminescence

Introduction

Colloidal quantum dots attract exciting attention due to their unique optical properties, capability to tune the emission energy or bandgap and stability. These advantages make them potentially useful for variety applications such as dual imaging and optoelectronic devices. Among numerous semiconductor material systems, lead sulphide (PbS) attract more attention due to their narrow bandgap of 0.41 eV at room temperature with a large exciton Bohr radius of ~20 nm, thus allowing the quantum confinement in relatively large sized QDs.

In this study, we report near-infrared (NIR) fluorescent PbS/MnS core shell colloidal QDs in an aqueous solution. PbS quantum dots (QDs) capped with MnS shell were synthesized via aqueous chemistry method in inorganic solvents. A thin layer of MnS was grown around PbS QDs via cation exchange in order to improve the optical properties of PbS QDs. Cation exchange is a new pathway to design novel NCs starting from well-developed synthesis QDs.

Experiment

A cation exchange method has been developed to synthesise PbS/MnS core/shell QDs. The exchange between Pb^{2+} and Mn^{2+} on the PbS QDs surface formed a layer of MnS shell, giving an additional confinement to the carriers. The samples were prepared with different concentration of Mn^{2+} precursor, to control the thickness of the shell. Then the samples were characterized by micro-photoluminescence at room temperature and the emission was monitored for several weeks. The increasing of PL energy can be observed could be due to the presence of MnS shell.

Result and discussion

Optical charasterisation of the QDs has been done through photoluminescence (PL) spectroscopy at room temperature. Figure 1 shows the PL peak emission for PbS and PbS/MnS over 7 weeks. Decreasing trend of PL peak energy with aging has been observed for PbS bare core sample and probably attributed to coalescence. In contrast, the PbS/MnS core shell samples with various thickness shows the blue-shifts trend could be due to quantum confinement effect by formation of MnS shell. This also could be due to reduction in the size of the core PbS QDs.

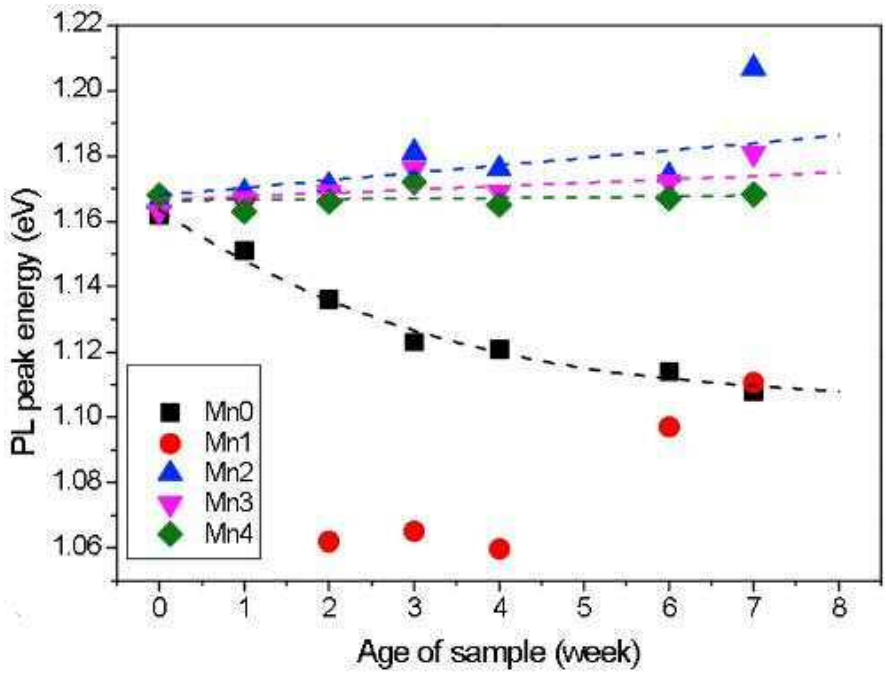

Figure 1

Please choose: Oral
Presentation session: Applied Chemistry
Presenter name: Tossapon Phromsatit

Silver(II) porphyrin complexes; the paramagnetic and electrochemistry study

Tossapon, Phromsatit[1], Peter, Liu[2], Ming-Li, Tsai[2], Supakorn, Boonyuen[1]

[1]Department of Chemistry, Faculty of Science and Technology, Thammasat University, Pathumthani 12120, Thailand
[2]Faculty of Chemistry, National Sun Yat-Sen University, Lienhai Rd., Kaohsiung 80424, Taiwan

Email: tossapon.phr@dome.tu.ac.th

Abstract: A series of silver(II) porphyrin complexes that contain different *meso*-substituent groups (phenyl, methoxyphenyl, butyloxtphenyl, octyloxyphenyl, and dectyloxyphenyl) were synthesized and fully characterized. Mass spectrometry and CHN elemental analysis were used to confirm the structure of all synthesized compounds. The silver(II) ion was founded in each complex which can be confirmed by the present of ESR signal. The g value of all complexes was calculated. The silver(II)porphyrin complexes exhibited one reversible oxidations occurring at range from +0.47 V to +0.57 V and one reduction at range from -0.87 V to -0.93 V. All silver(II) porphyrin complexes showed energy band gap around 1.40 V. The silver(II) porphyrin complexes have potential to use in energy application.
Keywords silver(II) porphyrin, cyclic voltammetry, electrochemistry, EPR spectroscopy

Introduction

Porphyrins play a vital role in biological systems, and their synthesis is of interest in biological, material, and inorganic chemistry. The normal coordination geometry around the metal ion in the former species would be square planar. Nowadays, there are several routes to the synthesis of *meso*-substituted porphyrin.[1-2] Porphyrin can undergo additional reaction without loss of the aromatic properties. The functionalized porphyrin finds multiple applications in biology, medicine, and materials. The *meso*-positions are the most electronically reactive, and preferential sites for substitution and addition.[3] and particular interest because the *meso*-substituted porphyrins have been used in many applications.[4] Although *meso*-substituted porphyrins are not a naturally occurring compound, it has provided chemists and other scientists with a multitude of applications and fundamental studies. Their syntheses are based on condensation of pyrrole and aldehyde under various reaction conditions. In the present work, the Adler-Longo synthesis method was applied to the free base porphyrin synthesis. The silver(II) porphyrin complexes were prepared and purified. Then, their properties were characterized by, mass spectrometry (MS), CHN analysis, cyclic voltammetry and electron paramagnetic resonance spectroscopy (EPR).

Experiment

The silver(II) porphyrin complexes were synthesized by refluxing each free base porphyrins (TPP, TOMPP, TOBPP, TOOPP, and TODPP 0.14 mmol) with excess $AgNO_3$ in DMF (20 mL). The reaction was refluxed for 5 hour. The compound was isolated by column chromatography (silica gel, hexane: dichloromethane) as a purple solid more than 50% yield.

Result and Discussion

Table 1 The characteristic data for silver(II) porphyrin complexes.

Compounds	Empirical formula	Yield (%)	Formula weight [a]	MS (m/z)	Elemental analysis ([b]) %		
					C	H	N
AgTPP	$AgC_{44}H_{28}N_4$	74	720.6	719.2	72.98(73.34)	4.11(3.92)	7.57(7.78)
AgTOMPP	$AgC_{48}H_{36}N_4O_4 \cdot 1.25X$	57	840.7	841.6	62.63(62.47)	4.53(4.10)	6.13(5.92)
AgTOBPP	$AgC_{60}H_{60}N_4O_4$	48	1009.0	1010.1	74.51(71.42)	6.25(5.99)	5.76(5.55)
AgTOOPP	$AgC_{76}H_{92}N_4O_4 \cdot 0.15X$	63	1233.4	1233.9	73.19(73.39)	7.71(7.47)	4.21(4.50)
AgTODPP	$AgC_{84}H_{108}N_4O_4 \cdot 1.5X$	52	1345.7	1346.0	69.66(69.71)	7.70(7.59)	3.88(3.80)

$X = CH_2Cl_2$ [a]calculate with out solvent, [b]the theoretical value

The silver(II) porphyrin were characterized by CHN elemental analysis and mass spectrometry. The elemental analysis data have been strongly confirmed the expected their structure and the result data was agreed with the theoretical value. However, some silver(II) porphyrins, were afforded difference theoretical composition due to the trace of solvent (CH_2Cl_2) in their molecule. The mass spectra of all silver(II) porphyrins showed very intense molecular ion peaks due to they had high energy from the delocalized electrons in the molecule.

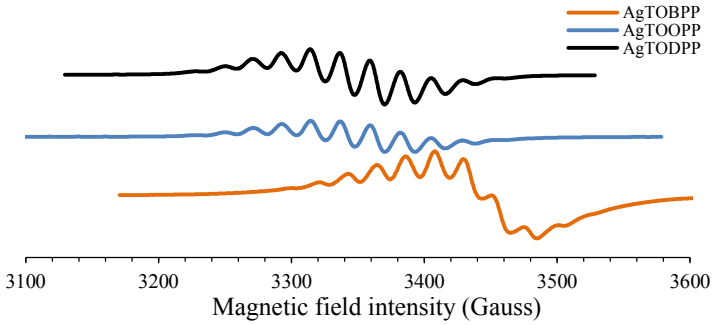

Figure 1 The EPS spectrum of AgTOBPP, AgTOOPP, and AgTODPP.

The Figure 1 how the electron paramagnetic resonance (EPR) spectra of silver(II) porphyrins, with an consist of eleven lines with an equal separation of approximately 21 Gauss. This splitting, together with the observed peak ratios, can be explained by assuming an overlap of the expected two sets of nine nitrogen hyperfine lines, where each spectrum corresponds to hyperfine interactions between the unpaired electron from Ag(II) ion and four equivalent nitrogen atoms from porphyrin ligand with a nuclear spin of one. The splitting into two sets is due to the hyperfine interaction with the spin of one half of the silver nucleus. From the spectra, we obtain an isotropic g-value of 2.03 - 2.05. These values are in close agreement with those reported from Mohamed *et. al*.[5] Thus, the appearance of these EPR signals from Ag(II) porphyrins unequivocally shows that they have an unpaired electron with a high density on the Ag, All silver(II) porphyrin must contain Ag^{2+} ion.

Cyclic voltammetry

The electrochemical properties of silver(II) porphyrin complexes were investigated by cyclic voltammetry in dichloromethane containing by 1.0 M $TBAPF_6$ as the supportind electrolyte. All silver(II) porphyrin complexes show one reversible one electron oxidation and reduction. The results are conclude in **Table 2**. The result show that the oxidation potential of silver(II) porphyrins were decrease when the number of carbon in alkyl long chain substituent group were increase, that the alkyl long chain substituent porphyrin are easier to oxidize compare to AgTPP due to the electron donating group at *meso*-position. Moreover the energy gab of silver(II) porphyrin complexes were calculate by difference of first ring oxidation and first ring reduction potential. All compounds show energy gab around 1.40 V.

Table 2 The redox potential and energy gab of silver(II) porphyrin complexes.

Compounds	First ring oxidation (V)	First ring reduction (V)	Energy gap
AgTPP	0.57	-0.90	1.46
AgTOMPP	0.51	-0.92	1.43
AgTOBPP	0.47	-0.94	1.40
AgTOOPP	0.47	-0.91	1.37
AgTODPP	0.46	-0.91	1.37

Conclusion

The series of silver(II) porphyrin complexes were successfully synthesized and characterized. The structure of all compound were confirmed by CNH elemental analysis and mass spectrometry. From the EPR spectra, it obtains an isotropic g-value of 2.03 - 2.05. The appearance of EPR signals confirmed that they have an unpaired electron with a high density on the silver ion. The electrochemical studies all silver(II) porphyrin complexes exhibited one reversible oxidation and reduction peak. The oxidation potential of silver(II) porphyrin complexes decrease with an increase the number of carbons at *meso*-substituent groups due to the high electron density on carbon alkyl long chains. The energy bands gap of all compound were found around 1.40 V. So, the silver(II) porphyrins have potential to use in energy application.

Acknowledgement

We are grateful to the Department of Chemistry, Faculty of Science and Technology, Thammasat University and Science Achievement Scholarship of Thailand (SAST), for financial and all experiments support.

Reference

1. Lee, C.-H.; Park, J.-Y.; Kim, H.-J. *Bull. Korean. Chem. Soc.* **2000**, 21, 97 - 100.
2. Fedulova, I. N.; Bragina, N. A.; Novikov, N. V.; Ugol'nikova, O. A.; Mironov, A. F. *Russ. J. Bioorganic Chem.* **2007**, 33, 589-593.
3. Temelli, B.; Unaleroglu, C. *Tetrahedron* **2009**, 65, 2043-2050.
4. Zhang, Z.; Duan, Y.; Zhang, L.; Yu, M.; Li, J. *Inorg. Chem. Commun.* **2015**, 58, 53-56.
5. Mohamed, G.; Morsy, A.; Krister, L.; Örjan, H.; Adel, A.; Toomas, T.; Lars Ö.; *Inorg. Chem. Commun.* **2008**, 11, 1019 - 1022.

Please choose: Oral
Presentation session:
Presenter name: Ahmad Muhaimin bin Roslan

Zero-Waste Concept for Phytoremediation of Industrial Wastewater

Ahmad Muhaimin Roslan[1,2], Nor Farhana Aziz Ujang[1], Nurul Atiqah Osman[1]

[1]Faculty of Biotechnology and Biomolecular Sciences, Universiti Putra Malaysia, 43400 UPM Serdang, Selangor, Malaysia
[2]Laboratory of Biopolymers and Derivatives, Institute of Tropical Forestry and Forest Products, Universiti Putra Malaysia, 43400 UPM Serdang, Selangor, Malaysia

Email: ar_muhaimin@upm.edu.my

Keywords:

constructed wetland, phytoremediation, industrial wastewater, zero waste concept, biosugars

Introduction

As the world is progressing towards Industrial Revolution 4.0, the common industries will still be relevant to sustain the daily need of people around the globe. However, industry that produce wastewater such as agricultural mill, is facing challenges due to the stringent standard discharge limit. Although the standard impose is important to conserve the environment and protect its content, such challenge can affect the business revenue, which will eventually affect the labor forces. In this study, a zero-waste concept was developed to treat a selected industrial wastewater (palm oil mill effluent final discharge). The system started with a phytoremediation using a modified constructed wetland system, to treat the wastewater to a river water quality. This is then followed by harvesting the plant biomass from phytoremediation and hydrolyzed it for biosugars production. The plant biomass was also characterized to ensure that the pollutants from the wastewater will remain immobilized, while the biosugars can be used as fermentation feedstock to produce non-food products. The rest of the biomass can either be utilized as for composting process, or it can be ashed to recover the metals. The application of this strategy at industries will assist them to satisfy standard discharge limit for effluent, while at the same time, generating more profit through the selling of their products. This allow the industry to conduct their business as usual, while at the same time, conserve the environment.

[Experiment]

The concept surrounding the system is to treat wastewater from agricultural industry using a phytoremediation system, followed by utilization of the biomass from the phytoremediation for non-food product application. Wastewater from food-based industry such as palm oil mill effluent final discharge (POME FD) was used as the wastewater input, and Napier grass in a constructed wetland as the phytoremediator. The POME FD was flowed through the constructed wetland, which consist of layers of rocks, sand, and fine sand, and the Napier grass was grown on top of it. The matured Napier grass biomass was then extracted and characterized to identify its potential for further bioconversion. The three selected application for the Napier grass biomass was proposed are; (1) pressing for sugar extraction in juice form, (2) enzymatic hydrolysis of the biomass to produce more biosugars, and (3) composting of the remaining biomass to recover metals.

[Result and Discussion]

During the phytoremediation of the POME FD, it was observed that the Napier grass show substantial growth over the control Napier grass, which is mainly due to the organic nutrients content inside the POME FD. The

stem is bigger in diameter and the plant consist of higher moisture content. The moisture, which can be extracted using pressing machine in a juice form, are rich in glucose (~ 18.0 g/L) and fructose (~ 23.6 g/L). This suggest that the juice can be readily used as fermentation feedstock. Furthermore, the increment of the biomass is parallel to the increase of lignocellulose (cellulose, hemicellulose, lignin) amount in the Napier grass. The biomass, which has been partially ground during juice extraction, undergo hydrolysis by cellulase enzyme. This hydrolysis further releases more sugars (glucose, xylose, arabinose, fructose) which can also be used as fermentation feedstock. The remaining biomass from hydrolysis will finally be added into a composting as additional nutrients.

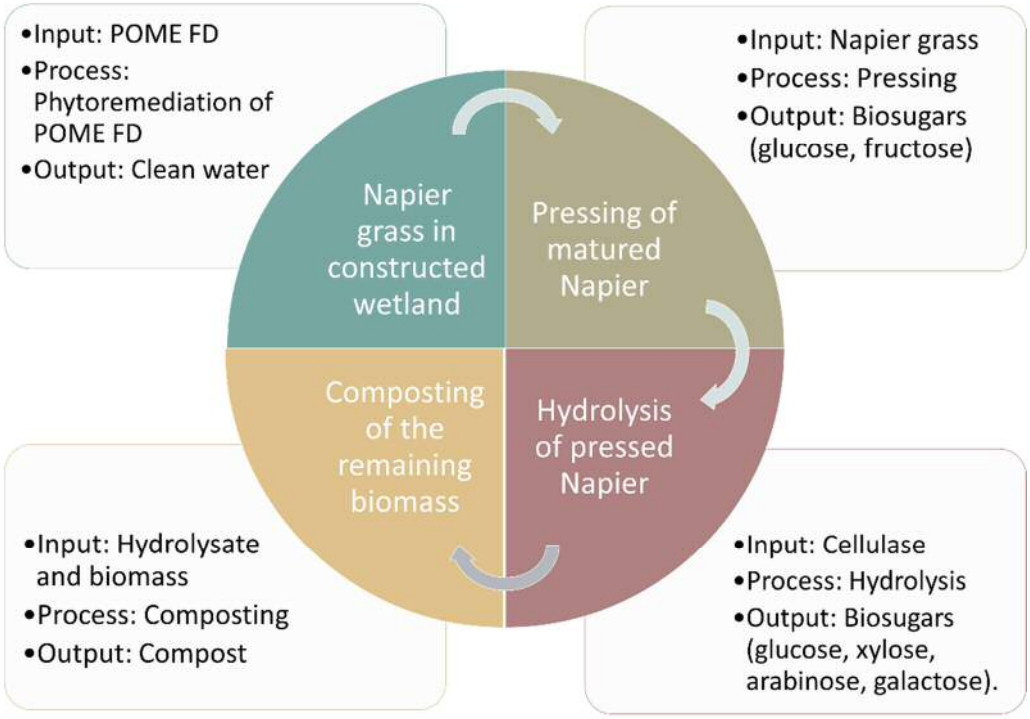

Fig. 1. The zero waste concept of the phytoremediation of POME FD using Napier grass in a constructed wetland

Please choose: Oral
Presentation session: 15 December 2018
Presenter name: Nadiah Mad Nasir

DEVELOPMENT OF NEW METHODS FOR THE SYNTHESIS OF DIOSPONGIN B

Nadiah Mad Nasir[1], Paul A. Clarke[2]

[1]Faculty of Science, University Putra Malaysia, 43400 UPM Serdang, Selangor, Malaysia
[2]Department of Chemistry, University of York, York, YO10 5DD, United Kingdom.

Email: nadiahmadnasir@upm.edu.my

Recently the group has focused on the development of new methods, based on the Maitland-Japp reaction,[1] for the formation of dihydropyrans (DHP)[2] and tetrahydropyrans (THP),[3] which are structural units found in many biologically active natural products. Extension of the Maitland-Japp reaction now allows for the synthesis of DHPs which can be converted into highly functionalised THPs found in natural products like Diospongin B **1**. Which is the 2, 6-*trans*-THP ring of Diospongin B **1** can be produced from DHP by conjugate addition. The development of this reaction and its scope and limitations will be discussed further.

Organic Synthesis, Tetrahydropyran

[Introduction]
The advent of improved methods in organic synthesis have greatly contributed to the drug discovery and promise greater success in developing new pharmaceuticals. Tetrahydropyran (THP) rings are common and important building blocks in natural products as they are found in many biologically active compounds. Their derivatives are widely distributed in various plants and they show the variety of biological properties such as anti-inflammatory, anticancer properties, antimicrobial properties and anti-osteoporotoc activity.

[Experiment]

General procedure for the synthesis 2,6-*trans*-tetrahydropyran- 4-ones.

Phenyl lithium 1.9 M in dibutyl ether solution (0.58 mL, 0.90 mmol) was added to a suspension of copper iodide (86.3 mg, 0.45 mmol) in THF (3.00 mL) at 0 °C. The mixture was stirred at this temperature for 20 minutes then cooled to −78 °C. Addition of chlorotrimethylsilane (0.18 mL, 1.4 mmol) was followed by addition of DHP (0.28 mmol) in THF (2.00 mL) at −78 °C. The reaction

mixture was stirred at this temperature for 30 minutes then at 0 °C for 1.5 hours. The reaction was quenched with sat. aq. NH4Cl (2.50 mL) and allowed to warm to rt with vigorous stirring. The mixture was diluted with sat. aq. NH_4Cl (10.0 mL) and extracted with EtOAc (5 × 15.0 mL). The combined organic extracts were washed with H_2O (15.0 mL) and brine (15.0 mL), then dried over MgSO4 and concentrated in vacuo. Flash column chromatography (hexane–ethyl acetate) afforded the product as a mixture of enol/keto tautomers

[Results and Discussion]

Based on the structure of the Diospongin B **1** showed high compatibility to be synthesized by using Clarke group stereocontrolled method, which would allow stereocontrol the construction of either *trans* or *cis* THP ring (Clarke 2015 and Clarke 2016). The *trans*-THP ring can be achieved by treatment of dihydropyran (DHP) with the carbon nucleophile (Clarke 2016), meanwhile, an addition of hydride nucleophile to DHP and trapping with carbon electrophiles can lead to the formation of *cis* THP ring (Clarke 2015). These prototype reactions were successfully applied on the total synthesis of Diospongin B (*trans*-THP) and synthesis of the A-ring of Lasonolide A (*cis*-THP).

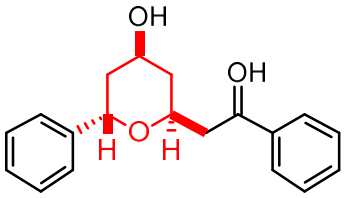

Diospongin B **1**

References:

1. F. R. Japp and W. Maitland, *J. Chem. Soc*. **1904**, *85*, 1473–89
2. P. A. Clarke, P. B. Sellars and N. Mistry, *Tetrahedron Lett*. **2011**, *52*, 3654.
3. P. A. Clarke, W. H. C. Martin, J. M. Hargreaves, C. Wilson and A. J. Blake, *Org. Biomol. Chem*. **2005**, *3*, 3551.
4. P. A. Clarke, P. B. Sellars and N. M. Nasir, *Org. Biomol. Chem*. **2015**, *13*, 4743.
5. P. A. Clarke, N. M. Nasir, P. B. Sellars, A. M. Peter, C. A. Lawson, and J. L. Burroughs, *Org. Biomol. Chem*. **2016**, *14*, 6840.

Please choose: Oral/ Poster/ Either
Presentation session:
Presenter name: Dr Mohd Rafein Zakaria

Valorization of biodiesel side stream waste glycerol for biosurfactant production by *Pseudomonas aeruginosa* WG

Shobanah Menon Baskaran[1], Mohd Rafein Zakaria[1, 2], Helmi Wasoh[1], Toshinari Maeda[3], Hidayah Ariffin[1,2], Mohd Ali Hassan[1], Ibrahim M. Banat[4]

[1] Department of Bioprocess Technology, Faculty of Biotechnology and Biomolecular Sciences, Universiti Putra Malaysia, 43400, UPM Serdang, Selangor, Malaysia.
[2] Institute of Tropical Forestry and Forest Products (INTROP), Universiti Putra Malaysia, 43400 UPM Serdang, Selangor, Malaysia.
[3] Department of Biological Functions Engineering, Graduate School of Life Science and Systems Engineering, Kyushu Institute of Technology, 2-4 Hibikino, Wakamatsu-ku, Kitakyushu 808-0196, Japan.
[4] School of Biomedical Sciences, Faculty of Life and Health Sciences, University of Ulster, Coleraine BT52 1SA, Northern Ireland, UK.

Email: mohdrafein@upm.edu.my

Keywords; Biosurfactant, rhamnolipid, emulsification index, waste glycerol, *Pseudomonas aeruginosa*

[Introduction]

Biosurfactants are the best environmentally friendly alternative for the synthetic surfactant. In general, biosurfactants are derived directly from a natural source such as animal, plant or microorganism (Xu et al., 2011). Microbially derived surfactant have more advantage when compared to plant-derived surfactant due to the capacity to scale-up production, multifunctional useful properties and rapid production by fast growing microorganisms (Randhawa and Rahman, 2014). The interest in biosurfactants increased because of the limitations of synthetic surfactants which are toxic, low biodegradability and effectiveness in a narrow range of pH and temperature (Suryanti et al., 2009). Biosurfactant are classified according to their chemical composition into mainly glycolipids, lipopeptides, lipopolysaccharides and oligosaccharides (Eraqi et al., 2016). Based on microbial origin members of the *Pseudomonas* sp. are known for their capacity to produce rhamnolipids, *Bacillus subtilis* and other bacilli's are known to produce lipopeptide biosurfactants while sophorolipids are produced by *Candida* sp. which belong to yeast group (Silva et al., 2014). One of the most promising type of biosurfactants is rhamnolipids produced by *Pseudomonas* species (Marchant and Banat, 2012b).

[Experiment]

Preparation of P. aeruginosa WG

P. aeruginosa WG was obtained from Institute of Bioscience, UPM and stored as a glycerol stock at -80°C. *P. aeruginosa* WG was streaked onto a nutrient agar plate and incubated at 37°C for 24 h.

Medium and cultivation conditions for rhamnolipid production

About 10% (v/v) inoculum was inoculated into freshly prepared basal salt media (BSM) according to formulation proposed by Zhang et al. (2012). The BSM was autoclaved at 121°C for 20 min separately from the carbon source, waste glycerol. For optimization purpose, the *P. aeruginosa* WG was incubated at different temperature, initial medium pH, concentrations of carbon sources, nitrogen sources, nitrogen concentrations and working volumes (oxygen-limiting environments) for 72 h.

Analyses

Quantitative emulsification index (E_{24})

Two mL of the supernatant was added into 2 mL of hydrophobic substrate such as cooking oil and diesel oil in a test tube. The mixture was mixed thoroughly by vortex for 2 min. Then, the mixture was left for 24 h to react. According to Aparna et al. (2012), the emulsion index (E_{24}) was calculated as a percentage of the height of emulsion layer over total height of mixture as expressed below:

$$\text{Emulsion Index } (E_{24}) = \frac{\text{The height of emulsion layer}}{\text{The total height of mixture}} \text{ x } 100$$

[Result and Discussion]

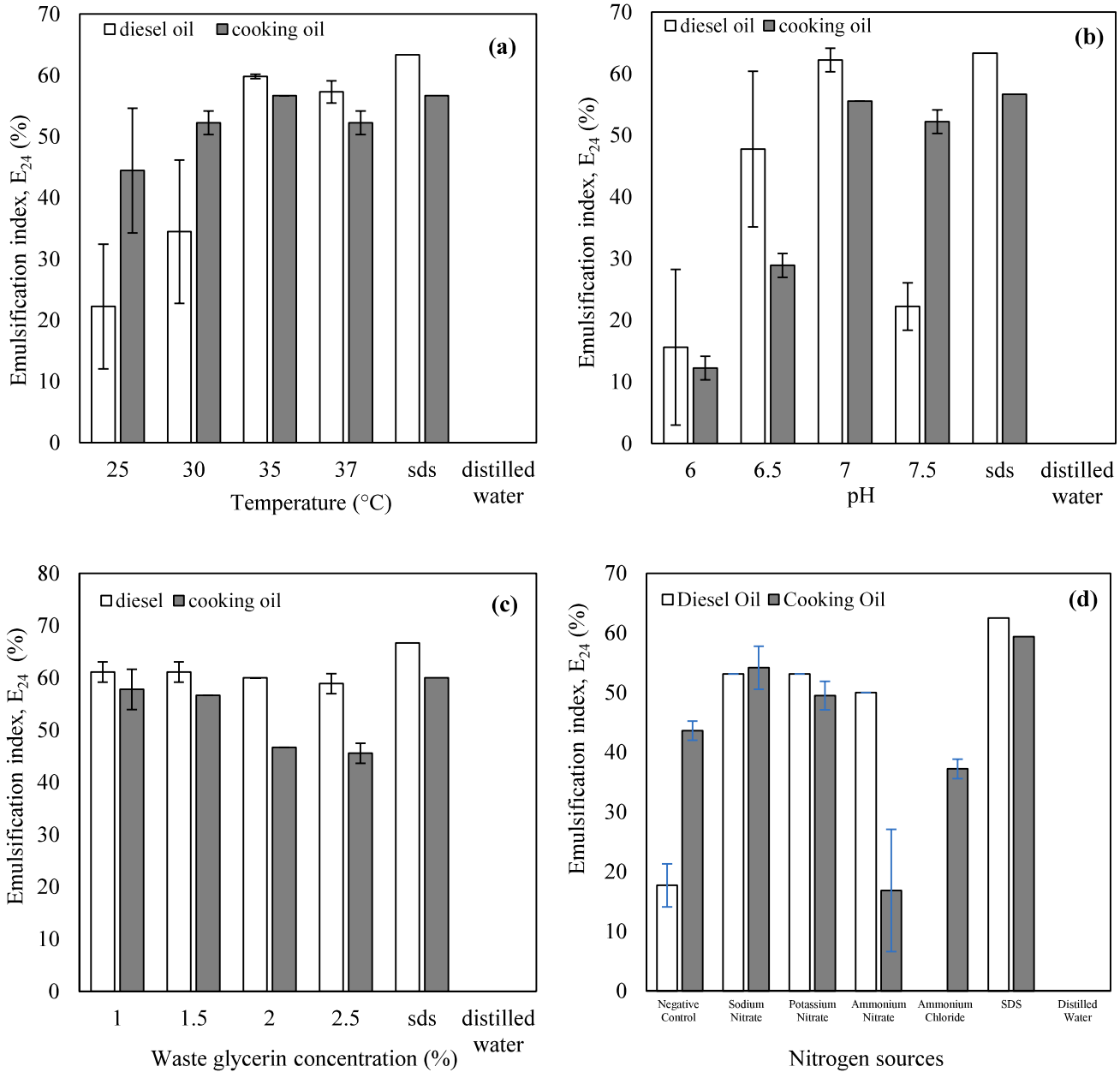

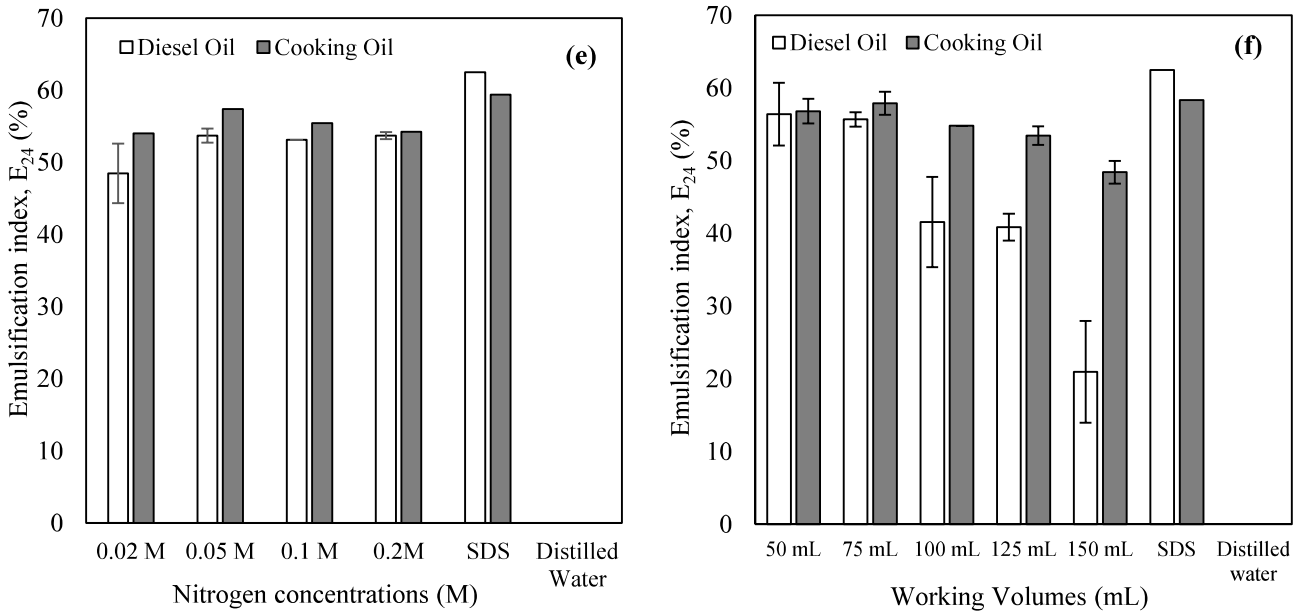

Fig. 1. Emulsification activity of biosurfactants produced by *P. aeruginosa* WG at different (a) different temperatures (°C), (b) initial medium pH, (c) waste glycerine concentrations, (d) nitrogen sources, (e) nitrogen concentrations, and (f) basal salt medium working volumes against diesel oil and cooking oil. Values are mean ± S.D. of triplicate experiments.

Please choose: Oral/ Poster/ Either
Presentation session:
Presenter name:DR. SITI EFLIZA ASHARI

Development of Kojic Monooleate Enriched Oil-in-Water Nanoemulsion as Potential Carrier for Hyperpigmentation Treatment

Sharifah Nurfadhlin Afifah Syed Azhar [1], Siti Efliza Ashari,[1], Norazlinaliza Salim[1]

[1]Integrated Chemical Biophysics Research, Universiti Putra Malaysia, 43400 UPM Serdang, Selangor, Malaysia

Email: ctefliza@upm.edu.my

Keywords: kojic monooleate, anti-tyrosinase, nanocosmeceutical, optimization, hyperpigmentation

1.0 Introduction

Kojic acid ester, which derived from a kojic acid (production of a fungal metabolite from many species of *Aspergillus, Acetobacter* and *Penicilium*) act as tyrosinase inhibitor to treat overproducing melanin in human skin (Uher et al., 2000). Since enzymatic esterification method with fatty acid claimed to be the best technique to synthesize kojic acid ester, the derivatives also are more excellent characteristics than the original starting material making more profitable especially for the cosmetic application (Ashari et al., 2009). Research by Kim et al. (2004) stated that kojic acid ester has higher storage stability and almost more stable under ambient stored conditions with lower toxicity than kojic acid itself. Moreover, kojic acid derivatives were relatively higher with tyrosinase inhibitory activities than that of kojic acid. Apart from that, kojic monooleate (KMO), a palm-based fatty acid derivative of kojic acid (KA) was found to have significantly inhibited mushroom tyrosinase superior than kojic monolaurate (KML) and kojic monopalmitate (KMP). The inhibitory effect of mushroom tyrosinase activity of KMO was not significantly different to KA at doses ranging from 62.5 to 250 µg/mL (Lajis et al., 2012). Therefore, the KMO can be used as active ingredient for cosmeceutical purposes.

To enhance the active ingredient, oil-in-water (O/W) nanoemulsion was used as a carrier and claimed better than water-in-oil nanoemulsion (W/O) for topical delivery system because O/W gives better penetration into skin, increased the effectiveness to deliver the active ingredient and contain a counter ion that can be used to optimize targeting active compound without a concomitant increase in systemic absorption (Grampurohit et al. 2011). Nanoemulsion (NE) is an emulsion, which consists of oil and water stabilized by a surfactant. NE is considered to be the most advanced nanoparticulate system for cosmeceutical which contain droplet size varied from 20-200 nm (Gutierrez et al., 2008.) This NE is designed to possess high stability towards droplet aggregation and gravitational separations showing improved and efficient activity, mainly antimicrobial activity (Chen et al. 2002).

Besides, optimization of mixture composition to obtain a product with required characteristic is one of the common issues in the pre-formulation of cosmeceutical products. There are several statistical techniques used for the optimization of mixture compositions and processing parameters to obtain desirable properties such as Response Surface Methodology (RSM) and D-Optimal Mixture Design. According to Borhan et al. (2014), D-optimal has been practiced in product formulation in food, pharmaceutical, and cosmeceutical industries. There are several advantages of D-optimal mixture design including a reduction in the number of experimental run and the ability to identify interaction statistically to overcome the shortcomings of traditional formulation method. To date, there are no reported studies on the optimization of KMO enriched nanoemulsions using D-optimal mixture design and only a few reported works on optimization of cosmeceutical products using this type of mathematical tool. Therefore, in this work, the D-Optimal mixture design was used as a tool to optimize KMO enriched nanoemulsions. The interaction effects between factors (surfactant, oils, xanthan gum, and deionized water) were evaluated against droplet size as a response.

2.0 Experiment

2.1 Preparation of KMO oil-in-water nanoemulsion

The nanoemulsion was prepared using both high and low energy emulsification techniques. The oils used was a mixture of castor oil, (CO) and lemon essential oil (LO) in a ratio of 9:1. Castor oil was chosen to be used as a carrier oil to blend with the lemon essential oil for better enhancement of nanoemulsion. A non-ionic surfactant, (Tween 80) was chosen to obtain better solubilization and stability of the dispersion system developed. Thus, due to its suitable HLB value, it was chosen as an oil-in-water emulsifier. The oil phase was carried out by mixing KMO and CO while the aqueous phase, Tween 80 and xanthan gum were added into the deionized water. Both oil and aqueous phase were separately heated up to 30 °C with continuously stirring using a magnetic stirrer to form homogenous solution. Then, both phases were separately sonicated using ultrasonic bath sonicator (Power Sonic 405, Korea) where it cavitated bubbles induced by high frequency pressure (sound) waves to agitate a liquid for 20 min. Using high shear homogenizer (T25 digital, IKA-Werk, Germany), the oil phase was gradually added dropwise into the aqueous phase until completed for 15 min at 6000 rpm. The final mixture was further homogenized for 3 h while adding lemon essential oil and 0.7% w/w of potassium sorbate dropwise using overhead stirrer (RW20 digital, IKA-Werk, Germany) at 250 rpm.

2.2 Experimental Design

D-optimal mixture design of five-factor was utilized to determine the effect of Tween 80 (A), CO: LO with ratio of 9: 1 (B), KMO (C), xanthan gum (D), and deionized water (E) on response taken as droplet size. The amount of potassium sorbate as an antimicrobial agent was kept constant (0.7% w/w). By using Design Expert software (Version 7.1.5, Stat. Ease Inc., Minneapolis, USA), the design matrix was generated. According to the D-optimal mixture design, the input variables are non-negative proportionate amounts of mixture.

3.0 Results and Discussion

3.1 D-optimal analysis

There is a high demand for the production of cosmeceutical products with a smaller droplet size (20–200 nm) due to the small size of nanoemulsions that would enhance the permeability of actives through stratum corneum of the skin. For the optimization of KMO enriched O/W nanoemulsions, contour and three dimensional surface graphs were plotted using Design Expert software. Based on Figure 1, increasing the surfactant concentration (Tween 80) will decrease the droplet size. Since emulsifier plays a vital role in the formation of the emulsion, it helps to lower the interfacial tension, thus reduced the *Laplace* pressure, *p*, and the stress required for particle deformation (Zainol *et al*., 2012). However, this behavior different for the concentration of oils in the KMO enriched nanoemulsion. When the concentration of oils increased, the droplet size decreased.

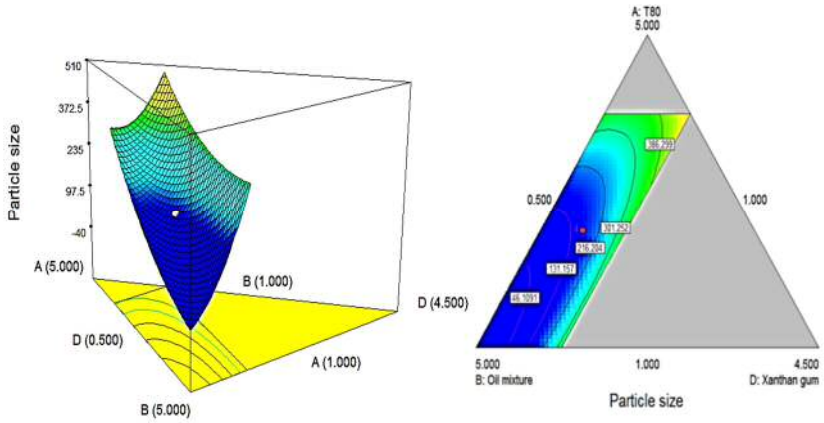

Fig. 1 Contour plot of 3D surface and 2D plot showing the interaction effect between variables: (A) (T80), (B) (Oils), (D) (xanthan gum) on droplet size (nm) of the nanoemulsion, (C) (KAE) and E (water) are kept constant

From Fig. 2, increasing xanthan gum concentration, will decrease the droplet sizes. Increasing the amount of xanthan gum concentration at the high amount of water was enough to make the water phase more viscous for

the formation of the network. However, at the low amount of water, increasing xanthan gum's concentration cause the emulsion to be highly viscous and therefore hard to be homogenized. As the viscosity increases, particle disruption efficiency decreased and led to the formation of larger droplet size. The same observation was reported by Krstonosic *et al*. 2015 and Rodd *et al.* 2000 in the presence of xanthan gum as an emulsifier. Decreasing the active ingredient content and increasing the surfactant concentrations seems to give a smaller droplet size of the emulsion. However, at a certain point, decreasing and increasing active ingredient and surfactant respectively shows an increase in droplet size. This happened because both surfactant and oil mixture reached the overlap concentration in which individual polymer molecules begin to physically interact. Therefore, after that concentration, the flocculation occured and promoted a large droplet size (Rodd *et al*. 2000).

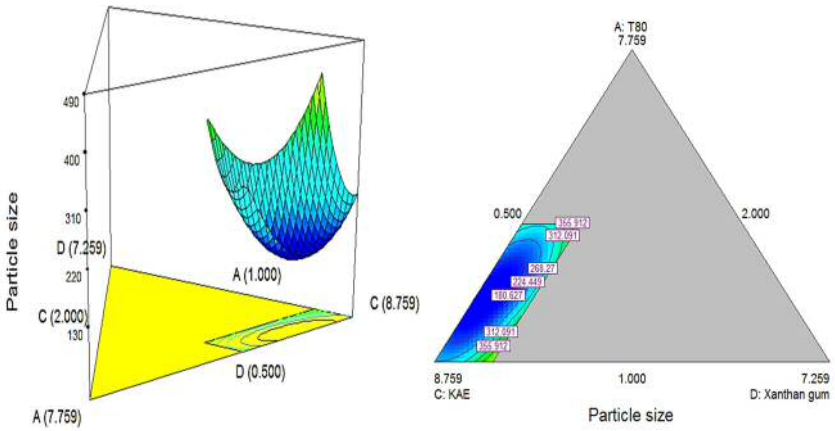

Fig. 2 Contour plot of 3D surface and 2D plot showing the interaction effect between variables: (A) T80, (C) KAE, (D) xanthan gum on droplet size (nm) of the nanoemulsion, (B) Oils and E (water) are kept constant

3.2 Optimization of the Responses

The optimum formulation was obtained based on minimum droplet size of nanoemulsion and maximum amount of KMO. Based on the D-optimal MED, the optimum formulation with the composition of KMO (10.00% w/w), Tween 80 (3.19% w/w), CO: LO (3.74% w/w), xanthan gum (0.70% w/w) and deionized water (81.68% w/w) was predicted that the nanoemulsion would have droplet size of 110.01±0.14nm. Table 1 shows predicted and actual responses values of the KMO optimum formulation. The desirability of the optimum KMO formulation was 1.00. This showed that the formulation quality was regarded to be acceptable and excellent. However, it was reported that when the value was 0.63 the formulation quality regarded as poor (Masoumi *et al.* 2015).

Table 1 Optimum formulation of KMO enriched O/W nanoemulsion

Variables					**Droplet size (nm)**		**Desirability**
Tween 80 (%)	**CO: LO (%)**	**KMO (%)**	**Xanthan gum (%)**	**Deionized water (%)**	**Actual**	**Predicted**	
3.19	3.74	10.0	0.70	81.68	110.01±0.14	111.73	1.00

Please choose: Oral
Presentation session:
Presenter name: Noor Azira Abdul Mutalib

Microbiological safety of kitchen sponges and its correlation with hygiene level of food establishments

Noor Azira Abdul Mutalib[1,3], Risa Yunisari Iskandar[1], Son Radu[2,3]

[1]Department of Food Service and Management, Faculty of Food Science and Technology, Universiti Putra Malaysia, 43400 UPM Serdang, Selangor, Malaysia
[2]Department of Food Science, Faculty of Food Science and Technology, Universiti Putra Malaysia, 43400 UPM Serdang, Selangor, Malaysia
[3]Food Safety and Food Integrity, Institute of Tropical Agriculture and Food Security, Universiti Putra Malaysia, 43400 UPM Serdang, Selangor, Malaysia

Email: n_azira@upm.edu.my

Keywords: Kitchen sponges, cross-contamination, *Staphylococcus aureus, Escherichia coli,* and *Salmonella* spp.

Introduction

Malaysia hot and humid climate is an important factor that leads to bacterial growth, especially in the food service establishment. Lack of food safety knowledge could lead to cross-contamination from food contact surfaces to food item. Study also shown that unhygienic food handling procedure is the most significant contribution to foodborne outbreaks at school (Soon, Singh, & Bainesa, 2011). Food handlers usually neglect the fact that kitchen sponges used to clean the utensils can become media for cross contamination. Although contaminated dishes have a low potential of microbial contamination to food, kitchen sponges used to clean and wash is more of a concern in spreading foodborne illness related pathogens (Mattick, et al., 2003). The objectives of this study were to determine the contamination of *Salmonella*, *S. aureus* and *E. coli* in kitchen sponges collected from various food premises in Serdang, Malaysia and to analyze the correlation between the contamination level of kitchen sponges and the storing condition & food residue. The data from this study will give an overview of kitchen sponges contamination level and to educate consumers on the safety issue in food service establishment.

Methodology

Used kitchen sponges were taken from food premises using aseptic technique. Each sampling bag was labeled with the number that represents the food premise, usage duration, and type of sponge as well as the date of sample collection. 15cm^3 of the kitchen sponge were cut aseptically using a sterile blade and mixed with 0.1% of peptone water. Next, 10 times serial dilution until dilution 10^{-4} was prepared. Spread plate method on Eosin Methylene Blue (EMB), Xylose Lysine Deoxycholate (XLD) and Mannitol Salt Agar (MSA) was performed to determine the presence of *Salmonella, E. coli,* and *S. aureus* respectively. Mean bacterial number and correlation analysis was analyzed using SPSS version 22.

Result and Discussion

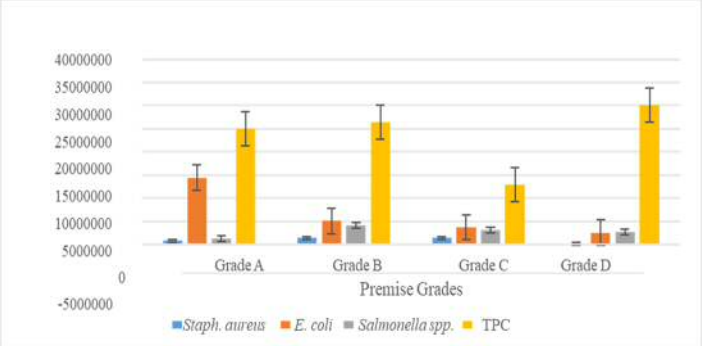

Figure 1: The number of foodborne bacteria in kitchen sponges based on premise grades

Total plate count shows that the mean number of foodborne bacteria were 2.49×10^7, 2.63×10^7, 2.49×10^7 and 3.00×10^7 CFU/cm^3 isolated from grade A, B, C, and D food premises, respectively. The least contamination was caused by *S. aureus* followed by *Salmonella* and *E. coli.* The kitchen sponges were found to be dominated by *E. coli* which range from 2.51×10^6 to 1.44×10^7 CFU/cm^3. This bacterium represents the fecal contamination (Price & Wildeboer, 2017) which could be caused by the transfer from raw food to the sponges during manual washing. Poor food handling will further lead to the contamination of cooked food which could cause illness to the consumers. The analysis also shows that premise grades & usage duration and the number of foodborne bacteria were not significantly correlated. This strengthens the need for a better cleaning method for utensils and food contact surfaces.

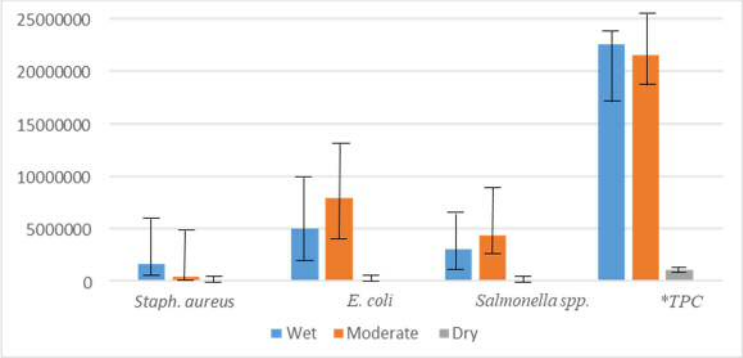

Figure 2: The number of foodborne bacteria in kitchen sponges based on storing condition.

Storing the sponges in a dry condition with fewer food residues showed a significantly lower number of total plate count ($p<0.05$). This is because wet or moist sponges provide a suitable environment for microbial growth (Hernandez, 2014). Having the sponges contact with dishwashing liquid was also found to be ineffective to reduce the number of molds, yeast and some bacteria (Erdoğrul & Erbilir, 2005). Thus, storing kitchen sponge in dishwashing liquid does not make the level of contamination lower. To top it off, storing wet kitchen sponges with some food residues will increase the number of bacteria on it, thus, increase the risk of cross-contamination to food contact surfaces.

In conclusion, the number of foodborne pathogens was not significantly correlated with premise grades, usage duration and the types of sponges used ($p>0.05$). However, bacterial count was found to be influenced by storing condition and residues on kitchen sponges. Hence, keeping sponges dry and replace periodically is a best practice and could reduce possible bacterial growth and prevent cross-contamination in the food premises.

References

Erdoğrul, Ö., & Erbilir, F. (2005). Microorganism in kitchen sponges. *Internet Journal of Food Safety*, 17-22.

Hernandez, J.M. (2014). Human Pathogens and Antibiotic-Resistant Bacteria in Polar Regions. Uppsala: Acta Universitatis Upsaliensis, 1-174.

Mattick, K., Durham, K., Domingue, G., Jørgensen, F., Sen, M., Schaffner, D. W., & Humphrey, T. (2003). The survival of foodborne pathogens during domestic washing-up and subsequent transfer onto washing-up sponges, kitchen surfaces and food. *International Journal of Food Microbiology*, 213-226.

Price, R.G. and Wildeboer, D. (2017). In Amidou Samie (Eds). *E. coli* as an Indicator of Contamination and Health Risk in Environmental Waters. IntechOpen, DOI: 10.5772/67330.

Soon, J.M., Singh, H., & Bainesa, R. (2011). Foodborne diseases in Malaysia: A review. *Food control*, 823-830.

Please choose: Oral
Presentation session: Biological Science
Presenter name: Mahmuda Akhtar

Late embryogenesis abundant peptide co-expression system, the unique method for adequate expression of insecticidal crystal proteins in *Bacillus thuringiensis*

Mahmuda Akhtar[1], Kazuhiro Mizuta[1], Tomoko Shimokawa[2], Minoru Maeda[2], Shinya Ikeno[1]

[1]Department of Life Science & Systems Engineering, Faculty of Graduate School of Life Science & System Engineering, Kyushu Institute of Technology, 2-4 Hibikino, Wakamatsu-ku, Kitakyushu, Fukuoka, 808-0196, JAPAN
[2]Bioindustory Division, Kyushu Medica Co., Ltd., Fukuoka Bio Incubation Center (F-BIC) 1F Hyakunen-kouen 1-1 Kurume, Fukuoka, 839-0864 JAPAN

Email: akhtar.mahmuda662@mail.kyutech.jp

Keywords: *Bacillus thuringiensis*, crystal protein, late embryogenesis abundant, peptide

[Introduction]

According to World Health Organization (WHO), *Bacillus thuringiensis* (Bt) is identified as a worthy candidate for the control of mosquito pest by virtue of its efficiency and safety. Mosquito is the utmost dangerous creature on the planet as it is the principal vector for transmitting the life threatening and mostly dangerous deadly diseases like Malaria, Dengue, chikungunya, Zika virus, yellow fever, West Nile virus and Lymphatic filariasis that are still threatening half of the world's population. Morphologically it is characterized by an aerobic, ubiquitous gram-positive, spore-forming bacterium Regarding the biological control of insects today, Bt is the most widely used microorganism worldwide by virtue of specific to a limited number of insect species with no toxicity against humans or other organism. Even though it is regarded the most appeal biological alternatives to chemical insect pests and have acknowledged the augmented recognition in the last few years on account of the presence of resistant insects, deficient in evolution of new molecules. So the best strategy to control the mosquito by using the pathway that is alternative to chemical insecticide is Bt, the reliable biological weapon. The distinctive attribute of Bt to synthesize the insecticidal protein crystal inclusion during sporulation phase that has the capability to work out against larvae of mosquito and ultimate death. So nowadays, commercially numerous groups of bio insecticide is being used this crystal protein to exterminate pests. But it is still being challenging to use it in industrial purpose on account of low productivity and expensive than compared to chemical pesticide.

To resolve this problem, research has been directed towards the development of new technologies by the employment of Late embryogenesis abundant (LEA) peptide co-expression system is one of the unique methods for efficient expression of crystal protein, which has been developed in *Escherichia coli* (*E.coli*). The LEA peptide was designed with reference to the sequence of group 3 LEA protein consisting of a repetitive sequence of 11 amino acid which has the role to protect the cell against desiccation, cold or high salinity in a variety of organism. Besides, this short peptide co-expression system have been developed to enhance protein expression level in host cell [1, 2]. In this study, the co-expression system was applied to pursue the efficient expression of crystal protein in Bt to kill the mosquito larvae.

[Experiment]

To execute our current research for enhancing the crystal protein expression of Bt. D142 we applied the LEA peptide co-expression system that has already been developed in our lab. *E. coli* (NovaBlue strain) was used for gene recombination. *Bacillus thuringiensis* (strain D142, dispensed

from Kyushu Medical Co., Ltd.) was used as an expression host of insecticidal protein and LEA peptide. To proceed the experiment, firstly we constructed the expression vectors based on the pHT01 which is an intracellular expression plasmid of the Bacillus system capable of inducing expression with isopropyl-β-thiogalactopyranoside (IPTG) was used. After that, the LEA peptide (LEA-I, II, K) was constructed by the expression vector, pHT01 for efficient expression of recombinant protein. pHT 01 - LEA vector was introduced into the bacterium Bt (D142) by the electroporation method to construct trans-formant (Bt - LEA). The transformants introduced pHT 01-LEA plasmids were cultured in Tryptone Soya Broth (Cm^{+}) medium with 100x stock solution containing baffle flask and for each LEA peptide (LEA-I, II, K) we ran four sample. For each experiment LEA-I, II & K and Bt were used as a control and different concentration of IPTG (0.01 M, 0.1 M, 0.5 and 1 M) were added at the different time interval of 4h, 8h, 12h, 16h, 20h and 24h to this culture solution by maintaining the rotation and temperature 150 rpm and 27°C respectively in bio shaker incubator to induce expression of LEA peptide. After 48 hours later harvesting of cell by taking optical density value, centrifugation 12000 rpm, processing of sample and SDS-PAGE to know the expression level of the above mentioned three peptides. Finally the toxicity level of protein was evaluated by the insecticidal assay on mosquito larvae.

[Result and Discussion]

The spore formation and crystal protein expression were started in vegetative cells after 20-22 hours and 30-32 hours respectively and was confirmed after 48 hours. The expression level of the insecticidal protein was increased in most transformants compared to the non transformants and was confirmed by SDS-PAGE analysis. The staining result of SDS-PAGE was evaluated by using ImageJ, a Java-based image processing program. Here the marker was used as a reference and the average of the density of the non-transformant or control sample band was taken as 1, the density of the band around 66 kDa of each sample was quantified. According to protein quantification result, the bioassay was performed in mosquito larvae to know the toxicity of expressed by deriving the LC_{50} of the purified toxin protein in nanograms per milliliter and effectivity was confirmed after 24 hours to observe the dead insect. Finally among all these three LEA peptides, LEA-II peptide was most effective and it was confirmed by the protein expression level as well as the toxicity assay. So finally we may conclude that LEA peptide co-expression system is expected to be the key factor for efficient expression of insecticidal crystal protein in Bt.

[References]

[1] Shinya Ikeno, Tetsuya Haruyama, “Boost Protein Expression through Co-Expression of LEA-Like Peptide in Escherichia coli” PLOS ONE, vol.8 (12), 2013

[2] Nishit Pathak, Hiro Hamada, Shinya Ikeno, “Construction and characterization of mutated LEA peptides in Escherichia coli to develop an efficient protein expression system” Journal of Molecular Recognition, vol.31 (1), 2018

Please choose: ~~Oral~~/ Poster/~~ Either~~
Presentation session:
Presenter name: Nurul Shazini Ramli

Total phenolic content and antidiabetic activity of *Mangifera odorata* fruit

Nur Fatimah, Lasano[1], Azizah, Haji Hamid[1], Roselina, Karim[1], Nurul Shazini, Ramli[1]

[1]Faculty of Food Science and Technology, Universiti Putra Malaysia, 43400 UPM Serdang, Selangor, Malaysia

Email: shazini@upm.edu.my

Keywords (Diabetes mellitus, polyphenols, solvents extraction, *kuini*)

Introduction

Diabetes mellitus (DM) becomes a major public health concern due to increasing prevalence of DM among adults aged 18 years from 4.7% in 1980 to 8.5% in 2014 globally (WHO, 2016). In Malaysia, the DM prevalence increased by more than doubled from 1996 to 2015 (Institute for Public Health, 2015). *Mangifera* species is a tropical plant that is proven to have pharmacological properties such as anticancer (Noratto et al., 2010), anti-diabetic (Bhowmik, Khan, Akhter and Rokeya, 2009), and anti-inflammatory (Dhananjaya and Shivalingaiah, 2016). There are eight underutilized *Mangifera* species have been discovered and one of them is *M. odorata* (Porcher, 1995). *M. odorata* belongs to family *Anacardiaceae* and the fruit is a hybrid between *M. foetida* (*bacang*) and *M. indica* (mango) (Teo et al., 2002). It was previously reported that *M. odorata* showed potent antioxidant activities compared to other species, however, there is still lack of information on the anti-diabetic properties and the compounds that contribute to its bioactivity. Therefore, the present study is conducted to determine the total phenolic content and anti-diabetic properties of *M. odorata* fruit extracted using different solvents. This study could serve as a basis for identification of compounds responsible for anti-diabetic and it can be used as a pharmaceutical ingredient or as a functional food in future.

Experiment

Sample preparation and extraction. *M. odorata* fruit was obtained from fresh market Serdang, Selangor. The sample were dried using freeze dryer and further ground into fine powder using electronic grinder at room temperature (24˚C). The extraction procedures were conducted according to the method of Addai et al., (2013). Three different solvent-water extraction systems were used (methanol, ethanol, and acetone) at 60% v/v concentrations and 100% distilled water. All analyses were performed in triplicate.

Total phenolic content (TPC). The TPC was determined using Folin-Ciocalteu reagent as adapted from Velioglu et al. (1998).

Anti-diabetic activities. The anti-diabetic properties of the samples were analyzed using α-amylase and α-glucosidase inhibition assay. α- amylase inhibition assay was performed based on the starch-iodine test according to Kusano et al. (2010) and Chakrabarti et al. (2014) while the enzyme inhibition activity against alpha glucosidase was measured according to the modified method of Al-Zuaidy et al. (2016).

Statistical analysis

All experiments were carried out in triplicates and data were reported as a mean ± standard deviation. All statistical analyses were conducted using Minitab version 16.0.

Result and Discussion

Total phenolic content (TPC) of *M. odorata* fruit extracted using 60% of ethanol, methanol, and acetone are presented in Figure 1. The results showed that the recovery of phenolic compounds is significantly varied depending on the type of the solvents used. *M. odorata* extracted using acetone contained the highest amounts of TPC. In addition, the water extracts showed the lowest amounts of TPC. The present work showed that TPC value of pulp from *M. odorata* was higher than previous work on an edible portion of *M. odorata* fruit with 2.57mg GAE/g. (Mirfat et al., 2015). Ikram et al. (2009) reported that TPC of the edible portion from *M. odorata* was 26.64 mg GAE/ g which is comparable to present work.

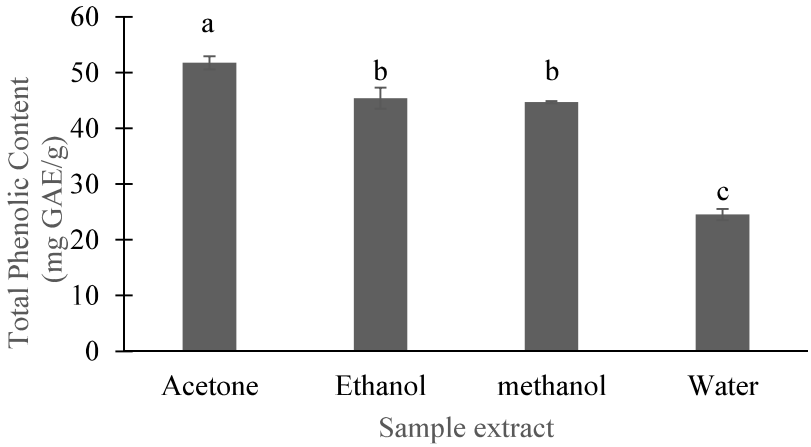

Figure 1. Total phenolic content (TPC) of a different solvent extract of pulp from *M. odorata* fruit. The concentration of each solvent is at 60% v/v. Mean with different subscript letters are significantly different at ($P<0.05$).

Results of α- amylase inhibitory activity of a different extracts of pulp are presented in Table 1. Ethanol extract showed the most potent α- amylase inhibitory activity compared to other solvents. This finding was contradicting with Thouri et al. (2017) who found water extract from date seed contain the highest inhibitory activity against α-amylase. On the other hand, α-glucosidase inhibition assay revealed that acetone extract had lower IC_{50} value compared to other solvents, indicating excellent inhibitory activity against α-glucosidase. However, this finding contradicts with that reported by Al-Zuaidy et al. (2016), who found that 60% ethanol extract of Melicope lunu-ankenda showed the highest inhibition of α- glucosidase activity.

Table 1. α- amylase and α- glucosidase inhibitory activities of different solvent extract of pulp from *M. odorata* fruit

Sample extract	**IC_{50} value (mg/ml)**	
	α- amylase	**α- glucosidase**
Acetone	127.84 ± 1.26^{a}	93.71 ± 12.31^{d}
Ethanol	20.86 ± 0.32^{c}	188.99 ± 10.09^{b}
Methanol	52.18 ± 1.29^{b}	262.24 ± 5.10^{a}
Water	51.22 ± 9.02^{b}	129.17 ± 4.79^{c}
Acarbose	0.94 ± 0.05^{d}	3.53 ± 0.59^{d}
Quercetin	-	0.40 ± 0.02^{e}

Results are expressed as IC_{50} mg/ml dry sample (mean ± standard deviation of three replicates). Each type of solvent at a concentration 60% v/v except water. Means followed by different letters in the same row are significantly different by Fisher test at 5% probability.

Please choose: Oral
Presentation session: Biomaterial
Presenter name: Khanom Simarani

Recovery of Xanthan Gum from fermentation broth using Ultrasound

Khanom, Simarani

[1]Institute of Biological Sciences, Faculty of Sciences, University of Malaya, 50603 Kuala Lumpur, Malaysia.

Email: hanom_ss@um.edu.my

Abstract
The highly viscous xanthan gum produced by *Xanthomonas sp* leads to difficulties in removing bacterial cell mass from the fermentation broth. Thus, cell free xanthan gum is hard to be recovered. The used of ultrasound as an alternative to the current process of microbial cells removal from fermented xanthan gum was investigated. After 72 hrs fermentation process, the mixture of xanthan gum slurry was subjected to sonication at 20kHz for 20 min. The amount of DNA concentration of lysed cell was measured using uv spectrophotometer. The rheological characterization of the biopolymer was determined using viscometer. The removal of cell mass after sonication was determined using FTIR and SEM. The results showed the decrease in A_{260}/A_{280} ratio indicated the reduction of DNA concentration and increasing concentration of protein in a sample simultaneously. The reduction in viscosity of the gum with respect to time of irradiation revealed the integrity of xanthan gum is compromised due to the sonication treated and the clumps of bacterial cells are detached from the xanthan gum. This result indicates that sonication helps in loosen the attached cells from the xanthan gum in the broth, hence helping in the recovery process.

Keywords: Biopolymer, Natural Polysaccharide, Sonication, Food thickening, *Xanthomonas sp.*

Introduction

Xanthan gum is a natural polysaccharide and an important industrial biopolymer. Xanthan gum has unique structure displaying pseudoplastic properties, high viscosity and solubility, enhanced stability over a wide range of pH values and temperatures, compatible with many salts, food ingredients and other polysaccharides used as thickening agents. This material is an extracellular hetero polysaccharide produced by *Xanthomonas sp.* that are secreted outside the cell wall into the extracellular medium. The main steps in recovery of xanthan gum is removal of microbial cells and precipitation of the biopolymer. Recovery of the xanthan from fermentation broth is difficult due to the broth is highly viscous which also contain residual nutrients and other metabolites. This high viscosity complicates the biomass removal from broth. Ultrasound is able to inactivate bacteria through a number of physical, chemical and mechanical effects arising from acoustic variation. As to date no work has been carried out to separate xanthan gum from cell biomass in fermentation broth using ultrasound. Hence, this preliminary study is to observe the effects of ultrasound on xanthan gum and microbial cells during the recovery process.

Materials and Methods

The potential *Xanthomonas* sp. used in this study was previously isolated and screened for xanthan gum production. Fermentation was carried out at 30C, 200rpm for 72 hrs. Fermentation broth was sonicated using Ultrasound at frequency of 20kHz under irradiation time 0 – 20 min. Analysis on lysed cell was performed using spectrophotometer on the ratio of absorbance of the sample at 260 (A260) and at absorbance of 280 (A280). SEM was used to observe the distribution of bacterial cell on the xanthan gum. The viscosity of sonicated xanthan gum was also measured.

Results and Discussion

Ultrasonication of cells suspension for 20 minutes at 20kHz causes bacterial cells to lyse. The collapse of cavitation bubbles produced by sound wave creates energy strong enough to lyse the cells. The amount of cell lysis in the treated sample is depicted using A_{260}/A_{280} ratio, represents the amount of DNA/protein concentration in a sample, which is presence in the supernatant of cells suspension after sonication process.

The decrease in A_{260}/A_{280} ratio is due to the reduction of DNA concentration and increasing concentration of protein in a sample simultaneously. Thus, the increase in protein fraction in a sample indicates the increases of lysed cells over irradiation time. As shown in Fig 1a, the concentration of lysed cells increases with respect to irradiation time. The reduction value in viscosity of the gum indicates the integrity of xanthan gum is compromised due to the treatment mentioned above (Fig 1b).

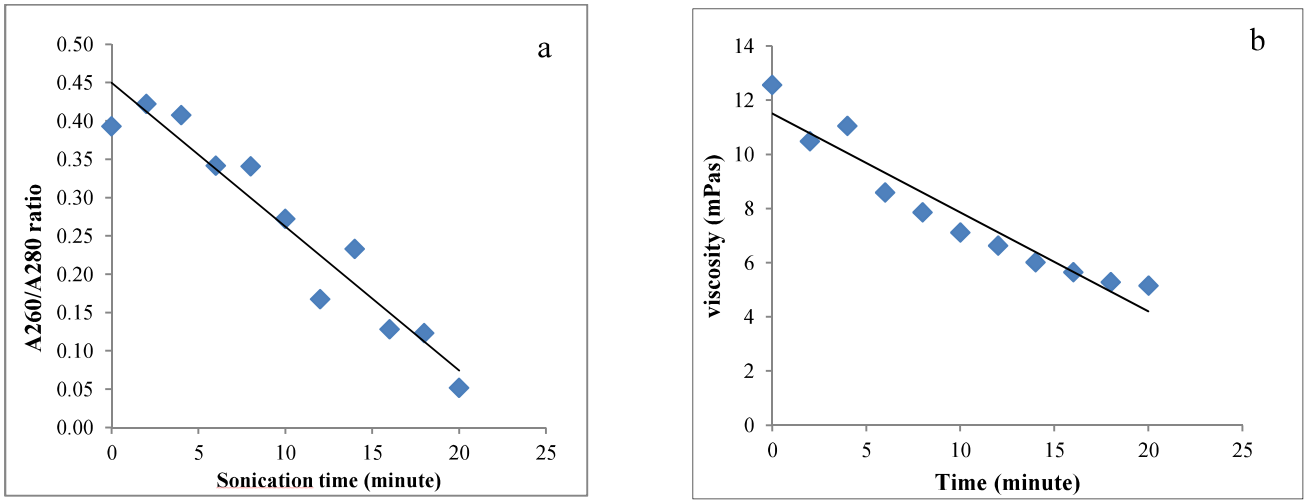

Fig 1. Effect of sonication irradiation on bacterial cell (a) and viscosity profile of sonicated xanthan gum (b).

SEM was employed to observe the behaviour of the microbial cells when attached to xanthan gum in the fermentation broth. Fig.2 a,b shows the SEM of control sample i.e. broth before sonication with clumps of bacterial cells and xanthan gum. However, cells are no longer attached to xanthan gum in the irradiated sample with ultrasound (Fig. 2c,d). This result indicates that sonication helps in loosen the attached cells from the xanthan gum in the broth, hence helping in the recovery process.

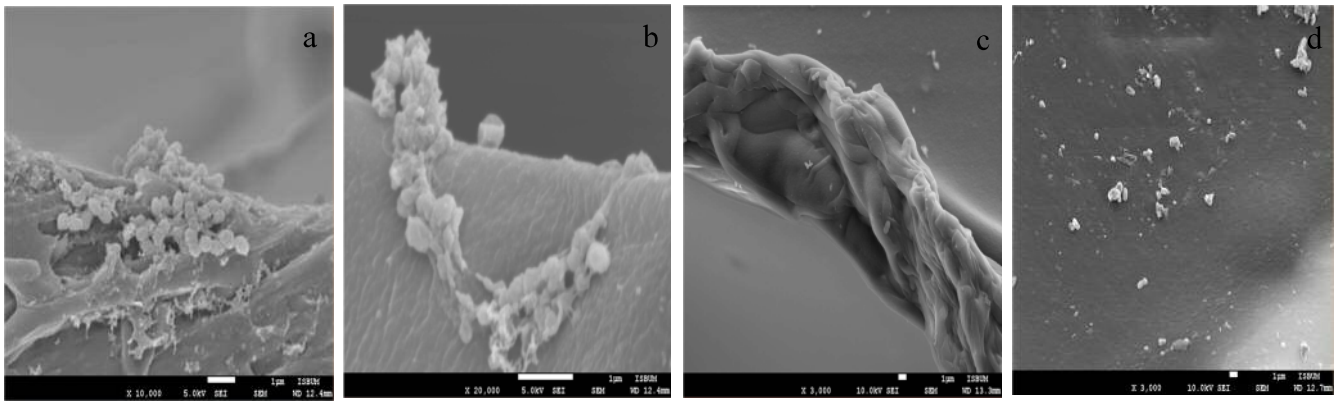

Figure 2.0: SEM of xanthan gum fermentation broth before sonication (a, b) under magnification of 10000 X and after sonication (c, d) under magnification of 3000 X.

Conclusion

Sonication process has the potential to be developed as an alternative method in aiding the xanthan gum recovery process from fermentation broth.

Please choose: Oral
Presentation session: Biological Science
Presenter name: Khaled Metwally

The effect of mutated LEA peptide over acid tolerance in *Escherichia coli*

Khaled Metwally[1], Kouki Sato[1], Shinya Ikeno[1]

Kyushu Institute of Technology, 2-4 Hibikino, Wakamatsu-ku, Kitakyushu 808-0196, Japan

Email: metwally.khaled-abdelfatteh735@mail.kuutech.jp

Keywords: Late embryogenesis abundant protein, LEA peptide, point mutation, acid tolerance, *Escherichia coli*

[Introduction]

Abiotic or environmental stresses such as increased soil salinity, extreme temperature, water deficiency, and unsuitable pH represent the major limiting factor for the growth and productivity of all organisms. Most living organisms have a well-defined range of pH tolerance. Death of the organism will be resulted, when pH falls below the tolerance range, by the effect of the osmoregulatory or respiratory failure [1]. pH is considered to be the most important factor affecting the determination of the bacterial community composition compared to factors such as temperature and moisture in the soil [2]. Acid soils significantly limit crop production worldwide because approximately 50% of the world's potentially arable soils are acidic. Genetic manipulation was one of the physiological and biochemical strategies that were developed to help organisms better adapt to or tolerate various abiotic stress conditions. In higher plants late embryogenesis abundant (LEA) proteins which were first identified in cotton and wheat plays an important role after suffering from environmental stresses [3]. LEA proteins have been described not only throughout the entire plant kingdom but also in other organisms as invertebrates to prokaryotes. Although several studies were carried out focusing on the role, function of LEA proteins in tolerating environmental stresses including salinity, drought, temperature [4] and radiation [5] there were no study focusing on its effect over the acid tolerance however the great role the pH plays in vital activities of organisms.
This study was conducted to investigate the effect of mutated LEA peptides constructed in our previous study [4] over acid tolerance, using *Escherichia coli* (*E.coli*) BL21 (DE3) transformed with these constructed LEA peptides for elucidation of the tolerance mechanism.

[Experiment]

We constructed five different LEA peptides (LEA I, II, E, K and S) (Table 1), and these LEA peptide were inserted in pRSFvector and this recombinant vector was transformed to *E. coli* BL21 (DE3), and the transformants were cultured in LB (Kam) medium. After confirming that OD (600nm) of the main culture reached 0.5, IPTG was added as inducer for expression induction with five different concentrations (0, 0.01, 0.1, 0.5, 1 mM). The capacity of acid tolerance were studied in four levels of pHs (2, 3, 4, 7).

Table1 Amino acid sequences of designed LEA peptides used in our study

LEA Peptide	Amino acid sequence
LEA I	(Glycine) MDAKD**GT**KEKA**G**E
LEA II	(Leucine) MDAKD**GL**KEKA**G**E
LEA E	(Glutamic acid MDAKD**EL**KEKA**E**E)
LEA K	(Lysine) MDAKD**KL**KEKA**K**E
LEA S	(Serine) MDAKD**SL**KEKA**S**E

[Results and Discussion]

LEA K showed the highest capacity of acid tolerance in comparison with other LEA peptides, but all LEA peptides showed capacity of acid tolerance in comparison with control (without IPTG). The maximum expression was resulted from using IPTG with concentration 0.1 mM.

[References]

[1] W. G. Kimmel, "No Title," *impact mine Drain. stream Ecosyst. Pennsylvania coal Resour. Technol. Util. Pennsylvania Acad. Sci. Publ.*, pp. 424–437, 1983.
[2] J. Rousk *et al.*, "Soil bacterial and fungal communities across a pH gradient in an arable soil," *ISME J.*, vol. 4, no. 10, pp. 1340–1351, 2010.
[3] D. K. Hincha and A. Thalhammer, "LEA proteins: IDPs with versatile functions in cellular dehydration tolerance," *Biochem. Soc. Trans.*, vol. 40, no. 5, p. 1000 LP-1003, Oct. 2012.
[4] N. Pathak, H. Hamada, and S. Ikeno, "Construction and characterization of mutated LEA peptides in Escherichia coli to develop an efficient protein expression system," *J. Mol. Recognit.*, vol. 31, no. 1, pp. 1–6, 2018.
[5] A. Huwaidi, N. Pathak, A. Syahir, and S. Ikeno, "Escherichia coli tolerance of ultraviolet radiation by in vivo expression of a short peptide designed from late embryogenesis abundant protein," *Biochem. Biophys. Res. Commun.*, vol. 503, no. 2, pp. 910–914, 2018.

Please choose: Oral
Presentation session:
Presenter name: Nadia Mei Lin Tan

Low-Load Efficiency Improvement of a Three-Phase Bidirectional Isolated DC-DC Converter (3P-BIDC) via Enhanced Switching Strategy

Nuraina Syahira Mohd Sharifuddin[1], Nadia Mei Lin Tan[1,2], Hirofumi Akagi[3]

[1]Department of Electrical Power Engineering, Universiti Tenaga Nasional, Malaysia
[2]Institute of Power Engineering, Universiti Tenaga Nasional, Malaysia
[3]Department of Electrical and Electronic Engineering, Tokyo Institute of Technology, Japan
Email: SE22704@utn.edu.my

Keywords

Bidirectional isolated dc-dc converter; burst-mode; phase-shift modulation; efficiency

Introduction

A bidirectional isolated dc-dc converter (BIDC) also known as the dual active bridge plays a significant role in battery-energy storage systems for electric vehicles or grid connection and more recently, the solid-state transformer (SST). Fig. 1 shows simulation circuit of a three-phase (3P) BIDC connected to a battery bank. It consists of two three-phase bridges that has a high-frequency transformer for galvanic isolation. The two dc-link capacitors C_1 and C_2 can handle high switching current ripples and maintain a nearly constant dc bus voltage. The output power the 3P-BIDC is described as [1],

$$P_o = \frac{V_1 N V_2}{2\pi f_s L}\delta\left(\frac{2}{3} - \frac{\delta}{2\pi}\right), \qquad (1)$$

where V_1 is the dc-link voltage of bridge 1, V_2 is the dc-link voltage source of bridge 2, N is the transformer turns ratio, δ is the phase-shift angle between ac voltage of bridges 1 and 2, L is the total leakage inductance per phase of the transformer, referred to bridge 1 side, and f_s the switching frequency.

Phase-shift modulation (PSM) has been traditionally used to operate the 3P-BIDC. The technique is simple to understand and implement. The PSM can be simply controlled by adjusting the phase-shift angle δ, which is the angle difference between the two AC phase volt-ages of bridges 1 and 2 in the 3P-BIDC. The optimum operation of the 3P-BIDC is when the ratio of the dc voltages is equal to N. However, hard-switching is likely to occur if the 3P-BIDC only depends on PSM in the low-load power transfer conditions, increasing switching losses and decreasing the converter efficiency. This paper presents an enhanced switching strategy combining burst-mode (BM) and PSM. Burst mode enables intermittent power transfer to the output during a low-load operation. The PSCAD simulation verification shows that the combination of burst-mode and phase-shift modulation techniques improves the efficiency of the 3P-BIDC at low-load conditions.

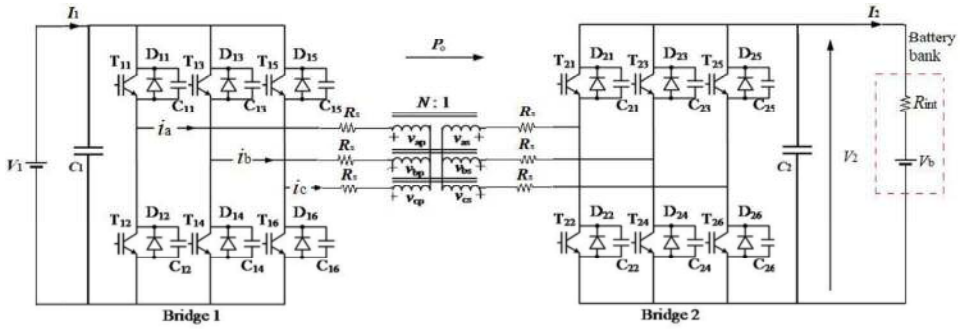

Figure 1: The simulation model of a 3P-BIDC.

Methodology

The circuit in Fig. 1 is simulated using PSCAD for charging the battery bank in non-ideal conditions. PSM is employed when the power transfer is 20% of rated power to the rated power. However, the combination of PSM and BM is employed when the power transfer is less than 20%. The combination strategy is generated by multiplying a signal of 50% duty cycle at 20-kHz with another signal of variable duty cycle or conducting period m and varying frequency $10\ \text{Hz} \le f_{\text{BM}} \le 50\ \text{Hz}$. The conducting period m controls the range of output power at a fixed phase-shift angle δ.

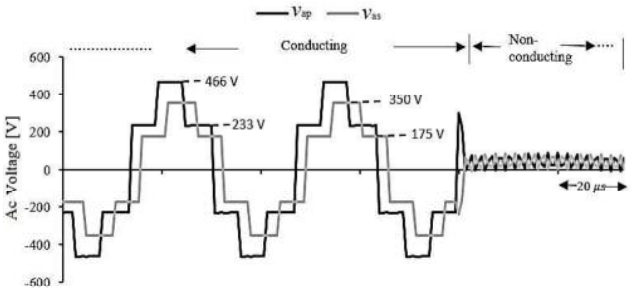

Figure 2: Time-expanded ac voltage waveforms in phase A of bridges 1 and 2 when m=10%, f_{BM} = 20 Hz, and δ=24°.

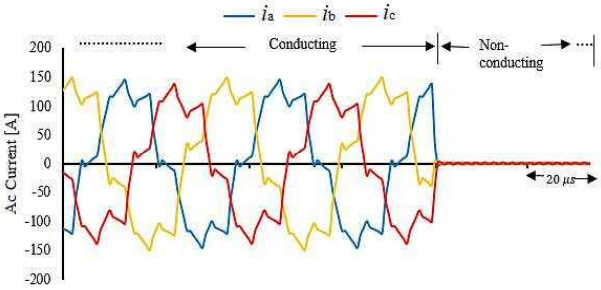

Figure 3: Time-expanded ac voltage waveforms of phase A in bridges 1 and 2 when m=10%, f_{BM} = 20 Hz, and δ=24°..

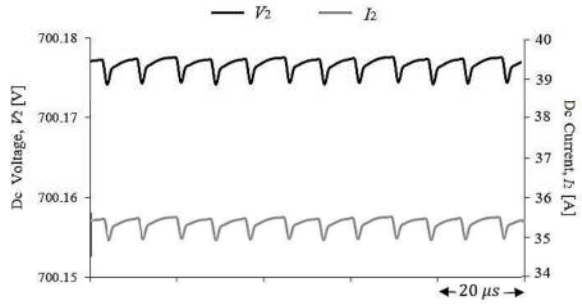

Figure 4: Dc voltage and current waveforms bridge 2 when m=10%, f_{BM} = 20 Hz, and δ=24°.

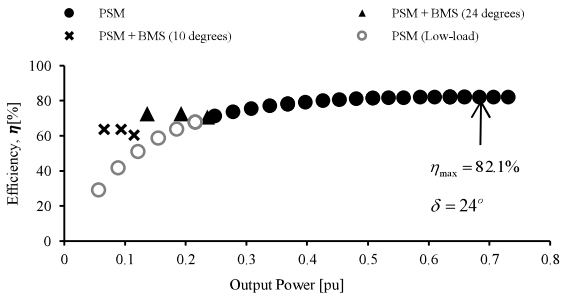

Figure 5: Converter efficiency at varying output power when only PSM employed and when the PSM and BM is employed ($10\ \text{Hz} \le f_{\text{BM}} \le 30\ \text{Hz}$).

Simulation Results and Discussion

Figs. 2–4 are obtained when the conducting period m is 10%, f_{BM} = 20 Hz, and $\delta = 24°$ at V_1 = 525 V and V_2 = 525 V. Fig. 2 shows the last two cycles (of 100 cycles) of the high-frequency (HF) transformer ac voltage in phase A. Fig. 3 demonstrates the HF transformer three-phase current waveforms. The current is zero in the non-conducting period. Fig. 4 shows the dc voltage V_2 and dc current I_2 at bridge 2 side. The voltage and current ripple percentage are lower than 1%, respectively. Fig. 5 presents the relation of the converter efficiency with change in output power at V_1 = 700 V and V_2 = 525 V. In the PSM only mode, the highest efficiency achieved is 82.1% at $\delta = 24°$. The combination of PSM and BM is carried out at δ = 10° and δ = 24°. With δ is 10°, the converter efficiency improves by 30% at the output power of 0.066 pu. When the δ is 24°, the efficiency is improves by 21% at the output power of 0.137 pu. Therefore, during the transfer of power from 0% to 20% of the rated power, the combined PSM and BM mode is seen to enhance the performance of the 3P-BIDC.

References

[1] R. W. A. A. De Doncker, D. M. Divan, and M. H. Kheraluwala, "A Three-Phase Soft-Switched High-Power-Density DC/DC Converter for High-Power Applications," IEEE Trans. Ind. Appl., vol. 27, no. 1, pp. 63–73, 1991.

Please choose: Oral
Presentation session: Applied Engineering
Presenter name: Akihiko Watanabe

Real-Time Monitoring for Improvement of Reliability of Power Devices

Akihiko Watanabe[1], Shingo Hiroyoshi[2] and Ichiro Omura[2]

[1]Department of Electrical Engineering/Electronics, Kyushu Institute of Technology,
1-1 Sensui, Tobata-ku, Kitakyushu, 804-8550, Japan
[2]Department of Biological Functions Engineering. Kyushu Institute of Technology,
2-4 Hibikino, Wakamatsu-ku, Kitakyushu 808-0196, Japan

Email: nave@elcs.kyutech.ac.jp

Keywords : Power devices, Reliability, Failure analysis, Real-time monitoring, Scanning Acoustic Microscopy

1. Introduction

A power semiconductor device is an electronic device that converts electric energy to match the purpose of use, and it is a key component indispensable for constructing a power network from home appliances to hybrid cars, photovoltaic power generation, wind power generation, and furthermore DC power transmission. To meet growing demand in the future, demand for reliability of power semiconductor devices is also increasing.

A power cycling test is often used for failure analysis of power devices due to long term fatigue. The power cycling is acceleration test reproduces a failure mode of power devices. Bond wire lift-off and solder fatigue are the main failure mechanisms in standard power modules. In a conventional failure analysis with power cycling test, an electrical and thermal condition monitoring and internal structure observation by a post failure or sampling are often used for the analysis. However, it is often difficult to determine the primary failure mechanism by this method. Due to the interdependency of the failure modes, power cycling tests require a careful failure analysis [1].

To solve the problem of conventional failure analysis with power cycling test, we have proposed a method based on a real-time monitoring [2-4]. In this method, a process to failure of a device is continuously observed from initial condition by several analysis techniques. The obtained data enables us to analyze the relation of physical phenomena occurs in the failure process and to clarify the failure mechanism of power devices.

In this paper, we present a novel apparatus “A power cycling degradation inspector [4]” which has been developed for our concept of failure analysis and demonstrate a result of real-time monitoring of a failure process of a power MOSFET.

2. Power cycling degradation inspector

The power cycling inspector is a multi-functional real-time monitoring system (shown in Fig.1). This apparatus enables the real-time monitoring of (1) inside structure of device, (2) electrical condition and (3) temperature condition during a power cycling test. For non-destructive inspection of inside the device, we employed a scanning acoustic microscopy (SAM). The SAM enables non-destructive observation inside power devices with fine resolution. Applied power stress and power consumption on the device are also monitored. The semiconductor chip temperature is estimated from an on-state voltage drop at low current. Temperature of the package is monitored by an Infrared camera through an open window at the back side of the DUT.

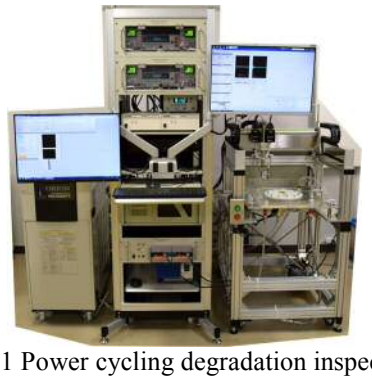

Fig.1 Power cycling degradation inspector

3. Experiment

To accelerate a process to failure, the excessive power stress was applied to the device. The power stress was

applied to achieve a junction temperature Tj≧250℃ and a package temperature Tp≧150℃ to the specimen MOSFET device which rated operating temperature is 150□.

4. Result and Discussion

The results of T_j and T_p is shown in Fig. 2. The device was failed after 9th cycle. The results indicated that the behavior of T_j and T_p was not changed just before the failure, but there is a transient change of temperature behavior was observed after 1st and 7th cycle. As for electric property, it is not change before 9th cycle as shown in Fig.3. The internal structural change is shown in Fig. 4. The white area at the semiconductor region which propagated dueling power cycle is indicated a fatigue of a chip attach. The black area in the observation region was less than 50% after the failure.

From these results, the failure mechanism of this case is discussed. For the temperature behavior, the remarkable change can be observed when stress is applied for the 1st, 7th and 9th cycle. No remarkable change was observed in the electric properties before 9th cycle. The internal structure change at the observation area is 60%, 55% and 45% after 1st, 3rd and 9th cycle, respectively. The structural change at 1st cycle could be affected to thermal condition, but that of 3rd cycle was not affected. The temperature behavior change at 7th cycle could be related to a change of thermal dissipation manner because the electrical property was not changed, but the cause cannot be pointed out from the parameters monitored this time. Finally, the failure occurred by degradation of thermal dissipation caused by propagation of the fatigue at solder layer.

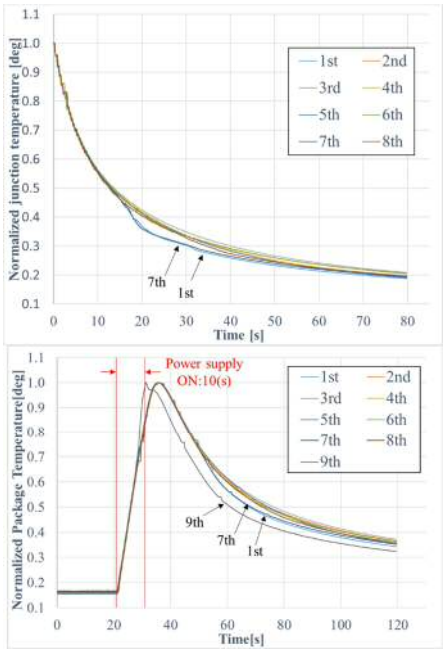

Fig.2 Variation of temperature of T_j (upper) and T_p (lower)

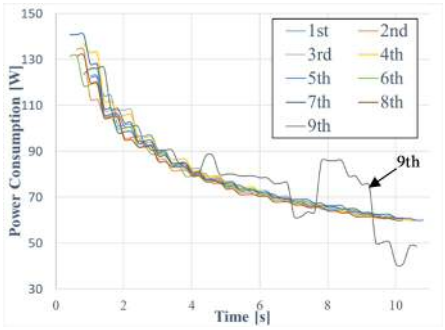

Fig.3 Variation of electric power

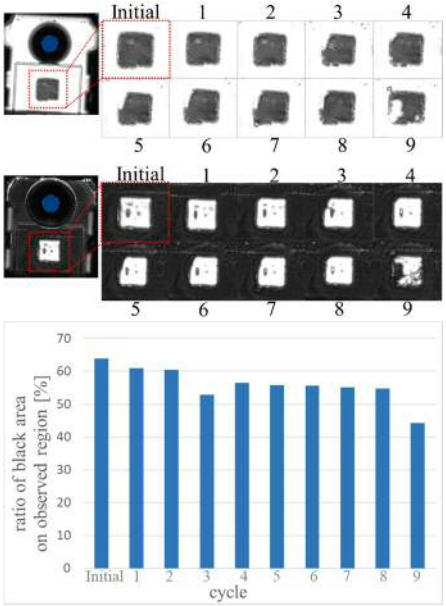

Fig4. Progress of degradation of solder layer

5. Conclusions

We proposed a method based on a real-time monitoring to increase a reliability of power devices. The real-time monitoring of a process to failure of a power MOSFET was demonstrated by a Power cycling degradation inspector developed for the concept.

Acknowledgment

A part of this work was supported by Sumika Chemical Analysis Service (SCAS).

Reference

[1] J. Lutz, H. Schlangenotto, U. Scheuermann, R.D. Doncker, Semiconductor Power Devices, Springer, 2011.

[2] A. Watanabe, M. Tsukuda, I. Omura, Real time degradation monitoring system for high power IGBT module under power cycling test, Microelectronics Reliability 53 (2013) 1692-1696.

[3] A. Watanabe, M. Tsukuda, I. Omura, Failure analysis of power devices based on real-time monitoring, Microelectronics Reliability 55 (2015) 2032-2035.

[4] A. Watanabe, I. Omura, A power cycling degradation inspector of power semiconductor devices, Microelectronics Reliability 88–90 (2018) 458-461.

Model and Motion Control of Lower Limb Exoskeleton

Asnor Juraiza Ishak, Madihah Mohd Zin, Naagajoothi Adin Naraina
Department of Electrical and Electronic Engineering
Faculty of Engineering
Universiti Putra Malaysia
43400 UPM Serdang, Selangor Darul Ehsan, Malaysia

Keywords: Exoskeleton Robot, Assistive Device, Humanoid, Rehabilitation, Maneuver Control

Introduction

Sit-to-stand (STS) movement is an essential precursor to walking. If elderly or patients loss the ability to rise from a seated position or chair, they will remain prisoners in their chairs. Therefore, it is necessary to develop assistive device to assist disable people to regain the ability to stand, sit and walk, and release therapist from heavy work of rehabilitation training. Exoskeleton robot is one of the most significant examples of human assistive device. This paper present the work implemented to model and motion control of humanoid model and lower limb exoskeleton model that only focuses on standing-up and sitting-down phases. This project consists of two main parts, which are the development of model using SOLIDWORKS and controller development using MATLAB. The completed model in SOLIDWORKS is exported to MATLAB using SimMechanics. Feedback closed loop control system and PID controller have been used to simulate the sit-to-stand (STS) movement of the model. Lastly, the PID controller and joint torque saturation is compromised to obtain the optimal sit-to-stand (STS) movement

Experiment

The process of model development for humanoid model and lower limb exoskeleton model in SOLIDWORKS and development of motion control for the model in MATLAB is outlined in the flow chart in Figure 1.

The development of the humanoid model and lower limb exoskeleton model is being completed in SOLIDWORKS as illustrated in Figure 2 and Figure 3. The completed models then being exported to MATLAB to obtain the SimMechanics block diagram. This project focused on the lower part, the joint included are hip joint, knee joint and ankle joint. Feedback closed loop system and PID controller is developed at each joint to control the movement of each joint. Saturation block is included in the system to limit the minimum and maximum torque of each joint.

Result and Discussion

The aim of this project is to develop a feedback control system which enables the joints to tracking the desired joints' angle trajectory that performing STS movement. The PID gain for each joint is being done from one limb to another. The simulation process with is starting with only hip joint and other two joint is in rigid. After the output signal satisfies the desired output, the knee joint is change to revolute joint. This tuning process is a bit risky as there are two different joint connected together. Table 1 show the PID gain when hip joint and knee joint are combined.

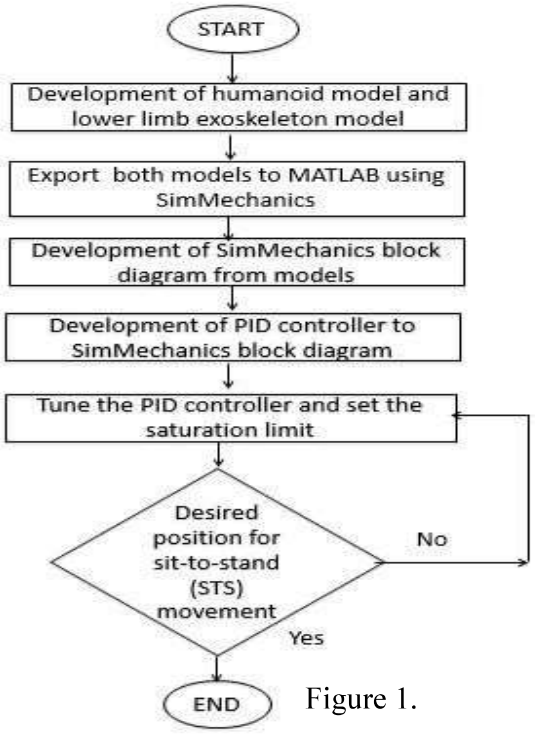

Figure 1.

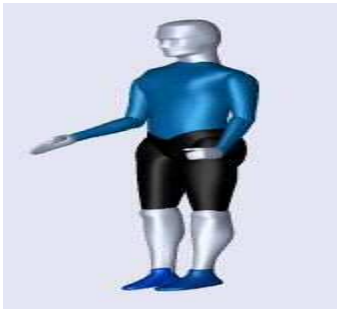

Figure 2. Humanoid model

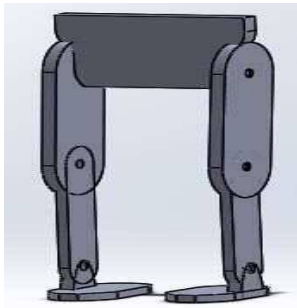

Figure 3. Lower limb exoskeleton model

Table 1: PID Gain and saturation value for each hip and knee joint

	Hip	Knee
K_P	16	16
K_I	1.6	3.2
K_D	2	8
Saturation	160 to -160	210 to -210

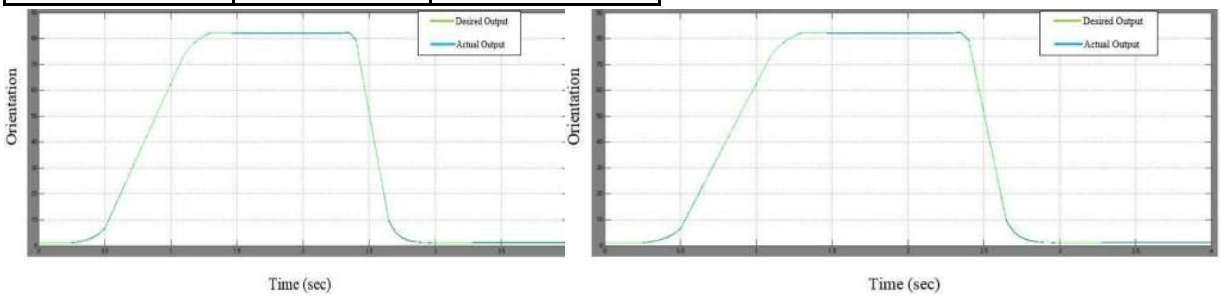

(a) Hip joint (b) Knee joint

Figure 4: Graph of orientation versus time using STS trajectory

Please choose: Presentation
Presentation session:
Presenter name: Ipsita Mishra

Comparative analysis of continuous PWM and discontinuous PWM for PMSM drive

Ipsita Mishra[1], Vijay Kumar Singh[1], Ravi Nath Tripathi[2], Tsuyoshi Hanamoto[1]
[1]Department of Biological Functions and Engineering, Graduate school of Life Science and Systems Engineering,
Kyushu Institute of technology, 2-4, Hibikino, Wakamatsu, Kitakyushu, Fukuoka, 808-0196, Japan
[2]Next Generation Power Electronics Research Center
Kyushu Institute of technology, 2-4, Hibikino, Wakamatsu, Kitakyushu, Fukuoka, 808-0196, Japan

Email: ipsitamishra713@gmail.com

Keywords
Permanent magnet synchronous motor (PMSM), Field oriented control (FOC), space-vector pulse width modulation (SVPWM), bus-clamping pulse width modulation (BCPWM), Xilinx system generator (XSG)

Introduction

Variable speed drives are nowadays used in every sector of life. In the midst of all variable speed drives permanent magnet synchronous motor (PMSM) drives are obtaining worldwide attention due its higher efficiency, higher torque to weight ratio and high power density. The vector control of PMSM can be classified as Field-oriented control (FOC) and direct torque control (DTC). The switching signal generation for power switches can be performed by using sine pulse width modulation (SPWM), space-vector PWM (SVPWM) or bus-clamping PWM (BCPWM). The digital signal processing (DSP) is most commonly used technique to implement these types of controllers. But DSP tends to exhaust CPU resources and suffers from a poor timing performance [1].

Recently, due to the advantages of higher speed, simple and low cost with parallel processing functionality, field programmable gate arrays (FPGA) have been getting attention among the researchers for the AC drives applications [2]. The algorithm complexity of AC drives requires high bandwidth which can be accomplished by the parallelism nature of FPGA. For the real-time applications, FPGA needs a deep knowledge of the hardware description language (HDL codes). However, it is a tedious task even for a skilled programmer with increase in complexity. Xilinx Inc. has provided a platform for the automatic HDL code generation using Xilinx system generator (XSG) tool [3]. XSG is a digital platform integrated with the MATLAB-Simulink.

In this paper, the FOC of PMSM drives based on a continuous PWM (SVPWM) and a discontinuous PWM (BCPWM) is considered for the in depth analysis. The voltage source inverter (VSI) model with PMSM is developed in MATLAB-Simulink and the control section is designed in XSG environment. The performance of developed system is compared on the basis of total harmonic distortion (THD) and switching losses of VSI.

XSG based simulation of PMSM drive

The schematic diagram representing the field oriented control is represented in Fig.1. It uses one outer speed controller and inner two current controllers. The discretized speed control based on the forward Euler method is obtained as follows:

$$i_q(K+1) = i_q(k) + K_{iw} w_{err} T_s + K_{pw}(w_{err}(k+1) - w_{err}(k)) \quad \ldots (1)$$

Where $w_{err} = w_{ref} - w_m$

In a similar way the discretized inner current control can also be obtained by using forward Euler method. For generation of the switching signals, the SVPWM and BCPWM is used. In this paper a carrier based approach is adopted for the simulation of PWM techniques instead of the traditional sector based calculation.

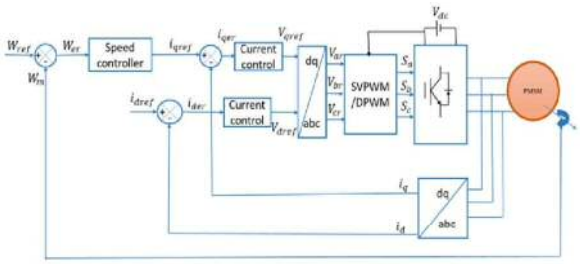

Fig.1 FOC of PMSM drive

Table I System Parameters

Parameter	Value
No of pole pair	4
Stator resistance (ohm)	0.869
Stator inductance (H)	0.0039
Rotor flux (Wb)	0.03
Power switch	IGBT
Switching frequency (KHz)	7
Rotor inertia (kg-m^2)	3.63e-5

Result and Discussion

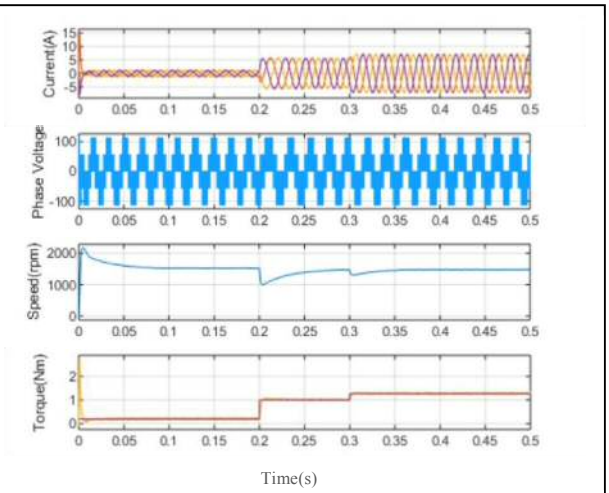

Fig.2. top to bottom: stator current of PMSM drive, output Phase voltage of VSI, Rotor speed and dynamic torque response for SVPWM FOC

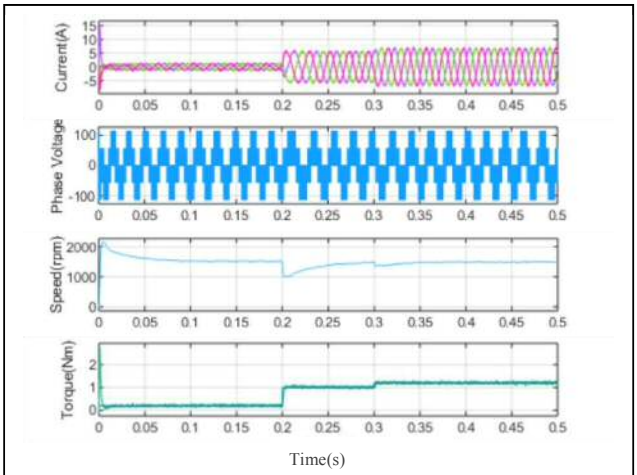

Fig.2. top to bottom: stator current of PMSM drive, output Phase voltage of VSI, Rotor speed and dynamic torque response for SVPWM FOC

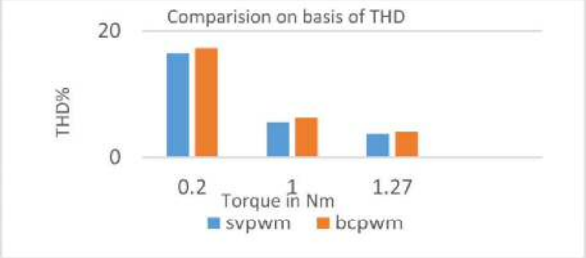

Fig.4 THD comparison of two technique

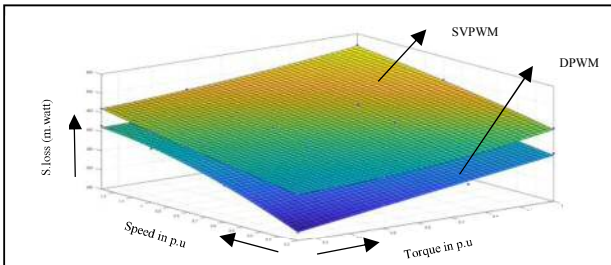

Fig.5 switching loss comparison of two technique

Fig 2 and 3 represent the speed and torque response PMSM drive for both the techniques. From Figure 4 and 5 it can be observed that the DPWM technique have lower switching losses than compared to the SVPWM without compromising much in THD. It is observed that the losses in case BCPWM are 2/3 of that of SVPWM at same frequency. As the losses are less the heat generation is also less, hence by using DPWM technique the cost of inverter can be reduced by reduction of the size of the heat sink.

Reference

[1] N. K. Quang, N. T. Hieu, and Q. P. Ha, "FPGA-Based Sensor less PMSM Speed Control Using Reduced-Order Extended Kalman Filters," *IEEE Trans. Ind. Electronics*, vol. 61, no. 12, pp- 6574 – 6582, Dec. 2014.
[2] B. Alecsa and A. Onea, "An Optimized FPGA Implementation of the Modified Space Vector Modulation Algorithm for AC Drives Control," 21st International Conference on Field Programmable Logic and Applications, pp-393-395, Sept. 5-7, 2011.
[3] V. K. Singh, R. N. Tripathi and T. Hanamoto, "HIL Co-simulation of Finite Set-Model Predictive Control using FPGA for Three Phase VSI System," Energies, 11(4), 909, April 2018.
Fig.4 THD comparison of two technique

Please choose: Oral/ ~~Poster/ Either~~
Presentation session:
Presenter name:

Performance of Gabor Transform on SEMG Signal in FCE's Work Level Categories Identification

Ezreen Farina, Shair[1,3], Siti Anom, Ahmad[1,2], Abdul Rahim, Abdullah[3], Mohammad Hamiruce, Marhaban[1], Shamsul Bahri, Mohd. Tamrin[4]

[1] Department of Electrical and Electronic Engineering, Faculty of Engineering, Universiti Putra Malaysia, Serdang, Selangor, Malaysia
[2]Malaysian Research Institute of Ageing, Universiti Putra Malaysia, Serdang, Selangor, Malaysia
[3]Centre for Robotics and Industrial Automation, Faculty of Electrical Engineering, Universiti Teknikal Malaysia Melaka, Durian Tunggal, Melaka, Malaysia
[4]Department of Environmental and Occupational Health, Faculty of Medicine and Health Sciences, Universiti Putra Malaysia, Serdang, Selangor, Malaysia

Email: ezreen@utem.edu.my

Keywords – surface electromyography (SEMG), functional capacity evaluation (FCE), time-frequency distribution (TFD), Gabor transform

1. INTRODUCTION

Industrial-related lower back and upper limb injuries are common musculoskeletal disorders (MSDs) evaluated by physical therapists in rehabilitation centers. These injured workers are required to undergone treatment and after they are fully recovered, they are routinely evaluated to determine their residual functional capacity before they return to work.

Functional capacity evaluation (FCE) is a test used to check a worker's physical ability to perform specific work errands and to determine his/her physical preparation to work. One of the FCE task available is the core-lifting task. A worker's lifting limit is essential to determine if the worker is fit enough of handling either the light, medium, heavy, or very heavy physical job requirements. To test a worker's working limit, he/she needs to perform the core-lifting task to a maximal limit and only the therapist's visual perception is utilized to determine whether the he/she has reached his/her maximal limit. However, a vital constraint innate to this FCE is the likelihood that the therapist's decision could be influenced by information other than visual perception. In order to improve the FCE's reliability and validity, surface electromyography (SEMG) signal is considered in this study to determine the work levels categories of each worker. SEMG signal is a profoundly complex non-stationary signal which speaks to the neuromuscular activation with a contracting muscle.

Previously, different techniques have been proposed for the SEMG signal analysis. The earliest technique is the Fourier transform. In any case, this technique is only suitable for stationary signal. Since SEMG signal is a non-stationary signal, to satisfy the stationary condition of the Fourier transform, long-haul signals are divided into small segments and the Fourier of each segment is taken. This technique is known as short-time Fourier transform (STFT). Another technique is the Gabor transform which has been proven to be superior that the STFT in terms of the time resolution and frequency resolution. Thus, this study depicts the usage of Gabor transform to enhance the FCE's work levels categories identification based on the SEMG signal.

2. EXPERIMENTAL METHOD

Eleven SEMG recordings were evaluated in this study. These SEMG signals were recorded from right and left biceps brachii, and right and left erector spinae muscles of eleven control subjects which comprised of 6 males and 5 females aged between 22 and 30 years old. Subjects were asked to perform core-lifting task which consists of six lifting phases in a single cycle using the Valpar - Joule premium package work centre. After one cycle, weights were added to the weightlifting container. Weight progression flip-chart in conjunction with the T-handled color-coded weights were used to propel the subject through the core-lifting task. Lifting cycle was repeated until the subject experiences fatigue or reached their maximum lifting capacity. Spectrogram was utilized as a pre-processing approach for auto-segmentation of the EMG signal and for the feature extraction. This set of features was extracted to accurately differentiate the FCE's work levels categories. The work levels

categories definition used at the SOCSO Tun Abdul Razak Rehabilitation Centre are taken from the Dictionary of Occupational Titles as in Table 1. However, this study only focuses on classifying the medium work level and heavy work level due to subject constraint. These features were then reduced using linear discriminant analysis (LDA) and support vector machine (SVM) acts as a classifier. The whole core-lifting task was performed at the Social Security Organization (SOCSO) Tun Abdul Razak rehabilitation centre, Melaka, Malaysia and follows the convention set by the association to ensure the reliability and validity of the results.

Table 1. Work levels categories definition

Light work	Medium work	Heavy work	Very heavy work
Exerting up to 4.5 kg of force to lift.	Exerting up to 4.5 - 11 kg of force to lift.	Exerting up to 11- 23 kg of force to lift.	Exerting in excess of 23 kg of force to lift.

3. RESULTS AND DISCUSSION

From the time-frequency representation of the Gabor transform, the average RMS voltage was calculated and plotted (Figure 1). It can be seen that the RMS voltage increases as the cycle proceeds. However, the erector spinae muscle shows a much smaller increment compared to the biceps brachii. The erector spinae muscle is appeared to have less reaction to the load increment. From the plot of the average RMS voltage, the SEMG signal features (muscle power, muscle strength, and muscle endurance) were estimated. These features were then passed to the classifier for the work levels categories classification. The accuracy, sensitivity, and specificity of the classification based on the extracted features were found to be 93%, 97%, and 89%, respectively. This shows that the system adequately classifies the work levels categories of the FCE's core-lifting task.

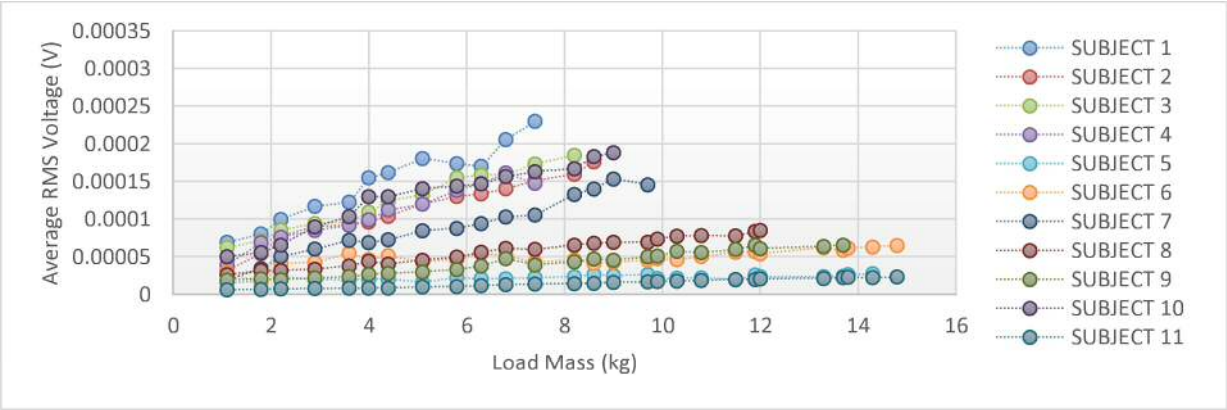

(a)

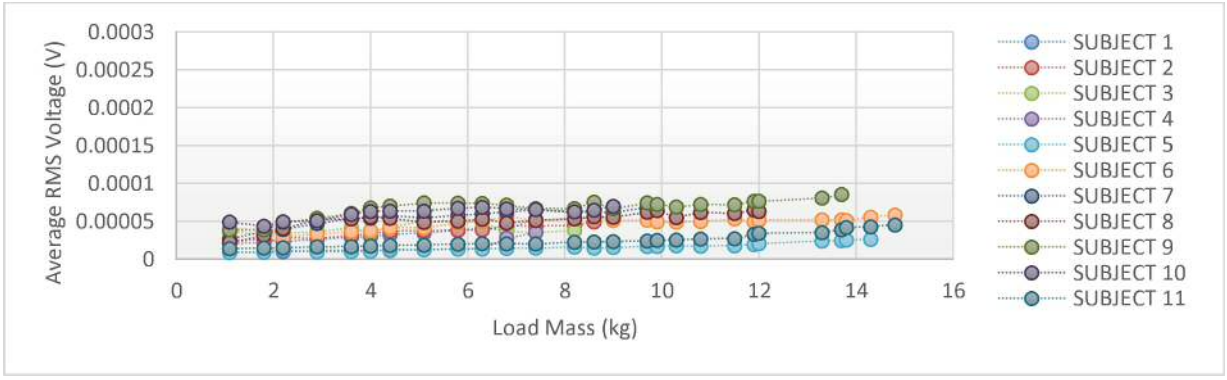

(b)

Figure 1 Mean average RMS voltage for (a) biceps brachii and (b) erector spinae muscles

Please choose: Oral/ Poster/ Either
Presentation session:
Presenter name: Rahimah binti Abdul Rafar

[Multiple Inclined or Curved Cracks Problem in Circular Positions in Plane Elasticity]

[Rahimah, Abdul Rafar][1], [Nik Mohd Asri, Nik Long][1,2], [Norazak, Senu][1,2], [Nao-Aki, Noda][3]

[1]Faculty of Science, Mathematics Department, University Putra Malaysia, 43400 UPM Serdang, Selangor, Malaysia
[2]Institute for Mathematical Research, University Putra Malaysia, 43400 UPM Serdang, Selangor, Malaysia
[3]Faculty of Engineering, Kyushu Institute of Technology, 1-1 Sensui-cho, Tobata-ku, Kitakyushu-shi, Fukuoka, 804-8550, Japan

Email: [eimah7178@gmail.com]

Keywords Stress intensity factor, inclined crack, curved crack, circular position, hypersingular integral equation.

[Introduction]

The problems of multiple inclined or curved cracks in circular positions is treated by using the hypersingular integral equation method. The cracks center are placed at the edge of a virtual circle with radius R. The first crack is fixed on the x-axis while the second crack is located on the boundary of a circle with the varying angle, θ. A system of hypersingular integral equations is formulated and solved numerically for the stress intensity factor (SIF). Numerical examples demonstrate the effect of interaction between two cracks in circular positions are given. It is found that, the severity at the second crack tips are significant when the ratio length of the second to the first crack is small and it is placed at a small angle of θ.

[Stress analysis for multiple cracks]

The problems of multiple cracks in circular positions in plane elasticity have been formulated into the hypersingular integral equation by using a complex potential method. Here a simple description of our approach is made. Suppose, for an infinite plate having the multiple cracks that are placed in a circular form. The center of the cracks are placed at the edge of a circle with radius R. The first crack is fixed on the x-axis while the second crack is located on the boundary of a circle with the varying angle. The remote stresses is assumed to be zero, the applied normal and tangential forces on both edges of each crack are the same in magnitude and opposite in direction. For solving this problem, it is assumed that at the prescribed points of both edges of a single crack a pair of normal and tangential concentrated forces are applied. The stresses, the resultant force functions and the displacement are related to complex potentials. The complex variable function method plays an important part in plane elasticity in formulating the equation for the multiple crack problems. In general, the problems of multiple crack in an infinite plate can be considered as a superposition of many single crack problems. By using superposition principle, the system of hypersingular integral equation for multiple crack problems can be obtained. The obtained hypersingular integral equations for the problems are then transformed into hypersingular integral equation on the real axis by using curve length coordinate method. This method requires less collocation points, thus give faster convergence. It is also very efficient for solving various crack positions and configurations of the multiple crack problems. Then, with the help of particular quadrature rules, the resulting system of hypersingular integral equations are solved numerically for the unknown coefficients. From the obtained values of the unknown coefficients, the stress intensity factors (SIFs) can be evaluated. Thus it can be used to investigate the behavior of two cracks in circular position in plane elasticity.

[Result and Discussion]

Figure 1 shows the interaction between inclined and curved cracks in circular positions in an infinite plate. Both cracks are placed on the virtual circle. Figure 2 shows the result for the SIFs at the crack tips A_1, A_2, B_1 and B_2. Since the angle θ is varied, the shielding effect on the curved and inclined cracks is easily seen.

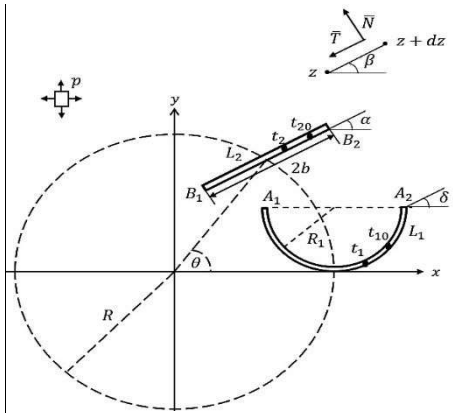

Figure 1 Inclined and curved cracks

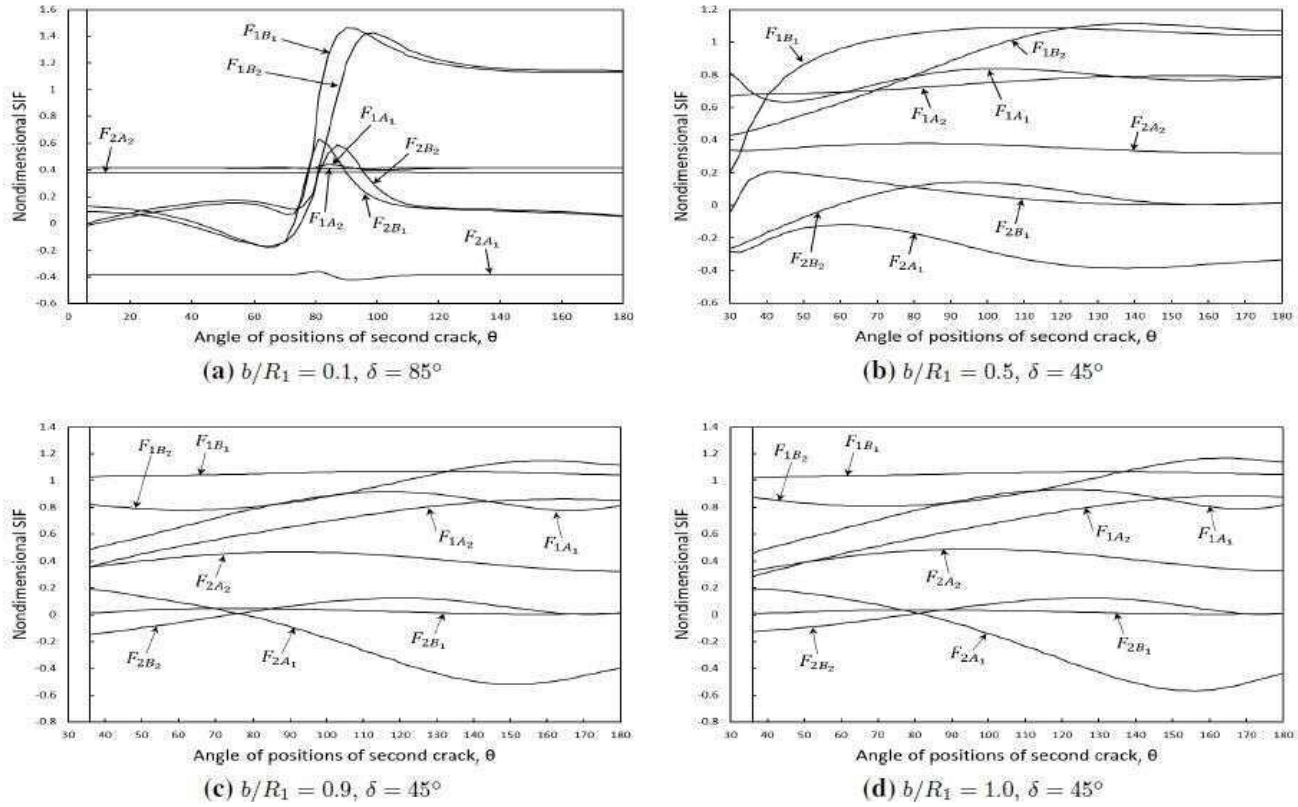

(a) $b/R_1 = 0.1,\ \delta = 85°$ **(b)** $b/R_1 = 0.5,\ \delta = 45°$

(c) $b/R_1 = 0.9,\ \delta = 45°$ **(d)** $b/R_1 = 1.0,\ \delta = 45°$

Figure 2 Nondimensional SIF for $\alpha = 20^{\circ}$ when θ changing.

[Conclusion]

The multiple cracks problems in a circular position in plane elasticity are studied. The hypersingular integral equation for two cracks have been formulated. The numerical examples showed the behaviour of the stress state at the crack tips. Since the angle is varied, it is obvious that the second crack tips is most affected than the first crack tips. In addition, with an increase of the length ratio of the second to the first crack, the shielding effect for the cracks at the angle $\theta \leq 90^{\circ}$ is obvious.

Please choose: Oral/ Poster/ Either
Presentation session:
Presenter name: Ibai Gorordo Fernandez

Performance Evaluation of a Commercial Electromagnetic Tracking Controller for Motion Capture

Ibai, Gorordo Fernandez[1] and Chikamune, Wada[1]

[1] Graduate School of Life Science and Systems Engineering, Kyushu Institute of Technology, 2-4 Hibikino, Wakamatsu-ku, Kitakyushu 808-0196, Japan

Email: ibai.gorordo@hotmail.com

Keywords: motion capture, electromagnetic tracking, optical tracking, kinematics

INTRODUCTION

Optical motion capture and inertial measurement units (IMU) systems are the most common technologies for human motion capture. However, both of these technologies have various limitations. In the case of optical motion capture systems, they suffer from occlusion when the markers are blocked by the subject's body, have high cost and can only analyze movement inside a limited area. On the other hand, IMU sensors suffer from time varying noise and since the position is obtained using integration, it produces drift over time.

Besides those technologies, other techniques such as magnetic motion capture are also used for position tracking. Magnetic motion trackers consist of two main elements: one magnetic source and one or several magnetic sensors. The transmitter generates a magnetic field by applying a current through a coil and the position and orientation are calculated by measuring the field strength in the receiver coils. Despite being easily affected by ferromagnetic materials, magnetic motion capture systems can provide position and orientation with high accuracy and are not affected by occlusion nor drift.

In this test, the game controller Razer Hydra (Sixense) was analyzed. It consists of one base, that contains a 3-axis coil, connected with wires to two controllers that contain 3 small receiver coils. The base generates a sequence of 20 KHz AC pulses for each of the three axes (X, Y, Z). Then, these pulses are measured by the receiver coils in order to calculate the position and orientation of the controllers with respect to the base. The objective of this test was to validate the accuracy of the Razer Hydra to measure the distance by comparing it with an optical motion capture system.

EXPERIMENT

For the optical motion capture system, 8 cameras Flex 13 (OptiTrack) were placed in a 25 m^2 room to track the position of the Razer Hydra's base and controllers. In order to do that, 4 markers were placed in each controller and another marker was placed in the top of the base (Figure 1). The output rate for the motion capture system was set to 100 Hz and the data was stored in a computer for later analysis.

Figure 1. Razer Hydra base and controllers with the attached markers.

On the other hand, the data from the Razer Hydra, 3D position and orientation of both receivers, was stored in the computer at a sampling rate of 250 Hz. The base of the Razer Hydra was placed in the middle of the room at a 60 cm height while the controllers were moved around the base at a distance between 20 to 120 cm. The test was performed in two parts of 4 minutes, one for each controller of the Razer Hydra.

RESULTS AND DISCUSSION

After the test, the data from both devices was post-processed in MATLAB®. First, the data from the Razer Hydra was downsampled from 250 Hz to 100 Hz using linear interpolation so that the data from both devices were sampled at the same instants. Moreover, all the signals were adjusted with offsets to have an initial value of 0. Finally, the Root Mean Square Error (RMSE) was calculated for the distance difference between the Razer Hydra and the optical motion capture system. The RMSE value was calculated for the whole range of distances and also for the range between 0-20 cm, 20-40 cm, 40-60 cm, 60-80 cm, 80-100 cm and 100-120 cm as shown in Table 1.

Table 1. RMSE values (cm) at different distance ranges and for the whole range.

	20 cm	40 cm	60 cm	80 cm	100 cm	120 cm	Total
Left	2.16	4.93	6.71	6.83	6.47	6.73	6.42
Right	3.85	6.69	8.15	9.46	9.21	8.95	8.35

As the distance between the controller and the base of the Razer Hydra increases, there is also an increase in the RMSE value and it barely does not change at distances between 80 to 120 cm. Furthermore, the accuracy of the right controller seems to be smaller than the accuracy of the left one with a difference of 2 cm for the RMSE.

After visually comparing both signals, even though all the signals had been fixed to have an initial value of 0, it was observed that the distance from the Razer Hydra tended to be higher that the distance from the motion capture system. For this reason, the distance from the Razer Hydra was multiplied with a reducing coefficient k ($k < 1$), to improve the RMSE. The coefficient was selected by applying a linear regression that minimized the RMSE value, obtaining a coefficient k of 0.9268 for the left controller and 0.895 for the right one. Table 2 shows the RMSE values after applying a reducing coefficient to the distance from the Razer Hydra.

Table 2. RMSE values (cm) at different distance ranges and for the whole range after applying a reducing coefficient.

	20 cm	40 cm	60 cm	80 cm	100 cm	120 cm	Total
Left	1.21	2.67	2.72	1.85	1.71	2.15	2.02
Right	2.76	3.69	3.04	2.59	2.79	3.68	2.97

Compared to the high end electromagnetic trackers such as Fastrak® (Polhemus) that have a static accuracy below 1 mm, the Razer Hydra has a significant lower accuracy, even after applying a reducing coefficient to the distance from the Razer Hydra. One of the possible reason for the low accuracy might be caused by the environment in which the test was performed, the walls of the room were metallic and there were several electronic devices placed around the room. As mentioned previously, magnetic capture systems are affected by ferromagnetic materials; therefore, in the future a similar test will be performed in a proper environment to analyze how the Razer Hydra is affected by metallic objects.

Finally, in this test only the accuracy of the distance was analyzed. The measurement of the distance can be useful for certain application such as measuring the distance between the two feet while walking to calculate the step length. However, most of the motion capture applications require the knowledge of the position and orientation of different segments of the body. Thus, further analysis will be performed in the future to measure the accuracy of the position and orientation of the Razer Hydra.

Please choose: Oral/ Poster/ Either
Presentation session: Appiled Engineering
Presenter name: Watcharin Tangsuksant

Comparison of HSV and RGB Color Models using Color Moment for Obstacles Matching along the Road

Watcharin Tangsuksant[1], and Chikamune Wada[1]

[1]Graduate School of Life Science and Systems Engineering, Graduate School of Life Science and Systems Engineering, Kyushu Institute of Technology, Hibikino 2–4, Wakamatsu–ku, Kitakyushu, Fukuoka 808–0196, Japan

Email: w.tangsuksant.m@hotmail.com and wada@brain.kyutech.ac.jp

[Keywords]
Blind people, Color moment, Height estimation, Images similarity measurement, Obstacles

[Introduction]

According to World Health Organization, in 2017, the report shows the number of completely blind people is about 36 million [1]. Bind individuals have to face many problems in daily life, especially in the underdeveloped countries which cannot provide the support system for them. However, the smartphone become useful assistive device for blind people recently, because it can contain various useful applications such as bank reader and color detection. Although, there were appearance of many researchers focusing on such problems, this research concerns the situation of public bus waiting for blind people.

Image processing method is widely used for various applications including the assistive system of bus waiting for blind individuals. The proposed bus number recognition techniques [2-3] also used some image processing methods in order to inform the blind user of the oncoming bus. However, when the blind users captures scenarios for the image processing method by a camera without any assistances, some obstacles along the road might be captured instead of oncoming bus number. For example, the blind user want to capture the oncoming bus while they are standing behind the huge or high obstacles. Because existing researches did not consider the situation of obstacles appearance, final goal of this research emphasizes to estimate the height of obstacles based on color moment technique [4] as shown in Figure 1, in order to detect the oncoming bus number.

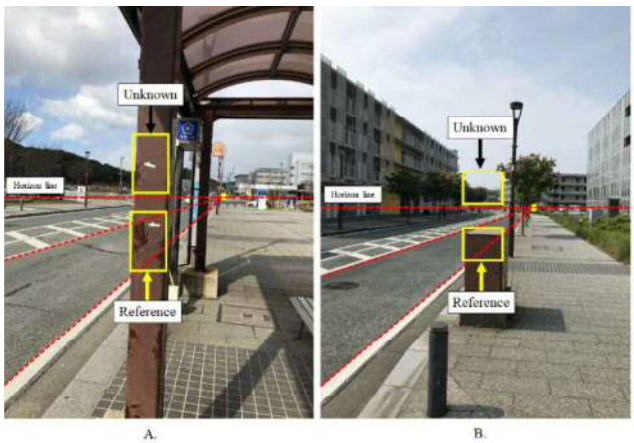

Figure 1. (A.) Matching obstacles example (B.) Non-matching obstacles example.

[Experiment]

The color moment generally is applied on the image retrieval application. Based on the traditional method of color moment technique, there were three important parameters such as mean (E), standard deviation (σ), and skewness (s) as shown in Eq. 1. Moreover, weight (w) was adjustable parameter that was defined manually depending on application.

$$d_{mom}(H,I) = \sum_{i=1}^{r} w_{i1}\left|E_i^1 - E_i^2\right| + w_{i1}\left|\sigma_i^1 - \sigma_i^2\right| + w_{i1}\left|s_i^1 - s_i^2\right| \quad (1)$$

For this research, we apply the color moment for matching two area of obstacles along the road. To distinguish between the matching and non-matching images, the criteria setting between two categories was necessary. Two types of dataset were provided for matching and non-matching images, which contained fifty pair images for each dataset. This experiment compared two color models of HSV and RGB using color moment which HSV color model was proposed in traditional method [4] for image retrieval application. Moreover, the weight in Eq. 1 was selected as the basic number of 1, 2, and 3 with permutations, but not included cases (1, 1, 1), (2, 2, 2) and (3, 3, 3). Therefore, there are 18 cases of testing for HSV and RGB color models.

[Result and Discussion]

The trend of graph between HSV and RGB were shown in Figure 2. Basically, the color moment value of non-matching cluster, which shows as the red mark in Figure 2, is higher than another. Obviously, the RGB color model, as shown in Figure 2(B), could separate the data between matching and non-matching images with mean $\pm$ S.D. for all weight testing. value. On the other hand, HSV color model cannot separate those data in all weights testing.

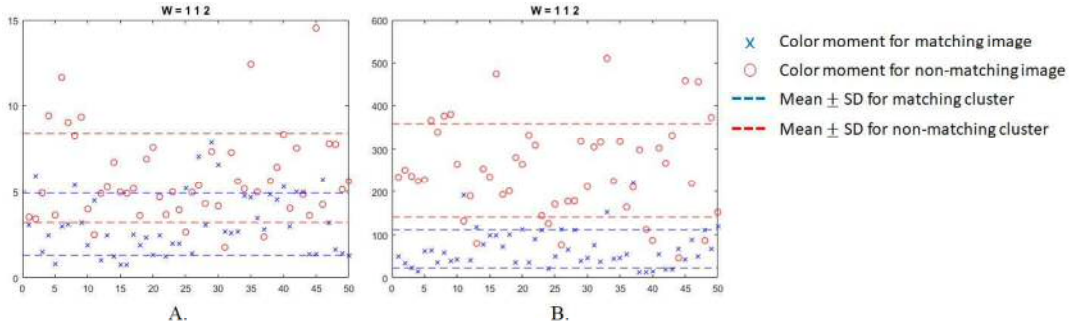

Figure 2. (A.) Example of HSV with weight 1,1,2 (B.) Example of RGB with weight 1,1,2

Based on the experimental results with 18 weight cases, the RGB color model was feasible to apply for clustering the matching and non-matching images with mean $\pm$ S.D. criteria. For future work, the optimization is necessary to select the suitable weight value.

[References]

[1] World Health Organization [Online]. Available: http://www.who.int/news-room/fact-sheets/detail/blindness-and-visual-impairment, Accessed on: Oct. 11, 2017.

[2] P. Wongta, T. Kobchaisawat, and T. H. Chalidabhongse, "An automatic bus route number recognition," in Proc. of the IEEE Int. Conf. on Computer Science and Software Engineering (JCSSE), Khon Kaen, Thailand, 2016, pp. 1–6.

[3] C. C. Cheng, C. M. Tsai, and Z. M. Yeh, "Detection of bus route number via motion and YCbCr features," in Proc. of the IEEE Int. Conf. on Computer, Consumer and Control (IS3C), Taichung, Taiwan, 2014, pp. 31–34.

[4] M. A. Stricker, M. Orengo, "Similarity of color images", In Storage and Retrieval for Image and Video Databases III (Vol. 2420, pp. 381-393). International Society for Optics and Photonics, 1995, March.

Please choose: Oral
Presentation session: Applied Engineering
Presenter name: Takeshi Jouyashiki

Comparison of Body-conducted sound sensor and Air-conducted sound Sensor via a lung sound simulator

Takeshi Jouyashiki[1], and Chikamune Wada[1]

[1]labratory of Human-function substitution systems Kyushu Institute of Technology
2-4, Hibikino, Wakamatsu-ward, Kitakyusyu-city, Fukuoka, 808-0196, Japan

Email: o899019t@edu.brain.kyutech.ac.jp

Keywords Body-conducted sound sensor frequency response, Lung sound simulator.

[Introduction]

Body-conducted sound sensors (BCS) was developed to detect non-audible murmur (NAM). BCS was using urethane elastomer in acoustic propagation layer, and it was a bio-acoustic sensor with high sensitivity and resistance to external noise [1, 2]. On the other hand, in the study of pulmonary sound, an Air-conducted microphone sensor (ACS) was used [3-6]. There was a coupler was attached to the tip of the microphone to provide an air chamber. In this study, we analyzed the characteristics of the BCS, compared with the air conduction type, and examined the usefulness of the BCS.

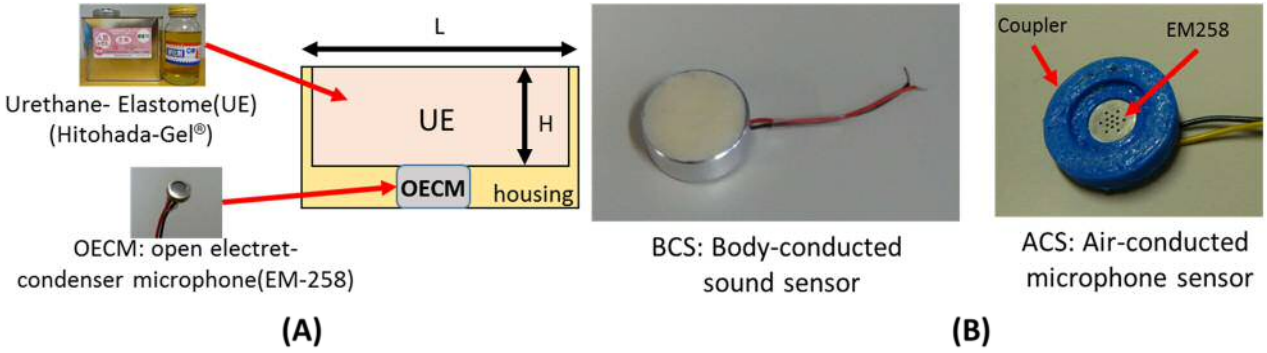

Fig.1 (A) Stricture of Body-conducted sound sensors (BCS), (B) BCS and ACS.

[Experiment]

We have produced the BCS and ACS, shown in Fig. 1. The diameter of BCS was 20 mm, and the propagation layer shape was filled with urethane elastomer in a cylinder type with 1mm thickness. The ACS had the same shape as the BCS, but the propagation layer was filled with air.

In the experiment, the following two steps were performed;

(1) Production of sensitivity measurement system [2], and sensitivity measurement of BCS and ACS. Fig. 2(A) shows a diagram of the system used to calibrate. The measurement system was composed of DAQ-6212, frequency analyzer software (LabVIEW2012; National Instruments Corporation), a .reference sensor (8001; B&K), a vibrator (4810; B&K), and a urethane elastomer cylinder of 75mm diameter and 50mm height, which simulates the soft tissues. The frequency characteristics of BCS and ACS were measured and frequency measurement range was 10-3kHz. The reference sensor was used to measure force/contact area, it was defined of stop-surface pressure. Let the measured frequency response of force/contact area be $P_0(\omega)$, measurement objetc puressure be $P(\omega)$; then $P(\omega)/P_0(\omega)$ gives the pressure frequency response of BCS and ACS.

(2) The spectrogram measured of the BCS and ACS were measured using a lung sound simulator [3]. Lung sound spectrogram measured using audio-interface (Rubix22; Roland) and analysis software (EasyLSA[4, 5]). The sample sound was used a white noise and trachea sound[5, 6]. Fig. 3(A) shows a diagram of the lung sound simulator system.

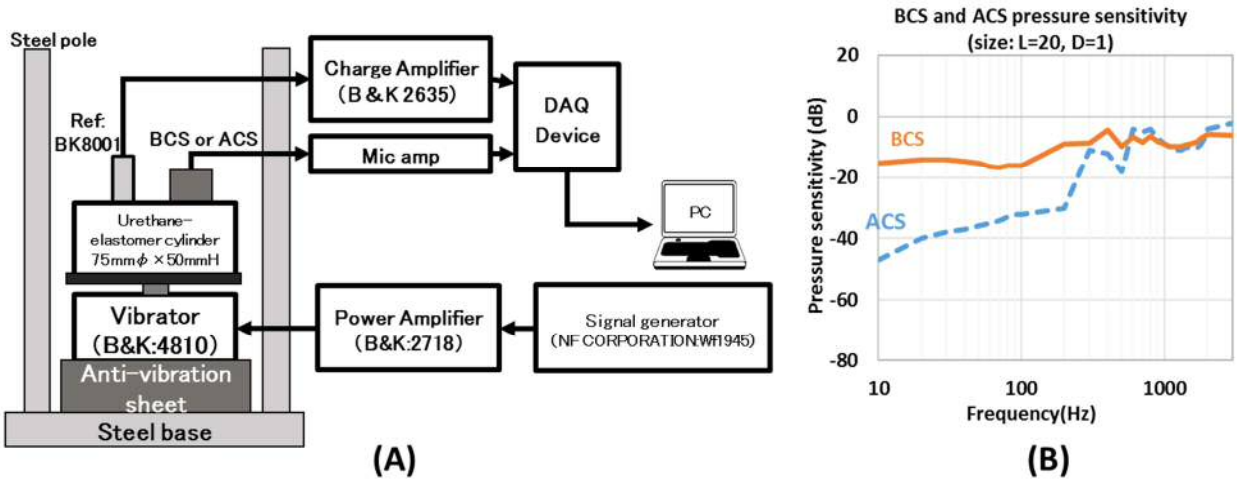

Fig.2 (A) Block diagram of the sensitivity measurement system,
(B) Frequency response of BCS and ACS.

[Results and Discussion]

Fig. 2(B) shows the frequency characteristic results of BCS and ACS. BCS showed higher sensitivity than ACS. Fig.3 (B) shows the observation results of white noise and trachea sound spectrogram. The white noise and tracheal sound spectrogram in BCS was responded with high sensitivity. Furthermore, spectral waveform of BCS was responded with 10dB higher sensitivity than ACS in below 800Hz. The lung sounds were dominated by below 1000 Hz segment. BCS had higher sensitivity than ACS, and it was considered useful. From the results, we think the sensor can be used as a bioacoustics sensor with high sensitivity and resistance to external noise by covering the sensor with a urethane elastomer. In the future we need to observe and verify of many lung sounds.

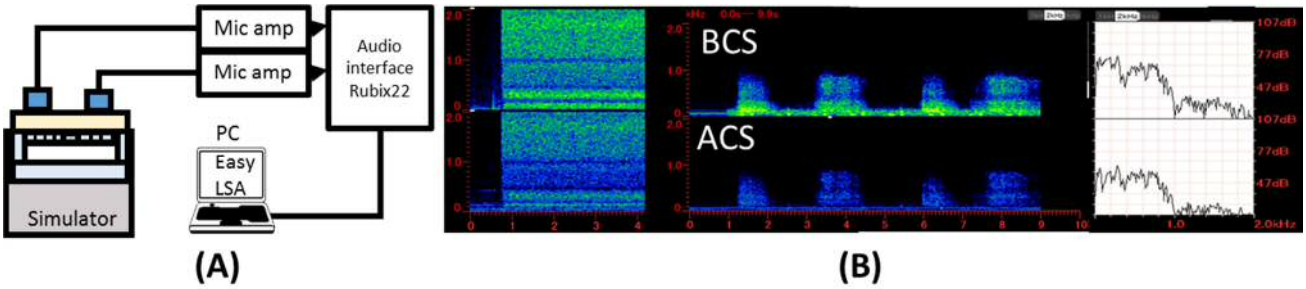

Fig.3 (A) Lung sound simulator, (B) lung sound observation.

Reference

[1]Y Nakajima, H Kashioka, N Campbel, K Shikano: Non-Audible Murmur (NAM) Recognition. IEICE Trans.Inf. & Syst. vol.E89-D, no.1, pp.1-8, 2006.

[2]T Hirahara, M Otani, S Shimizu, T Toda, K Nakamura, Y Nakajima, K Shikano: Silent-speech enhancement using body-conducted vocal-tract resonance signals. Speech Communication. Vol.52, no.4, pp.301–313, 2010.

[3]S Kraman, G Pressler, H Pasterkamp, G Wodicka: Design, Construction, and Evaluation of a BioAcoustic Transducer Testing (BATT) System for Respiratory Sounds. IEEE Transactions on Biomedical Engineering, vol.53, no.8, pp.1711-1715, 2006.

[4]T Shimoda,Y Obase,Y Nagasaka, H Nakano, R Kishikawa, T Iwanaga: Lung sound analysis can be an index of the control of bronchial asthma. Allergology International. Vol.66, no.1, pp.64-69, 2017.

[5]H Nakano, M Hayashi, E Ohshima, N Nishikata, T Shinohara: Validation of a New System of Tracheal Sound Analysis for the Diagnosis of Sleep Apnea-Hypopnea Syndrome. SLEEP. vol.27, no.5, pp.951-957, 2004.

[6] A Yadollahi, Z Moussavi: A Robust Method for Estimating Respiratory Flow Using Tracheal Sounds Entropy. IEEE Trans Biomed Eng. Vol.53, no.4, pp.662-668, 2006.

Please choose: Oral
Presentation session:
Presenter name: AHMAD SHUKRI MUHAMMAD NOOR

Lipids Sensing using Optical Fiber Sensor

C.H.C. Lah[1,2], N. Jamaludin[5], F.Z. Rokhani[1,3], S.A. Rashid[4,5], A.S.M.Noor[1,2]

[1] Department of Computer and Communication Systems Engineering, Faculty of Engineering, Universiti Putra Malaysia, 43400 UPM Serdang, Selangor, Malaysia.

[2] Research Centre of Excellence for Wireless and Photonic Network, Faculty of Engineering, Universiti Putra Malaysia, 43400 UPM Serdang, Selangor, Malaysia.

[3] Halal Research and Product Institute, Universiti Putra Malaysia, 43400 UPM Serdang, Selangor, Malaysia.

[4]Department of Chemical and Environmental Engineering, Faculty of Engineering, Universiti Putra Malaysia, 43400 UPM Serdang, Selangor, Malaysia.

[5]Materials Processing and Technology Laboratory (Nanomaterials and Nanotechnology Group), Institute of Advanced Technology, Universiti Putra Malaysia, 43400 UPM Serdang, Selangor, Malaysia

E-Mail: ashukri@upm.edu.my; Tel: +603-8946 6446

Keywords—Optical Tapered fiber; Optical Fiber sensor; Graphene Quantum Dots; Lipids; Fats.

I. INTRODUCTION

Graphene quantum dots (GQDs), as a new kind of quantum dots, having emerged and ignited tremendous research interest. Due to the pronounced quantum confinement and edge effects, GQDs has numerous novel chemical and physical properties [1]. GQDs also show considerably low toxicity, excellent solubility, high stability, stable photoluminescence, better surface grafting, high electrical conductivity and high thermal conductivity, thus making them promising potential in fields like fluorescent probe, optoelectronic devices, sensors, and cell imaging [2].

Lipids such as lard from pork and not ritually slaughtered meats are forbidden for Muslims and Jews [3]. For this reason, several analytical methods either physical or chemical based-methods have been developed to identify it [4]. In some countries, lard is one of the cheapest edible lipids; consequently, lard is deliberately added into the food products to reduce the production cost [5]. Structure and composition of fatty acids in fats and oils could be used as an indicator for determination adulteration. Therefore, this study was directed to studies the intensity of lard in the present of GQD as a sensing medium. The result could be used as a basis for detection of lard adulteration in products with complex composition.

II. EXPERIMENTAL

1. Sample preparation

Lipids were extracted by rendering different batches of subcutaneous fat from the back part of pig's body which were obtained from several local markets in Seri Kembangan, Selangor, Malaysia. The rendering process was carried out according to previously reported publication [4]. The filtered fats sample is kept in tightly closed container under a nitrogen blanket in -20°C. Before being used for analysis, the lard were thawed at water bath at 60°C until they melt.

2. Sensor Fabrication

Vytran glass processing workstation (GPX 3000 series) was used to taper the standard multimode fiber (62.5μm core and 125μm cladding). A taper profile of fiber with a waist diameter W of 20 mm, a waist length L of 10 mm, and a length of the stretching L of 5 mm were prepared. The GQDs were synthesized in-house based on [6]. The tapered fiber region were then coated with GQD using drop casting method.

The experimental setup of the project is shown in Fig. 1. Ocean optic whitelight source (HL 2000) and spectrophotometer (USB 4000) were used as the input and detector respectively. The tapered fiber was placed in a flow cell and the intensity of the light from the tapered fiber was captured via a computer.

III. RESULTS AND DISCUSSION

Shown in Fig. 2, the intensity drops as the lard concentration increases because the higher the concentration of lard combine with the GQD, will absorb more light when it travel to tapered or sensing region. Fig. 3 show the FESEM image of the tapered fiber coated with GQD. It reveals that the thickness of lard coated on tapered fiber. The thickness of the grapheme quantum dots is estimated to be approximately 2.30-2.40μm. This FESEM is performed to verify the uniformity of the coating of GQD on the tapered fiber.

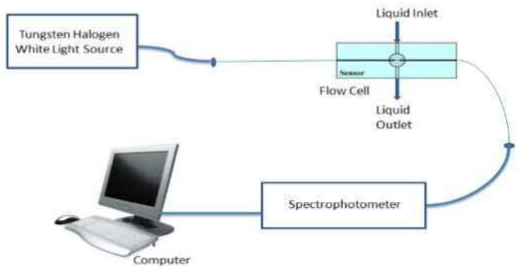

Fig 1: Experimental Setup

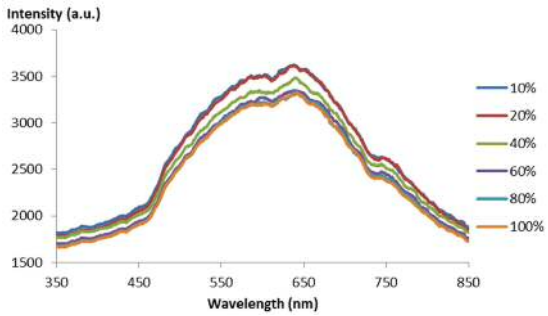

Fig. 2: Intensity Spectrum of tapered fiber coated with GQD

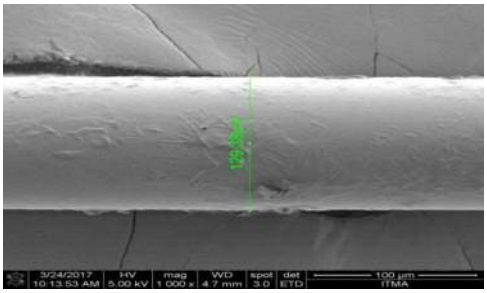

Fig. 3: FESEM image of tapered fiber coated graphene quantum dots (GQD)

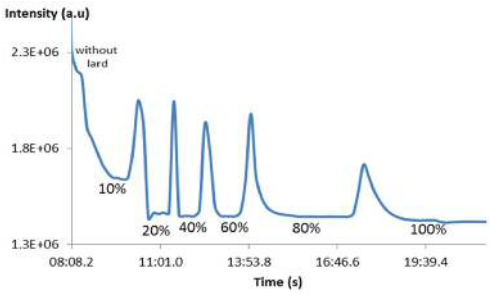

Fig. 4: Dynamic response of GQD coated tapered fiber

The presence of lard is detected by both tapered fiber coated and uncoated GQDs as shown in Fig. 4. The tests were performed at room temperature. The shows the dynamic response of coated tapered fiber tip exposed towards different concentrations of lard. It shows the dynamic response is inversely proportional to the different concentrations of lard solutions exposed to the tapered multi-mode tapered fiber coated with GQD. The response from the GQD coated fiber changes according to the lard concentration.

I. CONCLUSION

We have successfully fabricated a tapered fiber sensor with a graphene quantum dots sensing layer to detect lard concentrations. The tapered fiber coated with GQD gives a stable repeatable response towards lard concentrations as well as high sensitivity.

II. ACKNOWLEDGMENT

The work reported in this paper supported by the Universiti Putra Malaysia's Putra *Grant* - Putra Graduate Initiative (IPS) (Vote Number 9499000).

III. REFERENCES

[1] X. Zhou, Y. Zhang, C. Wang, X. Wu, Y. Yang, B. Zheng, H. Wu, S. Guo and J. Zhang, Photo-Fenton Reaction of Graphene Oxide: A New Strategy to Prepare Graphene Quantum Dots for DNA Cleavage, **ACS Nano**, 6, 6592–6599, 2012.

[2] L.A. Ponomarenko, F. Schedin, M.I. Katsnelson, R. Yang, E.W. Hill, K. S. Novoselov, et al., Choatic Dirac billiard in graphene quantum dots, **Science** 320, 356-358, 2008.

[3] K. Bonne and W. Verbeke, Muslim consumer trust in halal meat status and control in Belgium. **Meat Science**, 79, 255-260, 2008.

[4] A. Rohman and Y.B. Che Man, FTIR spectroscopy combined with chemometrics for analysis of lard in the mixtures with body fats of lamb, cow, and chicken. **International Food Research Journal** 17: 519 – 527, 2010.

[5] Y.B. Che Man and A.Q. Sazili, "Food production from the halal perspective. In: Isabel Guerrerov Legarreta and Y.H. Hui (Ed.), **Handbook of Poultry Science and Technology**, 1, 183 -215, 2010.

[6] S. Abdul Rashid, S. Mohd Zobir, S. Krishnan et al., **J Nanopart Res** 17: 225. DOI:10.1007/s11051-015-3040-3, 2015.

Please choose: Oral/ Poster/ Either
Presentation session:
Presenter name: Dr Mohamad Aizat bin Abas

[EFFECTIVENESS OF VARIABLE STENT DESIGNS FOR TREATMENT OF RENAL ARTERY ANEURYSM]

Abas, Mohamad Aizat[1], Muhammad Haziq, Abu Bakar[1], Norizham, Abdul Razak[2], Mohd Zulkifly, Abdullah[2]

[1]School of Mechanical Engineering, University Sains Malaysia, 14300 Nibong Tebal, Penang, Malaysia
[2]School of Aerospace Engineering, University Sains Malaysia, 14300 Nibong Tebal, Penang, Malaysia

Corresponding author email: aizatabas@usm.my

Keywords: RAA; FSI; stent; flow modulator

Introduction

The rising trend of aneurysm patients should gain more attention not just from the medical sector but also from the engineering sector especially in the design of stent and devices that can improve blood flow in aneurysm bulge. An aneurysm is a balloon-like bulge in an artery due to blood being pushed against the weakened or burned walls. If not controlled, aneurysm artery will rupture causing dangerous internal bleeding within the body. There are many sorts of aneurysm, for instance intracranial aneurysm, abdominal aortic aneurysm and renal artery aneurysm. The bulging in aneurysm can then be classified into saccular, fusiform and pseudo-aneurysm.

Of all the listed aneurysm types, Renal Artery Aneurysm (RAA) is by far the least aneurysm type being researched due to its minimal occurrences. However, RAA occurrence have increased in number and can be harmful especially for pregnant women. Symptomatic RAAs can cause hypertension, pain and renal infection. Asymptomatic RAAs could appear benign, however the potential for rupture and fistulation will increase with size. Asymptomatic patients are often referred for elective repair but if patients are symptomatic, additional investigation with possible surgical intervention is required. Though surgical clipping is the popular choice, it can lead to harmful effect of Subarachnoid Hemorrhage (SAH) after surgery. Additionally, other treatment method like Endovascular coiling or Coil embolization is difficult for wide neck aneurysm. Therefore, a mesh stent that can improve the flow of blood in the bifurcation aneurysm region can be employed to reduce the risk of rupture of the aneurysm.

A stent design based on Abbott RX Herculink and a flow modulator (FD) with 65% porosity level are simulated and compared with RAA model alone to monitor the effectiveness of different design of stent in improving the hemodynamic of the blood. Fluid-structure interaction (FSI) simulations are performed in this study using coupling of finite volume method (FVM) and finite element method coupling solver. A 3-D model of RAA, stent and FD are drawn using SolidWorks 2017 are as shown in Fig. 1.

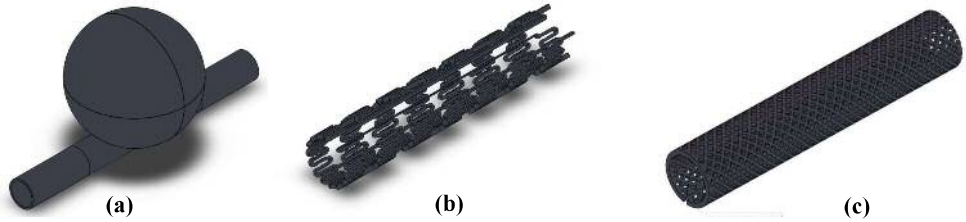

Figure 1. (a) RAA model; (b) Abbott RX Herculink stent; (c) FD 65% porosity

Result and Discussion

1. Flow patterns

The blood flow inside the aneurysm sac reduces due to the presence of stent and FD managed to obstruct the blood from entering and circulating inside the aneurysm. The velocity reduced to about 26% when stent is placed and about 60% further reduction when FD is implemented. This will reduce the potential of rupture and promotes thrombosis formation inside the aneurysm. Figure 2 shows the velocity streamlines for all cases of RAA, RAA with stent and RAA with flow modulator.

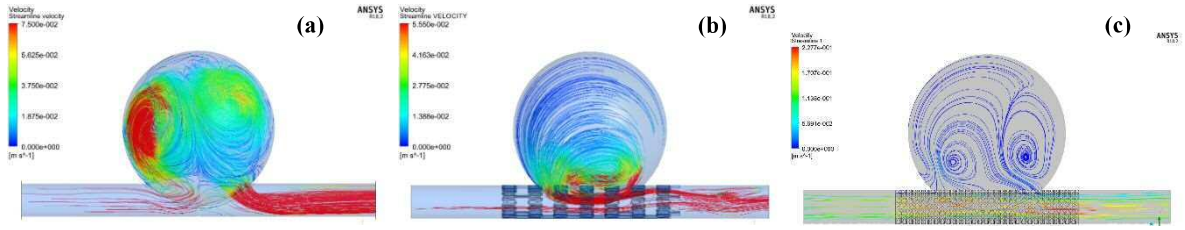

Figure 2. velocity streamlines for: (a) RAA; (b) RAA with stent; (c) RAA with flow modulator

2. Wall shear stress (WSS) of aneurysm

The WSS distribution at the aneurysm wall reduces significantly for the case of stent and FD installed inside the RAA model as depicted in Fig.3. An approximation of 66% and 84% reductions are recorded for the stent and FD respectively. This proved the capability of stent and FD to reduce the risk of rupture of the aneurysm.

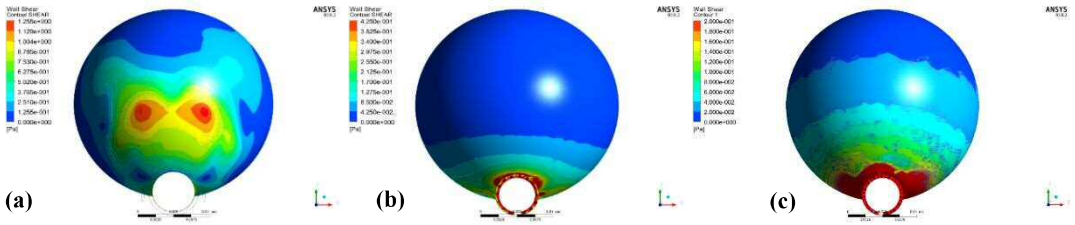

Figure 3. Maximum WSS at aneurysm wall for: (a) RAA; (b) RAA with stent; (c) RAA with flow modulator

3. Total deformation

The presence of stent and FD managed to alter the total deformation distributions in the RAA model as shown in Fig.4. The percentage reduction is around 78% for stent placement and 31% for FD placement. The placement of stent and FD provides a strong support to the RAA and prevented it from excessive buckling.

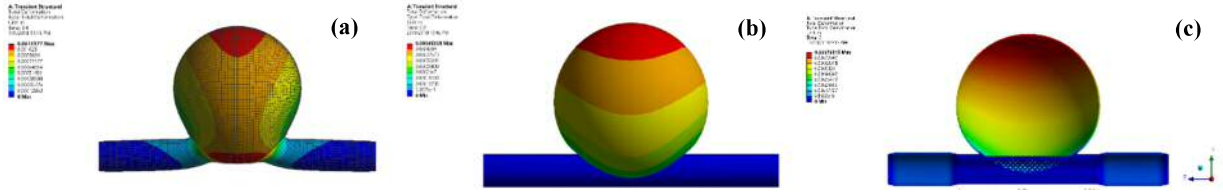

Figure 4. maximum total deformation for: (a) RAA; (b) RAA with stent; (c) RAA with flow modulator

Conclusion

The presence of stent and FD have beneficial effects on the RAA model simulated. In addition, the stent design plays a great role in the hemodynamic of blood thus reducing the risk of rupture in aneurysm.

Please choose: Oral/ Poster/ Either
Presentation session: Applied Engineering
Presenter name: Yingming YI

Development of Novel Hybrid Method Combining FDM with DPD to Simulate Concentration Distribution of Platelet in Thrombus Formation

Yingming, YI[1], Masaaki, TAMAGAWA[1]

[1]Graduate School of Life Science and Systems Engineering, Kyushu Institute of Technology, 2-4 Hibikino, Wakamatsu-ku, Kitakyushu-shi, Fukuoka, 808-0196, Japan

Email: yi-yingming@edu.life.kyutech.ac.jp

Keywords
Thrombus, Hybrid method, FDM, DPD, Concentration distribution

1 Introduction

White thrombus always occurs in artificial hearts. So the investigation of white thrombus is an important issue. Concentration transport of blood species has been simulated by finite difference method (FDM)(1). And platelet aggregation and separation have also been simulated by dissipative particle dynamics (DPD)(2). The demerit of FDM is that concentration modification caused by platelet aggregation and separation can't be simulated. The demerit of DPD is that the chemical reactions between blood species can't be simulated. In this paper, a hybrid method combining FDM with DPD is proposed to overcome the demerits of FDM and DPD. And by the hybrid method, concentration transport, platelet aggregation and separation can be simulated.

2 Computational method

2.1 Governing equation of FDM

Concentration transport with consideration of chemical reactions was simulated by convection and diffusion equations. And the equation used to simulate the transport of activated platelet (AP) is;

$$\frac{\partial [AP]_{\mathrm{FDM}}}{\partial t} + \mathbf{div}(\boldsymbol{u}\ [AP]_{\mathrm{FDM}}) = \mathbf{div}(D_{\mathrm{AP}}\ \mathbf{grad}[AP]_{\mathrm{FDM}}) + k_{\mathrm{pa}}\ [RP]_{\mathrm{FDM}}, \quad (1)$$

where $[AP]_{\mathrm{FDM}}$ is the concentration of activated platelet, $[RP]_{\mathrm{FDM}}$ is the concentration of unactivated platelet, D_{AP} is the diffusivity of AP, k_{pa} is the reaction rate of activation of unactivated platelets.

2.2 Governing equations of DPD

DPD is a method which can simulate the motion, aggregation and separation of particles(2). The governing equation of DPD method is Newton's law of motion. In this investigation, particle means AP. The discretized numerical equations are;

$$\Delta \boldsymbol{X}_i = \boldsymbol{V}_i \Delta t + \frac{1}{2}\frac{\boldsymbol{F}_i}{m}\Delta t^2, \quad (2)$$

$$\boldsymbol{F}_i = -\frac{4}{3}\pi a^3(\rho_{\mathrm{P}} - \rho)\frac{\mathrm{d}\boldsymbol{V}_i}{\mathrm{d}t} + \boldsymbol{F}_{\mathrm{inter}}, \quad (3)$$

where $\Delta \boldsymbol{X}_i$ is the displacement of ith AP, $\boldsymbol{V}_{\mathrm{i}}$ is velocity vector of ith AP, $\boldsymbol{F}_{\mathrm{i}}$ is the force exerted on ith AP, m is mass of single AP, Δt is time step, a is platelet radius, $\boldsymbol{F}_{\mathrm{inter}}$ is the interaction force between ith AP with other AP. The interaction force term includes a repulsive portion when the platelet has come within a specific distance of another platelet or wall surface. There is also an attractive force, when the distance is larger. If the distance is outside of the effective force region, the

force is zero.

2.3 Governing equations of hybrid method

The concept of the hybrid method is that particles in DPD represent for a certain number of AP $N_{AP,i}$ in FDM. The computation region is divided according to the particles. So every particle has its own region. $N_{AP,i}$ is equal to the integration of AP concentration in the area of ith region. Then $N_{AP,i}$ is reversed to concentration modification of AP $[AP]_{\mathrm{DPD}}$. In the computation of $[AP]_{\mathrm{DPD}}$, the first step is the computation of $N_{AP,i}$ multiplying distribution function at the ith particle position after aggregation and separation and before aggregation and separation. The second step is the computation of the difference between the results at first step after aggregation and separation with the results before aggregation and separation. The $[AP]_{\mathrm{DPD}}$ is the sum up of the difference of all particles. Then AP concentration by hybrid method $[AP]_{\mathrm{H}}$ is;

$$[AP]_{\mathrm{H}} = [AP]_{\mathrm{FDM}} + [AP]_{\mathrm{DPD}}. \quad (4)$$

3 Results and Conclusions

3.1 Results of concentration modification by hybrid method

By DPD, particle aggregation and separation occur during particle motion. If particle aggregation occurs, particles get closer; if particle separation occurs, particles get farer. According to the hybrid method, AP moves from the place before aggregation and separation to the place after aggregation and separation. It means that AP concentration increases at the place of platelet aggregation, and AP concentration decreases at the place of platelet separation. It is thought that the hybrid method we propose can simulate the concentration modification when platelets aggregate and separate.

3.2 Conclusions

In this paper, the hybrid method is used to simulate platelet aggregation and separation in thrombus formation. And the hybrid method can also be used to other cases of particle aggregation and separation. Mixing or dispersion enhancement under the effect of turbulence; condensation, coalescence and precipitation in the formation of droplets; and the clustering of dust particles in planet formation are the examples of particle aggregation and separation. And the local high and low particle concentration is caused by particle aggregation and separation.

References

(1) Yi, Y, Tamagawa, M, and Shi, W, "Prediction of Thrombus Formation on the Wall by High Shear Rate on Couette and Orifice Flows", *Journal of Medical Imaging and Health Informatics*, Vol. 7, No. 1 (2017), pp. 79-84.

(2) Yi, Y, and Tamagawa, M., "Simulation of Platelet Aggregation on Orifice Flows by Dissipative Particle Dynamics", *ICIC Express Letters, Part B: Applications*, Vol. 9, No. 7 (2018), pp. 665-672.

Please choose: Either
Presentation session: Applied Engineering
Presenter name: Daiki Masumoto

In-plane thermal diffusivity measurement of Polyimide thin film using periodic heating technique

[Daiki, Masumoto][1],[Koji, Miyazaki][1], [Tomohide, Yabuki][1], [Shrikant, Saini][1]

[1]Faculty of Engineering, Kyushu Institute of Technology, 1-1 Sensui-cho, Tobata-ku, Kitakyushu-shi, Fukuoka, 804-8550, Japan

Email: [o104113d@mail.kyutech.jpl]

Keywords (5 words)
In-plane thermal diffusivity, Periodic heating, Infrared laser, Phase difference, Polyimide,

[Introduction]

It is well known that the thermal properties of thin film and bulk are different, due to the effects of microstructures and interfaces. Thermal conductivity or diffusivity of thin films can be measured by several techniques. However, not many techniques are developed for in-plane thermal conductivity measurement. In-plane thermal conductivity is important as some of the materials have anisotropic properties. In this study, we report the in-plane thermal diffusivity of polyimide thin film using a periodic heating technique.

[Experiment]

Periodic heating method is based on the AC calorimetric method developed by Hatta et al[1]. The schematic of the technique is shown in Fig 1. In this technique, a thermocouple was deposited on the polyimide film to measure the thermal response by periodic heating. A mechanically chopped laser beam was used to heat the sample. We changed the distance between the laser beam spot and thermocouple to generate thermal response delay. The temperature rise of the sample can be expressed as[2].

$$T(x) = \left[Q / 4\pi f\rho ch\right]\exp\left[-mx - i(mx + \frac{\pi}{2})\right] \quad \textbf{(1)}$$

where m is $(\pi f/\alpha)^{2}$, here α is the thermal diffusivity of the film along the in-plane direction, c is the specific heat, f is the modulation frequency, h is the film thickness, Q is the absorbed heat flux, and ρ is the density of the film.

The amplitude of the temperature signal (T) as the function of distance (L) (in between laser spot and thermocouple) is indicated below.

$$\ln T(L) = \ln\left(\frac{Q}{4\pi f\rho ch}\right) - mh \quad \textbf{(2)}$$

The thermal diffusivity of the film can be derived from the slope of $\ln T(L)$ *vs* L plot. The relation between the phase difference (φ) and distance (L) can be written as.

$$\varphi(L) = -mL - \frac{\pi}{2} \quad \textbf{(3)}$$

By solving these equations, we can write thermal diffusivity as.

$$\alpha = \frac{\pi f}{\left(d\varphi/dL\right)^2} \qquad \textbf{(4)}$$

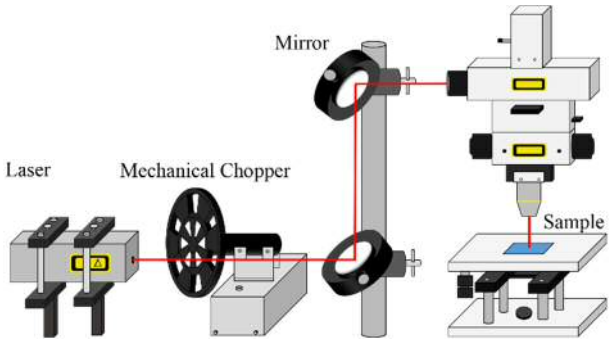

Fig. 1 Schematic of periodic heating method for in-plane thermal diffusivity

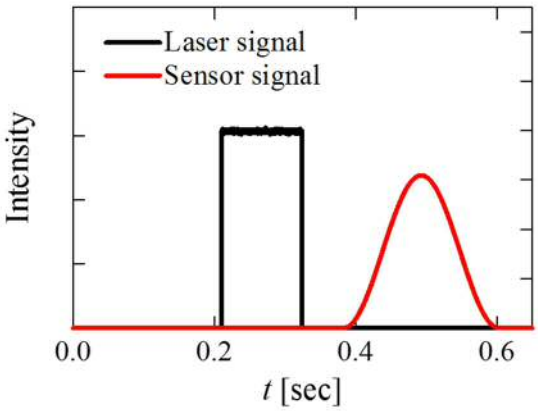

Fig. 2 Phase difference between Laser signal and Sensor signal

[Result and Discussion]

We plotted the phase difference vs distance (Fig 3). The value of in-plane thermal diffusivity of polyimide thin film is about α=1.1 × $10^{-7}$$m^2$/s from this technique. The reported value of thermal diffusivity of polyimide thin film is about α= 0.85 × $10^{-7}$$m^2$/s [3] which is close to our observed value. The detail description and analysis will be shown in the presentation.

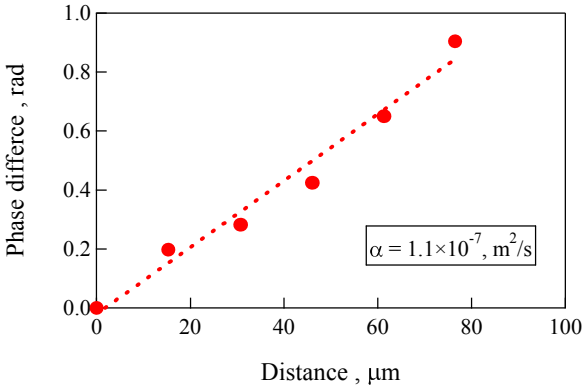

Fig. 3 The phase difference vs distance plot for in-plane thermal diffusivity

References:

[1] I. Hatta, *Int. J.Thermophys.*, **11**(2), 293, (1990).
[2]Chen, G., Tien, *et al.J. Heat Trans.*, **116**, 325, (1994).
[3]K. Kurabayashi,et al, *thin solid film,***339**, 160 (1999)

Please choose: (Oral) Poster/ Either
Presentation session: Applied Engineering
Presenter name: Shoji YAMAGUCHI

Visualization of thrombus formation on shear flows in Paravalvular leak model

Shoji YAMAGUCHI[1] and Masaaki TAMAGAWA[1]

[1]Graduate School of Life Science and Systems Engineering, Kyushu Institute of Technology, 2-4 Hibikino, Wakamatsu-ku, Kitakyushu 808-0196, Japan

Email: yamaguchi.shoji327@mail.kyutech.jp

Keywords
Thrombus formation, Optical visualization, TAVI, PVL

1. Introduction

In recent years, TAVI (Transcatheter Aortic Valve Implantation) in which the artificial valve is located by catheters is popular method for treating aortic stenosis. Compared with conventional aortic valve replacement, TAVI is minimally invasive treatment for patients. But there is a specific trouble called PVL (Paravalvular Leaks) in TAVI. PVL is blood leaks from the gap between artificial valve and aorta, and it is considered to be one of risks of thrombosis [1]. However, flow field and mechanism of thrombus formation around the PVL are not elucidated yet. In our previous studies, thrombus formation in orifice flow was quantified [2], and flow field using model of artificial valve was also analyzed by PIV (Particle Image Velocimetry) [3]. In this paper, thrombus formation around the PVL model is visualized. In addition, the effect of the gap size on thrombus formation is investigated.

2. Experiment

In this experiment, thrombus is generated in the flow circuit and thrombus formation is observed by using optical systems. The flow circuit is composed the roller pump, thermostat bath and test section part. The test section part is an acrylic straight pipe. The length and diameter is 140 [mm] and 20 [mm] respectively. And the PVL model is attached in this part. The PVL model have an orifice and a gap. The orifice diameter is 7.25 [mm] and the gap h in the radial direction is 0.5 [mm] or 1.0 [mm]. To observe thrombus formation in the acrylic straight pipe, plasma, which is extracted from the fresh blood of pig, is filled in the flow circuit. With increasing of the flow rate, thrombus is occurred around the PVL model. Flow rate of the circuit Q is 5.0 [ℓ/min] and temperature T at inlet is 31 [°C]. By using the laser sheet, only plane on the axis is illuminated. Then thrombus formation can be observed around the PVL. This thrombus formation is recorded by the high speed camera.

In order to visualize thrombus formation, a recorded image is normalized by the difference between brightness of the initial image and the target image. Regarding as thrombus formation rate, the area above threshold of brightness is defined as the thrombus area S. From the history of the thrombus area S, the maximum gradient during thrombus formation is defined as the thrombus formation rate R_s, and the time from start to initial thrombus formation is defined as the thrombus formation time τ_s [s]. Effects of the gap size on the thrombus formation are examined by R_s and τ_s.

3. Result and Discussion

3･1 Visualization of initial thrombus formation

From the results of the visualization of initial thrombus formation, in case of the gap h is 1.0 [mm], it was found thrombus formation is clearly observed around the gap, but not clearly in case of the gap h is 0.5 [mm]. It was suggested that the thrombus formation is affected by the flow field around the gap.

3･2 Effects of the gap size on the thrombus formation

In the previous sub-section, initial thrombus is expected to occur on the wall surface around the PVL model. The analysis region treated by taking thickness (1.0 [mm]) times length (40 [mm]) on the pipe wall and length (5.0 [mm]) behind the PVL. As a result, thrombus formation rate R_s is 0.0028 in case of h= 0.5 [mm] with n *(sample number)* = 6, and R_s is 0.0057 in case of h= 1.0 [mm] with n= 10. This suggests that thrombus is

generated earlier in the large gap. Regarding as the thrombus formation time, τ_s is 552 [s] in case of h= 0.5 [mm] with n= 6, and τ_s is 431 [s] in case of h= 1.0 [mm] with n= 10. This suggests that thrombus formation start earlier if the gap is large. From these results, it was found that effects of the gap size on the thrombus formation rate and thrombus formation time are large.

4. Conclusion

In this study, thrombus formation in the PVL model was visualized, and it was found that initial thrombus is generated around the gap. It was also found that the thrombus formation rate is high and the thrombus formation time is small if the gap is large.

References

[1] Dimitry Schewel, Christian Frerker, Jury Schwel, Peter Wohlmuch, Felix Meincke, Thomas Thielsen, Felix Kreidel, Karl-Heinz Kuck, Ulrich Schafer, Catheterization and Cardiovascular Interventions 85:502-514, 2015

[2] Ryosuke Motooka, Masaaki Tamagawa, Proc. of JSME Bioengineering Conference, 2C07, 2013

[3] Yuji Sanjo, Masakki Tamagawa, Proc. of 2017 Annual Meeting of JSME, MECJ-17, J0210102, 2017

Please choose: Oral
Presentation session: Applied Engineering
Presenter name: Taisei Hidaka

Stability Analysis of Wnt-ERK signal transduction system by Nyquist stability criterion

Taisei,Hidaka, Takashi Nakakuki

[1]Kyushu institute of Technology, 680-4 Kawazu, Iizuka, Fukuoka 820-8502, Japan

Email: hidaka.taisei875@mail.kyutech.jp
nakakuki@ces.kyutech.ac.jp

Keywords (5 words)
Systems biology , Signal transduction, Feedback systems, Stability analysis, Nyquist Criterion

[Introduction]

System biology is discipline to understand behavior by constructing mathematical models for complex biochemical reaction systems. This field is indispensable in the today's advanced medical development.

However, it is difficult to analyze the biological system because it is a high-dimensional nonlinear system, and in addition contains some complicated feedback regulations, and cross-talk regulations.

In this study, we apply the Nyquist stability discrimination method to a practical model of a cancer cell signaling, a Wnt-ERK model [1] as an example case. By calculating the gain margin and the phase margin with the Nyquist stability discrimination method, we discuss about the relation between stability property of the whole system and six main feedback loops.

[Analysis target and analysis method]

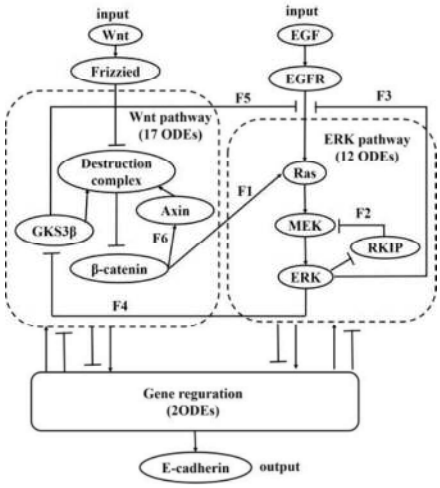

Fig.1 Wnt-ERK pathway

First, we explain the Wnt-ERK routes used in this study The Wnt-ERK pathway is a system in which Wnt and EGF are input and E-cadherin related to the expression of cancer cells is output. This system is divided into three parts as shown in Fig. 1, and it is indicated by a total of 31-dimensional differential equations. Furthermore, this system includes six feedback loops, and there are feedback loops in which both Wnt and ERK paths are involved. Such a phenomenon is called crosstalk.

In addition, the feedback in the biochemical reaction system is impossible to construct the subtractor, and deviation cannot be taken. For this reason, feedback is performed by a reaction called an inhibition reaction. This is called subtraction type feedback. Thus, the Wnt-ERK pathway has several characteristic points in the biochemical reaction system, and we thought that analysis can be performed on other multidimensional biochemical reaction systems by establishing analysis method of this system, It was set as the analysis target.

So, in order to apply the control theory, linear transformation using Taylor expansion is used for the nonlinear differential equation of Wnt - ERK pathway. Please see the reference[2] for details. The nonlinear differential equation in Fig.2 is expressed by Equation (1).

$$\begin{cases} \dot{x}_1 = f_1(x) + g(x_n, \bar{x}) \\ \dot{x}_2 = f_2(x) \\ \quad\vdots \\ \dot{x}_n = f_n(x) \end{cases} \tag{1}$$

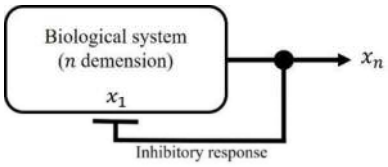

Fig.2 Example model

x_1 adjusts the output of x_n by feedback. $x \in \mathbb{R}$ is state vector. $\bar{x} = [x_1, x_2 \cdots, x_{n-1}]^T \in \mathbb{R}^{n-1}$ is a vector excluding the feedback element x_n. f is Known nonlinear function. g is nonlinear function showing feedback element. Linear transformation yields the equation (2).

$$\begin{cases} \dot{\xi} = A_o(x^*, u^*)\xi + g_o(\bar{x}^*)b\eta \\ y = \gamma(x^*)c\xi \end{cases} \quad (2)$$

$\eta \in \mathbb{R}$ is a virtual input. y $\in \mathbb{R}$ is the output. $\xi \in \mathbb{R}$ is the redefinition state vector: $\xi = x - x^*$. x^* is function point. For more information, please refer to References[2] .
Correspondence with the state space representation was taken for the expression that underwent linear transformation in this way. I converted that expression into a transfer function and analyzed by program.

[Results and Discussions]
1)comparison of gain margin
The gain margin when the gain margin is the smallest in each loop is compared. The results are shown in Table.1.

Table.1 Comparison of gain margin

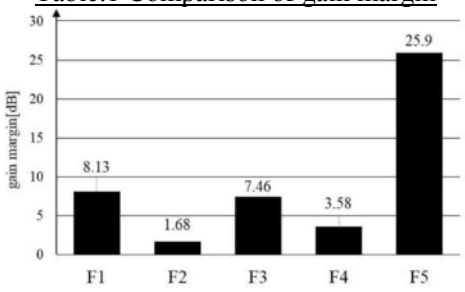

The gain margin of F5 is very large. Therefore, it is excluded from Table 1. F5 have a larger gain margin than other loops. F1, F2, F4andF5 starts from the second quadrant and is the direction of rotation going toward the fourth quadrant through the first quadrant. Among them, F5 has a particularly large gain margin.

2) Changes in the complexity of a Nyquist diagram by the input
Next, the result of F4 is shown in Fig.3. The arrow indicates the direction of rotation. F4 has a Nyquist diagram crossing when Wnt and EGF are 1. This is very different from the shape of the Nyquist diagram when both Wnt and EGF are zero.
This phenomenon suggests that the changing shape of the trajectory due to the variation of the input value in the biochemical reaction system.

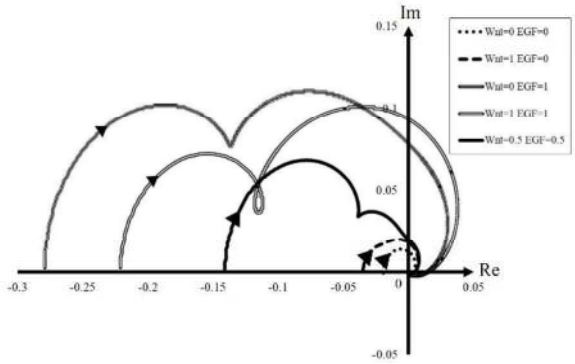

Fig.3 Result F4

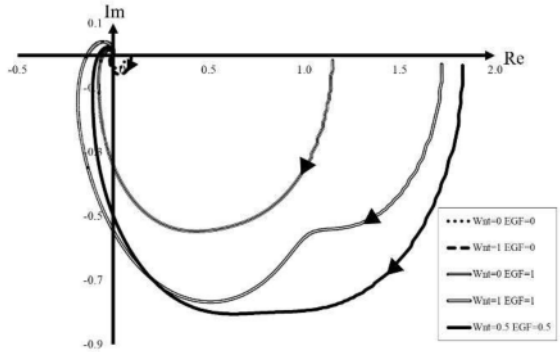

Fig.4 Result F3

3) An implication of phase margins
The result of F3 is shown in Fig.4. The arrow indicates the direction of rotation. Characteristic phenomena were seen in F3. Other loops have an infinite phase margin, but depending on the input value the phase margin of F3 may not be infinite. Also, if Wnt and EGF compare both 1 and 0.5, the phase margin will be smaller for 0.5. Therefore, simply decreasing the input value can't increase the phase margin. However, the gain margin is small when Wnt and EGF are 1. Therefore, from the viewpoint of phase margin, Wnt and EGF are more unstable with 0.5, and from the viewpoint of gain margin, it can be said that Wnt and EGF are 1 more unstable. We will further examine this difficult F3.

[1] Sung-Young Shin et al ”Functional Roles of Multiple Feedback Loops in ERK and Wnt Signaling Pathways that Regulate Epithelial-MesenchymalTransition”,
Cancer Res,2010,70(17),pp.6715-6724.
[2] T. Nakakuki, A Stability Analysis Method for Biochemical Reaction System with Inhibitory Feedback Loop, IEEJ Transactions on Electronics, Information and Systems, 136(5), 617-624, 2016.

Please choose: Oral/ Poster/ Either
Presentation session:
Presenter name: Hiroyuki, Tsurumaru

[Interfacial creep simulation for shrink-fitted bimetallic work roll]

[Hiromasa, Sakai][1], [Hiroyuki, Tsurumaru][1], [Rahimah Binti, Abdul Rafar][1], [Nao-Aki, Noda][1], [Yoshikazu, Sano][1], [Yasushi, Takase][1]

[1]Department of Mechanical and control, Kyushu Institute of Technology, 1-1 Sensui-cho, Tobata-ku, Kitakyushu-shi, Fukuoka, 804-8550, Japan

Email: [noda@mech.kyutech.ac.jp]

Keywords Shrink-fitting, Roll, Shaft, Sleeve, Interfacial creep

[Introduction]

The bimetallic roll is used at the roughing stands of hot rolling stand mills as shown in Figure 1. The bimetallic roll is usually manufactured by using centrifugal casting method. However, so-called assembled rolls are sometimes used for large diameter roll having more than 1000mm and H-shaped steel rolling rolls by connecting a hollow sleeve and shafts due to shrink-fitting. Although the wear and surface roughness soon appear on the roll body, the shaft can be reused in this assembled structure. Furthermore, it is easy to provide high wear resistance property to the sleeve. However, the shrink-fitted structure has some inherent problems such as roll residual bending deformation, shaft breakage due to fretting cracks and interfacial creep. This creep often causes damage to the roll, although few studies are available. Therefore, in this study, the interfacial creep phenomenon will be realized by finite element method simulation.

[FEM Modelling to Realize the Interfacial Creep in Work Roll]

Figure 2 shows 2D FEM model where the sleeve is elastic and the shaft is rigid. Here, the sleeve and shaft are fixed and the concentrated load P and distributed load p are rotated. (N-A. Noda, D. Suryadi, S. Kumasaki, Y. Sano, Y. Takase: Engineering Failure Analysis, 57(2015), 219-235) to simulate the rotation of the work roll. In this FEM analysis, a tetrahedron primary element with plane strain is used and the number of elements is 46080. MSC marc/ mentat 2012 with full Newton-Raphson iterative spare solver of multifrontal method is

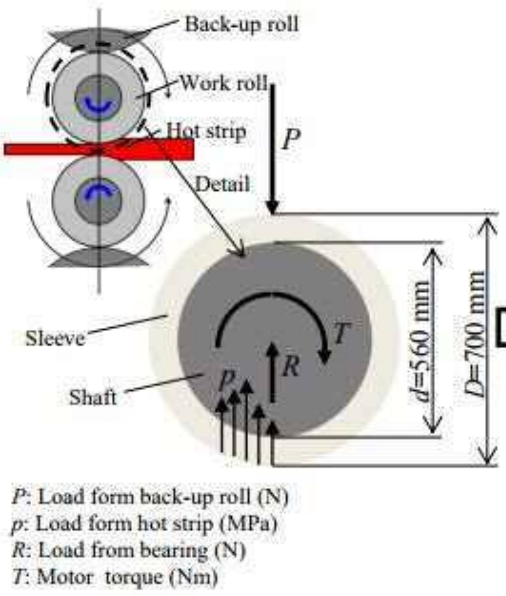

Figure 1 Real rolling roll diameter and Load

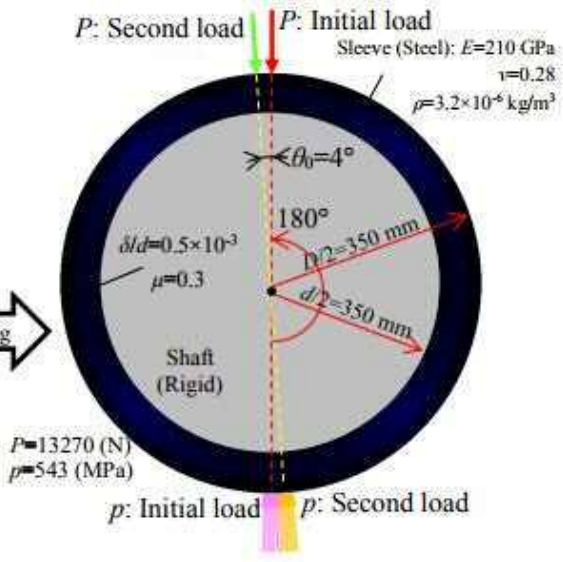

Figure 2 2D FEM model and boundary conditions.

used for the static structure analysis and the rotation speed of the work roll is not considered. Define the shrink fitting ratio as δ/d, where δ is the diameter difference with the diameter d. In this analysis, we used δ/d=0.5 × 10-3. Assume that the roll is subjected to concentrated load P=13700 N/mm and distributed load p=543 MPa/mm at outer surface of the sleeve as shown in Figure 1.

[Results and Discussion]

Figure 3 shows the circumferential relative displacement along the interface of the sleeve and the shaft due to the static loading in the vertical direction. It is seen that the average interfacial displacements =0 in Fig.3. Figure 4 shows the accumulation of the relative interfacial displacement. Due to the load rotation, the relative displacement is accumulation and the average displacement increases.

Figure 5 shows the average interfacial displacements increases almost linearly by changing loading directions. The loading direction change contributes to the accumulation of the circumferential relative displacement and increase the average displacement. Figure 5 indicates that the interface creep phenomenon can be regarded as the accumulation of the circumferential relative displacement and once the rotate starts the interfacial creep occurres. The interface creep phenomenon was realized by the continuous quiz-static analysis by changing the loading direction in the 2D model. As this result, it was found that as soon as the load began to rotate, the interfacial creep occurred.

[Conclusion]

In this study, the interface creep between the sleeve and the shaft was realized by applying FEM analysis. The interfacial creep can be regarded as the accumulation of the circumferential relative displacement due to rotation force.

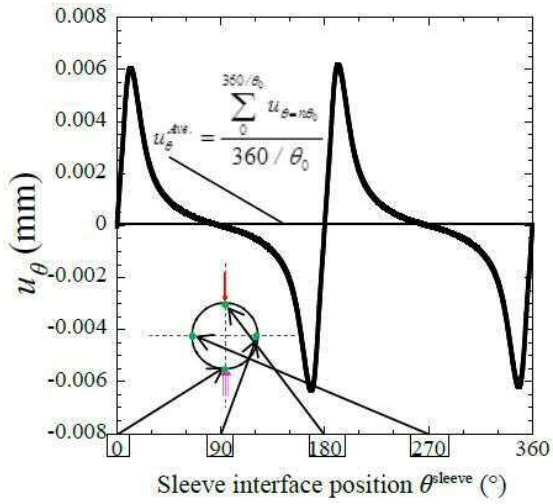

Figure 3 Displacement distribution of sleeve interface due to initial loads are

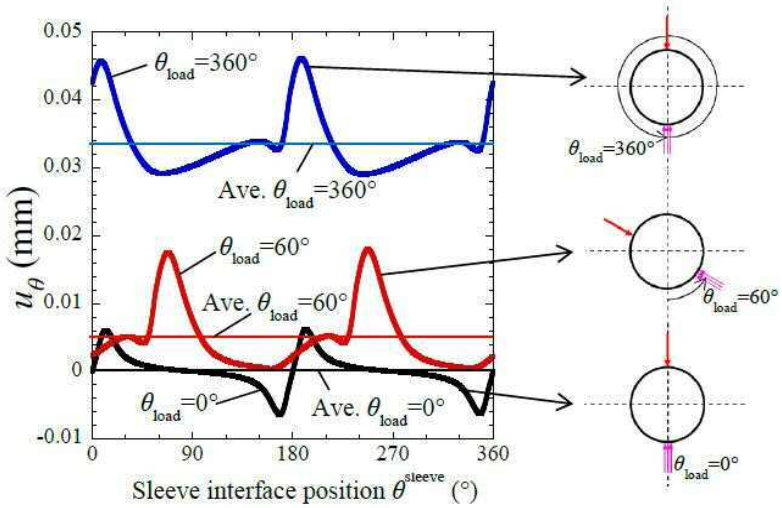

Figure 4 Displacement distribution of Sleeve interface when *P* and *p* are shifted.

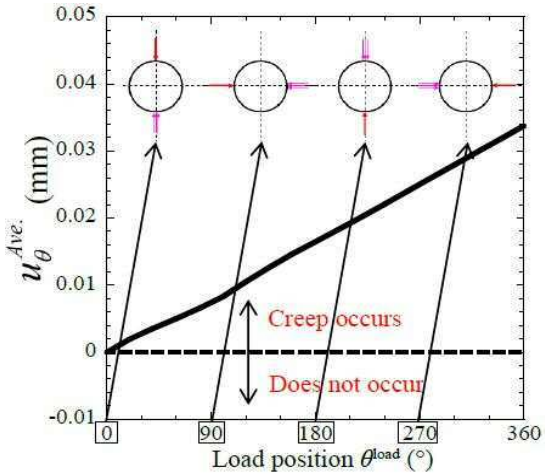

Figure 5 Average of displacement of Sleeve interface when *P* and *p* are shifted.

Please choose: (Oral) Poster/ Either
Presentation session: Applied Engineering
Presenter name: Kosuke Tateishi

[Proposal of Suitable Pitch Difference for Various Bolts-Nuts Diameter to Realize Anti-loosening Performance]

[Kosuke, Tateishi][1], [Shutaro, Kubo][1], [Xi, Liu][1], [Nao-Aki, Noda][1], [Yoshikazu, Sano][1], [Yasushi, Takase][1]

[1] Department of Mechanical and control, Kyushu Institute of Technology, 1-1 Sensui-cho Tobata-ku, Kitakyushu-shi, 804-8550, Japan
Email: [noda@mech.kyutech.ac.jp]

Keywords bolt-nut joint, pitch difference, anti-loosening performance, Fatigue Life, prevailing torque

[Introduction]

In a wide industrial field, bolt-nut joint is unitized as a machine element and is of great importance. However, the anti-loosening and anti-damage performances are always required. When vibration is added, the rotational loosening force on the spiral shape of the screw becomes larger than the friction between the screw surfaces, then the loosening occurs. Most previous studies have been mainly focusing on anti-loosening performance. Only a few studies contribute toward improving fatigue strength. To improve both the fatigue life and the performance of anti-loosening, a slight pitch difference between bolt and nut was previously proposed. Figure 1 shows a contact status between bolt and nut threads during the tightening process. Then, the anti-loosening performance was confirmed for M16 bolt-nut connection by using FEM simulation as well as experiment. However, other bolt-nut diameters have not been considered yet. Therefore, in this paper, the anti-loosening will be studied for different bolt-nut diameter to clarify the suitable pitch difference theoretically and experimentally.

[How to estimate suitable pitch difference]

Suitable pitch difference will be considered for various thread nominal diameters. In the following discussion, loosening force Fl and anti-loosening force Fa are assumed. Figure 2 shows the relationship between Fl and Fa. Loosening force Fl can be proportional as Eq. (1) since Fl should be proportional to the nut weight. On the

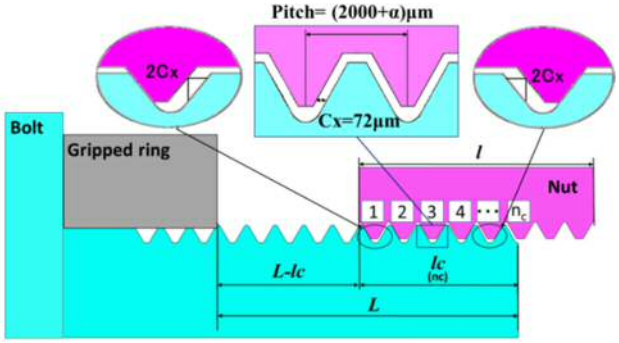

Figure 1. Schematic diagram of bolted joint

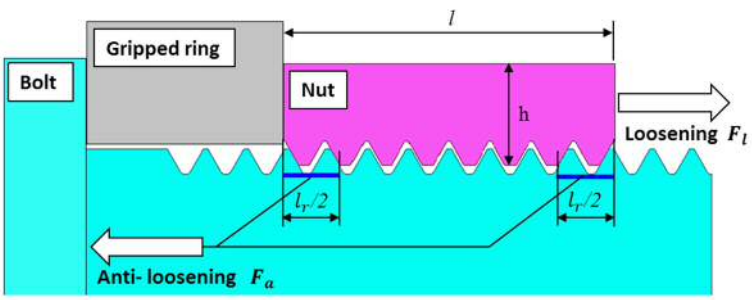

Figure 2. Relationship between loosening force F_l and anti-loosening force F_a

other hand, anti-loosening force Fa can be proportional as Eq. (2) since Fa should be contact surface area between the nut and bolt threads. Therefore, loosening condition can be expressed as Eq. (3) assuming loosening and anti-loosening forces should be balanced.

$$F_l \propto \gamma V \cong \gamma(\pi d)hl \tag{1}$$

$$F_a \propto \tau_s(\pi d)l_r \tag{2}$$

$$F_l = KF_a \tag{3}$$

Here, γ= specific gravity, V= the volume of nut, l= the length of nut, τ_s= average shear stress between the nut and bolt threads, l_r= the length of the nut threads in contact in Figure 2.
Therefore, we have

$$\gamma(\pi d)hl = K\tau_s(\pi d)l_r$$

$$K = \frac{\gamma hl}{\tau_s l_r} = \frac{\gamma}{\tau_s}K', \qquad K' = \frac{lh}{l_r} \tag{4}$$

Here, K and K' are proportional constants.
Since the values of the proportional constants K and K' are unknown, in this study, the loosening experimental results for M16 is used. From these conditions, Suitable pitch difference range can be expressed by the Eq. (5).

$$\frac{2.9764d + 82.478}{\mathrm{n}\left(1 - \frac{0.3099\mathrm{d} + 0.4253}{14.3}\right) - 1} < \alpha < \frac{2.9764d + 82.478}{\mathrm{n}\left(1 - \frac{0.3099\mathrm{d} + 0.4253}{11.4}\right) - 1} \tag{5}$$

[Result and Discussion]
Suitable pitch difference can be estimated by using Eq.(5). Table 1 shows suitable pitch difference obtained from Eq.(5) for M12~M16 bolt-nut connection. As an example, for M12 the suitable α can be expressed as $38.6\mu m < \alpha < 44.8\mu m$. By using Junker vibration test, we have confirmed that $\alpha = 40\mu m$ have no loosening Eq.(5) is valid. Therefore, the validity of Eq.(5) is confirmed for M12.

[Conclusion]
In the previous study, a suitable pitch difference between the bolt-nut was obtained as α=33μm for M16 JIS bolt-nut through loosening experiment and FEM simulation for tightening process. In this paper, suitable pitch difference was considered for other nominal thread diameters to realize anti-loosening performance. Suitable pitch difference was determined by assuming that loosening force should be balanced to the anti-loosening force. Then, the suitable pitch difference was expressed as approximate formula. By using Junker vibration test, we have confirmed that the proposed formula is valid for M12 since α=40μm have no loosening Eq. (5) is valid.

Table 1. Suitable pitch difference estimated for M12~M16

Diameter	Pitch p(mm)	Nut length l(mm)	Number of threads n	Nut thickness h(mm)	Clearance C_x(μm)	Suitable Pitch difference range α(μm)
M12	1.75	10	5.7	4.1	59.1	38.6<α<44.8
M14	2	11	5.5	4.8	62.1	46.5<α<56.4
M16	2	13	6.5	5.4	65.1	42.6<α<53.5
	2	16	8	5.4	65.1	32.6<α<40.4

Please choose: Oral/ Poster/ Either
Presentation session: Applied Engineering
Presenter name: Kenji Tsuboi

[Adhesive strength evaluation method focusing on the intensity of singular stress field distributions along interface for three-dimensional butt joint]

[Kenji Tsuboi[1]],[Nao-Aki Noda[1]] , [Rei Takaki[1]], [Fei Ren[1]], [Mohd Radzi Bin Aridi[1]], [Yoshikazu Sano[1]], [Yasushi Takase[1]] [Tatsyujiro Miyazaki[2]]

[1] Department of Mechanical Engineering, Kyushu Institute of Technology Sensui-Cho 1-1 Tobata-Ku, Kitakyushu-Shi, Fukuoka, Japan
[2]Department of Mechanical Engineering, University of the Ryukyus Azasenbaru 1, Nishihara-Cho, Nakagami-Gun, Okinawa, Japan

Email: [noda@mech.kyutech.ac.jp]

Keywords Intensity of singular stress field (ISSF), Adhesion, Interface, 3D butt joint

[Introduction]

Adhesive joints are extensively used in various manufacturing processes in different industrial sectors because of its high fatigue resistance. Different materials properties cause the singular stress field, whose intensity is depending on the adhesive joint geometry. Our previous studies show that debonding strength can be expressed as a constant value of the critical intensity of singular stress field (ISSF) by using two-dimensional butt joint models. By considering real specimen geometry, in this paper, the ISSFs on the interface outer edges of three-dimensional butt joints are analysed by varying the adhesive thicknesses.

[Three-dimensional mesh-independent technique to obtain ISSF]

The most popular ISSF is known as the stress intensity factor for cracks. To obtain more general ISSF for evaluating interface strength, several analytical techniques were applied One of the most used numerical modelling techniques is the finite element method, which can be used for many engineering applications conveniently .

By considering the real specimen geometry, in this study, 3D butt joint will be analysed. To apply the mesh-independent technique to 3D problem, a reference 3D solution is necessary. Therefore, 3D butt join is analysed under arbitrary material combinations.

The FEM stress values near the outer of interface sides are inaccurate since they are different depending on the mesh size. This is due to the singular stress field along the outer interface side. Focusing on the outer interface side from y=0 to y=W/2 (see table 1), the constant FEM stress decreases first and then increases rapidly when y is close to the outer interface corner. This is because another stronger singular stress field exists around the outer interface corner. In this paper, the ISSF distribution along the outer interface side in the three-dimensional joint will be focused.

Table 1 shows the FEM stress distribution along the outer interface side in three-dimensional butt joint for and . It is seen that the FEM stress and are inaccurate since they are different depending on the mesh size. However, the FEM stress ratio is very accurate since they are the same independent of the mesh size. Therefore, for example, by focusing on the middle point of the side, the ISSF ratio can be expressed as the FEM stress ratio as shown in equation (1).

$$\frac{K_\sigma^{3D}}{K_\sigma^{REF}}=\frac{F_\sigma^{3D}\sigma_z^\infty W^{1-\lambda}}{F_\sigma^{REF}\sigma_z^\infty W^{1-\lambda}}=\frac{\lim_{r\to 0}\left[r^{1-\lambda}\times\sigma_z^{3D,Real}(r)\right]}{\lim_{r\to 0}\left[r^{1-\lambda}\times\sigma_z^{REF,Real}(r)\right]}=\lim_{r\to 0}\left[\frac{r^{1-\lambda}\times\sigma_z^{3D,FEM}(r)}{r^{1-\lambda}\times\sigma_z^{REF,FEM}(r)}\right]=\frac{\sigma_z^{3D,FEM}(0)}{\sigma_z^{REF,FEM}(0)} \quad (1)$$

To discuss the ISSF distribution along the outer interface side, 3D butt joint is considered as the new reference solution in the next section under arbitrary material combination.

Table 1. FEM stress distributions for three-dimensional joint under tension obtained by different mesh sizes when E_1=210 GPa, ν_1=0.3, E_2=3.14 GPa and ν_2=0.37.

y	Smallest mesh size e_{min}=1/3200 around the edge			Smallest mesh size e_{min}=1/12800 around the edge		
	$\sigma^{3D}_{y,h/W=0.01}$	$\sigma^{3D}_{y,h/W\geq1}$	$\frac{\sigma^{3D,FEM}_{y,h/W=0.01}}{\sigma^{3D,\mathrm{FEM}}_{y,h/W\geq1}}$	$\sigma^{3D}_{y,h/W=0.01}$	$\sigma^{3D}_{y,h/W\geq1}$	$\frac{\sigma^{3D}_{y,h/W=0.01}}{\sigma^{3D}_{y,h/W\geq1}}$
0.000	3.282	13.006	0.252	4.941	19.540	0.253
0.053	3.282	12.991	0.253	4.939	19.513	0.253
0.105	3.283	12.978	0.253	4.939	19.498	0.253
0.158	3.284	12.956	0.253	4.941	19.471	0.254
0.211	3.285	12.931	0.254	4.942	19.418	0.255
0.263	3.287	12.908	0.255	4.945	19.390	0.255
0.316	3.290	12.900	0.255	4.950	19.382	0.255
0.368	3.294	12.944	0.254	4.957	19.444	0.255
0.421	3.303	13.129	0.252	4.970	19.718	0.252
0.447	3.311	13.374	0.248	4.982	20.082	0.248
0.474	3.302	13.933	0.237	4.968	20.931	0.237
0.500	4.483	31.002	0.145	7.538	52.086	0.145

Figure 1 shows the normalized critical ISSF distributions for various . The critical ISSF distributions are nearly the same for different adhesive thickness .

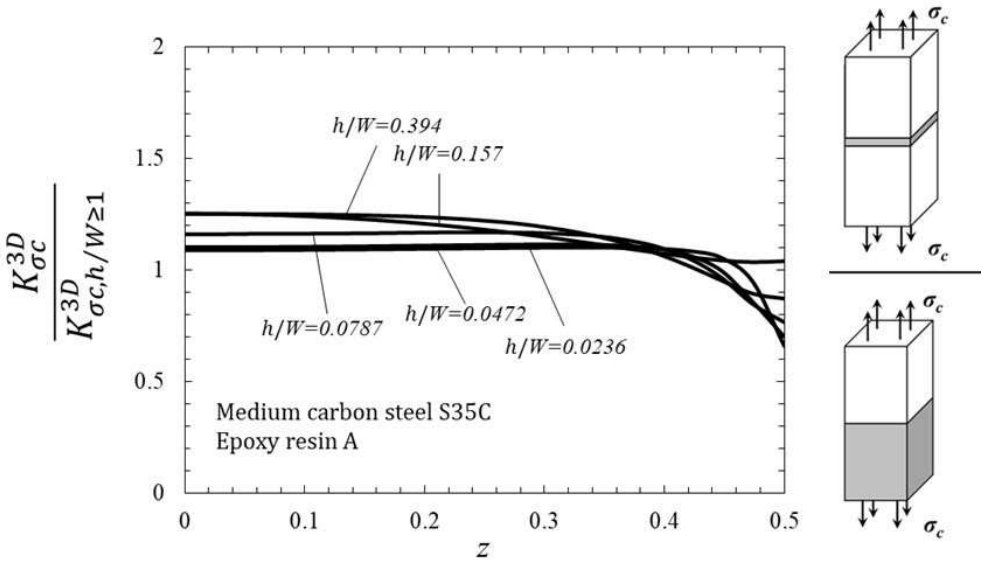

Figure 1. Critical ISSF distribution on the outer edge of the three-dimensional butt joint.

[Conclusion]

In this study, the three-dimensional butt joint has been analyzed in terms of the intensity of singular stress field. Without considering any defects and residual strain, the elastic and homogenous adhesive is assumed to evaluate the debonding strength. The FEM stress distributions of three-dimensional butt joint are obtained by using different mesh sizes. The results show that FEM stress ratio stay constant near the middle of the outer interface side independent of element size. It is found that the adhesive strength can be evaluated by the critical constant ISSF by focusing on the middle point on the outer interface side.

Please choose: Oral
Presentation session:
Presenter name: Guowei ZHANG

Generation Mechanism of Driving Out Force of the Shaft from the Shrink Fitted Ceramic Roll by Introducing Newly Designed Stopper

Guowei ZHANG[1], Nao-Aki NODA[1], Yoshikazu SANO[1] , Hiromasa SAKAI[1]

[1]Faculty of Engineering, University Putra Malaysia, 43400 UPM Serdang, Selangor, Malaysia
[1]Dept. of Mechanical and Control Engineering, Kyushu Institute of Technology, Sensui-cho 1-1
Tobata-ku Kitakyushu-shi Fukuoka 804-8550
Email: mouedi@163.com

Keywords : shrink fitting; ceramic roller; driving out; stopper; residual displacement

Introduction

Figure 1 shows new ceramic roller consisting of the steel shaft connected at both ends and the ceramic sleeve having high heat resistance, high wear resistance and high corrosion resistance. Previous studies indicated that the shrink fitting system may be the most suitable joining method for ceramic cylindrical structures to reduce maintenance time and cost for shaft replacement. However, since most of the ceramics are quite brittle, only a small shrink fitting ratio can be used. During operation, the coming out of the shaft may happen, and therefore, we have to prepare for this new failure.

As a further development of those previous studies, this study will focus on a stopper newly installed on the sleeve to evaluate the driving out force generated on the shaft. In the first place, a two-dimensional model will be improved to prevent the coming out. To design the stopper, the contact force will be investigated between the stopper and the inner plate. Note that this contact force can be regarded as the driving out force generated on the shaft. The discussion shown in this paper is therefore useful for understanding the coming out mechanism as well as the practical aspect of the coming out prevention.

[Experiment]
FEM simulation.
[Result and Discussion]

(1) Shear forces are generated along the upside and downside at the fitting portions of the inner plate to balance the alternate bending load. The inner plate comes out gradually when the shear forces in the coming out direction exceeds the shear force in the opposite direction.

(2) When the alternate loading is applied under the condition of (1), the inner plate and the stopper come into contact with each other. The contact force generated on the stopper can be regarded as the driving out force.

(3) In order to clarify the coming out phenomenon and generation mechanism, no-load interval was introduced into the alternate bending loading cycle. As a result, it was found that the residual displacement appears during the no-loading interval. The coming out process can be explained by the accumulation of this residual displacement.

(4) The driving out force can be generated by the shrink fitting force, the friction force, and the bending load as shown in Fig. 10.

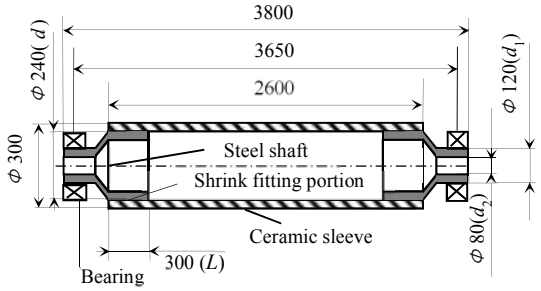

Fig.1. Structure and dimensions of a real ceramic roller (mm)

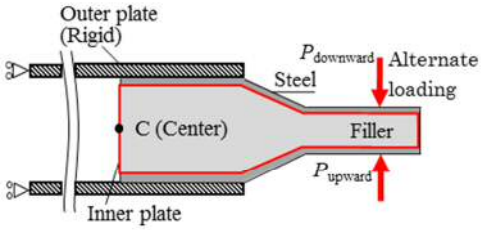

Fig. 2. 2D model in the previous paper [16]
(Online version in color.)

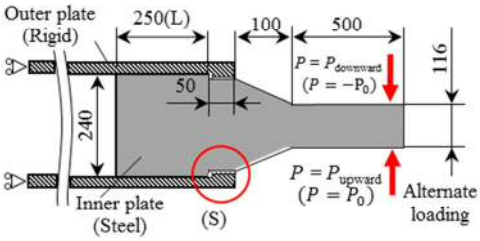

(a) 2D model with stopper(mm)

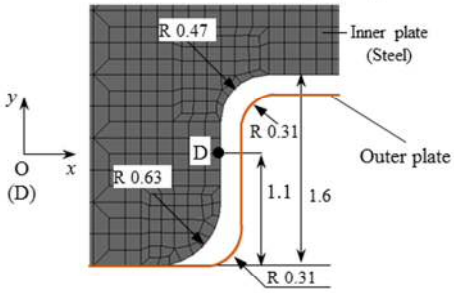

(b) Mesh detail of the inner plate around stopper (S) (mm)

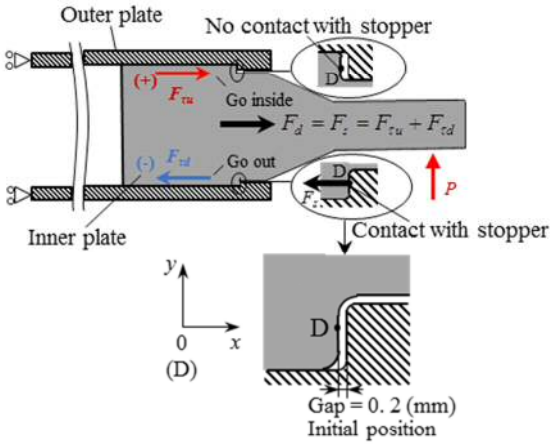

Fig.3 Generation mechanism of the driving out force F_d occurs on the inner plate(Online version in color.)

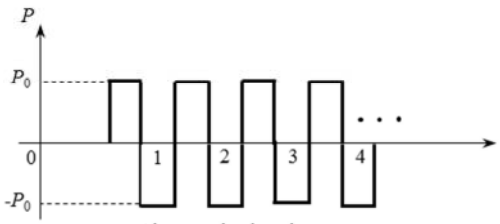

(c) Alternate loading

Fig. 4. New simplified 2D model with stopper
(Online version in color.)

Presentation session:
Presentation: Oral
Presenter name: Norhisam Misron

Effect of Parametric Analysis on Double Stator Permanent Magnet Generator Integrated with Magnetic Gear

Norhisam Misron[1,2], Sheshu M. Salehu[1], Nisa Syakirah Kamal Azhar[1], Tsuyoshi Hanmoto[3]

[1]Department of Electrical & Electronic, Faculty of Engineering, Universiti Putra Malaysia, 43400 UPM Serdang, Selangor, Malaysia
[2]Institute of Advanced Technology, Faculty of Engineering, Universiti Putra Malaysia, 43400 Serdang, Selangor, Malaysia
[3]Department of Biological Functions Engineering, Graduate School of Life Science and Systems Engineering, Kyushu Institute of Technology, 2-4 Hibikino Wakamatsu-ku, Kitakyushu 808-0916, Japan

Email: [nsyakeerah@yahoo.com, norhisam@upm.edu.my]

Abstract

This paper presents about double-stator permanent magnet generator (DSPMG) integrated with a novel magnetic gear structure which is proposed to address problems of mechanical geared generators for low-speed applications. To improve the torque performance, a parameterized design approach using 2-D finite-element method (FEM) is proposed to calculate the transmission torque and analyze the relationship between the geometrical parameters and maximum torque. The geometrical design parameters include thickness of the iron ring pole pieces, thickness and width of the permanent magnets. The operating principle is based on three rotors consisting of prime permanent-magnet (PM) poles in the middle rotor and field PM poles in the inner and outer rotors respectively. The simulation results show that the parameterized design approached can improve the torque density and Back EMF voltage of the magnetic geared PM machine.

Keywords : Magnetic gear (MG), permanent-magnet (PM), double-stator, optimized, prime magnet

Introduction

Recently, research on permanent magnet (PM) machines with a double-stator topology has increased because of its greater performance characteristics, compared to conventional single-stator permanent magnet machines as reported in some studies [1]. Various types of double-stator permanent magnet machines have been found by researchers [2] to produce higher output torque with high-torque densities. Magnetic gearing and magnetic geared PM machines have gained many interest in the last decade because magnetic gears have developed to new emerging technologies that have potential to replace mechanical gears and address problems of oil, lubrication, friction, non-contact transmission and inherent overload protection. The concept of integrating a magnetic gear with a conventional PM machine results to a new class of magnetic geared PM electrical machines which can be designed as magnetic geared motors or magnetic geared generators. Also the integration of magnetic gears with double-stator PM machines has resulted to various proposed designs of double-stator magnetic geared PM machines (MGDSPMMs).

This study aims to improve the torque capability of a magnetic geared generator and to achieve an optimal design with high torque density. In this paper, a parameterized magnetic geared double-stator PM machine to improve transmission torque performance and reduce cogging is proposed and analyzed. In addition, the performance characteristics of the parameterized machine are compared with the proposed original structure shown in Fig. 1.

Parametric studies

Parametric analysis is an analytical method for finding a parametric solution to optimizing an electrical machine design. A variable is assigned to various geometrical structures of the electric machine and the simulation steps are conducted within the upper and lower boundary limits. For the parameterized design, geometric parameters such as thickness of the PMs and pole pieces are parametrically solved to obtain the optimal values of the MG machine design for improving transmission torque. In this study, parametric

analysis is conducted on the magnetic gear part only in order to obtain an optimum level of physical dimensions for the proposed magnetic geared generator. Those parameters are field magnet thickness (T_{outer}, T_{inner}), prime magnet thickness (T_{prime}) and pole piece thickness T_{pp1},T_{pp2}). The analysis is given as an effect of variable pole piece thickness on Back EMF voltage.

Effect on Back EMF Voltage

The effect of back EMF as a result of varying the magnet thickness is shown in Fig. 2. The Back EMF increases as the magnet thickness is increased. The voltage waveform from the original model in Figure 5a is better than the parameterized model in Fig.5b but the voltage waveform from the improved model is greater in amplitude because the electromotive force produced from the field magnets is higher due to increased width and thickness. The induced peak-to-peak voltages from the original and parameterized model are 55 V and 100 V respectively for a double layer three-phase concentrated winding. It can be observed that both induced voltage waveforms are not perfectly sinusoidal due to the presence of harmonics but it can be reduced by proper selection of coil winding design.

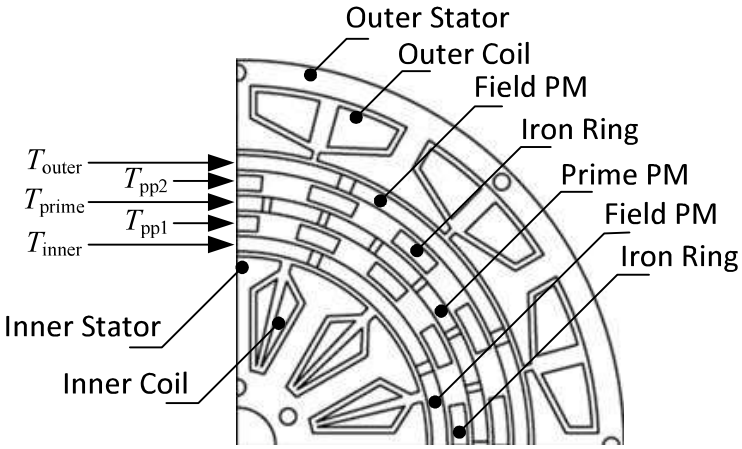

Fig. 1 Magnetic geared double-stator PM generator and the parametric analysis .

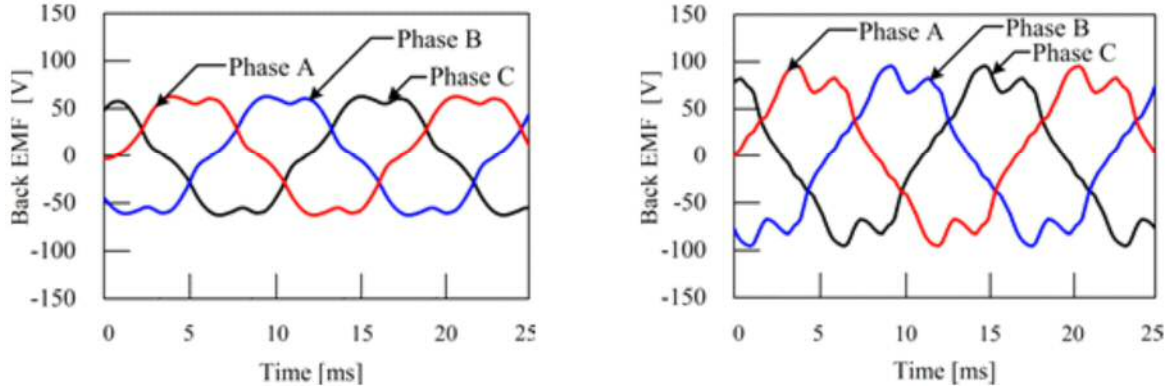

(a) Back EMF of original MG generator model (b) Back EMF of parameterized MG generator model

Fig. 2 Back EMF waveforms of both models at prime speed of 200 rpm.

References

[1] S. Niu, K. Chau, J. Jiang and C. Liu, "Design and Control of a New Double-Stator Cup-Rotor Permanent-Magnet Machine for Wind Power Generation", IEEE Transactions on Magnetics, vol. 43, no. 6, pp. 2501-2503, 2007.

[2] Wang, Y., Cheng, M., Chen, M., Du, Y. and Chau, K.T., 2011. Design of high-torque-density double-stator permanent magnet brushless motors. IET Electric power applications, 5(3), pp.317-323.

Please choose: Oral
Presentation session: Applied Engineering
Presenter name: Mohamad Nasrun bin Mohd Nasir

Dominant Mode Frequency Assessment of Malaysia Power System based on Phasor Measurement Data of Campus WAMS

Mohamad Nasrun bin Mohd Nasir[1,2], Minoru Yonezawa[3], Yoshiaki Matsukawa[3], Masayuki Watanabe[3], Mohammad Lutfi bin Othman[1], Noor Izzri bin Abdul Wahab[1], Yasunori Mitani[3]

[1]Faculty of Engineering, University Putra Malaysia, 43400 UPM Serdang, Selangor, Malaysia
[2]Faculty of Engineering Technical, University Tun Hussein Onn Malaysia, 84600 Pagoh, Muar, Johor, Malaysia
[3]Faculty of Engineering, Kyushu Institute of Technology, 1-1 Sensui-cho, Tobata-ku, Kitakyushu-shi, Fukuoka, 804-8550, Japan

Email: nasrun.nasir@student.upm.edu.my

Campus WAMS, Phasor measurement, Phase Difference, FFT analysis, power system stability
Keywords (5 words)

[Introduction]

Recent development in Synchronized Measurement Technology (SMT) that enables synchronization of phasor measurement with Universal Coordinated Time (UTC) have triggered the utilization of phasor measurement unit (PMU) in Wide-Area Monitoring, Protection and Control (WAMPAC). The application of PMUs in monitoring power system provides a possibility to realize real-time analysis especially monitoring dynamic characteristics of the power system. Time-stamped synchrophasor data make it possible to compare with relative data from wide area.

A survey from North American SynchroPhasor Initiative (NASPI) indicated that SMT is capable of successfully monitoring phase angle across important locations and alarming for conditions that indicate increased stress across the system which perturb system stability. This new technology could identify growing angular separation which benefits electric utilities and grid operators by increasing awareness of system conditions in which corrective action may require to ensure the grid is operated in a safe and reliable manner.

This study describes a practical demonstration of SMT network that has been built in universities named Campus Wide Area Monitoring System (WAMS). The network was established in each utility region in Japan, between Malaysia and Singapore, and also in Thailand. Campus WAMS enables the researcher to monitor and analyze the data offline based on voltage angle measurement and its oscillations from power socket which can assess the small signal stability of the power system. This paper describes the monitoring method using phase angle data by using FFT analysis to the Malaysia power system.

[Analysis Method]

Phase angle differences is an indicator of grid stress. A sudden rise in angle difference implies an impedance increase mostly caused by the change of system topology, or an increase in power transfer between the monitored two locations. Either of the above causes will result in increased grid stress. Grid disturbances can be detected and characterized by rate-of-change of phase angle whether it is line trip or generator loss. Monitoring angle separation can increase transmission system reliability by indicating and identifying excessive stress if the safe limits are approached or exceeded.

The Fast Fourier transform (FFT) is employed in campus WAMS to extract oscillation data for center frequency of dominant mode from phase different raw data obtained from PMU. The FFT is very effective to find the synchronicity existing in it from the stationary signal. A signal in the time domain is converted to the frequency domain by using FFT, then the single oscillation mode is extracted to calculate the center of frequency.

[Result and Discussion]

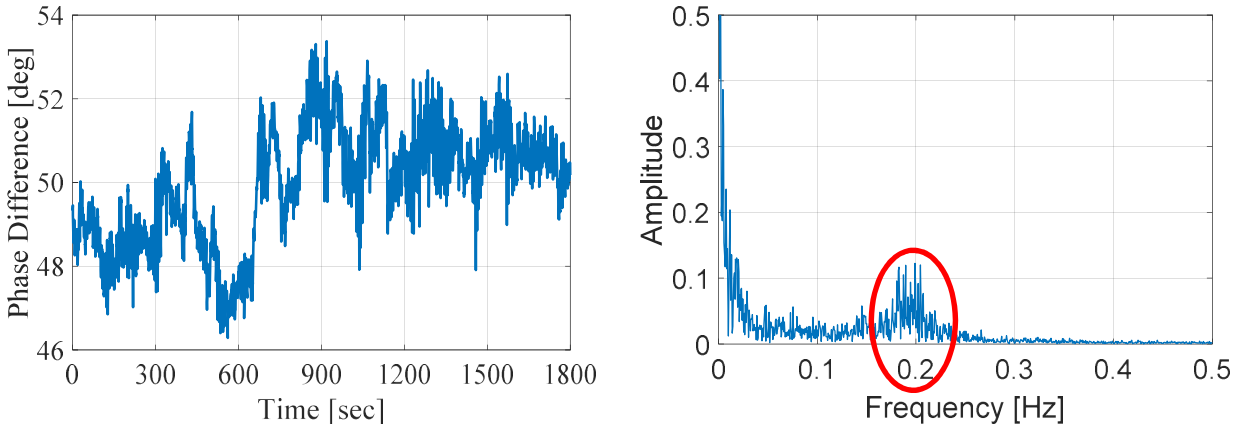

(a) (b)

Figure 1 : (a) Phase difference in degree between two points of PMU measurements, and (b) a FFT analysis of phase different by PMU measurements

This study analyzes data obtained based on the phase difference information in order to grasp the dynamic characteristics of the interconnected line between Malaysia and Singapore and to evaluate the stability in the wide area as real system data. Phase difference information of phasor data is obtained from PMU measurement at two distant points between University Putra Malaysia (UPM), Malaysia and Nanyang Technological University (NTU), Singapore. Figure 1(a) shows the phase difference between UPM and NTU. Figure 1(a) shows the phase difference waveform of 12:20 to 12:50 on 1st December 2008 and figure 1(b) shows FFT analysis of oscillation mode generated from actual data calculation of figure 1(a). The center of frequency can be identified from phase difference data as illustrated in figure 1(b). The red circle in figure 1(b) shows the oscillation mode of the phase difference. The oscillation mode frequency is around 0.2 Hz which indicate the dominant mode of the phase difference between Malaysia and Singapore.

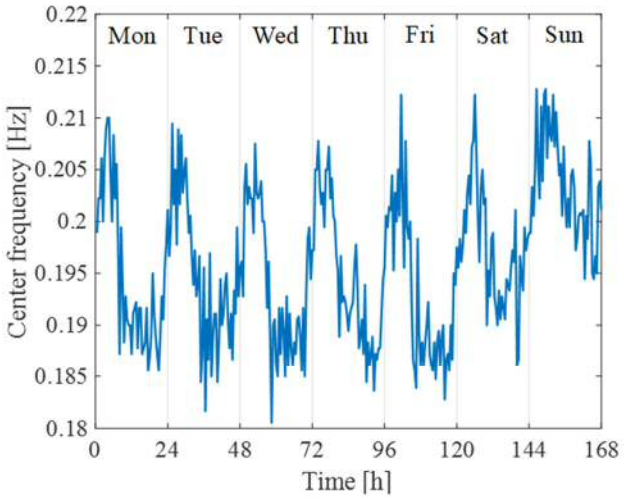

Figure 2: Centre frequency of inter connection between Malaysia – Singapore in a week

The waveforms also represent power oscillation. Thus, the center frequency was derived from the oscillation mode. Figure 2 shows the center frequency obtained by extracting power oscillation from FFT analysis. The center frequencies are different between weekdays which are from Monday to Friday and weekends. Where the center frequency is larger for holidays than for weekdays. This is due to lower electric power demand in weekends compared to weekdays.

Even the comparison of the center frequency in one day, it also can be confirmed that there is a big difference in center frequency fluctuation component in daylight when electric power demand is high and in nightfall when electricity demand is low. Therefore, the center frequency extracted from the phase difference information between Malaysia and Singapore reflects the tendency of electric power demand variation. Here, the center frequency shows a correlation with the electric power demand where higher demand reflects the increased number of generators connected to the grid, causes the lower frequency of the dominant mode.

Please choose: Poster
Presentation session:
Presenter name: Siti Amalina Enche Ab Rahim

The Performance of BIRDS-2 Nano-satellites by Observation from UiTM Ground Station

Afifah Taat, Siti Nadhirah Mohamad Rahim, S.A. Enche Ab Rahim, Mohamad Huzaimy Jusoh

[1]Center for Satellite Communication, Faculty of Electrical Engineering, Universiti Teknologi MARA (UiTM) 40450 Shah Alam, Selangor, Malaysia

Email: amalinaabr@uitm.edu.my

Keywords (BIRD-2, Nano-satellites, UiTM Ground Station, CW)

[Introduction]

The emerging of nano-satellites has changed the game scenario in space and satellite technology. Famously known as CubeSat due to its cubic shape, the nano-satellites are small satellites that weigh from 1kg -10kg. The standard 1U cubic structure has a dimension of 10 cm x 10 cm x 10 cm, and it can be stacked to form 2U or 3U nano-satellite. The nano-satellites can be built by using the commercial-off-the-edges (COTS) components, which greatly reduces the building period and costs of these small satellites, make them suitable to universities, small companies and organizations, that have limited funding. Furthermore, compared to the big and heavy satellites, the small size of the nano-satellite makes it a lot easier to be launched into space where more than two nano-satellites can be put together on-board of a rocket. Despite its small size, a nano-satellite has capabilities to carry specific missions like the conventional satellite, through a constellation of many nano-satellites [1-4].

Universiti Teknologi MARA (UiTM), Malaysia has participated in a programme called Joint Global Multi-nation BIRDS-2 Project, which is an international collaboration between Japan and two other countries, Bhutan and the Philippines. In this project, 10 post-graduate students; three (3) from Japan, two (2) from the Philippines, three (3) from Bhutan and two (2) from Malaysia developed and tested three identical nano-satellites or CubeSats, at the Laboratory of Spacecraft Environmental Interaction Engineering (LaSeine), Kyushu Institute of Technology (Kyutech), Japan. The main objective of this project is to expose and to provide the participants with a comprehensive hands-on experience in developing nano-satellites. The three BIRDS-2 nano-satellites, UiTMSAT-1, MAYA-1 and BHUTAN-1 were successfully deployed from the International Space Station (ISS) to the orbit on 10 August 2018 by using Kibo, the Japanese experimental module at ISS.

In preparation for the satellite launching, UiTM has arranged for an installation of the ground station at the Faculty of Electrical Engineering, UiTM for remote operation and data acquisition. UiTM`s ground station has been fully operational since December 2017.

This extended abstract presents the analysis on the telemetry data of the BIRDS-2 nanosatellites for a period of 2 months, specifically on the temperature of the nanosatellites in order to verify the good functionality of the nanosatellites. The results obtained were compared with the values obtained from the Thermal Vacuum Test. Based on the comparison, the temperature of the nanosatellites never exceed the ones obtained during the test, and thus indicates that the nanosatellites are well-function.

[Experiment]

The UiTM Ground station is one of the BIRDS Ground Station Networks that has the main mission for monitoring BIRDS-2 nanosatellites. The ground station is installed with two difference of Yagi Antenna which operates in Amateur Band in range of; 144 MHz -148 MHz for Very High Frequency (VHF) and 430 MHz - 438 MHz for Ultra High Frequency (UHF).To date, two (2) months of telemetry data have been analyzed after the deployment of BIRDS-2 nanosatellites on 10th August 2018. The 20 Hex characters of Morse code was decoded by using BIRDS-2 CW Morse Code Beacon Analysis Software. There are seven (7) telemetry status of UiTMSAT-1, BHUTAN-1 and MAYA-1 have been closely monitored which are battery

voltage (mV), battery current (mA), battery temperature (°C), OBC temperature (°C), backplane temperature (°C), COM96 TRx temperature (°C) and VHF TRx temperature (°C). The status of satellites was observed during daytime and nighttime of Malaysia local time (LT) as shown in Figure 1.

[Result and Discussion]

Based on the plots, the temperature results during nighttime (battery, OBC, backplane, COM96 TRx, and VHF TRx) of UiTMSAT-1, MAYA-1 and BHUTAN-1 are slightly higher compared to the daytime results. The addition temperature of satellite is usually due to the heat radiation by Sun or the own internal heat production [5]. The heat is not suddenly reduced, and some time can fluctuate during orbit. Besides, the average values of each type of temperature of UiTMSAT-1, MAYA-1, and BHUTAN-1 were calculated, and based on comparison, the values do not exceed the results obtained during the Thermal Vacuum Test. Conclusively, the overall performance of BIRDS-2 nanosatellites within these 2 months period was considered well-functioning and regulated even though sometimes the decoded values from the nanosatellites were unstable.

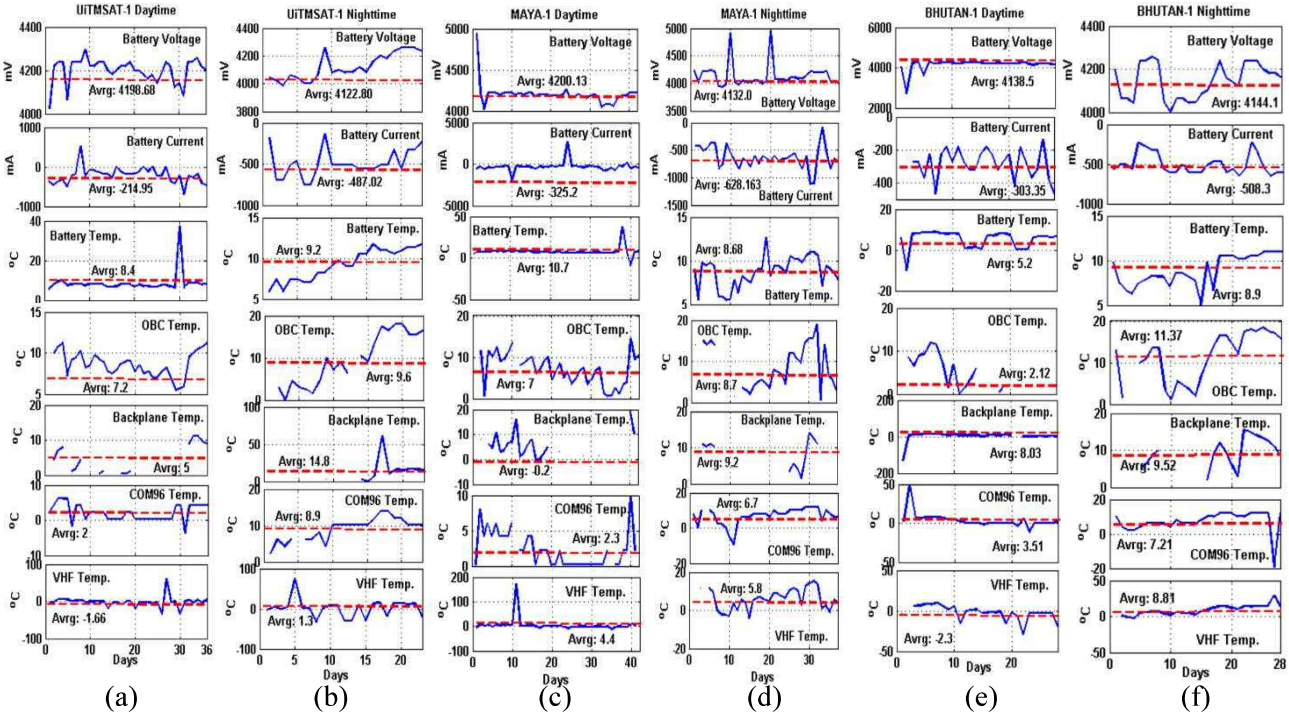

Figure 1. Telemetry status of BIRDS-2 nanosatellites during daytime and nighttime. (a)-(b) UiTMSAT-1, (c)-(d) MAYA-1, (e)-(f) BHUTAN-1.

[References]

[1] E. Hand, "Weather forecasting: Cubesats promise to fill weather data gap," Science. vol. 350, no. 6266, pp. 1302-1303, Dec. 2015.

[2] D. H. A. Maithripala and S. Jayasuriya, " Radar deception through phantom track generation," in Proc. Amer. Control Conf., vol. 6, pp. 4102-4106, Jun 2005.

[3] J. Kim and J. P. Hespanha, "Cooperative radar jamming for groups of unmanned air vehicles," in Proc. IEEE Conf. Decis. Control, pp. 632-637, Bahamas, Dec. 2004.

[4] F. Y. Hadaegh, S.-J. Chung, and H. M. Manohara, "On the development of 100-gram-class spacecraft for swarm applications," IEEE Syst. J., vol. 10, no. 2, pp. 673-637.

[5] J Meseguer, I Pérez-Grande, A Sanz-Andrés, "Spacecraft Thermal Control", Elsevier, Technology and Engineering, August 2012, pp 412.

Please choose: Oral/ ~~Poster/ Either~~
Presentation session: Engineering
Presenter name: Farhan Abdullah

Development of a Method for In-Situ Measurement of Carbon Fiber/ Polyether Ether Ketone (CF/PEEK) Composite Thermal Expansion in Low Earth Orbit

Farhan, Abdullah[1], Kei-ichi, Okuyama[1], Isai, Fajardo Tapia[1], Naoya, Urakami[1]

[1] Department of Applied Science for Integrated System Engineering, Kyushu Institute of Technology, 1-1 Sensui-cho, Tobata-ku, Kitakyushu-shi, Fukuoka, 804-8550, Japan

Email: abdullah.farhan835@mail.kyutech.jp

Keyword: Atomic Oxygen, Coefficient of Thermal Expansion, Carbon Fiber/PEEK, Low Earth Orbit, Ultraviolet

The Low Earth Orbit (LEO) environment exposes spacecraft structures to factors such as ultraviolet (UV) radiation, atomic oxygen (AO), vacuum and extreme temperature variation. Carbon Fiber/ Polyether Ether Ketone (CF/PEEK) composite can be an ideal material to counter such factors due to properties which includes dimensional stability, resistance to radiation and thermal cycling.[1)] However, there are limited data on the space performance of CF/PEEK composite when exposed to the LEO environment. The lack of data can be attributed to limited opportunities to send samples to space, limited retrieval methods and inaccuracy in the ground test to simulate simultaneous space environment factors.[2)] This presentation discusses the development of a space exposure experiment which allows in-situ measurements of changes in the coefficient of thermal expansion (CTE) of CF/PEEK composite samples in LEO. This presentation will also describe the preliminary tests carried out prior to launch. The experiment eliminates the need for sample retrieval by transmitting results to the ground. The experiment is a payload onboard Ten-koh satellite. Ten-koh was successfully launched on 29th October 2018 and was designed to perform several experiments in the LEO environment. Fig. 1 illustrates the flight model of Ten-koh satellite.

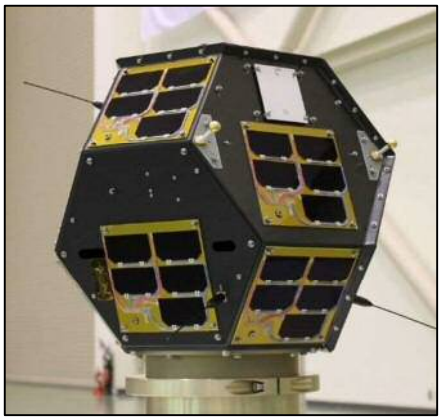

Fig. 1. Flight Model of Ten-koh Satellite

Strain gauges and temperature sensors were used to measure changes in the CTE due to space environment factors. Three sets of CF/PEEK samples were attached externally to the top part of the satellite structure. Each set contains a strain gauge attached between two pieces of thermally welded CF/PEEK. The strain gauges and temperature sensors measure the change in strain and temperature of each sample respectively. The measured data would then be transmitted to the ground station for CTE calculation. Two sets of the samples were separately coated with UV and AO protective coating to observe the effect of UV and AO on CTE values. Fig.

2 illustrates the 3D CAD model of the experiment assembly. Preliminary results indicate that the space exposure experiment can measure changes in strain and temperature required to calculate CTE values.

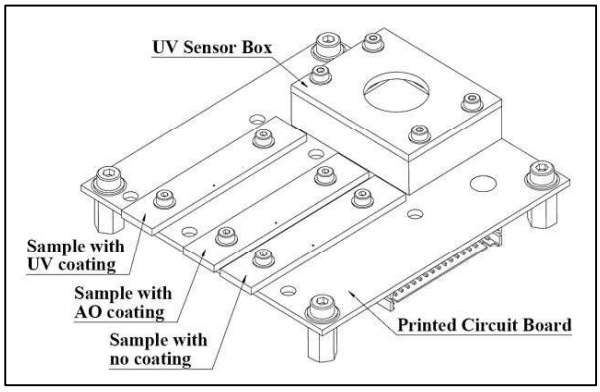

Fig. 2. 3D CAD Model of Experiment Assembly

References

[1] Cogswell, F.N.: *Thermoplastic Aromatic Polymer Composites*, Butterworth-Heinemann, Oxford, 1992, pp. 215.

[2] Tagawa, M. and Yokota, K.: Issues and Consequences of Space Environmental Effect on Materials, *Transactions JSASS Space Technology Japan*, **7**, ists26 (2009), pp. Tr_2_21–Tr_2_26.

Please choose: Oral/ Poster/ Either
Presentation session:
Presenter name: Dr Mohd Sharizal Abdul Aziz

[INFLUENCES OF FILLING LEVEL ON PTH SOLDER JOINT DURING WAVE SOLDERING]

Mohd Sharizal Abdul Aziz [1], Mohd Zulkifly Abdullah [2], CY Khor [3]

[1]School of Mechanical Engineering, University Sains Malaysia, 14300 Nibong Tebal, Penang, Malaysia
[2]School of Aerospace Engineering, University Sains Malaysia, 14300 Nibong Tebal, Penang, Malaysia
[3]Faculty of Engineering Technology, Universiti Malaysia Perlis, UniCITI Alam, Sungai Chuchuh, Padang Besar, Perlis, Malaysia

Corresponding author email: msharizal@usm.my

Keywords: solder joint, wave soldering, PTH

Introduction

The process parameter, physical design and assembly conditions are the key factors that influenced the quality of the solder joint during the wave soldering process. Solder joint failure typically causes by the mismatch of coefficient of thermal expansion. Besides, other factors (i.e., chip size, underfill and substrate materials, board material, interface metallurgy and solder joint geometry) also influenced the solder joint reliability. Therefore, proper control and better understanding are very important in the solder joint assembly process. Finite element (FE) based simulation is useful to provide the better understanding and visualization of the displacement stress behavior of the solder bumps during a thermal cycle via fatigue law and constitutive law methods. The small size of PTH has created the challenges to visualize the solder joint defects such as cracks, void formation and unfilled PCB hole (<50%). Thus, in the current study, the effect of several filling levels and fillet geometrical to solder joint strength are investigated via commercial FEA tool ABAQUS. Five different fillet radius and five different filling level configurations are considered in this study.

Results and Discussion

1. Effect of filling level to PTH displacement

The PCB hole is occupied by the molten solder via capillary motion once the PCB passes the molten solder fountain during the wave soldering process. In the filling process, the PTH interacts with molten solder and solidification of molten solder lead to the displacement. The variation of the filling level of PTH may induce the unintended defect of the solder joint. Fig. 1 demonstrates the finite element results for the effect of filling level on the PTH displacement at t= 28s and t= 55 s. The displacement results indicated as the pin deformation due to filling level of molten solder. The investigation revealed that the increase of PTH displacement was attributed by the variation of capillary force that driven the molten solder to fill the empty PCB hole. The difference of solder joint displacements at different filling levels is plotted in Fig. 2.

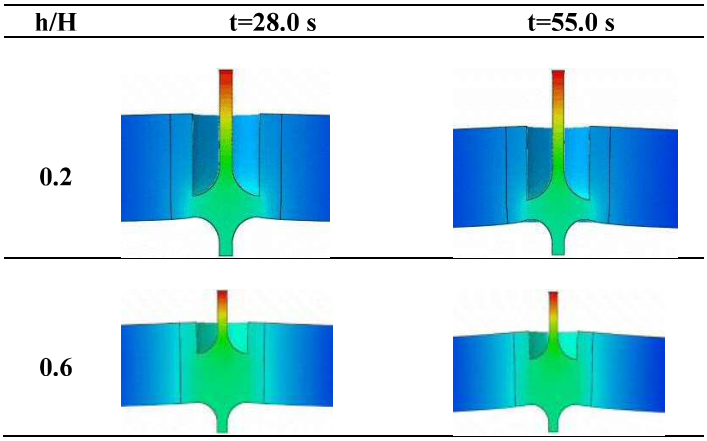

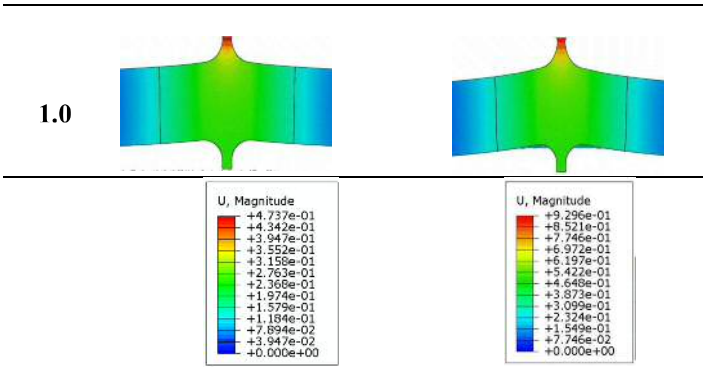

Fig.1 PTH displacement at t= 28s and t= 55s

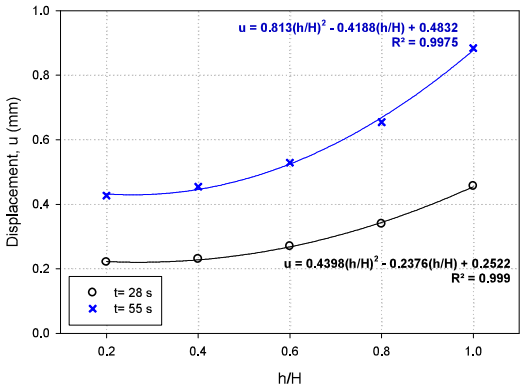

Fig. 2 Solder joint displacements at 28 s and 55 s

2. Effect of fillet to stress of solder joint

Von Mises stress along the solder joint fillet (line A-B) is plotted (Fig. 3). The stress is concentrated at the top of the PTH along line A-B as clearly illustrated in Fig.3. The simulation results indicated that highest stress imposed on the 1.0 fillet profile at 42 MPa and lowest stress (37 MPa) was on 0.2 fillet profile. This situation clearly implies the fillet design on the solder joint correlates with the concentrated stress at top region of PTH. Hence, proper control of the solder joint fillet is significant to minimize the stress of the PTH and sustain its reliability.

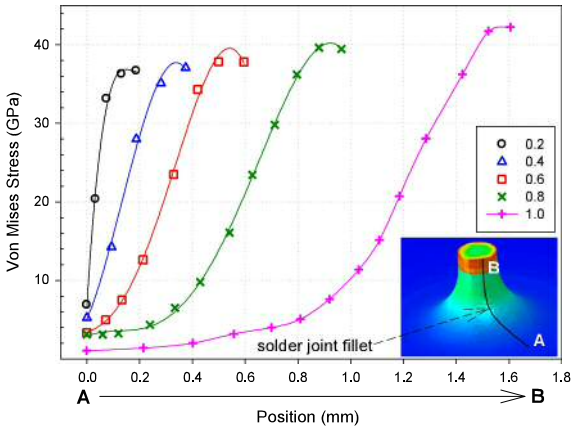

Fig. 3 Solder fillet stress at t= 55s

Conclusion

The FE based simulation has demonstrated the influence of filling level and fillet profile on the solder joint strength. Both factors should be considered to attain the optimum strength and reliability. The numerical method and results are useful for researchers and engineers to anticipate trends and provide firsthand information in the microelectronics industry.

Please choose: (Oral)/ Poster/ Either
Presentation session: Engineering
Presenter name: Ryo SAKAI

Fundamental Investigation of Generating Laser-induced Shock Wave for Development of Regenerative Cell-culture System

Ryosuke TERAJIMA[1], Ryo SAKAI[1] and Masaaki TAMAGAWA[1]
[1] Graduate School of Life Science and Systems Engineering, Kyushu Institute of Technology, 2-4 Hibikino, Wakamatsu, Kitakyusyu 808-0196, Japan

Email: terajima.ryousuke591@mail.kyutech.jp, sakai.ryou185@mail.kyutech.jp

Keywords: Femtosecond Laser, Laser-induced Shock Wave, Regenerative Medical System, Microcapsule, Image Processing

1.Introduction

This paper describes a regenerative culture system which is composed of acceleration of cell-culture and destruction of capsule by shock wave. In this system, shock waves are applied to microcapsules containing bubbles for DDS to stimulate cells simultaneously and disintegrate capsules. The capsule have an important role as a scaffold for cell-culture in regenerative medicine. However, the control method of the shock wave has not been established because there are three physical phenomenon such as shock waves, bubbles and micro-jet in the micro region. In this study, for the cell stimulation, the generation of micro shock wave by using femtosecond laser is measured. Especially, the shock waves generated in water are observed by visualization of particles and the pressure of the shock wave is investigated.

2.Experiment

In this experiment, underwater shock waves are generated by using femtosecond laser device and optical lens. A laser outputted from a femtosecond laser device (FK 3000, wavelength 1030nm, pulse width 260fs, pulse output 2.1μJ, laser diameter 2mm) with fiber type can be redirected vertically downward with a hot mirror. Finally, the laser is focused at a point whose position is 1mm from water surface by an objective lens (M PLAN APO NIR 100X, NA 0.5, aperture angle 30degrees). By using a pulse generator (DG535), the repetition frequency of laser is set up to be 10Hz. For confirmation of the generation of shock waves, the particles (HE-3040, diameter 11μm, density 960kg/m^3) are suspended in water and the motion of the particles around the focal area is taken from the upper side by a CCD camera (WAT-910HX, frame rate 29.97fps, shutter speed 1/250s pixel 720×480). Also, to observe the particles easily, light emission at the focal point is adjusted with a band-pass filter (central wavelength 625nm±50nm).

Since the frame rate of the CCD camera is larger than the pulse width of the laser, time resolution is low. Also, time synchronization of laser and CCD camera has not been done. Therefore, images taken by a CCD camera are analyzed and the motion of the particles is examined. From the particle velocity, the pressure of the shock wave in the focal area when the laser is irradiated is obtained. Regarding as image processing, the moving distance $\boldsymbol{X}_n(t)$ of the particle n is obtained from two images (t and $t+\Delta t$), and V_0 is the particle velocity at $\boldsymbol{X}_n(t)$. At first, an equation about the motion of the particle in the fluid is made and the pressure is calculated based on the equation. Table 1 shows physical conditions used in the equation. Also, equation (1) shows the motion of the particle in the fluid. $P(t)$ is the pressure worked by the particle, P_{max} is the maximum pressure at the focal area and r_0 is the distance between the particle and the focal point.

Table 1 Physical conditions of following

Density of water ρ	1000kg/m^3
Density of particle ρ_s	960kg/m^3
Diameter of particle d	11μm
Radius of focal area r_1	1.255μm
Image time interval Δt	33.36ms（29.97fps）

$$\left(1+\frac{\rho}{2\rho_s}\right)\frac{\rho_s d^3}{6}\cdot\frac{d\mathrm{v}}{dt}+3d\mu\mathrm{v}=r_1{}^2\cdot P(t) \qquad \mathrm{P(t)}=\begin{cases}\frac{r_1{}^2}{r_0{}^2}\cdot P_{max} & (t=0)\\ 0 & (t>0)\end{cases} \tag{1}$$

When equation (1) is solved as an ordinary differential equation of v, it becomes the following general solution.

$$\mathrm{v}(t)=V_0 exp\left\{\frac{-36\mu}{(2\rho_s+\rho)d^2}\cdot t\right\} \tag{2}$$

Since v varies exponentially rather than linearly from equation (2), it is assumed that the moving distance $\boldsymbol{X}_n$ in the two images also varies exponentially, and the particle velocity V_0 is expressed by the following.

$$V_0=\frac{\left|ln|\boldsymbol{X}_n(t)|-ln|\boldsymbol{X}_n(t+\Delta t)|\right|}{\Delta t}\cdot|\boldsymbol{X}_n(t)| \tag{3}$$

The pressure in the focal area at the time of laser irradiation ($t=0$) is calculated by the equations (1) to (3).

3.Result and Discussion

By analyzing images taken by a CCD camera, the velocity at each time was obtained from the equation (3). As a result, it was found that the velocity at each time have a peak of the speed corresponding to the laser repetition frequency of 10Hz. In this study, since the value of the velocity of these peaks is not constant, the maximum velocity was taken as the particle velocity, and it was obtained to be 9.18mm/s.

Finally, the pressure in the focal area was estimated. The distance from the focal point to the particle was 48.9μm. From equations (1) and (2), it was found that the pressure worked by the particle was 192Pa and the pressure in the focal area was 0.29MPa. According to the study by Hosokawa et al.[(2)], a pressure of about 0.3MPa has been confirmed. Therefore, the pressure value estimated in this study is almost same as 0.3MPa, and an impulse pressure wave is considered to be generated at the focal area.

4.Conclusion

In this study, underwater shock waves were generated by a femtosecond laser, and particles around the focal point were taken with a CCD camera. And, by image processing, the generation of shock wave for local stimulation on the cell was confirmed and the pressure was measured. As a result, it was found that the pressure at the position of 48.9μm from the focal point was 192Pa. And it was estimated that the pressure in the focal area was 0.29MPa.

References

(1) A. Vogel, *et al.*, Appl. Phys. B. 81 (2005), pp. 1015-1047.
(2) Y. Hosokawa, *et al.*, Appl. Phys. A. 79 (2004), pp. 795-798.
(3) Y. Hosokawa, *et al.*, Rev. Laser Eng. 32 (2004), pp. 94.
(4) H. Misawa, *et al.*, Appl. Phys. 70 (1991), pp. 3829.

Please choose: Oral/ Poster/ Either
Presentation session:
Presenter name: AHMED ALMASSRI

Development of Real-time Secured Grasping System for Wearable Robotic Hand Glove

Ahmed M. M. Almassri [1,2,*], W. Z. Wan Hasan [2], Chikamune Wada [1], Keiichi Horio[1], Siti Anom Ahmad[1] and Suhaidi Shafie[1]

[1]Graduate School of Life Science and Systems Engineering, Kyushu Institute of Technology, 2-4 Hibikino, Wakamatsu-ku, Kitakyushu 808-0196, Japan
[2]Department of Electrical and Electronic Engineering, Faculty of Engineering, University Putra Malaysia (UPM), 43400 Serdang, Selangor, Malaysia
Email: eng.ahmed8989@gmail.com

Keywords: robotic hand glove; pressure sensors; secured grasping system; self-calibration; artificial neural network;

[Introduction]

The number of world's patients with a disability in a part of the body as a result of a cerebral vascular accident (CVA) or stroke is increasing concurrently with the aging of the world population [1]. 15% of the world population have some form of disabilities. In fact, some of people suffer from impaired hand while others have paralysed due to stroke and spinal cord injury. Stroke is the most common cause of serious long-term disability. The leading cause of paralysis was stroke (29%), followed by spinal cord injury (23%) and multiple sclerosis (17%). Thus, the current research focuses on improving the performance of rehabilitation method but the recovery of upper limb, after stroke and spinal cord injuries, is still complex and requires multidisciplinary and multifactorial approaches [2].

The paralysed patients need timely and insistent rehabilitation to recover their lost abilities and resume their normal daily activities such as grasping and manipulation objects [3]. Particularly, patients with paralysed situation, need something to secure grasp during the rehabilitation system. A solution to this, is a device with smart rehabilitation system that allows the patients with disability to independently and securely perform the rehabilitation exercises [1]. Thus, we propose a wearable lightweight robotic hand glove that able to enhance the grasping mechanism and create a secure grasp.

[Experiment]

The block diagram of the developed robotic hand glove based on pressure sensors was introduced as shown in Figure 1 (a). Five FlexiForce sensors were used to capture the pressure data of calibration process, which were later distributed to the five fingers of the developed glove to detect the grasping pressure as shown in Figure 1 (b). An analogue conditioning circuit based on the pressure measurement system was employed to calibrate and extract data from the utilized sensors to be processed. The data set of the calibration experiments were collected in real time, including the output voltage from the sensors. The LABVIEW program was used to analyse the output signal and to export the calibrated data into Excel file. The collected data set were integrated together for the proposed self-calibration algorithm. In order to create a secure grasp with an

accurate measurement pressure, a self-calibration algorithm using the dynamic calibrated data set based on artificial neural network was implemented.

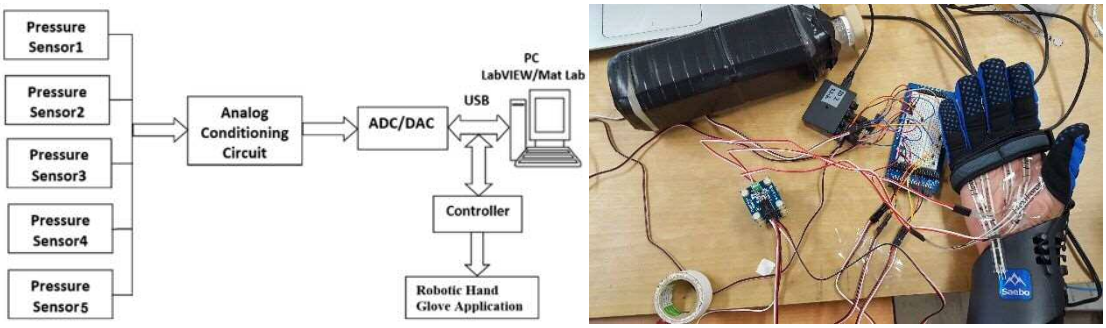

a b

Figure 1. Developed Robotic Hand Glove System and Application

[Result and Discussion]

Multi pressure sensors stitch onto a robotic hand glove (SaeboGlove) to investigate the sensing mechanism in which can restore the sensory function of paralysed hand and to come out with an accurate pressure measurement in excellent sensitivity and response times. Figure 2 illustrates the output of the proposed algorithm based on real time experiment using actual data set input. The predicted pressure pattern (red color) was effectively presented relative to either with target pressure (reference) or without target pressure. It can be observed how the predicted output tracked the target successfully during the whole time of experiment. The results verify that the proposed self-calibration algorithm using ANN can effectively correct and accurately measure the input pressure, which proves sufficient performance. This work also shows that the proposed model exhibited a remarkable performance than traditional methods with a max mean square error of 0.17325 and an R-value over 0.99 for the total response. In return, this can be used to enhance the durability of the grasping mechanism, leading to a more robust and secure grasp for paralysed hands.

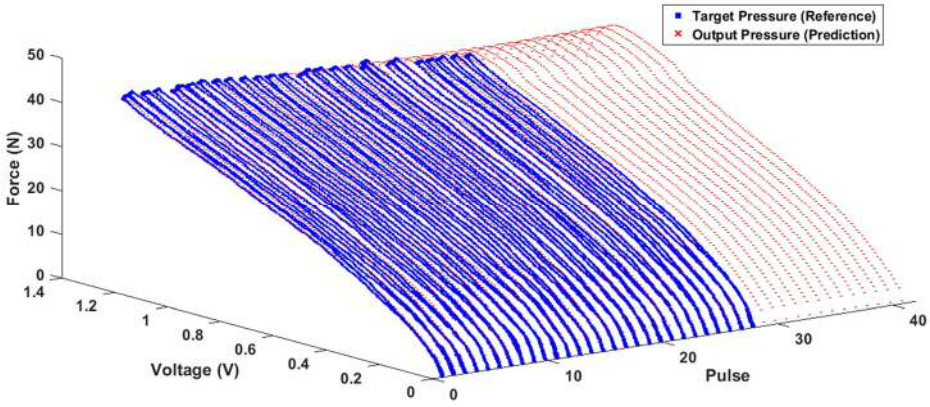

Figure 2. Output estimation pressure sensor versus the target (reference) using the proposed ANN algorithm

[1] S. Ueki, H. Kawasaki, S. Ito, Y. Nishimoto, M. Abe, T. Aoki, *et al.*, "Development of a hand-assist robot with multi-degrees-of-freedom for rehabilitation therapy," *Mechatronics, IEEE/ASME Transactions on,* vol. 17, pp. 136-146, 2012.

[2] P. Sale and M. Franceschini, "Action observation and mirror neuron network: a tool for motor stroke rehabilitation," *European journal of physical and rehabilitation medicine,* vol. 48, pp. 313-318, 2012.

[3] A. M. Almassri, H. W. Wan, S. A. Ahmad, S. Shafie, C. Wada, and K. Horio, "Self-Calibration Algorithm for a Pressure Sensor with a Real-Time Approach Based on an Artificial Neural Network," *Sensors (Basel, Switzerland),* vol. 18, 2018.

Please choose: Oral

Presentation session: Engineering

Presenter name: Minoru Yonezawa

Investigation of estimation method of inertia using inter-area oscillation modes extracted from measured phasor and power flow information in power system

M.Yonezawa[1] , Y.Mitani[1]

[1]Faclty of Engineering, Kyusyu Institute of Technology, 1-1Sensui-cho ,Tobata-ku, Kitakyusyu-shi, Fukuoka,804-8550,Japan

Email:[yonezawa.minoru346@mail.kyutech.jp]

[Keywords(5 words)]

・Inertia of power system
・inter-area oscillation
・phasor measurement unit
・phasor information
・flow information

[Introduction]

In recent years, there has been rapid development of PV systems. There is concern that the resistance to disturbance decreases such that the frequency fluctuates more than estimated from the power loss amount due to the increase in the introduction amount of renewable energy not having inertia. Therefore, it is important to estimate the inertia possessed by the focused on region. In this research, focusing on two power systems in the East Japan 50Hz system, we evaluate estimation method of inertia using phase difference and flow information.

[Experiment]

In order to confirm inter-area oscillation modes of East Japan 50Hz system, we use phase difference information of the remote tow points of Yokohama National University and Hachinohe Institute of Technology got from phasor measurement unit (PMU) and flow information of active power in Tokyo-Tohoku line. Figures1 and 2 show graphs obtained by FFT analysis on phase difference and flow information of 300 seconds.

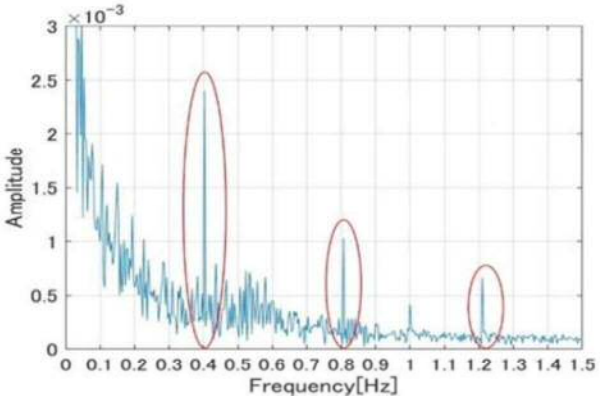

Figure1. Frequency spectrum of flow information

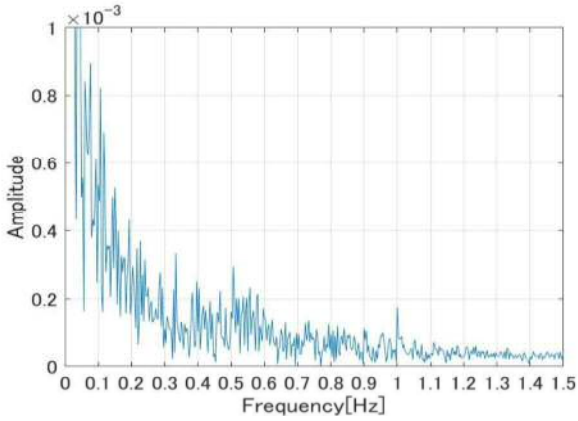

Figure2. Frequency spectrum of phase difference information

From figure1, the peak of the single frequency component appears conspicuously around 0.4 Hz, and the peak of the spectrum can be confirmed even at the frequency of the multiple frequency component. From this, it is expected that the fluctuating component of flow information constitutes a standing wave. By extracting the peak frequency component per 0.4 Hz from the phase

difference and flow information using FFT filtering, plotting the phase difference information on the horizontal axis, and flow information on the vertical axis data, one of the P - δ curves as shown in figure3 Curve can be obtained.

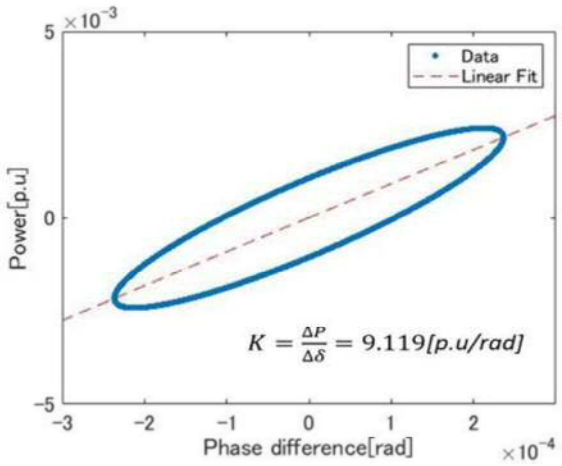

Figure3. P- δ Curve

From figure3, it can be seen that the phase difference and flow information oscillates while maintaining a constant phase difference. Based on these facts, the main oscillation mode of East Japan 50 Hz is a component of 0.4 Hz, and analysis is carried out focusing on its inter-area oscillation mode.

[Result and Discussion]

The frequency at which the fundamental vibration peak appears is taken as oscillation frequency f_0. The synchronization power K is obtained from the ratio of the amplitude of the phase difference and flow spectrum at the oscillating frequency (1-1). Inertia is calculated from the obtained synchronization force and oscillation frequency(1-2).

$$K = \frac{\Delta P}{\Delta \delta} = \frac{Amplitude\ of\ P(f_0)}{Amplitude\ of\ \delta(f_0)} \quad \cdots\cdots (1\text{-}1)$$

$$M = \frac{K}{(2\pi f_0)^2} \cdots\cdots (1\text{-}2)$$

The oscillating frequency f_0 and the synchronizing power K of 2018/3/16 (Fri) and 2018/3/18 (Sun) were estimated. The fluctuation frequency and synchronization power every three hours are estimated, and the change over the course of the day is shown in figure4 and figure5

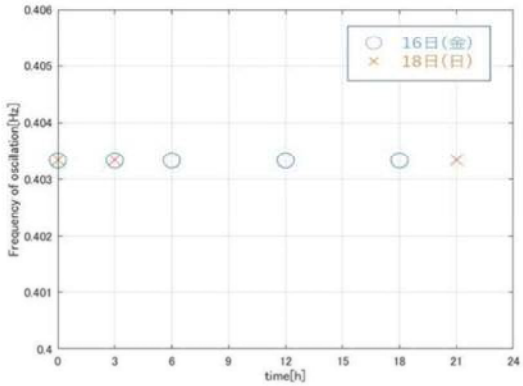

Figure4. Transition of oscillating frequency

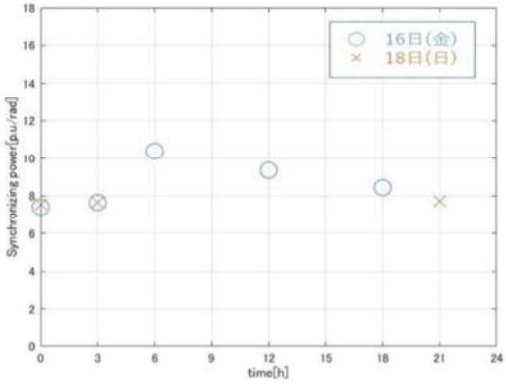

Figure5. Transition of synchronization power

The oscillation frequency was always almost constant for one day at f_0= 0.4033 [Hz] on both days. Synchronization power showed a certain value to some extent although some change was seen (Fig. 5). The average value of the synchronizing power is K = 8.276[p.u/rad]. Calculating the value of inertia from equation 3 yields M = 1.29 [p.u * s ^ 2]. From the result that the synchronizing power and the oscillating frequency are changing to a certain degree to a certain extent, it is expected that the inertia will also remain almost constant based on this value.

Please choose: Poster
Presentation session:
Presenter name: Haizum Hanim Binti Ab Halim

A New Smart Meter Model Integrated with Portable Communication

Haizum Hanim Ab Halim[1], Nashiren Farzilah Mailah[1], Mohammad Lutfi Othman[1], Noor Izzri Abdul Wahab[1]

[1]Faculty of Engineering, University Putra Malaysia, 43400 UPM Serdang, Selangor, Malaysia

Email: nashiren@upm.edu.my, haizumhanim_88@yahoo.com

Abstract

This paper presents a new smart meter model integrated with three types of wireless communication; there is GSM, WiFi, and RF. The proposed model has been designed to solve poor networking system that contributes to overload data and backlog data issues in meter system. The model development divided into two parts; there is hardware development and programming using Arduino IDE software. To ensure that the smart meter system works well, a data center is develop as a data collection and monitoring center.

Keywords
Smart Meter, GPRS, WiFi, RF, Communication.

Introduction

Malaysia has ongoing a pilot test project on the SM system (from August 2014 until August 2016) and as the main purpose of the project is to test the reliability of the meter system and the effectiveness of different types of communication technology. The project is a part of TNB's smart grid initiative and funded by the Malaysian Government Fund (MESITA fund). A 1000 smart meters have been installed in the states of Melaka (800) and Putrajaya (200). Based on the network performance report from 1st June 2015 until 15 September 2015 [1], it can be concluded that the network issues are the major problem in the pilot test. As an example, data delays due to weak RF links, poor GPRS coverage and LAN interface on PLC DCU were down. Poor networking has caused delays and backlog data stored in the meter, hence, it is contributing to overload data issues because data is too big to be pushed to HES through GPRS network. Besides, communication failures will affect the data transfer process and needs a backup system to resolve the problem [2].

Based on the result, a new smart meter model has been designed to solve the problems. The model uses a microcontroller unit ATMega 2560, Energy Meter IC MCP 3905 with three types of communications (GPRS, WiFi, and RF). The selection of communication types are based on its ability, availability, costing and ease of maintenance. Every communication technologies has their own advantages and limitation that is the integration of these three communication is able to address the network issues to be solve.

Experiment

The model development divided into two parts; there is hardware development (circuit design using Proteus software, printed circuit board (PCB) fabrication, components assembly and circuit testing) and programming using Arduino IDE software (coding and program execution). To ensure that the smart meter system works well, a data center is develop as a data collection and monitoring center. Figure 1 shows the illustrated of smart meter systems with data monitoring center.

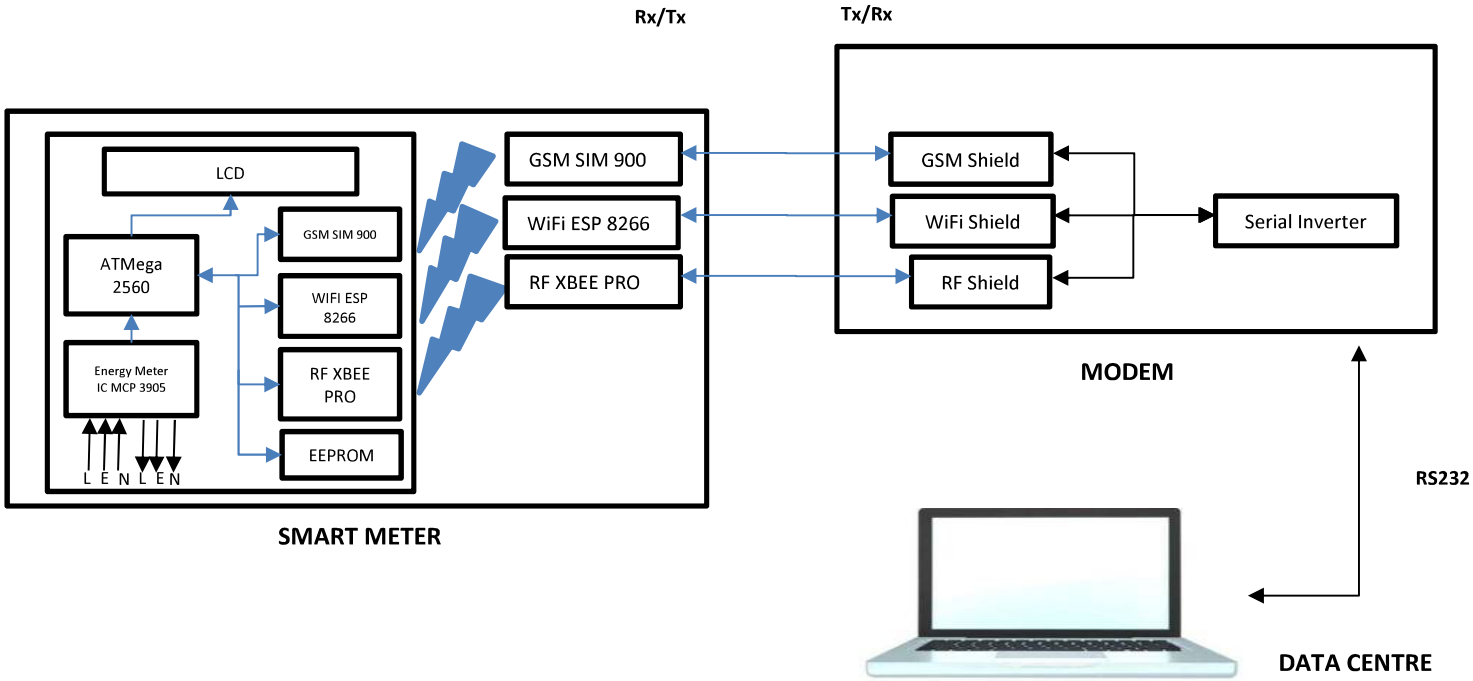

Fig. 1 An illustrated of smart meter system with data monitoring center.

Expected Results and Discussion

In the proposed model, the meter will measure and record a parameter on Voltage (V), Current (A), Peak Voltage (V), Peak Current (A), Frequency (Hz), Power (W) and Energy (kWh). MCU ATMega 2560 will acts as a heart of the smart meter to control all the meter system processes, while energy metering IC MCP 3905 will measure current and voltage. The data will kept safely in EEPROM for a certain period until it send to data center by using selected communication. The network selection technique based on the strength of Received Signal Strength Indicator (RSSI) signal. However, if the entire purpose network failed to reach the specified RSSI signals, an emergency signal will be sent to data center for further action. A received data from smart meter will be collected, save in data center for monitoring purpose and load profiling.

Conclusion

A new smart meter with integrated communication has proposed to resolve network issues in power system. Switching communication techniques based on RSSI signals strength is able to avoid overload data and backlog data issues in meter system. Besides, the purpose of smart meter system in order to improve the conventional system will achieved successfully.

Please choose: Oral
Presentation session: Engineering
Presenter name: Junpei Jike

Research of Peak Cut and Peak Shift Operation Using Thermal Radiative Cooling/Heating System

J.Jike[1], A. Satake[1], Y. Mitani[1]
[1]Faculty of Engineering, Kyushu Institute of Technology, 1-1 Sensui-cho, Tobata-ku, Kitakyushu-shi, Fukuoka, 804-8550, Japan

Email: [jike.junpei140@mail.kyutech.jp]

Keywords (5 words)
▪Thermal Radiative Cooling/Heating System
▪Peak Cut
▪Peak Shift
▪Contract Power
▪Maximum power

[Introduction]
Peak cut operation is an operation to suppress power consumption of air conditioning and heating, and it aims to lower the demand peak. By doing peak cut operation, there is a merit that it leads to a stable supply of power on the supply side, and contract power can be lowered also to the customer side. In this laboratory, power management of Thermal Radiative Cooling/Heating System is studied. Compared with the air conditioner, the Thermal Radiative Cooling/Heating System has a characteristic that the response of the room temperature change to the input power is slow, and it is considered that the influence on the room temperature when performing the peak cut operation is small. Therefore, in this paper, it is proposed a peak cut operation method using Thermal Radiative Cooling/Heating System, and evaluated effect of the maximum power reduction and accompanying room temperature change. The change in room temperature is studied when performing peak shift operation to turn on power before peak cut.

[The way of peak cut operation and peak shift operation]
Since room temperature simulation of room 407 (floor area 50m^2) which is located in No. 10 Building of Kyushu Institute of Technology can be performed by the previous study [1], It have assumed that the situation where 16 rooms are arranged in the whole this building, evaluate the room temperature change when carrying out peak cut operation in reference to the electric power record of No. 10 building (July 21, 2017). At this time, since the cooling power is not known, the cooling power per room have assumed from the outside air temperature when constant at room temperature of 26℃. It is converted into 16 rooms, and the power consumption by cooling is estimated. Figure 1 shows the cooling and heating power estimated as the actual performance of the 10th building. As shown in Figure1, the maximum power is set 30 kW. So, the maximum power have reduced by 6 kW. During the actual power exceeds 30 kW, the operation to cut the excess of electric power from the cooling power consumption is assumed. The room temperature change at this time is calculated by simulation.

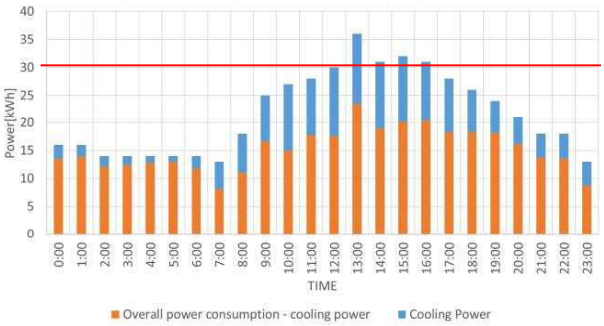

Figure1. Power performance and estimated cooling power at July 21, 2017

In addition, It have assumed that additional power is input of the cooling power so that the maximum power of entire facility don't over 30 kW when the maximum power of the entire facility does not exceed 30 kW. At this simulation, the time when inputting additional power is 10: 00 to 12: 00. Peak shift operation is examined by this way.

[Simulation Result]
Figure2 shows the power consumption data at the time of peak cut and combining peak shift and peak cut operation. Figure3 shows the room temperature simulation result during peak cut and peak shift operation.

Figure2. Power consumption during peak cut and peak shift operation

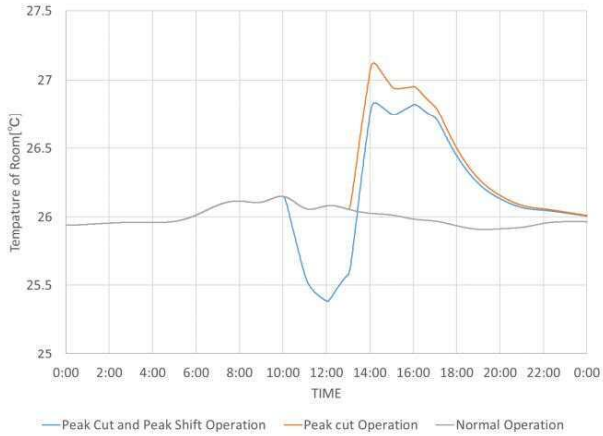

Figure3. Room temperature change during peak cut and peak shift operation

As shown in Figure3, when the peak cut operation was performed, the maximum value of the room temperature was about 27.1℃, and it can be said that the maximum power was reduced by 6 kW without largely deviating from 26 ℃. Also, it can be seen that the peak at room temperature is as low as about 26.8℃. When comparing the peak shift operation with the peak cut operation, doing peak shift operation have told us that doing it less influence room temperature. It is considered that by effectively utilizing the peak shift operation in addition to the peak cut operation, the influence on the room temperature can be reduced and the peak power consumption can be cut to a greater extent.

[Conclusion]

In this paper, a peak cut operation using Thermal Radiative Cooling/Heating System is proposed and is showed that the maximum power can be reduced without changing the room temperature considerably with respect to the actual electric power performance of the target customer. Peak shift operation have studied and have showed that the peak at room temperature can be lowered.

[References]

[1] Naoto Kubo, Akihiro Satake, Yasunori Mitani" Examination of Power Smoothing Operation Method by Dynamic Heat Transfer Model Simulation of Thermal Radiative Cooling/Heating System"
It was announced in Joint technical meeting on “Power Engineering” and ”Power Systems Engineering”, IEE Japan (2017).
Announcement number is “PE-17-155, PSE-17-155”.

Investigation of electric vehicle driving support system using Geographic In formation System

Keita Tsuruhara, Yasunori Mitani, Atsushi Shiota

[1]Faculty of Engineering, Kyushu Institute of Technology, 1-1 Sensui-cho, Tobata-ku, Kitakyushu-shi, Fukuoka, 804-8550, Japan

Email: [tsuruhara.keita611@mail.kyutech.jp]

Keywords (5 words)

・Electric Vehicle・GIS・Regenerative brake・Driving support system・Drive characteristics

1 Introduction

In recent years, shifting from an internal combustion vehicle to an electric vehicle (EV) that does not emit carbon dioxide while driving is progressing against the background of environmental problems.

However, the electric vehicle has a problem that the cruising range is shorter than that of the internal combustion vehicle and the charging time is long. Also, like the regenerative brake, there is action specific to electric cars. Therefore, energy management while driving is important. This research is conducted to construct a system to teach driving method with low power consumption by using geographic information system(GIS). The driving characteristic is indicated by comparing the measured value with the estimated value of the power consumption when traveling 0.5 kilometer for each driver.

2 Methods

Estimated expression of power consumption from plural person's driving data was derived.

$$\text{Up}: \quad W = \frac{x}{8740} + 0.0045h \qquad (1)$$

$$\text{Down}: \quad W = \frac{x}{8740} + 0.0044h \qquad (2)$$

x is the mileage. h indicates the difference in elevation. Estimate the power consumption using GIS road data and estimation formula. Compare the estimated values of power consumption with measured value.

Estimation of power consumption was conducted in the section from the departure point of the Fig.1 to the destination.

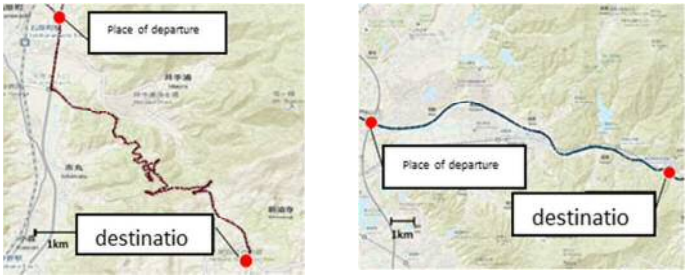

Fig.1 Route chart of experiment (routeA, routeB)

3 Results

The bar graph in Fig. 2 shows the difference between the estimated power consumption and the measured power consumption every 0.5 kilometers. A positive value indicates that power is consumed more than the estimation, and a negative value indicates that the power consumption is smaller than the estimation. Further, the line graph shows the altitude of each traveling distance point. In the case of traveling on the route A, more electric power is consumed than the estimated value when traveling on an uphill slope, and traveling with less power consumption is performed on a flat portion or a downhill slope. On the other hand, in the case of traveling on the route B, the power consumption of the uplink portion is a value close to the estimated value or a power consumption amount smaller than the estimated value.

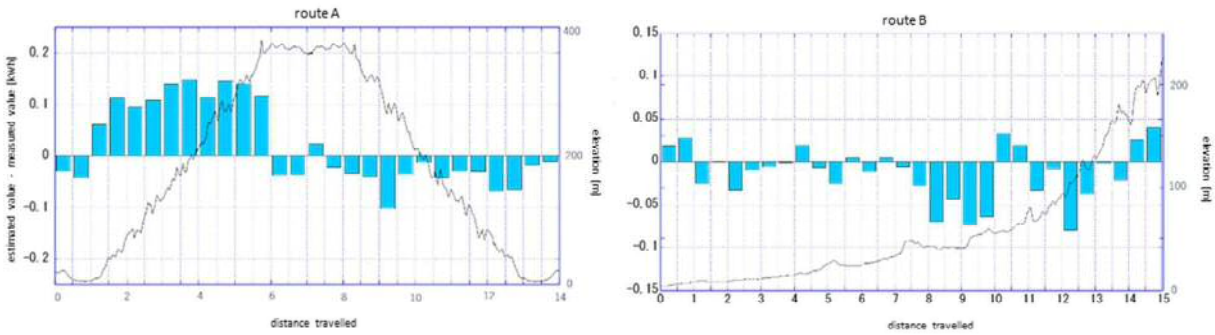

Fig.2 Comparison of estimated value of power consumption and measured value

Fig. 3 shows the transition of the actual amount consumed up to each traveling point and the value of the estimated total consumed up to the destination. In the route A, the power consumption increases in the section where the power is consumed more than the standard value. That is, the accelerator opening degree is large in the uphill slope and the accelerator opening degree is small in the downhill slope. In the case of traveling on route B, the difference between the estimated amount and the measured amount is small. Therefore, it is close to the running characteristic based on the estimation formula. In the route B, it is traveling without stepping on the accelerator on the uphill slope.

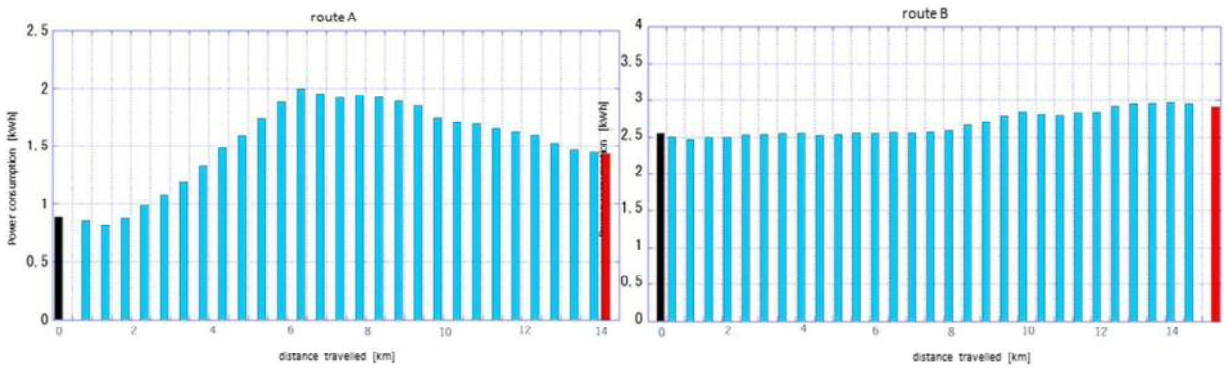

Fig.3 Trend of power consumption

4 Conclusions

By comparing the estimated value with the measured value, it was possible to show the op erating characteristics. The future task is to use driving characteristics and propose driving w ith less consumption.

Please choose: Oral
Presentation session: Engineering
Presenter name: Hirotaka Ihara

[Reduction of supply and demand adjustment costs of retail electricity companies using contract batteries for contract power reduction installed in customers]

H.Ihara[1], Y. Mitani[1]
[1]Faculty of Engineering, Kyushu Institute of Technology, 1-1 Sensui-cho, Tobata-ku, Kitakyushu-shi, Fukuoka, 804-8550, Japan

Email: [ihara.hirotaka998@mail.kyutech.jp

Keywords (5 words)
Battery. Contract power. Retail Electricity Company. Supply and Demand Adjustment. Photovoltaics.

[Introduction]

In recent years, the introduction amount of Photovoltaics (PV) is increasing due to the influence of Feed-in Tariff in Japan. The amount of electricity generated by PV in Kyushu gradually increases from the morning as shown in Fig.1, and decreases with the peak of daytime as the boundary. For this reason, electric power surplus is likely to occur in the daytime when PV generation amount increases, conversely electric power shortage tends to occur in the morning and evening. The actual power shortage status of the electric power system and the transaction price of the power market conducting power trading are linked, and as a result it tends to be high in the morning and evening as shown in Fig.1. In the future, as the PV increases, the price difference as shown in Fig.1 is considered to become even bigger. A retail electric power company forecasts demand by the day before and creates a supply-demand curve. After that, we adjust supply and demand by buying electricity to satisfy that. For this reason, it is necessary to procure expensive electric power in a time zone when power shortage is likely to occur, which may increase the burden. As a countermeasure against this, in this paper we will consider using storage batteries owned and operated by customers for contract power reduction. Supply and demand adjustment costs can be reduced by using this storage battery by a retail electricity company to store inexpensive surplus electric power and discharge it in a time zone where electricity shortage tends to occur and price is high.

[Combination of contract power reduction and supply and demand adjustment cost reduction]

Figure.2 is a curve drawn for one year for the day maximum value of the electricity demand accumulated for 30 minutes by a customer of the scale of several hundred kW. The electricity fee paid by the customer consists of the basic charge and the metered amount, and the basic charge is determined by the maximum value of 30 minutes accumulated demand. Therefore, as shown in Fig2, if the 30-minute accumulated demand is large even once, the contract power is determined by the green line, and the basic charge for one year becomes high.

However, customers can discharge electricity using a storage battery and reduce contract power by reducing demand. The customer in Fig. 2 controls the storage battery and reduces the contract power from the green line to the red line. As can be seen from Figure 2, the day when the customer uses the battery, is several ten days when the blue line exceeded the red line. The battery is rarely used out of the year. Therefore, on the day when customers do not use batteries, retail electricity companies can use it to reduce supply and demand adjustment cost. Reduce purchase cost by storing inexpensive surplus electric power in the storage battery and discharging in high time period of electricity price to reduce supply and demand adjustment cost. In this research, in addition to traditional contract power reduction operation, a reduction operation of supply and demand adjustment cost is added.

[Transition of electricity price by season and Seasonal storage battery control method and effect]

Electricity trading is being conducted in Japan Electric Power Exchange in Japan. In this research, based on spot price information in the Kyushu area published in Fiscal Year 2017, we consider May as spring, August summer, November as fall, December as winter and analyze. The price of this power trading changes from season to season because of reasons such as different electricity demand for each season.

Here, in order to grasp how the electricity price changes each season, the average value for each season is calculated. Electricity demand is greatly different between weekdays and Saturdays, Sundays and holidays. Also, electricity prices are dependent on weather as other factors. Most of the year is fine weather. This time, we extracted and averaged the electricity price only in the day when the peak of the PV generation amount is 2000 MW or over in Kyushu. The results are shown in Fig. 3.

From Fig. 3, it can be seen that the electricity price fluctuates in one day, especially, it fluctuates greatly in summer and winter. From Fig.3, control of the storage battery for each season is decided. The electricity price has the characteristics as shown in Fig.3, but the peak time goes up and down depending on circumstances. For this reason, the charging and discharging time of the storage battery is made to have a certain width. Based on

these, the storage battery control is defined as Fig.4 and Fig.5. In Fig.4 and Fig.5, the charging is negative and the discharge is positive. The charge / discharge efficiency is set to 90%.

Control the storage battery for one month for each season. In that case, in the case of customers with a demand scale of 200 kW, the supply and demand adjustment cost of 135 yen in the spring, 681 yen in the summer, 673 yen in the fall, 1202 yen in the winter was reduced on average per day. In the spring, although the effect of reducing supply and demand adjustment cost is small, since the price difference is large and there are two peaks, the effect is great in winter.

[Conclusion]

Grasping the operation status of the storage battery when contract power reduction was carried out, the supply and demand adjustment cost reduction operation have done. In the result of this time, the effect of reducing supply and demand adjustment cost in spring is small, and it is big in winter. In the future, consider the situation of each customer and the influence on the distribution system.

[References]

[1]Kento Kobayashi, Takanori Kodou, Mr. Yasunori Mitani: "Integrated control of electric power system for massive introduction of solar power generation using fuel cell cogeneration and storage batteries" Joint meeting of electric engineering / electric power system technology (2017)

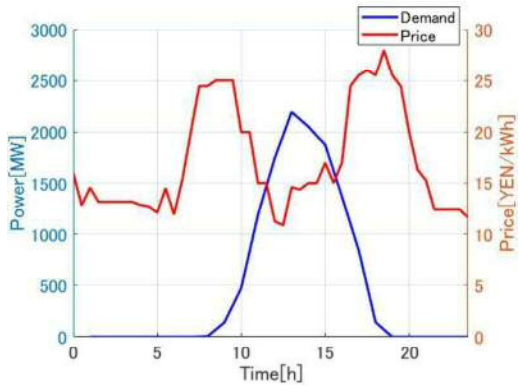

Figure.1. Trends in PV power generation and electricity price

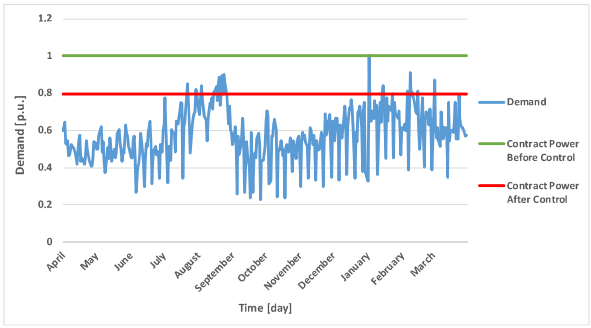

Figure.2. Customer demand and contract power

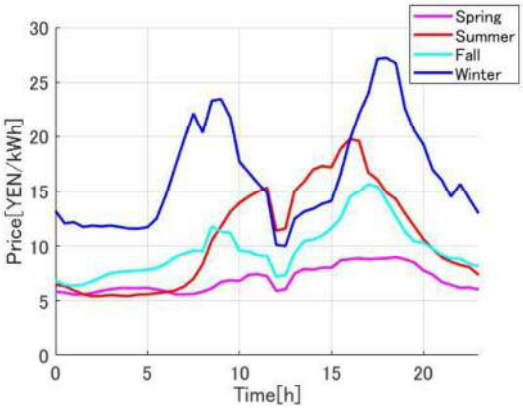

Figure.3. Transition of electricity price by season

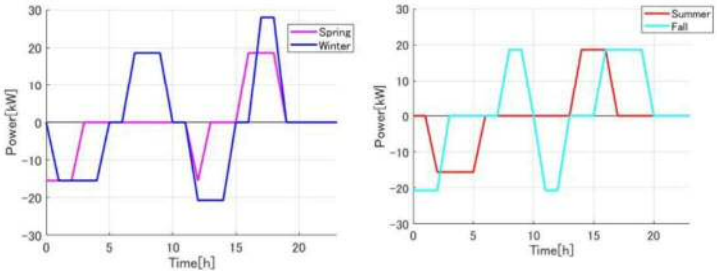

Figure.4. Storage battery control

Presentation choose: Oral

Presentation session: Engineering

Presentation name: Yoshimasa Kaneda

DC Hot carrier effect of a thin-film SOI Power p-MOSFET at high temperature

Y. Kaneda, A. Watanabe, S. Matsumoto

Faculty of Engineering, Kyushu Institute of Technology, Sensui-cho, Tobata-ku, Kitakyushu-shi, Fukuoka, 804-8550, JAPAN

e-mail: kaneda.yoshimasa774@mail.kyutech.jp

Keyword

hot carrier effect, SOI power MOSFET, DC stress, high temperature

Introduction

Silicon on insulator (SOI) power MOSFETs have attracted attention as one of the promising candidates for high temperature applications because they can reduce thermally induced leakage current and prevent luch-up[1,2].

In this paper, we describe the temperature dependence of the DC hot carrier effect and NBTI (Negative Bias Temperature Instability) of thin-film SOI power p-MOSFET.

Experiment

The schematic cross section of the thin-film SOI power p-MOSFET used in this study is shown in Fig. 1. The body contacts were formed to suppress the parasitic bipolar effect. The main structural parameters are listed in Table 1.

Results and Discussion

Dependence of the threshold voltage shift on the stress gate voltage is shown in Fig.2. The threshold voltage shift is positive when the gate voltage is near threshold voltage (Vth + 0.2 V) because hot electrons are injected by DAHC (drain avalanche hot carrier injection). The threshold voltage shift is negative when the gate stress voltage is more than 2.5 V. The threshold voltage shift increases with increasing temperature and stress gate voltage when the temperature is more than 473K because NBTI occurs. Dependence of degradation rate of on-resistance on stress gate voltage is shown in Fig.2. Degradation rate of on-resistance is negative when the gate voltage is near the threshold voltage (Vth + 0.2) and positive when the stress gate voltage is more than 2.5V. These results indicate that DAHC which electrons are injected actively occurs

near the threshold voltage, and CHC (Channel Hot Carrier injection) which holes are injected actively occurs when the stress gate voltage is large.

Figure.4 shows dependence for each channel length. Dependence of threshold voltage shift on stress gate voltage is shown in Fig.5. From Fig.4 and 5, both the degradation rate of on-resistance and the threshold voltage shift are larger as the channel length is shorter even at the same electric field because of parasitic bipolar effect. The parasitic bipolar effect is stronger as the channel length decrease because the base resistance of the parasitic bipolar transistor smaller.

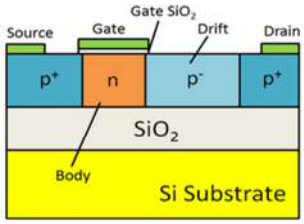

Fig.1 Schematic cross section of SOI p-MOSFET

The name of parameter(μm)	Parameter
Top Si layer(μm)	0.14
Buried oxide(μm)	0.4
Gate oxide(μm)	20
Channel length(μm)	0.5
Drift Length(μm)	0.5
Gate Width(μm)	10

Table.1 The main structural parameter

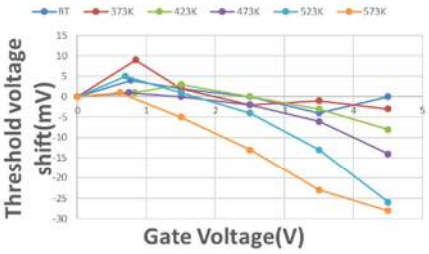

Fig.2 Dependence of threshold voltage shift of p-MOSFET on stress gate voltage

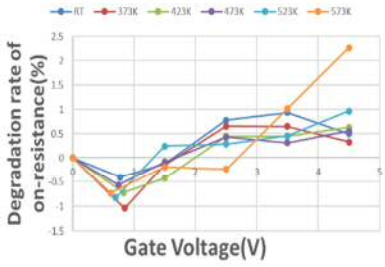

Fig.3 Dependence of degradation rate of on-resistance of p-MOSFET

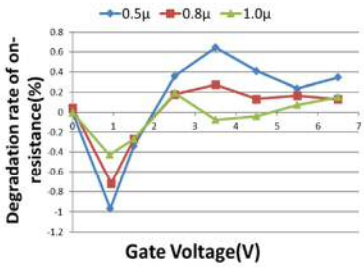

Fig.4 Dependence of degradation rate of on-resistance for each channel length

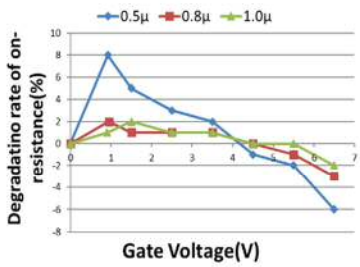

Fig.5 Dependence of threshold voltage shift for each channel length

Reference

[1] H. Tomita, H. Eguchi, S. Kijima, N. Honda, T. Yamada, H. Yamawaki, H. Aoki, and K. Hamada, Proc. ISPSD2011, p. 28, 2011.

[2] J. P. Colinge, Silicon-on-Insulator Technology: Materials to VLSI (Kluwer, Dordrecht, 2004) 3rd ed., p. 200.

[3] K. Ikeno and S. Matsumoto, “Ext. Abs. SSDM2016” PS-14-04, 2016

Presentation session: Oral
Presentation session: Applied Engineering
Presenter name: Nashiren Farzilah Mailah

Design and Development of Modular Structure Neutral-Point-Clamped Multilevel Inverter

Nashiren F., Mailah[1], Nur Aleeya, Bahrin[1]
[1]Faculty of Engineering, University Putra Malaysia, 43400 UPM Serdang, Selangor, Malaysia
Email: nashiren@upm.edu.my

Keywords
Neutral-Point-Clamped, Multilevel Inverter, Total Harmonic Distortion, Graphical Method Analysis

Introduction

Multilevel Inverter is an inverter where its DC supply input is divided into several equal smaller voltages and then generates a staircase output AC voltage of desired magnitude and frequency [1]. The desired stepped level of AC output is achieved when the multiple DC voltages are combined with the help from arrays of power electronics switches. The triggering angles of each switch are calculated using the devised Graphical Method Analysis (GMA) and its switching sequence are determined from the specified Neutral-Point-Clamped Multilevel Inverter (NPCMI) sequence. The multilevel inverter offers the advantages of producing higher power and voltages, producing lower Total Harmonic Distortion (THD) value with the increasing number of level, lower switching stress on devices and low power dissipation of the power switches [2].

Methodology

The process of designing the modular structure for several levels of NPCMI using GMA as the switching algorithm involves a few important steps. There are two steps involved in this work, first is the development of modular structure for 3-Level, 5-Level, 7-Level, 9-Level and 11-Level of NPCMI and second is using Graphical Method Analysis (GMA) [3] to determine the triggering angle. The NPCMI is designed with a DC supply of 400V and frequency of 50Hz. Figure 1 shows the Matlab/Simulink model of modular structure of NPCMI that starts with 3-level. This modular structure then being added one on top rail and one on bottom rail when the level is increased by 2, that is 5-level. With an increment of 2 level, another modular structure is added to top and bottom rail. Whilst GMA calculates the triggering angle that could produces an output staircase stepped output voltage with a lower THD value. Figure 2 shows how a 3-level NPCMI triggering angle is calculated.

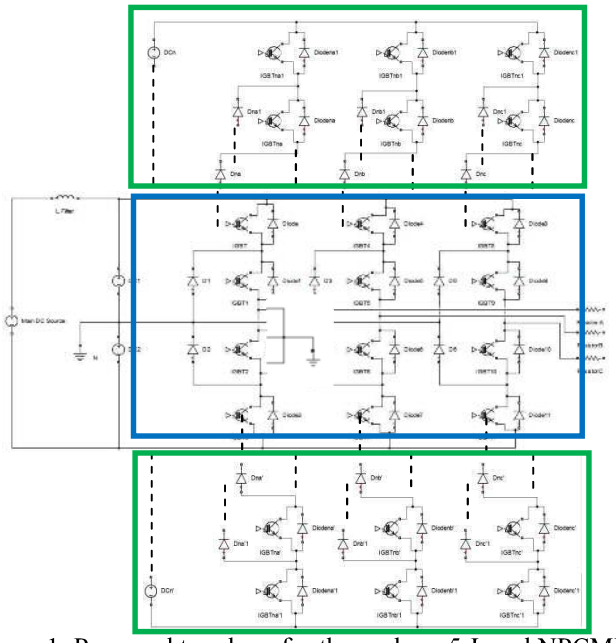

Figure 1: Proposed topology for three-phase 5-Level NPCMI

Result and Discussion

Table 1 shows the THD value obtained in this work. As it can be seen, with an increment of NPCMI level, the THD value of line-to-line voltage, V_{LL} decreases. While in Table 2 shows the comparison of the proposed work to others researcher works.

Table 1: The THD values for each level of NPCMI using GMA

THD (%)	No. of Level of NPCMI				
	3-Level NPCMI	5-Level NPCMI	7-Level NPCMI	9-Level NPCMI	11-Level NPCMI
V_{LL}	16.78	11.09	8.87	7.57	6.13

Table 2: The comparison of THD values with others work for each level of NPCMI.

3-Level NPCMI			
	3-Level NPCMI using Proposed GMA	3-Level NPCMI using LSPWM [3]	3-Level NPCMI using PODPWM [4]
THD of V_{LL} (%)	16.78	17.53	39.12
5-Level NPCMI			
	5-Level NPCMI using Proposed GMA	5-Level NPCMI using PODPWM [5]	5-Level NPCMI using IPD and APODPWM [6]
THD of V_{LL} (%)	11.09	27.78	17.57
7-Level NPCMI			
	7-Level NPCMI using Proposed GMA	7-Level NPCMI using SPWM [7]	7-Level NPCMI using PWM [8]
THD of V_{LL} (%)	8.87	N/A	10.47
THD of V_{LN} (%)	12.45	13.73	N/A
9-Level NPCMI			
	9-Level NPCMI using Proposed GMA	9-Level NPCMI using SPWM [7	9-Level NPCMI using PWM [8]
THD of V_{LL} (%)	7.57	NA	7.84
THD of V_{LN}(%)	9.65	11.73	N/A
11-Level NPCMI			
	11-Level NPCMI using Proposed GMA	11-Level CHBMI using SPWM [9]	11-Level CHBMI using PWM [10]
THD of V_{LL} (%)	6.13	3.68	N/A
THD of V_{LN}(%)	7.83	N/A	10.41

Conclusion

The results obtained from the THD value of proposed modular structure NPCMI and GMA produced a THD value compared to others researcher works.

References

[1] Ahuja, K. Rajesh, and A. Kumar. (2014). "Analysis and Control of Three Phase Multi level Inverters with Sinusoidal PWM Feeding Balanced Loads Using MATLAB". http://www.ijergs.org/files/documents/ANALYSIS13.pdf

[2] Pandey, A. (2014). "Study of multilevel inverter and analysis of three level Inverter (FCMI)". https://www.ijser.org/researchpaper/Study-of-multilevel-inverter-and-analysis-of-three-levels-Inverter.pdf

[3] N. F. Mailah, S. S. T. Othman, I. Aris, N. Misron, Hanamoto, T. And Yamada. H. (2014). "Determination of Triggering Anglethrough A Novel Graphical Method Analysis". http://jestec.taylors.edu.my/Special%20Issue%20SAES2013_9_5_2014/SAES%202013_090_097.pdf

[4] T. Prathiba, P Renuga,. (2012). "A comparative study of Total Harmonic Distortion in Multilevel inverter topologies." http://pakacademicsearch.com/pdf-files/eng/512/26-36%20Vol%202,%20No%203%20(2012).pdf

[5] Pandey, S., Wadhwani, S. and Bansal, P. (2014). "Analysis of Three Level Diode Clamped Multilevel Fed Induction Motor Drive."

[6] C. R. Balamurugan, S. P. Natarajan and R. Bensraj. (2012). "Investigations on Three Phase Five Level Diode Clamped Multilevel Inverter."

[7] Xu, Z., Li, S. and Pan H. (2012). "Study of Five-level diodes-clamped Inverter Modulation Technology Based on Three-harmonic Injection Method."

[8] S. Kumar, R. R. Kumar. (2016). "Design and Simulation of Seven and Nine Level Diode Clamped Inverter." http://www.ijatir.org/uploads/213645IJATIR11118-280.pdf

[9] S. Kiruthika, S. Sudarsan, M. Murugesan and B. Jayamanikandan. (2012). "High Efficiency Three Phase Nine Level DiodeClamped Multilevel Inverter."

[10] Preeti, R. Gupta. (2015). "Switching of Three Phase Cascade Multilevel Inverter Fed Induction Motor Drive". Retrieved from http://www.krishisanskriti.org/vol_image/24Sep201509093410%20Preeti%202.pdf

[11] Ankita, S., Jyoth, D. and Prtima G. (2015)."Comparison of Nine level and Eleven level Inverter for Induction Motor Drives."

Please choose: Oral
Presentation session: Applied Engineering
Presenter name: Yukito Tanaka

Seismic performance of temporary structure made of steel pipes

Yukito Tanaka[1], Takeshi Itoh[2], Eiki Yamaguchi[3]

[1]Graduate School of Engineering, Kyushu Institute of Technology, 1-1 Sensui-cho, Tobata-ku, Kitakyushu-shi, Fukuoka, 804-8550, Japan
[2]MK Engineering, Sando Komazawa Building, 2-16-1 Komazawa, Setagaya-ku, Tokyo, 154-0012 Japan
[3]Ph.D., Graduate School of Engineering, Kyushu Institute of Technology, 1-1 Sensui-cho, Tobata-ku, Kitakyushu-shi, Fukuoka, 804-8550, Japan

Email: tanaka.yukito399@mail.kyutech.jp

Keywords: Temporary Structure, Steel Pipe, Seismic Performance, FEA

1 Introduction

A temporary structure is necessary in many construction sites to provide a work platform and an access road. The service period of such a structure tends to become longer in recent years, sometimes exceeding ten years. Therefore, its seismic performance and durability are getting important. Yet those aspects are not paid much attention to, since it is still for a temporary use.

There was a temporary structure subjected to a large earthquake. Although it was not prepared for such a large earthquake, no damages occurred. The potential strength of the temporary structure might be quite larger than expected.

Against the background of the above information, the seismic performance of the temporary structure was investigated in the present research. To be specific, a temporary structure made of steel pipes subjected to a strong earthquake, the 2000 Tottori-ken Seibu earthquake, was analyzed numerically. The temporary structure is shown schematically in Figure 1.

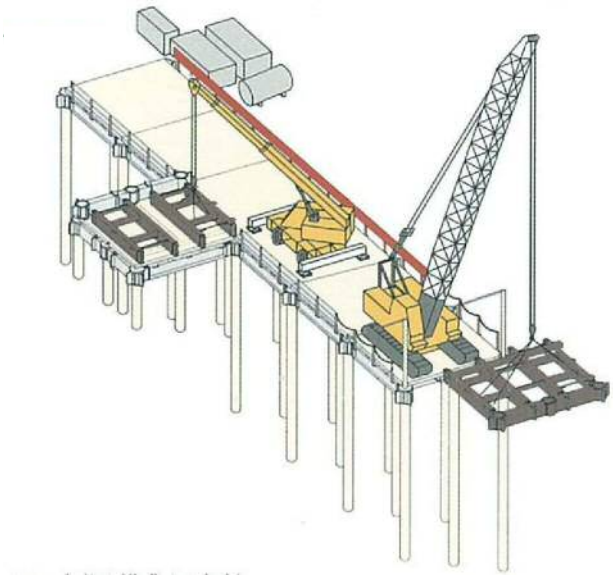

Figure 1. Temporary structure

2 Modeling and input waveform

The analysis model is presented in Figure 2. It is 54 m long and 6 m wide. It was installed over a valley. Therefore the length of the columns varies from 1 m to 16 m.

Nonlinear dynamic analysis was conducted and the time histories of stress and displacement were obtained. Acceleration recorded in the 2000 Tottori-ken Seibu earthquake was employed for this analysis. The software used in this analysis is SeamFEM [1].

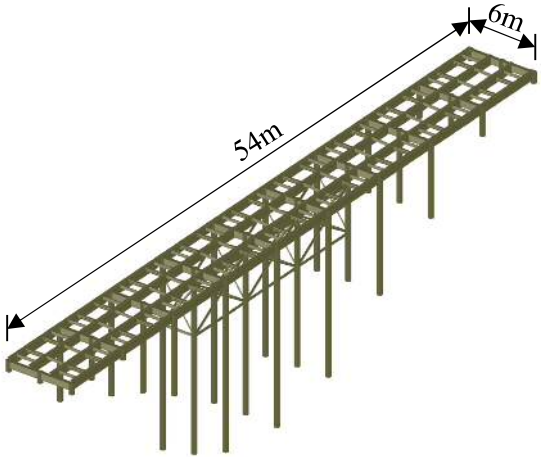

Figure 2. Analysis model

3 Analysis result

The induced stress is shown in Figure 3. This stress state is observed at the time of the maximum displacement occurrence when the seismic acceleration was applied in the lateral direction. The maximum displacement is 27 mm and its location is in the vicinity of the center of the main frame. The residual displacement is 0 mm. The maximum stress is 194 N/mm^2 at the lower end of the support pile near the center.

The above is for the completed temporary structure. In addition, the temporary structure under construction was also analyzed.

The maximum displacement occurred at the central part of the protruding portion. The value is 50 mm. The maximum stress of 133 N/mm^2 is observed in the main frame near the center.

It is noted that the displacement is less than 1/10 when the seismic acceleration is applied in the longitudinal direction.

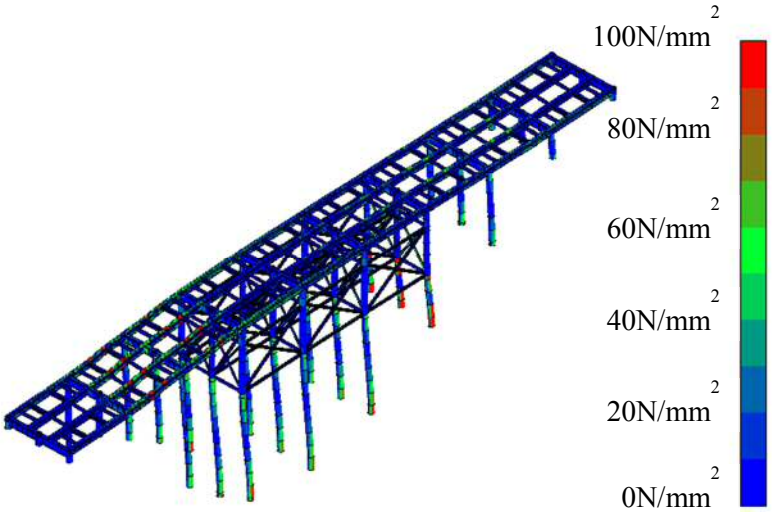

Figure 3. Stress contour diagram of the completed temporary pier model

4 Discussion and future tasks

The temporary structure could be subjected to twice larger displacement during its construction. This is because the rigidity is much smaller. Careful attention is therefore required during the construction of this structure.

The effect of the underground parts of the piles are not taken into account in the present study. This needs to be investigated in the future. Furthermore, the structure can be very different depending on the site conditions. The remaining task is therefore to provide information on the seismic performance of this temporary structure under various site conditions.

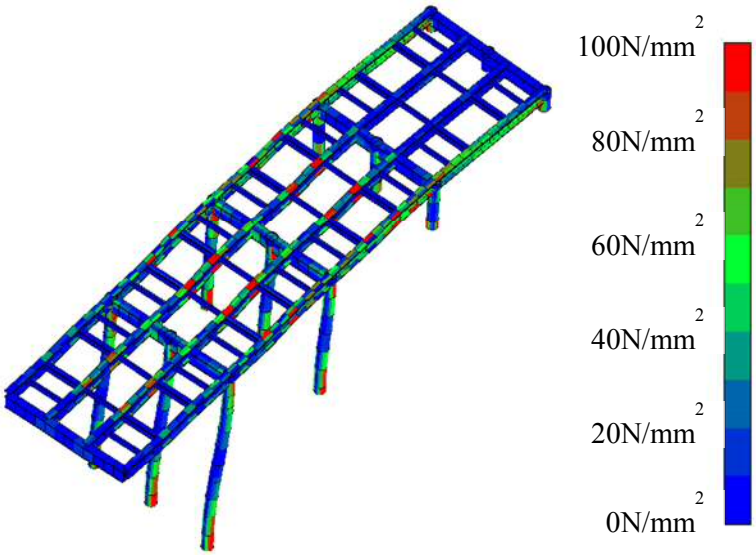

Figure 4. Stress contour diagram of the temporary pier model under construction

Reference

[1] Seismic Analysis Research Inc., SeamFEM, 2017.

Please choose: Oral/ Poster/ Either
Presentation session: Applied Engineering
Presenter name: Syahrim Azhan Ibrahim

Study of solar disturbance torque on CubeSats deployable solar panels

Syahrim Azhan, Ibrahim[1], Eiki, Yamaguchi[1]

[1]Department of Civil Engineering,
Kyushu Institute of Technology, 1-1 Sensui-cho, Tobata-ku, Kitakyushu-shi, Fukuoka, 804-8550, Japan

Email: [p595303a@mail.kyutech.jp]

Keywords
CubeSats, Deployable Solar Panels, Solar Radiation Torque, Low Earth Orbit

Introduction

For satellites in Low Earth Orbit (LEO), major sources of external disturbances that can perturb satellites motion are the gravity gradient, magnetic field, and aerodynamic drag. Solar radiation pressure can also cause significant disturbance torque for satellites with large surface areas. In the present, small satellites like CubeSat have begun carrying advanced missions that require high power that can be realized using deployable solar panels. However, higher area of solar arrays facing the sun would add up and change characteristics of the total external disturbances on the satellite.

The use of deployable solar panels on CubeSat can be based on the purpose to maximize solar power generation and to accomplish specific missions. A number of papers are available for the former application as in the following references [1–3] whereby novel solar panel configurations are designed and solar energy harnessing studies are made. For the latter, one example of a mission is a technology demonstration in manipulating the strong atmospheric drag at orbit below 500 km to achieve attitude stability [4,5]. The present study, on the other hand, will focus on solar radiation torque resulted from the increased area of solar cells on board the CubeSats. Two prominent deployable solar panel configurations are used for a defined reference mission for comparison purpose. Recognizing and including more precise disturbance impact that can influence satellites motion would be helpful when designing the attitude control system for CubeSats.

Methodology

For the present analysis, two 3-Unit sized CubeSat models with prominent deployable solar panels configurations as depicted in Figure 1 and Figure 2 are used. Model 1 has four deployable solar panels attached 90° at the short edges of the satellite body. Model 2 has its extendable solar panels angle deployed at fixed 30° angle with respect to the +z-axis of the satellite body. Solar cell and radiator surface properties are assigned accordingly to respective outer body parts. Both CubeSats are positioned at Local Vertical Local Horizontal coordinate frame with body vector towards nadir as shown in both figures.

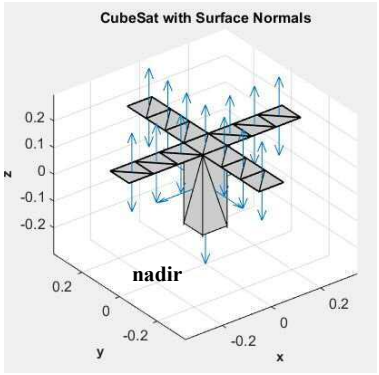

Figure 1: CubeSat Model 1

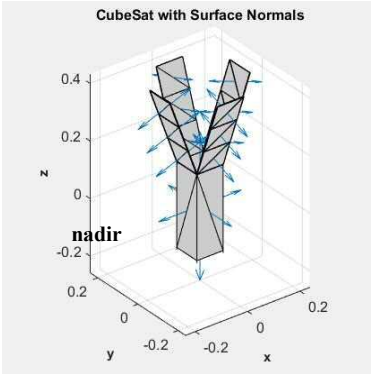

Figure 2: CubeSat Model 2

Disturbances computation is implemented using Princeton Satellite Systems MATLAB Toolbox [6]. Figure 3 shows the flow chart of the software program. In the first step, the CAD model is designed using patch function in MATLAB. In the second step, CubeSat properties which can be affected by external disturbances are defined. They are mass, the center of mass and optical surface properties. Disturbance parameters consist of environment information on solar radiation, magnetic dipole and aerodynamic drag are also defined to be included in their respective models. This information is then used in preselected orbital dynamics and rigid body dynamics equations.

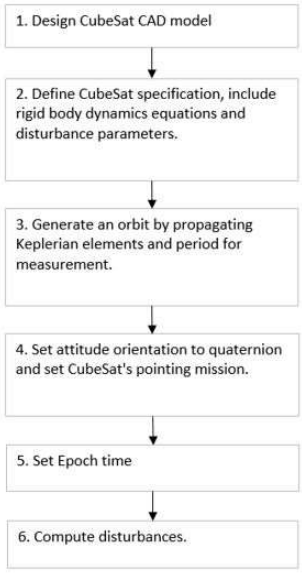

Figure 3: Flow chart of disturbances computation

Next, steps 3 to 5 consist of specific mission data for the CubeSat that are used to change the default equations in Step 2. So in this paper, the CubeSats' mission is as described in Methodology section before. Hence specific Keplerian elements, simulation time, pointing directions and the initial position of the CubeSats are specifically reprogrammed before computing the external disturbances. Disturbances are computed for each component on a body by body basis. Disturbances that are a function of the surface geometry are computed for each triangle that makes up the component meshes. Propagation of the orientation of the CubeSat is done with quaternions as they are much simpler and computationally more efficient.

Result and Discussion

A simulation was performed with orbital parameters as in Table 1. The CubeSats' orbit path is depicted in Figure 4. Solar radiation torque results on both models are shown in Figure 5. It can be seen that eclipse effects can be seen on the x and y-axes of Model 1 (see Figure 5-a). The effect can also be seen on z-axis of Model 2 (see Figure 5-b) but at magnitude level about 20 times lower. Hence, the deployable solar panels configuration of Model 2 minimizes the eclipse effect. However, this is actually at the expense of much lower power generation than Model 1 as proven in previous study [3].

TABLE I ORBITAL PARAMETERS

Orbit Altitude	400 km
Orbit Inclination	50°
Right Ascension of the Ascending Node (RAAN)	0°
Argument of Periapsis	0°
Eccentricity	0
Mean anomaly	0°
Simulation time	6 hours

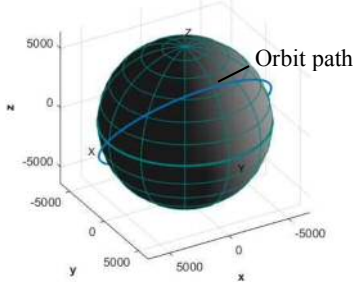

Figure 4: CubeSats' Orbit

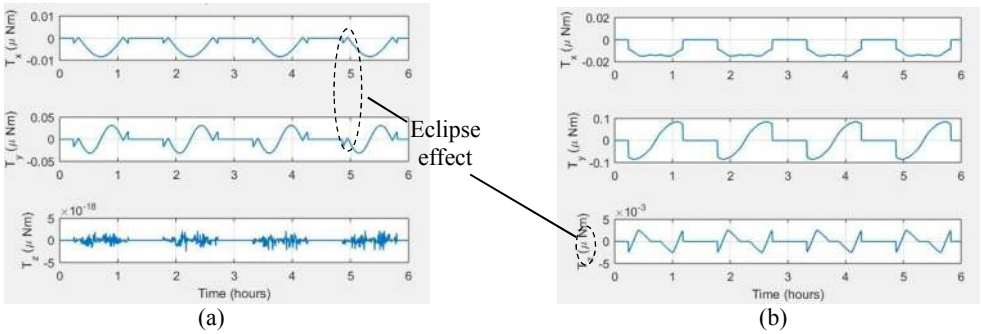

(a) (b)

Figure 4: Solar radiation torques of (a) Model 1 and (b) Model 2

References

[1] F. Santoni, F. Piergentili, S. Donati, M. Perelli, A. Negri, M. Marino, An innovative deployable solar panel system for Cubesats, (2014).

[2] W.J. Ubbels, A.K. Bonnema, Delfi-C3 : A student nanosatellite as a test-bed for thin film solar cells and wireless onboard communication, (2000).

[3] D. Young, J.W. Cutler, J. Mancewicz, A.J. Ridley, Maximizing photovoltaic power generation of a space-dart configured satellite, (2015).

[4] S.A. Rawashdeh, J.E. Lumpp, Aerodynamic stability for CubeSats at ISS orbit, (2013).

[5] J. Armstrong, C. Casey, G. Creamer, G. Dutchover, Pointing control for low altitude triple CubeSat space darts, (2009).

[6] http://www.psatellite.com/products/sct/ (accessed October 4, 2018).

Please choose: Oral
Presentation session: Applied Engineering
Presenter name: Takuya Amamoto

Influence of collision on mechanical behavior of steel girder

Takuya Amamoto[1], Eiki Yamaguchi[2], Naohiro Kaya[1]

[1]Graduate school of Engineering, Kyushu Institute of Technology, 1-1 Sensui-cho, Tobata-ku, Kitakyushu-shi, Fukuoka, 804-8550, Japan
[2] Ph.D., Graduate school of Engineering, Kyushu Institute of Technology, 1-1 Sensui-cho, Tobata-ku, Kitakyushu-shi, Fukuoka, 804-8550, Japan

Email: amamoto.takuya332@mail.kyutech.jp

Keywords : Steel Girder, Bridge, Collision, Damage, Load-Carrying Capacity

1. Introduction

An overpass bridge is damaged by collision of a truck running under the bridge occasionally. The steel girder is deformed by the collision, and it is required to evaluate the influence of the accident on the bridge to ensure the safety of traffic. However, the influence of the damages on the steel girder has not been investigated much and there is only a few research on collision damage in railway steel bridge. [1,2] Therefore, in this study, the load-carrying capacity of the damaged girder (*Fig.1.,2.*) is studied numerically so as to reveal the influence of the damage due to the collision on the mechanical behavior of steel girder. For this research analysis, ABAQUS [3] is used.

Fig.1. Damaged part

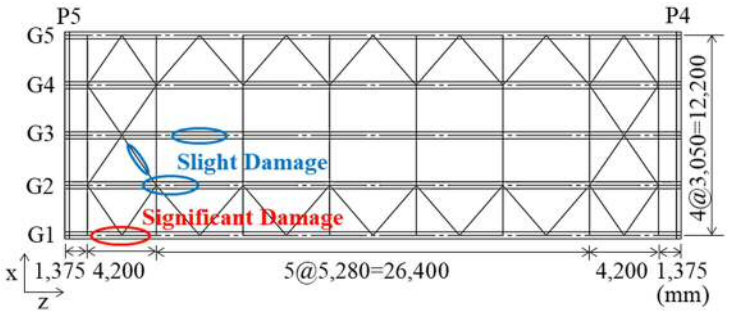

Fig.2. Overview of damaged bridge

2. Experiment

2-1. Overview of bridge

The overpass bridge across National Route 3 damaged by collision is a 37.8m long simple plate girder bridge. The superstructure consists of five steel girders, from G1 to G5, and a reinforced concrete slab. The main girder has vertical and horizontal stiffeners, lower lateral bracings and cross beams.

2-2. Damage

Three main girders, from G1 to G3, are found damaged. (*Fig.2.*) One of the three main girders has significant damage, which is G1 (*Fig.1.,2.*). The other two girders, G2 and G3, have slight damage. Therefore, G1 is the subject of this research. Typical collision damages observed in a steel girder bridge are follows; a lower flange is deformed in the vertical direction and/or in the horizontal direction; a web plate is bent; vertical stiffeners are buckled.

2-3. Collision load

To compare the mechanical behavior of the damaged girder with the undamaged girder by analysis, it is necessary to reproduce the analysis model of the damaged steel girder which has the deformation equivalent to actual residual deformation. For this reason, it is required to estimate the collision load for references to the damage marks and the residual displacement by the collision.

Shell elements are employed for all the members except for the lower lateral bracings that are modelled by beam elements. This analysis model does not reproduce the reinforced concrete slab. This bridge, however, is a composite girder bridge; hence, the upper flange is completely constrained at all nodes, and the girder is

simply supported. Also, it is necessary to consider the influence of G2 on the collision, and thus the cross beams and the lower lateral bracings are constrained at the locations of the connections with G2.

2-4. Influence of collision damage

To research the influence of the damage caused by the collision, the load-carrying capacity of the only G1 girder both the no damaged girder and the damaged girder given the deformation by using the collision load estimated by the nonlinear finite element analysis. The girder is simply supported. To prevent the steel girder from lateral buckling, the bridge-axial rectangular direction, the rotation around the vertical axis are constrained at the top of the girder. The load condition is shown in *Fig.3*.

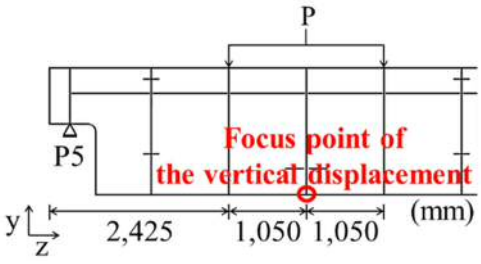

Fig.3. Loading condition

3. Result and Discussion

3-1. Collision load

The *Fig.4*. shows that the vertical displacement computed by ABAQUS are approximately equivalent in the measured deformation data. In addition, other residual displacements are similarly equivalent and vertical stiffeners also are buckled. Consequently, this damaged girder model on analysis can be reproduced.

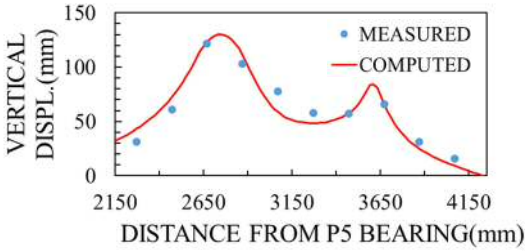

Fig.4.Vertical displacement of lower flange

3-2. Influence of Collision Damage

The numerical results in terms of the load P and the vertical displacement at the focus point of the vertical displacement (*Fig.3*.) are presented in *Fig.5*. The figure shows that the maximum load of the no damaged girder is found 1430.4kN and the damaged girder is found 1366.4kN. Therefore, the collision has reduced the load-carrying capacity of the main girder by about 4.5% and the stiffness by about 11.2%. As the result, it is found that the damage due to the collision have an effect on the steel girder. Nakayama et al. research [2] also shows that the load-carrying capacity of the steel girder having both the local deformations at a lower flange and the out-of-plane deformation of a web plate has reduced and the similar result is obtained. On the damaged girder, the steel yields at the lower part of the web plate by the collision. Therefore, it is considered that the stiffness of the damaged girder during the evaluation of the load-carrying capacity is lower than that of the no damaged girder. Although both the damaged girder and the no damaged girder occur local buckling at the upper flange, this failure mode is different from the actual bridge since the bridge is the composite girder bridge with a reinforced concrete slab as previously written. Consequently, it is possible to confirm the influence on the only one steel girder by the collision in this analysis; however, the influence on the composite girder bridge cannot be confirmed. Thus, in order to evaluate the safety of the actual bridge, it is necessary to consider how to reproduce the reinforced concrete slab. Moreover, in the future, it is necessary to examine the influence of the local deformation at the lower flange and the out-of-plane deformation of the web plate on the steel girder which has the damage by the collision, respectively.

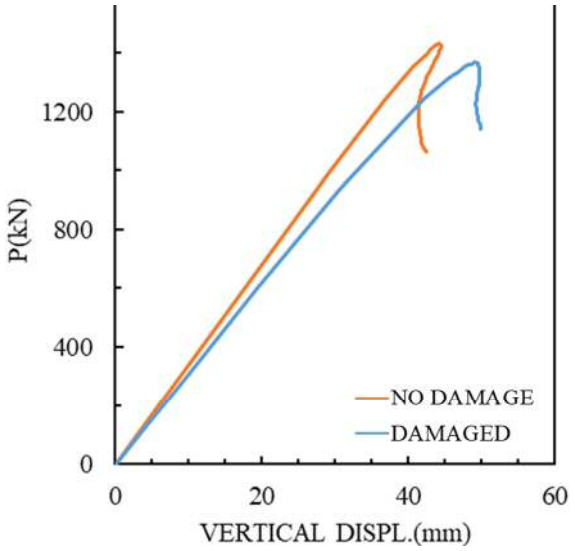

Fig.5. Vertical load-displacement relationship

References

[1] T.Nakayama, M.Kimura. et al. Residual load carrying capacities of riveted steel girders subjected to collision deformation, Structural Engineering, JSCE, Vol. 54A, pp.68-79 (2008).
[2] T.Nakayama, M.Kimura. et al. Study on index to reopen for service of steel railway bridges subjected to local damage due to collision of vehicles passing through, Journal of Japan Society of Civil Engineers, Ser.A, Vol.66, No.Ⅲ, pp.467-476 (2010).
[3] User's Manual, ABAQUS Ver.6.8, Dassault Systemes Simulia Corp. (2008).

Industrial Revolution 4.0: Are We Ready?

Dr. Manzoor Ahmed Hashmani

Abstract

Each Industrial Revolution (IR) improves the way we live, work and interact with each other using state of art technologies. IR-4.0 describes a future state of industry characterized thorough digitization of economic and production flows. The nine pillars of IR-4.0 are dependent on Big Data Analytics, Artificial Intelligence, Cloud Computing Technologies and Internet of Things (IoT). The core of this revolution is to improve the industries business processes through implementation of these technological advancements for achieving the aspiration of digital transformation.

The adaptation of IR 4.0 in current industries demands systematic migration of legacy systems (hardware, software) and employee skill development. Certainly, it is unendurable for industries to compete or sustain in upcoming markets without taking some serious action towards the implementation of IR 4.0. However, due to increase of demand for specialized skills personnel from industries, academia needs to revise their existing curriculum towards IR 4.0. In addition, research community also needs to further investigate possible threat and optimization techniques to securely and smoothly step into IR 4.0.

This talk discusses some major concerns for the industries, academia and research community to set up their directions towards IR 4.0.

The Mitigation of Concept Drift (Big Data) through Pre-Trained Deep Learning Networks

Syed Muslim Jameel[1,2] Manzoor Ahmed Hashmani[1,3], Hitham Alhussain[1,4]

[1] Universiti Teknologi PETRONAS, Sri Iskandar, Perak, Malaysia
[2]muslim_16000370@utp.edu.my, [3]manzoor.hashmani@utp.edu.my,
[4]seddig.alhussian@utp.edu.my

Industrial Revolution (IR) improves the way we live, work and interact with each other by using state of the art technologies. IR-4.0 describes a future state of industry which is characterized through the digitization of economic and production flows. The nine pillars of IR-4.0 are dependent on Big Data Analytics, Artificial Intelligence, Cloud Computing Technologies and Internet of Things (IoT). Image datasets are most valuable among other types of Big Data. Image Classification Models (ICM) are considered as an appropriate solution for Business Intelligence. However, due to complex image characteristics, one of the most critical issues encountered by the ICM is the Concept Drift (CD). Due to CD, ICM are not able to adapt and result in performance degradation in terms of accuracy. Therefore, ICM need better adaptability to avoid performance degradation during CD.

CD issue frequently takes place in the Online Supervise Learning (OSL) environment. In OSL environment, ICM is trained by image dataset to know the predictor features. The ultimate goal is to assign class labels to testing instances (we categorize images according to generic feature space in a unique class and train our ICM to classify different images accordingly). Starting from the hypothesis model, the aim is to maximize this model towards target function, so that ICM can predict the class of un-labelled images correctly. The training mood, being dependent on the environment in which ICM is deployed, can be batch, online or both. In batch learning, the best predictor, is generated after the training of entire image dataset at once. However, in online learning, the best predictor is generated once the model undergoes successive sequential training after the discretization of image data into sizeable chunks. Due to the non-stationary environment of online learning, the statistical properties of images may vary at different time step. For example, a set of class example has legitimate class labels at the onetime step and different labels at another time step (called as CD issue) which substantially decreases the performance in terms of accuracy in ICM. The change in features (among both time span) are due to various conditions. It could be due to the data format (variety), distribution (variability) or sources (complexity) which change over time. Another term for Concept Drift refers to the classification boundary or clustering centers that continuously change with time

elapsing [04]. In studies the term CD is modeled based on Bayesian decision theory for class output 'c' and input data 'X' as below.

$$P\left(\frac{c}{X}\right) = P(c)\, P\left(\frac{X}{c}\right) / P(X)$$

Where P(c/X), P(c), P(X/c) and P (X) are posterior, prior, conditional and feature based probabilities respectively. The possible conditions of Concept Drift arise P(c/X) undergo changes and causes the shift in class boundary or conditional probabilities (the number of classes increase), this type of Concept Drift is referred as Real Drift. Furthermore, if the P (X) (feature wise distribution of data changes) due to insufficient or partial feature representation of existing data distribution (new additional feature adds or some feature updates) called as Virtual Drift. However, Hybrid Drift as a conditions P(c/X) and P (X) occurred consequently. In literature, this problem of CD is tackle through below approaches;

1. Non-Adaptive Shallow Learning Approaches
2. Adaptive Shallow Learning Approaches
3. Non-Adaptive Deep Learning Approaches
4. Adaptive Deep Learning Approaches
5. Adaptive Hybrid Deep Learning Approaches

In this study, we examine some existing Shallow Learning, Deep Learning and Pre-Trained Deep Learning Networks, to identify their suitability or otherwise to overcome Concept Drift. From the results of the experiment of this study, we can safely state that the Image Classification model degrades their performance (in terms of accuracy) due to Concept Drift. However, the Hybrid drift causes more accuracy degradation then Real or Virtual Drift. Moreover, the complexity of image dataset also directly proportional to the accuracy degradation after Concept Drift (e.g. MNIST images accuracy degradation is less then CIFAR 10). Interestingly, in most of the experiments CNN model having better accuracy than others (because it is extracted not hand-crafted features). However, pre-trained network (ResNet-50) accuracy is better than CNN. **Therefore, through these experiments, we can conclude that to handle Concept Drift the Pre-Trained networks are a better solution. These networks are capable to train on new features through Transfer Learning. However, a dynamic adaptation approach (to train additional features during testing) is mandatory for Online Supervised Learning scenarios.** This contribution is providing a direction research community for handling CD through Pre-Trained networks, which will helpful towards the improvement in various practical applications areas of Business Intelligence which are relevant to IR-4.0 and TN50 (e.g., Automation Industry, Autonomous Vehicle, Expert Agriculture Systems, Intelligent Education System, and Healthcare etc.).

Oral/Poster (Either)
Presentation session:
Presenter name: Utkarsh Shashank

Enhancement of spin-orbit-torque by introducing S^+ impurities in Pt

U. Shashank[1], R. Medwal[2], S. Gupta[1,*], R. Nongzai[3], M. Bala[3], R. S. Rawat[2], K. Asokan[3], H. Asada[4], Y. Fukuma[1*]

[1]Kyushu Institute of Technology, Iizuka 820-8502, Japan
[2]National Institute of Education, Nanyang Technological University, Singapore 637616
[3]Inter-University Accelerator Center, New Delhi 110067, India
[4]Yamaguchi University, 2-16-1 Tokiwadai, Ube 755-8611, Japan
*Email: gupta@cse.kyutech.ac.jp, fukuma@cse.kyutech.ac.jp

Keywords (Spin orbit torque, ferromagnetic resonance, spin, charge)

Introduction

Efficient generation, transport and detection of spin current is crucial in spin-based technologies where spin current can be understood as flow of spin angular momentum without any physical flow of electric charge. In presence of strong spin-orbit interaction, a non-zero spin current is generated in perpendicular direction of applied charge current, known as spin Hall effect (SHE) is the widely studied technique. Various phenomena have been probed by spin current, such as control of magnetization by spin-transfer torque, possible transmission of electric signals through insulators and electric probing of insulator magnetization. Thus, to detect and utilize these spin-based phenomena, interconversion efficiency of spin $\leftrightarrow$ charge current (also known as spin Hall angle, SHA) need to be high. Finding new materials suitable for spin-to-charge conversion is indispensable and one of the popular methods to quantify the SHA is based on the studies of the broadband spin-torque ferromagnetic resonance (ST-FMR).

Experiment

In present work, we show that widely used heavy metal Pt become more efficient in spin-charge conversion through low energy 12keV S^+ ion implantations (5×10^{16} cm^{-2}). For ST-FMR measurement, an rf current was applied in longitudinal direction with in-plane external magnetic field H at an angle of 45° to the sample. This rf charge current generates both spin-orbit torque (due to SHE) as well as Oersted field (Ampere Law), and that drives the magnetization precession in top $Ni_{80}Fe_{20}$ layer. The precession

leads to oscillation of the resistance due to anisotropic magneto-resistance property of $Ni_{80}Fe_{20}$, which is measured as rectified voltage using a bias tee.

(a) **(b)**

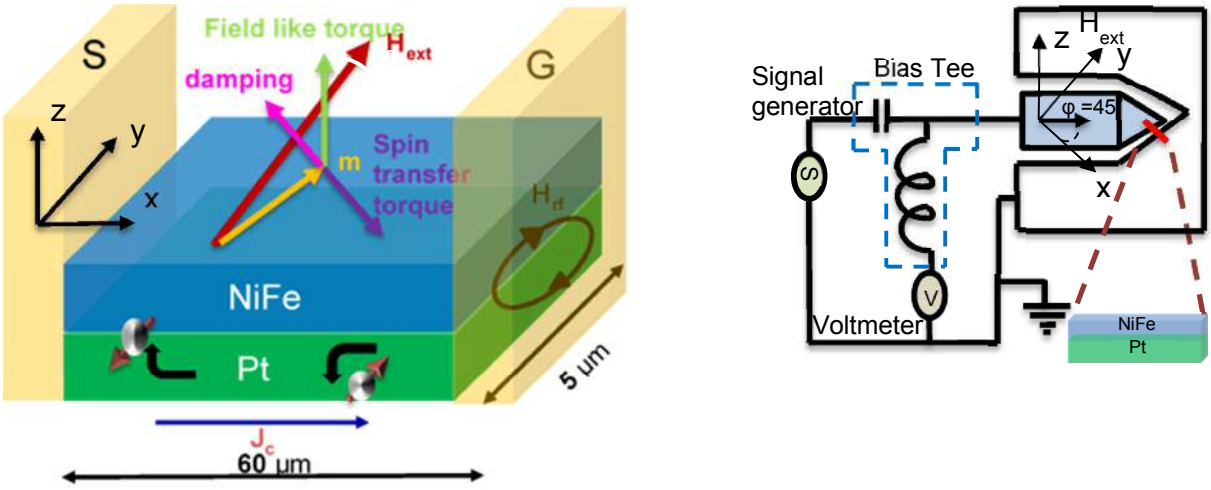

Fig 1: (a) Schematic of a Pt/NiFe bilayer thin film illustrating the spin transfer torque, field like torque and damping torque. ***θ*** denotes the angle between the magnetization m and the sample. H_{ext} is the applied external field. **(b)** Schematic circuit of the ST-FMR experiment.

Result and discussion

We notice a decrease in the ST-FMR signal in S^+ implanted Pt/ $Ni_{80}Fe_{20}$ compared to Pt/$Ni_{80}Fe_{20}$. This is due to the less amount of rf current flowing in the S^+ sample due to increase in electrical resistance. However, when we separate the symmetric (S) and antisymmetric (A) components from the ST-FMR signal, we observe the ratio of S/A is more in S^+ implanted Pt/ $Ni_{80}Fe_{20}$ indicating a higher charge to spin conversion. We observed three-fold increase in SHA from 10% to approx. 30% in S^+ implanted Pt. These results provide a way of engineering the conversion efficiency by controlled implantation.

Oral/Poster (Either)
Presentation session: Computer Science
Presenter name: Mohan John Rex

Micromagnetic Simulation study of Exchange interaction of off stoichiometric FePt/Pt bilayers

M. John Rex[1], R. Medwal[1,2*], S. Gupta[1] R. S. Rawat[2], S. Annapoorni$_3$, Y. Fukuma[1*]
[1]Kyushu Institute of Technology, Iizuka 820-8502, Japan
[2]National Institute of Education, Nanyang Technological University, Singapore 637616
[3]Department of Physics, University of Delhi 110007

*Email: rohit.medwal@nie.edu.sg, fukuma@cse.kyutech.ac.jp

Keywords Magnetic storage devices, HAMR, FePt, Micro magnetic Simulations, LLG

Introduction: Heat Dot Magnetic Recording (HDMR) is one of the possible candidate to improve the areal density after the upcoming technology of heated assisted recording media (HAMR) [1-3]. HDMR, combines the both bit patterning media (BPM) and HAMR, where, the ultra-small magnetic nanoparticle with strong perpendicular magnetic anisotropy were pattern to store the information. In, HDMR, bit writing process is done at a higher temperature 850 K above the curie temperature, where the anisotropy of the magnetic materials is almost negligible. To realized HDMR, L10-FePt, which is composed of alternating layers of Fe and Pt stacked along the [0 0 1] direction, is important because it has one of the largest anisotropy energy densities among all known magnetic nanomaterials (up to 4.5 MJ m−3) [4,5]. As synthesized FePt nanostructures are in are found to be in the disordered face centred cubic (fcc) A1 phase with the random occupancy of Fe and Pt in the A1 FePt unit cell. The disordered FePt, nanostructures can be converted into the magnetically hard ordered phase with large monocrystalline anisotropy. The annealing treatment perform to convert the disorder phase to ordered phase, sintering, and agglomeration of the as prepared FePt nanoparticles takes place, the particle sizes are enhanced [6,7] and the polydispersity in the sample also increases. Agglomeration reduces the interparticle distances, leading to a greater effect of interparticle interactions in the system. Considerations and careful tailoring of these interactions are essentials for high media performance as the size of individual grain (3-10 nm) is of the same order of the exchange length (4 nm). Micro magnetic simulations are predominantly used to bridge the gap between the theoretical predictions and experimental observations. It helps in understanding the underlying physical principles of experimental results. In this report we present a numerical Micro magnetic simulation for thin magnetic structures with FePt/Pt, designed based on our experimental work, to understand the effect of off stoichiometry elemental composition of Fe and Pt in FePt and interactions on the magneto-crystalline anisotropy.

Experiment: The off stoichiometry $Fe_{60}Pt_{40}$ alloy nanoparticles were synthesized by chemical co reduction method. The synthesized nanoparticles were drop casted on silicon substrate and platinized silicon substrate and subjected to thermal annealing at 400 °C to 750 °C. We investigated two systems (1) $Fe_{60}Pt_{40}$/Si and (2) $Fe_{60}Pt_{40}$/Pt/Si. The structural and magnetic phase transformation has been studied by X-ray diffraction and vibrating sample magnetometer. To further investigate the effect of interparticle exchange interaction on the

anisotropy, Micro magnetic Simulations were performed using the commercial Micro magnetic Simulator. The stimulated 3D model media design consists of volume 640 X 640 X 10 nm^3 with a mesh size is of 4 X 4 X 1 nm^3, which is approximately equal to the exchange length of FePt. To mimic irregular gran size, we have used media boundary condition with Voroni tessellation method. The external magnetic field was applied in the film normal direction and uniform Z direction initial magnetization was chosen. The simulations were carried by varying anisotropy constant and keeping fixed exchange length and vice versa.

Result and Discussion: XRD results of Fe60Pt40/Si and Fe60Pt40/Pt/Si systems clearly reveals the transformation of chemically disordered phase to ordered phase at 600 °C followed by magnetic phase transformation from A1 to L10 phase. In 750 °C annealed $Fe_{60}Pt_{40}$/Pt/Si, there mixed phase of A1 and L10 phase which clearly indicated the diffusion of Pt buffer layer into FePt layer. The magnetic behavior of two systems is shown in the figure 1 (i) and (ii). The samples annealed at 500 °C exhibit coercivity of 2.3 KOe. The simulated coercivity is larger than the experimental value. This is because, simulations do not consider the effects of defects, inhomogeneity present in real films as well as the thermal effect. However, the simulation provided same trend as the anisotropy value reduces the coercivity values also changed. The magnetic properties of $Fe_{60}Pt_{40}$/Pt/Si, showed that the coercivity reduction followed by anisotropy reduction caused by Pt diffusion into FePt layer. The coercivity value calculated from the simulation for only FePt layer structure is 4.3 KOe and $Fe_{60}Pt_{40}$/Pt/Si, structure is 3.5 KOe. This implies the reduction of coercivity values in soft hard layer is because of Pt.

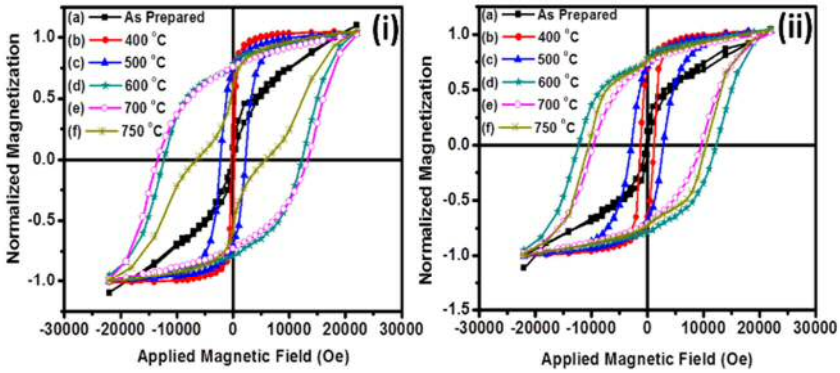

Fig 1: M-H loop of the (i) $Fe_{60}Pt_{40}$ and (ii) Pt/ $Fe_{60}Pt_{40}$

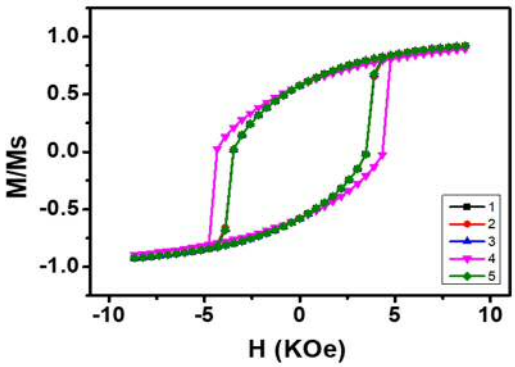

Fig 2: MH loop simulated by LLG micromagnetic simulator with anisotropy value of 4.5X 10^7 erg/cm^3

References:

1. Marinero E, et al. IEEE Trans. Magn., 49, 773, (2013).
2. Medwal R. IEEE magnetic letter, 9, 5504105 (2018).
3. Antoniak C, et al. Nature Comm., 2, 528, (2011).
4. Chen C T, et al. Phys. Rev. Lett., 75, pp. 152–155, (1995).
5. Kim C, et al. Appl. Phys. Lett., 91, 172508 (2007).
6. Medwal R, et al. J. Phys. D, Appl. Phys., 45, 055001 (2012).
7. Medwal R, et al. J. Nanopart. Res., 15, 1423 (2013).

Please choose: Oral
Presentation session: Applied Engineering
Presenter name: Abdallah Alsayed

Design and Fabrication Pinch Force Measurement Based on Strain Gauge for Post-Stroke Patients

[Abdallah, Alsayed], [Raja Mohd Kamil, Bin Raja Ahmad], [Hafiz Rashidi, Harun Ramli], [Azizan, As'arry]

Faculty of Engineering, University Putra Malaysia, 43400 UPM Serdang, Selangor, Malaysia

Email: eng.abdallah.2013@gmail.com

Hand strength is an indicative measurement of hand impairments.Traditionally, Fugl Meyer Upper Limb Assessment (FMA-UE) remains the primary clinical standard evaluation tool to measure pinch strength of post-stroke patients. However, the evaluation method performed by therapist is subjective and exposed to inter-rater reliability and intra-rater reliability. Recently, Force-sensing resistors were implemented to measure two fingers force, but it have drawbacks of nonlinearity, high hysteresis, and drifting over time. This paper presents a new design of pinch force measurement based on strain gauge as sensing element resulting in high linearity (0.0001%), low hysteresis error (0.5%), and low voltage drifting (20mV over 20 minutes).

Keyword: pinch, stroke, Fugl Meyer, strain gauge, finite element.

Introduction

Stroke is a blockage of blood supply to the brain that causes death to its tissue [1]. The motor cortex is often affected by a stroke that results in a lack of signal transmission to upper limb and lower limbs muscles [2, 3]. Hand strength is often impaired after stroke [4, 5]. This disability may cause limitations to motor control, hence limiting hand movements use for daily activities [6]. As the demands for quick hand fingers strength recovery is increasing, physical performance assessments are of importance in order to facilitate the rehabilitation interventions and monitor the progress of recovery [7, 8]. Clinically, the therapists evaluate the pinch strength performance using standard assessments such as FMA-UE, Action Research Arm Test (ARAT), and Wolf Motor Function Test (WMFT) [9]. FMA-UE remains the main instrument in research and in clinical practice to assess pinch strength impairment [10]. The primary focus of motor evaluation in FMA-UE for hand pinch grasp is to evaluate patient's ability to grasp an cylindrical object and exert enough strength against applied resistance [11].The therapist evaluates the pinch strength manually by exerting pulling force against hand grasp. However, this assessment is based on subjective observation [12, 13]. Moreover, its evaluation time is long [14].

Recently, researchers have implemented force-sensing resistors (FSR) sensors to measure fingers force exerted by patient [15]. The results have shown that severe to moderate stroke patients have difficulty in wearing the FSR sensors [16]. For that reason, clinicians do not encourage to use body-worn sensors for patients. Practically, FSR sensors are nonlinear and temperature dependent, exhibit large amounts of hysteresis, when dynamic forces are exerted on them, and also drift, when the application involves static forces [17]. Hence, researches have been conducted to understand FSR's behaviour and also at complementing their usage with appropriate electronic conditioning circuits and data processing techniques that could provide less complexity and less cost. On the other hand, strain gauge load cells provide high linearity, minimal hysteresis, and temperature independent [18]. Also, they are not body-worn sensors.
This paper presents a new apparatus to measure pinch strength based on Fugl Meyer assessment using strain gauge sensing. Thus, the patients do not require to either wear gloves or touch the sensor surface. Firstly, the design is simulated using finite element analysis. Then, the fabricated device is testing under experimental condition.

Design and Finite Element Analysis

Fig.1 shows hand pinching a cylindrical object as in FMA-UE. The therapist instructs the patient to grasp a cylindrical object (e.g. pen, pencil) by opposing the thumb and index finger tips around the cylindrical object. Once the object is retrieved, the therapist test hand pinching against resistance. The scoring is based on ability of patient to hold the cylindrical object and keeping it in place against resistance.

The pen, which is cylindrical object, is replaced by cylindrical copper object having a slot which allows the object to be deformed while fingers applied the force. The strain gauge resistance changes linearly according to the amount of object deformation. The strain gauge is positioned where the highest stress point. Finite element analysis (FEA) simulation is

used to predict the position of the maximum elastic stress while applying linear force at the pinching area. Fig. 2 shows the highest stress point and the position of pinching.

Fig. 1 Pinch Grasp as in FMA-UE

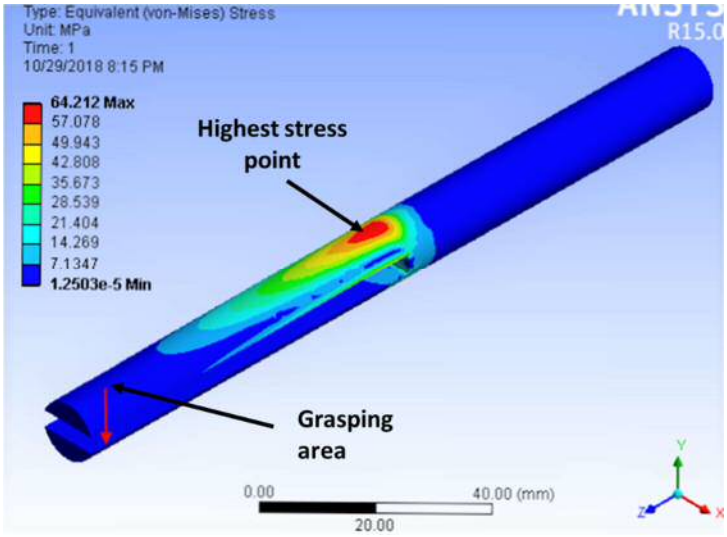

Fig. 2 FEA stress analysis

To measure small deformation, the strain gauge is connected to a full Wheatstone bridge through an amplifier (Wachendorff Strain Gauge Converter). The load cell (Pinch sensor) calibration is shown in Fig. 3. The compression and tensile universal testing actuator (INSTRON 3366) with dynamic force of 0 to 45N (loading) and 45N to 0N (unloading) is used during calibration. Synchronously, the readings of output voltage are recorded using Arduino microcontroller.

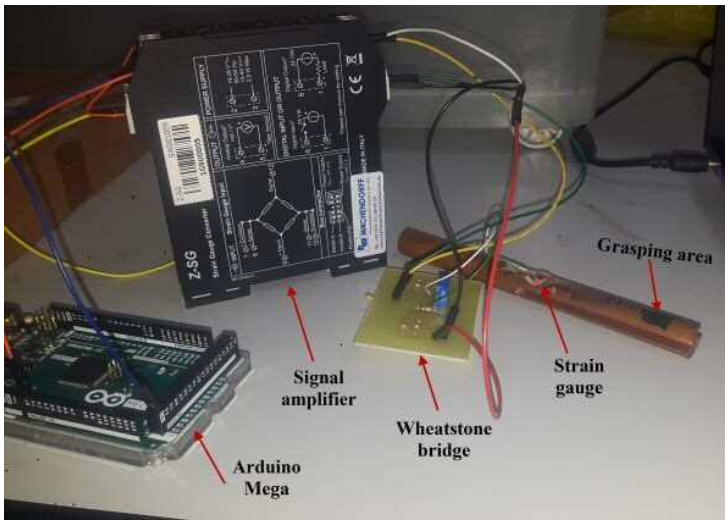

Fig. 3 Experimental Setup

Result and Discussion

FEA deformation analysis shows that the deformation of cylindrical object is linear (R^2 =1) to the applied dynamic force. The deformation is sensed by the change of strain gauge resistance. The results shows that the relation between strain gauge output voltage and force applied is linear. However, it may decrease due to electronic noises. In the lab, the cylindrical object was placed on the platform while vertical dynamic force was applied on the grasping area. The linearity error of strain gauge voltage output to force applied is 0.0001% and 0.0008% for loading and unloading respectively over the range of 0 to 45N with 0.05N increment (Fig. 4). The hysteresis error of loading and unloading is derived from the mean error of the loading and unloading curves which equals to 0.5%. The average voltage drift is 20 mV over 20 minutes. The drifting errors resulted from the noise of signal amplifying, wires, electronic components (e.g. resistors and capacitors), and power supply. The design meets the description of the pinching strength assessment. Further work will be involved to use linear actuator to apply the resistance replacing the therapist. Besides that, we will use the pinch strength measurement device to recruit volunteers in order to establish the baseline of force measurement.

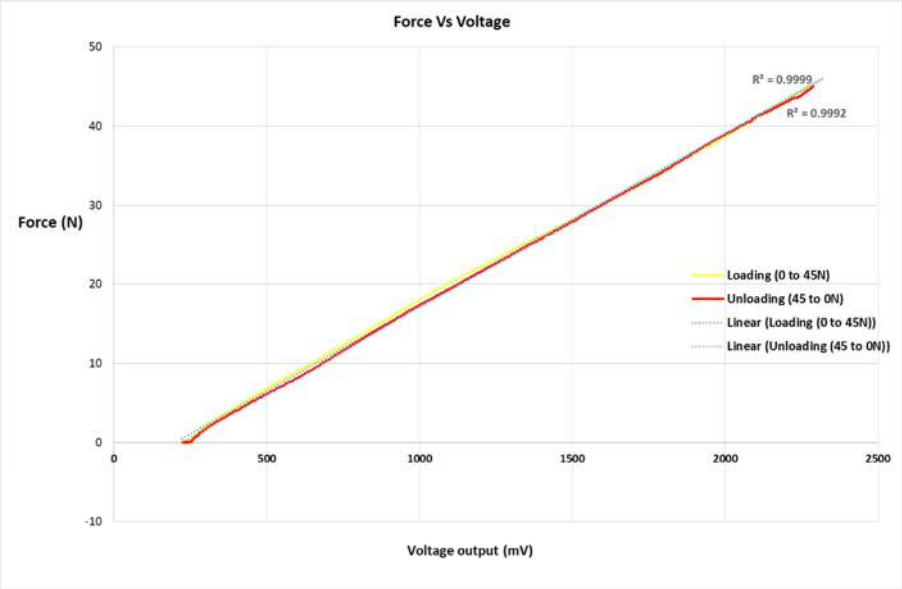

Fig. 4 Calibration results of loading and unloading

References

[1] C. W. Kooi, H. C. Peng, Z. A. Aziz, and I. Looi, "A review of stroke research in Malaysia from 2000-2014," Med J Malaysia, vol. 71, pp. 58-69, 2016.

[2] H. C. Persson, Upper extremity functioning during the first year after stroke. 2015.

[3] R. T. Pinzon and R. D. L. R. Sanyasi, "Complications as important predictors of disability in ischemic stroke," Universa Medicina, vol. 36, no. 3, pp. 197-204, 2017.

[4] K. Baker, L. Barrett, E. D. Playford, T. Aspden, A. Riazi, and J. Hobart, "Measuring arm function early after stroke: is the DASH good enough?," Journal of Neurology, Neurosurgery & Psychiatry, pp. jnnp-2015-310557, 2015.

[5] V. Repšaitė, A. Vainoras, K. Berškienė, D. Baltaduonienė, A. Daunoravičienė, and E. Sendžikaitė, "The effect of differential training-based occupational therapy on hand and arm function in patients after stroke: Results of the pilot study," Neurologia i neurochirurgia polska, vol. 49, no. 3, pp. 150-155, 2015.

[6] P. Raghavan, "The nature of hand motor impairment after stroke and its treatment," Current treatment options in cardiovascular medicine, vol. 9, no. 3, pp. 221-228, 2007.

[7] G. Kwakkel, B. J. Kollen, and H. I. Krebs, "Effects of robot-assisted therapy on upper limb recovery after stroke: a systematic review," Neurorehabilitation and neural repair, vol. 22, no. 2, pp. 111-121, 2008.

[8] C. E. Lang, M. D. Bland, R. R. Bailey, S. Y. Schaefer, and R. L. Birkenmeier, "Assessment of upper extremity impairment, function, and activity after stroke: foundations for clinical decision making," Journal of Hand Therapy, vol. 26, no. 2, pp. 104-115, 2013.

[9] G. M. Johansson, "Clinical and kinematic assessments of upper limb function in persons with post-stroke symptoms," Umeå universitet, 2015.

[10] W. W. Lee et al., "A smartphone-centric system for the range of motion assessment in stroke patients," IEEE journal of biomedical and health informatics, vol. 18, no. 6, pp. 1839-1847, 2014.
[11] J. W. Krakauer and S. T. Carmichael, Broken Movement: The Neurobiology of Motor Recovery After Stroke. MIT Press, 2017.
[12] L. Yu, D. Xiong, L. Guo, and J. Wang, "A remote quantitative Fugl-Meyer assessment framework for stroke patients based on wearable sensor networks," Computer methods and programs in biomedicine, vol. 128, pp. 100-110, 2016.
[13] J. H. van der Lee, H. Beckerman, G. J. Lankhorst, and L. M. Bouter, "The responsiveness of the Action Research Arm test and the Fugl-Meyer Assessment scale in chronic stroke patients," 2001.
[14] E. J. Woytowicz et al., "Determining levels of upper extremity movement impairment by applying a cluster analysis to the Fugl-Meyer assessment of the upper extremity in chronic stroke," Archives of physical medicine and rehabilitation, vol. 98, no. 3, pp. 456-462, 2017.
[15] P. Otten, J. Kim, and S. H. Son, "A framework to automate assessment of upper-limb motor function impairment: A feasibility study," Sensors, vol. 15, no. 8, pp. 20097-20114, 2015.
[16] S.-H. Lee, M. Song, and J. Kim, "Towards clinically relevant automatic assessment of upper-limb motor function impairment," in Biomedical and Health Informatics (BHI), 2016 IEEE-EMBS International Conference on, 2016, pp. 148-151: IEEE.
[17] E. R. Komi, J. R. Roberts, and S. Rothberg, "Evaluation of thin, flexible sensors for time-resolved grip force measurement," Proceedings of the Institution of Mechanical Engineers, Part C: Journal of Mechanical Engineering Science, vol. 221, no. 12, pp. 1687-1699, 2007.
[18] A. Matute, L. Paredes-Madrid, G. Moreno, F. Cárdenas, and C. A. Palacio, "A Novel and Inexpensive Approach for Force Sensing Based on FSR Piezocapacitance Aimed at Hysteresis Error Reduction," Journal of Sensors, vol. 2018, 2018.

Please choose: Oral
Presentation session: Engineering
Presenter name: Takayuki Okabe

A Discussion on Knowledge Systematization for Basic Design Support of Distribution Centers

Takayuki Okabe[1],Masanobu Umeda[1],Keiichi Katamine[1]
[1] Kyushu Institute of Technology, 680-4 Kawazu, Iizuka 820-8502, Japan

Email: p237203t@mail.kyutech.jp

Keywords (5 words)
Distribution center, Basic design, Design pattern, Design support, Knowledge Systematization

1. Introduction

Distribution centers (DCs) play an important role in adjusting the imbalance of supply and demand in supply chains, and high quality and high efficiency of logistics operations is required for DCs while severe requirements of retailers and manufactures are satisfied. Therefore, it is necessary for the design of DCs to optimally determine an operation architecture, equipment such as storages and carriers, and their layout according to the requirements, such as items, time, and a frequency of shipping. However, it is not easy to find an optimal solution while considering initial construction costs and daily operation costs because there are many combinations of possibilities, such as the types, the numbers, and layout methods of equipment. It is strongly required to support the design of DCs for increasingly complex logistics requirements.

In this paper, we propose design patterns of equipment, layouts, and operation methods in the basic design of DCs and a systematization method of domain knowledge about DCs, which focuses on attributes and relationships between them based on the design patterns. A knowledge base for the basic design support of DCs is also briefly described.

2. Overview of DC Operations and the Design of DCs

Fundamental operations in a DC are to inspect arrived items, once store them in the storage areas such as piece ball storage area, and then pick items from the storage areas upon request orders, assort them by shipping destination, and finally load them up delivery cars according to predetermined orders and loading methods[1].

Generally, DCs are designed through three steps, that is, outline design, basic design, and detailed design, and the designs are refined step by step. The basic design determines major specifications, which affect performance and costs, of a DC based on an operation architecture and a rough layout of operation areas determined in the outline design. Key performance indicators of the basic design are labor productivity which is the throughput per a worker, area productivity which is the throughput per unit area, and equipment operation productivity which is the throughput per equipment unit. This paper focuses on operation architecture design in the outline design and the basic design. In the following, these designs are collectively referred to as the basic design.

3. Knowledge Systematization of DCs

3.1 Design Pattern of DCs

There are many trade-offs which affect performance and costs of DCs in the basic design. For example, racks with high picking efficiency often occupy a large area. Therefore, if many such racks are used, the time required for picking items from the racks is shortened. On the other hand, travel time required for the picking is lengthened due to an increase in area for the picking. Because the basic design is a kind of combinatorial problems, it is difficult to find the most suitable combination of equipment, sizes, counts, and methods while considering trade-offs arising from the characteristics of equipment and methods. Therefore, a design pattern approach was proposed for this combinatorial problem[1]. The proposed method determines an operation architecture and mechanism from design patterns based on the numbers of item types and shipping containers in requirements. It is, however, insufficient for the basic design because specific patterns of equipment, layouts, and operation methods are not discussed.

This paper extends the design patterns to types of equipment, layouts, and various methods more specifically. The design patterns introduced in this paper include picking methods, layouts of storage areas, allocations of items to storage areas, storage methods of items, layouts of aisles, and transport methods.

3.2 Modeling of Domain Knowledge of DCs

DCs and related concepts can be characterized by attributes, and there are often natural, physical, or causal dependencies among these attributes. For example, a total travel time required for picking items is determined from the average of walking speeds of workers and the total distance walked. Relationships between these attributes are referred to as attribute dependency, and the total travel time and the average of walking speeds are expressly called superior and inferior attributes, respectively.

Domain knowledge of DCs is systematized by focusing on attributes and relationships between attributes and represents relationships as attribute dependency graphs. Because parts of the relationships regarding the basic design of DCs vary according to the design patterns, the attribute dependency graphs are organized by the design patterns. As an example, the attribute dependency graph for the labor productivity in the case of total-picking system, which picks items delivered to different shipping destination at once and assorts later, is shown in Fig.1. The graph indicates that the labor productivity is determined from the total processing time and the total shipments, and the total processing time is determined from the total travel time and the total picking time.

4. Design and Implementation of Knowledge Base for DCs Design

A knowledge base for supporting the basic design of DCs was designed according to the systematized knowledge and implemented in the knowledge representation language DSP[2]. Fig.2 shows a data-flow diagram of the basic design module for a DC.

For given stocked items, ordered items, and rough area sizes, the module first assumes design patterns in (1), and then designs piece ball storage areas according to the patterns by assuming the types, numbers, and layouts of equipment in (2). The module also designs assorting areas by assuming the numbers and layouts of equipment in (3). Performance indicators such as the labor productivity are calculated for assumed design plans in (4).

The knowledge base was applied to an example of a DC for convenience stores. The experiments showed that multiple basic design results of a DC were obtained and could be compared with one another.

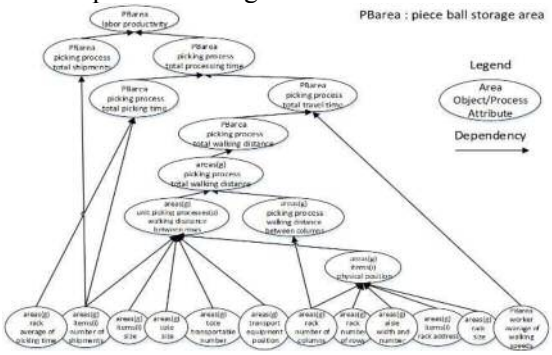

Fig.1 Attribute dependency graph for labor productivity of a DC

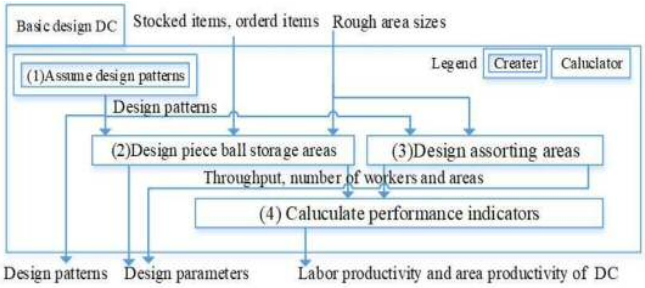

Fig.2 Data-flow diagram of the basic design module

5. Conclusion

This paper proposed a knowledge systematization method for supporting the basic design of DCs. A knowledge base for basic design of a DC was developed according to the systematized knowledge, and experiments using the knowledge base showed that different design plans could be compared with one other. Some of the design patterns have not been implemented yet, and the extension of the knowledge base is left for future work.

Reference

[1] T. Eguchi, S. Hashimoto, M. Hashimoto, I. Nagasawa, C. Takizawa, M. Umeda, K. Katamine, "Modeling and Design Method of Warehouse Operation -Design Pattern Based Method-," IEICE Technical Report, Vol.107, No.331, pp.55-60, 2007.

[2] M. Umeda, I. Nagasawa, and T. Higuchi, "The elements of programming style in design calculations," In Proceedings of the Ninth International Conference on Industrial and Engineering Applications of Artificial Intelligence and Expert Systems, pp.77–86, 1996.

Please choose: Oral
Presentation session: Engineering
Presenter name: Kosei Ueno

Design and Implementation of Operation Management Support System for Shared Vehicles in a Large University Campus

K. Ueno[1], M. Umeda [1], K. Katamine [1], Shaiful J. Hashim[2], Syed Al-Haddad[2]
Rusli Abdullah[3], Khaironi Y. Sharif[3]
[1] 1Department of Creative Informatics, Graduate School of Computer Science and Systems Engineering,
Kyushu Institute of Technology, 680-4 Kawazu, Iizuka 820-8502, Japan
[2] Universiti Putra Malaysia, 43400 UPM Serdang, Selangor, Malaysia.
[3]Information Technology, Universiti Putra Malaysia, 43400 UPM Serdang, Selangor, Malaysia.

Email: k.ueno@cad.ci.kyutech.ac.jp

Keywords (5 words)
Car sharing, Booking management, State management, Operation management

1. Introduction

Instead of owning a car individually, sharing cars in a community is attracting attention from the viewpoint of economic efficiency and natural environment protection [1]. For example, it is planned to share a small number of vehicles among many people in a large campus of Universiti Putra Malaysia. However, it is not easy to operate a limited number of vehicles without decreasing user convenience and the usage efficiency of vehicles. That is, it is necessary to pay attention to user convenience so that vehicles are available when requested, consider operation efficiency of vehicles by reducing spare time of vehicles, introduce a simple and safe key management system because the management of physical keys is often troublesome, and pay attention to the security of vehicle usage because normal operation must be affected by unauthorized use of vehicles or rule violation in use. Therefore, a framework for supporting operation management which also takes account of the characteristics of a society and local communities is required.

In this research, we have been developing an operation management support system of shared vehicles for the university campus to solve common issues of sharing a small number of vehicles in a large community. This paper describes the design and implementation of the operation management support system.

2. Booking and State Management of Vehicles

2.1 Booking Management

If a booking is fixed at a certain time by a reservation, a vehicle must be available at a starting point by the start time of the reservation. If a vehicle is restrained at a start point when a booking is fixed, user convenience and operation efficiency may decrease because inactive time of a vehicle occurs. The following two booking management methods are proposed for this issue.

Time Frame-based Booking This method divides an available time of a day into a set of short time frames and allows to book only the next time frame at a current time.

Constraint Satisfaction-based Booking This method introduces two booking states: fixed and temporary, and allows any temporary bookings which may affect fixed bookings. Temporary bookings are fixed at once when a new booking request counteracts the influence of temporary bookings to fixed bookings.

2.2 State Management

It is necessary to manage detailed state such as the location of a vehicle in order to provide high quality and safe service of shared vehicles to the users. For example, if a running vehicle encounters troubles such as malfunction of a vehicle, or rule violation such as going of a designated route, the operation of shared vehicle service may be affected. In order to cope with such problems, the state of a vehicle must be

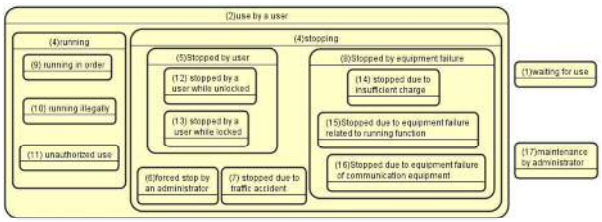

Fig.1 State machine diagram of a vehicle

managed precisely as shown in Fig. 1.

The state of a vehicle consists of twelve states, such as waiting for use, forced stop by an administrator, stopped due to traffic accident, running in order, running illegally, unauthorized use, stopped by a user while unlocked, stopped by a user while locked, and stopped due to insufficient battery charge.

3 Design and Implementation of Operation Management Support System

3.1 System Overview

A prototype of the operation management support system implements the time frame-based booking. The configuration of the system is shown in Fig.2. The system provides two user interfaces: a client application running on smart phones for users and a web application for administrators. The former provides functions for the shared vehicle services such as booking and digital keys while the latter provides functions for administration of vehicles.

The vehicle operation management database stores the information about users, vehicles, and booking. The data manager consistently manages the data stored in the database. The operation manager realizes the operation management service using the database through the data manager. The app façade and web facade provide the operation management functions through the operation manager. The client API provides an abstract programming interface to the operation management functions realized in the server side for the client application.

3.2 Data Model for Operation Management Support

The data model represented in UML classes is shown in Fig. 3. The classes of the data model are User, Booking, Route, Location, Vehicle, RidingState, VehicleState, and VehicleLog. User class represents personal information of users and administrators and has attributes such as *name* and *id_number*. Booking class represents reservation information of vehicles and has attributes such as *start_time*, *end_time,* and *route*. Route class represents predefined routes and has attributes such as *start_ location* and *end_location*. Location class represents locations get on and off and has attributes such as *latitude* and *longitude*. Vehicle class represents fundamental information of a vehicle and has attributes such as *id_number*. RidingState represents actual usage records of users and has attributes such as *vehicle*, *start_time, end_time, and route*. VehicleState represents states of vehicles, and VehicleLog represents actual usage records of vehicles.

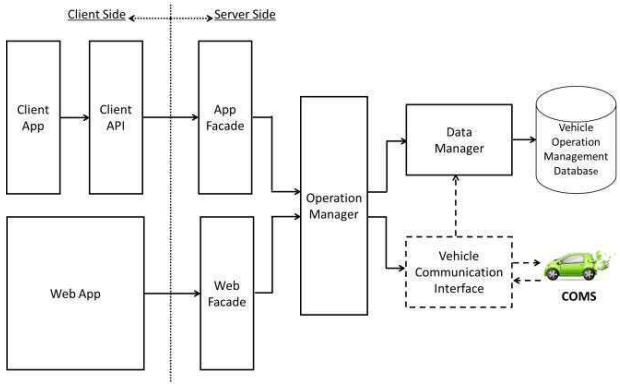

Fig.2 System configuration of the operation management support system

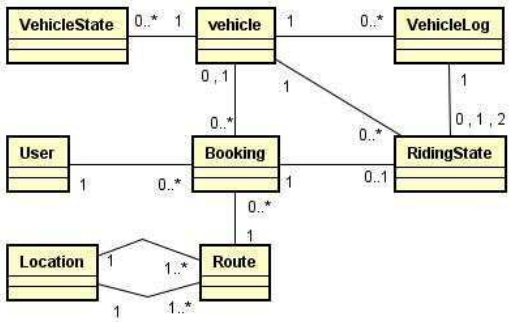

Fig.3 Data model for operation management

4 Conclusions and Future Work

This paper described the design and implementation of the operation management support system for sharing a small number of vehicles among many people in a large university campus. The time frame-based and constraint satisfaction-based booking methods are proposed. The precise state management of vehicles for high quality and safe services is also discussed. The field evaluation of the system in Universiti Putra Malaysia is left for future work.

References

[1] Ayako Taniguchi, ”Introduction for development of Car sharing system on University of Tsukuba“, Proceedings of infrastructure planning , Vol.42, P33, 2010.

Presentation session: Engineering
Presentation: Oral
Presenter name: Shaiful Jahari Hashim

Toward Optimization of One-Way EV Carsharing System in University Campus

Omar S. Abahussen[1], Shaiful J. Hashim[1], Syed. A. R. Al-Haddad[1], Nasri Sulaiman[1], Raja Kamil[1], Fakhrul Z. Rokhani[1], Siti M. Shafie[1], Rusli Abdullah[2], Khaironi Y. Sharif[2], M. Umeda [3], K. Katamine [3],

[1]Faculty of Engineering, Universiti Putra Malaysia, 43400 UPM Serdang, Selangor, Malaysia.

[2]Faculty of Computer Science and Information Technology, Universiti Putra Malaysia, 43400 UPM Serdang, Selangor, Malaysia.

[3]Department of Creative Informatics, Graduate School of Computer Science and Systems Engineering, Kyushu Institute of Technology, 680-4 Kawazu, Iizuka 820-8502, Japan

Email: sjh@upm.edu.my

Abstract

This paper presents the optimization of one-way electric vehicle (EV) carsharing system in university campus. The area that has been chosen is Universiti Putra Malaysia (UPM) campus located in Serdang, Malaysia. Two main objectives are needed to be optimized namely the quality of service (QoS) and the cost. The most crowded spots are easy to select because they are close to the faculties' buildings thus the locations of the stations have been placed accordingly. The simulation model is responsible on generating the demands based on different times and locations with the Non-equal Distributed Demand (NEDD) and the Equal Distributed Demand (EDD) scenarios. The multi-objective optimization is performed using heterogeneous NSGA-II with simulation parameters threshold variations across stations for cars' battery charging level and relocation threshold. Simulation of homogeneous NSGA-II technique, however, only support fixed threshold across stations. The unserved demand for heterogeneous NSGA-II is only around 10% while for the homogeneous NSGA-II the unserved demand can be as high as 30% for NEDD. However, for EDD scenario both heterogeneous and homogeneous NSGA-II have approximately similar results. Furthermore, heterogeneous NSGA-II also has lowered the cost to nearly double for both NEDD and EDD scenario over homogeneous NSGA-II.

Keywords*: simulation , optimization, carsharing , EV, genetic algorithm, one-way.*

1 Introduction

Carsharing system is classified into one-way or two-way based on the type of journeys. For two-way journey, the car can be used and booked until the users return from their destinations, while for one-way carsharing the car will be booked only during the initial journey from the source to destination. A further classification is flexible ("free-floating") or restricted ("non-floating") based on the parking space allowance. For the former, users can park their car as they wish inside the campus while the latter has restricted parking only inside the designated area or parking spaces. In the "free-floating" models, normally it is not possible to make a reservation, whereas in the "non-floating" approach, one-way trip is guaranteed upon vehicle reservation. Generally, majority of the non-floating systems of the one-way carsharing operation works with partial reservations without provision for destination parking space reservation. This is due to more planning is required for full reservation to be made available toward a better service delivery and customer satisfaction.

In most cases, large environment or cities are considered in the existing carsharing systems in literature. In this study, carsharing system design for small scale environment in university campus has been addressed with customized features that generate demands between sources and destination similar to the large scale systems. For small scale type of environments like university or company campus demands generation is related to working scenario which makes it possible to include some assumptions in the carsharing system. These assumptions make it more efficient from the perspective of serving time, cost, and balance of vehicles. This study is addressing the problem of one-way EV carsharing system for UPM university campus for the total area around 1000 hectares, with 25 stations representing faculties and institutes and estimated 20,000 persons population of potential users.

2 EV Carsharing Simulation Measures

The measure that has been generated is the percentage of the number of unserved demand over the total number of generated demand with respect to time. It can be observed from Figure 2 that heterogeneous Non-dominated Sorting Genetic Algorithm (NSGA-II) multi-objective optimization has achieved better performance than the benchmark of homogeneous NSGA-II for Non-equal Distributed Demand (NEDD). During steady-state the different in percentage of the unserved demand for the homogeneous NSGA-II can be as high as 30% compared to only 10% for heterogeneous NSGA-II. Both approaches, however, have achieved around 20% of unserved demand for Equal Distributed Demand (EDD). From Figure 2 heterogeneous NSGA-II has lowered the cost to nearly double for both Non-equal Distributed Demand (NEDD) and Equal Distributed Demand (EDD) scenarios over homogeneous NSGA-II multi-objective optimization.

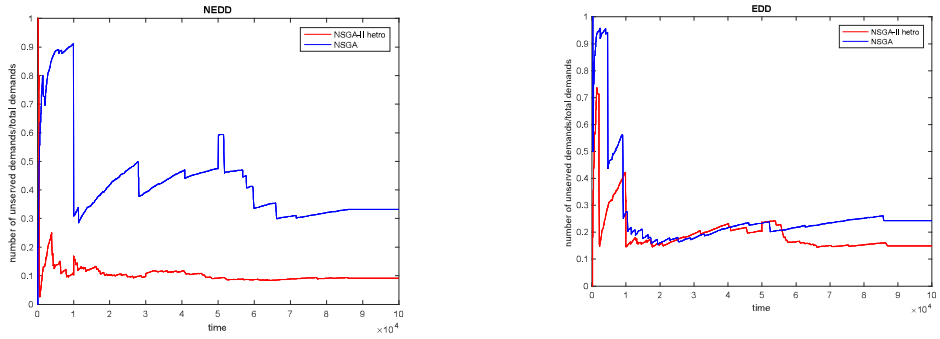

(a) (b)

Figure 2: Demand Percentage for NSGA-II and NSGA-II Heterogeneous of NEDD (a) and EDD (b)

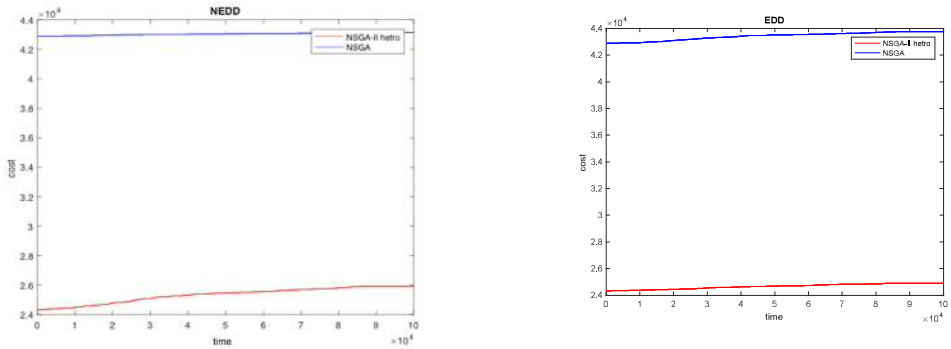

(a) (b)

Figure 2: Cost for NSGA-II and NSGA-II Heterogeneous of NEDD (a) and EDD (b)

Oral
Presentation session: Computer science
Presenter name: Md. Mamunur Rashid

Title: A Coupled Feedback Oscillatory Model Provides a Robust and Entrainable Oscillator

Md. Rashid[1], ABM Hasan[2], Yuka Umezaki[3], Hiroyuki Kurata[3]
[1,3]Department of Bioscience and Bioinformatics, Kyushu Institute of technology, Iizuka, Fukuoka, Japan
[2]University de Montreal, Montreal, Canada
Email: rashid.md-mamunur327@mail.kyutech.jp

Keywords: Circadian rhythm, Coupled feedback oscillator, Robustness, Entrainability and Phase shift curve

1. Introduction

Oscillatory rhythms are generated at the cellular level to maintain their 24-h variation in behavior and physiological activities. Many studies have been conducted to confirm the molecular mechanisms by which the circadian clock produces sustained oscillation, and recognized that coupled transcription-translation feedback loops form the core of this network in many organisms[1]. In general, several types of feedback loop are suggested to affect the robustness and entrainability of circadian rhythms. To uncover the mechanism by which such a coupled feedback molecular network produces robustness to dynamic environment, we quantify the robustness of phase, period and amplitude by activator coupled feedback oscillator (ACO) that belong to drosophila circadian clock[1,3] and repressor coupled feedback oscillator (RCO-proposed). Therefore, to examine the global properties of both feedback models, all plausible kinetic parameter estimates that generate sustained circadian oscillations are searched to characterize their oscillatory features. To efficiently investigate the robustness, we used parameter random perturbations and stochastic simulation. Using kinetic symmetry, our findings first show that RCO provides most robust oscillators with respect to phase and amplitude to parameter random perturbations and molecular noise, while ACO easily generate anti-phase trajectory and both model produces robust period. We also show that both ACO and RCO readily entrains to a wide range of master clock cycles.

2. Method and Results

2.1 Biochemical network and System analysis

To understand how coupled feedback oscillators, generate robust oscillations, we developed two coupled feedback oscillators, ACO and RCO model where, two delay induced feedback oscillators mutually activated or repressed, as shown in Fig.1. The wiring diagram in Fig.1 shows coupled feedback oscillators biochemical network and their corresponding DDEs. Symmetry kinetics value for both models are as bellow: n=2, b=0.1, $\tau_1=\tau_2=\tau_3=\tau_4=5$, $k_1=k_2=10$, $Kb_1=Kb_2=Kb_3=Kb_4=1$, $kd_1=kd_2=0.96$(ACO) & 1.1(RCO). Where n: hill coefficients, b: leaky expression, τ: time delay, k& kd: synthesis and degradation rate kinetics, Kb: critical threshold values responsible for activation and repression. For comparison between ACO and RCO, we compute a mathematical analysis for robustness via parameter random perturbations using deterministic models[2] and stochastic simulation by modified Gillespie algorithm[4,5]. Additionally, we also clarify the entrainability of ACO and RCO model. All the computational analysis was carried out through MATLAB software R2017b.

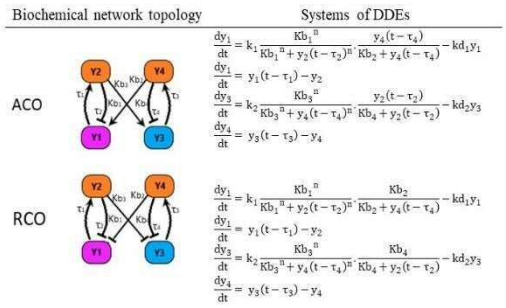

Fig.1: Biochemical network for coupled feedback oscillators and

2.2 Sensitivity Analysis

The robustness is an important charecteristics of a circadian rhythm to parameter uncertainity, including external and internal variations and molecular noise. Along with Period and amplitude of the rhythm, phase is a key characteristic of biological oscillators. Sensitivity is computed by parameter random perturbations and stochastic simulations to charecterize the mechanism of how coupled feedback loops generate robust properties to parameter fluctuations. Stochastic simulations was computed by delay induced modified gillespie algorithm. For the purpose of parameter random perturbations, we assume that all parameters corresponding to rate kinetics follows normal distributions with mean μ, defined as the symmetric parameter values and standard deviation σ, defined as .08μ. This implies that random perturbations of each parameter lying within $\mu \pm 0.24\mu$ are included in approximately 99.7% of the normal distribution. A total of 4000 runs for both, parameter random perturbations and stochastic simulations of each models are made to

verify the sensitivity of period, amplitude and phase movement as shown in Fig.2. We found that, it is very hard to change the phase of RCO (Fig.2(D)) in response to external and internal variations, while ACO easily generate anti-phase oscillations,Fig.2(A). In order of insensitivity RCO and ACO shows robust period in the sense that most period approximately 72% of all random perturbations lie within 24 ± 0.5 hours while the period default value is 24 hours. RCO model also shows robust amplitude in the sense that most amplitude approximately 74% of all perturbations lie within 8.05±0.8 while the default value is 8.04 on the other hand, ACO shows approximately 66% of all perturbations lie within 9.20 ± 1 while the default value is 0.89.

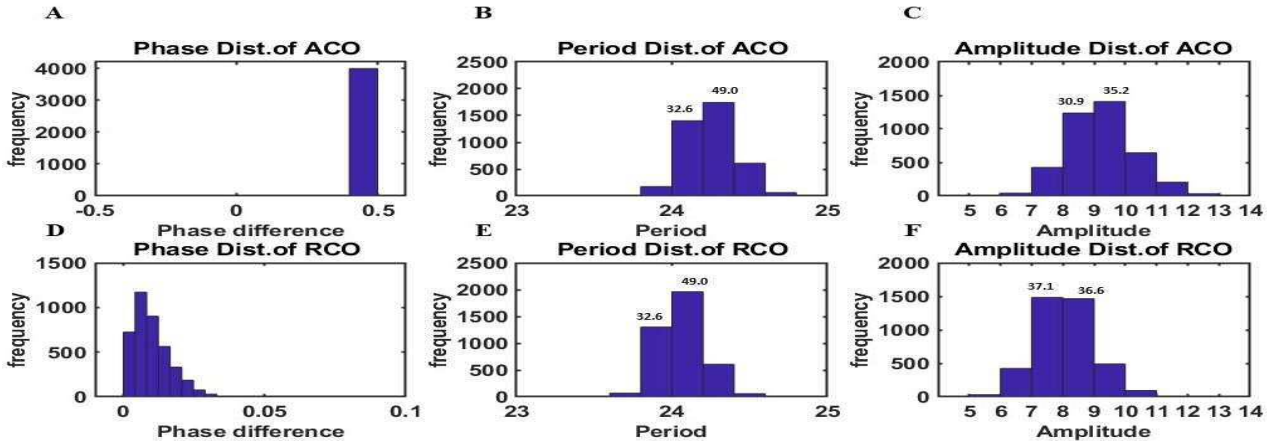

Fig.2: Phase, Period and Amplitude distributions to parameter random perturbations

In natural conditions living organisms are subject to the alternation of day and night and hence must undergo a periodic LD cycle. For adapting to such a cyclical environment a proper entrainment of the circadian clocks required. Here we find that both ACO and RCO shows period entrainability in a certain range with master clock cycles as shown in Fig.3.

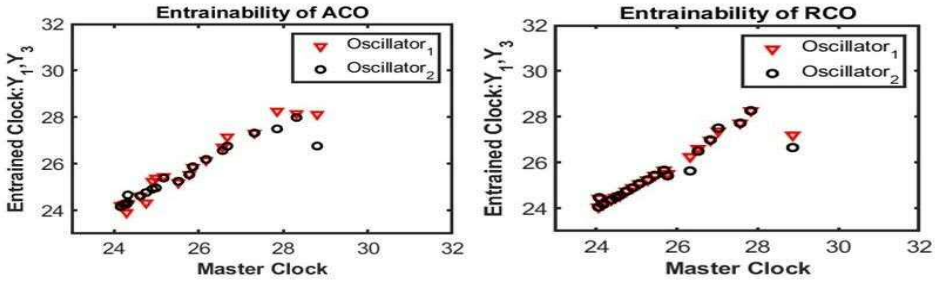

Fig.3: Entrainability

3. Discussion

To understand how coupled feedback oscillators generating robust oscillations in the cellular level, we performed a mathematical analysis of two deterministic and stochastic models in terms of robustness to parameter random perturbations and molecular noises. One is the activator coupled oscillator and the other is repressor coupled oscillator (proposed) model. We found that RCO is robust in phase and amplitude to parameter random perturbations and molecular noises.

4. References

[1]. Ueda, H.R., Hagiwara, M. and Kitano, H., 2001. Robust oscillations within the interlocked feedback model of Drosophila circadian rhythm. Journal of theoretical biology, 210(4), pp.401-406.
[2]. Caicedo-Casso, A., Kang, H.W., Lim, S. and Hong, C.I., 2015. Robustness and period sensitivity analysis of minimal models for biochemical oscillators. Scientific reports, 5, p.13161.
[3]. Cheng, Ping, Yuhong Yang, and Yi Liu. "Interlocked feedback loops contribute to the robustness of the Neurospora circadian clock." Proceedings of the National Academy of Sciences98.13 (2001): 7408-7413.
[4]. Gillespie, Daniel T. "Exact stochastic simulation of coupled chemical reactions." The journal of physical chemistry 81.25 (1977): 2340-2361.
[5]. Barrio, Manuel, et al. "Oscillatory regulation of Hes1: discrete stochastic delay modelling and simulation." PLoS computational biology 2.9 (2006): e117.

Oral

Presentation session: Computer Science

Presenter name: Mst Shamima Khatun

[Title: A Machine Learning Approach for the Identification of Autoimmunity Peptides]

[Khatun, Mst Shamima][1], [Hasan, Md Mehedi],[1] [Kurata, Hiroyuki][1,2]

[1]Department of Bioscience and Bioinformatics, Kyushu Institute of Technology, 680-4 Kawazu, Iizuka, Fukuoka 820-8502, Japan.

[2]Biomedical Informatics R&D Center, Kyushu Institute of Technology, 680-4 Kawazu, Iizuka, Fukuoka 820-8502, Japan.

Email:[shammistat@gmail.com]

Keywords: Inflammatory diseases, Anti-inflammatory peptides, Feature encoding, Feature selection, Random forest

[Introduction]

An autoimmune disease is a disorder of cell that systems mistakenly attack in the body. The immune system normally guards against germs like bacteria and viruses [1]. In order to understand the molecular mechanism of autoimmune disease, it is important to identify immunogenic peptides. To date, several experimental methods have been developed to identify immunogenic molecules, but these experimental methods are generally laborious and costly. Therefore, computational methods that can accurately predict potential immunogenic peptides based on protein sequence information are highly desirable [2]. In this work, the author focuses on the prediction of inflammatory molecules. The development of the novel in silico predictors is desired to classify potential anti-inflammatory peptide (AIP) prior to in vitro investigation. Herein, a novel predictor, called PreAIP (Prediction of Anti-Inflammatory Peptides) was developed by integrating multiple complementary features. It was implemented as a web application. The PreAIP predictor achieved high performance on both the training and test datasets compared with existing methods. It can provide valuable insights into the processes and functions of AIPs. A flowchart of proposed method is shown in **Figure 1**.

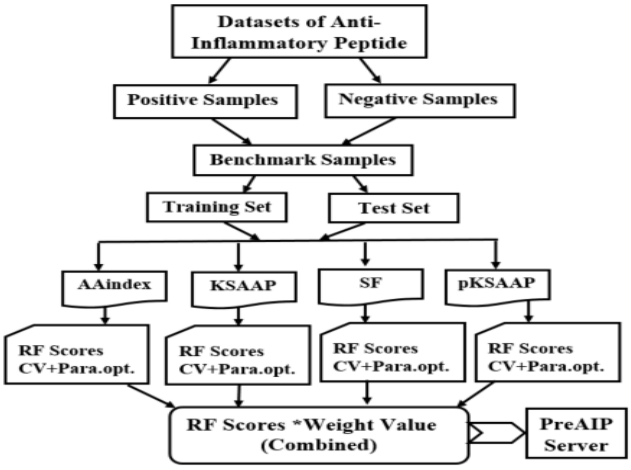

Figure 1: A flowchart of the employed methods.

[Materials and Methods]

Dataset preparation

After collecting positive and negative AIPs from the AIPpred tool [2], the datasets were encoded by primary, evolutionary and structural features sequence encoding. These features were trained by a random forest (RF) classifier. After combining the optimum prediction scores of RF, a stringent cutoff was considered and online server of PreAIP established to identify the AIPs.

Random Forest

RF is an ensemble and supervised statistical learning algorithm for classification, which employs a group of decision trees to decrease the output variance of individual trees [3].

AAindex

The AAindex database (version 9.1) has the 534 indices of physicochemical properties of amino acid [4-7]. After evaluating different types of AAindex, we selected 8 informative amino acid indices were used in this study.

pKSAAP

After generating the PSSM profile, we calculated the k-space amino acid pair from the PSSM matrix, i.e., pKSAAP on the AIP peptides [5,6]. The PSSM has been shown to provide useful evolutionary information about proteins [8-11]. This matrix contains the substitution probability of each amino acid in a protein with all the amino acids of the genetic code.

Structural features (SF)

Secondary feature provides useful information to understand the local 3D structure of proteins. This structure can be studied by looking at the amino acid contributions to local protein structures, namely, helix, strand and coil.

KSAAP

The possibe K-spaced amino acid pairs i.e., KSAAP was measured from the protein seqeunces[11-13]. A sequence of a 2000-dimension feature vector was obtained through KSAAP encoding.

[Results and Discussion]

The final PreAIP model achieved an AUC value of 0.833 in the training dataset via 10-fold cross-validation test, which was considerably better than that of other existing models (Table 1). Moreover, the performance of PreAIP was assessed on a test dataset to demonstrate that the proposed method outperformed the existing two methods, with an AUC value of 0.840. These results indicated that PreAIP is a suitable predictor for identifying anti-inflammatory peptides and contributes to the development of anti-inflammatory peptides therapeutics and biomedical research. The curated datasets and the PreAIP predictor are freely available at http://kurata14.bio.kyutech.ac.jp/PreAIP/.

Table 1. AUC values for prediction performance of the training dataset by 10-fold CV test

Methods	Specificity	Sensitivity	Accuracy	AUC
pKSAAP	0.798	0.647	0.738	0.789
AAindex	0.795	0.644	0.735	0.774
SF	0.765	0.434	0.633	0.739
KSAAP	0.805	0.656	0.745	0.813
PreAIP*	0.806	0.709	0.767	0.833

* PreAIP is the combined method of k-spaced amino acid pairs (KSAAP), amino acid index (AAindex) and profile-based composition k-space of amino acid pair (pKSAAP) encoding schemes and their weight coefficients are 0.15, 0.25, and 0.6, respectively via RF scores.

References

[1] Ferrero-Miliani L, Nielsen OH, Andersen PS, Girardin SE. Chronic inflammation: importance of NOD2 and NALP3 in interleukin-1beta generation. Clin Exp Immunol. 2007; 147: 227-35. doi: 10.1111/j.1365-2249.2006.03261.

[2] Manavalan B, Shin TH, Kim MO, Lee G. AIPpred: Sequence-Based Prediction of Anti-inflammatory Peptides Using Random Forest. Front Pharmacol. 2018; 9: 276. doi: 10.3389/fphar.2018.00276.

[3] M.M Hasan, H. Kurata, "GPSuc: Global Prediction of generic and species-specific succinylation sites by aggregating multiple sequence features," PloS one 2018 (in press).

[4] M.M. Hasan, Y. Zhou, X. Lu, J. Li, J. Song, Z. Zhang. Computational identification of protein pupylation sites by using profile-based composition of k-spaced amino acid pairs. PloS one 2015, 10(6):e0129635.

[5] M.M. Hasan, S. Yang, Y. Zhou, M.N. Mollah. SuccinSite: a computational tool for the prediction of protein succinylation sites by exploiting the amino acid patterns and properties. Molecular bioSystems 2016, 12(3):786-795.

[6] M.M Hasan, M.S. Khatun, H Kurata. A comprehensive review of in silico analysis for protein S-sulfenylation sites. Protein & Peptide Letters 2018, *25,* 1-7.

[7] M.M. Hasan, M.S. Khatun, M.N.H. Mollah, C. Yong, D. Guo. A systematic identification of species-specific protein succinylation sites using joint element features information. International journal of nanomedicine 2017, 12:6303-6315.

[8] M.M. Hasan, D. Guo, H. Kurata. Computational identification of protein S-sulfenylation sites by incorporating the multiple sequence features information. Molecular BioSystms 2017, 13(12):2545-2550.

[9] M.M. Hasan H. Kurata. Prediction of protein Post-Translational Modification sites: an overview. Annal Proteom Bioinform 2018, 2:049-057.

[10] M.M. Hasan, M.S. Khatun, H. Kurata. Computational modeling of lysine post-translational modification: an overview. Curr Synthetic Sys Biol 2018, 6:137.

[11] M.M. Hasan, M.S. Khatun, M.N.H. Mollah, Y. Cao, D. Guo. NTyroSite: Computational identification of protein nitrotyrosine sites using sequence evolutionary features. Molecules 2018, 23(7): 1667.

[12] M.M. Hasan, M.S. Khatun. Recent Progress and Challenges for Protein Pupylation Sites Prediction. EC Proteom Bioinform, 2017, 2(1): 36-45.

[13] M.M. Hasan, H. Kurata. iLMS, computational identification of lysine-malonylation sites by combining multiple sequence features. IEEE of BIBE Conf. Tiwan (2018) (accepted).

Please choose: Oral/ Poster/ Either
Presentation session:
Presenter name:

Cross-Site Scripting Vulnerabilities Detection Techniques and their Limitations

Isatou Hydara, Abu Bakar Md Sultan, Hazura Zulzalil, Novia Admodisastro

Faculty of Computer Science and Information Technology, University Putra Malaysia, 43400 UPM Serdang, Selangor, Malaysia

Email: ishahydara@gmail.com

Abstract
Web applications have become very important tools in our daily activities as we use them to share and get information, conduct businesses, and interact with family and friends on social media through the Internet. Despite their importance, web applications are plagued with many security vulnerabilities that enable hackers to attack them and compromise user information and privacy. Cross-site scripting vulnerabilities are a type of injection vulnerabilities existing in web applications. They can lead to web application attacks due to lack of proper validation of input data in the affected web pages of an application. Many approaches and techniques have been proposed to mitigate this type of vulnerabilities in web applications. However, these solutions have some limitations and cross-site scripting vulnerabilities still remain as a major security problem for web applications. This paper explores and presents the existing approaches and techniques for detecting cross-site scripting vulnerabilities in web applications. It gives an overview of cross-site scripting as a security issue in web applications and its different types. The advantages as well as the limitations of each proposed approach or technique are highlighted and discussed. Based on the limitations, some possible future research directions are identified and recommendations are given as reference for researchers interested in this topic.

Keywords: Cross-site scripting, cross-site scripting vulnerabilities, cross-site scripting attacks, web application security, security testing

Introduction

As technology advances, we rely on the Internet to accomplish daily transactions through Desktop and mobile web applications. Banking websites enable customers to transfer money online, pay bills, and conduct many transactions without having to visit any bank branch. Many online stores are also available to support the E-commerce businesses around the world. Social and other sites enable people to consume and share information online. However, this has made web applications more complex [1], resulting to a lot of security issues affecting them including cross-site scripting (XSS). It is reported that 80% of all websites are vulnerable to XSS [2].

Background of Cross-Site Scripting Vulnerabilities

XSS vulnerabilities are among the top security vulnerabilities that are in desktop web applications[1] as well as mobile web applications [3] and are exploited through XSS attacks on web applications that are available and running online[1]. Hackers can inject or input malicious code where these applications accept user inputs such as providing username and password when login to an application. If the website does not verify the user input or it does it incorrectly, it allows the hacker the opportunity of exploiting for vulnerabilities and conduct malicious activities. There are three types of cross-site scripting vulnerabilities, which are Reflected, Stored and DOM-based cross-site scripting [1]. Reflected and stored cross-site scripting attacks occur on the server side while DOM-based cross-site scripting attacks occur on the client side of an application. Successful XSS attacks allow attacker to steal cookies, transfer private information, hijack a user's account, manipulate the web content, cause denial of service, and many other malicious activities.

Existing Detection Techniques and Their Limitations

This section briefly discusses the existing techniques and approaches for the detection of XSS vulnerabilities in desktop and mobile web applications. They can be categorized into static analysis, dynamic analysis, modeling, and hybrid analysis.

Static Analysis
Static analysis techniques are solutions that carry out XSS vulnerability detection at the source code level of web applications [4]. They help to tract and identify vulnerable parts of a source code thereby detecting XSS vulnerabilities. The most common detection techniques under static analysis are static taint analysis, data flow analysis, string analysis, precise alias analysis, program slicing, and symbolic execution. The major limitation of these techniques is their high rate of false positives. This is as a result of the conservative nature of these techniques. Another limitation is the source codes of applications are needed to conduct these security tests.

Dynamic Analysis
Dynamic analysis techniques detect XSS vulnerabilities in web applications that are already deployed online during runtime [3]. They intercept and analyze input data coming into an application from users and determine whether it is harmful or not. Such techniques include penetration testing, web monitoring, filtering, dynamic analysis, taint tracking, and flow analysis. The limitations of these techniques are that attackers can use obfuscation to hide their attack patterns and carry out successful XSS attacks. Also, these techniques require more computing resources to simulate the running environment of web applications.

Modeling
Modeling techniques [5] are not as commonly used in XSS detection as the previous two categories, but they are still important solutions. Existing modeling techniques for XSS detection include model checking, finite state machine, data mining, and threading. Most models are design to provide guidelines to developers and security testers during coding and testing. The major limitation of these is that in most cases the guidelines are not read and followed while coding due to time constraints of development projects.

Hybrid Analysis
Due to the limitations of the previous techniques and approaches, most research studies are now combining different techniques of XSS detection known as hybrid analysis [6]. It is used in order to reduce the limitations of using a single technique or approach. Combining static and dynamic analyses as well as modeling provides more coverage in terms of security testing of the code and the running application, as well as guiding the developers. Hybrid analysis still have their limitations, however, they are an improvement on previous techniques.

Conclusion
In this study, we have investigated the various methods that have been proposed by previous researchers to solve XSS problems. We have identified the limitations in those techniques as well as the needed improvements. Based on the limitations identified, new areas of research should be explored continuously with the hope of finding better ways of developing secure software and preventing more XSS attacks.

References

[1] OWASP, "Cross-site Scripting (XSS) - OWASP," *OWASP Foundation*, 2018. [Online]. Available: https://www.owasp.org/index.php/Cross-site_Scripting_(XSS). [Accessed: 26-Sep-2018].

[2] A. Javed and J. Schwenk, "Towards elimination of cross-site scripting on mobile versions of web applications," *Lect. Notes Comput. Sci. (including Subser. Lect. Notes Artif. Intell. Lect. Notes Bioinformatics)*, vol. 8267 LNCS, pp. 103–123, 2014.

[3] G. Kaur, B. Pande, A. Bhardwaj, G. Bhagat, and S. Gupta, "Efficient yet Robust Elimination of XSS Attack Vectors from HTML5 Web Applications Hosted on OSN-Based Cloud Platforms," *Procedia Comput. Sci.*, vol. 125, pp. 669–675, 2018.

[4] A. Kurniawan, B. S. Abbas, A. Trisetyarso, and S. M. Isa, "Static Taint Analysis Traversal with Object Oriented Component for Web File Injection Vulnerability Pattern Detection," *Procedia Comput. Sci.*, vol. 135, pp. 596–605, 2018.

[5] D. Gol and N. Shah, "Detection of Web Appication Vulnerability Based on RUP Model," in *National Conference on Recent Advances in Electronics & Computer Engineering (RAECE)*, 2015, pp. 96–100.

[6] R. Wang, Y. Zhu, J. Tan, and B. Zhou, "Detection of malicious web pages based on hybrid analysis," *J. Inf. Secur. Appl.*, vol. 35, pp. 68–74, 2017.

6th International Symposium on Applied Engineering and Sciences (SAES2018)
Kyushu Institute of Technology, 15th–16th, Dec 2018

Oral
Presentation session: Computer Science
Presenter name: **Md. Mehedi Hasan**

Title: SulCysSite, A Bioinformatics Tool for the Prediction of S-sulfenylation Sites

[Hasan, Md. Mehedi][1] and [Kurata, Hiroyuki][1,2*]

[1]Department of Bioscience and Bioinformatics, Kyushu Institute of Technology, 680-4 Kawazu, Iizuka, Fukuoka 820-8502, Japan. Email: mehedicuhk@gmail.com

[1,2]Biomedical Informatics R&D Center, Kyushu Institute of Technology, 680-4 Kawazu, Iizuka, Fukuoka 820-8502, Japan. Email: kurata@bio.kyutech.ac.jp

Keywords: S-sulfenylation, feature extraction, feature analysis, sequence analysis, machine learning

1. Introduction

Cysteine S-sulfenylation is a type of mutable covalent oxidation reaction of protein posttranslational modification (PTM) [1]. In this process, the thiol group of cysteine is transformed to a sulfenic acid group mainly through the reaction with H_2O_2 *in vivo* [1,2]. This modification is involved in various biological processes including cell signaling, signal processing, protein function, and binding to interaction partners [1]. Therefore, due to the advancement technologies on sequence analysis, the computational identification scheme of S-sulfenylation is needed before experimental verification. Until now, a few of computational methods focused on predicting the S-sulfenylation [2,3]. Despite all these efforts, the S-sulfenylation site prediction is still not accurate enough and more efficient algorithms are still desirable.

In this study, a novel predictor SulCysSite has been developed for accurate identification of S-sulfenylation by the integrated of complementary features. The SulCysSite predictor achieved an AUC score of 0.899 on a cross-validation set and outperforms other existing methodologies on a comprehensive independent dataset. The SulCysSite is suggested to be a helpful computational resource for biomedical researchers.

2. Materials and Methods

The training and independent dataset was collected from the recently published article [2,3]. To thwart the overestimation of the prediction model, less than 40% similarity sequences were removed [2].

2.1 Feature extraction

To develop a binary classification prediction model, the individual sequence fragment was encoded into a numeric feature vector through diverse sophisticated methods, namely, evolutionary, structural, amino acid properties and sequence information to represent the S-sulfenylation sequence fragments [4-13]. The combined features vectors were optimized via information gain.

Table 1. The performances of proposed method using training and independent samples

Predictors	Training	Independent
specificity	0.897	0.711
sensitivity	0.823	0.766
accuracy	0.896	0.719
MCCC	0.678	0.343
AUC	0.899	0.757

3. Results and Discussion

Best performance was observed after combining the multiple encoding methods including evolutionary, structural, amino acid properties and sequence information to represent the S-sulfenylation (**Table 1**). Then, we optimized these features using the IG feature selection scheme. After several trials, the top feature vectors were collected from the all-features for S-sulfenylation sites prediction. The collected feature vectors were transformed into a new ordered feature based on low to high IG values. The final

feature vectors were trained by the RF, SVM, and NB classifiers. The consecutive model parameters were optimized via training dataset based on the 10-fold cross-validation. Then the final features scores were combined through linear regression model. The proposed method provided the highest AUC values of 0.899 on the training dataset. The performance indexes in terms of specificity, sensitivity, accuracy, and MCC were summarized in the training and independent datasets **(Table 1)**.

Table 2. The performance comparison with existing methods on the independent set

Predictors	specificity	sensitivity	accuracy	MCC
SOHSite	0.710	0.710	0.710	0.278
MDD-SOH	0.710	0.720	0.711	0.300
SulCysSite	0.711	0.766	0.719	0.343

Moreover, the performances indexes were found robust in the independent datasets. In addition, the proposed model SulCysSite greatly outperformed the others existing algorithms (**Table 2**). Indeed, all performance measures in the SulCysSite were higher than those of the other methods, thus indicating the superiority of the SulCysSite in S-sulfenylation prediction.

4. References

[1] Beedle, A.E.; Lynham, S.; Garcia-Manyes, S. Protein Ssulfenylation is a fleeting molecular switch that regulates nonenzymatic oxidative folding. Nat. Commun., 2016, 7, 12490.

[2] Bui, V.M.; Lu, C.T.; Ho, T.T.; Lee, T.Y. MDD-SOH: Exploiting maximal dependence decomposition to identify S-sulfenylation sites with substrate motifs. Bioinformatics, 2016, 32(2), 165-172.

[3] M.M. Hasan, D. Guo, H. Kurata. Computational identification of protein S-sulfenylation sites by incorporating the multiple sequence features information. Molecular BioSystms 2017, 13(12):2545-2550.

[4] M.M Hasan, H. Kurata, "GPSuc: Global Prediction of generic and species-specific succinylation sites by aggregating multiple sequence features," PloS one 2018 (in press).

[5] M.M. Hasan, Y. Zhou, X. Lu, J. Li, J. Song, Z. Zhang. Computational identification of protein pupylation sites by using profile-based composition of k-spaced amino acid pairs. PloS one 2015, 10(6):e0129635.

[6] M.M. Hasan, S. Yang, Y. Zhou, M.N. Mollah. SuccinSite: a computational tool for the prediction of protein succinylation sites by exploiting the amino acid patterns and properties. Molecular bioSystems 2016, 12(3):786-795.

[7] M.M Hasan, M.S. Khatun, H Kurata. A comprehensive review of in silico analysis for protein S-sulfenylation sites. Protein & Peptide Letters 2018, *25,* 1-7.

[8] M.M. Hasan, M.S. Khatun, M.N.H. Mollah, C. Yong, D. Guo. A systematic identification of species-specific protein succinylation sites using joint element features information. International journal of nanomedicine 2017, 12:6303-6315.

[9] M.M. Hasan H. Kurata. Prediction of protein Post-Translational Modification sites: an overview. Annal Proteom Bioinform 2018, 2:049-057.

[10] M.M. Hasan, M.S. Khatun, H. Kurata. Computational modeling of lysine post-translational modification: an overview. Curr Synthetic Sys Biol 2018, 6:137.

[11] M.M. Hasan, M.S. Khatun, M.N.H. Mollah, Y. Cao, D. Guo. NTyroSite: Computational identification of protein nitrotyrosine sites using sequence evolutionary features. Molecules 2018, 23(7): 1667.

[12] M.M. Hasan, M.S. Khatun. Recent Progress and Challenges for Protein Pupylation Sites Prediction. EC Proteom Bioinform, 2017, 2(1): 36-45.

[13] M.M. Hasan, H. Kurata. iLMS, computational identification of lysine-malonylation sites by combining multiple sequence features. IEEE of BIBE Conf., Tiwan (2018) (accepted).

Please choose: Oral/ Poster/ Either
Presentation session:
Presenter name: Shahrel Azmin Suandi

Oil Palm Tree Counting using Fast Region-Convolutional Neural Network (Fast R-CNN)

Muhamad Faris, Che Aminudin [1], Shahrel Azmin, Suandi [1,2], Hazry, Desa [2], Muhamad Azizi Azizan [2]

[1]Intelligent Biometric Group, School of Electrical and Electronic Engineering, Universiti Sains Malaysia, Engineering Campus, 14300 Nibong Tebal, Pulau Pinang, MALAYSIA
[2]Centre of Excellence for Unmanned Aerial System, Universiti Malaysia Perlis, 02600 Arau, Perlis, MALAYSIA

Email: shahrel@usm.my

Keywords (5 words): Oil palm tree counting, convolutional neural network (CNN), fast region-convolutional neural network (fast R-CNN), smart agricultural management system

Introduction

Malaysia has huge amount of oil palm plantations and is one of the biggest palm oil producers and exporters in the world. This makes oil palm trees important economic crops in Malaysia. With the current demand for palm oil, more efficient agricultural mechanism is desired to manage the plantations in more effective way. One of them is to count the oil palm trees. Having in hand the number of oil palm trees in a plantation area, one can predict the yield, monitoring the growth and healthiness of palm trees etc. to maximize the productivity [1]. There are techniques which have been proposed earlier and most of them are remote sensing-based technologies. However, with the rising of unmanned aerial vehicle (UAV) such as drones, tree counting process can be performed merely from UAV images and is nearly to 'on-demand' technology. The drawback in this technology is that it is not as sophisticated as satellite imaging in remote sensing, which has more information such as near infra-red, medium infra-red, long infra-red, multispectral frequencies. In our work, we proposed to use the most recent advanced technique for object detection, which is Fast Region-Convolutional Neural Network (Fast R-CNN) [2], [3] to detect and count oil palm trees. In contrast to existing techniques, we need to solve the problem where Malaysia oil palm trees are planted quite near to each other. This makes the existing computer vision algorithms to detect tree crown etc. are not viable. Figure 1 shows an example of not crowded and crowded oil palm tree plantation in Malaysia. To train our Fast R-CNN model, a few examples of oil palm tree were prepared. We initially focused on adult and small oil palm tree. To validate our proposed method, comparison with template matching and Haar cascaded (AdaBoost) methods were conducted.

(a) (b)

Figure 1: (a) Not crowded example, (b) Crowded oil palm tree plantation in Malaysia.

Experiments

In the experiments, we prepared 11 oil palm tree images taken in northern Malaysia. The number of trees in each image was manually annotated by human. This amount is later used as the ground truth data (GT) to benchmark our proposed method.

Results and Discussions

The performance of proposed method was compared with template matching and Haar casdaded techniques in terms of precision, recall and overall accuracy. Here, we compute accuracy as the averaged between precision and recall, i.e., $accuracy = (precision + recall)/2$. Table 1 shows the summary of results obtained from the experiments. From the results, Fast R-CNN achieved the highest overall accuracy, 0.915, compared to TM and HC, which achieved 0.7 and 0.774, respectively.

Table 1: Summary of results obtained from each method in terms of Precision, Recall and Accuracy.

Image #	Ground Truth, GT	Template Matching, TM		Overall Accuracy	Haar Cascade, HC,		Overall Accuracy	Fast R-CNN,		Overall Accuracy
		Precision	Recall		Precision	Recall		Precision	Recall	
Image 1	1755	0.755	0.679	0.717	0.866	0.903	0.885	1.00	0.829	0.915
Image 2	1753	0.842	0.785	0.814	0.862	0.942	0.902	1.00	0.791	0.896
Image 3	1828	0.862	0.700	0.781	0.604	0.798	0.701	1.00	0.859	0.930
Image 4	393	0.703	0.471	0.587	0.606	0.654	0.630	1.00	0.888	0.944
Image 5	1187	0.666	0.919	0.793	0.731	0.911	0.821	1.00	0.961	0.981
Image 6	1289	0.700	0.902	0.801	0.715	0.850	0.783	1.00	0.801	0.901
Image 7	1219	0.630	0.844	0.737	0.714	0.964	0.839	1.00	0.811	0.906
Image 8	1103	0.811	0.607	0.709	0.869	0.695	0.782	1.00	0.876	0.938
Image 9	1108	0.451	0.105	0.278	0.694	0.530	0.612	1.00	0.651	0.826
Image 10	1200	0.745	0.651	0.698	0.831	0.634	0.733	1.00	0.790	0.895
Image 11	1478	0.735	0.831	0.783	0.720	0.924	0.822	1.00	0.870	0.935
Averaged	-	**0.718**	0.681	**0.700**	**0.747**	**0.800**	**0.774**	**1.000**	**0.830**	**0.915**

Conclusion

From the results shown in Table 1, it is revealed that Fast R-CNN has the most superior performance compared to others. Although the time processing is a little bit more expensive than the other two techniques, we believe that accuracy issue should be solved with higher priority since the speed issue can be solved by using higher speed computer. However, since the allowable error in actual oil palm tree counting problem is merely 1%, we will further improve the performance by exploring the Mask R-CNN. This method considers the object of interest in more detail manner, which we believe could be a good solution to our current limitation.

References

[1] W. Li, H. Fu, L. Yu, A. Cracknell, W. Li, H. Fu, L. Yu, and A. Cracknell, "Deep Learning Based Oil Palm Tree Detection and Counting for High-Resolution Remote Sensing Images," *Remote Sens.*, vol. 9, no. 1, p. 22, Dec. 2017.

[2] A. Mhalla, T. Chateau, H. Maâmatou, S. Gazzah, and N. E. Ben Amara, "SMC faster R-CNN: Toward a scene-specialized multi-object detector," *Comput. Vis. Image Underst.*, vol. 164, pp. 3–15, Nov. 2017.

[3] L. K. Cheong, S. A. Sundi, and S. Rahman, "Defects and Components Recognition in Printed Circuit Boards Using Convolutional Neural Network," in *The 10th International Conference on Robotics, Vision, Signal Processing & Power Applications (ROVISP2018)*, 2018, pp. 1–6.

Poster

Please choose: Poster
Presentation session: Applied Chemistry
Presenter name: Tatsuki Shinoda

Measurement of the Energy Distribution of Trapped Electrons in Titanium(IV) Oxide Photocatalyst Powders by Photoacoustic FTIR spectroscopy

Tatsuki Shinoda[1], Naoya Murakami[1,2]

[1]Graduate School of Life Science and Systems Engineering, Kyushu Institute of Technology, 2-4 Hibikino, Wakamatsu-ku, Kitakyushu 808-0196, Japan
[2]Faculty of Engineering, Kyushu Institute of Technology, 1-1 Sensui-cho, Tobata-ku, Kitakyushu-shi, Fukuoka, 804-8550, Japan

Email: shinoda.tatsuki830@mail.kyutech.jp

Keywords (5 words)
Photocatalyst, Titanium(IV) oxide, Trapped electrons, Energy distribution, Photoacoustic FTIR spectroscopy

[Introduction]

Photocatalytic reactions over semiconductor materials are photochemical reactions induced by photoexcited electrons and positive holes, which are generated by above-band gap excitation. However, estimating the quantum yield of many photocatalytic reactions, most of the photoexcited electrons and positive holes recombine without contributing to the reactions. This mostly occurs due to defects which behave as electron/hole trap sites and recombination centers, and defects dominating recombination are important factors that decide to photocatalytic activity, as with the crystal structure, specific surface area and particle size. Crystal defects in titanium(IV) oxide (TiO_2) are trivalent titanium (Ti^{3+}) species, which form by accumulation of trapped electrons at unsaturated titanium atoms with oxygen vacancies. Previous studies have shown that amount of Ti^{3+} species in TiO_2 powders can be quantified by a photochemical method using methylviologen[1] and a photoacoustic (PA) measurement in ultraviolet (UV) to visible region[2]. Also, energy levels of Ti^{3+} species in TiO_2 powders have been investigated in mid-infrared (MIR) region, i.e., photon energy from electron-trap levels to the bottom of the conduction band (CB) (0-0.4 eV).[1, 3] Recently, we reported that energy levels of Ti^{3+} species in TiO_2 powders, i.e., energy distribution of trapped electrons in band gap, largely depend on the crystal structures by detecting MIR absorption (0.1-0.7 eV) of Ti^{3+} species using photoacoustic Fourier transform infrared spectroscopy (FTIR-PAS).[4] Here, photoacoustic spectroscopy (PAS) is an effective technique which can be applied to scattering solid materials such as TiO_2 powders because photoabsorption is detected by photothermal waves. Besides, FTIR-PAS, which applies PAS to Fourier transform infrared spectroscopy (FTIR) system, is a convenient method for analysis of energy distribution of trapped electrons in semiconductor photocatalyst powders. In the present study, energy distribution of trapped electrons in TiO_2 powders were measured by FTIR-PAS in near-infrared (NIR) to MIR region, i.e., wider-wavenumber (photon energy) range (800-15000 cm^{-1} (0.1-1.8 eV)).

[Experiment]

TiO_2 powders from reference catalysts supplied by the Catalyst Society of Japan (JRC-TIO series) and commercial products were used without any pretreatment. TiO_2 powder samples with adsorbed iron(III) ion (Fe^{3+}/TiO_2) were obtained by an impregnation method using an aqueous iron(III) nitrate ($Fe(NO_3)_3$). Platinum was photochemically deposited on the TiO_2 powder samples (Pt/TiO_2) from an aqueous solution containing hexachloroplatinic acid (H_2PtCl_6) and ethanol. For FTIR-PAS measurements, about 100 mg of sample was placed in the PA cell, and nitrogen gas containing gaseous ethanol (N_2-EtOH) was flowed through the gas flow passage to the PA cell and then the cell was closed tightly. The sample was photoexcited by UV irradiation using a light-emitting diode (emitting around 365 nm). The measurements were performed in the wavenumber range of 800-15000 cm^{-1} using FTIR spectrometers (Frontier NIR; mirror velocity: 0.1 cm s^{-1}, Nicolet is10; mirror velocity: 0.3165 cm s^{-1}) as probe light at room temperature, and the PA signal, corresponding to NIR-MIR absorption of the sample, was acquired before and after UV irradiation.

[Result and Discussion]

Fig. 1a and b show FTIR-PAS spectra of rutile TiO_2 powders (JRC-TIO-6) under N_2-EtOH before and after UV irradiation. The broad absorptions at around 3200 cm^{-1} and 11000 cm^{-1} before UV irradiation were attributed to adsorbed H_2O as in the previous studies.[5] In NIR region, a broad absorption in the range of 15000-3000 cm^{-1} was observed under UV irradiation, and the absorption peak at 6866 cm^{-1} corresponds to 0.86 eV of photon energy. In MIR region, an upward shift of FTIR-PAS spectrum was observed under UV irradiation, and the PA intensity decreased with a decrease in the wavenumber. Also, the monotonic increase in PA intensity in the low-wavenumber range below 1000 cm^{-1} is attributed to the interband transitions of free electrons in the CB or the electron transitions of trapped electrons from shallow-trap levels to the CB. Thus, photoexcited electrons in rutile TiO_2 powders (JRC-TIO-6) are mostly trapped at deep-energy trap sites. Fig. 1c and d show FTIR-PAS spectra of Fe^{3+}/JRC-TIO-6 under N_2-EtOH before and after UV irradiation. The intensity of absorptions at around 3200 cm^{-1} and 11000 cm^{-1} before UV irradiation decreased by comparing with bare JRC-TIO-6. In NIR to MIR region, a broad absorption in the range of 15000-3000 cm^{-1} and an upward shift were observed under UV irradiation; however, the PA intensity decreased clearly after iron(III) ion (Fe^{3+}) was adsorbed on the surface and then the absorption peak at 7629 cm^{-1} corresponds to 0.95 eV of photon energy. This suggests that photoexcited electrons in the CB and trapped electrons at shallow-trap states transfer to Fe^{3+}, whereas trapped electrons at deep-trap states are localized. Similarly, FTIR-PAS measurements for Pt/TiO_2 were carried out. The detailed results will be presented at the symposium.

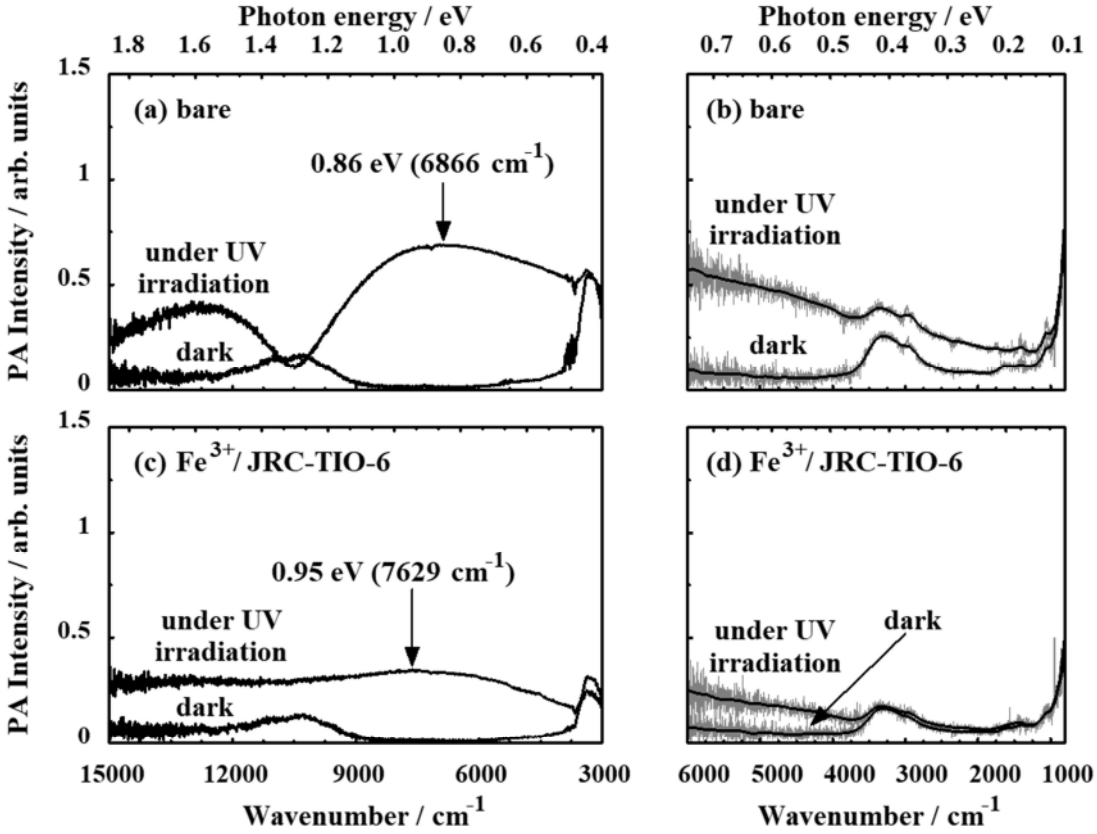

Fig. 1. FTIR-PAS spectra of (a) and (b) bare JRC-TIO-6, (c) and (d) Fe^{3+}/JRC-TIO-6 under N_2-EtOH before and after UV irradiation. The measurements were carried out by use of (a) and (c) NIR (mirror velocity: 0.1 cm s^{-1}), (b) and (d) MIR (mirror velocity: 0.3165 cm s^{-1}) spectrometers.

(1) S. Ikeda *et al.*, *Phys. Chem. Chem. Phys.*, **5**, 778-783 (2003)
(2) N. Murakami *et al.*, *J. Phys. Chem. C*, **111**, 11927-11935 (2007)
(3) A. Nitta *et el.*, *Chem. Commun.*, **52**, 12096-12099 (2016)
(4) N. Murakami *et al.*, *Phys. Chem. Chem. Phys.*, **20**, 24519-24522 (2018)
(5) T. Makoto *et al.*, *J. Phys. Chem. C,* **111**, 9811-9817 (2007); T. Makoto *et al.*, *J. Phys. Chem. B*, **109**, 7387-7391 (2005)

Please choose: Poster
Presentation session: Applied Chemistry
Presenter name: Wataru Ishitobi

Electric Orientation of Liquid Crystalline Binary Nanosheet Colloids Composed of Niobate and Clay Nanosheets

Wataru Ishitobi, Miho Yabuuchi, Emiko Mouri, Teruyuki Nakato

Department of Applied Chemistry, Kyushu Institute of Technology, 1-1 Sensui-cho, Tobata-ku, Kitakyushu-shi, Fukuoka, 804-8550, Japan

Email: nakato@che.kyutech.ac.jp

Keywords: Liquid crystal, Inorganic nanosheets, Colloid, Electric orientation

Introduction

Inorganic nanosheets obtained by exfoliation of layered crystals in water forms colloidal liquid crystals. Liquid crystalline nanosheets are oriented parallel to electric fields to generate macroscopic textures.[3] Since binary liquid crystalline nanosheet colloids composed of two different nanosheets exhibit complex phase behavior compared with single-component colloids, they will give unusual textures that cannot be achieved by the single-component colloids.[1, 2, 4] We report herein the electric orientation of nanosheets in binary nanosheet colloids of niobate and clay nanosheets.

Experiment

Binary nanosheet colloids of niobate and clay were prepared by mixing colloidal nanosheets obtained by exfoliation of layered niobate $K_4Nb_6O_{17}$ and synthetic hectorite. While the average lateral length of the niobate nanosheets was 1.75 μm, that of clay was 30 nm. A small portion of the mixed sample was injected into a thin-layer ITO cell, and applied by an AC electric voltage of 10 $V_{p\text{-}p}$, 50 kHz (Figure 1). Structural changes were observed with an optical microscope. The electric field was applied in the direction perpendicular to the cell surface; this direction was parallel to that of microscope observations.

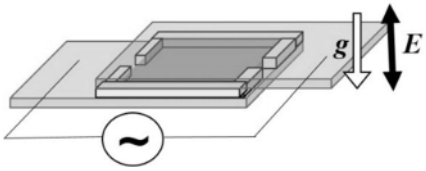

Figure 1. Schematic image of electric field application experiment

Result and Discussion

Figure 2 exhibits bright field microscope (BFM) images, polarized optical microscope (POM) images, and fluorescent optical microscope (FOM) images of a binary nanosheet colloid of niobate and clay nanosheets before and after the application of an electric field. In the BFM image before applying the electric field (Figure 2a), nanosheets are dispersed almost homogeneously, but some spots, in which nanosheets are aligned perpendicular to the cell surface, are also observed. The observed nanosheets are assigned to niobate

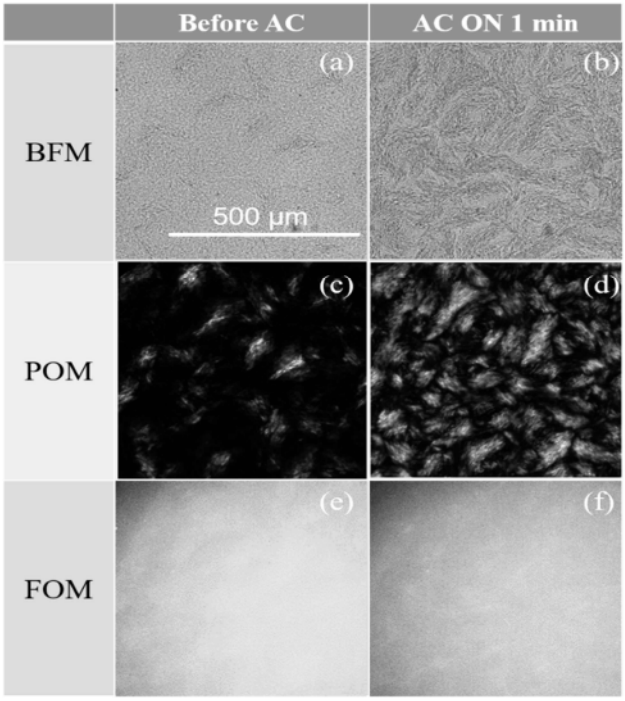

Figure 2. Microscopic images of before and after application of an electric field (sample: Niobate 5 gL^{-1}-Hectorite 1 gL^{-1} /Rhodamine 6G 2.0×10^{-6} $molL^{-1}$)

nanosheets because of their size. The aligned niobate nanosheets form μm-sized domains as observed in the POM image (Figure 2c), agreeing with the aligned spots seen in the BFM image. On the other hand, clay nanosheets are located among the niobate nanosheets as shown in the FOM image (Figure 2e), where the fluorescence indicates the location of clay nanosheets because of selective adsorption of fluorescent dye (rhodamine 6G) onto clay nanosheets.

After applying the electric field, niobate nanosheets are oriented in parallel to the electric field to form many large domains of aligned nanosheets as seen in the BFM image (Figure 2b). The orientation change is also observed in the POM image (Figure 2d). On the other hand, clay nanosheets are distributed similarly to those before the application of electric field (Figure 2f). The results indicate that only the niobate nanosheets respond to the electric field in the binary colloid of niobate and clay nanosheets. Moreover, it was confirmed that the clay nanosheets and niobate nanosheets are spatially separated at μm-level length scale.

Reference

1. N. Miyamoto, T. Nakato, Liquid Crystalline Colloidal System Obtained by Mixing Niobate and Aluminosilicate Nanosheets: A Spectroscopic Study Using a Probe Dye. *Langmuir,* **2003**, 19, 8057-8064

2. N. Miyamoto, Y. Yamada, S. Koizumi, T. Nakato, Extremely Stable Photoinduced Charge Separation in a Colloidal System Composed of Semiconducting Niobate and Clay Nanosheets. *Angew. Chem.,* **2007**, 119, 4201-4205

3. T. Nakato, Y. Nono, E. Mouri, M. Nakata, Panoscopic Organization of Anisotropic Colloidal Structures from Photofunctional Inorganic Nanosheet Liquid Crystals. *Phys. Chem. Chem. Phys.*, **2014**, 16, 955-962

4. T. Nakato, S. Terada, T. Ishiku, S. Abe, S. Kamimura, E. Mouri, T. Ohno, Photoinduced Electron Transfer in Semiconductor-Clay Binary Nanosheet Colloids Controlled by Clay Particles as a Turnout Switch. *Appl. Catal. B: Envir.* **2019**, 241, 499-505

Please choose: Poster
Presentation session: Applied Chemistry
Presenter name: Kota Tsubaki

New synthetic methods of phosphate triesters and their applications

Kota Tsubaki[1], Hirokazu Shimooka[1], Mitsuru Kitamura[1], Tatsuo Okauchi[1]
[1]Faculty of Applied chemistry, Kyushu Institute of Technology, 1-1 Sensui-cho, Tobata-ku, Kitakyushu-shi, Fukuoka, 804-8550, Japan, Email: kotatsubaki.0620@gmail.com

Keywords
transesterification, phosphate triester, new phosphorylating agents, phosphate diester, phospholipid

Introduction

Phosphate esters are of great importance in the pharmaceutical, agrochemical, medicinal, and materials chemistry. Accordingly, many methods for preparing organophosphates have been reported. Phosphoryl chloride ($POCl_3$) and phosphorus trichloride (PCl_3) are widely used as phosphorylating agents. The phosphorylation of alcohols using $POCl_3$ or PCl_3, however, often gives complex mixtures and/or low yields due to their strong reactivity. Although several phosphorylating agents have been developed for the synthesis of the desired phosphate ester, the problem is that they are unstable against heat, water and oxygen[1]. Recently, Sano *et al* reported the novel method for the synthesis of phosphate diesters using a Horner-Wadsworth-Emmons reagent (Scheme1 (a))[2]. In this report, a trifluoroethoxy group can act as a leaving group for the selective transesterification. However, this method can not be used for the preparation of phosphate triesters.

Herein we describe the synthesis of phosphate triesters by introducing different three alcohols via transesterification of tris(trifluoroethyl) phosphate **1** in the presence of DBU, ^{t}BuOLi or ^{n}BuLi. (Scheme1 (b)).

(a) Synthetic method using Horner-Wadsworth-Emmons (HWE) reaction (b) This work

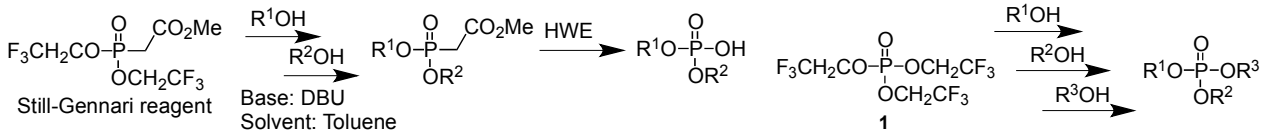

Scheme 1. Synthesis of phosphate esters

Result and Discussion

Synthesis of phosphate triesters using tris(trifluoroethyl) phosphate

We tried the selective transesterification between tris(rifluoroethyl) phosphate **1** and an alcohol in the presence DBU according to Sano's conditions. The reaction proceeded selectively and the desired product was obtained in high yield. We next examined the transesterification of 2nd alcohols. The reaction didn't proceed under the condition used for the transesterification of 1st alcohols. After screening the various reaction conditions, we found that ^{t}BuOLi or ^{n}BuLi promoted the transesterification with 2nd and 3rd alcohols. These sequential transesterifications proved to be an effective strategy for selective transesterification to synthesize phosphate triesters derived from three different alcohols (Scheme 2).

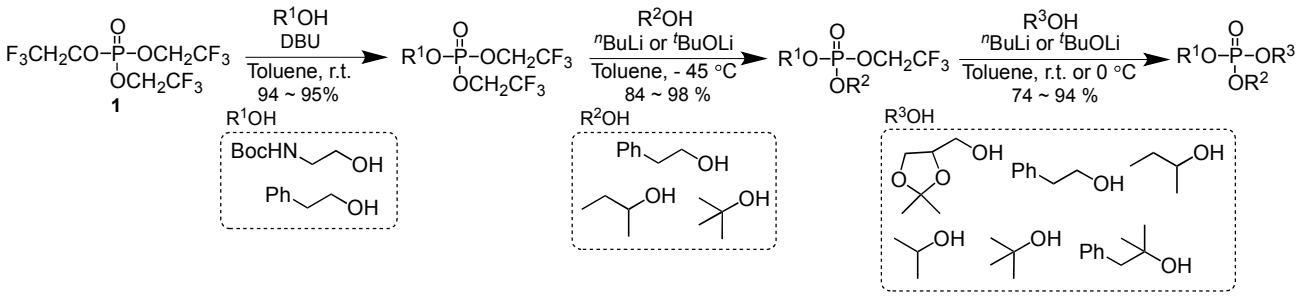

Scheme 2. Synthesis of phospholipid derivatives using tris (2,2,2-trifluoroethyl) phosphate

Synthesis of new phosphorylating agents and phospholipid derivatives.

The intermediates in these transesterifications were stable to water and oxygen. We expect to be able to develop new phosphorylating agents **2a**~**c** for the preparation of phospholipid derivatives. (Scheme 3). New phosphorylating agents **2a**~**c** were synthesized under the conditions used for the transesterification of 1st and 2nd alcohols.

We synthesized phospholipid **3** and its derivatives by using new phosphorylating agents **2a**~**c** (Scheme 4). The desired products were obtained after the transesterification, the functional transformation (R→ $COC_{17}H_{35}$), and the deprotection of protecting groups (PG^1 and PG^2).

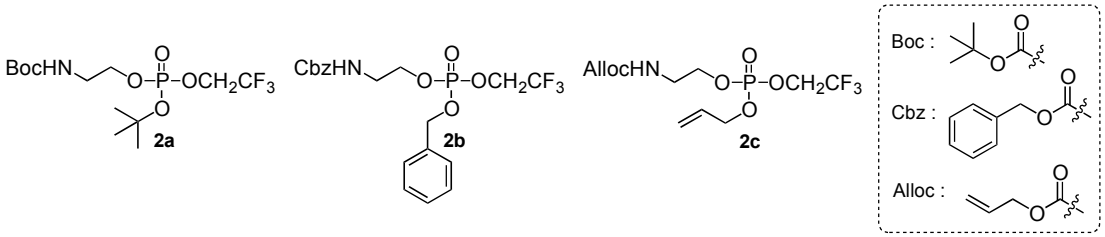

Scheme 3. New phosphorylating agents

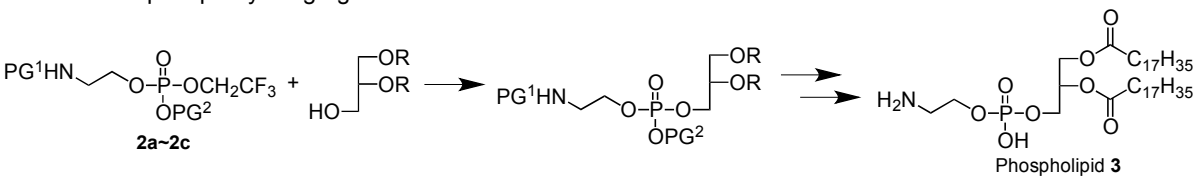

Scheme 4. Synthesis of phospholipid

Synthesis of phospholipid derivatives using tris(trichloroethyl) phosphate

We also tried the transesterification of tris(trichloroethyl) phosphate **4** to synthesize phospholipid derivative **5** (Scheme 5). The desired phospholipid derivative **5** was obtained from tris(trichloroethyl) phosphate **4** via the transesterification and the deprotection. This is the first example in which chloroethoxy group can act as a leaving group for the selective transesterification and a protecting group.

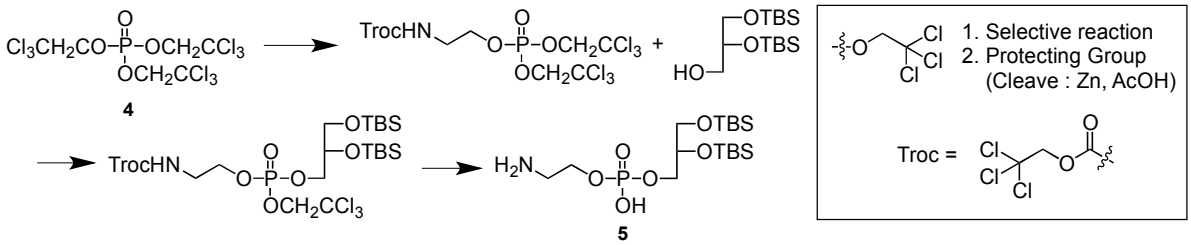

Scheme 5. Synthesis of phospholipid derivatives using tris (2,2,2-trichloroethyl) phosphate

CONCLUSION

We have developed the selective transesterification of tris(trifluoroethyl) phosphate **1** and tris(trichloroethyl) phosphate **4**. This method turned out to be effective for the synthesis of phospholipid and its derivatives.

REFERENCES

[1] a) ND Sinha, J. Biemat, J. McManus, H. Koster, *Nucleic Acid Res.,* **1984**, *12*, 4539. b) J. Shin, D. H. Thompson, *J. Org. Chem.*, **2003**, *68*, 6760.

[2] S. Sano, H. Sumioshi, A. Handa, R. Tokizane, M. Nakao, *Tetrahedron Lett.,* **2015**, *56*, 4686.

Presentation session: Poster
Presenter name: Dina I. A. Othman

Synthetic Study of Eleuthoside A; Application of Rh-Catalyzed Intramolecular Cyclization of Diazonaphthoquinone

Dina I. A. Othman[1, 2], Kota Ohtsuka[1], Shuhei Takahashi[1], Khalid B. Selim[2], Magda A. El-Sayed[2], Atif S. Tantawy[2], Tatsuo Okauchi[1], Mitsuru Kitamura[1]

[1] Department of Applied Chemistry, Kyushu Institute of Technology, 1-1 Sensui-cho, Tobata, Kitakyushu, Fukuoka, 804-8550, Japan
[2] Department of Pharmaceutical Organic Chemistry, Faculty of Pharmacy, Mansoura University, Mansoura 35516, Egypt.

Email: [dondn_21@ hotmail.com]

Keywords (Diazonapthoquinone, Eleutherol, Intramolecular cyclization, Glycosidation, Eleuthoside A)

[Introduction]

Recently, the efficient and short directed diazo transfer reaction finds wide spread uses in the field of total synthesis of natural compounds with the aid of metal-catalyzed reactions. On the other side, Eleuthosides A (**1**) has been found in the bulbs of Eleutherine palmifolia (Iridaceae), which is an Indonesian medicinal plant used traditionally as anticancer agent (Figure 1). The interesting biological activities of this substance **1** have inspired us toward its synthesis, making good use of this developed diazo transfer methodology. 2-Azido-1,3-dimethylimidazolinium chloride (ADMC) is the diazo transfer reagent used to convert appropriate naphthol to its corresponding diazonaphthoquinone which could be served as a precursor of Eleuthoside A.
In this investigation, the first total synthesis of the cytotoxic natural Eleuthoside A (**1**), was examined *via* metal-catalyzed intramolecular C-H insertion cyclization reaction of the appropriate diazonaphthoquinone, followed by selective *β*-glycosidation and resolution of the final product. This developed strategy takes the advantage of both diazo transfer reaction and metal catalyzed reaction. (Figure 1).

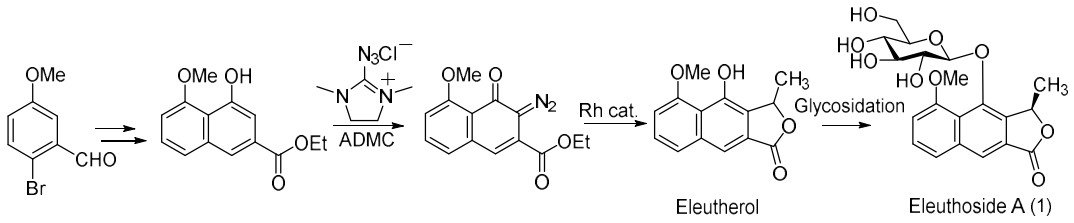

Figure 1. Structure and synthetic pathway of Eleuthoside A (**1**).

[Experiment]

In this work, the experimental procedures involve 2 main steps. First, the synthesis of aglycone part, which is Eleutherol. Second, glycosidation step which has been investigated to get Eleuthoside A (**1**). As shown in scheme 1, naphthalene **4** has been smoothly obtained after several steps starting with phosphonoacetate **2** and aldehyde **3**. Then, it was subjected to debromination and deacetylation to afford the corresponding naphthol **5**. The latter compound was anticipated to form eleutherol (**8**) *via* efficient one step diazo transfer reaction using ADMC (**6**) followed by Rh-catalyzed intramolecular cyclization of the obtained diazonaphthoquinone **7** in refluxing benzene. The challenging glycosidation step was attempted by joining both eleutherol (**8**) and

glucosyl donor **9** together into our final desired glycoside **1**. Several trials have been done, such as Mukaiyama-Suzuki conditions or BF_3-Et_2O catalyzed Schmidt glycosidation reaction. Unfortunately, all these attempts gave back the starting material **8**.

Interstingly, the best conditions found for smooth *O*-glycosidation involved the treatment of eleutherol (**8**) with two equivalents of acetobromoglucose **9** in quinoline in the presence of Ag_2O at room temperature. Finally, subsequent deacetylation, using K_2CO_3 in methanol, and purification, using (PTLC, $CHCl_3$/MeOH, 6:1) were achieved to furnish 20% Eleuthoside A (**1**) in β-configuration. The spectral data of both eleutherol (**8**) and Eleuthoside A (**1**) matched strongly with those previously reported for the natural one.

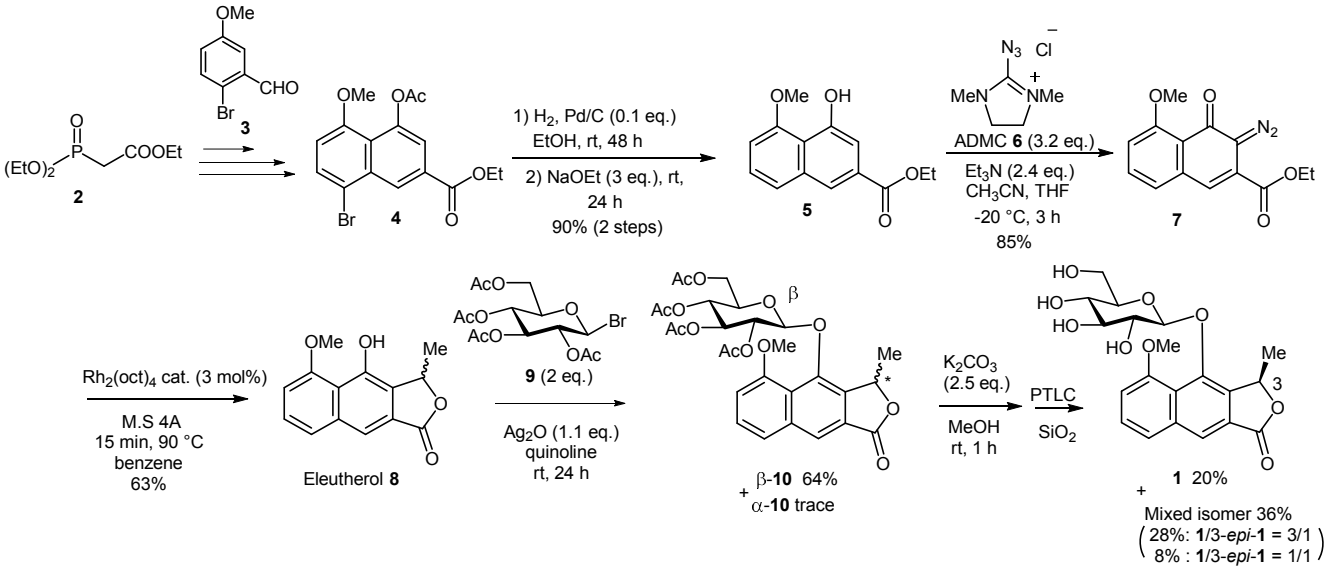

Scheme 1. The synthetic steps toward the total synthesis of Eleuthoide A (**1**).

[Result and Discussion]

We have developed the first total synthetic method of Eleuthoside A (**1**), involving simple and readily accessible starting materials, such as glucose and bromomethoxy aldehyde. Eleutherol (**8**) was synthesized through 9 steps with the aid of diazo transfer chemistry approach and Rh-catalyzed C-H insertion cyclization reaction. Then, several glycosidation routes were experimented to reach effective *O*-glycosidation of Eleutherol (**8**).

In this investigation, the main challenge was that finding proper reaction conditions for both intramolecular cyclization reaction and glycosidation reaction. In brief, the presence of 3 mol % of Rh catalyst, preactivated powdered molecular sieve, and anhydrous benzene were essential to avoid OH- or benzyl-insertion side reactions and get eleutherol (**8**) as a sole product. In addition, the only successful strategy for glycosidation reaction has involved Koenigs-Knorr reaction using peracetyl glycosyl bromide in the presence of Ag_2O and quinoline. This strategy furnished our desired acetylated glycoside **10** of β-configuration, regioselectively. Finally, subsequent deacetylation and purification was done to furnish 20% eleuthoside A (**1**) as single isomer. This reported chemistry allows not only access to the rare naturally occurring substances but also to attractive designed analogues as a new class of potential anticancer agents for future investigation.

[References]

1) H. Shibuya, T. Fukushima, K. Ohashi, A. Nakamura, S. Riswan, I. Kitagawa, *Chem. Pharm. Bull*. **1997**, 45, 1130. 2) D. I. A. Othman, M. Kitamura, *Heterocycles*. **2016**, 92, 1761. 3) A. Frackowiak, P. Skibinski, W. Gawel, E. Zaczynska, A. Czarny, R. Gancarz, *Eur. J. Med. Chem.* **2010**, 45, 1001.

Please choose: Poster
Presentation session: Applied Chemistry
Presenter name: Tomoaki Nishimura

Synthesis of benzodioxane derivatives from diazonaphthoquinones

Tomoaki Nishimura [1], Kota Ohtuka [1], Hirokazu Shimooka [1], Tatsuo Okauchi [1], Mitsuru Kitamura [1]

[1]Faculty of Engineering, Kyushu Institute of Technology, 1-1 Sensui-cho, Tobata-ku, Kitakyushu-shi, Fukuoka, 804-8550, Japan

Email: kita@che.kyutech.ac.jp

Keywords : diazonaphthoquinone, naphthalenediol, benzodioxane, rhodium, cyclization

[Abstract]

1,4-benzodioxane derivatives are often found in pharmaceutical compounds. We have been studying Rh-catalyzed O-H insertion reaction of diazonaphthoquinones and alcohols. In this study, we examined the reaction of diazonaphthoquinones and propargyl alcohols. When terminal alkyne was used as propargyl alcohol, benzodioxane derivative was formed selectively. In the reaction with the propargyl alcohol of internal alkyne, O-H insertion product, naphthol, was formed as major products.

[Introduction]

Substituted aromatic compounds are often found in various useful organic compounds, such as functional materials, and bioactivity natural products. Therefore, development of the new synthetic methods of aromatic compounds are strongly demanded.

Previously, we reported that 1,2-diazonaphthoquinones could be synthesized in high yields by diazo-transfer reaction to naphthol with 2-azido-1,3-dimethyl imidazolium chloride (ADMC)[1)]. We have been studying the reaction of diazonaphthoquinones for the synthesis of substituted aromatic compounds.

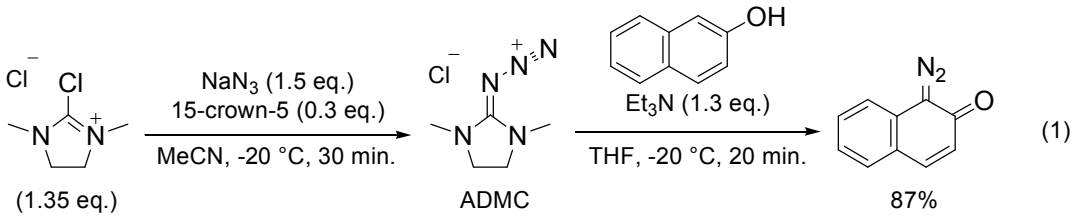

(1)

It is generally known that diazo compounds react with metal catalyst to form metal carbene, which react with alcohol to give corresponding ether via O-H insertion reaction. Naphthalenediol was formed by the O-H insertion reaction of the alcohol and diazonaphthoquinone in the presence of Rh(II) catalyst. Interestingly, benzodioxane derivative was formed as major product when propargyl alcohol was used as the alcohol[2)]. This result prompt us to study this reaction in detail.

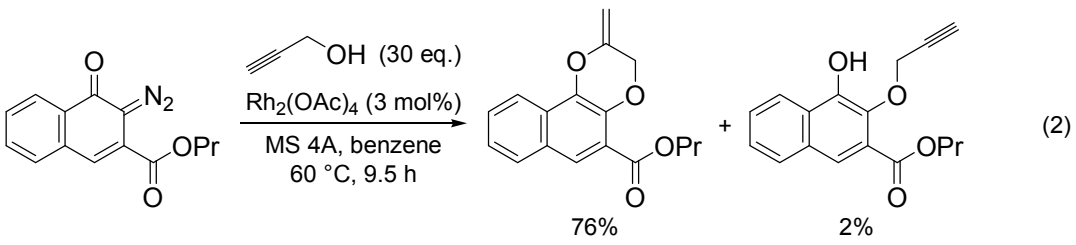

(2)

[Result and Discussion]

Optimization of the Reaction Conditions

We examined the reaction of diazonahthoquinone **1** and propargyl alcohol in the presence of rhodium catalyst (Table 1). When the concentration was 0.01 M, desired benzodioxane **2** was obtained in 51 % yield. Increasing of concentration, the yield of benzodioxane **2** was improved (entry 1~3). When other rhodium catalyst was used, the yield of benzodioxane **2** was decreased and O-H insertion product **3** was obtained (entry 4~6).

Table 1. Optimization of the reaction conditions

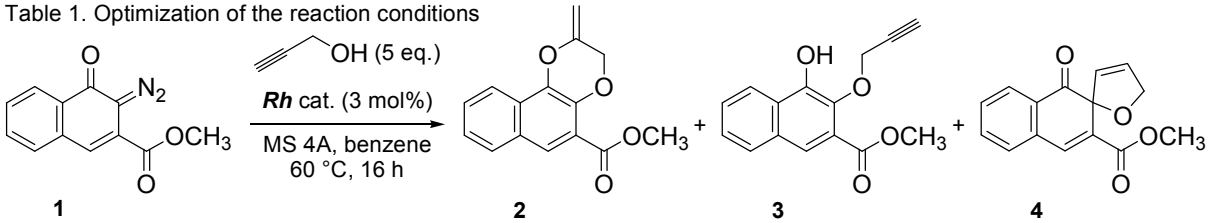

1 **2** **3** **4**

entry	Conc. (M)	*Rh* cat.	yield (%) **2**	**3**	**4**
1	0.01	$Rh_2(OAc)_4$	51	-	1
2	0.05	$Rh_2(OAc)_4$	81	-	6
3	0.1	$Rh_2(OAc)_4$	94	-	1
4	0.1	$Rh_2(Oct)_4$	76	-	-
5	0.1	$Rh_2(OCOCF_3)_4$	0	22	-
6	0.1	$Rh_2(OCOC_3F_7)_4$	11	65	-

Substrate Scope

To a solution of diazonaphthoquinone **1** in benzene, $Rh_2(OAc)_4$ and propargyl alcohol was added at room temperature. The mixture was stirred at 60 °C. When we use diazonaphthoquinone bearing ester, major product is benzodioxane derivative (eq 3). Also, propargyl alcohol of terminal alkyne was used, benzodioxane derivative was selectively formed (eq 4). On the other hand, O-H insertion product and spirocompound were preferentially formed with propargyl alcohol of internal alkyne (eq 5).

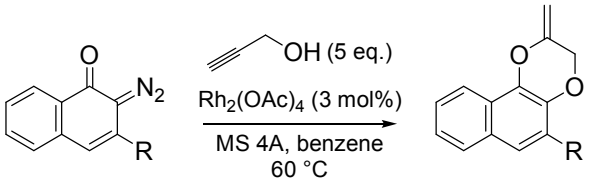

R = CO_2Et 90%
R = CONHPh 79%
R = COPh 84%
R = CHO 54%

(3)

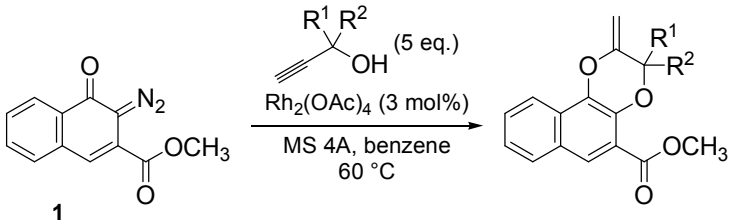

1

$R^1 = H, R^2 = CH_3$ 66%
$R^1, R^2 = CH_3$ 31%

(4)

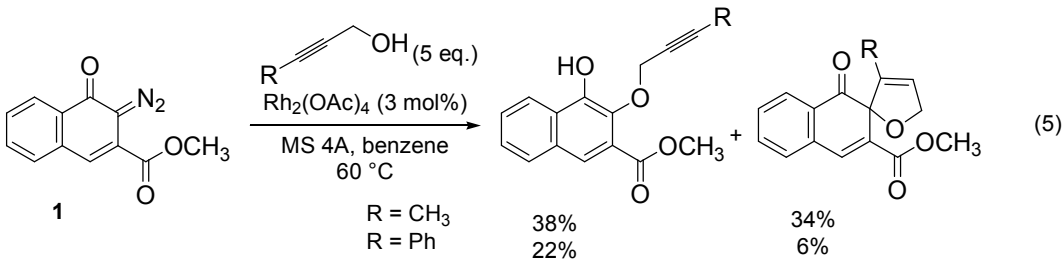

1

R = CH_3 38% 34%
R = Ph 22% 6%

(5)

[Reference]

1) M. Kitamura, N. Tashiro, R. Sakata, T. Okauchi, *Synlett*, **2010**, *16*, 2503.
2) M. Kitamura, K. Otsuka, S. Takahashi. T. Okauchi, *Tetrahedron Lett.*, **2017**, *58*, 3508-3511.

Presentation session: Poster

Presenter name: Yukihiro Yamaguchi

Synthetic study of teadenol derivatives

Yukihiro Yamaguchi, Kosuke Hoshino, Hiroki Suetake, Hirokazu Shimooka,
Tatsuo Okauchi, Mitsuru Kitamura

Faculty of Engineering, Kyushu Institute of Technology, 1-1 Sensui-cho, Tobata-ku, Kitakyushu-shi, Fukuoka, 804-8550, Japan

Email: kita@kyutech.ac.jp

[Keywords] Hetero-Diels-Alder, tea catechin, polyphenol

Abstract

Teas show a good effects for life style diseases and contain polyphenol called tea catechin. The tea catechins are regaraded as main active compounds for the good bioactivity and have flavan skeleton in general. In 2011, new tea catechin named teadenol were isolated, and that don't have flavan skeleton. Teadenols show remarkable anti-diabetic influence and metabolic syndrome improvement activity. We planned the synthesis of teadenols and its derivatives were synthesized by Hetero-Diels-Alder reaction of vinyl ether **4**/**5** and unsaturated keto ester **6** as a key step. Vinyl ether **4a**/**5a** were synthesized from the salicyl aldehyde **9** in 5 steps. Vinyl ether **5b** were prepared from the phloroglucinol dihydrate in 7 steps.

Introduction

Teadenols A (**1a**) and B (**1b**) were isolated from tea fermented by Aspergillus sp. (PK-1, FARM AP-21280),[1] and possess unique biological activities to increase adiponectin and decrease protein-tyrosine phosphatease 1B (PTP1B), which are relevant to the treatment of diabetes.[2] Most of tea catechins have flavan structure, however, teadenols don't have this structure. Stimulated with the unique structure and biological activity, we started synthetic study of teadenols.

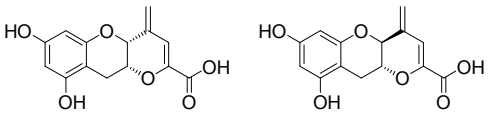

teadenol A (**1a**) teadenol B (**1b**)

Fig.1 Teadenol

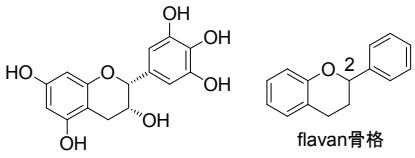

(-)Epigallocatechin (**1c**) flavan骨格

Fig.2 Tea catechin

Result and Discussion

We planned the teadenols and its derivatives were synthesized by Hetero-Diels-Alder reaction with vinyl ether **4**/**5** and unsaturated keto ester **6** as a key step as show scheme 1. Tricyclic compound **7**/**8** would be transformed to teadenols and teadenol derivative **2** with olefinaton, deporotection and hydrolysis.

Scheme 1. Synthetic plan of teadenol and teadenol derivative

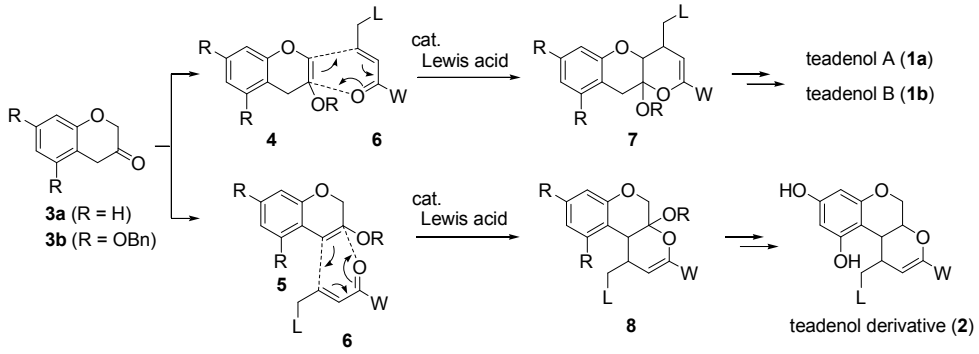

Synthesis of enol ether 4a/5a

Nitrile **10** was synthesized from salicyl aldehyde **9** with Morita-Baylis Hillman reaction. Nitrile **10** was transformed to ketone **3a** with Crutius rearrangement via carboxylic acid **11**. After protecting carbonyl group with dimethylacetal, enol ether **4a**/**5a** were obtained by treating TMSOTf and diisopropylethylamine. (Scheme 2)

Scheme 2. Synthesis of enol ether 4a/5a

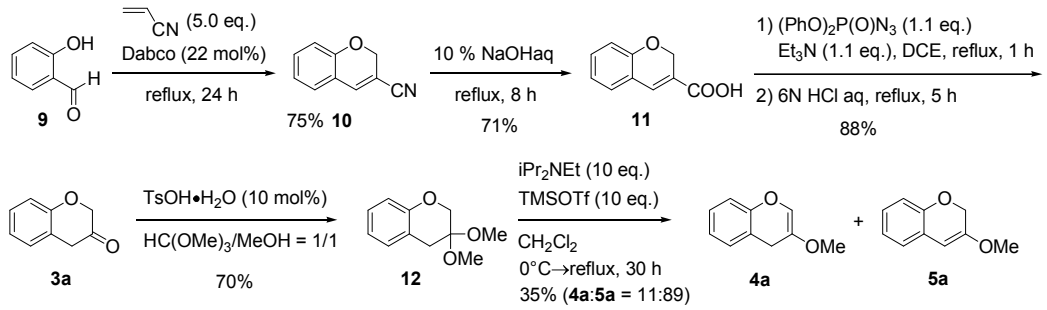

Synthesis of enol ether 5a

Aldehyde **14** was synthesized from phloroglucinol dihydrate **13** with Vilsmeier-Haack reaction. After protecting phenolic hydroxyl group with Bn ether, in the same way as synthesis of ketone **3a**, ketone **3b** was synthesized. Ketone **3b** was transformed to enol ether **5b** with LiHMDS and Me_2SO_4. (Scheme 3) Now, Hetero-Diels-Alder reaction between enol ether **5b** and unsaturated keto ester **6** is under investigation.

Scheme 3. Synthesis of enol ether 5b

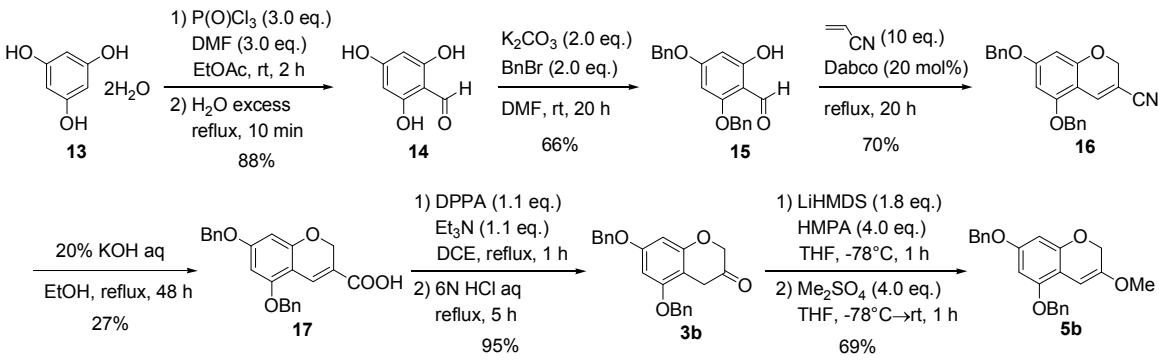

Reference

1) K. Ishimaru, R. A. Wulandari, M. Amano, T. Yanagita, T. Tanaka, I. Kouno, D.Kawamura, *J. Nat. Med.* **2011**, *65*, 594.

2) T. Yanagita, K. Ishimaru, T. Tanaka, K. Koba, H. Miyazaki, N. Aoki, D. Kawamura, PCT Int.Appl, WO2011034217A1, **2011**

Please choose: Poster
Presentation session: Applied Chemistry
Presenter name: Hiromasa Ando

Synthesis and structure of pseudo aza[5]helicenediol derivatives

Hiromasa Ando, Hiroaki Fukuma, Mitsuaki Kobayashi, Hirokazu Shimooka, Tatsuo Okauchi, Mitsuru Kitamura
Faculty of Engineering, Kyushu Institute of Technology, 1-1 Sensui-cho, Tobata-ku, Kitakyushu-shi, Fukuoka, 804-8550, Japan

Email: n109004h@mail.kyutech.jp

Keywords (5 words)
organic synthesis, heterocycles, azahelicenes, helical chirality, quinolone

Introduction

Various asymmetric reagents have been synthesized and applied for asymmetric reactions. As the chiral source for asymmetric reactions, center chirality and axial chirality have been used commonly. Recently, exploration for new chiral source has been conducted and planar chiral compounds were found to be used in several reactions. In nature, helical compounds offer good environment for the reaction to maintain its lives, such as DNA/RNA and alpha-helix in proteins. Therefore, helical compounds are good candidate for the asymmetric reagents in organic reaction. Actually, exploration for helical chirality has been conducted as new chiral source and helical chiral compounds were used in several reactions. [1]

Helical 1,14-diaza[5]helicene (**1**) seems to be efficient new asymmetric organic base catalyst, because good asymmetric environment is constructed around pyridine nitrogen in **1** (Figure 1). However, aza[5]helicene **1** cannot be used for the purpose because of low barrier for helicity of **1**. [2] We supposed that *trans*-pseudo aza[5]helicenediol **2** and its derivative would be used as efficient helical chiral base (Figure 2). Environment around nitrogen in **2** is similar to that of aza[5]helicene **1**. Diol **2** has two conformers, such as diaxial conformer and diequatorial conformers. When the *trans*-diol **2** is obtained as enantiomerical pure form, the helicity of **2** could be controlled by the conformer. That is, the helicity of (*R*,*R*)-diol is controlled (*P*) (clockwise) when **2** was obtained as diequatorial conformer, and (*M*)-helicity (anti-clockwise) was induced by diaxial conformer.

Then, we started to synthesize **2** and achieved synthesis of **2** in racemic form. We also examined changes of its conformers of diol **2** by ^{1}H NMR.

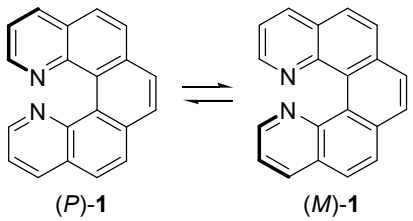

Figure 1. 1,14-diaza[5]helicene

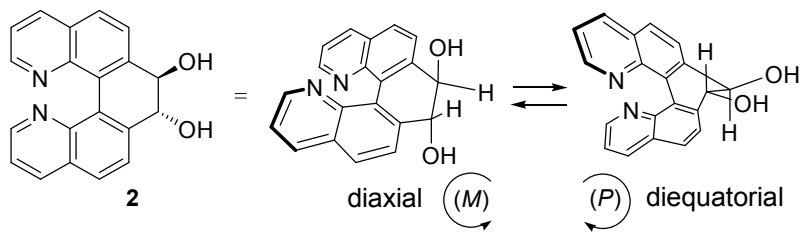

Figure 2. Structure and helicity of (*R*,*R*)-pseudo aza[5]helicenediol **2**

Result and Discussion

Started from 7-methylquinoline (**3**), 8-bromo-7-methylquinoline (**4**) was synthesized by the bromination with NBS in H_2SO_4, quantitatively. Successively, dibromination on benzylic position was conducted to give **5** in 77% yield. Dibromomethyl group in **5** was transformed to formyl group by heating in DMSO (dimethylsulfoxide) to afford aldehyde **6** in 84% yield. Intermolecular pinacol coupling of **5** proceeded by treating $TiCl_4$ and Zn in THF/CH_2Cl_2 at 0 °C giving *dl*-diol **7** as major product. In this pinacol coupling reaction, temperature is very important for good reproducibility. Then, diol part in **8** was transformed to orthoester for making two bromo groups close aiming good reactivity in the next biaryl coupling reaction.General Ullmann coupling reaction of **9** using Cu reagents did not proceed efficiently probably due to the effect of quinoline nitrogen atoms. To our delight, intramolecular biaryl

coupling of **8** proceeded by treating $Ni(cod)_2$ (biscyclooctadiene nickel) to give pseudo aza[5]helicene **9**. Finally, deprotection of orthoester in **9** was achieved by treating formic acid affording *trans*-diol **2**.

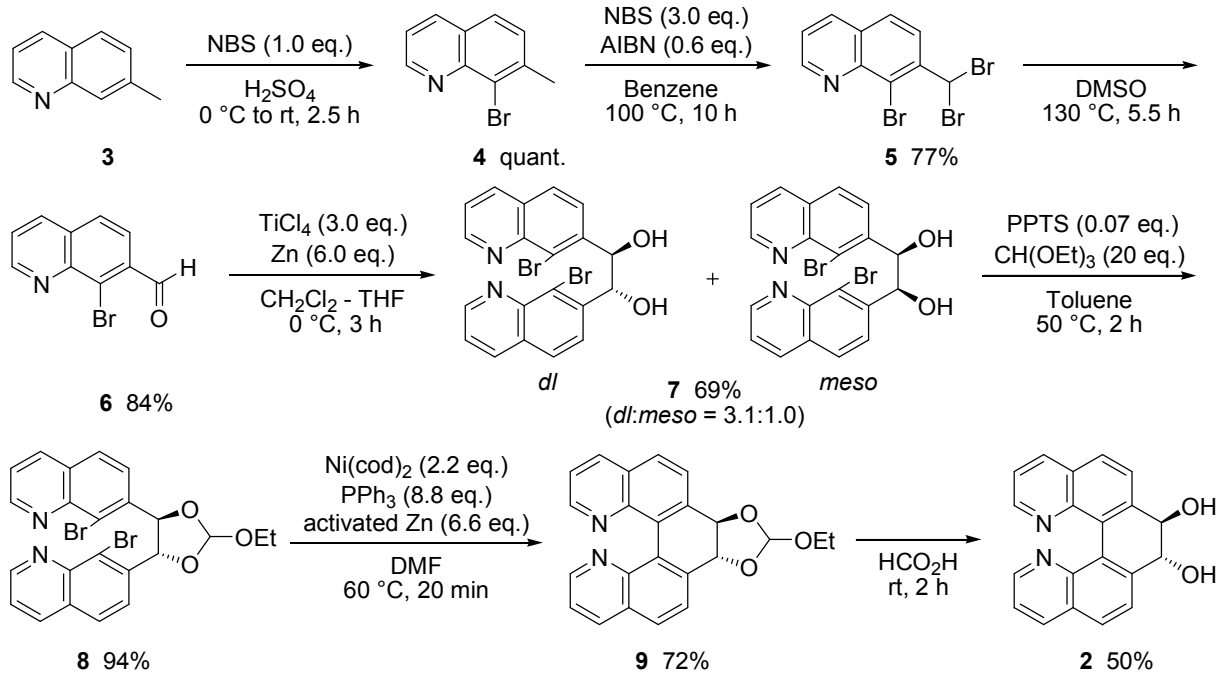

Scheme 1 Synthesis of pseudo aza[5]helicenediol **2**

Protected pseudo aza[5]helicenediol **10** and **11** were also synthesized. By treating DIBAL-H (diisobutylaluminium hydride) to pseudo aza[5]helicenediol **9**, alcohol **10** was synthesized in 85% yield. By the acetylation of hydroxyl group in **10**, **11** was obtained.

The coupling constant between H_A and H_B in **10** were 7.0 Hz (^{1}H NMR), which suggested that alcohol **10** was existed as a diequatorial conformer. On the other hand, **11** shows two kinds of coupling constants, 2.6 and 11.4 Hz on H_A and H_B. That suggest two conformers, diequatorial and diaxial, were existed on the confomers of **11**.

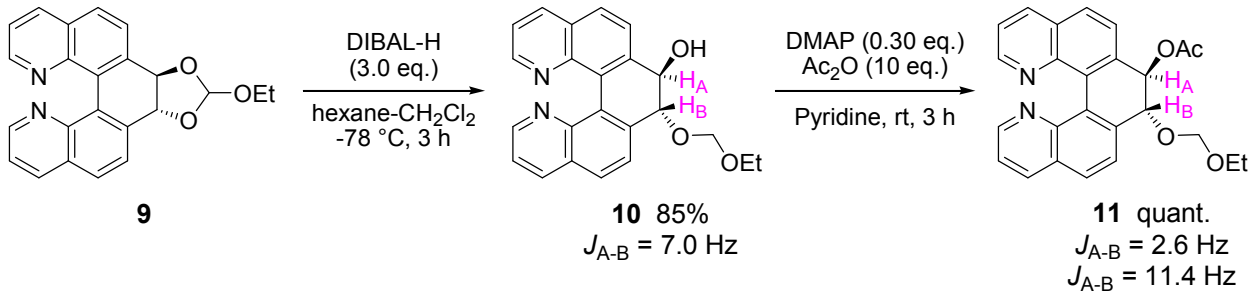

Scheme 2 Synthesis of derivatives **11**

References

[1] K. Yamamoto, T. Shimizu, K. Igawa, K. Tomooka, G. Hirai, H. Suemune, K. Usui, *Sci. Rep.* **2016**, *6,* 36211.
[2] P. Ravat, R. Hinkelmann, D. Steinebrunner, A.Prescimone, I. Bodoky, M. Juricek, *Org. Lett.* **2017**, *19*, 3707.

Please choose: Poster
Presentation session: Applied Engineering
Presenter name: Juhyo Lee

Development of New Material Structure Based on Carbon Fiber for Aircraft

Juhyo Lee[1], Yasuhiro Akahoshi[1], Takao Koura[1], Taito Hayashi[1]

[1]Department of Mechanical and Control Engineering, Kyushu Institute of Technology
1-1 Sensui-cho, Tobata-ku, Kitakyushu-shi, Fukuoka, 804-8550, Japan

Email: lee.juhyo123@mail.kyutech.jp

Keywords (5 words)
Bird Strike, Aircraft, Jet Engine, Material, Carbon Fiber

[Introduction]

Currently, as globalization progresses, the amount of cargo and people being transported by aircraft is increasing. Therefore, the demand for aircraft is increasing every year. Air-fuel usage increases as the volume of air traffic increases. The problem of environmental degradation is cited. Bird strikes also tend to increase as the number of aircraft increases. Bird strikes are hard to predict, and if an accident occurs, it is highly likely that the aircraft will crash and cause fatal damage. For these reasons, future aircraft requires lower fuel efficiency and improves safety. Carbon Fiber Reinforced Plastic (CFRP), a composite material with high specific strength, is attracting attention as a countermeasure. Carbon fiber is superior to the resin in the shear and tensile strength of CFRP, and researches are actively progressing to improve impact resistance. In this study, the strength of CFRP is noteworthy and the purpose of the development of materials for high-performance aircraft is to use the fiber's properties more efficiently.

[Experiment]

In the CFRP, fibers are fixed with resins, and the friction between fibers and the absorption of energy by the elongation of fibers are small against shearing force. In this research, CFHT (Carbon Fiber Held Tube) was produced with the aim of increasing absorption energy through friction and elongation by increasing the degree of freedom of fiber. CFHT is a new material made by bundling carbon fibers with a heat shrinkable tube. Since CFHT does not use resin, the degree of freedom of carbon fibers can be improved. The kind of carbon fiber is T800SC that used in CFRP. Both ends of the CFHT are knotted. It allows the target to measure the absorption energy without separating it from the jig when the impact experiment. CFHT is shown in Fig.1 and CFHT fixed with a jig is shown in Fig.2. The launcher uses an air gun for launching a projectile by releasing high-pressure compressed air. In this research, the target has impacted by the rectangular projectile, and impact resistance is evaluated from absorbed energy calculated from the speed difference between before and after the impact. Also, the absorbed energy of CFRP and CFHT are compared.

Fig.1 CFHT

Fig.2 CFHT fixed with a jig

[Result and Discussion]

Since CFHT and CFRP differ in mass and shape, it is not appropriate to compare only absorbed energy them with each other. In order to unify the parameters, the surface density showing the mass per unit area is introduced. The absorbed energy per unit surface density is calculated by dividing the absorbed energy by the surface density obtained from the projection area and the mass. By using this parameter, the comparison of the absorbed energy can be performed regardless of the mass and shape of the test piece. Experimental results are shown in Fig.3. In the graph, the open symbol means non-penetrating and closed symbol means penetrating.

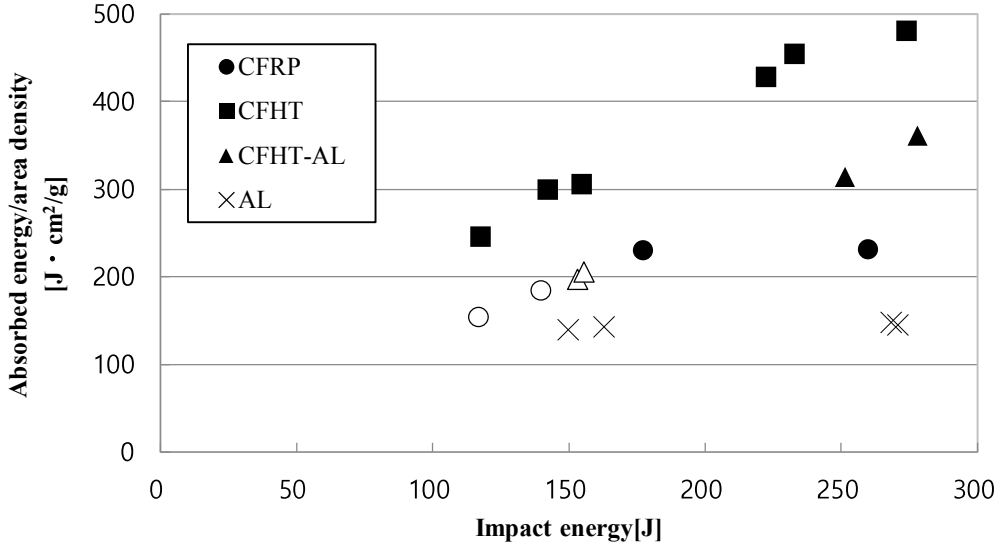

Fig.3 Experimental results

In experimental results, what characterized the CFHT is that the absorbed energy increases proportionally to the impact energy and shows a value of 1.5 to 2 times superior to absorbed energy for the CFTP. This is because we were able to increase the absorbed energy due to friction between fibers and elongation of fibers as this research aims. However, if the impact energy is around 150J, CFRP is non-penetrated, but CFHT is pierced by the rectangular projectile. In order to be used as a material for aircraft engines, a containment property is required to confine splinters in a fan case without escaping, when fan-blades are broken as a bird strike or an impact occurs. From results, it can be seen that CFHT has superior ability to absorb energy than CFRP, but has inferior containment property. In order to improve the containment property of CFHT, CFHT-AL is manufactured by superposing an aluminum plate (A2017) on CFHT. According to the result of the experiment, impact becomes non-penetrated when its energy is in the vicinity of 150J, and the absorbed energy per unit surface density is 1 to1.5 times superior to CFRP. As a result, it is expected that CFRP, which is superior in containment properties, and CFHT, which is superior in energy absorption, will be used in combination to achieve higher impact resistance.

Please choose: Poster
Presentation session: Applied Chemistry
Presenter name: Takahiro Saiki

[Electromagnetic shielding of cellulose nanofiber/polyaniline composite with various dopants]

[Takahiro, Saiki][1], [Taku, Omura][1], [Minato, Wakisaka][1]
1 Graduate School of Life Science and Systems Engineering, Kyushu Institute of Technology

Email: [saiki.takahiro922@mail.kyutech.jp]

Keywords (5 words)
Cellulose nanofiber, Conductive Polymer, Dopant, Electromagnetic Shielding

[Introduction]

Since the mid-1980s, accidents such as machine / device malfunction due to electromagnetic waves generated from electronic devices, radio information leakage, and so forth have occurred frequently and become serious. Electromagnetic shielding (EMS) is one of the key technology which is an electrically conductive material and covers the periphery of the device. In order to solve these problems, researches on electromagnetic wave shielding materials has been actively studied.

EMS material which replacing metal with light and tough with good forming processability are necessary. Thus, composite of polymer with conductive materials attract great attention.Typical conductive materials include carbon materials such as carbon nanotubes. Although these carbon materials are currently being improved in terms of cost, they emit a large amount of CO_2 in the process from production to disposal. Therefore it is necessary to overcome the environmental burden problem for general purpose utilization. Conductive polymer could be synthesized considerably lower cost and environmental friendly way compared to carbon materials. Among varieties of conductive polymers, uniqueness of polyaniline is controllable conductivity and stability in environment. But, polyaniline is stiff and brittle, so composite with flexible support is necessary for wide range of application with shape desired.Cellulose nanofiber (CNF) is renewable polymer derived from plant resources. CNF is expected as light and strong filler to produce excellent polymer composite. CNF has almost same strength characteristics as carbon nanotubes and has various features, it is expected to be used in a wide range of fields. However, in order to exhibit the potential of cellulose nanofibers as an electromagnetic wave shielding material, it is necessary to improve compatibility with the matrix resin. Surface modification of CNF by conductive polymer, PANI expected to be a good solution to improve compatibility. It is possible to improve the electromagnetic wave shielding function by doping the polyaniline with a base to a dedoped state to form an emeraldine base and doping an optically isomeric dopant to the base state polyaniline to obtain a doped state. In this study, it is investigated how to influence electromagnetic wave shielding effect when changing dopant of polyaniline in conjunction with cellulose nanofibers.

[Experiment]

PANI-coated CNF (CNF/PANI) was prepared by the oxidative polymerization of aniline in water medium. Bamboo-derived CNF dispersion gel (1 wt% in water in, Chuetsu Pulp Co., Ltd., Japan) 10g (100 mg as solid weight) was added into a 100mL of 1 M HCl aq., followed by addition of anilin (1.4 mmol) and lithium chloride (0.2 mol) before stirring at -10 ℃ for 1 h . Oxidizing agent: ammonium persulfate (1.75 mmol) aq. 100 mL was slowly added dropwise into the solution. After completion of the dropwise addition, the solution was further stirred for prescribed periods. After the reaction, the solution, which changed in color to dark green, was filtered with PTFE membrane filter (pore size 1.0 μm) under a reduced pressure before washed with acetone to obtain PANI-Cl coated CNF. PANI-Cl coated CNF gel before drying was added into a 100 mL of 1 M ammonia aq. and

stirred at r.t. for 3 h to de-dope the chlorine ions. To recover de-doped PANI coated CNF, previously obtained blue black solution was filtrated and purple-colored residue was washed with acetone. The de-doped PANI coated CNF gel before drying was added into a 50 mL of m-cresol solution with dopant (Camphor sulfonic acid (CSA) or phytic acid (PA) (0.1, 0.25, 0.5, 0.75, 1.0 mmol) and stirred at r.t. for 3 h. After filtration of this dark green solution, PANI-PA coated CNF with various dopant finally obtained followed by washing with acetone and following vacuum drying. Electromagnetic shielding (EMS) effectiveness of each sample were measured at room temperature in the range from 0.45 to 15 GHz (including X-bonds: 8.2~12.4 GHz) by using networks analyzer (Anritsu corporation, Japan, model MS202C) and coaxial sample holder complying with the test standard.

[Result and Discussion]

Fig. 1 shows the digital images of PANI-Cl coated CNF which is before dedoping (a) and dedoped PANI-Cl coated CNF which is after dedoping (b). PANI coated CNF film showed blue-black in color without dopant, and color changed to greenish black in color with dopant. Various dopant dedoped PANI coated CNF film was thin and flexible. EMS effect of PANI/CNF with various dopants (Cl, PA and CSA) were shown in Fig.2. On the other hand, by treating with various dopants such as Cl, PA, CSA, or the like, the surface of the film changes to greenish black which shows conductivity. It is said that this state generally shows electrical. As shown in Fig. 2, The EMS effect of PANI-Cl coated CNF was around – 3dB. On the other hand, the EMS effect of PANI-PA coated CNF increased around – 17 dB and PANI-CSA coated CNF increased around -30 dB after changing the dopant with m-cresol. In case of PANI/CNF composite, EMS effect could be controlled by simply changing dopant of PANI. Especially, CSA showed excellent EMS effect as a dopant. It is attributed to the magnitude of the electron attracting property in each dopant. Sulfo groups are present in CSA, and S atoms are positively affected by the influence of large electronegativity O atoms existing around the S atom in the sulfo group. Therefore, the sulfo group has electron withdrawing property. The phosphate group in PA is also the same reason. These groups having electron-withdrawing properties attract electrons of polyaniline, whereby polyaniline develops conductivity. Since this electron withdrawing property differs depending on each group, it seems that the electromagnetic shielding effect also showed a high value when CSA having a sulfo group having a higher electron attracting property was used as a dopant. Further investigation will be conducted on PANI/CNF composite to improve EMS effect with a lower cost.

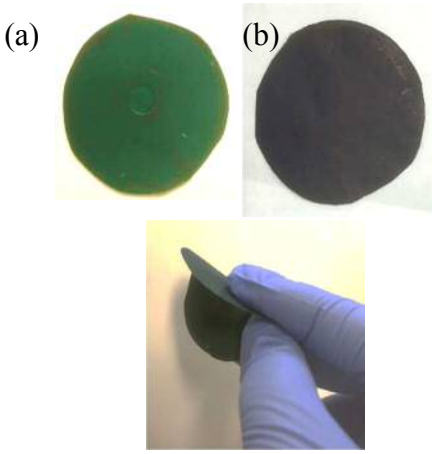

Fig.1. Flexible PANI coated CNF composite PANI-Cl coated CNF (a), dedoped-PANI coated CNF (b)

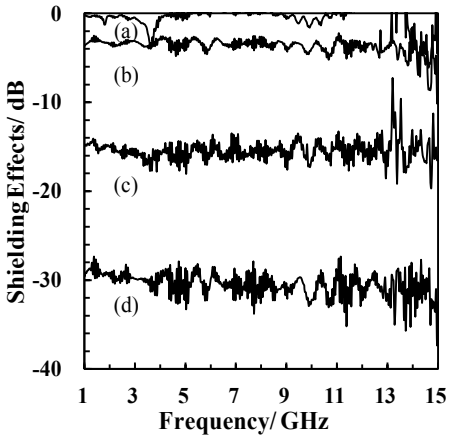

Fig. 2. EMS effect of dedoped-PANI coated CNF (a), PANI-Cl coated CNF (b), PANI-PA coated CNF (c), PANI-CSA coated CNF (d)

References

[1] L. Tang, J. Han, Z, Jiang, S, Chen, and H. Wang, *Carbohydr. Polym.,* 117, 230-235 (2015).

Please choose: poster
Presentation session: Applied Chemistry
Presenter name: Tessei Kawano

Mechanism of Cellulose Nanofiber Dissolution in Lithium Hydroxide/Urea Solution and Regeneration

Tessei Kawano, Yoshito Andou

Department of Biological Functions Engineering, Graduate School of Life Science and Systems Engineering, Kyushu Institute of Technology, 2-4 Hibikino, Wakamatsu-ku, Kitakyushu-shi, Fukuoka, 808-0196, Japan

Email: kawano.tessei758@mail.kyutech.jp

Keywords: Cellulose Nanofiber, Regenerated Cellulose, Lithium Hydroxide/Urea aq., Dissolution Cellulose

Introduction

Cellulose nanofiber (CNF), from biomass have recently attracted much attention as an advanced material with high strength, lightweight, and biodegradability. In most commercial products such as films and plastics, regenerated cellulose (RS) were used as one of the components. These products are known to be transparent and tough due to its unique structure resulting from hydrogen bonding. Usually, RS materials are prepared directly from cellulose solution via physical dissolution, shaping, regeneration, and drying process. However, it is very difficult to dissolve RS in common solvents, because of their strong intra- and intermolecular hydrogen bonds. To overcome the issues, many methods have been developed to dissolve cellulose. Hence, to address this issue, a simple route using alkali/urea aqueous solution has been developed for fabricating RS materials without discharging hazardous byproducts. In addition to dissolution of cellulose, shaping and drying of RS are very difficult because shrinkage occurs during restructuring process when RS is formed. The mechanism and how to solve these problems were discussed. The structure of the RS were studied by ATR-FTIR measurement.

Experimental

In this study, 5 wt% CNF (IMa-1005, Sugino Machine Limited, Japan) was used. At the start, 50g of CNF sample, 0.2mol of LiOH, and urea was mixed and cooled at -14□ for 2 hours. The mixture was stirred, subsequently forming a transparent and viscous solution. The CNF solution obtained was degassed by centrifugation (8500rpm, 5□, 7min), spread on a glass plate, and then immersed in

a coagulation bath at room temperature. The sheet-like hydrogels of RS was washed with DI water, fixed on a plastic cup to avoid shrinkage, and air dried at ambient temperature.

Result and discussion

A schematic process describing the dissolution and regeneration process of cellulose in LiOH/urea aqueous solutions at low temperature and is depicted in Figure 1. Before the cooling process, CNF doesn't dissolve in solution and a transparent solution cannot be obtained due to the its close packing through numerous hydrogen bonds, Figure 1(a). As temperature droped below the freezing point of free water, ice started to form, and then concentration of LiOH and LiOH adsorbed on CNF increased, Figure 1(b). The volume expansion occured due to crystal growth in free water, and severing of hydrogen bonding between cellulose chains. Subsequently, cellulose chains are interacted with the LiOH, are overcoated by urea hydrates in free water as an overcoat, the resulting is dispersed in the solution to form transparent solution, Figure 1(c). When LiOH and urea are removed by a neutralization, CNF is regenerated by restructuring, Figure 1(d). This process was also confirmed by ATR-FTIR measurement based on Figure 2. From the result of CNF/LiOH/urea aqueous solution without regeneration, several peaks due to urea such as N-H and C-N stretching were found, however, peaks attributed to CNF was not found. This result proved the structure of CNF/LiOH/urea solution at low temperature. After regeneration, lithium and urea were removed and the broad band in the 3600~3100 cm^{-1} showing increase of OH group were found. This proved that a transparent film could be obtained.

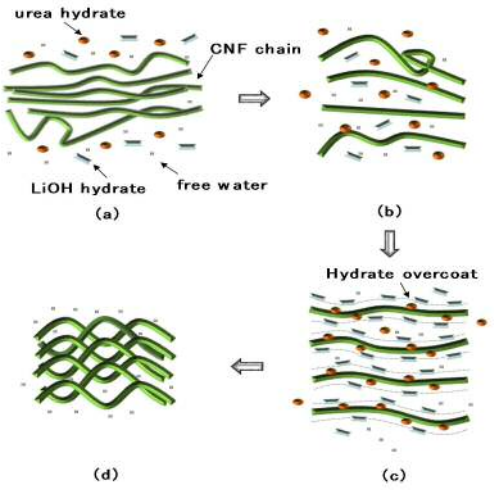

Figure 1. Schematic dissolution and regeneration process

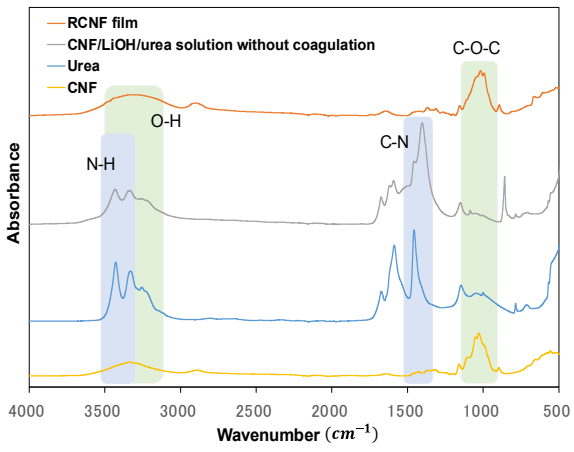

Figure 2. ATR-FTIR spectra

Please choose: Poster
Presentation session: Applied Chemistry
Presenter name: Satoko Takase

Enhanced Metal-phthalocyanine Crystalline Phase for Oxygen Reduction Electrocatalyst

Satoko Takase, Yuki Aoto, Daiki Ikeda and Youichi Shimizu

Department of Applied Chemistry, Kyushu Institute of Technology, 1-1 Sensui-cho, Tobata-ku, Kitakyushu-shi, Fukuoka, 804-8550, Japan

Email: satoko@che.kyutech.ac.jp

Keywords Oxygen Reduction, Metal Phthalocyanine, Crystalline Phase Conversion, Fuel Cell

Introduction Practical proton conductive polymer electrolyte membrane fuel cells (PEMFC) require a highly active electrocatalyst for oxygen reduction reaction (ORR), which have some slow electron transfer and transformation steps. At the present time, platinum-based catalyst are widely used. However, the high cost of the catalyst has prevented the expansion of a commercial market for PEMFC. The development of non-platinum catalysts has been conducted intensively. Low-cost 3d-metal phthalocyanines (MPcs), which are analogous with porphyrins compounds, have been studied on the application for electro-catalyst due to the high chemical and thermal stability. It is well known that the kinds of central metal in MPc have a large influence on the catalytic property of MPc. High catalytic activity for ORR requires that the energy level of 3d orbital of the central metal in MPc should be similar to the π* orbital of O_2. In addition, the types of configuration for O_2 adsorbed on MPc have a large effect on ORR properties. It has been reported that the type of the adsorbed oxygen configuration determines the ORR pathway. MPc have three major oxygen configurations: side-on, end-on, and bridge as shown in Fig. 1. [1] The side-on configuration have a driving force to rupture the O-O bond after protonation, therefore follow to produce H_2O via a 4-electron pathway. On the other hand, the end-on configuration follow to produce H_2O_2 via a 2-electron pathway without the rupture of the O-O bond. In the bridge configuration, an O_2 molecule binds the two central metals with similar bond types as an end-on configuration, but the O-O bond in an oxygen molecule extend and should rapture and produce H_2O with protonation because of bonding to two metals. The formation of the bridge configuration of oxygen needs a distance about 4 Å for two central metals.

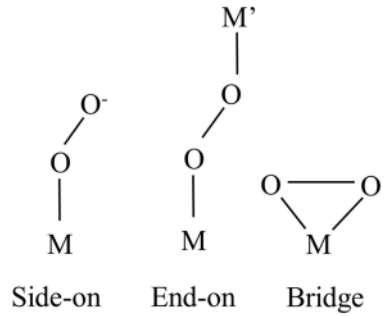

Fig. 1 Models for configuration of O_2 adsorption on active sites for catalyst.

We tried to align the MPc molecules through a selection of the crystallographic structures in MPc with a deposition at a hydrophilic-hydrophobic interface. In the two major crystallographic structures for MPcs, α phase (α-MPc) and β phase (β-MPc), MPc molecules are orderly arranged in parallel at a distance of 3.4 Å as shown in Fig. 2. [2] The distances for central metals are 3.8Å in α-MPc and 4.8Å in β-MPc due to parallel shifts of the molecular plane.

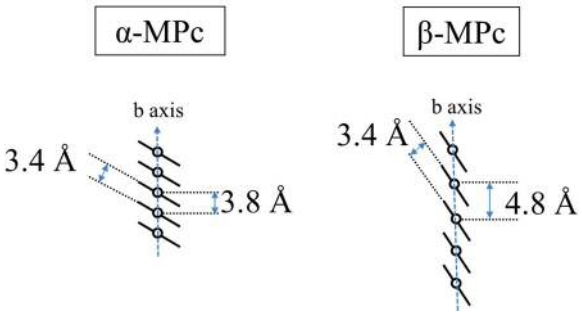

Fig. 2 Schematic representations of the arrangement of the MPc molecules in α- and β- phases.

The catalytic performance of various α-MPc compared with β-MPc in an acid medium, and the influence of the crystallographic structures on the ORR properties is discussed.

Experiment

The crystallographic conversion of MPc (M = Mn, Fe, Co, Ni, Cu, Zn) was conducted used organic MPc solution and aqueous solution. Commercial powders of MPcs were dissolved in CH_2Cl_2 containing CF_3COOH (1M). The MPc (1 mM) solution 200 mL was dropped in 300 mL KOH (1 M) aqueous solution and then filtered it and got powder. Finally, the powder was dried at 120ºC after washing with purified water. [3] The crystallographic structures of MPc were determined by X-ray diffraction (XRD) analysis, etc.

Electrochemical measurements were carried out used a three-electrode system with a gas diffusion electrode (GDE) with a nickel-mesh current collector as the working electrode, a reversible hydrogen reference electrode, and a platinum plate counter electrode. The electrolyte was a 1M H_2SO_4 solution at 70ºC. For testing the ORR activity, a staircase voltammetry (SV) was recorded with a potential step of 25 mV and a holding time at each potential of 3 min.

Result and Discussion

From XRD patterns, commercial CoPc, NiPc, CuPc, and ZnPc were identified with β phase. On the other hand, the patterns for commercial MnPc and FePc were identified with α phase. The patterns for the prepared powder of CoPc, NiPc, CuPc, and ZnPc were also attributed to α phase with high crystallinity. The prepared powder of MnPc and FePc were attributed to α phase with slight deterioration in crystallinity. These results indicated that the wet method in this study is appropriate for preparation of α-CoPc, α-NiPc, α-CuPc, and α-ZnPc, but is not suitable for α-MnPc and α-FePc.

For comparison of the ORR properties between α-MPc and β-MPc, polarization curves were measured with GDEs loaded with various MPcs (MPc-GDE) in an acid electrolyte (Fig. 3). The ORR current value for α-CoPc-GDE was about as high as double than that for the β-CoPc-GDE at the wider potential range. The ORR current value for α-CuPc-GDE also showed higher than that for β-CuPc-GDE, but it had a smaller current in comparison with the α-CoPc-GDE. From the Tafel curves obtained from these polarization curves, the Tafel slope (-50mV/dec.) for α-CoPc, was smaller than that for β-CoPc (ca. -60mV/dec.). Similarly, the slope for α-CuPc was smaller than that for β-CuPc. The results suggest that the conversion to α phase from β phase is very effective method in improving the catalytic performance of metal phthalocyanines such as CoPc and CuPc.

In the case for NiPc and ZnPc, their cathode currents were poor, and the difference in ORR between α- and β-phases were quite small. The results indicated that NiPc and ZnPc have less catalytic activity for ORR.

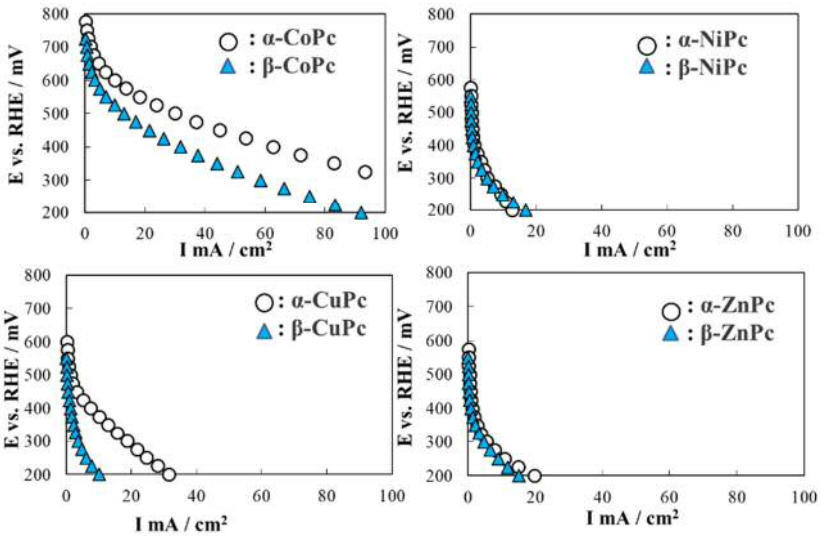

Fig. 3 Polarization curves for gas diffusion electrodes with CoPc, NiPc, CuPc, and ZnPc in O_2 saturated.

Reference

[1] E. Yeager, *Electrochim. Acta*, **29**(11) (1984) 1527-1537.
[2] C. Ercolani, C. Neri, and P. Porta, *Inorg. Chim. Acta*, (1967) 415-418.
[3] S. Takase, Y. Aoto, Y. Shimizu, *Chem. Lett*. **45**(9) (2016) 1066-1068.

Please choose: Oral
Presentation session: Applied Engineering
Presenter name: Mrs Nur Izzati Md Saleh

Influence of degree hydrolysis and enzymatic hydrolysis conditions on antioxidant activity of microalgae protein hydrolysate

Nur Izzati, Md saleh[1], Wan Azlina, Wan Ab Karim Ghani[1], Razif, Harun[1], Siti Mazlina, Mustapa Kamal[2]

[1]Department of Chemical and Environmental Engineering/ Sustainable Process Engineering, Faculty of Engineering, University Putra Malaysia, 43400 UPM Serdang, Selangor, Malaysia
[2] Department of Food and Processing Engineering, Faculty of Engineering, University Putra Malaysia, 43400 UPM Serdang, Selangor, Malaysia

Email: nurizzatims@gmail.com

Keywords: Enzymatic hydrolysis, degree hydrolysis, antioxidant activity, microalgae and protein hydrolysate

Introduction

Nowadays, many diseases that hit the global world such as neurodegenerative disorders, cardiovascular diseases, diabetes, Alzheimer's disease, retinal diseases and certain types of cancer which is associated with oxidative stress and free radicals (Elias et al., 2008; Homayouni-tabrizi, Asoodeh, & Soltani, 2016; Masuda, Shimazawa, & Hara, 2017; Poprac et al., 2017). The impact on human health arise from these two reactions; oxidative stress and free radicals are needed to prevent (Lobo, Patil, Phatak, & Chandra, 2010). In human body defense, antioxidant enzyme such as glutathione peroxidase, superoxide dismutase (SOD), and catalase (CAT) are used to induce the DNA damage from the free radicals and acts against oxidative stress. However, in certain conditions, the amounts of these antioxidants are less enough to overcome the reaction of free radicals and inhibit the damage (Mohankumar & Ramasamy, 2006). Thus, external sources of antioxidants are essential to prevent any damages and reduce the diseases associated with it (Crawford et al., 2000; Homayouni-tabrizi et al., 2016).

External sources of antioxidants can be either synthetic or natural based. According to (Caleja, Barros, Antonio, Oliveira, & Ferreira, 2017) the consumption of synthetic molecule has possibility associated with toxicity and several reports has claimed the side effects including carcinogenesis which led to usage restriction. Thus, natural antioxidant is necessary to replace the synthetic based and overcame the health problems related to free radicals and oxidative stress. Many research related to natural antioxidant has been investigated from various sources such as from Alaska pollack skin Y. Kim et al. (2001) ,whey protein isolate Jiang et al. (2017), African yam bean Ajibola et al. (2013),fish and chicken bones Prentice (2014),egg yolk Park et al. (2001) and many more. However, the microalgae have attracted attention from researchers all over the world to investigate more about this kingdom.

Microalgae have become incredible consideration as a potential feedstock in the production of biofuels and useful chemical since it can produce lipids, sugars and proteins in large amount in a very short period of time (Markou & Nerantzis, 2013; Nobre et al., 2013). Bioactive peptide derived from protein has been considered for antioxidant agent and in addition antihypertensive, anticoagulant or antimicrobial activity which could be utilized as a component in pharmaceutical healthcare products (S. Kim, Kim, Byun, Park, & Ito, 2001; Suetsuna, Maekawa, & Chen, 2004; Won, Rajapakse, & Kim, 2005). Peptides Enzymatic hydrolysis is a crucial step to release the antioxidative peptide from the microalgae protein. In order to produce microalgae protein hydrolysate with high degree hydrolysis (DH) and desired properties, the enzymatic hydrolysis parameters (eg. pH, temperature, substrate concentration and enzyme concentration) are needed to be controlled. Usually, high value DH contributes to the recovery of mixture peptides with small sizes and thus providing a good biological activity (De Jesus Raposo, De Morais, & De Morais, 2013). However, the information about the effect of enzymatic hydrolysis parameter particularly microalgae is limited. By having optimum enzymatic hydrolysis conditions, high degree of hydrolysis could be obtained and thus, improve antioxidant properties of microalgae protein hydrolysate. In this study, 1,1-Diphenyl-2-picrylhydrazyl (DPPH) assay and 2, 2'- azino-bis (ethylbenzthiazoline-6-sulfonic acid (ABTS) assay were used to evaluate the antioxidant activity of microalgae protein hydrolysate. Thus, the objective of this work is to study the

influence of enzymatic hydrolysis conditions on degree hydrolysis of MPH and the influence of degree hydrolysis on antioxidant activity.

Experiment

Four different parameters (enzyme concentration, substrate concentration, pH and temperature) were employed in the enzymatic hydrolysis. The initial amount of microalgae was varied from 0.2 g to 1.4 g with enzyme Alcalase (Sigma Pty Ltd., 2.4 U/g) for the enzymatic hydrolysis. The mixture containing microalgae biomass-enzyme was transferred into 100 mL of 50 mM sodium phosphate buffer with pH 7 and incubated in shaking incubator for 24 hours. Samples were taken out from the shaker and immersed in hot water bath at 90°C for 10 minutes to stop the hydrolysis process. The protein hydrolysate (sample) was centrifuged at 4000 rpm for 15 minutes to remove the residual. The samples were analysed for degree hydrolysis using O-Phthaldehyde (OPA) method according to Noble & Bailey (2009) and tested for antioxidant activity using 1,1-Diphenyl-2-picrylhydrazyl (DPPH) assay and 2, 2'- azino-bis (ethylbenzthiazoline-6-sulfonic acid (ABTS) assay.

Result and Discussion

In this study, microalgae protein hydrolysate was produced by hydrolysis using Alcalase enzyme. Based on the results obtained, two views of points can be discussed comprehensively. Firstly, is the influence of enzymatic conditions on degree hydrolysis and secondly, is the influence of degree hydrolysis on antioxidant activity. High antioxidant is usually associated with high degree of hydrolysis (DH). DH value can be controlled by several parameters during enzymatic hydrolysis parameters. In order to produce high DH value, parameters such as temperature, pH, enzyme concentration and substrate concentration should be at optimum condition. Apart from enzyme, antioxidant activity is also depending on hydrolysis conditions. Thus, an optimum range for each of parameters is considered for antioxidant activity to study the influence of the degree of hydrolysis towards antioxidant activity.

Table 1: Summary of degree of hydrolysis and antioxidant assays at optimum range

Enzymatic hydrolysis conditions	Degree of Hydrolysis (DH)	DPPH Assay	ABTS Assay
Temperature, °C			
50	33.68	56.68	17.51724
55	42.53	60.74	22.8276
60	24.84	59.75	19.6572
pH			
7	31.181	49.64289	37.6092
8	41.693	51.92861	43.67816
9	31.658	44.42861	39.95402
Enzyme Concentration, g/L			
0.2	37.67	40.28576	13.2184
0.3	43.96	52.14289	18.66667
0.4	43.78	50.14288	16.7586
Substrate Concentration, g/L			
2	37.393	65.85717	57.931
4	58.697	68.50002	69.28008
6	57.176	66.07146	49.754

Table 1 shows the degree of hydrolysis and antioxidant assay at different optimum range conditions. Based on the results, DPPH assay has high antioxidant activity compared to ABTS assay for the microalgae protein hydrolysate. The data showed that at high DH value, DPPH and ABTS free radical scavenging activity was high compared to low DH value. It could be due to the increasing number of electron and hydrogen donating properties of the active peptides (Sbroggio et al., 2016). These active peptides have high possibility to react with free radicals in producing more stable products, and hence the radical chain reaction could be terminated (Pazinatto et al., 2013). DPPH is a stable free radical with a maximum absorbance at 517 nm in ethanol. When DPPH encounters a proton-donating substance, the radical is scavenged and the absorbance is reduced (Cian, Alaiz, Vioque, & Drago, 2013) .

As we can see from the result, the effect of substrate concentration gives significantly high DH value and high antioxidant activity for both assays. It might be due to high amount of microalgae were converted in bioactive peptide. High bioactive peptide would have high chances in formation of various shorter peptides. This type of peptides is hydrophilic and water soluble, thus make it accessible to react with ABTS radical (Zhu, Jie, Tang, & Xiong, 2008). Similar result was reported for protein hydrolysate of fish and chicken bones (Prentice, 2014).

Please choose: Poster
Presentation session: Applied Chemistry
Presenter name: Ryo Watanabe

Development of measurement system for optimum film thickness of semiconductor photoelectrode

Ryo, Watanabe[1], Naoya, Murakami[1,2]

[1] Graduate School of Life Science and Systems Engineering, Kyushu Institute of Technology, 2-4 Hibikino, Wakamatsu-ku, Kitakyushu 808-0196, Japan
[2]Faculty of Engineering, Kyushu Institute of Technology, 1-1 Sensui-cho, Tobata-ku, Kitakyushu-shi, Fukuoka, 804-8550, Japan

Email: watanabe.ryo819@mail.kyutech.jp

Keywords (5 words)
Semiconductor photoelectrode, Photoabsorption, Photocurrent, Tungsten(VI) oxide

[Introduction]

Hydrogen has been expected as an alternative energy source, and hydrogen fuel cell can provide electricity without emitting carbon dioxide. However, hydrogen is currently produced by the steam reforming of natural gas, and the production method has harmful environmental impact due to a large amount of carbon dioxide emission. By contrast, water splitting reaction using inexhaustible sunlight energy is a potential method for low cost hydrogen production without environment burden. Photoelectrochemical (PEC) water splitting reaction using semiconductor electrode is known as Honda-Fujishima effect, and photoelectrode has been intensively studied in order to produce hydrogen efficiently. The PEC reaction on the semiconductor electrode is induced by photoexcited electron or positive hole generated by photoabsorption. Therefore, film thickness, which determines the amount of photoabsorption, is the most fundamental parameter for the properties of photoelectrode. However, electrode with thick film sometimes exhibit low PEC performance when film thickness is larger than diffusion length of electron or positive hole. Thus, this means that an optimal thickness exists for PEC reaction. Therefore, optimization of film thickness is conventional way to obtain the best PEC performance, and simultaneous measurement of photoabsorption and PEC performance is helpful for optimization of photoelectorde. However, it is not easy to estimation photoabsorption of porous film with high surface area because of light scattering. In the present study, PEC water-splitting was performed using tungsten(IV) oxide (WO_3) electrodes with porous structure, and photoabsorption of the electrodes were evaluated by photoacoustic spectroscopy (PAS), which is effective evaluation method for photoabsorption of strong scattering materials.

[Experiment]

The porous WO_3 electrodes were prepared by electrophoretic deposition in an acetone solution containing WO_3 powders (kojundo chemical laboratory) and iodine. Two parallel FTO-glass substrate were immersed in the solution with 8 mm separation, and a 20 V bias was applied between the two substrates. The WO_3-coated area of 1st layer was 1.5 cm × 2.0 cm. In order to make a thickness step, similar procedure was carried out again, and the WO_3-coated area of 2nd layer was 1.5 cm × 1.0 cm. Finally, as-prepared electrode was once calcined at 500 °C for 0.5 h.

PEC measurements were carried out using a potentiostat (Princeton Applied Research, 263A) and a three-electrode-type electrochemical cell with a Pt counter electrode, an Ag/AgCl reference electrodes, and Na_2SO_4 aqueous solution as an electrolyte respectively. Photocurrent was measured at 400 mV vs Ag/AgCl. PAS measurement was also carried out, simultaneously. A homemade PAS cell with an acrylic body and a quartz window was attached to a glass side of sample electrode. The digital PAS signal was acquired by a digital MEMS microphone buried in the cell, and recorded using a PC equipped with digital I/O interface. Time-series data was acquired by analog conversion of the digital PAS signal, followed by a Fourier transform with a Hamming window function. A laser diode module

emitting light at 455 nm was used as a light source, and the output intensity was modulated at 2.6 Hz. PEC and PAS measurement was carried out while changing the position of the irradiation at intervals of 0.3 mm.

[Result and Discussion]

Fig. 1 shows photoabsorption and photocurrent as a function of the laser irradiation position. Photoabsorption and photocurrent of sample was larger than that of FTO in any position. This indicates that both photoabsorption and photocurrent are attributed to WO_3. Moreover, large changes in these values were observed at 0 mm of laser position. This is attributed to film thickness of WO_3 layer. These results shows that difference of film thickness can be measured correctly using the present system.

For irradiation from FTO side (Fig. 1a, b), larger photocurrent was observed in thick-film area, compared to thin-film area. This is reasonable because photocurrent depend on photoabsorption, which is increased with film thickness. By contrast, smaller photocurrent was observed in thick-film area, compared to thin-film area for irradiation from WO_3 side (Fig. 1c, d). This is possibly due to the influence by electron and hole migration.

In order to carry out more detail discussion on the relationship between photoabsorption and photocurrent, samples with various kinds of film thickness profile are now being prepared. In the symposium, the results on the samples will be discussed.

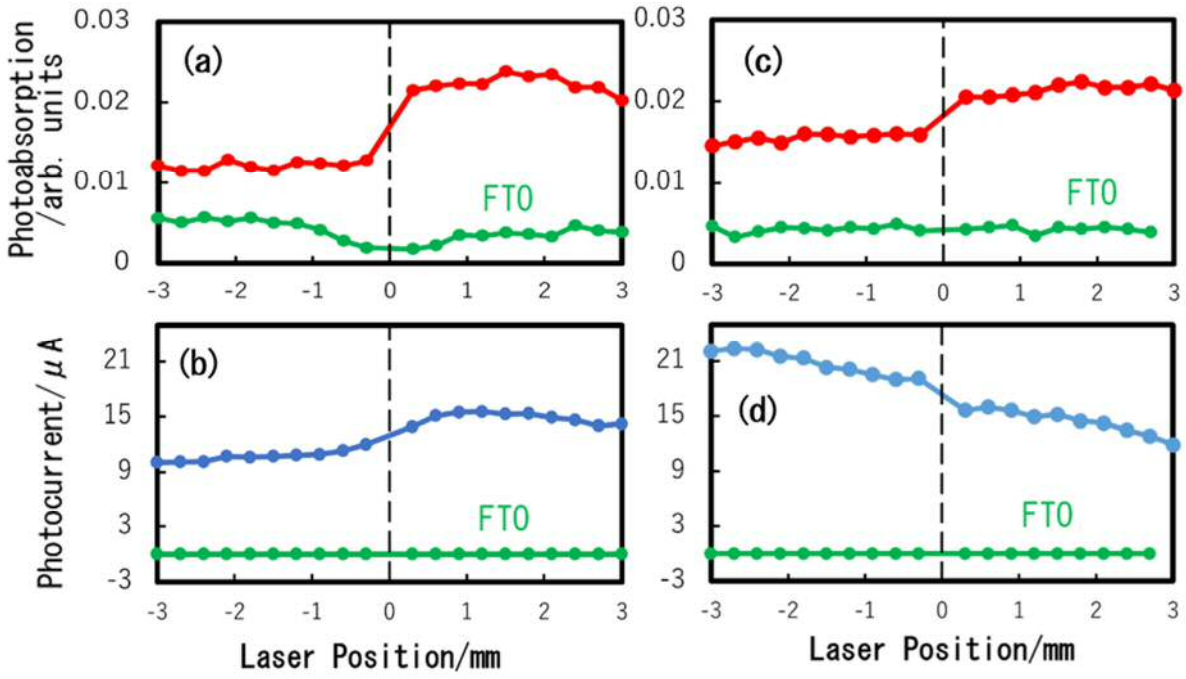

Fig. 1 Photoabsorption (a, c) and photocurrent (b, d) as a function of the laser irradiation position. Here, thick-film and thin-film area are defined as positive and negative direction of the position, respectively. Photoirradiation was carried out in two directions, thus, from (a, b) FTO substrate side and (c, d) WO_3 film side.

Please choose: Poster
Presentation session: Applied Engineering
Presenter name: Toui YOSHIDA

The Effect of Impactor Material on Momentum Transfer by Hypervelocity Impact

Toui YOSHIDA[1], Masaya IKEDA[1], Sota KOGA[1], Takao KOURA[1], Yasuhiro AKAHOSHI[1],

[1]Faculty of Engineering, Kyushu Institute of Technology, 1-1 Sensui-cho, Tobata-ku, Kitakyushu-shi, Fukuoka, 804-8550, Japan

Email: [yoshida.toui318@mail.kyutech.jp]

Keywords (5 words)
NEO(Near Earth Object), Planetary Defense, Hypervelocity Impact, MomentumTransfer

[Introduction]

Near Earth Objects (NEOs) are asteroids and comets which come close to Earth's orbit. So these have possibility of impacting, for example, February 2013, an asteroid created an airburst near Chelyabinsk State in Russia. In order to avoid the impact on Earth, it is necessary to execute NEO's orbit changing method early. One of the efficient methods is spacecraft impact. Spacecraft impact is efficient method because it is not necessary to attach equipment to NEO and it rarely causes splitting NEO.

The orbital change generated by spacecraft impact is performed by transference of momentum from spacecraft to NEO. There is β as an index of effect of the orbital change. β is defined the momentum ratio of spacecraft before the impact and NEO after the impact. Definition formula of β is shown in Eq. (1). It is known as an evaluation index in this field. β is affected by various factors. This research investigates the influence of the mechanical properties of the spacecraft on β.

$$\beta = \frac{M_A v_A}{m_i v_i} \tag{1}$$

M_A : Asteroid mass after impact
v_A : Asteroid velocity after impact
m_i : Impactor mass before impact
v_i : Impactor velocity after impact

[Experiment]

Two Stage Light Gas Gun (TS-LGG) installed in Kyushu Institute of Technology was used for accelerating impactor. This TS-LGG can launch aluminum Sphere (φ14, 4g) with 3 km/s.

The target was firebrick because its density is similar to asteroid and its physical property remains the same for different test.

Six types of spherical impactor of different materials were tested. The specifications of each impactor are shown in Table 1.

Table 1. Impactor's specification

material	Copper	Chromium Steel	Titanium	Aluminum		
				Low strength	Medium strength	High strength
density[kg/m^3]	8910	8030	4510	2700	2780	2810
strength[MPa]	118	193	106	95	612	716

[Result and Discussion]

Result of these experiments is shown in Fig.1.

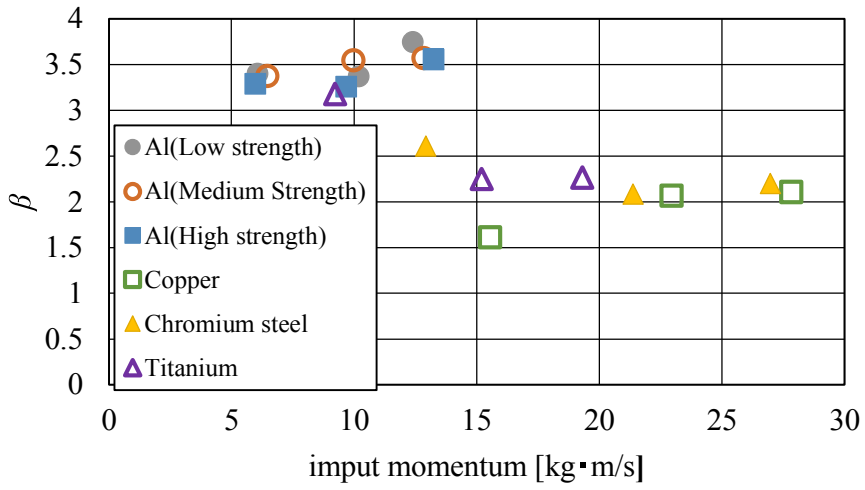

Fig.1. Experiment result

From Fig.(1), two things could be found. First, impactor's strength does not affect β. This is seen from the results of three types of aluminum. This is because the force applied to the impactor at the time of impact is large and immediately exceeds the strength of the target.

Second, impactor's density affects β. β is larger as the density of the impactors is smaller. However, if the density is too small, it is noted that the impactor is broken immediately after impact and β will be small. So, it can be said that the density ratio of the target and the impactor is related to β.

Poster
Presentation session: 15-16 December
Presenter name: Tuan Nurul Azura Binti Tuan Kob @ Yaakub

Thermostability of cutinase encapsulated with metal-organic framework; insights from molecular dynamics simulations

Tuan Nurul Azura Tuan Kob @ Yaakub[1,2], Mohd Farid Ismail[2] and Muhammad Alif Mohammad Latif[1,2,3]*

[1] Macromolecular Simulation Laboratory, Integrated Chemical BioPhysics Research, Faculty of Science, Universiti Putra Malaysia, 43400 Serdang, Malaysia
[2] Department of Chemistry, Faculty of Science, Universiti Putra Malaysia, 43400 Serdang, Malaysia
[3] Centre of Foundation Studies for Agricultural Science, Universiti Putra Malaysia, 43400 Serdang, Malaysia

*Corresponding author: aliflatif@upm.edu.my

Keywords: metal-organic framework; enzyme encapsulation; molecular dynamics;

Introduction

Chemical transformation using enzymes (biocatalysis) is a green alternative for production of chemicals. On industrial scale, the use of enzymes most of the time is limited due to extreme reaction conditions needed. The performance of enzymes can be increased by applying support systems like silica in order to limit their movement (immobilization). Enzyme immobilization have been widely studied since last century and many have been applied to produce commercial immobilized enzymes with increased performance. However, the issues with reaction conditions on industrial scale has not been properly addressed. Recently, metal-organic framework (MOF) has been tested as the potential solution. Some works have already produced positive results. Enzyme performance was increased when encapsulated with MOF. Even at elevated temperatures, MOF acted as protective layer enabling the enzymes to retain high activity (Liang K *et al.,* 2015).

The pores that resulted from the crystal arrangement of these MOFs should allow molecules to diffuse through them. This led to a variety of applications such as hydrogen gas storage and potential applications in catalysis, drug delivery, carbon capture and semiconductors (Jia et al., 2014). In this work, we are going to focus on the potential ability of MOF to improve enzyme productivity by encapsulation. Our target MOFs for enzyme encapsulation are IRMOF-74-VI (Deng *et al.,* 2017). These oligoethylene glycol–functionalized MOFs have pore apertures that are large enough for natural proteins to enter. Via isoreticular synthesis, the original one phenylene ring of MOF-74 can be increased for up to eleven which consequently produce larger pores (Deng *et al.,* 2014).

Although encapsulation of enzymes in MOF have been shown to improve their activity and maintain their stability at extreme conditions, the mechanism behind it haven't been studied at molecular level. This information is crucial in order to better understand how MOF affect the structure and dynamics of the protein structure, which in turn affect their stability and activity. Here, we proposed an atomic level investigation on the effect of IRMOF-74 MOFs towards the structure and dynamics of a model enzyme. In this project, the IRMOF-74-VI MOFs will be tested against the protein structure of a cutinase (PDB ID: 1CEX). By undertaking the computational methods such as ab initio calculations and molecular dynamics (MD) simulations, the properties and behavior of enzyme when encapsulated in the MOF can be acquired.

Experiment

Modelling of IRMOF-74 MOFs
- Model building
- Topology generation
- Force Field validation

Density Functional Theory Calculation
- Geometry optimization
- Atomic charges derivation
- Non-bonded interaction identification

Molecular Dynamics Simulation of IRMOF-74-encapsulated Enzymes
- Structural stability and flexibility
- Effect of temperature
- Binding energy analysis

Result and Discussion

a) **Effect of temperature -** The cutinase-MOF structures have thus been shown to have better conformational relative stability than cutinase-water structures.

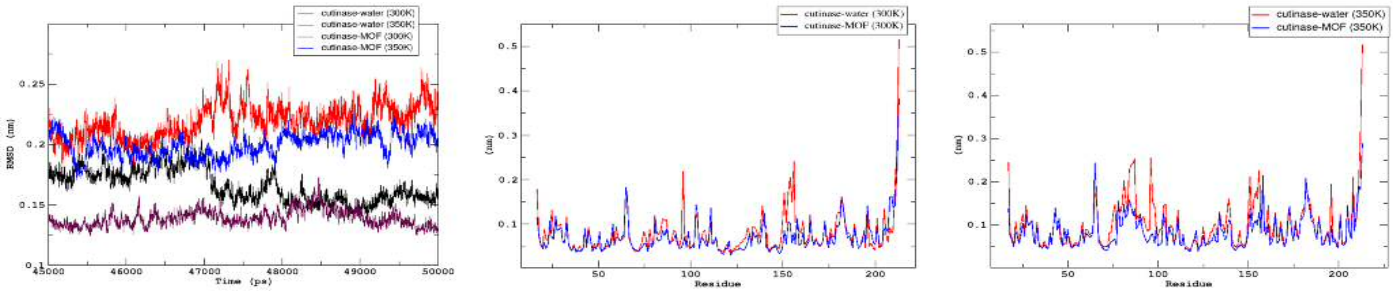

Figure 1 : RMSD and RMSF of cutinase-water and cutinase-MOF

b) **Binding energy analysis -** The key interactions that maintain the stability of cutinase were identified, such as hydrophobic interactions between Pro193 and Thr45 with aromatic ring of IRMOF-74-VI. In addition, ion pair interactions between Arg96 and carboxylate group of IRMOF-74-VI was found to have a distance of 4.53 Å and was classified as a strong salt bridge.

Table 1 : Interaction between Cutinase and MOF

	Residue	Amino Acids	Distance	MOF Atom
π-cation Interactions	156K	ARG	5.36	1180, 1192, 1204, 1228, 1234, 1408
Hydrophobic Interactions	193K	PRO	3.95	1794
	193K	PRO	3.96	1800
	45K	THR	3.81	2557
	17K	ARG	3.79	3115
	24K	ILE	3.92	3695
H-bonds	96K	ARG	3.34	1701
Salt Bridges	96K	ARG	4.53	1715, 1727

Please choose: Poster
Presentation session: Applied Engineering
Presenter name: Keno YOSHIDA

Evaluation of Pull-out Force in Novel Harpoon for Space Debris Capture

Keno YOSHIDA[1], Yasuhiro AKAHOSHI[1], Takao KOURA[1], Saika OHMORI[1], Satoshi FUJII[1]

[1]Faculty of Engineering, Kyushu Institute of Technology, 1-1 Sensui-cho, Tobata-ku, Kitakyushu-shi, Fukuoka, 804-8550, Japan

Email: yoshida.keno704@mail.kyutech.jp

Keywords (5 words)
Harpoon, Debris-capture, Active Debris Removal, Electrodynamic Tether

[Introduction]

The constant growth of space technologies has generated a significant increase on space debris. Avoiding self-multiplication of space debris with the active debris removal (ADR) is necessary to maintain the current number of space debris. NASA simulated that an increase of space debris in low earth orbit can be suppressed by removing at least 5 large debris every year.[1)] Removing large debris such as rocket bodies and abandoned satellites is one effective solution to keep the environmental safe for future missions.

One of promising ways of attaching electrodynamic tether (EDT) to debris is shooting a harpoon into it from an ADR satellite. The harpoon capturing device in harpoon system is a shot into debris with firearms as an anchor. In this method, it should be noted that arbitrary shaped debris can be attached and an accurate control of the attachment point is not needed. On the contrary, there is possibility of coming off the surface of debris because of the tensile load of electrodynamic tether. Therefore, an effective fixation method on the above mechanism should be added in order to avoid coming off that. The purpose of this paper is to evaluate the pull-out force in novel harpoon for debris capturing system. To evaluate it, harpoon shooting tests and tests of pull-out were conducted.

[Experiment]

The new harpoon with the barb is made with a double structure of an inner harpoon and an outer harpoon. Figure 1 shows a schematic diagram of the harpoon. The harpoon was deformed after the penetration and opened a barb on the tip. The type of tip is considered to the best penetration characteristic based on the previous research.[2)] The taper is structured in order to prevent deformation in process of penetrating a target. In addition, the tip of outer harpoon is crossed slit. Harpoon shooting tests were conducted by debris capture gun which was designed in the previous research, using harpoon and aluminum alloy plate made of A2042-T3. Figure 2 shows a schematic diagram of the debris capture gun. The gun has a structure in which the harpoon stops inside the launch tube and collides with the target. The harpoon was deformed after the penetration and opened a barb on the tip. After firing the test, a pull-out test was conducted by the universal tensile testing machine. Figure 3 shows a schematic diagram of the pull-out test. At the initial state in this test, a harpoon is attached to the target after the firing test. In this test, the maximum pull-out load while separating the harpoon and the target plate is measured.

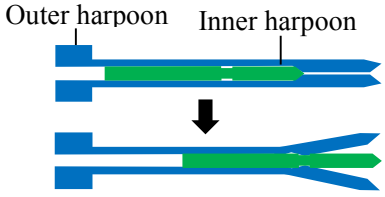

Figure 1. Harpoon

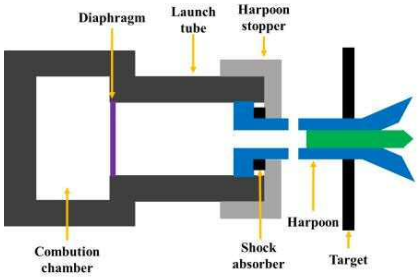

Figure 2. Debris capture gun

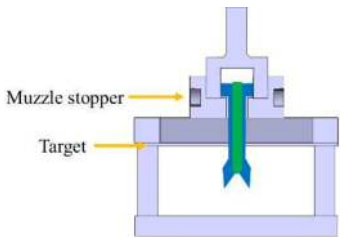

Figure 3. Pull-out test

[Result and Discussion]

To evaluate the function of barb system, firing and pull-out tests were conducted with two kinds of harpoon, namely barb and non-barb harpoons. In shot tests, the harpoon was deformed after the penetration and opened a barb on the tip, and the function of barb system could be confirmed. Table 1shows the result of pull-out tests. In the harpoon with the barb system, a pull-out load was over 10 kN and the maximum case was 13636 N. On the other hand, non-barb harpoons were around 6kN. It could be understood that the inner harpoon draws back and tip of outer harpoon was closed during the pull-out test. The present tests show that the effectiveness of the new harpoon system is confirmed by the firing test and pull-out tests. As the future plan, it is thought that fatigue tests could be required under cyclic loads during deorbiting manoeuvres after harpoon shooting.

Table 1. Result of pull-out test

Harpoon type	Experiment number	Pull-out load [N]	Inner harpoon movement of pull-out load measuring test [mm]
Non-barb	X-46	6867	-
Non-barb	X-50	6513	-
Barb	X-54	11694	0.5
Barb	X-55	13636	2.58
Barb	X-56	10399	1.11

[References]

1) J.-C. Liou, An active debris removal parametric study for LEO environment remediation, Advances in Space Research, Vol. 47, Issue 11, 2011, pp. 1865-1876
2) Mataki, T., Akahoshi,Y., Koura T., Kitazawa, Y., Shimamura, K., Izumiyama, T., Hashimoto, K., Kawamoto, S., Aoyama, J. and Fukuta, T.: Evaluation of Harpoon Tips for Debris Capture, Trans. JSASS Aerospace Tech. Japan, Vol. 14 (2016) No. ists30 (ISTS Special Issue: Selected papers from the 30th International Symposium on Space Technology and Science) pp. Pr_33-Pr_37.

Please choose: Poster
Presentation session: Applied Engineering
Presenter name: Shogo Tagami

Discharge on Solar Array by Space Debris Impact

Shogo Tagami[1], Takao Koura[1], Yasuhiro Akahoshi[1]

[1] Department of Mechanical and Control Engineering, Kyushu Institute of Technology
1-1 Sensui, Tobata, Kitakyushu, Fukuoka 804-8550, Japan

Email: tagami.shogo983@mail.kyutech.jp

Keywords (5 words)
Hypervelocity Impact, Space Debris, Plasma, Solar Array, Sustained Arc

[Introduction]

The number of debris has been increasing from the start of the space development, and the number of spacecrafts orbiting the Earth becomes larger. These mean that the risk of impact between spacecraft and debris is also growing. As solar arrays occupy the majority of spacecraft, the possibility of impact solar arrays is particularly high. The impact on solar arrays can causes not only mechanical damage but also electrical damage. High density plasma is generated by the energy transfer at the time of the collision, therefore electro static discharge might take place, and the insulating layer of the solar arrays is carbonized by Joule Heat generated due to the current flowing through the discharge and a permanent short circuit is considered to form, and it called sustained arc.

When sustained arc occurs, electricity does not flow to the payload and the power generation capacity is reduced. As a result, problems like difficulties to control the spacecraft from the ground will be caused by the power shortage, there is a possibility that spacecraft stops operation. At present, the occurrence of discharge by debris impact cannot be confirmed. However, there is a high possibility that discharge occurs by debris impact.

The purpose of this study is to analyze occurrence and characteristics of the discharge due to hypervelocity impact on solar arrays.

[Experiment]

Therefore the authors conducted hypervelocity impact tests on the solar array coupon using two-stage light gas gun. The projectile was 1 mm A2017 sphere. The impact velocity was around 4-5 km/s.

In this study, pseudo solar array coupon made of aluminum plate, Kapton tape, cooper plate and cover glass were used. The 0.8 mm thickness A1050 plate simulated substrate and the cooper plate simulated solar cell. The pseudo solar array coupon was connected an external circuit shown in Fig. 1. This external circuit was employed to simulate the operations conditions of the solar cell. The cooper plate connected to the positive terminal is called Hot cell, the other one connected to the negative terminal is called Cold cell. The gap between the cells is approximate 1 mm. The constant current power source supplied current of 192 V and 2.4 A. Three current probes are connected to an oscilloscope which measured the current change on pseudo solar array.

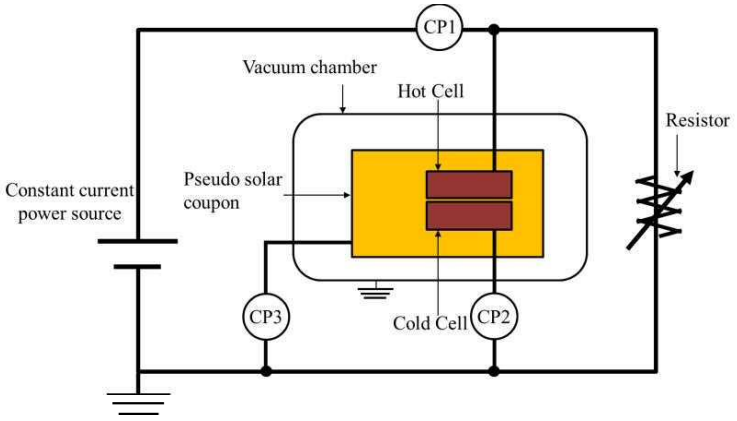

Fig. 1 External circuit

[Result and Discussion]

Figure 2 shows discharge waveform. Figure 2 (a) is impact at hot cell and Fig.2(b) is impact in neighborhood between two cells. Figure 3 shows targets after impact test.

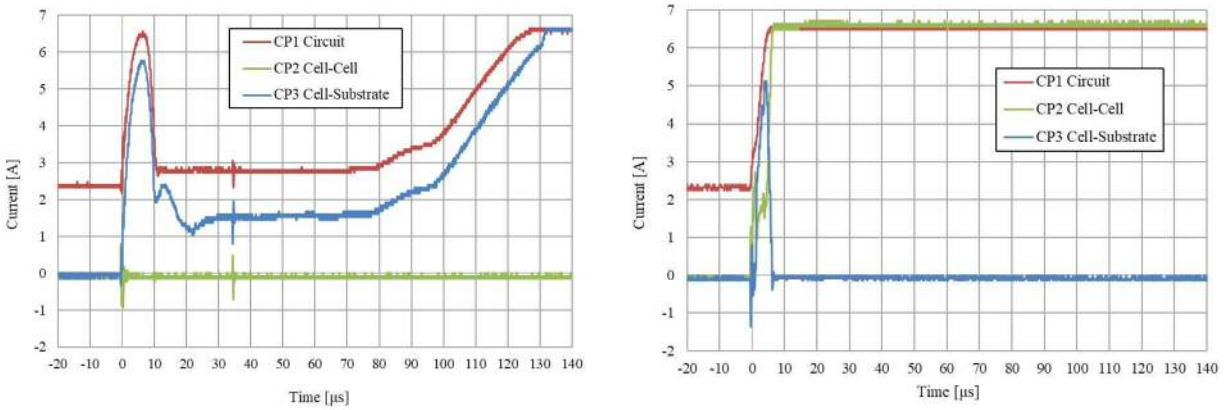

(a) 17-021 impact at hot cell (b) 17-024 impact near of between two cells

Fig. 2 Waveform of discharge

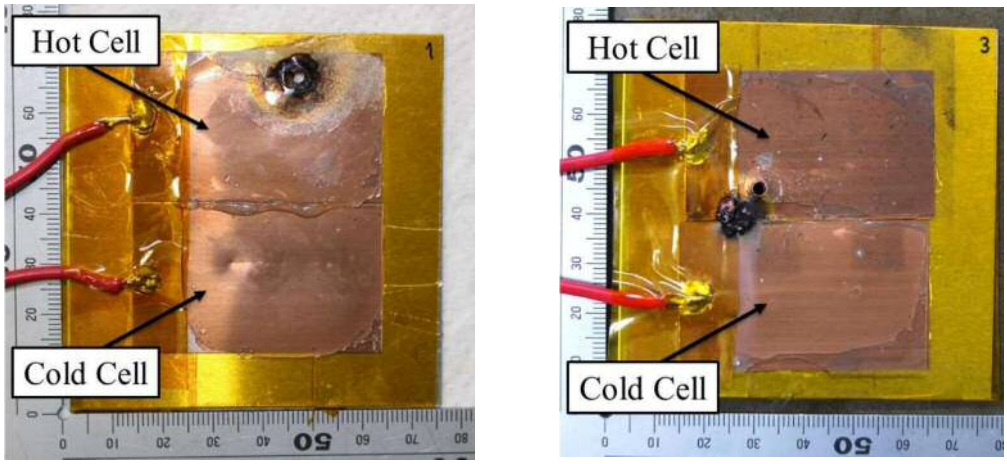

(a) 17-021 impact at hot cell (b) 17-024 impact near of between two cells

Fig. 3 Targets after impact test

In the case of impact at hot cell, discharge occurred between hot cell and substrate. Also, burn is observed at impact point. On the other hand, when a projectile impacts on the gap region between two cells, discharge occurred between two cells. At the same time burn occurred between two cells. As a cause of this, when a projectile impacts at hot cell, high density plasma is generated between hot cell and substrate and diffuses at there. In another case, plasma diffuses at not only impact point but also between cells. At that time, the electric resistance of the plasma was smaller than that between the cells. In this case, permanent sustained arc was confirmed, which was due to carbonization of Kapton tape by Joule Heat.

In this study, the authors confirmed the discharge phenomenon due to debris impact on the pseud solar coupon. It was confirmed that current waveforms flowing between the cells or between hot cell and substrate are different due to its impact position. In the future, the authors would be to use real solar array. And they would be able to determine impact and electric conditions under which discharge occurs.

Please choose: ~~Oral~~/ Poster/ ~~Either~~
Presentation session:
Presenter name: Syirrazie Che Soh

[Comparison EToU and ToU Possible Electricity Bills of Nuclear Research Reactor Operation in Nuclear Malaysia]

[Syirrazie, Che Soh][1], [Mohammad Lutfi, Othman][1], [Hashim, Hizam][1], [Nofri Yenita, Dahlam][2], [Mohd Fazli, Zakaria][3], [Mohd Sabri, Minhat][3]

[1]Faculty of Engineering, University Putra Malaysia, 43400 UPM Serdang, Selangor, Malaysia
[2]Faculty of Electrical Engineering, Universiti Teknologi Mara, 40450 Shah Alam, Selangor, Malaysia
Malaysia Nuclear Agency, 43500 Kajang, Selangor, Malaysia

Email: [syirrazie@gmail.com]

Keywords (5 words)

Demand Side Management, Time of Use, Energy Charge, Demand Charge, Tariff Scheme

[Introduction]

Enhanced Time of Use (EToU) is an extension of Time of Use (ToU) Tariff Scheme for Industrial and Commercial Consumers since 1st January 2016. This scheme offers with Energy Charge for three (3) respective time zones of Peak, Mid-Peak and Off-Peak Hour. And Demand Charge for two (2) respective time zones of Peak and Off-Peak Hour. Purpose of this scheme is to encourage Demand Side Management (DSM) through shifting a possible load to consume electricity from a time zone with higher charging rate onto a time zone with the lower one with more dynamic. Consumers may experience different electricity bill when switching tariff scheme from ToU to EToU Tariff. Then, this study will determine cost benefit both EToU ToU Tariff Scheme for Research Reactor Operation in Nuclear Malaysia. This will help consumers making a decision either to switch tariff scheme from ToU to EToU Tariff Scheme or vice versa. Then, also encourage a potential of Load Shifting Optimization that will benefit consumers to experience lower electricity bills either through EToU or ToU Tariff Scheme.

[Experiment]

Energy Charge and Demand Charge are the parameters that will be used to determine probable electricity bills for both EToU and ToU Tariff Scheme. Data of load consuming electricity will be gathered based on daily basis through daily load profile started from 00.00 at 5 November 2015 to 00.00 at 6 November 2015. Then, an assumption the load profile for all 22 working days is same, and this will be counted for monthly electricity bill.

[Result and Discussion]

Result of this study found that an Electricity bill of ToU is lower than EToU Tariff for Research Reactor Nuclear Operation in Nuclear Malaysia. This shows that consumer's tendency is to maintain with ToU Tariff Scheme because of experience lower electricity bill than EToU Tariff Scheme. However, consumer may also consider to switch onto EToU Tariff when Load Shifting Effort may potential to reduce electricity bill lower than ToU Tariff Scheme since EToU scheme offering lower Mid-Peak hour tariff rate that could not be offered by ToU Tariff Scheme.

Table 1: Electricity Bill's Breakdown Cost of EToU and ToU Tariff Scheme

Charges	EToU Scheme	ToU Scheme
Total Daily Amount Energy Charge (RM)	114.415	92.269
Total Monthly Amount Energy Charge (22 Working days) (RM)	2517.1333	2029.90986
Maximum Demand Charge Amount (RM)	1149.480	1181.41
Electricity Bill (RM)	**3666.6133**	**3211.31986**

Table 2: Tariff Scheme Charging Rate for Industrial E2 Tariff Category
(Source: [1]https://www.tnb.com.my/faq/etou/, [2]https://www.tnb.com.my/commercial-industrial/pricing-tariffs1)

Tariff Scheme	Demand Charge (RM per kW per Month)			Energy Charge (sen per kWh)		
	Off-Peak	Mid Peak	Peak	Off-Peak	Mid Peak	Peak
EToU[1]	0.00	36.00	40.00	21.90	33.30	59.20
ToU[2]	0.00	0.00	37.00	21.90	0.00	35.50

Table 3: Time of Tariff Scheme
(Source: https://www.tnb.com.my/faq/etou-bm/)

Time Zone	Hour																							
	0	1	2	3	4	5	6	7	8	9	10	11	12	13	14	15	16	17	18	19	20	21	22	23	24
EToU																									
ToU																									

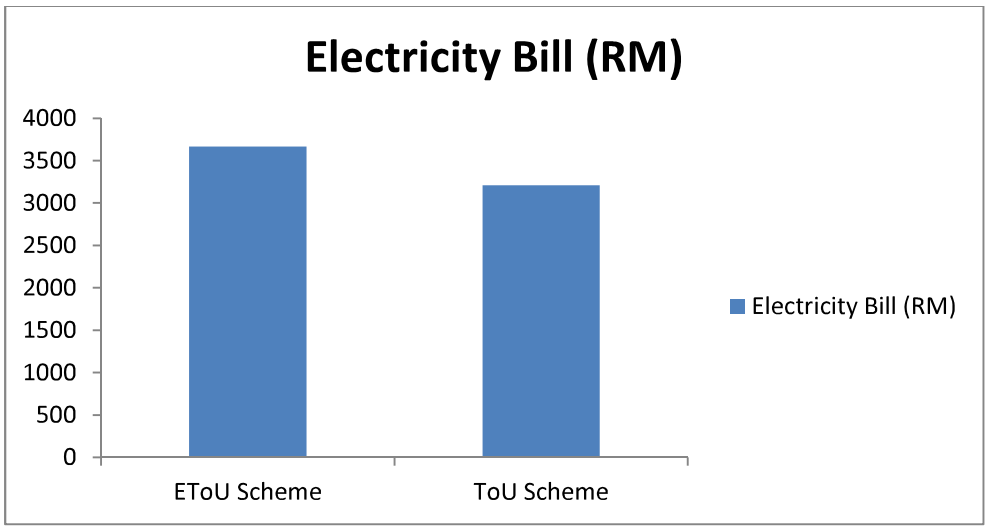

Figure 1: Electricity of EToU and ToU Tariff Scheme

Please choose: Poster
Presentation session:
Presenter name: Ryuya OHSAKI

Sensorless Initial Position Estimation and Start up Control of Surface Permanent Magnet Synchronous Motor

Ryuya OHSAKI, Ko MAEDA, Tsuyoshi HANAMOTO
Department of Biological Functions and Engineering, Graduate School of Life Science and Systems Engineering,
Kyushu Institute of Technology, 2-4, Hibikino, Wakamatsu, Kitakyushu, Fukuoka 808-0196, Japan

Email: ohsaki.ryuya437@mail.kyutech.jp

Keywords

SPMSM, Sensorless Initial Position Estimation, Start up Control, observer

Introduction

In recent years, synchronous motors have been widely used in industry such as robots and line conveying, for consumer products in compressors such as air conditioners and refrigerators, and motors for driving HVs. Among them, Permanent Magnet Synchronous Motor (PMSM) uses permanent magnets as a material for generating a magnetic field in the rotor, so it is used in a wide field because of high efficiency and small size. However, a position sensor used in PMSM has drawbacks such as high cost, large size, less durable and less reliable. To overcome these limitations, a sensorless control of PMSM is a possible solution.
The surface PMSM (SPMSM) used in this paper does not have the saliency so it is difficult to get the initial rotor position like the interior PMSM (IPMSM). We propose a sensorless start-up and initial position estimation method using nonlinear observer and induced voltage observer.

Experiment

The proposed control system is shown in Fig.1. In the proposed method, control is performed from the standstill to the rotation by combining two observers. At the time of startup, the inverter is controlled by the DSP to set the U phase of the motor to the rest phase and DC excitation to the V and W phases.

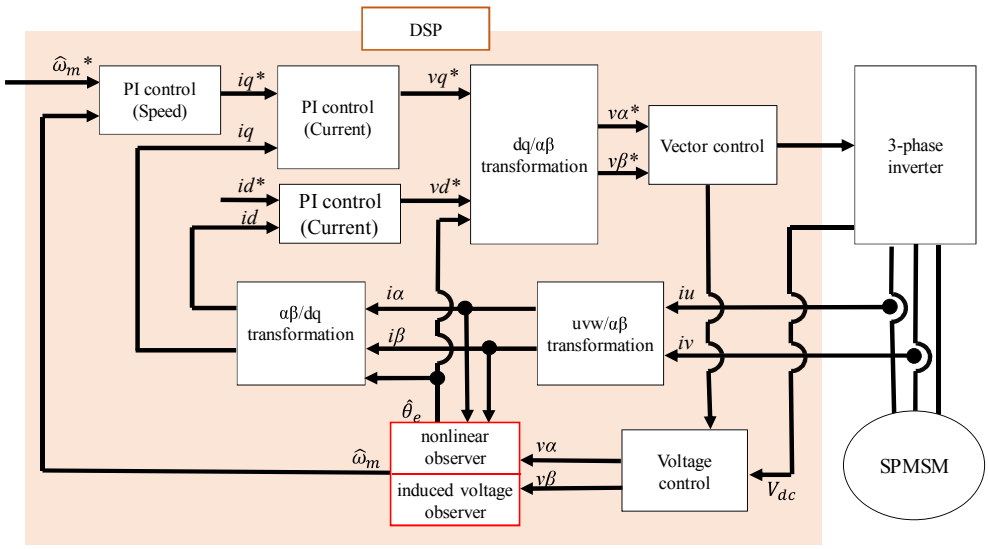

Fig.1 start up control of system

At that time, the rotor vibrates and an induced voltage is generated. Estimation of the rotor position is performed by the nonlinear observer based on the generated induced voltage. Then, the sensorless control is performed by the induced voltage observer.

Result and Discussion

In this research, when the rotor position estimation of the nonlinear observer is completed, the observer is switched and the rotation is performed before reversing. Fig.2 shows the estimated voltage waveform and the measured voltage waveform when DC excitation is performed with the U phase as the rest phase. The difference between the measured induced voltage and the estimated induced voltage goes below 2V, estimation counter is counted up. The counter value goes to 100, the observer is closed to the induced voltage observer and the rotational operation is started. When switching at 100 counts, it was confirmed to rotate from the stopped state without reversing between 0 ° and -180 °. (Fig.3) In addition, when the excitation direction was reversed, it was successfully started without reversing even in the range of 0 ° to 180 °. (Fig.4) Therefore, it was confirmed that by changing the excitation direction, it can rotate without reverse rotation at the initial position of the whole range.

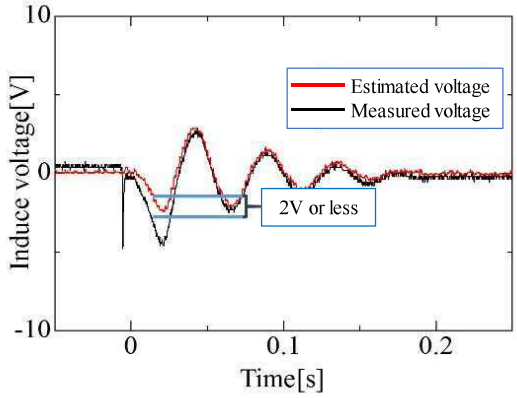

Fig.2 Measured voltage and estimated voltage during DC excitation

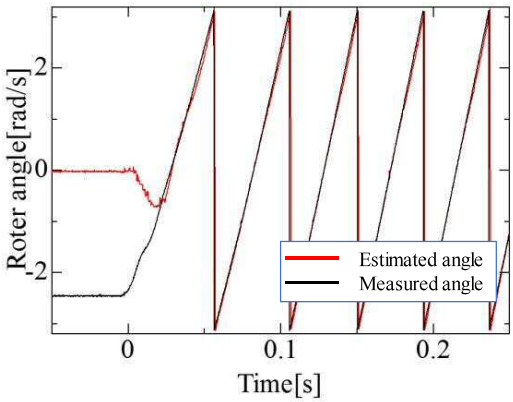

Fig.3 Startup at initial position 0 ° to -180 °

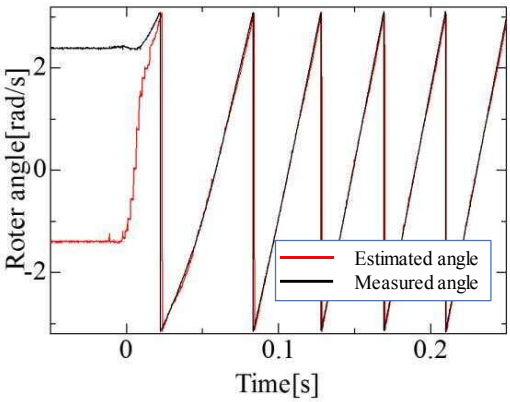

Fig.4 Startup at initial position 0 ° to 180 °

However, if control is performed without obtaining the position information of the rotor beforehand, it may be reversed at startup, which is difficult for practical use. Therefore, for future work, we would like to construct a system that obtains rough rotor position information. Finally, we would like to construct a system that performs sensorless control without reversing the SPMSM from the standstill by combining the initial position estimation system and the sensorless control algorithm.

Please choose: Poster
Presentation session:
Presenter name: Yasuhiro Ohta

Sensorless control of Synchronous Reluctance Motor

Yasuhiro OHTA, Kazumi ANDO, Tsuyoshi HANAMOTO

Department of Biological Functions and Engineering, Graduate School of Life Science and Systems Engineering,
Kyushu Institute of Technology, 2-4, Hibikino, Wakamatsu, Kitakyushu, 808-0196, Japan

Email: ohta.yasuhiro884@mail.kyutech.jp

Keywords
SynRM, sensorless control, flux observer, inductance nonlinearity

Introduction

This paper presents a sensorless control of Synchronous Reluctance motor (SynRM). Nowadays, Motors are widely used in many fields such as home appliances, industrial machinery, vehicles and so on. These motors are required to have high efficiency because of recent increased attention to energy problems. From this viewpoint, SynRMs are thought to be preferable because they can achieve high efficiency and saving resources due to their structures. SynRMs need a rotor position sensor for stable controls, but installing the sensor increases the cost and size of motors. For these reasons, the sensorless SynRM control is desired. SynRMs have the inductance nonlinearity so we have to take it into consideration in the sensorless control.

Experiment

To achieve the sensorless control, it is necessary to estimate the rotor position. We can estimate it by using the state observer. It is a mathematical model which can estimate unknown state from the system parameters and input-output values. The block diagram of the state observer used in this study is shown in Figure 1.

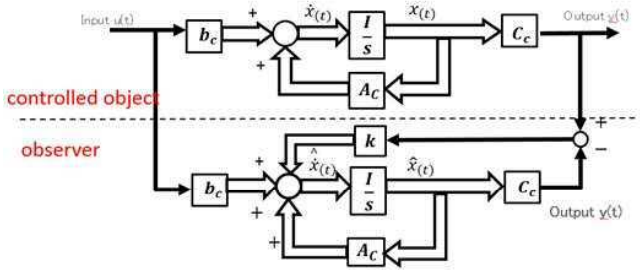

Figure 1. State observer

In this study, the state observer is designed by motor voltage equations. The SynRM voltage equation in α-β axes is described as follows:

$$\begin{bmatrix} v_\alpha \\ v_\beta \end{bmatrix} = \begin{bmatrix} R_a + pL_q & 0 \\ 0 & R_a + pL_q \end{bmatrix} \begin{bmatrix} i_\alpha \\ i_\beta \end{bmatrix} + \begin{bmatrix} e_\alpha \\ e_\beta \end{bmatrix} \quad (1)$$

Where, v: armature voltage, i: armature current, R_a: armature resistance, L: armature inductance, e: induced voltage, p: differential operator (d/dt).

Here, the induced voltages are modeled as a sinusoidal wave.

$$\begin{bmatrix} e_\alpha \\ e_\beta \end{bmatrix} = \begin{bmatrix} -k_e \omega sin\theta \\ k_e \omega cos\theta \end{bmatrix} \quad (2)$$

Where, ω: angular velocity, k_e: induced voltage constant, θ: rotor position.

From (1) and (2), and the relationship of the induced voltage and the flux φ, the state observer in α axis is derived as follows:

$$\frac{d}{dt}\begin{bmatrix}\hat{\imath}_\alpha \\ \hat{\varphi}_\alpha \\ \hat{e}_\alpha\end{bmatrix} = \begin{bmatrix}-\frac{R_a}{L_q} & 0 & -\frac{1}{L_q} \\ 0 & 0 & 1 \\ 0 & -\omega^2 & 0\end{bmatrix}\begin{bmatrix}\hat{\imath}_\alpha \\ \hat{\varphi}_\alpha \\ \hat{e}_\alpha\end{bmatrix} + \begin{bmatrix}\frac{1}{L_q} \\ 0 \\ 0\end{bmatrix} v_\alpha + \begin{bmatrix}k_1 \\ k_2 \\ k_3\end{bmatrix}(i_\alpha - \hat{\imath}_\alpha) \quad (3)$$

Where, $\boldsymbol{k} = [k_1\ k_2\ k_3]^T$: observer gain. In a similar way, the β axis observer is also derived as per equation (3).

By using the above mentioned observer, flux is estimated and the estimated rotor position is calculated by the following equation.

$$\hat{\theta} = tan^{-1}\frac{\hat{\varphi}_\alpha}{\hat{\varphi}_\beta} \quad (4)$$

In addition, L_q in the equation (3) changes according to the stator current, so we collected the data of the nonlinearity in advance and applied it to the observer estimation.

Result and Discussion

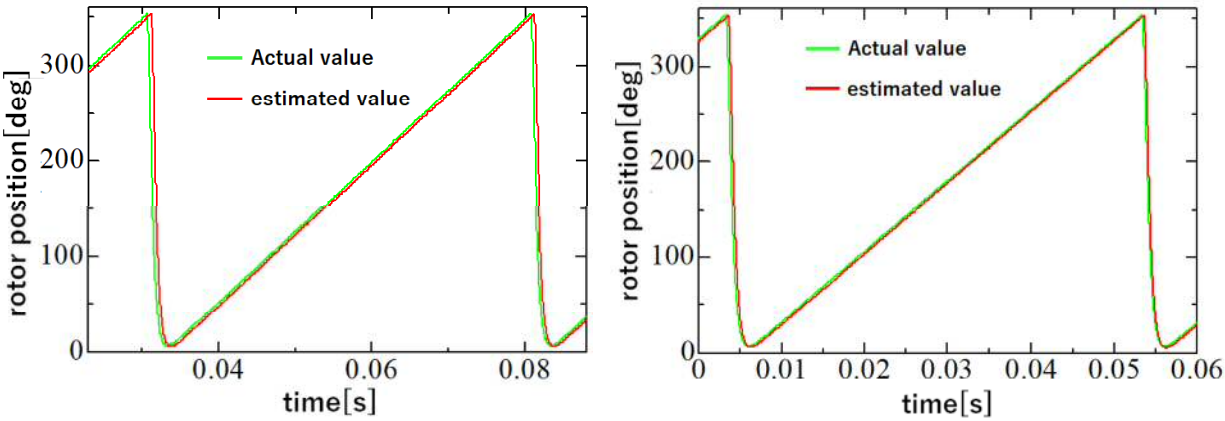

(a) I_d=1.5[A], constant L_q (b) I_d=1.5[A], variable L_q

Figure 2. Rotor position estimations at 600[rpm]

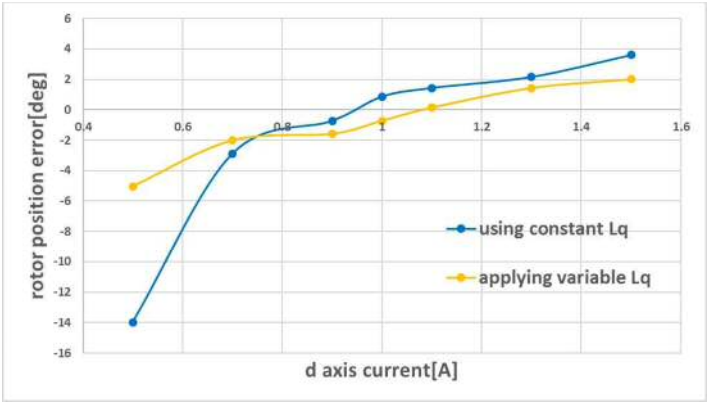

Figure 3. Rotor position estimation errors at 600[rpm]

Figure 2 shows the rotor position at a steady state when the motor speed is 600[rpm] and I_d = 1.5[A]. We have done the experiment using fixed L_q and applying the inductance nonlinearity (variable L_q). Figure 3 shows errors of the estimation at 600[rpm] for each I_d values.

From Figure 2 and 3, it can be observed that the sensorless control of SynRM has achieved under certain conditions. Also, estimation errors can be minimized by taking the inductance nonlinearity into consideration. The future goals are to achieve the sensorless control over a wide range and decrease estimation errors.

Please choose: Poster
Presentation session: Material Science and Technology
Presenter name: Wahyu Waskito Aji

Study on Capture Condition by Dielectrophoresis to Fabricate GNR Devices

[Wahyu, Aji][1], [Hirofumi, Tanaka][1]

[1]Graduate School of Life Science and Systems Engineering, Kyushu Institute of Technology, Kitakyushu 808-0196, Japan

Email: tanaka@brain.kyutech.ac.jp

Keywords: Capture condition, dielectrophoresis, GNR Devices, graphene nanoribbons, longitudinal unzipping.

Introduction

Graphene has attracted attention due to high carrier mobility and high conduction even low cross section. Various reports suggested to form graphene with sub-10 nm width, called graphene nanoribbons (GNR), to make the finite band gap. Sub-10 nm GNR can be obtained by longitudinal unzipping of single-walled carbon nanotubes (SWNTs) [1]. Although it can produce sub-10 nm width GNR by synthesis process and suitable for mass production, the application of unzipped GNR still limited because of the difficulty in assembly of the GNR to make electric devices. In the present study, we tried to capture the unzipped GNRs using dielectrophoresis (DEP) method.

Experiment

The GNR was synthesized by unzipping of Hipco SWNTs using poly[(*m*-phenylenevinylene)-*co*-(2,5 -dioctoxy-*p*-phenylenevinylene)] (PmPV) in dicloroethane solvent. After centrifugation of the solution, the supernatants were casted to electrodes and followed by DEP process. The frequency during DEP process was varried from 500 kHz to 20 MHz and the voltage from 5 to 10 Vpp. Atomic Force Microscopy (AFM) was used to analyze the DEP result.

Result and Discussion

Figure 1 shows the AFM result after the DEP process in 10 MHz of frequency and 10 Vpp of amplitude of applied AC voltage, which indicates successfully trapping the GNR using DEP method. Detail will be introduced at the presentation.

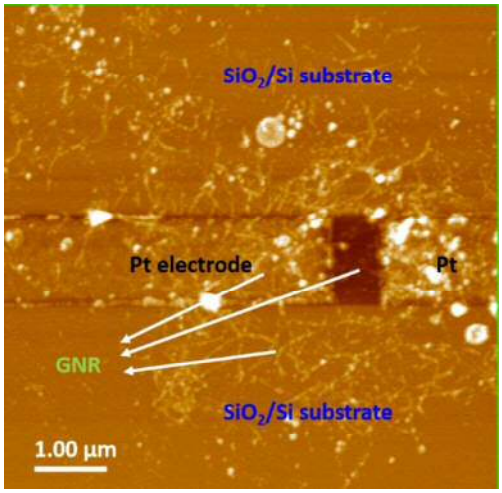

Fig 1. AFM result of GNR captured by DEP with 10 Mhz frequency and 10 Vpp

Reference: 1) M. Fukumori *et. al.,* Jpn. J. Appl. Phys. 56 06GG12 (2017).

Please choose: Poster
Presentation session:
Presenter name: Yoshiki Hashimoto

Vibration Suppression Control of Three-inertia Resonance System Using Fictitious Reference Iterative Tuning

Y.Hashimoto, Y.Takahashi, T.Hanamoto

Graduate School of Life Science and Systems Engineering, Kyushu Institute of Technology, 2-4 Hibikino, Wakamatsu, Kitakyushu, Fukuoka, 808-0196, Japan

Email: hashimoto.yoshiki920@mail.kyutech.jp

Keywords
Fictitious reference iterative tuning, motor control, parameter tuning, disturbance suppression, three-inertia system

Introduction

Recently the demand for high-speed and high-precision control increases more and more because of the requirement of increasing the production performance. In the case of controlling a load equipment using the motor, vibration may occur due to a disturbance or a change in the command value depending on the elastic connection of the load and the motor. In some cases that may become a resonance system. When multiple loads are connected, it is necessary to consider it as a multi-inertia resonance system. The purpose of this research is to design the speed and current controller of a three-inertia resonance system by using FRIT (Fictitious reference iterative tuning). FRIT is used for the designing of the controller parameters. The overall goal of this paper is to follow the target response, suppress overshoot, suppress disturbance, and suppress the vibration of the given three-inertia system.

Experiment

The design procedure of FRIT in a closed-loop system is shown in Fig. 1. The plant model (including a current control system) is defined as P, and PID controller that implements the initial parameters is defined as $C(\boldsymbol{\theta})$. The detailed explanation of FRIT control is described as follows:

Step 1: Enter set value signal $r_0(t)$ in closed-loop system to obtain input and output data $u_0(t)$ and $y_0(t)$.

Step 2: Obtain fictitious reference signal $\hat{r}(t)$ by the following formula using $u_0(t)$ and $y_0(t)$.

$$\hat{r}(\boldsymbol{\theta}, t) = C(\boldsymbol{\theta})^{-1} u_0(t) + y_0(t) \quad (1)$$

Step 3: Define reference model $M(s)$ that can provide an optimum speed response by using the following formula.

$$M(s) = \frac{1}{(\tau s+1)^3} \quad (2)$$

Step 4: Obtain a reference output $\hat{y}(\boldsymbol{\theta}, t)$ by the following formula using the fictitious reference signal $\hat{r}(t)$.

$$\hat{y}(\boldsymbol{\theta}, t) = M(s)\hat{r}(\boldsymbol{\theta}, t) \quad (3)$$

Step 5: Determine error signal $\hat{e}(t)$ and evaluation function $J(\boldsymbol{\theta})$ as the following formula using $\hat{y}(\boldsymbol{\theta}, t)$ and $y_0(t)$.

$$\hat{e}(\boldsymbol{\theta}, t) = y_0(t) - \hat{y}(\boldsymbol{\theta}, t) \quad (4)$$

$$J(\boldsymbol{\theta}) = \sum_{t=1}^{N} \left(\hat{e}(\boldsymbol{\theta}, t)\right)^2 \quad (5)$$

$$\boldsymbol{\theta} = \left(K_{ps}, K_{is}, K_{ds}, K_{pc}, K_{ic}\right)$$

Step 6: Change $\boldsymbol{\theta}$ (PID parameters) iteration for Step 2 to 5 until evaluation function $J(\boldsymbol{\theta})$ is minimized.

The minimum value of $J(\boldsymbol{\theta})$ is selected and accordingly, a parameter $\boldsymbol{\theta}$ is obtained for optimal speed response. In this paper, Particle Swarm Optimization (PSO) method is used as minimization of $J(\boldsymbol{\theta})$.

Fig. 2 shows a three-mass resonant system as a control target and the experimental conditions are shown in Table 1. Also, the block diagram of FRIT control is shown in Fig. 3. Here, C_1 and C_2 represent the m-IPD speed controller and the PI current controller respectively.

Result and Discussion

A command value is given as input so that the rotational speed of motor change from 0 [rpm] to 1200 [rpm]. After 2 seconds, a step disturbance of 0.3 [Nm] is given to the load2 in Fig.2. FRIT calculation is performed based on the obtained one set of the input-output data. The time constant shown in equation (2) is set as $\tau = 0.02$ [s]. The changes in the gains for the speed m-IPD controller and current PI controller are shown in Table 2. The step response and the disturbance response of the load side angular speed ω_L are shown in Fig. 4 and Fig. 5, respectively.

Therefore, by observing the Fig. 4 and 5, it is useful to design the speed and current controller using FRIT. By concurrently designing the speed controller and the current controller using FRIT, we think that a more desirable response can be obtained.

In this paper, we achieved designing the speed and current controller of a three-inertia resonance system by using FRIT. As a future goal, since the desired response was obtained in the simulation this time, we think that it is necessary to experiment with prototype system.

Table 1 Experimental conditions

Spring constant K_{s1}	64.3 Nm/rad
Spring constant K_{s2}	80.4 Nm/rad
Motor inertia J_M	3.65×10^{-5} Nm
Load1 inertia J_C	6.92×10^{-5} Nm
Load2 inertia J_L	3.18×10^{-5} Nm

Table 2 Parameter change of the controller

	Speed gain			Current gain	
	K_{ps}	K_{is}	K_{ds}	K_{pc}	K_{ic}
Before	1.00	20.0	0	1.00	20.0
After	1.30	26.7	0.00500	2.48	0.477

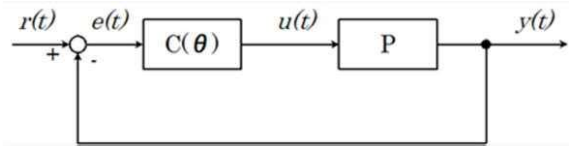

Fig. 1 Closed-loop system

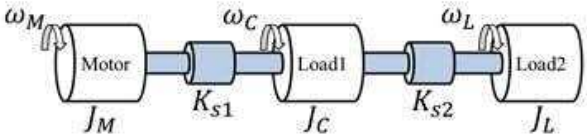

Fig. 2 Three-mass resonant system

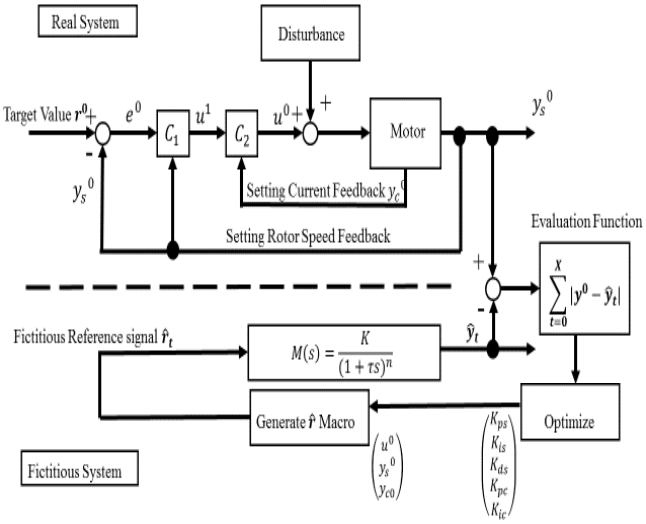

Fig. 3 Block diagram of FRIT

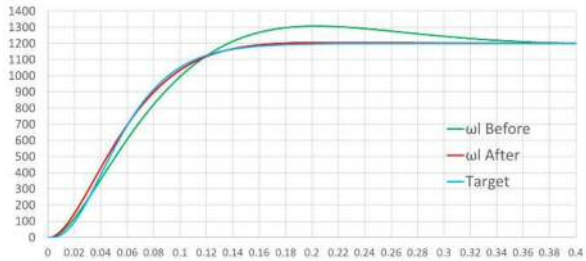

Fig. 4 Step response

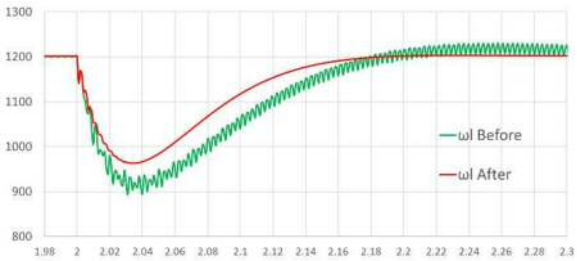

Fig. 5 Disturbance response

Please choose: ~~Oral/~~ Poster~~/ Either~~
Presentation session: Applied Engineering~~Poster~~
Presenter name: Sayako Chijiiwa

Evaluation of specificities of polymers prepared by vapor-phase assisted surface polymerization (VASP) on substrate surfaces.

○Sayako Chijiiwa[1], Haruo Nishida[2]

[1]Faculty of Engineering, University Putra Malaysia, 43400 UPM Serdang, Selangor, Malaysia
[2]Faculty of Engineering, Kyushu Institute of Technology, 1-1 Sensui-cho, Tobata-ku, Kitakyushu-shi, Fukuoka, 804-8550, Japan
[3]Faculty of Computer Science and Information Technology, University Putra Malaysia, 43400 UPM Serdang, Selangor, Malaysia

Email: chijiiwa.sayako634@mail.kyutech.jp

Keywords: Vapor-phase assisted surface polymerization, stereoregulity, polymethylmethacrylate, radical polymerization, NMR

[Introduction]

The vapor-phase assisted surface polymerization (VASP) is a controlled polymerization method, in which vaporized monomers are supplied to active sites on substrate surface (Fig. 1), initiating and propagating the polymerization. In 1995, anionic ring-opening VASP of β -propiolactone was determined to be a controlled polymerization process to confirm the immortality of active site [1], and in 2003, free-radical VASP was also a controlled process to prepare block copolymers[2]. The VASP has provided specific physical properties influenced by substrate surfaces, for example, epitaxial growing of polyester chains[3].

In this study, the influence of substrate surface structure on growing polymer chains by free-radical VASP was examined by analyses of thermal properties and Triad tacticity of polymer chains in comparison with conventional bulk polymerization products.

Fig. 1. H-shaped reactor for vapor-phase assisted surface polymerization.

[Experiment]

Methyl methacrylate (MMA) and styrene (St) was used as monomers. Uniaxial stretched isotactic polypropylene (USIPP) film (isotacticity > 98%) was employed as a substrate for VASP. Benzoyl peroxide (BPO) was used as free-radical initiators. The initiator 3 mg (1.23×10^{-5} mol) was dissolved in dichloromethane (1 mL) and cast on the substrate surface (2 × 8 cm). After drying, the initiator coated substrate was immediately used for polymerization experiments.

An H-shaped reactor (Fig. 1) was used for VASP experiments. Initiator catted substrate was placed on the bottom of reaction chamber. Monomer: MMA (1 mL) was supplied to reservoir, and freeze degasification treatment was repeated 3 times. After that, H-shaped reactor was retained under vacuum and put into an oven, which was thermostated at predetermined polymerization temperatures (50, 70, and 90 °C), to start polymerization.

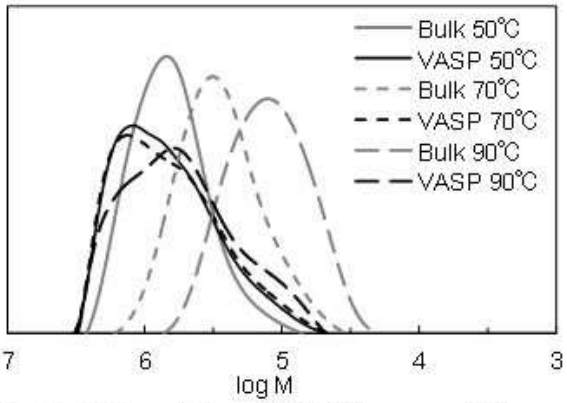

Fig. 2. SEC profiles of PMMA prepared by VASP and bulk polymerization.

After the polymerization, the polymer produced on the substrate was analyzed using ^{1}H-NMR, FT-IR, differential scanning calorimeter (DSC), X-ray diffractometer (XRD), and laser scanning confocal microscope (LSCM), which were measured on JEOL JNM-ECP 500 FT-NMR system, Thermo Scientific Nicolet iZ10 FT-IR spectrometer, Seiko Instruments Inc. EXSTAR 6000-DSC 6220, Rigaku X-ray powder diffractometer, KEYENCE 3D laser scanning confocal microscope model VK-X 100/105, respectively.

[Result and Discussion]High molecular weight polymethylmethacrylate (PMMA) was synthesized by VASP on USIPP film substrate (Fig. 2). Generated PMMA on the substrate surface was analyzed with FT-IR, microscopic FT-IR mapping system, XRD, and LSCM. FT-IR spectrum of VASP product is shown in Fig. 3. Carbonyl absorption peak $\nu_{C=O}$ at 1774 cm^{-1} derived from PMMA was appeared clearly on typical PP spectrum. Interestingly, this absorption peak shifted to higher wavenumber compared to 1730 cm^{-1} of bulk polymerization PMMA cast on USIPP, suggesting an interaction at interface of VASP-PMMA and USIPP.

Generated PMMA on the film was dissolved into deuterochloroform to measure ^{1}H NMR spectrum. In Fig. 4, ^{1}H NMR spectrum of PMMA prepared by VASP on USIPP film is shown. In order to evaluate first-order structure of PMMA, the triad tacticity analysis (Fig. 5) was applied to ^{1}H-NMR spectra of VASP samples in comparison with bulk polymerization products. As a result (Fig. 6), PMMA synthesized on USIPP film by VASP was predominant in the isotactic triad tacticity (mm). On the other hand, bulk polymerization PMMA was rich in the syndiotactic triad tacticity (rr), which is popularly seen in general radial polymer [4]. This result also suggets the interaction between VASP-PMMA and USIPP

In a previous study[3], it is reported that interaction occurred between CaO substrate surface and polypropiolactone prepared by VASP, indicating unusual thermal properties and crystal structure.

Above specific properties of VASP-PMMA would be influenced by the surface properties of highly isotactic and uniaxially oriented substrate USIPP.

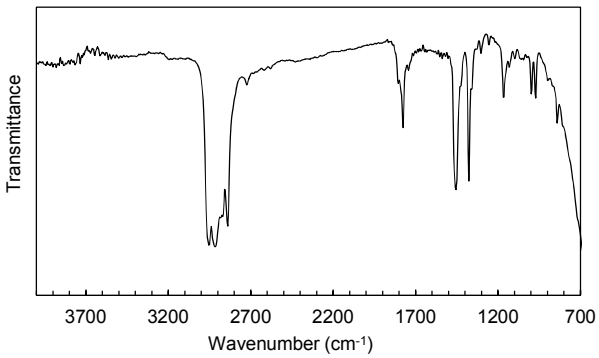

Fig. 3. FT-IR spectrum of PMMA on USIPP film prepared by VASP.

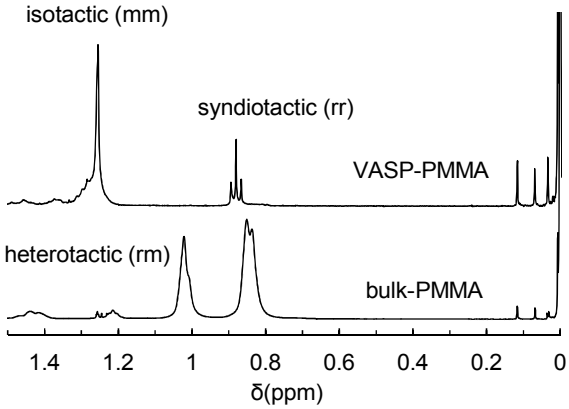

Fig. 4. ^{1}H NMR spectrum of PMMA prepared by VASP on USIPP film.

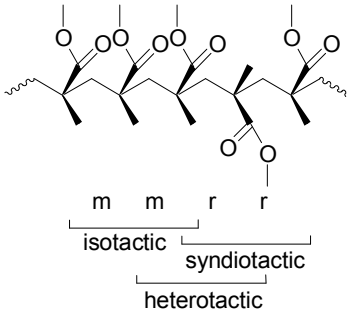

Fig. 5. Triad tacticity of PMMA.

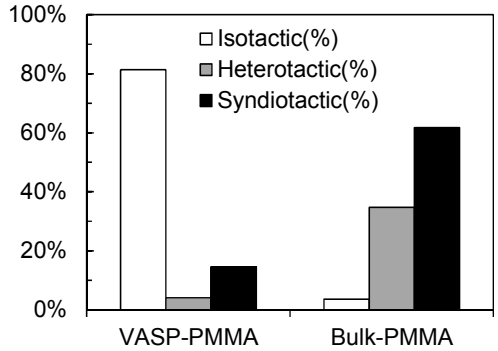

Fig, 6. Triad tacticity analysis of VASP and bulk polymerization products.

【References】

[1] H. Nishida, M. Yamashita, **1995**, JP 1995-82354-A1.
[2] M. Yasutake *et al.*, *Macromolecules*, **2003**, *36*[16], 5974-5981.
[3] H. Nishida *et al.*, *Macromol. Mater. Eng.*, **2005**, *290*, 848–856.
[4] C. Ducal-Terrie and L. Lebrun, *J. Chem. Education*, **2006**, *83* (3), 443-446.

Please choose: Poster
Presentation session: Applied Engineering
Presenter name: Subraya Krishna Bhat

Fitting Characteristics of Hyperelastic Ogden and Reduced Polynomial Models to Uniaxial Stress-Strain Relationships of Carotid Artery

Subraya Krishna Bhat[1], Hiroshi Yamada[1]
[1]Department of Biological Functions Engineering, Kyushu Institute of Technology, 2-4 Hibikino, Wakamatsu-ku, Kitakyushu-shi, Fukuoka, 808-0196, Japan
Email: bhat.subraya-krishna255@mail.kyutech.jp

Keywords
Fibrous cap, carotid artery, Ogden model, Reduced Polynomial model, Maclaurin series

Introduction

Various hyperelastic models have been proposed to describe the mechanical behaviour of biological tissues. In the previous studies, stress-strain relationships of carotid artery were modeled using various isotropic hyperelastic models[1), 2)]. However, interpreting the curve fitting characteristics of a hyperelastic model is a challenging task. Here, we present an approach to compare different hyperelastic models based on the Maclaurin series expansion of the Cauchy stress. Ogden model and reduced polynomial (RP) model, with same number of material constants were used for modeling. From the Maclaurin series expansion it can be seen that, the order of appearance of constants plays an important role in the modeling capability of the two models. While RP model showed better accuracy in highly nonlinear regions, its accuracy decreases in almost linear regions.

Methodology

A two-term Ogden model has been used as given by Eq. (1), wherein by assuming $\alpha_1 = 2$ and $\alpha_2 = \alpha$, the first term takes a Neo-Hookean form, and the total number of material constants reduces from four to three.

$$\mathrm{W} = \frac{\mu_1}{2}(I_1 - 3) + \frac{\mu_2}{\alpha}(\lambda_1^{\alpha} + \lambda_2^{\alpha} + \lambda_2^{\alpha} - 3) + \frac{H}{2}(J^2 - 1) \tag{1}$$

Here, μ_1, μ_2, and α are the three material constants. $\lambda_i (i = 1,2,3)$ are principal stretches, J is volume ratio, H is hydrostatic pressure, and $I_1 = \lambda_1^2 + \lambda_2^2 + \lambda_3^2$ is the first invariant of the right Cauchy-Green deformation tensor. A RP model with three parameters is given by Eq. (2).

$$\mathrm{W} = C_1(I_1 - 3)^1 + C_2(I_1 - 3)^2 + C_3(I_1 - 3)^3 + \frac{H}{2}(J^2 - 1) \tag{2}$$

Under incompressibility constraint, the uniaxial relationships between Cauchy stress and stretch, for Ogden and RP models are given by Eq. (3) and Eq. (4) respectively[3)]. From the stress-strain relationships it can be observed that, first term of the two equations are same, and the difference between the two models are the second terms.

$$\sigma_1 = \sigma_{Ogden1} + \sigma_{Ogden2} = \mu_1(\lambda_1^2 - \lambda_1^{-1}) + \mu_2\left(\lambda_1^{(\alpha)} - \lambda_1^{\left(\frac{-\alpha}{2}\right)}\right) \tag{3}$$

$$\sigma_1 = \sigma_{R1} + \sigma_{R2} = 2C_1(\lambda_1^2 - \lambda_1^{-1}) + 2C_2(\lambda_1^2 - \lambda_1^{-1})(\lambda_1^2 + 2\lambda_1^{-1} - 3) + 3C_3(\lambda_1^2 - \lambda_1^{-1})(\lambda_1^2 + 2\lambda_1^{-1} - 3)^2 \tag{4}$$

Curve fitting was performed by using the software Igor Pro 6.0 (WaveMetrics, Inc.). Accuracy of the estimated curves is evaluated by root mean square error (RMSE) as given by Eq. (5).

$$RMSE = \sqrt{\frac{\sum_{i=1}^{n}(\sigma_e - \sigma_t)^2}{n}} \tag{5}$$

Where, σ_e is experimental Cauchy stress, σ_t is estimated Cauchy stress, and n is the number of data values. Interpretations of the curve fitting characteristics of each model is made based on the Maclaurin series expansion

of Cauchy stress as a function of nominal strain ε. Maclaurin expansion was obtained using the MATLAB (Mathworks, Inc.) function, *Taylor*.

Results and Discussion

The curve fitting results of the two models with experimental stress-strain data of fibrous cap (CF) and normal intimal region (CN) of carotid artery is given by Fig. 1. From the RMSE calculated values given in Table 1, it is clear that RP model describes CF2 more accurately than Ogden model, whereas in case of CN4, Ogden model showed a better curve fit than RP model.

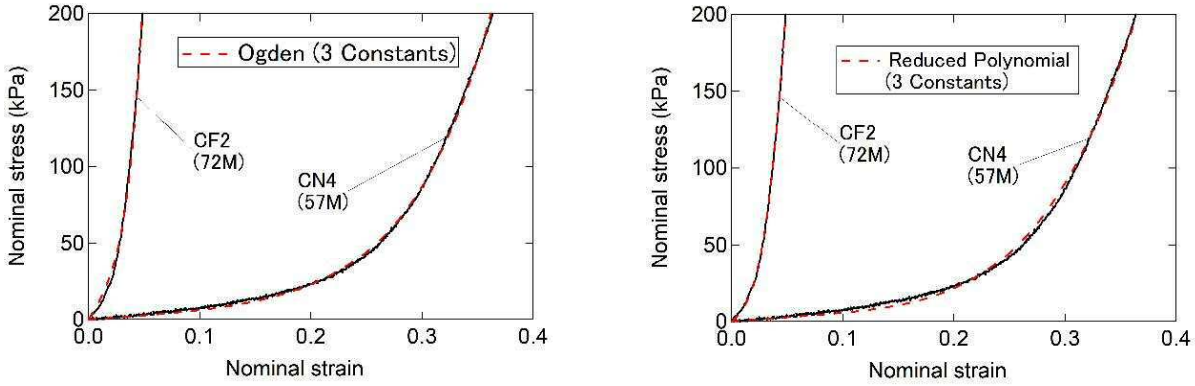

Fig. 1 Curve fit results for stress-strain relationships of fibrous cap and normal regions of carotid artery, using (a) Ogden model, and (b) reduced polynomial model. CF: carotid fibrous cap, CN: carotid normal.

Table 1 Root Mean Square Error (RMSE) of the estimated stress-strain curves

Specimens	Ogden Model	Reduced Polynomial Model
CF2 (72M)	4.19 kPa	1.34 kPa
CN4 (57M)	1.58 kPa	2.33 kPa

From the above results, it is clear that both models have certain advantages and limitations. Since, the first term of both models are the same, Maclaurin series of the second terms, given by Eq. (6) and (7) are compared. For simplification, in RP model, C_2, C_3 are taken as $\mu_2 C_2^*, \mu_2 C_3^*$ respectively, as given by (7). From this assumption, μ_2 becomes a common term in the two equations, and the constants inside the bracket need to be compared.

$$\sigma_{Ogden2} = \left(\frac{3\alpha\mu_2}{2}\right)\varepsilon - \left(\mu_2\left(-\frac{3\alpha^2}{8}+\frac{3\alpha}{4}\right)\right)\varepsilon^2 + \left(\mu_2\left(\frac{3\alpha^3}{16}-\frac{3\alpha^2}{8}+\frac{\alpha}{2}\right)\right)\varepsilon^3 - \left(\mu_2\left(-\frac{5\alpha^4}{128}+\frac{9\alpha^3}{32}-\frac{11\alpha^2}{32}+\frac{3\alpha}{8}\right)\right)\varepsilon^4 + \left(\mu_2\left(\frac{11\alpha^5}{1280}-\frac{5\alpha^4}{64}+\frac{21\alpha^3}{64}-\frac{5\alpha^2}{16}+\frac{3\alpha}{10}\right)\right)\varepsilon^5 - \left(\mu_2\left(-\frac{7\alpha^6}{5120}+\frac{11\alpha^5}{512}-\frac{85\alpha^4}{768}+\frac{135\alpha^3}{384}-\frac{137\alpha^2}{480}+\frac{\alpha}{4}\right)\right)\varepsilon^6 \quad (6)$$

$$\sigma_{R2} = \mu_2(36C_2^*)\varepsilon^3 - \mu_2(24C_2^*)\varepsilon^4 + \mu_2(36C_2^* + 162C_3^*)\varepsilon^5 - \mu_2(44C_2^* + 216C_3^*)\varepsilon^6 \quad (7)$$

From Fig. 1 it can be seen that, Ogden model deviates from the experimental curve CF2 in the low-stress nonlinear region. In case of RP model, it deviates from the experimental curve of CN4 in the almost linear portion of the curve. Now, observing the Maclaurin series it can be seen that, in case of RP model, the lower order terms of ε, $\varepsilon^2$are not present which seems to influence its capability to model lower order curves. Another observation from the RP model, is the order of appearance of constants C_2, C_3. It is seen that each constant appears to influence the nonlinearity of the curve independently. For instance, while C_2^* influences 3rd and 4th order curves, C_3^* plays an important role after 5th order. This order of appearance of constants increases the capability of the model to model nonlinearities, whereas in linear regions the accuracy decreases.

References

1) Yamada H., Esmaeili Monir H., Sakata N., Morita Y., and Nakashima, Y.: Mechanical characterization of the elastic properties of atheromatous plaques in the human carotid artery and thoracic artery. *Proc. of ATEM '15*, p.252, 2015.
2) Bhat S. K., Yamada H., and Sakata N.: Estimation of stress-strain relationships of fibrous cap in carotid artery using various types of hyperelastic models. *Journal of Japanese Society of Biorheology*, Vol.32, No.2, p.101, 2018.
3) Holzapfel, G. A.: Nonlinear Solid Mechanics – A Continuum Approach for Engineering. *John Wiley & Sons*, 2000.

Please choose: Oral/Poster/Either
Presentation session: Applied Engineering
Presenter name: Kodai Kitagawa

Prototype of Musculoskeletal Model for Assistance Motion of Standing-up

Kodai Kitagawa[1], Yoshiki Nishisako[1], Takayuki Nagasaki[2], Sota Nakano[3], and Chikamune Wada[1]

[1]Graduate School of Life Science and Systems Engineering, Kyushu Institute of Technology, Japan
[2]Department of Rehabilitation, Faculty of Medical Science and Welfare, Tohoku Bunka Gakuen University, Japan
[3]Department of Rehabilitation, Faculty of Nursing and Welfare, Kyushu University of Nursing and Social Welfare, Japan

Email: kitagawakitagawa156@gmail.com

Keywords (5 words)
Musculoskeletal Model, Assistance Motion, Lifting, Low-back, Simulation

[Introduction]
Generally, caregivers have low back pain from assistance motions such as supporting standing-up. Assistance motions have crucial risk factors for low back pain because it is strongly related to lifting, bending, and twisting. Moreover, various parameters are associated with the caregiver's lumbar load. From these backgrounds, we are studying the musculoskeletal model to simulate related parameters in order to find low-load assistance motions. The advantage of the simulation using the musculoskeletal model was that parameters could change quantitatively. In addition, the musculoskeletal model could examine the activity of the inner muscle which was difficult to be measured and the stress of the bone. However, since there might be differences between the simulated motion and the actual motion, verification of the musculoskeletal model was necessary. In this paper, we introduce the prototype of the musculoskeletal model and evaluation of this model.

[Experiment]
We used the AnyBody Modeling System (AnyBody Technology A/S, Denmark) as a musculoskeletal simulator. This AnyBody system can estimate the muscle activity and joint stress of each segment in assistance motions by inverse dynamics technique. The musculoskeletal model was tasked to simulate assistance motions. We evaluated whether our proposed musculoskeletal model could be applied to simulate lumbar joints stress in lifting motion for supporting standing-up (Figure 1). In this lifting motion, the 90 N load instead of human body was placed on the upper limb vertically. We compared the simulated compression force between the lumbar vertebrae and the sacrum (L5-S1) with measured compression force of previous researches [1-2].

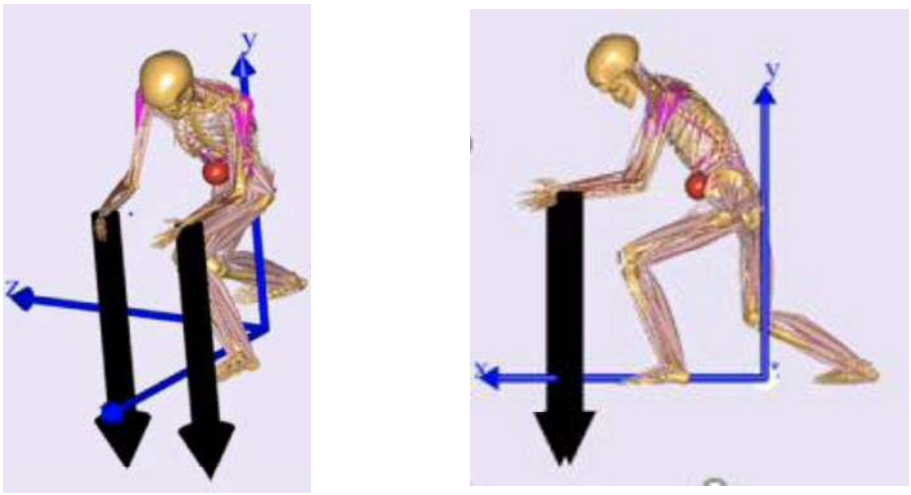

Fig.1 Lifting motion of musculoskeletal model

[Results and Discussion]

Figure 2 shows the time waveform of compressive force between the lumbar vertebrae and the sacrum, obtained from the proposed musculoskeletal model. The maximum compressive force during the simulated lifting motion was 5813 N. The maximum compressive force during the actual lifting motion measured in the previous study was 5400 N, and it was thought these two values were relatively close. In addition, the compressive force was found to decrease as the trunk became vertically, and this tendency was similar to that in previous studies. These results showed that the proposed musculoskeletal model could be applied to motion while supporting standing-up.

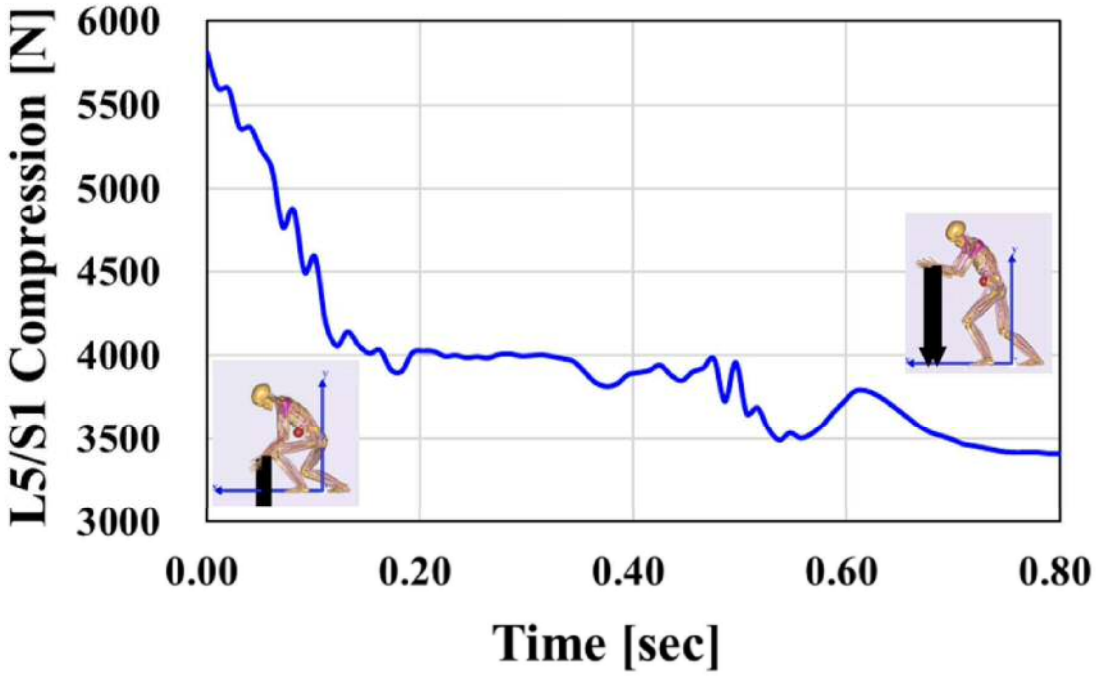

Fig.2 Time waveform of simulated compression force

[Conclusion]

In this paper, we introduced the prototype of the musculoskeletal model. We evaluated whether this model could estimate compressive force between the lumbar vertebrae and the sacrum in lifting motion. The results showed that the maximum compression force and tendency obtained by proposed musculoskeletal model were close to the measured values of the previous research. From these results, it was considered that the proposed musculoskeletal model could be applied to assistance motion research. In future works, we will analyze the relationship between parameters such as foot position and lumbar load during assistance motion.

[References]

[1] McGill, S. M., and Norman, R. W., “Dynamically and statically determined low back moments during lifting”. J. Biomech, Vol.18, No.12, pp.877-885, 1985.

[2] Chaffin D. B., "Primary prevention of low back pain through the application of biomechanics in manual materials handling tasks", G. Ital. Med Lav. Erg, Vol.27, No.1, pp.40-50, 2005.

Please choose: Poster
Presentation session: Applied Engineering
Presenter name: Yuki Yoshida

[Development of automated mismatch DNA base sequence designer]

[Yuki Yoshida][1], [Takashi Nakakuki][2*]

[1] Major of Interdisciplinary Informatics, Kyushu Institute of Technology,680-4 Kawazu, Iizuka, Fukuoka 820-8502 Japan
[2]Department of Systems Design and Informatics, Kyushu Institute of Technology,680-4 Kawazu, Iizuka, Fukuoka 820-8502 Japan
* Corresponding author

Email: [yoshida.yuki670@mail.kyutech.jp],[nakakuki@ces.kyutech.ac.jp]

Keywords (5 words)
DNA, Algorithm design and analysis, Design tool, DNA computing, Molecular circuits

[Introduction]

DNA computing is a field aimed at creating a wet system that can process information using biomolecules. DNA hybridization and DNA strand displacement reaction (DSD) based on DNA hybridization are one of the promising method for making DNA circuits with a wet system among designing methods which are the basis of DNA computing [1]. A DNA circuit having functions of a logic gate such as an AND circuit and an OR circuit is actually realized. Research in the field is progressing to create large-scale DNA circuits with practical functions. However, DSD-based circuits also cause unintended binding reactions between DNAs and the circuit may not operate as intended by the designer. Since it is technically difficult to ensure the specificity of the binding between two DNA molecules, the cause of such a phenomenon is based on the base sequence design consisting of a combination of only four bases that constitute the DNA in the circuit design. As a means for solving this phenomenon, there is "mismatch" base sequences. However, the method for designing base sequences using mismatch base sequences has not yet established an optimal method, and it is a situation requiring inspiration and labor for use. In this research, we aim to solve the problem by creating a tool that automatically designs. For that purpose, we devised an algorithm for automatic design. The algorithm was implemented as a program, and it was confirmed by practical examples of DNA switch circuit [2] and DNA feedback regulator [3].

[Experiment]

As mentioned above, this tool confirmed with a practical example of DNA switch circuit and DNA feedback regulator. The DNA switch circuit is a circuit which reacts as shown in Fig.1. Strand 1 performs DSD with Strand 2-3, and released Strand 3 binds with Strand 4 and Strand 5. However, unless the base sequence is skillfully designed, unintended reactions such as Strand 1-4-5 being generated due to complementation will occur. Therefore, it is necessary to redesign the base sequence. The DNA feedback regulator is a circuit that reacts as shown in Fig.2. This DNA circuit is larger in scale than the switch circuit. Specifically, the number of strands used and the number of DSD are large. Therefore, unintended reactions are more likely to occur. First, it is verified whether the base sequences of Switcher, which is a relatively simple DNA circuit, could be designed so that unintended reaction will not occur. Next, we verified whether the base sequences of a larger scale DNA feedback regulator can be designed as an application.

[Result and Discussion]

As a result of designing Switcher's base sequences with this tool and verifying the concentration at which each double stranded DNA is generated, as shown in Fig. 3, undesired reaction does not occur at all. The desired products are also generated at 94% or more against the concentration of the first prepared strands. From this, the design of Switcher using this tool succeeded.

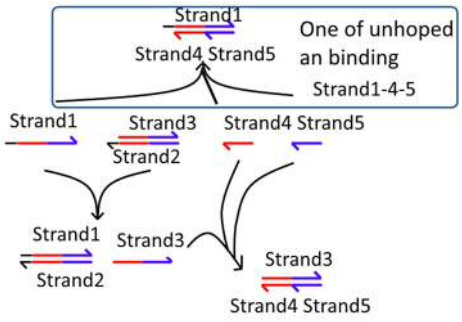

Fig.1 Reaction scheme of switch circuit

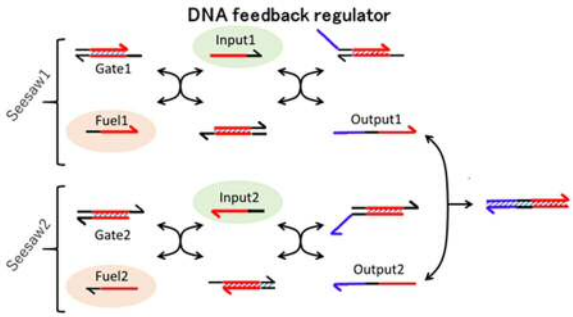

Fig.2 Reaction scheme of the two amplifier circuits in DNA feedback regulator

	Strand1	Strand2	Strand3	Strand4	Strand5
Strand1		100	0	0	0
Strand2			100	0	0
Strand3				97	94
Strand4					0
Strand5					

Fig.3 Summary of scores in Switcher (%)

	output1	gate1	input1	fuel1	output2	gate2	input2	fuel2
output1		100	0	0	100	0	0	0
gate1			100	100	0	4	2	0
input1				0	5	0	0	0
fuel1					7	0	0	0
output2						92	0	0
gate2							99	97
input2								0
fuel2								

Fig.4 Summary of scores in Switcher in DNA feedback regulator (%)

Next, a more complicated DNA circuit, DNA feedback regulator is designed and verified with this tool. As a result, as shown in Fig. 4, the undesired products are produced at a maximum of 7% or less, and the desired products are produced at a minimum of 92% or more. From this, the DNA feedback regulator was successfully designed. However, there are several problems with the tool at present. Firstly, if the DNA circuit design is even larger, the iterative process of design may not converge. The second problem is that the accuracy of the simulation used by this tool is not sufficient and an unintended reaction occurs in the experiment. Regarding the second problem, if you set certain parameters of the simulator, you can increase the accuracy, but the computation time increases dramatically. In order to solve these problems, a method of applying mismatch base sequence devised in our laboratory last year is expected. One of the advantages of applying the mismatch base sequence method over my proposed mismatch is that the number of base sequence rewriting processes decreases. For example, in my method, a process of checking the change in concentration is performed each time the base sequence changes one character, but in the case of the new method there is a difference that more than one character changes at a time, there may be a difference in efficiency. Also, since the way of rewriting changes, there is a possibility of convergence. Improvement is necessary to automate this new method because this method has to judge depending on the situation how the designer changes from which strand. Therefore, it is necessary to devise clear criteria that designers do not have to make judgment in order to automate. In the future I plan to solve the current problem by devising an algorithm for automating this new design method and implementing it in this tool.

REFERENCES

[1]D. Y. Zhang, and G. Seelig, Dynamic DNA nanotechnology using strand-displacement reactions, Nat Chem, vol. 3, pp. 103-113, 2011.

[2] K. Nishijima, T. Nakakuki, Y. Sato, and S. Nomura, DNA Switcher for a Molecular Robot, Proc. of ICTROBOT2016, Pusan, September, 2016.

[3] T. Nakakuki, and J. Imura, Molecular Governor:DNA Feedback Regulator for Molecular Robotics, SICE JCMSI, vol. 9, no. 2, pp. 60-69, 2016.

Oral/Poster/Either: Poster
Presentation session: Biological Science
Presenter name: Chandra SHEKHAR

Operon Mutant Library of *Escherichia coli* Hydrogenases to Understand the True Function of Hydrogen Metabolism

Chandra SHEKHAR, Ayaka IMABAYASHI, Toshinari MAEDA

Graduate School of Life Science and Systems Engineering, Kyushu Institute of Technology, 2-4 Hibikino, Wakamatsu-ku, Kitakyushu, Fukuoka, 808-0196, Japan

shekhar-chandra@edu.life.kyutech.ac.jp

Keywords:
Hydrogenase, operon, mutant library, hydrogen metabolism, P1 transduction

[Introduction]

Escherichia coli is a robust bacterium for hydrogen metabolism research based on genetic engineering because its whole genome sequence is available, operons & genes are annotated and its metabolic pathways are relatively well established which also makes genetic manipulations quite technically simpler than other strains. The KEIO Collection and ASKA library are the two most powerful tools which allows to evaluate rapidly the importance of each nonlethal gene and to perform systematic functional analyses not only of genes of unknown function but of those of known function to survey their function, respectively. In *E. coli*, four membrane-bound proteins, namely hydrogenase 1, 2, 3, and 4 (Hyd), play critical roles in H_2 metabolism. From these four hydrogenases classified as [NiFe] hydrogenases, Hyd-1 is encoded by *hyaABCDEF*, Hyd-2 is encoded by *hybOABCDEFG*, Hyd-3 is encoded by *hycABCDEFGHI*, and Hyd-4 is encoded by *hyfABCDEFGHI* operon. Under glucose metabolism, Hyd-1 and Hyd-2 generally act as hydrogen uptake, while Hyd-3 is involved in H_2 synthesis. In contrast, under glycerol metabolism, Hyd-2 seems to be important for glycerol metabolism as well as one report that Hyd-2 is most responsible for H_2 production at alkaline conditions. To date, the functions of hydrogenases in *E. coli* create a considerable controversy because it seems that the hydrogenases required in glucose or glycerol metabolism are different due to some unusual reports. The functional non-specificities and controversies motivated us to figure out this issue through mutational analysis targeting each operon rather than each single gene in hydrogenases to avoid any possibility that a cross-interaction between hydrogenases may be one of the reasons for the considerable controversy. In this work, *E. coli* four single hydrogenase mutants have been constructed by deleting each operon or three operons and analyzed for hydrogen metabolism to simply evaluate each function of the remaining one hydrogenase in *E. coli*.

[Experiment]

1. Making *E. coli* hydrogenase operon mutants

Each hydrogenase operon mutant was constructed according to a previous literature using a homologous recombination method (Datsenko and Wanner, 2000). A 50-nt extension homologous region to delete each hydrogenase was selected at the upstream or the downstream of targeted operons and primers were designed with a 20-nt sequence including FRT of pKD4.

2. Multiple chromosomal mutations by P1 transduction and mutant confirmation

P1 lysates of each single operon mutant containing Km^R were prepared by infecting P1 phage. These lysates were then employed for repeated rounds of P1 transduction to knockout all hydrogenase operons by selecting for the kanamycin resistance gene that is transferred along with each chromosomal deletion. Plasmid pCP20 was used to eliminate the Km^R gene from each intermediate operon mutant allele that was transferred to the chromosome via each P1 transduction so that multiple mutations could be introduced into a single strain.

Finally, four triple operon mutants of hydrogenases (TOMH-1, TOMH-2, TOMH-3, and TOMH-4) were successfully constructed in this way.

3. Hydrogen production assessment

Overnight cultures of mutants along with *E. coli* (control) was adjusted to OD_{600} 0.05 in fresh glycerol and LB medium separately. LB medium was supplemented with 2.25% glucose and mixtures (10 mL) transferred to crimp-top vial (65 mL). After that, all the vials were sealed with rubber cap and aluminum foil cap. Then, the vials are sparged for 5 min with nitrogen to remove oxygen, and anaerobically incubated at 37°C with 120 rpm. The amount of hydrogen generated in the headspace of the vial was measured by gas chromatography.

[Result and Discussion]

1. Hydrogen production, growth and glucose consumption in glucose media

Except TOMH-3 (meaning only Hyd-3 is present in the genome of *E. coli*), no other mutants showed H_2 production. It indicates that Hyd-3 is the main hydrogenase for hydrogen production. No significant difference in pH change recorded during the fermentation among all TOMHs. Reduced glucose consumption has been observed from TOMH-1 whereas TOMH-3 showed significantly increased consumption. A relative low growth observed in TOMH-2 than others.

3. Hydrogen production and growth in glycerol media

TOMH-1 and TOMH-4 showed no H2 production whereas TOMH-2 showed a little H_2 and TOMH-3 showed considerably H_2 production. No significant pH change and growth difference was observed.

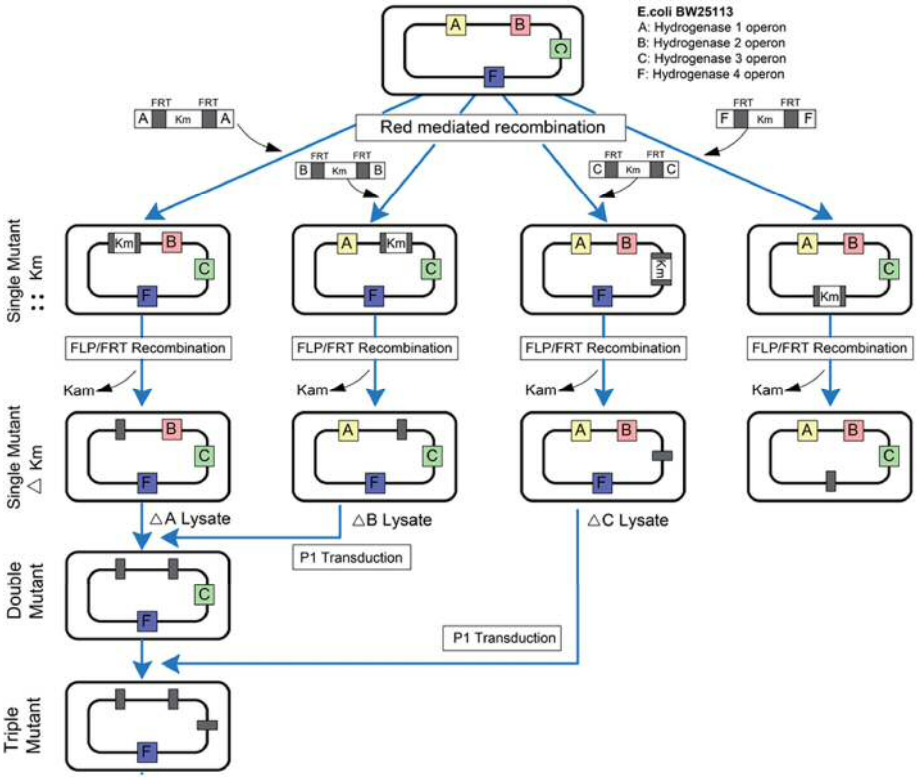

Fig.1. The procedural overview to describe the construction of triple mutants via successive rounds of P1 transduction

Reference:

Datsenko KA, Wanner BL. **One-step inactivation of chromosomal genes in Escherichia coli K-12 using PCR products.** PNAS. 2000 97 (12) 6640-6645.

Please choose: Poster
Presentation session: Biological Science
Presenter name: Kouki Sato

Efficient expression of Difficult to Expression Proteins by using LEA peptide co-expression system

Kouki Sato[1], Nishit Pathak[1], Takahiro Kikawada[2], Shinya Ikeno[1]

[1] Kyusyu Institute of Technology, 2-4 Hibikino, Wakamatsu-ku, Kitakyushu 808-0196, Japan
[2] National Agriculture and Food Research Organization

Email: sato.kouki316@mail.kyutech.jp

Keywords (5 words): LEA peptide co-expression system, Cas9 protein, Silicatein, *Escherichia coli*

[Introduction]

Cas9 protein is an RNA-guided DNA endonuclease enzyme for genomic editing technology called CRISPR / Cas9 system, and is widely used as useful protein because of the high accuracy of its genome editing. But it is a problem that Cas9 protein is very expensive because the expression level in bacterial production is small at bacterial production. Also, silicatein derived from marine sponge is an enzyme that catalyzes polymerization of amorphous silica nanospheres and is expected as a useful protein to promote formation of inorganic skeleton of silica through bioprocess. However, the bacterial expression is difficult like as a Cas9 protein, an efficient expression technology are required for it demand.

In our laboratory, we have found that an expression level of target protein (GFP) in *Escherichia coli* (*E.coli*) has been increased by co-expression of LEA peptides designed based on dehydration resistance protein (LEA protein) derived from *Polypedilum vanderplanki* [1]. The peptide consists of 13 amino acids and we have succeeded in increasing expression level of several proteins by co-expression of the LEA peptide or LEA peptide variant in microorganisms [2]. In this study, we have studied to efficient expression of above two proteins in *E.coli* through our original LEA peptide co-expression system.

[Experiment]

We constructed co-expression vectors that simultaneously expressed five different LEA peptides (LEAI, LEAII, LEAE, LEAK, LEAS) and Cas9 protein or silicatein by Isopropyl β-D-1-thiogalactopyranoside (IPTG) induction (Fig.1). These protein-LEA peptide co-expression vectors were transformed into *E. coli* BL21 (DE3), and the transformants were cultured in LB (Kam) medium. After confirming that OD (600nm) of the main culture was reached at 0.5, IPTG as an inducer was added into each culture solution for protein and each LEA peptide expression. Samples were collected from the culture solution in each times (8 h, 12 h, 24 h after addition of IPTG) to compare the expression levels. Expressed samples were analyzed by sodium dodecyl sulfate polyacrylamide gel electrophoresis (SDS-PAGE), and measured the luminance of the protein band in the SDS-PAGE gel with image processing software (ImageJ).

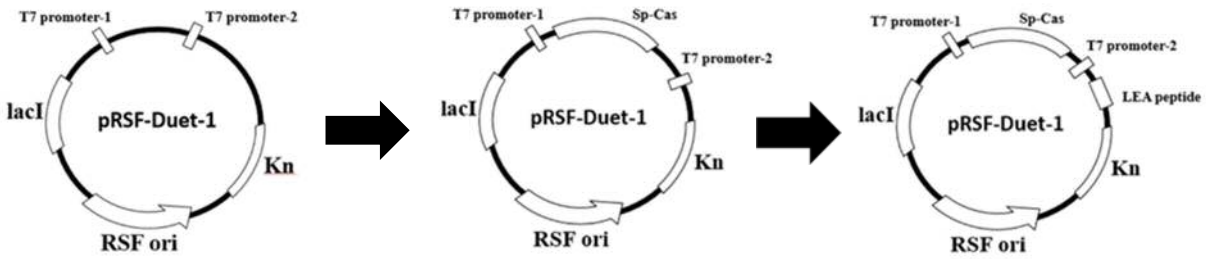

Fig.1 Cas9-LEA peptide co-expression vector

[Result and Discussion]

Protein expression by LEA peptide co-expression system were compared with the luminance level of the protein per number of bacteria. As a result, the expression level of Cas9 protein increased by co-expression of LEA II peptide slightly. In addition, enhancement of silicatein expression was done by the same experimental method, the expression level of silicatein was increased by co-expression of peptide designed based on LEAII. From this result, it is considered that the hydrophobic amino acid (leucine) in the LEA peptide are essential for enhancement of protein expression level.

[References]

[1] Shinya Ikeno, Tetsuya Haruyama, "Boost Protein Expression through Co-Expression of LEA-Like Peptide in *Escherichia coli*" PLOS ONE, vol.8 (12), 2013

[2] Nishit Pathak, Hiro Hamada, Shinya Ikeno, "Construction and characterization of mutated LEA peptides in *Escherichia coli* to develop an efficient protein expression system" Journal of Molecular Recognition, vol.31 (1), 2018

Please choose: Poster
Presentation session:
Presenter name: Norfatin Izzatie binti Mohamad Saimi

Development of aerosolized niosome formulation containing gemcitabine and cisplatin for lung cancer treatment

Norfatin izzatie Mohamad Saimi[1], Norazlinaliza Salim[1], Mohd Basyaruddin Abdul Rahman[1], Noraini Ahmad[2] and Siti Efliza Ashari[1]

[1]Integrated Chemical BioPhysics Research, Faculty of Science, Universiti Putra Malaysia, 43400 UPM Serdang, Selangor, Malaysia.
[2]Department of Chemistry, Faculty of Science, Universiti of Malaya, 50603 Kuala Lumpur, Malaysia

Email: norfatinizzatie115@gmail.com

Keywords: gemcitabine; cisplatin; niosome; lung cancer; aerosol

Introduction

Lung cancer has been the most common diagnosed cancer in the world for several decades (Torre *et al.*, 2015). Lung cancer is the leading cause of cancer-related deaths worldwide, estimated to be responsible for 1 in 5 (1.6 million deaths, nearly 20 %) of the total (Bhushan and Gopinath, 2016). Lung cancer can be divide into two categories types which are small cell lung carcinoma and non-small cell lung carcinoma (NSCLC), which contribute 15 % and 85 % of all lung cancer cases, respectively (Zappa & Mousa, 2016). Standard treatment options for lung cancer are surgery, chemotherapy and radiation depend on the stage and overall performance of the cell growth. Basic principle of chemotherapeutic drug is use to inhibit the proliferation of cells growing at an abnormal rate (Lee *et al*., 2015). Conventionally, a patient that undergoes chemotherapy will be given single or multi-drug at one time. For example, cisplatin or gemcitabine alone or combination of both drugs (Ma *et al.*, 2017). This combination of drugs usually used for patient with advanced non-small lung carcinoma (NSCLC) (Toschi *et al.*, 2005).

The demand on nano-carriers for drug administration in medical applications especially in chemotherapy treatment has been increased as drugs development become wider. Nano-carriers provide large surface area, have the potential to increase solubility, improve controlled released and enhance bioavailability (Majeed *et al*., 2016).There are a few of nanocarriers that usually use as cancer targeting drug delivery such as micelles, dendrimers, carbon-based nanoparticles, metallic, liposome and niosome (Kumari, Ghosh and Biswas, 2015). Hence, liposome and niosome are suitable vehicle for multiple drugs delivery due to their ability to encapsulate both hydrophilic drug into an aqueous compartment whereas hydrophobic drugs at the lipid bilayer (Kumar and Rajeshwarrao, 2011). Niosome is a system with bilayer spherical vesicles which formed by self-assemblies of nonionic surfactants and cholesterol in an aqueous medium (Ertekin *et al.*, 2015). Niosomes have advantages of chemically stable, has high compatibility with biological systems and low toxicity because of their non-ionic nature (Moghassemi & Hadjizadeh, 2014).

However, although gemcitabine and cisplatin were administered through intravenous at higher dosage about 1000mg/m^3 and 100mg/m^3, respectively, only limited quantity of drugs were delivered to lung tumor (Goel *et al*., 2013). This is due to less efficient carrier and higher dosages gave higher toxicity where most chemotherapeutics act on normal tissues leading to worsen side effects. Thus, the aerosol therapy with better carrier system such as niosome to deliver drug to the cancer cells at the same time minimum side effects can produce more opportunity in safer chemotherapy with better patient compliance.

Experiment

Screening and selection of niosome composition			
Drug	Surfactant	Cholesterol	Stabilizer

↓

Formulation of niosome using heating method and optimization niosome composition using MED

↓

Characterization of optimized niosome formulation			
Particle Size	Polydispersity Index	Morphology (TEM)	pH

↓

Stability evaluation of optimized niosome formulation	
Centrifugation test (4000 rpm, 15 min)	Storage test at 4˚C, RT, 45˚C

↓

Drug release studies
Franz cell diffusion

↓

Cytotoxicity tests using MTT assay	
Normal lung cell (MRC5)	Lung cancer cell (A549)

Result and Discussion

a) D-optimal analysis and validation

A special cubic model (**Figure 1**) was fitted by the D-optimal design. As for the p value, it is considered as significant when the values are less than 0.05 (Arbain *et al*., 2018). In this work, the final reduced model had a significant p value ($p < 0.0001$). The estimated regression coefficients (R2), adjusted R2, and standard deviation of the final reduced model were 0.9874, 0.9767, and ± 0.007, respectively and lack of fit 0.3217 (insignificant) which convinced the significance special cubic models.

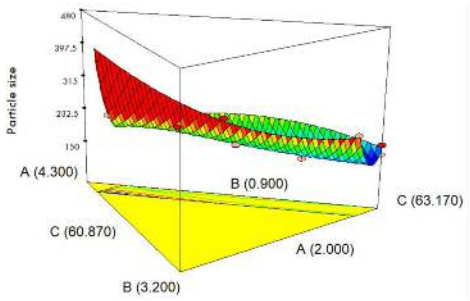

Figure 1

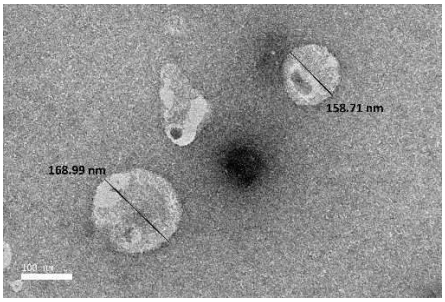

Figure 2

b) Optimization of D-Optimal mixture design of niosome and its characterization

By determining the optimization constraint and evaluating the interaction effect between independent variables, the optimized formulation was obtained based on minimum droplet size of niosome. Using this approach, optimized gem-cis niosome was obtained from D-optimal mixture design analysis with a composition of 2.000 wt.% of T65:S60, 1.01 wt.% of CHOL, and 63.06 wt.% of 3% Glycerol in PBS. The droplet size, PDI, and zeta potential of formulation obtained were 166.90 ± 11 nm, 0.16, -16.13 ± 1 mV, respectively. PDI value described the uniformity of particle distribution in the emulsion system. The lower PDI value of the optimized gem-cis niosome indicates a narrow size distribution of the droplet. The pH obtained from optimized gem-cis niosome was 6.70. Based on TEM analysis **(Figure 2)**, spherical shaped vesicles and exhibited large unilamellar vesicles for optimized niosomes. Particle sizes were estimated from TEM nanograph at the range of 150 – 170 nm, which agreed with the DLS results for the same sample. By observing the creaming or coalescence of the disperse phase, centrifugation test can be used to predict the shelf life under normal storage condition (Arbain *et al*., 2018). The centrifuge tests showed that the optimized niosome had good physical stability with no phase separation after centrifugation at 4000 rpm for 15 min.

Please choose: Poster
Presentation session: Applied Engineering
Presenter name: Keisuke, Watanabe

[Cell molecule simulation in contaminating reaction field]

[Keisuke, Watanabe][1], [Takashi, Nakakuki][1]

[1]Major of Interdisciplinary Informatics, Kyushu institute of Technology, 680-4 Kawazu, Iizuka, Fukuoka 820-8502, Japan
[2]Department of Systems Design and Informatics, Kyushu Institute of Technology, 680-4 Kawazu, Iizuka, Fukuoka 820-8502, Japan

Email: [watanabe.keisuke597@mail.kyutech.jp]

Keywords (system biology, signal transduction, intracellular signal, contaminating reaction field, particle simulation)

[Introduction]

A cell is the structure of the smallest unit that constructs human skin and organs. Cell size is about 5 μ m to 100 μ m, and a person is composed of about 60 trillion cells. Cells have various shapes and sizes, each working differently.

Cells are covered with cell membranes, which are composed of various biomolecules and organelles. The cytoplasm, which occupies the majority of cell volume consists of moisture and nucleus. Deoxyribonucleic acid (DNA) exists in the nucleus, which is response for the transfer and expression of genetic information in many organisms. A schematic diagram of the cell is shown in the Fig.1.

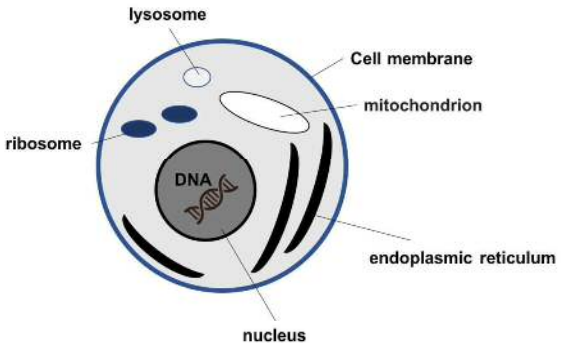

Fig.1 Schematic diagram of cells

A project to analyze the entire nucleotide sequence of human genome, Human Genome Project was completed in 2003, and all DNA sequences were clarified. After that, further detailed analysis, such as research to use the obtained information in the medical field, is being carried out.

On the other hand, researchers are trying to clarify how intercellular components transfer information and control cells. Since whole cell structure is very complicated and it is difficult to capture it in biochemical experiments, they have elucidated the intracellular control by mathematical modeling and simplifying. This study is called system biology.

Currently, the most representative cell simulation is a method using differential equations. In fact, molecular contaminants were mixed, and we thought it is necessary to conduct simulation considering them.

In this research, we aim to simulate in a more realistic simulation. Plasma membrane surface receives an external stimulus as an input and sends that signal into the cell. In brief, it is responsible for the switch function of the cell, and it is considered that abnormality of the switch function is the cause of cancelation. Therefore, we conducted simulation on the plasma membrane surface. For the simulation, we used Kholodenko[1] model, which is the EGF (Epidermal Growth Factor) signaling pathway. EGF plays an important role in cell growth and proliferation. We perfume deterministic and particle simulation. Deterministic simulation is a method using ordinary differential equations. Particle simulation is one of stochastic simulation by Mayawara[2]. We confirm the state, concentration change, and movement of molecules in contaminating reaction field using particle simulation.

[Simulation Method]

In this study, we aim to express contaminants on the surface of the cell membrane. In a

deterministic simulation using differential equation, it is impossible to express it. Therefore, we use particle simulation. This is a way to express the movement of a molecule by giving each molecule. It is a hybrid null-event Monte Carlo method proposed by Mayawara. As shown in the Fig.2, a two-dimensional plane is divided by a lattice, a molecule is arranged on a lattice point, and it is moved between lattice points. One molecule is randomly chosen and events occur on the basis of the probability. Events are binding, dissociation, activation, inactivation, internalization.

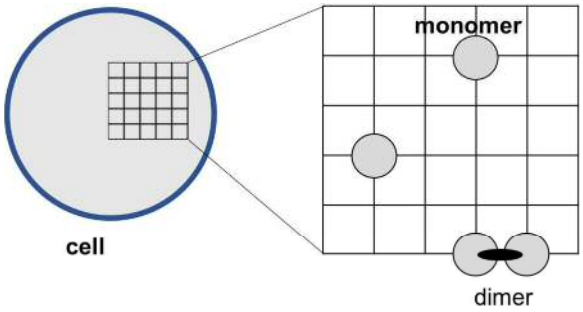

Fig.2 Expression of cell surface by lattice

We mixed contaminants other than EGFR and measured changes in reaction efficiency. It is assumed that contaminants diffuse like EGFR and chemical reaction doesn't occur.

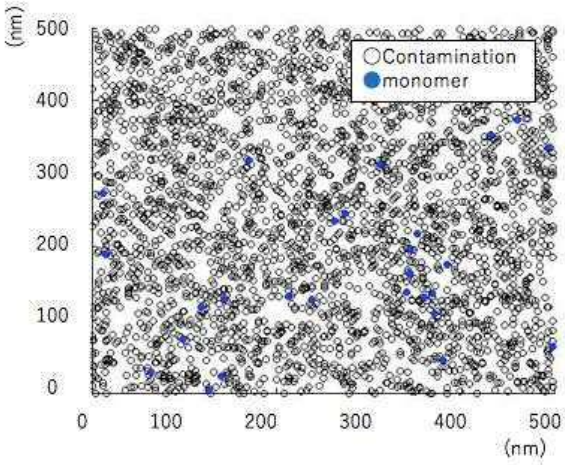

Fig.3 contaminating reaction field

[Result and Discussion]

We conducted a simulation with the number of contaminants is 100 times that of EGFR. Fig.4 shows the difference in the presence or absence of contaminants. Error bars indicate the respective standard errors.

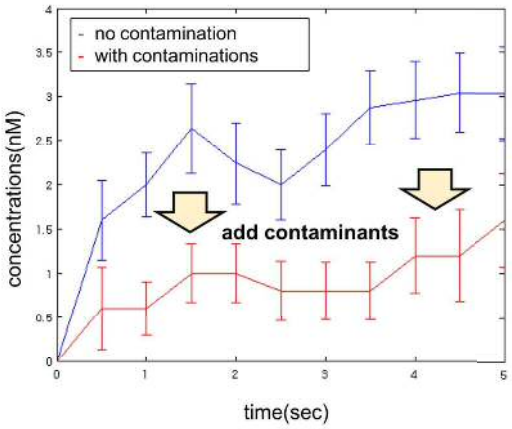

Fig4. Result of simulation

Fig.4 Change in reaction efficiency when contaminants are added. From this result, it was confirmed that the reaction efficiency of EGFR decreases due to contaminants.

In this steady, we conducted a new simulation in the contaminating reaction field. From now on, we think that it is necessary to use various simulations depending on the situation.

[References]

[1] Boris N.Kholodenko, Oleg V.Demin, Gisela Moehren and Jan B. Hoek, Quantification of Short term Signaling by the Epidermal Growth Factor Receptor, J.Viol. Chem, 1999, 274:30169-30181

[2] Kapil Mayawara, Dionisios G Blachos and Jeremy S Edwards, publishes, Computational modeling reveals molecular details of epidermal growth factor binding, BMC Cell Biology, 2005,6:41 doi:10.1186/1471-2121/6/41

Please choose: Poster
Presentation session: Applied Engineering
Presenter name: Michiko Misawa

Robustness of DNA feedback regulator including irreversible reaction

Michiko, Misawa[1], Takashi, Nakakuki[2]

[1]Graduate School of Computer Science and System Engineering, Kyushu Institute of Technology, 680-4 Kawazu, Iizuka, Fukuoka 820-8502, Japan
[2]Department of System Design and Informatics, Kyushu Institute of Technology, 680-4 Kawazu, Iizuka, Fukuoka 820-8502, Japan

Email: misawa.michiko601@mail.kyutech.jp

Keywords (5 words)
DNA Computing, Molecular Robotics, DNA Strand Displacement, Feedback Control, Robustness

[Introduction]

In recent years, manufacturing at the molecular level using biomolecules has attracted attention in the field of nanotechnology. Among them, a molecular robot[1] is an ultra-small robot that consists of all components such as a frame, a sensor, an actuator, and a controller as biomolecules. Molecular robot is a self-contained moving system composed of microcapsules, and driven and controlled by signal transmission by concentration of DNA chain. As a control problem, it is necessary to adjust the concentration of the DNA strand to the actuator relative to the target level of the concentration of the DNA strand from the sensor system. Therefore, the molecular robot needs a concentration adjuster.

We have proposed DNA feedback regulator[2] as controllers in previous studies. The operating principle of the control circuit is calculated based on the DNA strand displacement reaction. As a characteristic of the regulator, as shown in the Fig1, an autocatalytic amplifier is inserted in the circuit to improve the modularity of the DNA circuit.

There is a leakage response as a serious problem in DNA circuit design. The leakage reaction is a phenomenon in which a DNA chain is unintentionally reacted in the absence of a catalyst. Feedback regulator may suffer from unintended reaction due to fuel-fuel leaky binding. In the DNA feedback regulator, fuel exists in large quantities as an initial concentration, and plays an important role to drive a circuit. Therefore, how much trouble this circuit is against this fuel-fuel binding can be mentioned as a problem.

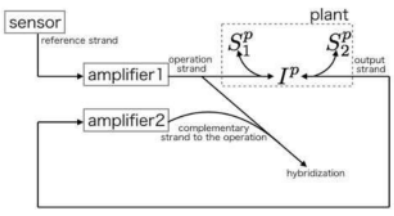

Fig. 1 Schematic of DNA feedback regulator

In our previous studies, we have experimentally verified the feedback regulator using seesaw gates consisting of reversible DNA reaction assemblies, but we could not get the intended behavior. As one of the causes, fuel-fuel leaky binding is suspected. Therefore, in this study, it is investigated by numerical simulations that seesaw gate and Zhang's gate including irreversible reaction make the DNA feedback regulator more robust against the leak reaction.

[Two types of amplifiers]

There are some candidates for the auto-catalytic amplifiers that can be used in the design of the DNA feedback regulator. Here we describe two types of typical automatic catalytic amplifiers, seesaw and Zhang's.

A. seesaw gate

The reaction scheme of the seesaw gate is shown in Fig. 2(a) where U and OB are the input and output DNA strands, respectively. F is the fuel and the strand I_1 to I_4 are the intermediates generated during a series of the reaction process.

B. Zhang's gate

The reaction scheme of the Zhang's gate is shown in Fig.2(b). As similar to the above discussion, U and OB are the input and output DNA strands, respectively. F is the fuel and the strand I1 to I7 are

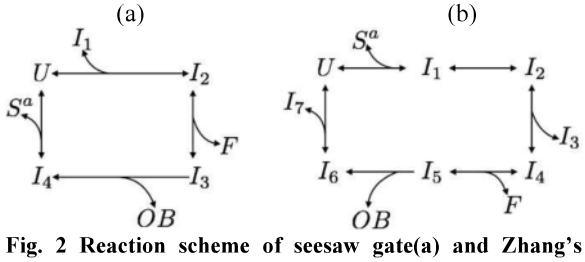

Fig. 2 Reaction scheme of seesaw gate(a) and Zhang's gate(b)

the intermediates generated during a series of the reaction process.

[Construction of DNA feedback regulator]

I In this chapter, we show the circuit implementation when seesaw gate is used and Zhang gate is used from the viewpoint of regulation performance.

A. Type A with the seesaw gates

We show the simulation result when the reference level sets r(0) = 1 in Fig. 3(a), respectively, under the ideal condition in the sense that unintended reactions are not occur in the system.

On the other hand, Fig. 3(b) shows the corresponding simulation results under a fuel-fuel leaky binding where the adverse influence of the undesired binding is adjusted by using the length of toehold regarding the unintended reaction according the following calculation[3]:

$$k_f = (5\times10^{n-10})\times10^{-2}\ [\mathrm{nM^{-1}s^{-1}}] \qquad (1)$$

It is noted that the longer the length of the toehold (n) is, the greater the association constant of the leaky binding becomes, where the length is changed from n = 1 to 6 in our test. The initial strand concentrations are shown in the Table. I.

B. Type B with the Zhang's gates

We show the simulation result when the reference level sets r(0) = 1 in Fig. 4(a), respectively, under the ideal condition in the sense that unintended reactions are not occur in the system.

On the other hand, Fig.4(b) shows the corresponding simulation results under a fuel-fuel leaky binding where the adverse influence of the undesired binding is adjusted by using the length of toehold regarding the unintended reaction according Eq.1. It is noted that the longer the length of the toehold (n) is, the greater the association constant of the leaky binding becomes, where the length is changed from n = 1 to 6 in our test. The initial strand concentrations are shown in the Table. I.

Table. 1 Initiation concentration

Parameter	Concentration[nM]
S_1^p, S_2^p	2×10^2
I^p	0
S^a	1×10^3
F	2×10^4
I_*	0

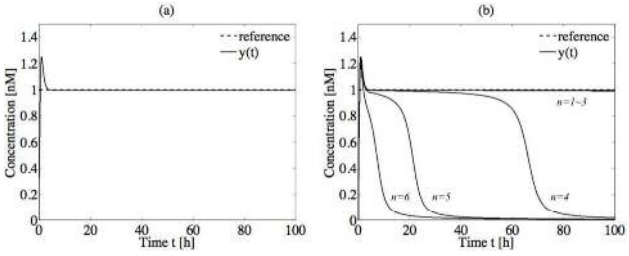

Fig. 3 Simulation result regarding Type A

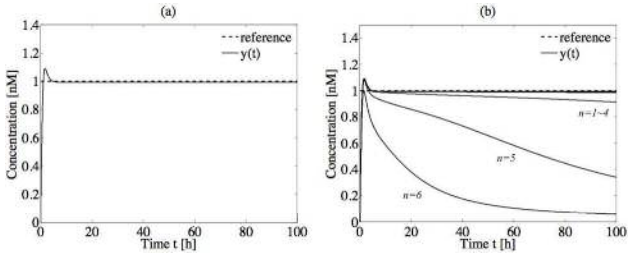

Fig. 4 Simulation result regarding Type B

[Discussions]

We compare the regulation performance of the two proposed DNA feedback regulators, where the concentration of output strand is evaluated. As we can see in Fig. 3(a) and 4(a) there are no essential differences between these two implementations when there is no fuel-fuel leaky binding in the system.

However, Fig. 3(b) shows that the output regulation fails to achieve with n = 4 the reference levels of 1 when there is leaky binding. On the other hand, Fig. 4(b) shows the better regulation performance with n = 4.

We speculate that the DNA feedback regulator consists with the Zhang's gates are more robust that consists with the seesaw gates. Our speculation is based on just numerical simulation with some limited conditions. Therefore, more investigation should be continued.

[Conclusions]

In this research, we discuss how the choice of DNA amplifier affects the robustness of DNA feedback regulator. From the viewpoint of suppressing the adverse influence of unintended fuel-fuel leak reaction, two candidate autocatalytic amplifiers as the insulating element of the DNA feedback regulator are compared by numerical simulation. It is numerically demonstrated that feedback regulator with the Zhang's gates, including irreversible reactions in the reaction scheme is more robust than it with the seesaw gates consisting only of reversible reactions.

References

[1] S. Murata, A. Konagaya, S. Kobayashi, H. Saito and M. Hagiya, Molecular Robotics: A New Paradigm for Artifacts, New Generation Computing, vol. 31, pp. 27-45, 2013

[2] M. Misawa and T. Nakakuki, Robust Design of DNA Feedback Regulator for Molecular Robot, 11th Asian Control Conference, pp2756-2759, 2017

[3] D. Y. Zhang and E. Winfree, Control of DNA Strand Displacement Kinetics Using Toehold Exchange, J. Am. Chem. Soc., Vol. 131, No. 47, pp. 17303-17314, 2009.

Please choose: Poster

Presentation session: Biological Science
Presenter name: Osamu Nakamura

A concerted spiking induced by a random pulse in uncoupled non-identical neuron models

Osamu Nakamura[1], Katsumi Tateno[2]

[1]Department of Life Science and Systems Engineering, Kyushu Institute of Technology, Kitakyushu, Japan
[2]Department of Human Intelligence Systems, Kyushu Institute of Technology, Kitakyushu, Japan

Email: p899014o@mail.kyutech.jp

Keywords: noise-induced synchronization, stochastic resonance, spiking neuron.

[Introduction]

A specific feature of a neuron is an action potential (also call spike). If a local graded potential, such as a receptor potential, reaches or exceeds a threshold, a neuron emits an action potential. A weak sensory signal does not cause spiking. A white Gaussian noise contributes to an improvement of a signal-to-noise ratio for detecting a subthreshold periodic signal in a neuron. It is known as stochastic resonance (SR). On the other hand, an adequate white Gaussian noise forcing induces synchronization in an uncoupled non-linear oscillators. This is known as noise-induced synchronization. The noise-induced synchronization has been found in neuron models and physiological experiments.

Synchronization of spikes is one of prominent phenomena in a neural network. Neural synchronization can be observed as an electroencephalogram (EEG). EEG is associated to a functional state of the brain. A phase synchronization augmented by random signal potentially in the human brain causes behavioral SR [1]. The noise input also arguments a long-range phase synchronization of EEG signals. They considered that an increase in phase synchronization increases signal transfer between neurons, and consequently induces behavioral SR.

We have previously presented that a common random pulse generated by an exponential distribution with a negative slope induced synchronization in a pair of uncoupled neuron models [2]. When an internal fluctuation is given, the common random pulse induces more robust synchronization of spiking than a common periodic pulse. SR has not been observed in the previous study. However, SR is induced by an irregular synaptic input in a conductance-based neuron model [3]. This indicates that random synaptic forcing causes SR in a neural network. In the present study, a phase synchronization and SR induced by a random pulse in a pair of conductance-based neuron models are presented. We revealed that a random pulse forcing induced a phase synchronization and SR in a pair of uncoupled non-identical conductance-based neuron models. Further, a degree of synchronization depended on a temporal pattern of a random pulse.

[Experiment]

The present neural network model comprises a pair of uncoupled non-identical conductance-based neuron models (Fig. 1). No interconnection existed between the two neurons. The neuron models received the common random or/and periodic pulse input. The neuron model emits an action potential if the pulse input is strong enough. We investigated output properties of spike trains: a degree of synchronization, a spiking frequency, and a periodicity.

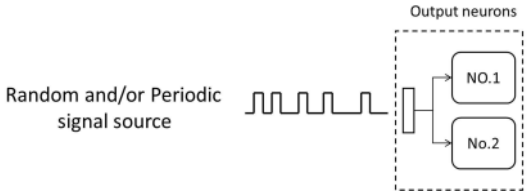

Fig.1 Outline of the neural network model

The neuron model is a $I_{Na,p}$+I_K neuron model [4], which consists of the persistent Na^+ channel and the delayed rectified K^+ channel. The equations are presented below:

$$C_m \frac{dV_i}{dt} = \bar{g}_{Na} m_{\infty,i}(E_{Na} - V_i) + \bar{g}_{K,i} n_i (E_K - V_i) + g_l(E_l - V_i) + I_{com}(t) + \xi(t)$$

$$\frac{dn_i}{dt} = \frac{n_{\infty,i} - n_i}{\tau_n}$$

where i = 1 or 2. Therein, $I_{com}(t)$ is a common pulse input current. $\xi(t)$ is the Gaussian noise.

Three stimulation patterns were applied to the two neuron models. First, a random pulse was applied to the neuron models. The pulse width (pulse on time) was fixed at 5 ms. The pulse off time y was selected from the gamma distribution $f(y) = \frac{\theta}{\Gamma(k)}(\theta y)^{k-1}e^{-\theta y}$ $(y \geq 0)$. Γ(k) is the gamma function. The mean frequency of a random pulse is determined by a shape parameter k (= 1, 3, 5) and a scale parameter θ. For k = 1, the gamma distribution is equivalent to the exponential distribution with a negative slope. The pulse amplitude was fixed at 5.5 μA/cm^2. This is a subthreshold stimulation. Second, the periodic pulse was applied to the neuron models. The input frequency of the periodic pulse was changed. Third, the periodic pulse and the random pulse were applied concurrently to the neuron models. The random pulse was selected from the gamma distribution. When two pulses arise coincidentally, the pulse was simply superposed with the other pulse while maintaining the pulse amplitude of 5.5μA/cm^2. The computation presented above was repeated 10 times. The computational time was 10 s.

A degree of synchronization in spiking of the neurons was quantified by a vector strength. We first defined a phase for a spike train, and then a phase difference $\Delta\phi(t)$ between the neurons were calculated. The vector strength ρ was calculated using the following equation: $\rho^2 = \langle \sin\Delta\phi \rangle^2 + \langle \cos\Delta\phi \rangle^2$.

[Result and Discussion]

When the common random pulse with k = 1 was given, the vector strength ρ increased up to approximately 0.9. Increasing k reduced ρ. For k = 5, ρ was near 0.6 (Fig. 2, filed triangle). The common periodic pulse caused low vector strength (ρ < 0.4). Those results indicate that a random bursty pulse input increased the degree of synchronization even in the neurons were non-identical.

The periodic pulse was applied with the random pulse with k = 5. The vector strength as a function of the mean frequency of the random pulse is shown by a red filled circle in Fig. 2. The common random pulse with the common periodic pulse improved the vector strength through the entire frequency range. In addition, the sensitivity in the lower frequency range was improved. The combined common pulse also periodic event rate up to about 30 % .

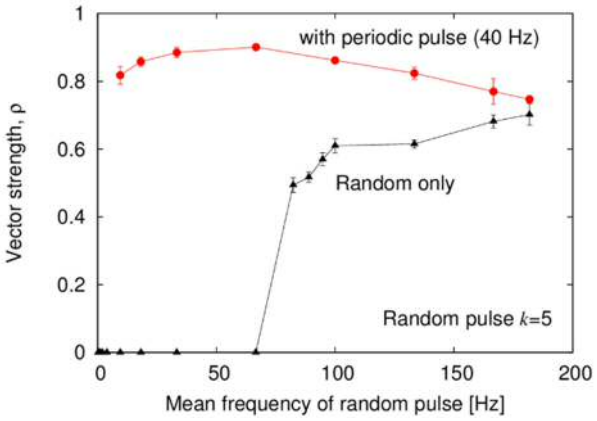

Fig. 2 Degree of synchronization in spiking of the neurons in response to the combined common pulse input

In the present neural network, the common periodic input with the common random pulse induces the periodic responses. This indicates that the random pulse uncovers the periodic responses of the neuron models. The common combined pulse also augments a phase synchronization of spiking in a pair of uncoupled non-identical neurons. The synchronization of spiking may support a signal transfer to a deep layer in the brain.

[References]

[1] Kitajo, K., Nozaki, D. Ward, L. M., and Yamamoto, Y. (2003) Behavioral stochastic resonance within the human brain. Physical Review Letters. 90:218103; Kitajo, K., Doesburg, S. M., Yamanaka, K., Nozaki, D., Ward, L. M., and Yamamoto, Y. (2007) Noise-induced large-scale phase synchronization of human-brain activity associated with behavioural stochastic resonance. EPL (Europhysics Letters) 80:40009.

[2] Tateno, K., Igarashi, J., Ohtubo, Y., Nakada, K., Miki, T., and Yoshii, K. (2011). Network model of chemical-sensing system inspired by mouse taste buds. Biological

[3] Yoshida, M., Hayashi, H., Tateno, K., and Ishizuka, S. (2002). Stochastic resonance in the hippocampal CA3-CA1 model: A possible memory recall mechanism. Neural Networks, 15:1171–1183.

[4] Izhikevich, E. M. (2007). Dynamical Systems in Neuroscience. Cambridge, MA: The MIT press.

[Acknowledgment]

This work was supported by JSPS KAKENHI Grant Number JP16K05869.

Please choose: Poster
Presentation session:
Presenter name: Mohd Khairi Zulkalnain

[Regulated Cascode Bandgap Reference for Improved PSRR and RF-DC Rectifier for Energy Harvesting Applications in 130nm Technology]

[Mohd Khairi, Zulkalnain][1], [Noor Ain, Kamsani][1], [Roslina, Mohd Sidek][1,2], [Fakhrul Zaman, Rokhani][2,3], [Shaiful Jahari, Hashim][3] , [Mohd Nizar, Hamidon]

[1]Faculty of Engineering, University Putra Malaysia, 43400 UPM Serdang, Selangor, Malaysia

Email: [mkhairizulk@gmail.com]

Keywords (5 words) RF Energy Harvesting, Bandgap Reference, Power Management, Analog IC Design, Low Power

[Introduction]

The emergence of IoT devices has aided mankind in ways never before possible. Advancement of cloud storage and IoT has brought upon the realization of a myriad of IoT applications namely health wearables and smart city. As with all electronics, an important factor that must be taken into consideration is how to power up these devices. RFEH has emerged as an interesting alternative to conventional power supply as it has the potential to provide power at a much cheaper cost and have longer lifetime. There is a need for high PSRR and clean power supply to ensure optimal functionality of IoT circuits, particularly sensitive circuits that degrade in functionality when subjected to noise travelling through power supply such as low power sensors and VCOs in frequency synthesizers. This work presents a power management designed on 130nm Silterra Technology achieving a PSRR of -81dB for bandgap reference at an output reference voltage of 0.416V and 1.1V of output voltage for a 5-stage rectifier at -1dBm.

[Experiment]

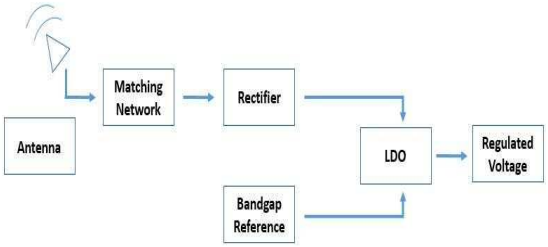

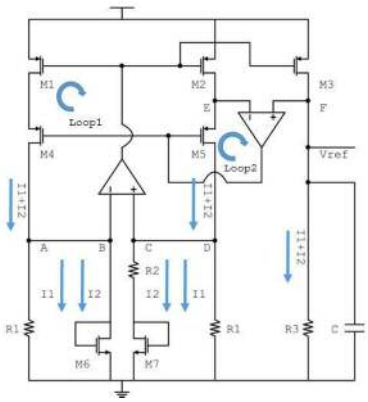

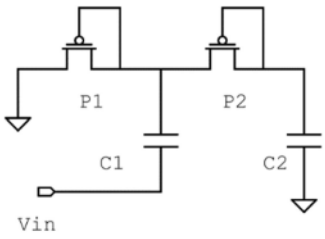

Top Level Architecture

Figure 1 shows an example of a RFEH system. The typical blocks in an RFEH system include a matching network and a rectifier. The ambient RF signal is first collected by the antenna and passes through the matching network. The function of matching network is to provide passive amplification and ensure maximum power transfer to the rectifier. The signal is then channeled to the rectifier where the conversion of RF signal to DC signal will take place. The converted DC signal then passes through a voltage regulator to provide a clean regulated voltage.

Bandgap Reference and Regulated Cascode Technique.

As can be seen in figure 1, transistors M1, M2, M3, M4 and M5 make up the current mirrors that will reflect or mirror the current to the output stage. M4 and M5 form a cascoded current mirror to boost the output

impedance at node E. It is a known issue that current mirrors suffer from channel length modulation problems. Op amp2 works in negative feedback to increase output impedance and hence PSRR. Opamp 1 functions in negative feedback to set nodes A, B, C and D to be equal. This is done so that the PTAT characteristic can be derived from M7 by obtaining the difference of voltage drop between M6 and M7 through the resistor R2. The current I1 is given by VDS6 divided by R1, where VDS6 represents the CTAT characteristic of the MOS. The current I2 is simply the the difference between VDS6 and VDS7 divided by R2 or the PTAT voltage divided by R2. It can be seen that the summation of I1 and I2 are reflected to the output branch by the current mirrors as described earlier. At the output branch, the reference voltage equals to the sum of I1 and I2 times R3 and can be expressed in terms of PTAT and CTAT variables.

Rectifier

The conventional rectifier used in many works in literature is a combination of both these circuits as shown in figure 3. The combined operation is as follows. During the negative cycle, P1 will turn on while P2 will turn off. This will charge capacitor C1 up to Vin. During the positive cycle, P2 will turn on while P1 will turn off. The charge stored in C1 will be discharged into C2. In order to achieve higher output voltage, the rectifier can be stacked in a cascode/cascade manner, in such a case, the output voltage will be multiplied proportional to the number of stages.

However, in reality, during the turning on of the transistors, the sinusoidal signal has to overcome the Vth of the device, causing a drop in the output voltage. The Vth of devices plays an important role in determining the output voltage. The higher the Vth of a device, the lower the output voltage. As such, many works have tried to address this issue by using different devices as the switching element or by means of circuit techniques as mentioned in Chapter 2.

[Result and Discussion]

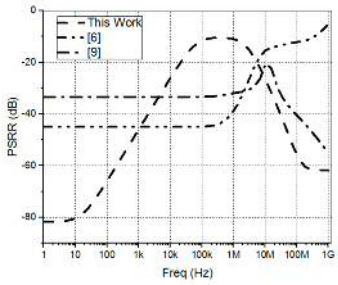

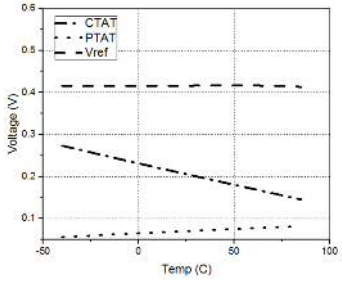

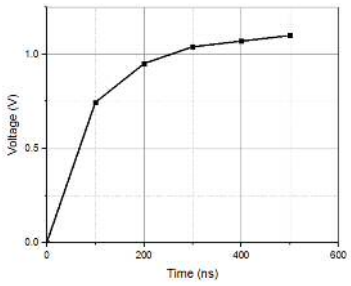

As can be seen, the proposed work shows significant improvement (30-40%) in terms of PSRR in contrast to previous design and conventional design. This is due to the increase in output impedance caused by the op amp in negative feedback and the cascode structure. The voltage reference is 0.416V and is suitable for low power applications. It exhibits small variation of around 3mV or 0.008% across temperature. The output of the 5-stage rectifier shows a DC voltage of 1.1V which is enough to power the bandgap reference circuit.

Conclusion

.This work presents a power management designed on 130nm Silterra Technology achieving a PSRR of -81dB for bandgap reference at an output reference voltage of 0.416V and 1.1V of output voltage for a 5-stage rectifier at -1dBm.Future work includes integrating the rectifier and bandgap reference as well as using a start-up circuit. Also, the physical layout will be designed and the parasitic extraction simulation will be run to test the functionality.

Please choose: Poster
Presentation session: Material Science and Technology
Presenter name: Masayuki Morimoto

Electrochemical reduction of CO_2 into CO and HCOOH using surface modified Zn electrodes

Masayuki Morimoto[1], Yukimasa Nakatsuru[1], Yoshiyuki Takatsuji[1], and Tetsuya Haruyama[1]

[1] Division of Functional Interface Engineering, Dept. of Biological Systems and Engineering, Kyushu Institute of Technology, 2-4 Hibikino, Kitakyushu Science and Research Park, Wakamatsu, 808-0196, Japan

Email: morimoto-masayuki@edu.life.kyutech.ac.jp

Keywords (5 words)
CO_2 reduction, Zn electrode, Anodization, CO selectivity, HCOOH selectivity

Introduction

In recent years, the global temperature has increased with an increase in the concentration of carbon dioxide, which is a greenhouse gas. Therefore, various methods have been studied to reduce carbon dioxide, and we focused attention on the electrochemical reduction of CO_2. Electrolytic reduction of CO_2 can be converted to carbon monoxide, formic acid, and hydrocarbons, and the metal electrode itself acting as a catalyst. However, most metal electrode progress H_2 evolution reaction as distinct from CO_2 reduction reaction. Ag, Au, and Zn electrode catalyze the reduction of CO_2 to CO, HCOOH is the main product of CO_2 reduction reaction on Sn, Pb, Hg, and In electrode[1]. Only Cu electrode produce hydrocarbons such as methane, ethylene, methanol, and ethanol from CO_2. This selectivity change depends on binding energy between metal and reaction intermediates[2]. Therefore, the understanding of binding strength between metal and reaction intermediates is important in selectivity control of CO_2 reduction reaction. In this study, we focused on Zn electrode that it can reduce CO_2 to CO with relatively high efficiency. We investigated the fundamental property of Zn electrode toward CO_2 reduction reaction, and increased CO and HCOOH selectivity by modifying electrode surface morphology.

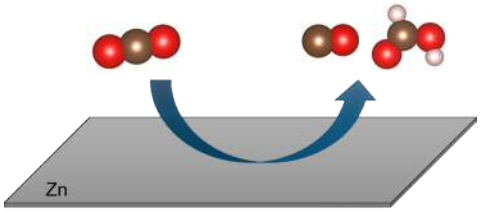

Fig. 1 electrochemical reduction of CO_2 on Zn electrode

Experiment

Preparation of Zn modified electrodes

The Zn electrode (0.2 mm) purchased from nilaco, and its surface washed by ultrasonic in acetone and ultrapure water (18.2 MΩ). Zn electrode carried out anodization in NaOH or Lactic acid solution using the two-electrode system. Zn electrode anodized in NaOH solution reduced surface ZnO to Zn in CO_2 saturated 0.1 M $KHCO_3$ solution at −1.5 V vs. Ag/AgCl[3]. Prepared electrode washed ultrapure water and dried at N_2, and it used CO_2 reduction quickly.

Characterization of Zn modified electrodes

The surface morphology of the prepared electrode analyzed by scanning electron spectroscopy (SEM). The acceleration voltage of SEM observation was set at 10 kV. The crystal structure of prepared electrodes analyzed X-ray diffraction (XRD) using powder and thin-film technique. The X-ray source used Cu Kα, measuring angle was set at 30° to

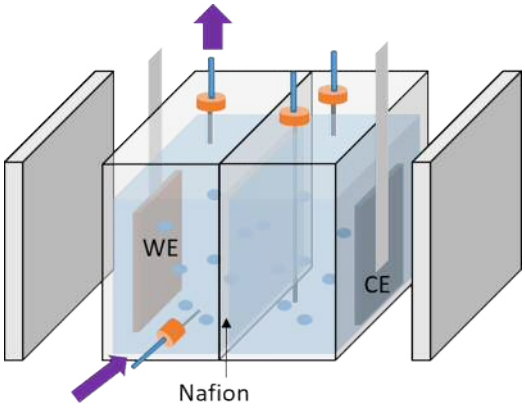

Fig. 2 Schematic illustration of CO_2 electrochemical reduction cell. WE, CE, and RE is working electrode, counter electrode, and reference electrode respectively.

100°. The chemical binding state of prepared electrodes analyzed X-ray photoelectron spectroscopy (XPS) with Al Kα as the X-ray source. The obtained spectra were calibrated as referenced with contaminant C-C bond at 284.2 eV.

Electrochemical reduction of CO_2

The electrochemical reduction of CO_2 was performed two-compartment flow cell (Fig. 2)[4]. CE and RE used Pt plate and Ag/AgCl electrode respectively. The electrolyte employed CO_2 saturated 0.1 M $KHCO_3$ (pH 6.8), the CO_2 flow rate was set at ~6 ml/min. CO_2 and formed gas products collected at gas bag during CO_2 reduction, it determined quantity using gas chromatography (GC-BID). The liquid product was analyzed anion chromatography after CO_2 reduction. The products from CO_2 reduction calculated Faradaic efficiency (FE).

Result and Discussion

Anodization of Zn was performed in NaOH and Lactic acid solution, surface morphology observed SEM (Fig. 3). The Zn electrode anodized in NaOH solution observed SEM after reduction at -1.5 V vs. Ag/AgCl. The Ad-SH-Zn electrode formed the porous structure, while the Ad-LA-Zn formed the terraced structure. The crystal structure of Ad-SH-Zn showed (002) and (101) orientation with similar to Zn plate. Ad-SH-Zn consisted with numerous Zn nanoparticles (50 to 200 nm), this phenomenon induced increase surface area and the unoccupied sites such as edge and step site. Ad-LA-Zn showed (101) orientation from XRD analysis, however, at low applied potential and low operation time, Zn formed (002) orientation. This results indicated that the crystal orientation could control by changing applied voltage and operation time in anodization.

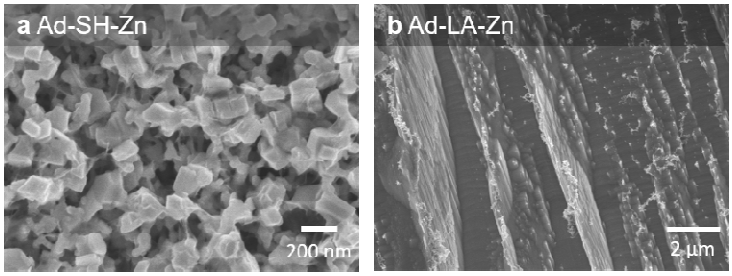

Fig. 3 SEM images of anodized Zn electrode in NaOH (a, Ad-SH-Zn) and lactic acid (b, Ad-LA-Zn).

The electrochemical CO_2 reduction on anodized Zn electrodes performed at various applied potential. The FE of CO_2 reduction products showed table 1. Ad-SH-Zn exhibited high FE for CO production at low applied potential as compared to Zn plate. This results suggested that the edge site of Zn nanoparticles possessed higher activity for CO_2 reduction than terrace site. Meanwhile, the selectivity for HCOOH production increased on Ad-LA-Zn electrode. This results showed that the (101) face of Zn has the higher selectivity for HCOOH production than (002) and (100) face. Additionally, both modified Zn electrodes inhibited H_2 evolution reaction relative to Zn plate. These results indicated that the surface modification of Zn electrode employing by anodization technique can control products selectivity of CO_2 reduction reaction.

Table 1 Faradaic efficiency for H_2, CO and HCOOH production on the anodized electrodes.

		FE / %		
	E / V vs. RHE	H_2	CO	HCOOH
Zn plate	−1.19	29.1	53.6	3.7
Ad-SH-Zn	−0.79	14.4	80.6	N.D.
Ad-LA-Zn	−1.19	20.0	24.0	45.1

References

1. H. Noda, S. Ikeda, Y. Oda, K. Imai, M. Maeda, K. Ito, Electrochemical reduction of carbon dioxide at various metal electrode in aqueous potassium hydrogen carbonate solution, *Bull. Chem. Soc. Jpn.*, **63**, 2459-2462 (1990)
2. K.P. Kuhl, T. Hatsukabe, E.R. Cave, D.N. Abram, J. Kibsgaard, T.F. Jaramillo, Electrocatalytic conversion of carbon dioxide to methane and methanol on transition metal surfaces, *J. Am. Chem. Soc.*, **136**, 14107-14113 (2014)
3. M. Morimoto, Y. Takatsuji, K. Hirata, T. Fukuma, T. Ohno, T. Sakakura, T. Haruyama, Visualization of catalytic edge reactivity in electrochemical CO_2 reduction on porous Zn electrode, *Electrochim. Acta*, **290**, 255-261 (2018)
4. M. Morimoto, Y. Takatsuji, R. Yamasaki, H. Hashimoto, I. Nakata, T. Sakakura, T. Haruyama, Electrodeposited Cu-Sn alloy for electrochemical CO_2 reduction to CO/$HCOO^-$, *Electrocatalysis*, **9**, 323-332 (2018)

Please choose: Oral/ Poster/ Either
Presentation session:
Presenter name: Nurul Atiqah Osman

The effect of Palm Oil Mill Effluent Final Discharge on the Growth of *Pennisetum Purpureum* Cultivars

Nurul Atiqah, Osman[1], Farhana Aziz, Ujang[1], Mohamad Faizal, Ibrahim[1], Mohd Ali, Hassan[1], Ahmad Muhaimin, Roslan[1,2]

[1]Department of Bioprocess Technology, Faculty of Biotechnology and Biomolecular Sciences, Universiti Putra Malaysia, 43400, Serdang, Selangor, Malaysia
[2]Laboratory of Biopolymer and Derivatives, Institute of Tropical Forestry and Forest Products (INTROP), Universiti Putra Malaysia, 43400, Serdang, Selangor, Malaysia

Email: nurulatiqah0194@gmail.com

Keywords (5 words)
Napier grass, palm oil mill effluent final discharge, biomass, bio-sugar, lignocellulose

[Introduction]
Napier grass (Pennisetum purpureum) also known as "elephant grass" was first introduced in Malaysia in the 1920's from East Africa and it is now the most popular fodder grass for livestock. The uses of Napier grass as a phytoremediation plant to remediate industrial and agricultural wastewater is mostly well-known and widely applied. This is because Napier grass has suitable features use in treating wastewater. This grass can grow fast and have high capability to absorb waters and nutrients from the soil to support the growth of the plant. It can also grow on low nutrient and water supply. Therefore, growing Napier grass on wastewater such as palm oil mill effluent (POME) final discharge is feasible since POME final discharge is a wastewater with a good supply of nutrients. POME final discharge consists of phosphorus and potassium which are vital element for plant. However, it is also contain metals that could be the inhibitor towards the growth of plant. Therefore, this study attempts to determine and evaluate the characteristic of Napier grass varieties, common and red cultivars supplied with POME final discharge in a constructed wetland system

[Experiment]
The 2 month old of Napier grass was transplant into the wetland system and they were watered with 5L of POME FD per day. The length of trees and the number of leaves were measured every week. The Napier grass was harvested from the system after 2 months treatment and were separated into its components, including stem and leaf. The Napier grass was pressed using a sugarcane pressing machine, and the dried pressed-biomass will be ground into 2.0 mm size using a hammer mill. The chemical composition of biomass was observed together with elemental composition, ash and moisture content. The structural composition was determined using acid hydrolysis.

[Result and Discussion]
There are increment of the height for both common and red cultivar of Napier grass which are 61.72% and 110%.

2 pages (A4 size) including figures.

Oral
Presentation session:
Presenter name: Muhammad Raznisyafiq bin Razak

Iminodiacetic acid modified kenaf fiber for waste water treatment

[Muhammad Raznisyafiq, Razak][1], [Nor Azah, Yusof][1,2], [Mohammad Jelas, Haron][1], [Norazowa, Ibrahim][1], [Faruq, Mohammad][3], [Sazlinda, Kamaruzaman][1], [Hamad A., Al-Lohedan][3],

[1]Department of Chemistry, Faculty of Science, Universiti Putra Malaysia, 43400 Serdang, Selangor, Malaysia
[2]Institute of Advanced Technology, Universiti Putra Malaysia, 43400, Serdang, Selangor, Malaysia
[3]Surfactant Research Chair, Department of Chemistry, College of Science, King Saud University, P.O. Box 2455, Riyadh 11451, Saudi Arabia

Email: raznisyafiq@upm.edu.my

Keywords (Surface modification, Modified kenaf fiber, Waste water treatment)

[Introduction]

In recent years, investigation into the application of chelating resins for environmental treatment purposes has become a significant area of research as it helps to provide suitable sorbent materials of low cost, environmental friendly and of suitable adsorption capacity for the trapping of toxic elements. Copper (Cu) and its ions is one of the pollutant which has considerable effects on the environment and natural water ecosystem due to its everyday usage in many consumables and industrial products. Elevated levels of Cu^{2+} can be responsible for the body disorders such as liver damage, Wilson's disease, insomnia, osteoporosis and leukaemia. Kenaf fiber are easy to find and are cheap lignocellulosic fibers which find advantages as biodegradable, renewable, economical, and of worldwide availability. These low dense materials allow for the attainment of high filling capacity by acting as sorbents and the materials can chemically be modified further for enhancing the metal binding ability by the introduction of new functional groups specific to a particular metal ion. Similarly, iminodiacetic acid (IDA) consists of both amino and carboxylic acid groups that are essential for increasing the adsorption capacity if grafted with any lignocellulosic fiber. Nowadays, the application for adsorption of heavy metals towards chelating resins IDA is not fully exploited as compared to the adsorption of organic pollutants. Thus, it is necessary to conduct further research regarding the adsorption behaviour and mechanism between heavy metal ions and IDA chelating functional groups.

[Experiment]

Preparation of kenaf modified iminodiacetic acid (K-IDA)

Kenaf fiber was supplied by the Institute of Tropical Forestry and Forest Products (INTROP),Universiti Putra Malaysia. The fiber was ground and sieved to obtain the desired particle size of <200 µm. In a 200 mL volumetric flask, 2.0 g of IDA and 2 mL of epichlorohydrin (BDH) were dissolved in 15 mL of distilled water which contained 2.0 g of sodium hydroxide (NaOH). The mixture was stirred for 4 h at 60 °C in an oil bath and following that, 4 g of NaOH was added with stirring until the contents get dissolved. Kenaf fiber (about 2 g) was then added and the reaction mixture was heated to 110 °C for 8 h in an oil bath; the product was filtered, washed with 0.5 M HCl followed by distilled water and air dried.

Characterization of adsorbent (unmodified kenaf fiber and K-IDA modified fiber)

The unambiguous structural information and properties of unmodified kenaf and K-IDA fiber were characterized by Fourier transform infrared spectroscopy (FTIR), CHNSO analysis, BET surface area analysis and scanning electron microscopy (SEM).

Metal adsorption of Cu2+ heavy metal solution

The adsorption measurements were carried out using inductive coupled plasma-atomic emission spectrometer (ICP-AES) model Perkin Elmer Optima 2000 DV instrument. The parameters used to optimised

the adsorbent is pH study, isotherm study, kinetic study, desorption study, reusability study and application to waste water sample analysis

[Result and Discussion]

A new kenaf chelating resin functionalized with IDA was synthesized and characterized to adsorb Cu2+ ions in waste water samples. Based on results, it was indicated that the maximum adsorption of IDA treated kenaf fiber of 91.74 mg/g, while only 54.95 mg/g for the untreated kenaf fiber was observed (at 0.1 g adsorbent dosage and pH 5). The Langmuir model fitted extremely well for the adsorption process with a correlation coefficient of 0.9934 by utilizing K-IDA as sorbent for the absorption of Cu2+ ions. From the kinetic studies, the pseudo second-order reaction kinetics were found to be the dominant mechanism. After the first desorption, the adsorbent was further desorbed to be reused in the study of carry-over effects. No improvements were detected in consecutive desorption studies, thereby indicating that the K-IDA has excellent reusability only for the first cycle. The applicability of K-IDA for removing Cu^{2+} ions was successfully tested by using the real waste water samples from electroplating and wood treatment waste industries are 96.5% and 78.2%, respectively. Based on the overall results therefore, we confirm that our functionalized chelating resin from kenaf fiber can serve as an alternative biodegradable sorbent and further study can be investigated in the treatment of waste water containing metal ions.

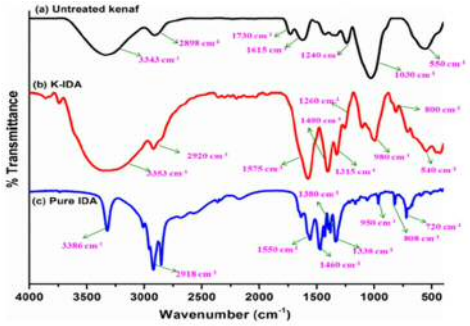

Figure 1

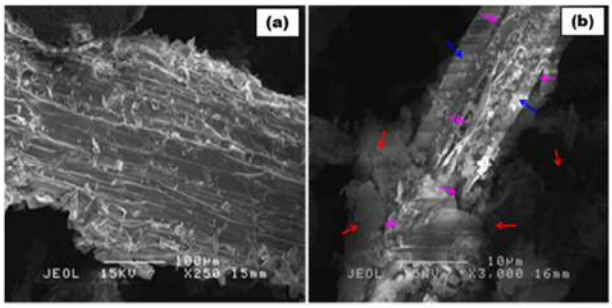

Figure 2

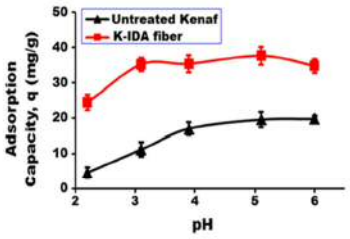

Figure 3

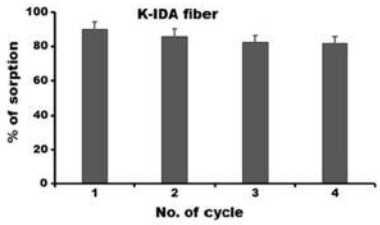

Figure 4

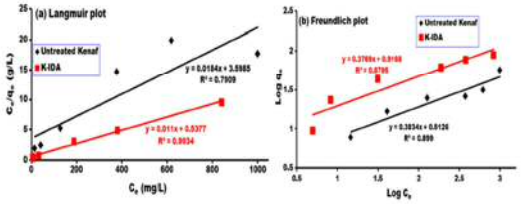

Figure 5

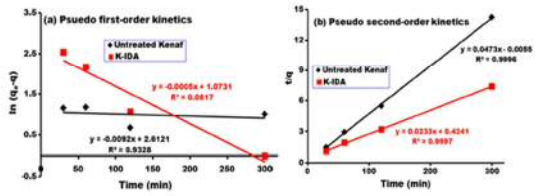

Figure 6

Figure 1: FTIR comparison of the spectrums of (a) untreated kenaf fiber, (b) K-IDA fiber, and (c) pure IDA.
Figure 2: Comparison of the SEM images of (a) untreated and (b) K-IDA fibers.
Figure 3: Comparison of the effect of pH
Figure 4: Reusibility studies towards K-IDA using 1–4 cycles
Figure 5: (a) Langmuir and (b) Freundlich, isotherm studies
Figure 6: (a) Pseudo first- and (b) pseudo second-order, kinetics studies

Please choose: Poster
Presentation session: Biological Science
Presenter name: Kazushige KONAI

Protein aggregation assay and computational analysis reveal the LEA peptide function and mechanisms

Kazushige. Konai[1], Nishit Pathak[1], Yuki Sakimura[1], Shinya Ikeno[1, 2]
[1]Graduate School of Life Science and Systems Engineering, Kyushu Institute of Technology
2-4 Hibikino, Wakamatsu-ku, Kitakyushu-shi, Fukuoka, 804-8550, Japan
[2]Reserach Center for Biomicrosensing Technology (RCBT), Kyushu Institute of Technology, Japan

Email: kounai.kazushige875@mail.kyutech.jp

Keywords: peptide, protein aggregation assay, DLS, simulations, PLS regression

[Introduction]

Late embryogenesis abundant (LEA) proteins is mainly accumulated in the late stages of embryo development in plant seeds and many plant species which has tolerance against drought, freezing, and salinity stresses. G3LEA proteins characterized by several tandem repeats of an 11-mer motif, although are so rich in polar residues. G3LEA proteins are very hydrophilic and disordered in aqueous solution, and they can develop predominantly α-helical structures when it's dried. We found that simple co-expression with the short peptide (LEA peptide) based on *Polypedilum vanderplanki* larvae G3LEA proteins repetitive units of 11-mer amino acids improves the target protein yield in *Escherichia coli* (*E.coli*). The expression of GFP with co-expression of LEA peptide was increased two times compared with control sample [1]. At the same time, measuring cell growth and mRNA amount, there is no effect by LEA peptide. It suggests that LEA peptide affects protein and enhance protein expression. In addition to that, the 6th and 12th residue of 13-mer motif has no homology, so we substituted the residues and redesigned new LEA peptide. As a result, LEA peptide whose 6th and 12th residue was replaced with K (LEAK) was most powerful in improving protein expression [2].

We hypothesized that the LEA peptide functions are same as G3LEA protein and acts as "molecular shield" to protect the target protein from lysozyme activity. In this study, *in vitro* role of LEA peptide against inhibition of protein aggregation have been investigated through Dynamic Light Scattering (DLS) measurement. Then, we focus on the LEA peptide *in vivo* mechanism and effect on the target protein with support by cheminformatics calculation.

[Experiment]

1. Aggregation assay using DLS

Green Fluorescent Protein (GFP) was expressed in *E. coli* BL21(DE3) cells and purified using His-tag affinity column and desalting column. GFP was determined by SDS-PAGE and GFP concentration was estimated using BCA protein assay kit. Bovine serum albumin (BSA) was purchased from FUJIFILM Wako Pure Chemical Corporation. LEA peptide (MDAKDGLKEKAGE) was synthesized by GenScript. Protein (GFP or BSA) and LEA peptide was mixed and incubated in 25 ^{o}C for 1 hour. Ammonium sulfate solution was applied in the mixture to process protein aggregation. DLS was performed in 25 ^{o}C a laser wavelength of 532 nm and scattering angle of 163.5. Repeating the addition of salt solution and DLS measurement, protein aggregation by increasing salt concentration was evaluated.

2. Docking simulation

Molecular calculations was performed using the software, Molecular Operation Environment (MOE). GFP molecule data, PDB code: 3EMK was downloaded in Protein Data Bank (PDB). LEA peptide was constructed and α-helix structure and applied energy minimization. Docking simulations was performed like candidate site is whole GFP surface and ligand is the energy minimized LEA peptide. Force field was Amber10: EHT.

3. PLS regression

We have performed GFP expression with various mutated LEA peptide co-expression. 54 descriptors of each 52 mutated helical LEA peptide was calculated by Amber10: EHT force field. Using expression data and descriptors, liner model was constructed by PLS regression method. Cross-validation, excluding the worst descriptor and reconstruction liner model was repeated to search the better liner model.

[Result and Discussion]

1. Aggregation assay using DLS

In each DLS measurement, dispersed protein was observed in nm order diameter (Fig.1). Protein aggregation was evaluated by dispersed protein abundance (%Mass) based on particle size distribution by DLS. Although both GFP and BSA %Mass was decreased by increasing salt concentration, the sample LEA peptide added did not aggregate in high salinity compared with control sample. These results indicate that LEA peptide prevents proteins from aggregation.

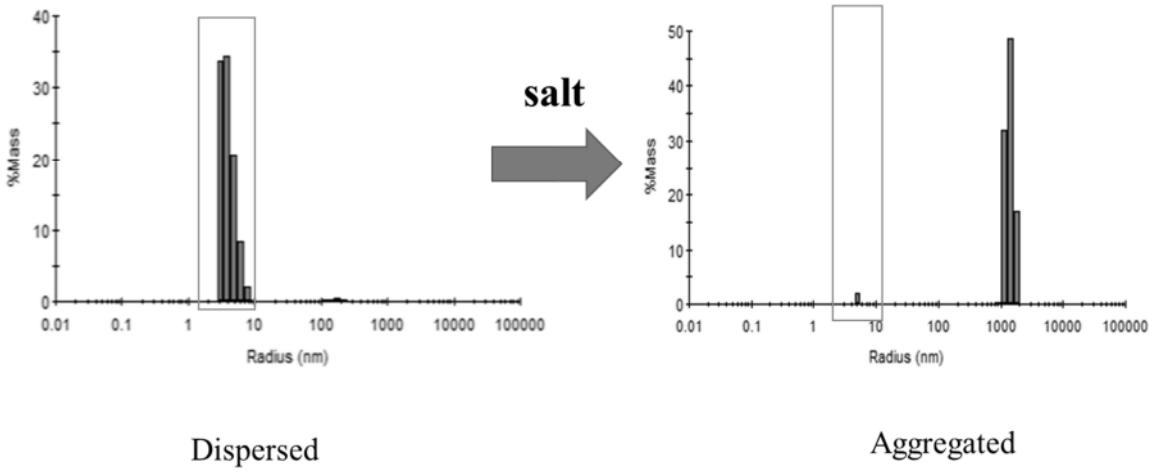

Fig. 1 Particle size distribution of protein in increasing salt concentration by DLS

2. Docking simulation

Top 30 GFP and LEA peptide interaction conformation was outputted by molecular simulation. The conformation was visualized by Protein–Ligand Interaction Fingerprints (PLIF) and it was revealed that the 30 conformations can be classified two types in rough and LEA peptide interact with two hydrophilic surface on GFP. This result insists that LEA peptide interact with GFP by hydrophilic or charged interactions.

3. PLS regression

Finally, the linear model equation with "adjusted R-square" of 65% was obtained. This liner model is constructed with 31 descriptors and coefficient of vsurf_A (amphiphilic moment) is the largest. Coefficient of vsurf_A is about ten times as large as dipole moment. This result insist that vsurf_A is so important than dipole moment for activity of LEA peptide. The result will not contradict the hypothesis that helical LEA peptide is amphiphilic and interact hydrophobically with proteins like a surfactants.

[References]

[1] Shinya Ikeno, Tetsuya Haruyama, "Boost Protein Expression through Co-Expression of LEA-Like Peptide in *Escherichia coli*" PLOS ONE, vol.8 (12), 2013

[2] Nishit Pathak, Hiro Hamada, Shinya Ikeno, "Construction and characterization of mutated LEA peptides in *Escherichia coli* to develop an efficient protein expression system" Journal of Molecular Recognition, vol.31 (1), 2018

Please choose: Oral
Presentation session: Biological Sciences
Presenter name: MOHD ZULKHAIRI MOHD YUSOFF

Towards waste reduction via utilisation of domestic waste for the green energy generation

Ahmad Aiman, ZULKIFLI[1], Mohd Zulkhairi, MOHD YUSOFF[1,2*], Yoshihito, SHIRAI'[3], Mohd Ali, HASSAN[1]

[1]Department of Bioprocess Technology, Faculty of Biotechnology and Biomolecular Sciences, Universiti Putra Malaysia, 43400 UPM Serdang, Selangor, Malaysia
[2]Laboratory of Biopolymer and Derivatives, Institute of Tropical Forestry and Forest Products (INTROP), Universiti Putra Malaysia, 43400 UPM Serdang, Selangor, Malaysia
[3]Department of Biological Functions Engineering, Graduate School of Life Science and Systems Engineering, Kyushu Institute of Technology, 2-4 Hibikino, Wakamatsu, Kitakyushu 808-0196, Japan

Email: mzulkhairi@upm.edu.my

Keywords: Anaerobic digestion; biogas; fermentation; municipal solid waste; renewable energy

Introduction

Municipal solid waste (MSW) is solid, other than emission or effluent, and is regarded as inevitable, valueless by-product due to human activities, and is generated at a rate and discarded after use when no longer needed by the generator. Waste consists of materials that are no longer considered valuable and subsequently disposed off. In Malaysia, urban waste generation increased 3 % annually due to urban migration, affluence and rapid development. In 2008, approximately 31,000 tonnes of waste were disposed into 260 landfills in Malaysia. MSW problems have been gaining prominence in Malaysia due to the ever-increasing waste generation and the ineffectiveness of the existing mechanism to tackle the problem holistically. Early management of solid waste involved very little effort since waste was generated at a manageable level and generally consists of organic materials such as food waste, paper, wood and others. This began to change with the increase in the human population and advancement in living standards. The quantity of waste generated increased together with the complexity of waste where plastic and other mixed waste became a significant portion of the waste stream. This called for an appropriate waste management system to avoid the proliferation of disease and the deterioration of environmental quality through pollution.

The problem of MSW disposal is likely to become more acute with the land available for landfills becoming scarce. In addition, landfill sites must be environmentally and socially acceptable so as to avoid any untoward problems and must be sufficiently buffered from human settlements to prevent odour, health risks and groundwater contamination. Thus, the aim of this study is to evaluate the current generation, composition, and disposal of solid waste in selected cities in Malaysia and to evaluate the feasibility of domestic waste generated towards the generation of green energy production.

Materials and methods

Survey question

A survey form consisted of questions related to operations such as type, capacity, methods of pretreatment, cost of operation, the frequency of collection, separation and utilization we drafted.

Field visits and interviews

Field visits were done at the restaurant, institutes, offices and personnel. An interview was conducted to obtain the information on the process, about complaints from the public and other issues in the MSW management

Characterization, generation and composition of municipal solid waste.

A sample of MSW from a few restaurants and institutes was collected and characterized based on the standard method

Biogas generation from organic matters via anaerobic digestion application

A feasibility study was performed for biogas generation from the waste obtained. The amount and the biogas quality was measured to estimate the potential used for electricity generation

Result and Discussion

The survey was done on the selected group that may contribute to the waste generation. In general, the Malaysia household waste generation is about 18,000 metric tonnes per day with the population 22 million in 2012. Waste generation is about 0.8 kg/capita/day. On average, the waste generation at urban (0.83 kg/capita/day) and rural (0.73 kg/capita/day), respectively (Fig .1)

From an interview survey from two municipalities in Kuala Lumpur and Putrajaya indicate the different composition of food waste was obtained. In Putrajaya for instance, the highest component in MSW is plastic followed by paper. Meanwhile, from one of the municipalities in Kuala Lumpur shows the highest component is food waste followed by comingle waste.

A survey from the restaurant shows about 80% are organic materials and the moisture is about 50-70%. The chemical oxygen demand of the organic is in the range of 200– 600 g/L. Theoretically, one kg of COD may generate 0.35 m^3 methane. Thus the organic available in the kitchen waste would be a good potential for the biogas generation using anaerobic digestion approach.

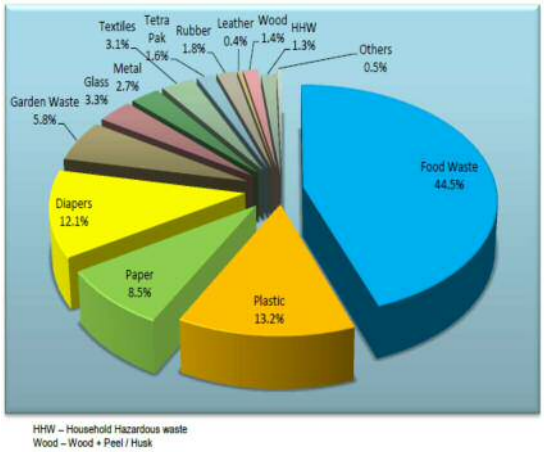

Fig. 1. Municipal solid waste composition in Malaysia

Table 1: Physical characterisation of kitchen waste.

Parameter	Average	Range percentage
Moisture Content	66.8%	50% – 70%
COD	348 g/L	200– 600 g/L

Please choose: Oral/ Poster
Presentation session:
Presenter name: **Nor Farhana Aziz Ujang**

Treatment of POME Final Discharge Using Napier Grass in Wetland System

Farhana, Aziz Ujang[1], Nurul Atiqah, Osman[1], Juferi Idris[4], Mohd Izuan Effendi, Halmi[3], Mohd Ali, Hassan[1] and Ahmad Muhaimin, Roslan [1,2]*

[1]Department of Bioprocess Technology, Faculty of Biotechnology and Biomolecular Sciences, Universiti Putra Malaysia, 43400 Serdang, Selangor, Malaysia
[2]Laboratory of Biopolymer and Derivatives, Institute of Tropical Forestry and Forest Products (INTROP), Universiti Putra Malaysia, 43400, Serdang, Selangor, Malaysia
[3]Department of Soil Management, Faculty of Agriculture, Universiti Putra Malaysia, 43400 Serdang, Selangor, Malaysia
[4]Faculty of Chemical Engineering, Universiti Teknologi MARA (UiTM), 94300, Kota Samarahan, Sarawak, Malaysia

Email: ar_muhaimin@upm.edu.my

Abstract.
POME is the most expensive and difficult waste to manage since it was generated in large volume in tons at a time. POME usually will discharge to nearby land or river since it is the easiest and cheapest method to disposal. Since the POME final discharge quality still not meets the river water quality, the approach that will use is the wetland system. This wetland system is more compatible compare to another system to treat the POME final discharge since it is more cost efficient and fewer side effects compared to the biological and chemical approach. The phytoremediation concepts were used. Phytoremediation is a process that uses plants to degrade and remove contaminants from the environment. Phytoremediation can degrade, remove, transform, or immobilize toxic compounds located in soils, sediments, and more recently in polluted ground water and wastewater in treatment. The plant that been use in this system is the Napier Grass. At the end of the experiment, this system shows good quality water by reducing the level of COD by 71.57%, TSS by 83.59% and ammonia by 85.97%. From this research, it has been prove that the wetland system can reduce the contamination from the final discharge to meet the river water quality.

Keywords (maximum 5 words)
Final discharge, wetland, phytoremediation, Napier grass.

[Introduction]
POME is the most expensive and difficult waste to manage since it was generated in large volume in tons at a time. POME usually will discharge to nearby land or river since it is the easiest and cheapest method to disposal. Since the POME final discharge quality still not meets the river water quality, the approach that will use is the wetland system. This wetland system is more compatible compare to another system to treat the POME final discharge since it is more cost efficient and fewer side effects compared to the biological and chemical approach

[Experiment]
The phytoremediation concepts were used. Phytoremediation is a process that uses plants to degrade and remove contaminants from the environment. Phytoremediation can degrade, remove, transform, or immobilize toxic compounds located in soils, sediments, and more recently in polluted ground water and wastewater in treatment.

[Results and Discussion]
The plant that been use in this system is the Napier Grass. At the end of the experiment, this system shows good quality water by reducing the level of COD by 71.57%, TSS by 83.59% and ammonia by 85.97%. From

this research, it has been prove that the wetland system can reduce the contamination from the final discharge to meet the river water quality.

Maximum 2 pages (A4 size) including figures/tables

Please choose: Poster
Presentation session: Biotechnology
Presenter name: Ayaka IMABAYASHI

Deletion of *Escherichia coli* Hydrogenase 2 Operon Impairs Glycolytic Pathway

Ayaka IMABAYASHI, Chandra SHEKHAR, Toshinari MAEDA

Graduate School of Life Science and Systems Engineering, Kyushu Institute of Technology, 2-4 Hibikino, Wakamatsu-ku, Kitakyushu, Fukuoka,808-0196, Japan

Email: imabayashi.ayaka927@mail.kyutech.jp

Keywords
hydrogen, fermentation, *Escherichia coli*, hydrogenase, glycolysis

[Introduction]

Hydrogenase is an enzyme capable of catalyzing the reaction $H_2 \rightleftarrows 2H^+ + 2e^-$. As shown fig. 1-(a), *Escherichia coli* has 4 types of hydrogenases which are hydrogenase 1 (Hyd-1), hydrogenase 2 (Hyd-2), hydrogenase 3 (Hyd-3), and hydrogenase 4 (Hyd-4). Hyd-1 (encoded by *hyaA-F*) and Hyd-2 (encoded by *hybO-G*) mainly consume hydrogen while Hyd-3 (encoded by *hycA-I*) involves to synthesize hydrogen. In *E.coli*, FHL (Formate Hydrogen Lyase) complex which consists of formate dehydrogenase (encoded by *fdhF*) and Hyd-3 produces 2 mol hydrogen from 1 mol glucose theoretically. Under a fermentative condition, glucose is converted into pyruvate; then pyruvate is converted into formate, lactate, and acetate. After that, formate is converted to hydrogen and carbon dioxide by the FHL complex.

Despite there are a lot of reports about the function of *E. coli* hydrogenases, functions of 4 hydrogenases are still unclear because the explanations regarding the function of *E. coli* hydrogenases are different among the researchers. Basically, a general approach to analyze each gene function is to use a mutant defective in a single gene; therefore, the gene function can be determined by comparing a target phenotype between the parent strain and the mutant. In case of *E. coli* hydrogenases, Hyd-1 and Hyd-2 or Hyd-3 and Hyd-4 are reported to have a high similarity in the protein sequences. Therefore, we hypothesize that the contrary opinion may be due to a full or a partial complementation by a homologous hydrogenase subunit for a lack of hydrogenase subunit (for example, the lack of HycE, the large subunit of Hyd-3 may be restored by HyfG, the large subunit of Hyd-4). Hence, the motivation of this study is to construct a mutant in which the operon rather than a single gene in each hydrogenase can be deleted and to analyze the phenotype regarding the function of hydrogenases by evaluating hydrogen metabolism.

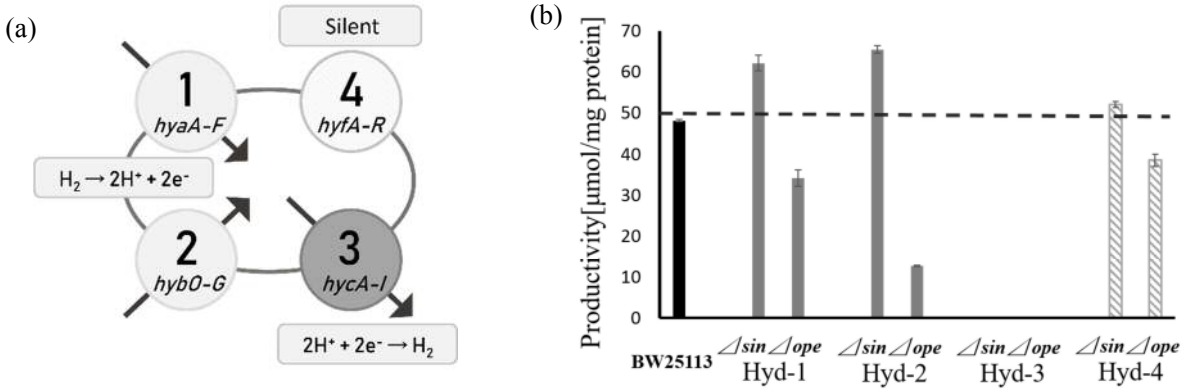

Fig.1 – (a) Roles of 4 hydrogenases reported in case of glucose as a substrate. (b) Hydrogen productivity at 24 h in each hydrogenase mutant when glucose was used as a substrate.

[Experiment]

1. Bacterial strains

4 single mutants (defective in the large subunit of each hydrogenase) and 4 operon mutants (the operon in each hydrogenase was deleted through homologous recombination) were used in this study. For example, Δ*2 single* indicates the deletion mutant of Δ*hybC* and Δ2*operon* indicates the deletion of Δ*hybO-G* which is the operon of Hyd-2. These strains were initially streaked LB medium with or without kanamycin (100 μg/mL) and incubated overnight at 37ºC aerobically. Then, 1 colony was transferred to fresh LB medium and cultivated in an aerobic condition at 37ºC with 120 rpm for 13 hours. The cultures were used for the following hydrogen fermentation.

2. Hydrogen fermentation

The cell turbidity of each *E. coli* overnight culture was adjusted to OD_{600} 0.05 with fresh LB medium supplemented with 2.25% glucose as well as pyruvate or formate (20 mM) and the mixtures (10 mL) were transferred to a vial (65 mL). After that, the vials were sealed with rubber stoppers and aluminum foil caps. Then, the vials are sparged for 5 min with nitrogen to remove oxygen, and anaerobically incubated at 37°C with 120 rpm.

3. Analysis

After 4 h and 24 h, gases produced in samples were measured by using a gas chromatography and cell turbidity was measured using a spectrophotometer. After the experiment, the cultures in vials were centrifuged at 12,000rpm for 1 min and each supernatant was taken to a new micro tube. Then, using the supernatant, pH and glucose concentration were measured by using a pH meter and a GOD method. The total protein was calculated by the following formula: 0.22 mg OD^{-1} mL^{-1}.

[Result and Discussion]

1. Hydrogen productivity using each single or operon mutant of *E. coli* hydrogenases

Fig. 1-(b) indicates hydrogen productivity at 24 h in each hydrogenase mutant when glucose was used as a substrate. Compared to the parent strain, BW25113, two single mutants of Hyd-1 and Hyd-2 increased hydrogen production whereas two operon mutants of Hyd-1 and Hyd-2 reduced hydrogen production. On the other hand, Hyd-3 mutants (single and operon) did not produce hydrogen gas, indicating that the Hyd-3 is the main hydrogenase responsible for the production of hydrogen gas as reported. In particular, inability of Hyd-2 operon mutant to produce hydrogen was due to the low growth (less than 0.5) while OD of Δ*2 single* was around 3.0 although there was no significant difference between these strains in an aerobic condition.

2. pH and glucose consumption in *Δ2operon*

In general, pH decreases through the anaerobic fermentation because *E. coli* consumes glucose and produces organic acid. Interestingly, pH of *Δ2operon* mutant showed more than pH 6.8 in aerobic and anaerobic conditions unlike Δ*2 single* mutant made acidic pH after the fermentation. Therefore, we hypothesized that Δ2*operon* may be not able to consume glucose. To investigate the hypothesis, glucose consumption in Δ2*operon* was evaluated during the fermentation. As a result, *Δ2operon* did not consume glucose during the fermentation; *Δ2operon* was not able to produce hydrogen gas due to the inability of glucose consumption. It was assumed that Δ2*operon* cannot acquire energy from glucose for the growth and for the production of organic acids. On the other hand, an interesting point of this study is that this phenomenon was observed in the *Δ2 single* mutant. This result was similar with our previous result that Hyd-2 mutant impairs glycerol metabolism by which low hydrogen production was observed. Therefore, Hyd-2 may be related to not only glycerol metabolism but also glucose metabolism. In the future, we may need to test all the single mutants of Hyd-2 (*hybO* to *hybG*) to verify what the subunit will be related to the glucose metabolism.

3. Hydrogen production from pyruvate and formate using *Δ2operon*

Two intermediates (pyruvate and formate) of glycolytic pathway were used as substrates to verify which pathways of glucose may be defective in *Δ2operon* mutant. In an experiment using formate, it was confirmed that *Δ2operon* mutant can produce hydrogen at a rate of 67 ± 8 μmol hydrogen mg $protein^{-1}$ after 24 h. In addition, an experiment using pyruvate also indicated 25 ± 2 μmol hydrogen mg $protein^{-1}$ after 24 h compared to 13 ± 0.2 μmol hydrogen mg $protein^{-1}$ at 24 h in case of glucose. Furthermore, interestingly, the growth of *Δ2operon* mutant was not inhibited in the presence of pyruvate or formate, indicating that an initial step of glycolytic pathway may be a rate-limiting reaction for the glucose consumption in *Δ2operon* mutant. Therefore, glucose uptake and initial steps of glycolysis can be targets to figure out the mechanism why *Δ2operon* mutant cannot produce hydrogen and cannot grow under an aerobic condition. In addition, a complementation study (to see if the current defective of glucose metabolism in Hyd-2 can be restored by providing a plasmid in which Hyd-2 genes are cloned) can be also required as the remaining study to complete the study.

4. Conclusion

In this study, the effect of deleting each operon of *E. coli* hydrogenases was investigated. In conclusion, as main results, Hyd-3 is a sole hydrogenase related to the production of hydrogen gas in *E. coli* and Hyd-2 may be a key hydrogenase essential to not only glycerol metabolism but also glucose metabolism. The detail function of Hyd-2 is still unknown; however, we assume that ATP synthesis or/and NADH production may be controlled by Hyd-2.

Please choose: ~~Oral~~/ Poster
Presentation session:
Presenter name: Lim Kah Yen (Kelly)

6th International Symposium on Applied Engineering and Sciences (SAES2018)
Kyushu Institute of Technology, 15th – 16th Dec 2018

Development of lignin-phenol-formaldehyde (LPF) adhesive by using black liquor from empty fruit bunches (EFB) pulp-making process

Lim Kah Yen[1,2], Hidayah binti Ariffin[3,4], Paridah binti Md Tahir[4,5], Chen Jun Zhi[6], Mohd Termizi bin Yusof[2*]

[1]*R&D Department, Nextgreen Pulp & Paper S.B., TTDI, 60000 K.L, Malaysia.*
[2]*Dep.of Microbiology, Faculty of Biotechnology and Biomolecular Sci., Universiti Putra Malaysia, 43400 UPM Serdang, Selangor D. E., Malaysia.*
[3]*Dep. of Bioprocess Technology, Faculty of Biotechnology and Biomolecular Sciences, UPM, 43400 UPM Serdang, Selangor D. E., Malaysia.*
[4]*Institute of Tropical Forestry and Forest Products (INTROP), UPM, 43400 UPM Serdang, Selangor D. E., Malaysia*
[5]*Dep. of Forest Production, Faculty of Forestry, UPM, 43400 UPM Serdang, Selangor D.E., Malaysia.*
[6]*Dep. of Chemical Engineering, Shaanxi University Of Science & Technology, Wei Yang District, 710021 Xi'an , Shaanxi Province, China.*

**Corresponding author: mohdtermizi@upm.edu.my*

Abstract

Lignin is a natural phenolic polymer which can be used as a substitute for phenol in phenolic adhesive production. Large quantity of lignin was produced in black liquor which is a by-product in pulp and paper industry. Pulp and paper-making using palm oil empty fruit bunches (EFB) as raw materials have started in Malaysia. To achieve 'zero-waste' in this industry, the components in black liquor, specifically lignin was exploited for its potential application. The objective of this study is to produce lignin-phenol-formaldehyde (LPF) adhesive by substituting phenol with lignin from black liquor in EFB pulping process. We hypothesised that it is possible to produce LPF adhesive by modifying the properties of lignin to enhance its chemical reactivity in the production of LPF adhesive. Different acids were tested to modify the properties of lignin for the substitution of phenol. Comparison between reference phenol-formaldehyde (PF) adhesive and LPF adhesives with various concentration of lignin based on LPF formulation will be made. The performance of each LPF adhesive was tested to identify the best methodology for the production of LPF adhesive. By utilising lignin, adhesive could be produced with smaller amount of phenol and formaldehyde which has been proven to be carcinogenic to human.

KEYWORDS: Empty fruit bunches (EFB), lignin-phenol-formaldehyde (LPF), pulp and paper, black liquor, industrial adhesives

Introduction

Black liquor is produced as a complex liquid by-product of the kraft pulping process, containing lignin residues, degraded carbohydrates and inorganic constituent (Annie Ng, 2008). The exact composition of black liquor components varies according to the pulping method and the properties of the raw material used (Humpert et al, 2016). In this study, lignin from black liquor was exploited for its potential application as a substitute for phenol in phenolic adhesive production, by establishing the production procedure for lignin-phenol-formaldehyde (LPF) resins and the ratio of phenol substitution with lignin.

Experiments

1. Preparation of Black Liquor from EFB

One kg of shredded EFB fiber was weighed and cut into 20-40 mm. Solvent (96% NaOH and 98% Na_2S) was mixed with fibers, soaked for 3 mins and then processed in a rotating digester for 20 mins [temperature: from room temperature to 168°C for 2.5 hr; pressure: 0.75 mPa]. Then pulp was screened through a 60-mesh sieve and the black liquor was collected. Concentrated lignin is collected by boiling black liquor to the concentration of 25- 30 Bé° in a flask.

2. Preparation of Adhesive &Plywoods

The substitution rates of lignin in this study were 50% and 40%, termed as A & B, respectively. The molar ratio of phenol (combination of lignin and phenol) to formaldehyde was kept constant at 1:2. Phenol and concentrated black liquor was mixed in a three-neck round bottom flask and heated at 50ºC. The pH of reaction mixture was adjusted to pH 10 for A; pH 11 for B and heated for 30 mins at 60ºC. 80% of the formaldehyde was then added. The temperature for A and B was increased to 87ºC and 80ºC, respectively within 1.5 hour. The remaining 20% of formaldehyde was added into the mixture and temperature was increased to 94ºC for A and 85 ºC for B within 30 minutes. Lastly, the temperature of mixture A was decreased to 82 ºC, 20% HCL and urea (7% of the total weight of the phenol and lignin) and calcium silicate powder (not added to B) were added to A for 30 mins, whereas mixture B was left as it is. Both reaction mixture A and B were cooled down to 40ºC to obtain LPF. Plywoods (50 mm × 50 mm × 10 mm) were prepared using the LPF adhesives. It were hot-pressed at 135 °C under 1.2 MPa for 5.0 min.

Results & Discussion

The resin obtained from Experiment A has poor adhesion. It is not even strong enough to hold the plywood. Methods used in Experiment A need to be revised. There are obvious differences from the physical observation between these two resins. The bonding strength of the LPF resin obtained from Experiment B has better adhesions; its bonding strength obtained is 0.35 MPa. However, the bonding strength does not meet the requirement of the first grade of plywood (⩾0.7 MPa) (Yang et al, 2015). The results of this study generally showed that lignin obtained from EFB can be used to prepare LPF resin adhesives for plywood adhesives in which 40% of phenol substitution by EFB lignin in Experiment B. However, there are other factors that influenced the results, such as cooking time (Ghorbani et al, 2018), curing temperature (Adhikari et al, 2016), pH and concentration of black liquor. Higher molecular weight of lignin tends to have quicker viscosity development (Ghorbani et al, 2018). Study showed that alkaline pulping results in low molecular lignin; this needs to be evaluated in the further study as it is one of the factors that affects the LPF resin network. This might be the greatest problem as the low reactivity of lignin due to its complicated molecular structure (Hemmila et al, 2013). The results presented are limited, but they give some indication of which bigger scale experiments should be conducted. Troubleshooting has been carried out to develop a procedure for the synthesis of LPF adhesives and to identify the possible influential factors in the study. Final product should have the final formula of LPF with specific process instruction and adjustment till reproducible adhesives with comparable bonding strength is achieved. The experiments carried out in this study showed that it is possible to achieve the objective of phenol substitution with EFB lignin to manufacture LPF resin adhesive for plywood lamination.

Please choose: Poster
Presentation session:
Presenter name: NOR AKHLISAH ZULKIPLI

[THERMAL STUDIES OF DIFFERENT PRETREATMENTS ON OIL PALM MESOCARP FIBER]

[Nor Akhlisah, Zulkipli][1], [Robiah, Yunus][1,2], [Zurina Zainal, Abidin][1], [Bo Yuan, Lim][2]

[1]Faculty of Engineering, University Putra Malaysia, 43400 UPM Serdang, Selangor, Malaysia
[2]Institute of Advanced Technology, University Putra Malaysia, 43400 UPM Serdang, Selangor, Malaysia

Email address: [akhlisahsolehah92@gmail.com]

Keywords (5 words)
Oil Palm Mesocarp Fibre, Thermogravimetric Analysis, Activation Energy, Pretreatments, Hydrolysis

[Introduction]

The purpose of thermogravimetric analysis (TGA) is to find out kinetic of oxidation and pyrolysis or thermal events of the solid biomass. This analysis can determine the measurement of weight loss of the biomass as a function of temperature and time. Basically, the kinetic of thermal behavior can be evaluated by the application of the Arrhenius equation which presented by the slopes of constant mass degradation in each thermal event with different frequency factor, activation energy, and reaction order. Thermal evaluation method developed by Broido (Broido et al., 1969) shows that TG curves provides the information to find out thermodynamic or kinetic paramters. The weight at any time is linked in proportionality with the fraction of initial biomass weight for this method. The parameters such as enthalpy, activation energy, free energy changes and entropy can be determined using this method. This paper only focus on one parameter which activation energy. The activation energy presents an excellect understanding of the thermal decomposition of biomass.

[Experiment]

Two different pretreatments, acid pretreatment and ultrasonic-assisted acid pretreatment were done followed by acid hydrolysis on oil palm mesocarp fibre (OPMF). For acid pretreatment, the parameter involved was temperature (60 □C, 80 □C and 100 □C) while the effect of sonication powers (40%, 60% and 80%) was investigated for ultrasonic-assisted acid pretreatment. The effect of pretreatments was evaluated based on the product generated during acid hydrolysis. After acid hydrolysis, activation energy (E_a) for a major stage of decomposition were determined by Broido's method (Broido *et al.,* 1969) using Eq. (3.8).

$$\ln(\ln\left(\frac{1}{y}\right)) = -\frac{Ea}{RT} + Constant \qquad (2.1)$$

Where, y refers to the normalized weight (w_t/w_i), w_t is the weight of the sample at any time t, w_i is the initial weight of the sample, T indicate the temperature in Kelvin and R refer to the gas constant (8.32 J/mol K). A plot of $\ln(\ln(1/y))$ against 1/T gives a straight line, the slope of which gives E_a. Although by using multiple heating rate methods, the kinetic parameters are better estimated, single heating rate methods are being used in several studies.

[Result and Discussion]

Senthamaraikannan and Kathiresan (2018) reported that the minimum energy needed to initiate degradation of fibre is called as activation energy (E_a). Activation energy can be calculated from the slope of the appropriate linear plot based on Figure 4.13 and 4.14 by using Broido equation.

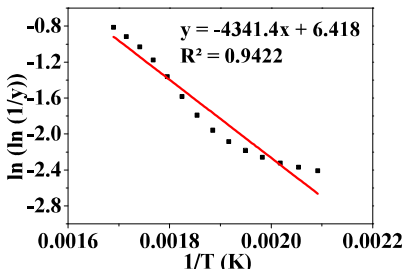

Figure 4.13. Broido's plot of raw OPMF

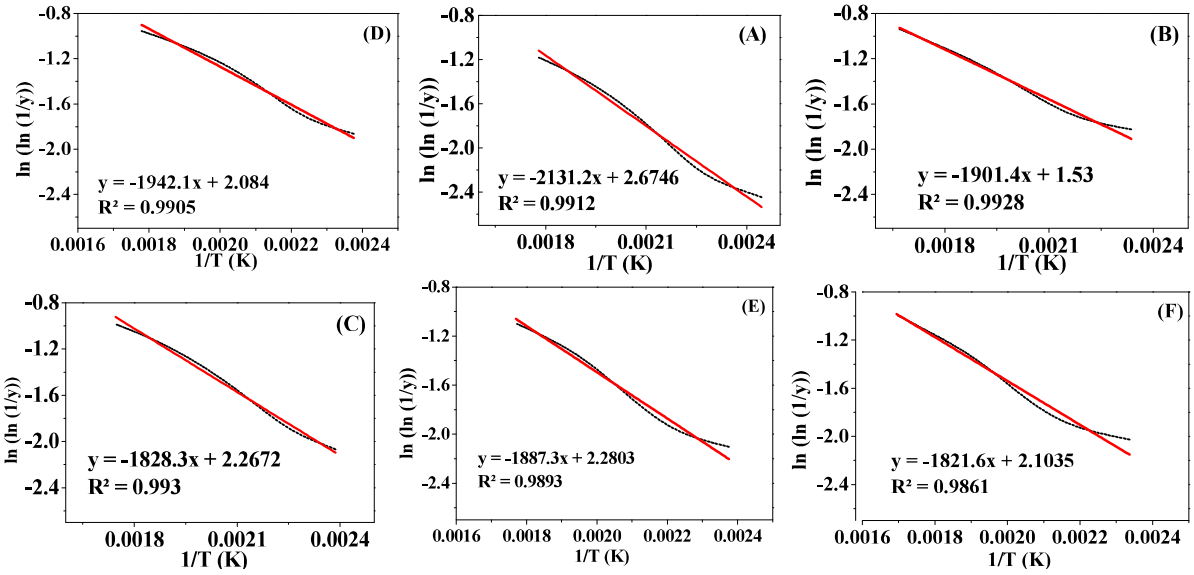

Figure 4.14. Broido's plot of direct-hydrolysed samples which pretreated by ultrasonic-assisted acid pretreatment. (A) 40%, (B) 60%, (C) 80% power and acid pretreatment (D) 60 □C (E) 80 □C (F) 100 □C.

As reported from Manimaran *et al.* (2018), normally the kinetic activation energy of plant fibres situated between 60-170 kJ/mol. However, the activation energy for OPMF from this study is low (35.76 kJ/mol) and this value is comparable with activation energy for combustion of OPMF from research by Asadieraghi and Wan Daud (2014) which was about 26.11 to 52.66 KJ/mol. Lower activation energy was observed at the pretreated samples compared to raw materials. This trend is similar to a study by Shinoj *et al.*, (2011) which found that chemical pretreatment on oil palm fibre resulted in lower activation energy. This is due to the lower energy needed to degrade lignocellulosic materials such as cellulose and hemicellulose at this decomposition stage and proved that pretreatment favoured the conversion of these materials.

Jamaludin *et al.* (2017) found that the condition of polysaccharides decomposition in biomass can influence the activation energy. The material in biomass which decomposed in this range of temperature is hemicellulose. Xylose is a product from hemicellulose while furfural is product of degradation of xylose. The highest activation energy was obtained from sample A (17.73 kJ/mol) which was pretreated by ultrasonic-assisted acid pretreatment at 40% power.

[Conclusion]

The results from different pretreatment methods accorded with each other, and were related through some kinetic parameters in thermal studies. Lower activation energy was observed at the pretreated samples compared to raw materials. The activation energy for OPMF from this study is low (35.76 kJ/mol). Ultrasonic-assisted acid pretreatment produced highest value of activation energy (17.73 kJ/mol) which obtained from the pretreatment condition at 40% power.

Please choose: Poster
Presentation session: Material Science and Technology
Presenter name: Yasufumi Morita

Distribution analysis of inorganic elements in the internal tissues of bamboo

Yasufumi Morita[1], Haruo Nishida[2]

Kyushu Institute of Technology, 2-4 Hibikino, Wakamatsu-ku, Kitakyushu-shi, Fukuoka-ken, 808-0135, Japan

Email: morita.yasufumi934@mail.kyutech.jp

Keywords (5 words): bamboo, internal tissues, inorganic elements, distribution behavior, analysis

[Introduction]

Bamboo is an abundant biomass available in Japan, and a homogeneous biomass resource. The abundance of bamboo is estimated to exceed 27 million ton in Japan and it grows rapidly to reach as high as 20 m in about 3 months. Even if all the culms were cut down, the bamboo forest will regenerate after 3 to 5 years. Thus, bamboo is the most promising renewable resource among woody materials in Japan. One of utilizations of bamboo is the renewable energy source for power generation. Although the usage as energy source has been examined many times, all the attempts have failed, because there are two problems when used as the energy source. Firstly, during the combustion, bamboo ash melts at low temperatures to form clinker due to the high concentration of potassium (K). Secondly, the containing chlorine (Cl) generates corrosive combustion gases and dioxins in incinerated bamboo ash. In recent years, a new technology to easily extract K and Cl in bamboo tissues has been developed, and a demonstration test also has been carried out. However, it is not yet clear where K and Cl are present in bamboo tissues, and how these are extracted easily. The purpose of this research is to clarify where K and Cl are present in bamboo tissues, and the extraction routes.

[Experiment]

Material

Phyllostachys heterocycla f. pubescens (Moso bamboo) sample was collected at Yame city in Japan.

Method

The bamboo culm was crosscut with 5 cm in length including a node. Each sample was dried in an oven at 80 °C for 26 h. Solutions of KCl and KI were prepared in beakers. The dried bamboo sample divided vertically by 1 cm in width. The sample were soaked its bottom side by 1.5 cm in the KCl solution, keeping the vertical direction of the original culm at room temperature (25 - 30 °C) for 22 h. The impregnation of the KI solutions into the dried bamboo tissues were achieved due to the capillary phenomenon or by suction (0.085 MPa). After impregnation, the sample were taken out and freeze-dried.

In order to observe cross section, the sample was cleaved, and the fracture section was analyzed by a field emission type scanning electron microscope - energy dispersive X-ray analyzer (SEM-EDS) JCM 6000 (JEOL) at an acceleration voltage of 15 kV after vapor deposition of Au.

Fibrovascular bundle structure of bamboo was observed on an X-ray computed tomography device (X-CT[1]) (Xradia 410 Versa, Zeiss, Oberkochen, Germany) at 20 kV with a tube current of 200 μA, and the scan time of sample was 10 s, repeating 1600 times exposure. Obtained X-CT images were then reconstructed using VGStudio MAX 2.2 (Volume Graphics GmbH, Heidelberg, Germany) to observe a cross-sectional image.

[Result and Discussion]

SEM-EDS analysis – Culm

In order to analyze the dynamics of KCl impregnation, SEM-EDS analysis was carried out. Typical tissue structures of bamboo culm were analyzed to explore the accumulation area of K and Cl. As an example, The SEM images and EDS analysis results of the medullary cavity surface after KCl impregnation are shown in Figure 1. In the EDS spectrum, two main peaks at 3.312 (K Kα) and 2.621 (Cl Kα) keV are derived from impregnated K and Cl. As expected, K and Cl were stored at the same area, suggesting the accumulation in

the salt form of KCl. From EDS results of all areas observed of bamboo culm tissues, the accumulation of KCl was in the following order:

medullary cavity surface > parenchyma cells > fibrovascular bundle

Interestingly, this result suggests that K and Cl are distributed to the parenchyma cells from pores of conduit and sieve pipe wall and reach to the medullary cavity surface, because the elements K and Cl must be transported through conduit or sieve pipes in the vascular bundle.

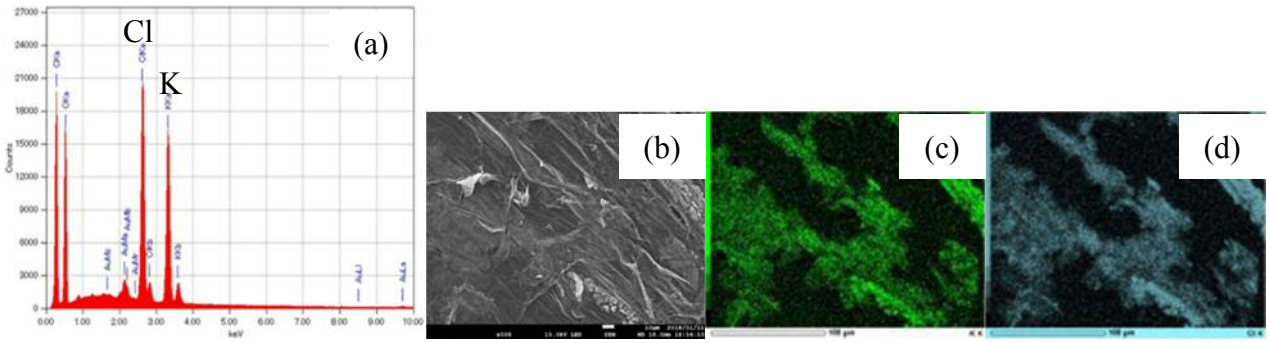

Figure 1. SEM-EDS analysis of medullary cavity surface of KCl impregnated bamboo. (a) EDS spectrum; (b) elemental mapping images; (c) K, (d) Cl.

SEM-EDS analysis - Node

When impregnated with KCl solution, the concentration of K and Cl remarkably increased at node, particularly, medullary cavity surfaces of node diaphragm. Other areas: parenchyma cells and fibrovascular bundle in node also showed the accumulation of K and Cl at corresponding concentrations to the culm tissues. From EDS analysis of node tissues, the accumulation of K and Cl was in the following order:

diaphragm surface > nodal parenchyma cells > nodal vascular bundle

The result stimulated us to reveal the internal tissue structures and their roles of bamboo node.

X-ray CT analysis

In order to clarify the internal tissue structures of node, X-ray CT analysis as a nondestructive observation method of bamboo internal tissues was carried out. As results, the X - CT analysis revealed that a part of the vascular bundles in bamboo culm was branched into node diaphragm, and the fibrovascular bundles were complicated and winding in the diaphragm as shown in Figure 2. In Figure 2, KI was impregnated as a salt instead of KCl because of higher contrast of accumulation state of salt in the node tissues. This result suggests that bamboo node tissues functions as a storage location of nutrients such as K.

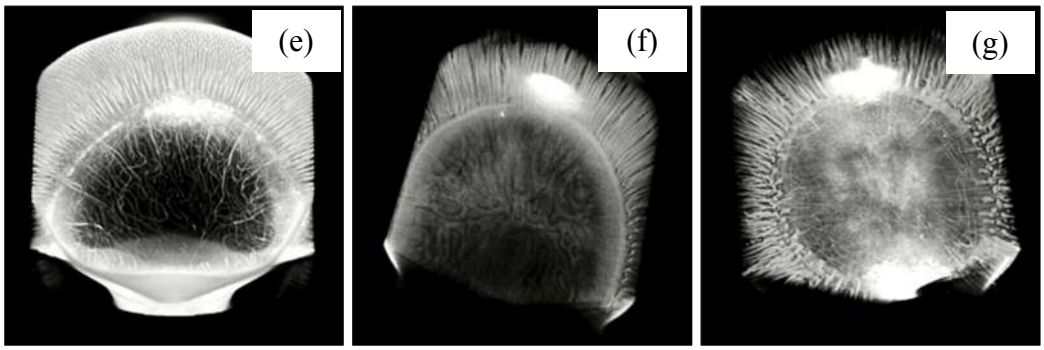

Figure 2. X-ray CT images of node part of Moso bamboo. (e) reference, (f) KI 1.5 g, (g) KI 7.5 g.

[Reference]

1. G. Peng *et al*., *Holzforschung*, **68**(2), 223–227 (2014).

Please choose: Poster
Presentation session: Material Science and Technology
Presenter name: Ikumi Nakata

Investigation into reaction pathway of CO_2 electrochemical reduction using Cu-Co electrodes

Ikumi, Nakata[1], Yoshiyuki, Takatsuji[1], Masayuki, Morimoto[1] and Tetsuya, Haruyama[1]

[1]Division of Functional Interface Engineering, Dept. of Biological System and Engineering, Kyushu Institute of Technology, 2-4 Hibikino, Kitakyushu Science and Research Park, Wakamatsu, 808-0196, Japan

Email: nakata.ikumi874@mail.kyutech.jp

Keywords (5 words)
CO_2 reduction, Copper, Cobalt, Plated electrode, Methane production selectivity

Introduction

Since CO_2 is a greenhouse gas, CO_2 cut down and convert into hydrocarbon fuels have attracted as a global issue. Converting CO_2 which is a stable compound needs external energy. CO_2 electrochemical reduction using a metal catalysis is one of approaches in order to convert CO_2. This reaction can obtain carbon monoxide, formic acid and hydrocarbons from CO_2 dissolved in the electrolyte. In the case, production selectivity is dependent on binding energy between metal catalysis and CO which intermediate of CO_2 reduction reaction. As Au and Ag have a low binding energy with CO, CO_2 electrochemical reduction using Au or Ag catalysis produce CO mainly. On the one hand, Pt, Ni and Co have a high binding energy with CO, CO_2 electrochemical reduction using them cannot reduce CO_2. When the method of convert CO_2 is performed using electrochemical reduction reaction on Cu catalytic electrode, hydrocarbon can be obtained as a product. Hydrocarbon is not obtained by other metals. To take advantage of this copper feature, the various studies about CO_2 electrochemical reduction using Cu catalysis have be reported. For example, CO_2 electrochemical reduction using Cu_2O is increased C_2H_4 selectivity compare to Cu metal.[1)] CO_2 electrochemical reduction using porous Cu, nano-particle Cu and dendrite Cu rise C2 selectivity.[2), 3)] Moreover CO_2 electrochemical reduction using Cu alloy can generate methanol and ethanol.[4)]

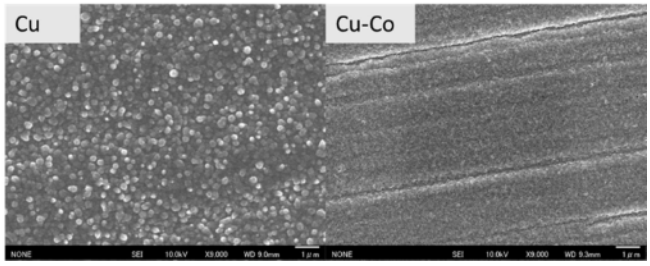

Figure 1. SEM images of Cu and Cu-Co catalysis on electrode

In previous study, we focused Cu-Co bimetal to increase the selectivity for hydrocarbon in excess of Cu (Figure.1). CO_2 electrochemical reduction using $Cu_{87}Co_{13}$ electrode generated 45.7% faradaic efficiency for CH_4 (Figure. 2)[5)]. In addition, it is necessary to reveal why Cu-Co catalysis is suited. In this study, we conducted CO_2 electrochemical reduction using pulse electrolysis. As the reaction produced hydrocarbons is multi electron reaction, it is step reaction. We followed step reaction by CO_2 electrochemical reduction using pulse electrolysis, and reaction was analyzed and discussed.

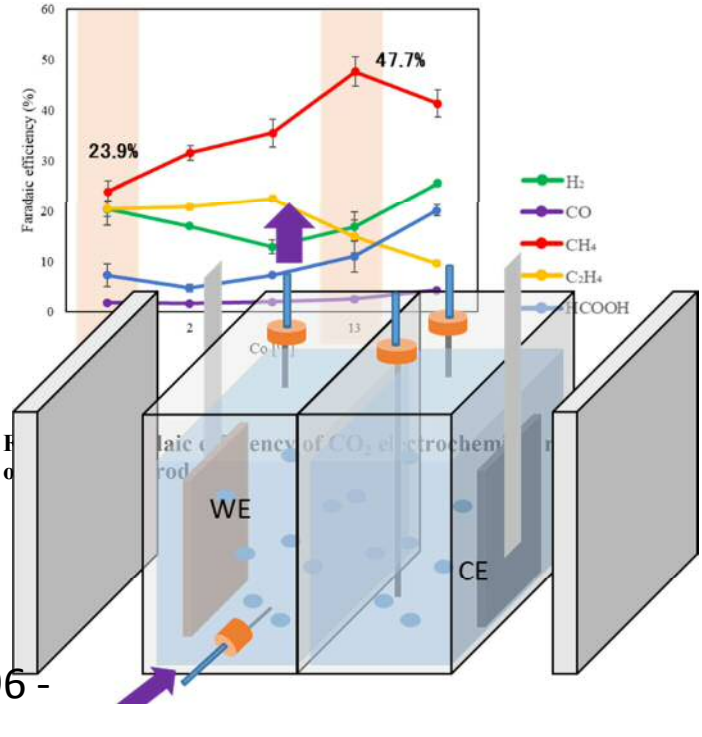

Experiment

Cu electrode and Cu-Co electrode were prepared by

electrodeposition.

CO_2 electrochemical reduction performed on H-type cell having three-electrode system (WE: Cu or Cu-Co, CE: Pt, RE: Ag/AgCl) (Figure. 3). The electrolyte used in the electrochemical CO_2 reduction reaction was 0.1M potassium bicarbonate saturated with CO_2 by bubbling for 40 min. Under the experiment, CO_2 gas at a flow rate of 6 ml/min was continuously supplied. Pulse electrolyte was performed by alternately applying REST potential and reducing potential (-1.19 V vs.RHE).

The gas phase of CO_2 reduction product was collected in a gas bag and analyzed by gas chromatography. The liquid phase of CO_2 reduction product was analyzed by anion chromatography. Faradaic efficiency (FE) was calculated from the amount of reduction products and measurement of electric quantity.

Figure 3. H-type cell

Result and Discussion

CO_2 electrochemical reduction products using Cu catalysis and Cu-Co catalysis were changed depending on the reaction time. In the case of 10ms pulse electro time, CH_4 FE of CO_2 reduction reaction using Cu catalysis was only 1%. However CH_4 FE of CO_2 reduction reaction using Cu-Co catalysis was achieved to 25%. Additionally with the long pulsed electro time, the amount of CO production from CO_2 reduction reaction using Cu-Co catalysis decreased than using Cu catalysis.CH_4 production amount of CO_2 reduction reaction using Cu-Co was increased than using Cu catalysis. These results showed that CH_4 product rate of CO_2 electrochemical reduction using Cu-Co catalysis is faster than using Cu catalysis.

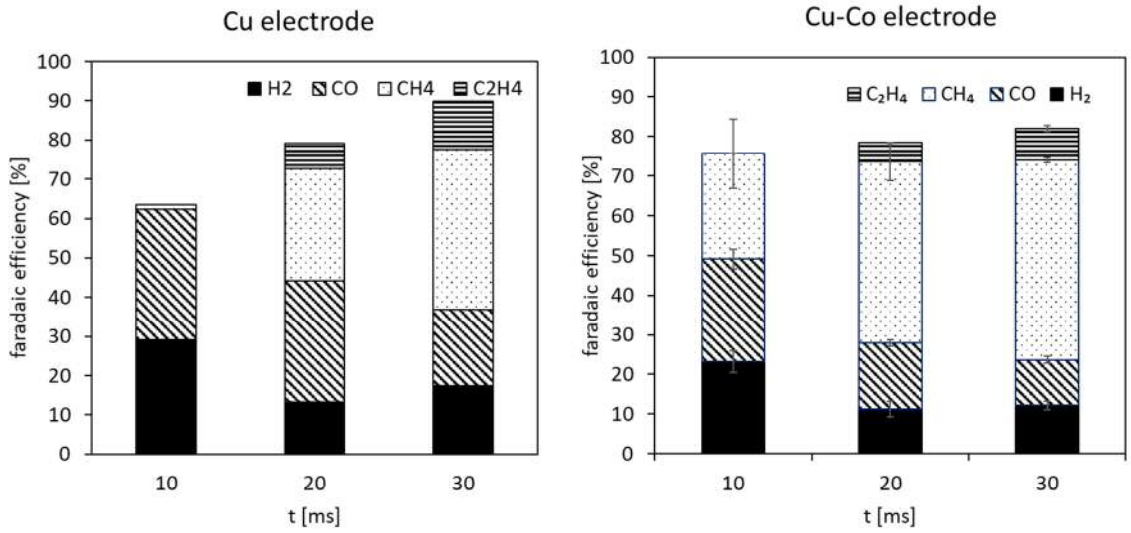

Figure 4. Faradaic efficiency of productions in electrochemical CO_2 pulse reduction reaction products

References

1) D. Ren, Y. Deng, A.D. Handoko, C. S. Chen, S. Malkhandi and B.S. Yeo, *ACS Catalysis*., **5**, 2814-2821(2015)

2) A. Dutta, M. Rahaman, N.C. Luedi, M.Mohos and P. Broekmann., *ACS Catalysis*., **3**,3804-3814(2016)

3) F. Jia, X. Yu and L. Zhang*., Journal of Power Sources,* **252**, 85-89 (2014)

4) D. Ren, B.S. Ang and B.S. Yeo., *ACS Catal.,* **6**,8239−8247(2016)

5) Y. Takatsuji, I. Nakata, M. Morimoto, T. Sakakura, R. Yamasaki and T. Haruyama, *Electrocatalysis*, ACCEPTED in 2018.9.11

Please choose: Poster
Presentation session:
Presenter name: Natrah Shafiqah bt Rosli

Comparative Study on Photocatalytic and Antibacterial Activity between TiO_2/G Nanocomposite and Magnetic TiO_2 Nanoparticles

Natrah Shafiqah Rosli [1,2,3] , Che Azurahanim Che Abdullah[1,2,*], Roshasnorlyza Hazan[3]

[1]Institute of Advance Technology (ITMA), University Putra Malaysia, 43400 UPM Serdang, Selangor, Malaysia.
[2]Department of Physics,Faculty of Science, University Putra Malaysia, 43400 UPM Serdang, Selangor, Malaysia.
[3]Malaysian Nuclear Agency, Bangi, 43000 Kajang, Selangor, Malaysia.
Email: azurahanim@upm.edu.my*

Abstract

This paper presents a new finding of synthesized Titanium dioxide combined with graphite powder (TiO_2/G nanocomposite) and Magnetic TiO_2 nanoparticles using synthetic rutile. In this work, the synthetic rutile was derived from natural Malaysian Ilmenite's waste to produce low cost and high quality of TiO_2 nanoparticles via environmental friendly process. These two types of samples were characterized using X-ray diffraction (XRD), Energy Dispersive X-Ray Fluorescence (EDXRF), UV-Vis Spectroscopy (UV-VIS), Field Emission Scanning Electron Microscopy (FESEM) and Particle Size Analyzer (PSA) in term of their structural and optical properties. Vibrating sample magnetometer (VSM) was used to investigate the magnetic properties of Magnetic TiO_2 nanoparticles. The functionality of the prepared samples in terms of photocatalyst and antibacterial activity was analyzed by degradation of methylene orange (MO) under the exposure to the ultra-violet (UV) light and by comparison of the bacteria *Escherichia coli* (*E-coli*) inhibition zone respectively. The result was found the degradation of MO by TiO_2/G nanocomposite can reach 90% compared to the magnetic TiO_2 nanoparticles, while the same result was shown in the antibacterial test. These results are promising for further practical application in nanotechnology.

Keywords (maximum 5 words)
Titanium dioxide, magnetic nanoparticles, Nano-composite, photodegradation, antibacterial

[Introduction]

Modified Titanium dioxide (TiO_2) nanocomposites have drawn increasing attention especially in photocatalytic and antibacterial properties due to their high performance for self-cleaning applications. Therefore, this paper focus on producing TiO_2/G nanocomposite and magnetic TiO_2 nanoparticles in anatase phase using low cost raw material and offers safer materials for the environment in contrast to the industrial and commercially available TiO_2 nanoparticles (TiO_2 P25). In our study, we used synthetic rutile derived from natural Malaysian Ilmenite's waste. Although this types of waste have low quality mineral but it has better potential to produce high quality metals and oxide (Mahdi *et al.* 2013). So, TiO_2/G nanocomposite and magnetic TiO_2 nanoparticles can be produce through a simple and low cost technique.

[Experiment]

The synthesized TiO_2/G nanocomposite was prepared in presence of graphite powder. Then the synthesized Magnetic nanoparticles was prepared by adding a base into an aqueous mixture of Ferrous ion (Fe2+) and Ferric ion (Fe3+) chloride at 1:2 molar ratios. After that, the magnetic nanoparticles were mixed with TiO_2 nanoparticles to become magnetic TiO_2 nanoparticles. The functionality of the prepared nanoparticles in terms of photocatalyst activity was analyzed by degradation of 10ppm of methylene orange. The synthesized samples were then test with inhibition zone of bacteria *E-coli*.

[Results and Discussion]

The TiO_2/G nanocomposite and Magnetic TiO_2 nanoparticles was successfully synthesized using alkaline fusion method and heteroagglomeration method, respectively. In term of characterizations, the XRD and EDXRF results was confirm that the TiO_2/G nanocomposite and Magnetic TiO_2 nanoparticles were in anatase phase and there no impurities. The result was found the degradation of MO by TiO_2/G nanocomposite can reach 90% compared to the magnetic TiO_2 nanoparticles, while the same result was shown in the antibacterial test. The possible reason for this result is due to the presents of graphite in the sample. Graphite was added to the pure TiO_2 nanoparticles during the leaching process as it has the ability to reduce the energy band gap of TiO_2 nanoparticles and increase the photocatalytic properties.

Please choose: Poster
Presentation session: Environmental Biotechnology
Presenter name: Yuki HOSHIKO

Effect of Hazardous Chemicals on Methane Fermentation using Sewage Sludge.

Yuki HOSHIKO, Shuto FUJIE, Nurul Asyifah MUSTAPHA, Toshinari MAEDA

Graduate School of Life Science and Systems Engineering, Kyushu Institute of Technology, 2-4 Hibikino, Wakamatsu-ku, Kitakyushu, Fukuoka, 808-0196, Japan

Email: n109060y@mail.kyutech.jp

Keywords (5 words)
Hazardous chemicals, methane fermentation, waste sewage sludge, water environment, Miseq

[Introduction]

To date, a lot of chemicals have been produced, and contributed to our convenient life. However, at the same time, many chemicals trigger the pollution to the environment. In fact, many kinds of chemicals (e. g. medicine, material of chemical products and so on) have been detected from the environment since 1970s, then the chemicals and their metabolites spread to the environment have been reported to be hazardous to ecosystem. The wastewater harvested from households, industrial sites, and hospitals is treated in wastewater treatment plants. Some reports indicate that numerous chemicals in wastewater remain without totally being degraded by bacteria and accumulate into sewage sludge. Therefore, sewage sludge produced from the process of wastewater treatment may influence the chemicals; in particular, the efficiency of wastewater treatment. On the other hand, methane fermentation using sewage sludge is one of the recycling approaches to reduce the amount of sewage sludge produced in a process of water treatment for a long time because 60-70% organic material derived from sewage sludge can be utilized for methane fermentation. Therefore, it would be important to understand how hazardous chemicals may influence the process of methane fermentation. Until now, there is no report on the methane fermentation in sewage sludge with hazardous chemicals. Hence, in this study, methane fermentation using sewage sludge with or without hazardous chemicals was investigated by seeing the influence of the chemicals at the processes of hydrolysis, acidogenesis, acetogenesis, and methanogenesis.

[Chemicals]

Fluorouracil (FU) - This chemical, known as an anticancer drug, has a high physiological activity and is one of the anticancer drugs being consumed and being detected in the world.
Bisphenol - This chemical, known as mainly an ingredient of practices, is an endocrine disruptor. In this study, bisphenol A (BPA), bisphenol F (BPF), and bisphenol S (BPS) were used.

[Experiment]

Wastewater sewage sludge was obtained from the Hiagari wastewater treatment plant in Kitakyushu City, Japan. The sludge was used within one week and washed with distilled water prior to the use.

1. Methane production

- Total 30 mL of sewage sludge (5%-w/w) with or without 50 mg/L of each chemical was mixed in a 66 mL vial and the mixture was incubated at 37°C with 120 rpm for 20 days under an anaerobic condition. Methane was measured by using a GC-TCD equipment and 50 µL of the headspace gas in the vials were used for the analysis of methane gas. Hydrogen sulfide (H_2S) was measured by a Gastec system at the end of experiments after 20 days.

2. Analyses to evaluate the effect on methane fermentation

- Each samples during the methane fermentation was harvested every 4 days and the supernatant after the centrifuge at 14,000 rpm for 1 min was used to measure protease activity, organic acids by HPLC, and pH. Bacterial and archaeal activities were measured by RT-PCR after RNA extraction and cDNA synthesis.

3. Effect of hazardous chemicals at the methanogenesis.

- Inhibition of methane fermentation was confirmed by evaluating methane production using *Methanosarcina acetivorans* C2A with or without each hazardous chemical in the medium with acetate as a carbon source.

4. Identification of bacteria related to methane fermentation using MiSeq

- RNA was extracted from the samples and used as the template for the analysis of bacterial community using MiSeq.

[Result and Discussion]

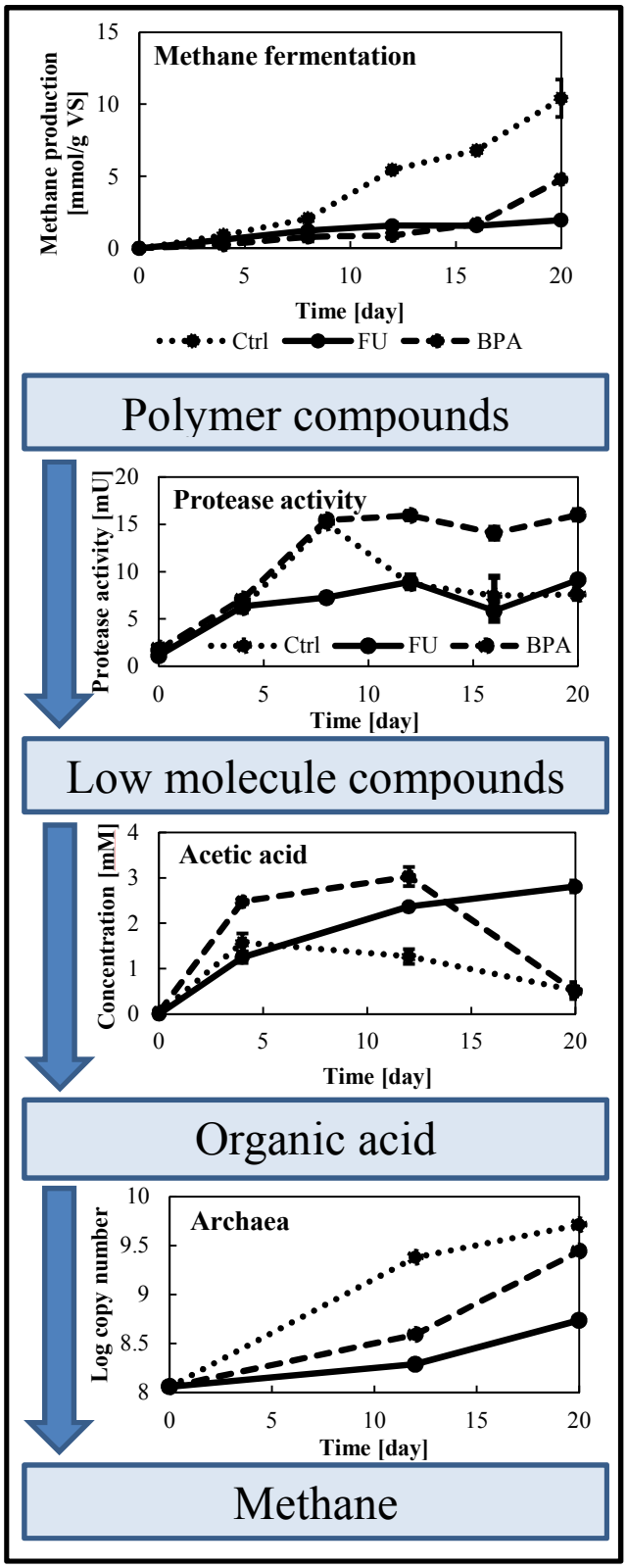

Fig. Methane fermentation in wastewater activate sludge with/without hazardous chemicals.

1. Methane fermentation using sewage sludge with hazardous chemicals.

Among the chemicals tested, FU and BPA remarkably inhibited methane production compared to the control without adding any chemical. At the same time, the amount of hydrogen sulfide which is known as an inhibitor of methane fermentation was 2-time higher than the control; therefore, the accumulation of hydrogen sulfide in FU sample may be a reason why methane production was inhibited. Methane fermentation in BPA sample was also inhibited by 16 days; however, at 20 days some amounts of methane were detected.

2. Understanding each step at methane fermentation

The three key steps for methane fermentation, hydrolysis, acidogenesis/acetogenesis, and methanogenesis were evaluated to see the impact of each chemical. First, in the hydrolysis process, both samples (FU and BPA) indicated same or more protease activity than the control; therefore, the inhibition of methane fermentation was not due to the hydrolysis process. Second, in the acetogenesis process, FU sample indicated the accumulation of acetate during the fermentation. Furthermore, in the methanogenesis process, archaeal activity was inhibited in the presence of FU. Thus, as a proposed mechanism how the chemical can inhibit methane fermentation, it seems that FU may be able to inactivate acetotrophic methanogens. On the other hand, sewage sludge with BPA was able to produce methane by supplying acetate whereas FU still had an inhibitory effect for methane fermentation.

3. Methane production using *M. acetivorans* in the presence of hazardous chemicals

M. acetivorans C2A was used to evaluate a direct impact of chemicals at the methanogenesis. As expected, FU and BPA inhibited methane fermentation by this strain.

4. Bacterial community analyses using MiSeq

MiSeq was used to analyze what the bacteria can be dominant in the chemicals. In FU sample, bacteria capable of consuming methane increased; therefore, the result also indicates that FU may not only inhibit methane production but also activate methane consumption. Moreover, bacteria capable of producing acetate and hydrogen disappeared in the presence of FU.

In BPA sample, bacteria able to degrade organic pollutants were detected. Thus, the bacteria may transform BPA to other metabolites; thereby, the inhibitory effect by BPA can be diminished by the degradation.

Others did not have the direct relation to methane fermentation; however, each sample has bacteria that grow by utilizing low molecule compounds and/or organic acids.

5. Conclusion

The existence of hazardous chemicals in sewage sludge had a certain impact to inhibit the methanogenesis process in methane fermentation, resulting in a low production of methane.

Please choose: Poster
Presentation session: Environmental Biotechnology
Presenter name: Shuto FUJIE

Understanding Virgin vs. Veteran Bacterial Community in the Degradation of 5-Fluoruracil

[Shuto FUJIE][1], [Toshinari MAEDA][1], [Nurul Asyifah MUSTAPHA][1]

[1] School Life Sci. Systems Eng., Kyushu Institute of Technology, 2-4 Hibikino, Wakamatsu-ku, Kitakyushu-shi, Fukuoka, 808-0196, Japan

Email: [fujie.syuto904@mail.kyutech.jp]

Keywords (5 words)
Water treatment, Sludge, Pharmaceutical, environmental adaptation, biodegradation

[Introduction]

Domestic wastewater and hospital wastewater flow in the wastewater treatment plant. At the wastewater treatment plant, wastewater is treated by various bacteria present in the sludge. Therefore, sewage sludge of wastewater treatment has many opportunities to contact with various chemical substances and it is considered that sewage sludge has a relatively- high biodegradability to these chemicals through the process that bacteria adapt the chemicals. In contrast, sludge which never has contacted chemical substances probably may not have resistance for such chemicals. Thus, it would be an interesting issue how bacterial community can gradually adapt a condition in which bacteria interact with chemicals for the first time; perhaps a highly adaptive sludge (sewage sludge in this study) and a virgin sludge (standard sludge in this study) may show different responses to the same chemical substances. The purpose of this paper is to elucidate the effect of adaptation of sewage sludge and standard sludge in microbial biodegradation of chemical substances. Biodegradation experiments using 5-fluorouracil (5-FU) by sewage sludge and standard sludge were conducted. In this process, biodegradability, change in the number of viable bacteria, change in bacterial flora before and after biodegradation were investigated.

[Experiment]

1. Sample preparation and biodegradation experiment

In this study, two types sludge were used. One is sewage sludge that used at the wastewater treatment plant (it was provided from the Hiagari sewage plant in Kitakyushu city), and the other is standard sludge that was removed the resistance for chemical substances by special culture method (it was provided by Chemicals Evaluation and Research Institute Kurume office). Each sludge were adjusted 50 % (w/v) using distilled water, 10 g of the adjusted sludge (50 %) was placed in a 300 ml sterilized flask and using sterile water and 100 mg of 5-FU aqueous solution, the sample was adjusted so that the concentration of sludge was 5% and the concentration of 5-FU was 50 mg / L. After preparing the samples, the culture was aerobically incubated at 30ºC with 120 rpm, and the degradation of 5-FU was evaluated with time. During this experiment, the concentration of 5-FU in each sample was measured by using HPLC with time, and the degradation rate of 5-FU in each sludge was calculated based on the first-order reaction. After a certain period of time of the samples, the powder of 5-FU was added to adjust the concentration of 5-FU in the sample to be 50 mg/L. By this way, continuous biodegradation of 5-FU in each sludge was examined.

2. Measuring the number of viable cells in each sludge

Sludge samples were sequentially diluted with saline solution at every sampling time and the number of viable cells in each sludge was counted after incubating LB agar plates at 30ºC for overnight in which the serial dilutions were spread.

3. Microbial community structure analysis

RNA and DNA were extracted from each sludge and microbial flora analysis was carried out by using Illumina Miseq and the experimental method was carried out according to the protocol of "16S Metagenomic Sequencing Library Preparation" provided by Illumina.

[Result and Discussion]

The first goal of this study was to compare the speed of 5-FU degradation in two sludge samples (sewage sludge vs. standard sludge). As shown in Fig. 1, compared to sewage sludge, the degradation speeds of 5-FU were remarkably slow. In addition, slow degradation was found by contacting the chemical continuously (Fig. 1). In agreement with the result, the number of viable bacteria reduced through every supplementation of 5-FU; however, the reduction of viable cells was not due to the toxicity of 5-FU because in control samples without 5-FU, the number of viable cells reduced. Therefore, the reduction of 5-FU degradation speed and viable cells may be due to the bacterial inactivation through a low nutrient condition. The same results were found in sewage sludge (Fig. 2). Through the contact with 5-FU, the degradation speed of 5-FU became slow although the number of viable cells did not reduce too much compared to the standard sludge. In detail, the number of viable bacteria in sewage sludge was higher than that in standard sludge at an initial stage. Through the incubation, the number of viable bacteria decreased in both sludge samples. Taken together, the initial degradation speed of 5-FU was higher in sewage sludge; however, an environmental adaption to 5-FU was not observed in both sewage sludge and standard sludge.

Next, bacterial communities in both sewage sludge and standard sludge were compared (Fig. 3). First, more diverse bacterial community was found in sewage sludge rather than standard sludge. The diversity may be related to a high speed of 5-FU degradation. Second, the pattern of bacteria detected in both sewage sludge and standard sludge was different, indicating that a large number of bacteria capable of degrading 5-FU may be present in sewage sludge compared to standard sludge. This may be a reason why sewage sludge can degrade 5-FU with a high rate. Third, microbe diversities in both sewage sludge and standard sludge remarkably reduced with time. The results indicate that only bacteria able to live in even conditions with a low nutrition; however, the remaining bacteria were unable to degrade 5-FU because in both sludge samples degradation speeds of 5-FU reduced with time. In this study, we tried to understand virgin and veteran bacterial communities for the degradation of 5-FU. We need to test more chemicals rather than only 5-FU for the study to see if other chemicals also show the same results. In addition, we need to add more nutrients to see bacterial adaptation to the chemicals.

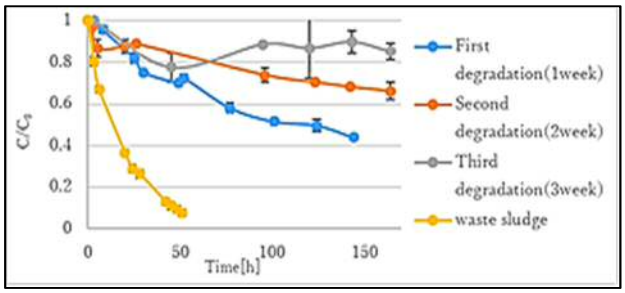

Fig.1. **Degrdation dynamics of 5-FU using standard sludge. Standard sludge was used as a bacterial source for the continuous biodegradation. The degradation was compared to the 1st, the 2nd, and the 3rd degradation.**

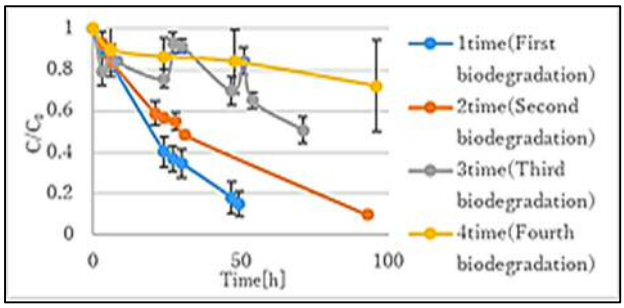

Fig.2. **Degradation dynamics of 5-FU using sewage sludge. Standard sludge was used as a bacterial source for the continuous biodegradation. The degradation was compared to the 1st, the 2nd, the 3rd, the 4th degradation.**

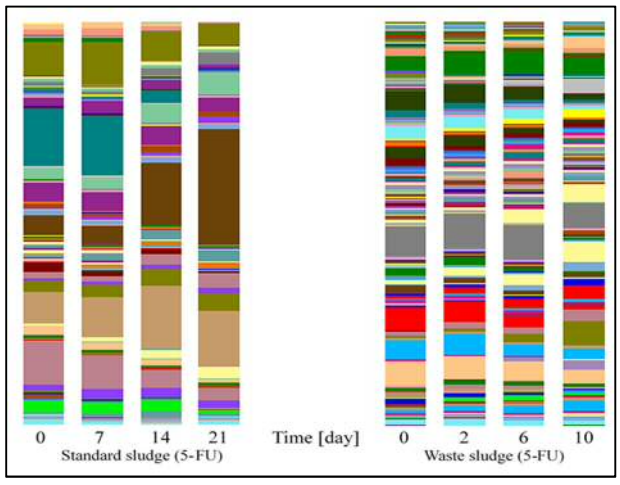

Fig.3. **Comparison of bacterial communities in standard sludge or sewage sludge during the degradation of 5-FU**

Please choose: Poster
Presentation session: Material Science and Technology
Presenter name: Xinguang Yu

Pulse Generation Behavior of Single-Walled Carbon Nanotube/ Polyoxometalate Complex Random Network

Xinguang Yu [1], Detiza Goldianto Octensi Hernowo [1], Tomoya Ishizuka [2], Takahiko Kojima [2], Takuji Ogawa [3], Hirofumi Tanaka [1,*]

[1] Graduate School of Life Science and Systems Engineering, Kyushu Institute of Technology, 2-4 Hibikino, Wakamatsu, Kitakyushu 808-0916, Japan
[2] Graduate School of Pure and Applied Science, Tsukuba University, 1-1-1 Tennoudai, Tsukuba 305-8577, Japan
[3] Department of Chemistry Graduate School of Science, Osaka University, 1-1 Machikaneyama, Toyonaka, 560-0043, Japan
Phone& Fax: +81-093-695-6157, * E-mail: tanaka@brain.kyutech.ac.jp

Keywords: SWNT/POM, $(TBA)_2[SW_{12}O_{40}]$, pulse generation, return map, Poincaré plots.

1. INTRODUCTION

The advancement of high-performance in information technology led us to solve complex computational problems easily. Very large scale integration, known as VLSI, of silicon-based transistor can be used to realize high performance computer with high processing speed. However, further miniaturization in integrated circuit (IC) based on Moore's law is reaching limitation process owing to high information processing capacity. Therefore, many researchers are developing high performance computer instead of silicon-based transistor to implement brain-inspired electronic devices, such as neuromorphic devices.

One of the promising materials to replace silicon is introduced to carbon-based neuromorphic devices that can exhibit remarkable electronic properties to realize VLSI of carbon nanotubes electronic devices. On the other hand, molecular functionalization of carbon nanotubes also takes part in developing brain-inspired electronic devices that may represent unique properties. Carbon nanotubes based on molecular devices are playing a role to generate large electrical noise with rich dynamics [1]. Thus, the purpose of this study is to investigate neural behavior of conjugated molecular wires that consists of single-walled carbon nanotube (SWNT) and polyoxometalate (POM), and to study behavior of neuron firing with intrinsic fluctuation or noise (Figure 1).

2. EXPERIMENTAL PROCEDURE

Firstly, fabrication process of SWNT/POM complex random network is as following. SWNT was annealed for 20 h, followed by washing in chloric acid to remove metallic catalysts and subsequently rinsing with DI water. To prepare the SWNT/POM complex, 1.6 mg of the purified SWNTs and 0.16 mg of POM were mixed and sonicated in 10mL of 1, 2-dichloroethane for 1 h. Then, continued to centrifuge solution with the speed at 50000 G for 1 h. The supernatant (1 mL) was vacuum-filtered using 1-μm-mesh nitrocellulose filter paper to fabricate the SWNT/POM network structure on the filter paper. The filtration surface of the filter paper was brought and tightly contacted with the surface of the glass substrate. The substrate was then placed upside-down on an open-mouth bottle filled with acetone, and the bottle was heated to 80 °C. Since evaporated acetone melted the filter paper, the network was transferred to the glass substrate. Next, aluminum electrodes was prepared by a sputtering method and electrical measurement was carried out. Current pulse generation was measured by applying various DC voltages between electrodes by using two-probe system.

3. Results and Discussion

Keggin POM has a stable and strong structure [2] and has been shown to be an 'electron sponge' that accumulates a large number of electrons [3]. We have investigated pulse generation characteristics using $H_3PMo_{12}O_{40}$ molecule, which has Keggin structure so far, as shown in Fig. 2 (a). As a result, we found that pulse generation occurs when 150 V was applied to the POM/SWNT random network [4] (Fig. 3). It was also found that POM, which is sandwiched between electron donors, two porphyrin rings [Fig. 2 (b)], could generate pulses that appeared to opposite direction to the current (call 'negative' hereafter). A similar experiment was carried out using $(TBA)_2[SW_{12}O_{40}]$ [Fig. 2 (c)] , having a highly reductive tetra (n-butyl) ammonium (TBA) group among POMs which have the same Keggin structure. Pulses were obtained at constant voltage (15 V) in

measurement of the current flowing through the network versus time. As shown in Fig. 4, the obtained pulses were negative and similar to the porphyrin sandwiched POM. As shown in Fig. 5 (a), return map [4] drawn by plotting all (t_n, t_{n+1}) plotted the interval of nth pulse between the pulse (n-1)th, and (n+1)th. As a result, the pulse intervals are centered around 0.1 s and dispersed. As a conclusion, pulse intervals show periodic property and pulse could be generated at low voltage level [Fig. 5 (b)].

REFERENCES

[1] P. G. Collins, M. S. Fuhrer and A. Zettl, Appl. Phys. Lett. **76**, 894 (2000). [2] T. Kojima *et al*., Dalton Transaction, **40**, 6445-6450 (2011). [3] H. Wang *et al*., J. Am. Chem. Soc. **134**, 4918-4924 (2012). [4] H. Tanaka *et al*., Nat. Commun. **9**, 2693 (2018).

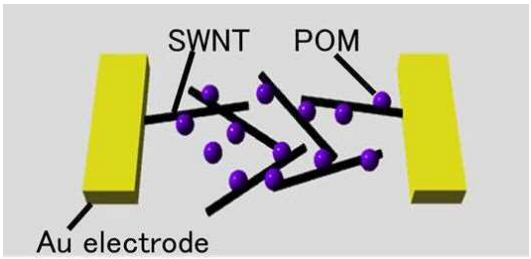

Figure 1. Model of SWNT/POM complex network between two Au electrodes.

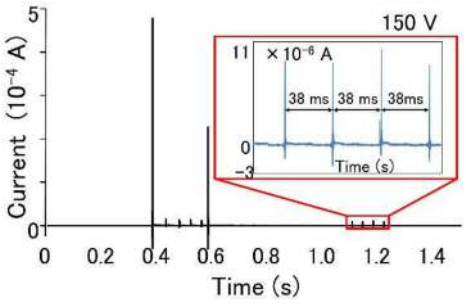

Figure 3. Current pulse generation on SWNT/ $H_3PMo_{12}O_{40}$ random network.

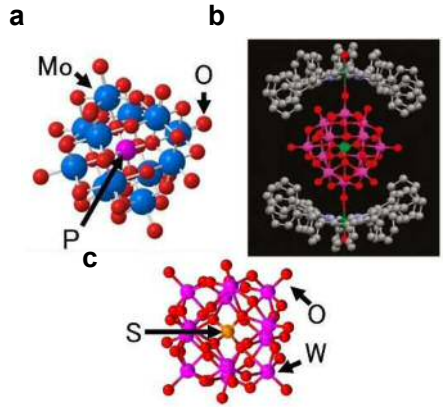

Figure 2. Structure of (a) $[PMo_{12}O_{40}]^{3-}$. (b) Porphyrin-POM. (c) $[SW_{12}O_{40}]^{2-}$.

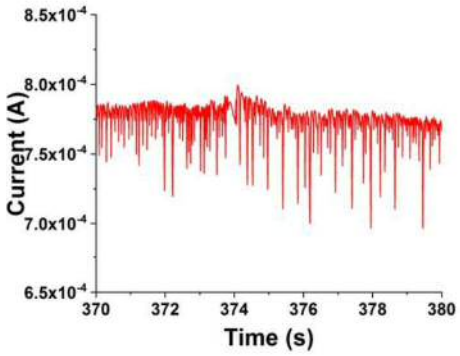

Figure 4. Negative pulse generation occurred in SWNT/ $(TBA)_2[SW_{12}O_{40}]$ network .

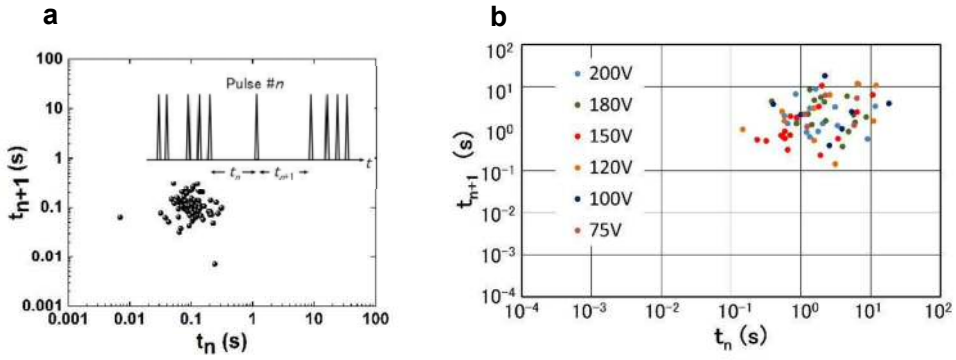

Figure 5. Return map of Poincaré plots. (a) Obtained from data in Figure 4 and insert explains the plotting method. (b) Poincaré plots on SWNT/$H_3PMo_{12}O_{40}$ network.

Please choose: Poster
Presentation session: Material Science and Technology
Presenter name: Taku Omura

Modification of Cellulose Nanofiber by Conductive Polymer and Properties of Composite with LDPE

Taku Omura[1], Chi Hoong Chan[1], Minato Wakisaka[1], Haruo Nishida[1]

[1] Graduate School of Life Science and Systems Engineering, Kyushu Institute of Technology, 2-4 Hibikino, Wakamatsu, Kitakyushu, Fukuoka 808-0196, Japan

Email: omura.taku263@mail.kyutech.jp

Keywords (5 words)
Modification, Cellulose nanofiber, Conductive polymer, Electromagnetic shielding, Composites

[Introduction]
Recently, in the fields of organic electronics and medical technology, many research papers of conductive nanocomposites combined nanocellulose (NCs) with conductive polymer (CP) have been reported [1]. The NCs/CP nanocomposite materials are expected for some applications, e.g., antistatic and chemically sensitive materials with the characteristic properties of NCs as reinforcements of conventional polymer sheets and composites.
Cellulose nanofibers (CNF) are promising nanofillers as reinforcements of plastics, however, they have poor compatibility with hydrophobic plastics because of hydrophilic groups such as hydroxyl group. In addition, CNF has a serious issue of re-aggregation behavior during drying process, resulting in ununiformed dispersion in matrix resin without expected performances. Therefore, in this study, we focused on coating the CNF surface with a conductive polymer not only to prevent re-aggregation of CNF during drying, but also to afford specific electrical properties on the CNF surface. The coating was carried out by oxidative polymerization of aniline to cover the CNF surface by a conductive polymer: polyaniline (PANI). Finally, nanocomposite materials were prepared by extrusion molding.

[Experimental/Theoretical Study]
PANI-coated CNF (CNF/PANI) was prepared by the oxidative polymerization of aniline in water medium. Bamboo-derived CNF dispersion gel (1 wt% in water, Chuetsu Pulp Co., Ltd., Japan) 10 g (100 mg as solid weight) was added into a 100 mL of 1 M HCl aq., followed by addition of aniline (1.4 mmol) and lithium chloride (0.2 mol) before stirring at -10 □ for 1 h. Oxidizing agent: ammonium persulfate (1.75 mmol) aq. 100 mL was slowly added dropwise into the solution. After completion of the dropwise addition, the solution was further stirred for prescribed periods. After the reaction, the solution, which changed in color to dark green, was filtered with PTFE membrane filter (pore size 1.0 μm) under a reduced pressure before washed with acetone to obtain PANI-Cl coated CNF. The chlorine-ion doped PANI-Cl coated CNF gel before drying was added into a 100 mL of 1 M ammonia aq. and stirred at r. t. for 3 h to de-dope the chlorine ions. Resulting blue black solution was filtrated and purple-colored residue was washed with acetone to recover de-doped PANI coated CNF. The de-doped PANI coated CNF gel before drying was added into a 50 mL of camphorsulfonic acid (CSA) (0.5 mmol) / m-cresol solution and stirred at r. t. for 3 h. Resulting dark green solution was filtered to recover dark green-colored PANI-CSA coated CNF before washing with acetone and following vacuum drying. The PANI-modified CNF samples were characterized using a field emission electron microscope-energy dispersive X-ray analyzer (FE-SEM/EDS), XRD, Fourier transform infrared (FT-IR, KBr), TG, UV-Vis, contact angle analyzer, electrical resistivity (four probe method) and electromagnetic shielding (EMS) property measurement apparatuses.

[Result and Discussion]
Morphology of PANI coated CNF samples was observed by FE-SEM/EDS. Fig. 1 shows SEM images of (a) freeze-dried pristine CNF, (b) control-CNF which was prepared under the same conditions of polymerization without adding oxidizing agent and aniline, (c) PANI-Cl coated CNF, and (d) PANI-CSA coated CNF, with inserted fiber-width histogram of each CNF. Widths of freeze-dried CNF and control-CNF were 36.1 ± 10.6

and 66.4 ± 24.8 nm, respectively, and their fiber surfaces were smooth. On the other hand, PANI-Cl coated CNF had a fiber width of 33.7 ± 12.6 nm and nano-size particles were observed on the CNF surface. The nano-size PANI particles uniformly distributed on the CNF surface, and no large aggregated particle was observed. Fiber width of PANI-CSA coated CNF was 36.5 ± 13.9 nm, showing smooth surface without the nano-particles. This suggests that free PANI particles were dissolved in m-cresol, while tethered PANI molecules remained on CNF surface. The tethered PANI molecules may have strong intermolecular hydrogen bonding with CNF hydroxyl groups in a manner of growing chains using the aligned hydroxyl groups as a template [2]. The uniform coating of PANI molecules effectively prevented the re-aggregation of CNF.

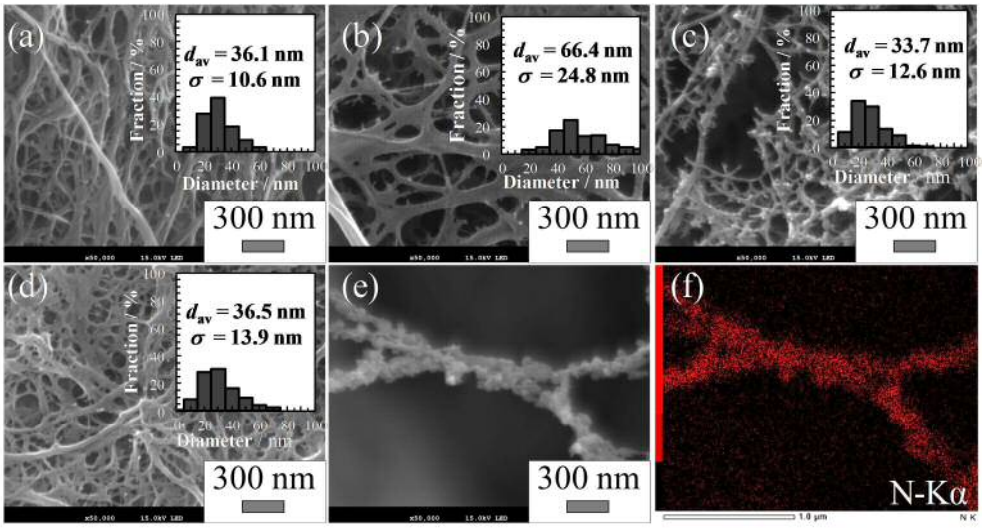

Fig. 1. SEM images of (a) freeze-dried pristine CNF, (b) control CNF, (c) PANI-Cl coated CNF, (d) PANI-CSA coated CNF, (e and f) PANI-Cl coated CNF and EDS element mapping image by nitrogene.

Electrical conductivity of PANI coated CNFs were measured by a four probe method. Pristine CNF showed very low electrical conductivity of 7.43×10^{-13} S/cm. PANI-Cl coated CNF achieved 0.20 S/cm. On the other hand, the conductivity of PANI-CSA coated CNF was 38.5 S/cm, showing 193 times higher value than that of PANI-Cl coated CNF. This is attributed to the change in dopant to CSA, which is known as an excellent dopant of PANI, and to the treatment with m-cresol, in which PANI chains change to an expanded coil-like conformation.

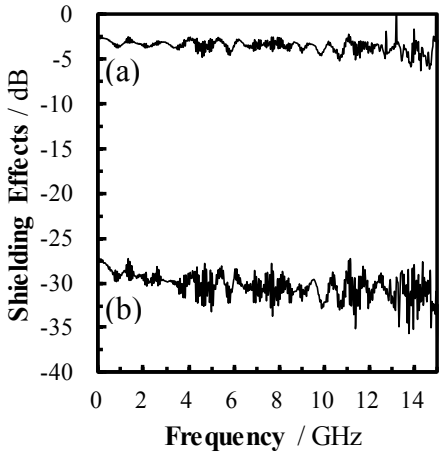

Fig. 2. Electromagnetic shielding effect of (a) PANI-Cl coated CNF film and (b) PANI-CSA coated CNF film.

Fig. 2 shows EMS effect of PANI coated CNFs at 0 to 15 GHz (including X-bands : 8.2~12.4 GHz). The shielding effectiveness (SE) of PANI-Cl coated CNF was around 3 dB. On the other hand, PANI-CSA coated CNF dramatically increased to 30 dB. Nevertheless the PANI-CSA coated CNF was much thinner (< 100 μm) than other carbon-based materials [3], it showed the very high SE value. From the results, it was determined that SE could be greatly improved by the CSA/ m-cresol treatment of PANI coated CNF.

References

[1] X. Du; Z. Zhang; W. Liu; Y. Deng *Nano Energy* **2017**, *35*, 299–320.
[2] W. Hu; S. Chen; Z. Yang; L. Liu; H. Wang *J. Phys. Chem. B* **2011**, *115*, 8453–8457.
[3] W. Yang *et al. J. Mater. Chem. C* **2017**, *5*, 3748–3756..

Please choose: Poster
Presentation session:
Presenter name: Takeru Nishimi

[Good die prediction modelling from limited test items]

[Takeru, Nishimi][1], [Seiji, Kajihara][1], [Yasuo, Sato][1], [Yoshiyuki, Nakamura][2]

[1] Kyushu Institute of Technology, Iizuka, Japan
[2] Renesas Electronics Corporation, Tokyo, Japan

Email: [nishimi@aries30.cse.kyutech.ac.jp]

Keywords (5 words)
test cost reduction ; big data analysis; burn-in test; machine learning, test result prediction

[Introduction]

With the advance of VLSI manufacturing technology, test cost has been increasing. Especially, the test cost of VLSIs used in safety-critical and/or mission-critical applications such as automobiles and medical equipment tend to increase rapidly. There is generally a positive correlation between test cost and test quality, test cost reduction without sacrificing high-test quality is strongly required.

Figure1 shows a conventional test flow. Among them, burn-in (BI) test, in which a stress such as high temperature or high voltage is applied to dies during enough time to activate the initial defects, is often mentioned as a big concern that increases test cost because of its long test time and expensive test equipment. Reduction of BI test cost, i.e., reduction of the number of dies applying BI test or reduction of BI test time, can contribute to reduction of total test cost.

This paper proposes a test cost reduction method using machine learning techniques. The proposed method tries to predict good dies among the manufactured dies on the way of test process. If a die is predicted as good before completing all of the test process, the die will be allowed to be shipped without going through the remaining test process which contains costly burn-in test and final test. By a SVM-based procedure together with K-fold cross validation, a prediction model to judge certainly good dies is created from known results of the selected test items. Figure2 shows the test flow with good die prediction. Figure3 shows the cost reduction with good die prediction.

We add the pre-learning step before the modeling to improve the model performance. Figure4 shows a modeling flow with pre-learning. In the pre-learning step, first, we divide failing dies into some groups based on fail test items. We use them to select some valid test items suitable for prediction. In particular, we create a model from all passing dies and one group of failing dies detected fail on one test item. In addition, we repeat this process with other groups of failing dies and some models are created. Next, we evaluate them. We select some high performance models. Then, test items used for modeling are selected. After the pre-learning step, we use failing dies that their test items for modeling.

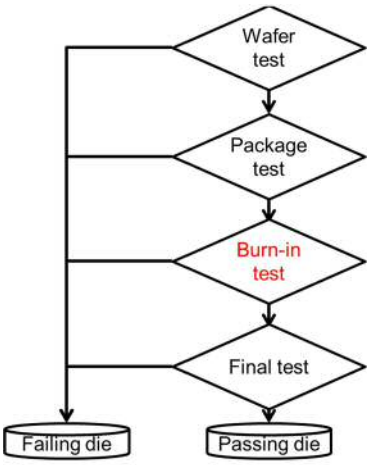

Figure 1. A test process

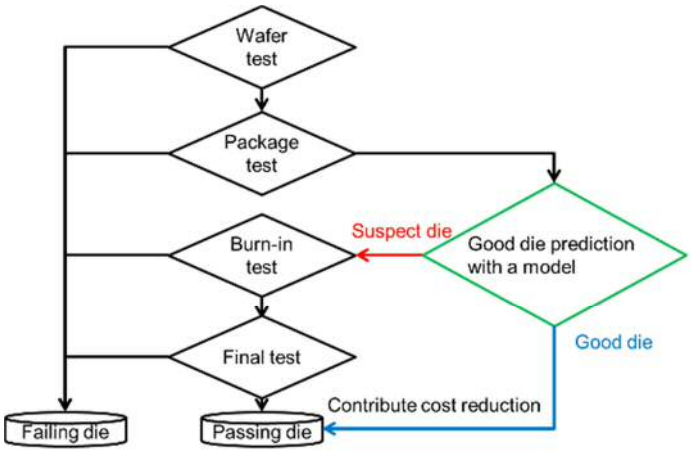

Figure 2. Test flow with good die prediction

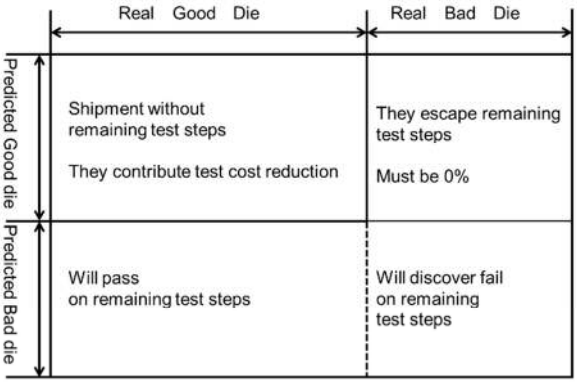

Figure 3. Good dies prediction

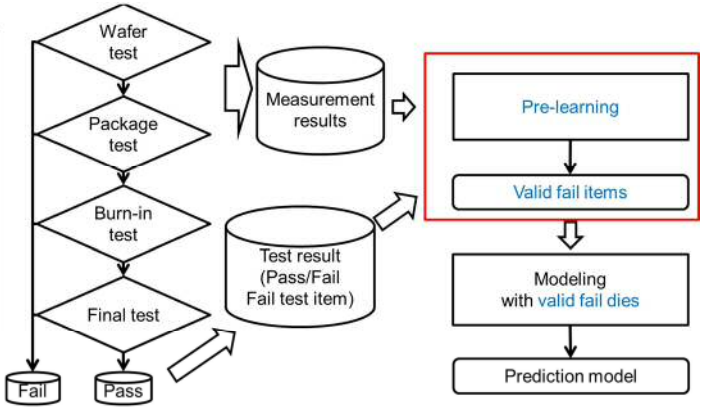

Figure 4. Improve the model performance by pre-learning

[Experiment]

We use data of 5 wafers. They are real chip data from one company. Each die has about 5000dies. We use 3 wafers for learning step. In the learning step, we create a model. In additional, we use remaining 2 wafers for validation step. In the validation step, we predict the final result of validation data and make sure that effectiveness of our method. In order to avoid influences by a peculiar case, we examine ten combinations of learning and validation data.

The results are evaluated by two measures:

a) AUC by all Pass/Fail

b) Our proposed cost reduction rate by all Pass/Fail without test escape

AUC is a general evaluation measure. However, when we use only AUC, we cannot observe the effectiveness without test escape. To observe the effectiveness without test escape, we define new evaluation measure.

[Result and Discussion]

Table1 shows result of our experiment. Unlike the case of AUC, the cost reduction rate of the proposed method improved by 11.2% on average. Especially for 8 out of 10 combinations, the cost reduction rates of the proposed method were significantly improved. From these results, it is concluded that the proposed method has advantages to predict good dies constraining bad dies escape rate 0%. In this paper, we propose a method for good die prediction and evaluate the method with test data for industrial dies. The method selects fail dies in the selected test items through pre-learning step. From evaluation results, it is found that the method is effective for test cost reduction. It achieves 20.7% test cost reduction, that is, cost reduction rate is improved by 11.2% keeping test escape at 0%. We confirmed the test cost reduction rate with most of the wafer combinations. Although AUC does not show the effectiveness of the method with some combinations of wafers, we confirmed the effectiveness with new measures with 0-defect quality.

There still remains room for further cost reduction. For example, we could not improve cost reduction rate with 2 combinations of wafers. More sophisticated selection of test items is required. In addition, we are investigating improvement of pre-process that shapes the data to a proper form for the subsequent processes, such as removing outliers.

Table 1. AUC and cost reduction rate result

ID		1	2	3	4	5	6	7	8	9	10	Avg.
Basic	AUC	0.636	0.644	0.653	0.662	0.648	0.613	0.595	0.580	0.687	0.639	0.636
	Cost reduction rate	5.8%	4.5%	18.0%	9.7%	20.8%	9.9%	1.4%	5.8%	10.6%	8.0%	9.5%
Proposed	AUC	0.703	0.688	0.741	0.725	0.740	0.611	0.538	0.581	0.534	0.634	0.650
	Cost reduction rate	28.7%	8.2%	47.3%	32.5%	43.6%	9.1%	8.6%	11.1%	3.5%	14.9%	20.7%

Please choose: Oral
Presentation session: Material Science and Technology
Presenter name: Nur Haryani binti Zabaruddin

Bio-Based Heterogeneous Catalyst for Biodiesel Production

Nur Haryani Zabaruddin[1,2], Nor Hasimah Mohamed[2], Luqman Chuah Abdullah[3], Masao Tamada[4], Yuji Ueki[4] and Noriaki Seko[4]

[1]Institute of Tropical Forestry and Forest Products, Universiti Putra Malaysia, 43400 Serdang, Selangor, Malaysia
[2]Radiation Processing Division, Malaysian Nuclear Agency, Kajang, Selangor 43000, Malaysia
[3]Department of Chemical and Environmental Engineering, Faculty of Engineering, Universiti Putra Malaysia, 43400 Serdang, Selangor, Malaysia
[4]National Institute for Quantum Radiological Science and Technology, 1233 Watanuki-machi, Takasaki-shi, Gunma 370-1292, Japan

Email: nurharyanizaba@gmail.com

Abstract (250 words)

In the present study, a novel solid catalyst derived from kenaf fiber was prepared by radiation graft polymerization for biodiesel synthesis. Initially, batch synthesis was carried out to obtain the catalytic transesterification of triolein/ ethanol into biodiesel. It was observed that the production of ethyl esters catalyzed by radiation grafted kenaf catalysts were influenced by graft chain length. Highest conversion yield of 92% obtained with short-chain kenaf catalyst.

Keywords: bio-based heterogenous catalyst, radiation graft polymerization, graft-chain, transesterification, kenaf catalyst.

1. Introduction

Recent increase in energy demand, global warming, and rapid decline in petroleum reserves, has results in the development of green, renewable and sustainable energy worldwide [1-4]. Biodiesel is one of the promising sustainable energy, which are found to be non-toxic and sulfur free [5]. It is a mixture of long chain fatty acid alkyl esters (FAAE) extracted from various kinds of vegetable oil or animal fats in the present of catalyst [6-7]. Generally, the commercial biodiesel production involves the use of homogeneous catalyst such (KOH, NaOH, H_2SO_4) in view of high reaction rates and mild processing conditions [8-10]. However, these catalysts require many steps of purification which generate large amount of alkaline or acidic wastewater, corrosion to equipment, high operational cost and high energy consumption. Therefore, number of studies on heterogeneous catalyst in relation to biodiesel production is increasing to address these difficulties. [11-14]. Lignocellulose fibers are abundant natural materials that are inexpensive to fabricate. It holds great promise as catalyst supports due to rich in surface functional groups (-OH, -C-O-C-) that promote surface modification. Using the method reported in our pioneering study on emulsion graft polymerization on lignocellulose [15], the anion exchange kenaf fiber will be beneficial as catalyst in transesterification reaction. Therefore, in this paper we reveal the effect of graft-chain on catalytic activity using batch transesterification process of ethanol and triolein into biodiesel.

2. Experimental

2.1 Materials

Kenaf fiber was obtained from Lembaga Kenaf Malaysia. Nonwoven polyethylene (NWPE) fiber (~13μm diameter) purchased from Kurashiki Textile Manufacturing Co., Ltd (Osaka, Japan) and spherical resin Diaion PA306s (particle size: 150-425 μm) purchased Mitsubishi Chemical Co. Japan. Palm oil was purchased from Seri Murni (PBB Group Berhad, Malaysia). 4-chloromethylstyrene (CMS) was obtained from AGC Seimi Chemical Co., Ltd. (Kanagawa, Japan) Trimethylamine (TMA) (30% aqueous solution), ethyl oleate, methanol, ethanol, 2-propanol, n-hexane, acetonitrile and sodium hydroxide (NaOH) were supplied by Wako

Pure Chemical Industries, Ltd. (Osaka, Japan). Triolein (purity: 60%), polyoxyethylene sorbitan monolaurate (Tween 20) were provided from Kanto Chemical Co., Inc. (Tokyo, Japan).

2.2 Preparation of kenaf catalyst by radiation graft polymerization

Radiation graft experiments were performed following the approached of N.H. Mohamed et al. (2013). Briefly, kenaf fiber (400 mg) was packed into polyethylene bags in nitrogen atmosphere and pre-irradiated with electron beam at dry ice temperature. Radiation dose was varied from 30 to 200 kGy at electron energy of 2 MeV and 3 mA. Radiated fibers were immerse in emulsion containing CMS monomer, Tween 20 and water in nitrogen condition at 30°C. Kenaf-g-CMS were rinsed with distilled water followed by methanol and dried at 30ºC under vacuum overnight. The yield of graft polymerization of kenaf fiber was evaluated by degree of grafting (Dg) which was calculated from the weight gained as follows:

$$\text{Degree of grafting: Dg [\%]} = \left(\frac{W_1 - W_0}{W_0}\right) \times 100 \qquad 1$$

Where W_0 and W_1 are the weight of the kenaf fiber and kenaf-g-CMS, respectively.

Kenaf-g-CMS fiber was then treated with 0.25M TMA solution at 50ºC for 1 hour. After amination, kenaf-g-CMS-TMA (radiation grafted kenaf catalyst) was rinsed with methanol and dried under vacuum at 30°C. TMA functional group was measured using elemental analyzer (CHNS/O Analyser 2400, Perkin Elmer).

2.4 Transesterification using batch reaction

Batch reaction was performed to screen the catalytic performance of catalyst. In this experiment, about 0.1 g (dry weight) of catalyst were mixed 10 g of triolein (65% purity) and ethanol (HPLC grade). The molar ratio of ethanol to triolein was kept constant at 50:1. Prior to transesterification, catalysts were treated with NaOH to replace Cl- with OH- group. Then transesterification reaction was carried out in a shaking water bath at 30ºC for 24 hours. The reaction products were drawn at regular intervals of time for analysis. To quantify the amount of ethyl oleate (biodiesel), the diluted samples were filtered through a 0.2 µm membrane filter and measured by high performance liquid chromatography (HPLC) system, in a similar manner to method described by M. Holčapek et al. [13].

3. Result and Discussion

3.2 Effect graft-chained lengths on catalytic activities

Individual chromatograms of aliquots obtained from batch transesterification of triolein/ethanol using long-chain (50 kGy) and short-chain (150 kGy) catalysts are shown in Fig 5. Transesterification experiments indicated that the areas of all triolein (TG) peaks decreased during the reaction. By increasing reaction time from 2h to 24 h, the peaks of ethyl oleate (FAEE) become higher for both catalysts. However, less TG conversion was achieved with 50 kGy catalyst with TG conversion of 57%, 74% and 77% was observed at 2h, 4h, and 24h respectively (Fig 5a). On the contrary, 150 kGy catalyst gave higher transesterification efficiency with TG conversion of 68%, 90% and 92% at 2h, 4h and 24h respectively (Fig 5b). The trend shows that the transesterification using grafted kenaf catalyst is affected by chain length rather than the degree of grafting. The explanation could lie in the accessibility of TG molecules to the active sites of kenaf catalyst. This observation suggests that the big molecule of TG is unable to penetrate between the gaps of graft chain to access the reactive sites on underlying surface of the long chain catalyst. Whilst, the short chain provides high accessibility of TG molecules to reactive sites, hence high TG conversion.

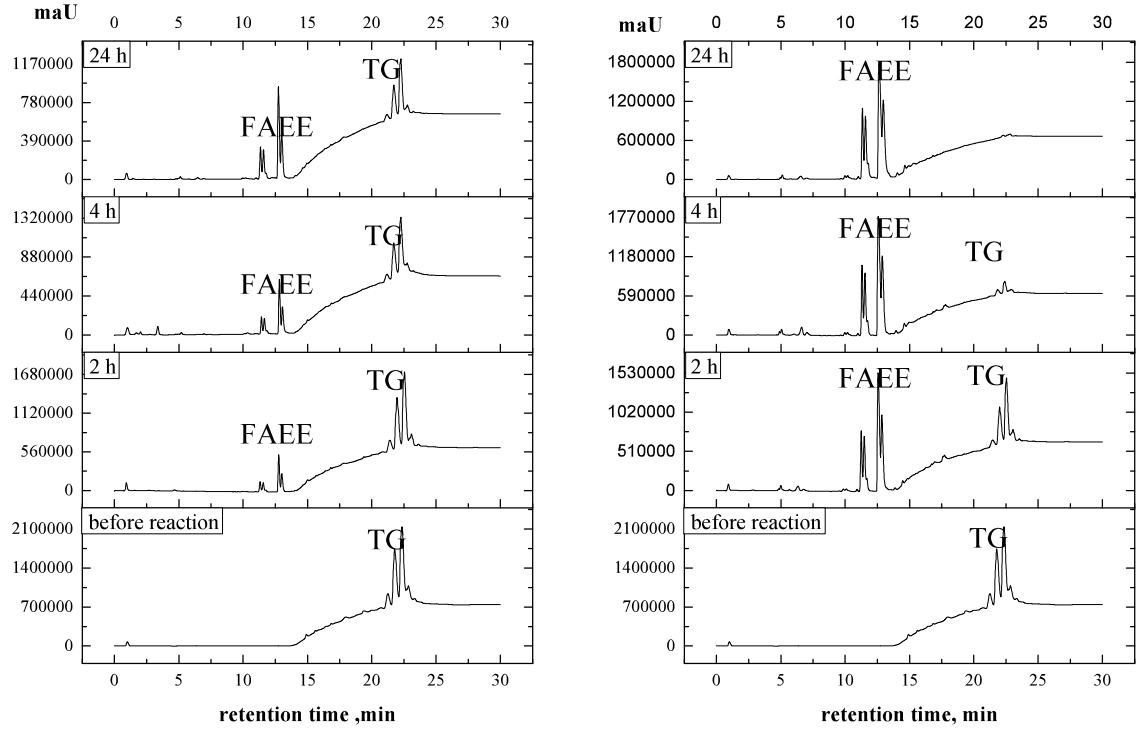

FIG. 5. HPLC chromatograms of effluents extracted from triolein/ethanol catalyzed with radiation grafted kenaf; (a) long chain catalyst (grafted with irradiation dose of 50 kGy) and (b) short chain catalysts (grafted with irradiation dose of 150 kGy).

References

1. Hajjari, M., Tabatabaei, M., Aghbashlo, M., Ghanavati, H., 2017. A review on the prospects of sustainable biodiesel production: A global scenario with an emphasis on waste-oil biodiesel utilization. Renewable and Sustainable Energy Reviews. 72: 445-464.
2. Mahmudul, H. M., Hagos, F.Y., Mamat, R., Abdul Adam, A., Ishak, W. F. W., Alenezi, R. 2012. Production, characterization and performance of biodiesel as an alternative fuel in diesel engines-A review. Renewable and Sustainable Energy Reviews. 113: 19-22.
3. Naylor, R. L., Higgins, M. M. 2017. The political economy of biodiesel in an era of low oil prices. Renewable and Sustainable Energy Reviews. 77: 695-705.
4. Markovska, N., Duic, N., Mathiesen, B. V., Guzovic, Z., Piacentino, A., Schlor, H., Lund, H. 2016. Addressing the main challenged of energy security in the twenty-first century-Contributions of the conference of sustainable development of energy, water and environment systems. 115(3): 1504-1512.
5. Knothe. G., Razon, L. F. 2017. Biodiesel Fuel. Progress in Energy and in Combustion Science. 58: 36-59
6. Fabián,S-C., J., Alberto, G-F. C. 2017. Methods for improving the cold flow properties of biodiesel with high saturated fatty acids content: a review. Renewable Sustainable Energy Reviews. 72:774–90
7. Baharak, Abdul, S. R. A.A ., Hamidreza, A. 2016. A comprehensive review on properties of edible and non-edible vegetable oil-based biodiesel: composition, specifications and prediction models. Renewable Sustainable Energy Reviews. 63:62–92.
8. Reyero, I., Arzamendi, G., Zabala, S., Gandia, L. M., 2015. Kinetic of the NaOH-catalyzed transeseterification of sunflower oil with ethanol to produce biodiesel. Fuel processing Technology. 129: 147-155.
9. Gebremariam, S. N., Marchetti, J. M., 2018. Economic of biodiesel production: Review. Energy conversion and management. 168: 74-84.

10. Soetaredjo, F. E., Ayucitra, A., Ismadji, S., Maukar, A. L., 2011. KOH/ bentonite catalyst for transesterification of palm oil to biodiesel. Applied Clay Science. 53: 341-346.
11. Sharma, Y. C., Singh, B., Korstad, J. 2011. Latest developments on application of heterogeneous basic catalysts for an efficient and eco friendly synthesis of biodiesel: a review.
12. Baskar, G., Aiswarya, R. 2016. Trends in catalytic production of biodiesel from various feedstocks. Renewable and Sustainable Energy Reviews.57: 496-504.
13. Mardhiah, H. H., Ong, H. C., Masjuki, H. H., Lim, S., Lee, H.V. 2017. A review on latest developmnets and future prospects of heterogeneous catalysts in biodiesel production from non-edible oils. Renewable and Sustainable Energy Reviews.67: 1225-1236.
14. Borges, M. E., Diaz, L., 2012. Recent developments on heterogenous catalysts for biodiesel production by oil esterification and transesterification reactions: A review. Renewable and Sustainable Energy Reviews.16: 2839-2849.
15. Mohamed, N. H., Tamada, M., Ueki, Y., Seko, N., 2012, Effect of partial delignification of kenaf bast fibers for radiation copolyerization. Journal of Applied Polymer Science. 127(4).

6^{th} International Symposium on Applied Engineering and Sciences (SAES2018)
Kyushu Institute of Technology, 15^{th}-16^{th} Dec 2018

Please choose: Oral/ Poster/ Either
Presentation session: Computer Science
Presenter name: Naoto Kashiwagi

[Automatic Classification of Auroral images using optical flow feature]

Naoto Kashiwagi[1], Eiji Miyano[1], Akiko Fujimoto[1], Terumasa Tokunaga[1], Yoshizumi Miyoshi[2], Yasunobu Ogawa[3], Keisuke Hosokawa[4]

[1]Kyushu Institute of Technology, 680-1 kawazu, Iiduka-shi, Fukuoka, 820-0067, Japan
[2]Institute for Space-Earth Environmental Research, Nagoya University, Furo, Chikusa, Nagoya 464-8601, Japan
[3]National Institute of Polar Research: 10-3, Midori-cho, Tachikawa-shi, Tokyo 190-8518, Japan
[4]The University of Electro-Communications: 1-5-1 Chofugaoka, Chofu, Tokyo 182-8585, Japan

Corresponding author's e-mail:p236015n@mail.kyutech.jp

Keywords: Aurora, Optical flow, Convolutional Neural Network

[Introduction]
The machine learning technique including the deep learning has been developed and the practical uses have increased on various field. On the study of auroral detection, the concern over the automatic image classification has risen using the approach of machine learning technique for the large statistical analysis of auroral images. The automatic auroral image classification has tried to use some techniques from computer vision, machine vision and pattern recognition. There are roughly two kinds of the selected feature: the color of image and the motion of aurora image sequences. The works based on the color feature of aurora image have been performed by Rao et al. (2014) and Tanaka et al. (2015). Rao et al. (2014) performed Support Vector Machines (SVM) classification with several local feature extraction techniques, and found that Scale Invariant Feature Transform (SIFT), OpponentSIFT, is the most effective feature for the automated classification of color aurora images. Tanaka et al. (2015) used the aurora area using the HSV model. They mentioned that it is difficult to classify the images including the diffuse aurora and cloud area. The color feature work well for the color auroral image, while the gray-scale (optically filtered) auroral images need other features on the automated classification. Blixt et al. (2006) applied the optical flow estimation to auroral image sequences. Their case study showed the useful tool for representing the motion of the aurora. In this study, we validate the optical flow estimation to extract the feature of auroral image, and automatically classify the large gray-scale auroral images using the machine learning with Convolution Neural Network (CNN).

[Experiment]
We use five categories for the preparation of supervised learning data, 1) aurora, 2) aurora and cloudy, 3) aurora and moon, 4) aurora, cloudy and moon, 5) clear/noaurora. We use three layer CNN structure in this work (Figure 1). We demonstrated the optical flow estimation on the auroral image (Figure 2a and 2b) and cloudy image (Figure 2c and 2d). It is clear from Figure 2 that the flow vector of aurora image is larger than that in the cloudy image. The optical flows have two vector (Vx: East-West direction and Vy: North-South direction) in the motion of auroral sequences. For the extracted feature of auroral images in the machine learning, we converted the two-dimensional calculated optical flow vector into each separated image map data.

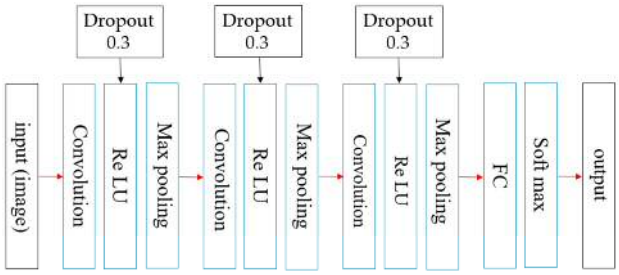

Figure 1: network structure of proposed method

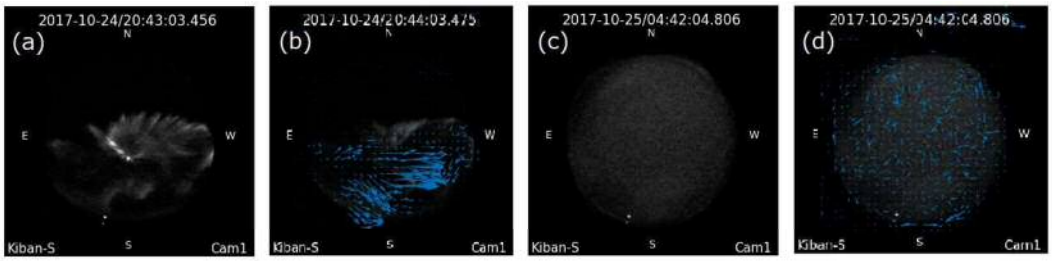

Figure 2: (a) aurora, (b) aurora's optical flow, (c) cloud, (d) cloud's optical flow

[Result and Discussion]
Figure 3 and 4 show the result of Vx image map derived from the Figure 2b (aurora) and Figure 2d (cloudy), respectively. These different characteristics clearly show that the useful extracted feature on the machine learning. We use 63,871 gray-scale aurora images in total, 51,097 images as training data, 6,378 images images as verifying data and 6,378 images images as testing data. We will show the result of the automatical auroral image classification using the machine learning with the optical flow feature in the presentation.

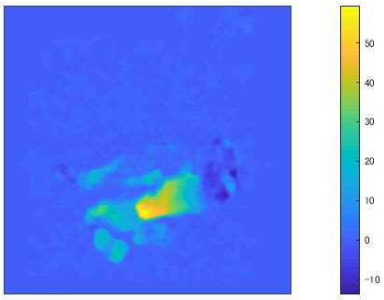

Figure 3: Aurora's Vx

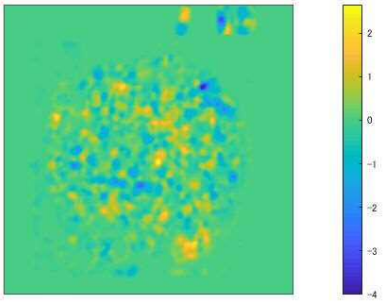

Figure 4: Cloud's Vx

References

[1] J. Rao, N. Partamies, O. Amariutei, M. Syrjasuo, and K. E. A. van de Sande, Automatic auroral detection in color all-sky camera images, IEEE J. Sel Topics Appl. Earth Observ. Remote Sens., pp. 4717-4725, (2014)

[2] Tanaka, Takanori; Tanaka, Yoshimasa; Sato, Yuka; Ikeda, Daisuke, Toward Automatic Classification of Auroral All-Sky Images to Forecast Auroral Behaviors, JAXA Research and Development Report: Journal of Space Science Informatics Japan: Volume 4, JAXA-RR-14-009, 127-134, (2015)

[3] Blixt, E., Semeter, J., & Ivchenko, N. Optical flow analysis of the aurora borealis, Transactions on Geoscience and Remote Sensing, 3, 159-163, (2006)

Please choose: Poster
Presentation session: Materials Science
Presenter name: Shoki Kondo

[Visualization of ribbing pattern in bar coating of non-Newtonian particle suspensions]

[Shoki, Kondo], [Yoshihide, Mawatari], [Masato, Yamamura]

[2]Faculty of Engineering, Kyushu Institute of Technology, 1-1 Sensui-cho, Tobata-ku, Kitakyushu-shi, Fukuoka, 804-8550, Japan

Email: [yamamura@che.kyutech.jp]

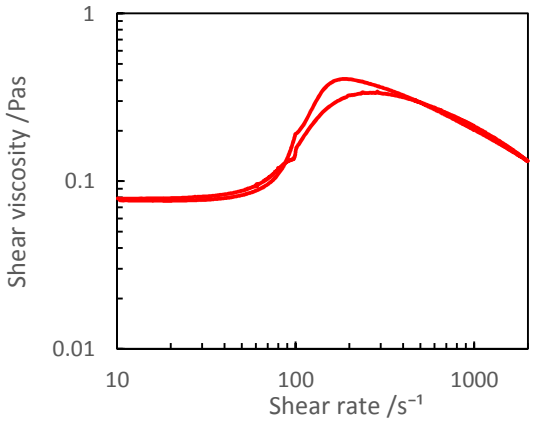

Fig. 1 Variations in shear viscosity with shear rates

Keywords (5 words)
non-Newtonian fluid, flow visualization, ribbing pattern, suspension, coating

[Introduction]

Liquid thin film coating of particle suspension on a moving solid substrate is widely used for the production of optical, magnetic, and adhesive films in a high-speed roll-to-roll process. However, periodic surface irregularities run in the coating direction and periodically align in the width direction when the liquid is too viscous or coated at too high speeds[1]. "Rib" is the name of the convex portion of the non-uniform surface. The sets of-adjacent ribs, referred to as ribbing pattern, are one of the serious defects in coating industries. To determine the critical condition of ribbing, extensive studies have been conducted in Newton fluids[2]. However, most of the practical particle dispersions in industries are non-Newtonian fluids [3]. Because the viscosity of non-Newtonian suspension depends on the shear rate, and even shows a time-dependent behavior, it is not yet well understood how the ribbing patterns develop in non-Newtonian suspensions. In this study, we aim at visualizing the ribbing pattern of silica-polyethylene oxide (PEO) aqueous dispersion as a model non-Newtonian fluid, and investigating the critical condition of the onset of ribbing instability.

[Experiment]

The coating fluids were prepared by dispersing silica nanoparticles (density: 1.209 g/cm^3, particle diameter: 10 to 20 nm, specific surface area: 130 to 280 m² / g, Nissan Chemical) in an aqueous solution of polyethylene oxide (PEO; Mw = 500000, Wako). The silica-PEO aqueous dispersions involved 6 vol% SiO_2, and 0.5 wt% PEO, respectively.

The shear-rate-dependent viscosity of silica-PEO suspension was measured using a rheometer HAAKE MARS II with the cone-plate geometry. Samples were sandwiched between the stationary plate, and rotating cone to measure the shear stress at 23 ± 0.5 ° C. To investigate a hysteresis of the viscosity curve, the shear rate ($\dot{\gamma}$) was first increased from 10 s^{-1} to 2000 s^{-1} and then decreased to 10 s^{-1}. The measurement was continued until the stress reached a constant at each shear rate. The shear viscosity was calculated by dividing the steady stress by the imposed shear rate.

The sample fluid was sandwiched in a narrow space between a cylindrical lens with a curvature radius of 63.9 mm and a flat plate maintained at a minimum clearance (h□) of 10 μm. To trigger the onset of ribbing, the flat plate was first moved at a constant speed (V□) ranging between 0.5 and 20 mm/s, and then moved in the reverse direction at constant speed of V□ = 15 mm/s, corresponding to the shear rate of 1500 s^{-1}, given by $\dot{\gamma}$ = V□/h□. The pattern was visualized using a high-speed camera (Detect, HAS-LIC) at 50 frame/s.

[Result and Discussion]

Fig. 1 shows the variations in shear viscosity with shear rates. The viscosity was almost

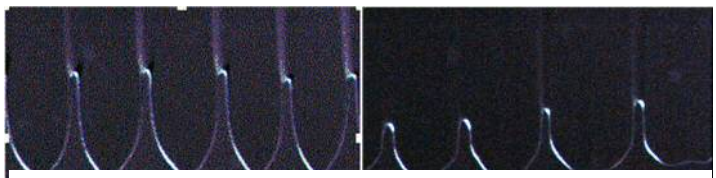

Fig. 2 Ribbing patterns of silica-PEO water dispersion visualized at 1500 s^{-1}. The flat plate moves from bottom to top in the figure.

constant at low shear rates of $\dot{\gamma}$ < 30 s^{-1}. At higher shear rates, the viscosity of the silica-PEO water dispersion first increased, reached a maximum at $\dot{\gamma}$ = 150～200 s^{-1}, and then decreased with increasing the shear rates upto 2000 s^{-1}. When we decrease the shear rates from 2000 s^{-1} to 10 s^{-1}, on the other hand, the viscosity showed a smaller peak at $\dot{\gamma}$ = 200～300 s^{-1} . In other words, the viscosity curve showed a hysteresis in a particular intermediate shear rate region between 100 and 400 s^{-1}. The existence of such flow hysteresis implies that the particle aggregate possibly change their size and/or orientation in the shear flow.

The flow visualization revealed that the flow was stable and showed no ribbing patterns when a constant shear rate was imposed on the fluid at 10-1500 s^{-1}. However, ribs appeared when we apply a stepwise change in shear rates from a certain initial value to a constant value of 1500 s^{-1}. Typical rib patterns at the initial shear rates of 200 and 1200 s^{-1} are shown in Fig.2 (a) and 2(b), respectively. The plate moved from bottom to top in the figure. The liquid film surface deformed to show triangular patterns that periodically aligned in the transverse direction. The rib spacing, i.e. the interspacing between neighboring downstream tips of the ribs, slightly increased with increasing the initial shear rates. Figure 3 shows the variations in the rib spacing with the initial shear rate. The flow was stable at γ˙ < 50 s^{-1} and γ > 2000 s^{-1}, as was in the case when a constant shear rate was imposed. However, a finite spacing was observed at initial shear rates ranging between 50 and 1500 s^{-1}. The previous theories for Newtonian fluids show that ribs appear when the viscosity exceeds a certain critical value. However, our supplemental viscosity measurements revealed that the viscosity at 1500 s^{-1} was almost constant and did not depend on the initial shear rates. The physical reason why we have ribbing patterns in such a particular intermediate range of shear rates remains unresolved.

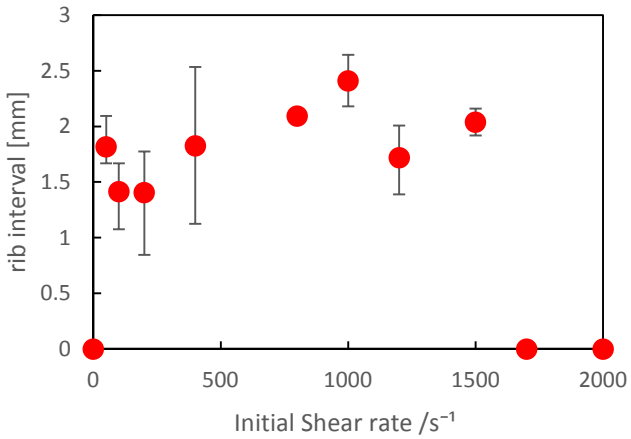

Fig.3 Effect of Initial shear rate on rib interval

[Conclusion]

The viscosity of silica-PEO water dispersion first increases and then decreases with increasing shear rates, showing a particular behavior of non-Newtonian fluids. The flow visualization revealed that no ribbing pattern appears at any shear rates of interests when a constant shear rate is imposed on the fluid. On the contrary, ribbing patterns develop in a particular intermediate range of shear rates when we apply a stepwise change in shear rates from a certain initial value to a constant value of 1500 s^{-1}.

[References]

1) Greener et al., Chemical Engineering Communications 5(1980), 73-83.
2) Coyle et al., Journal of Fluid Mechanics 216(1990), 437-458.
3) Saito et al., Colloids and Surfaces A; Physicochemical and Engineering Aspects 384(2011) 40-46.

Please choose: Poster
Presentation session: Material Science and Technology
Presenter name: Hideaki Furuki

Electric properties of single layer graphene nanoribbons fabricated by unzipping of single-walled carbon nanotubes

Hideaki Furuki[1], Hirofumi Tanaka[1]

[1] Department of Human Intelligence Systems, Graduate School of Life Science and Systems Engineering, Kyushu Institute of Technology, 2-4 Hibikino, Wakamatsu-ku, Kitakyushu-shi, Fukuoka, 808-0196, Japan

Email: tanaka@brain.kyutech.ac.jp

[Keywords]
graphene nanoribbon, electric property, unzipping, p-methoxyphenol, PCI-AFM method

[Introduction]
Large-scale integrated circuits based on silicon have followed the Moore's Law to be allowed by miniaturization of devices and to improve processing performance. Since the miniaturization is, however, facing to the limit of fabrication size, a new substitute material is required.[1)] Particularly in wiring materials, due to miniaturization, electron scattering by wiring side walls and grain boundaries becomes conspicuous, and further miniaturization is difficult. Especially since graphene nanoribbon (GNR) has been successfully isolated, it has been found that there are phenomenal features in electronic properties, mechanical properties and physical properties, and so many researchers are trying to use semiconductor substitute devices. While the current wiring thickness is about 30 nm, the thickness of GNR which is a good conductor is about 0.3 nm. If the GNR can substitute the wiring of LSI, the wiring thickness becomes a hundredth of present electric wiring in LSI. Further miniaturization of electronic products and semiconductor devices is expected in the future. There is a possibility that further lower power consumption and high speed processing of 1000 times or more can be realized. Unzipping of single-walled carbon nanotubes (SWNTs) was successfully performed to obtain single layer GNR with 5 nm wide by following reported procedure.[2)] Electric properties of the individual GNRs were measured by using conductive AFM method.[3) 4)] In addition, PmPV is expensive, it does not work well in unzip unless PmPV is in a state with moderate deterioration. So we are challenging unzip with a polymerization inhibitor called p-methoxyphenol which is a partial structure of PmPV. Furthermore, we compared the electric property of GNRs unzipped by p-methoxyphenol with that of GNRs unzipped by conventional unzipping chemicals.

[Experiment]
We used unzipping method for fabricating GNR from SWNT (Fig. 1). The catalyst was removed from SWNT synthesized by the HiPco method by acid treatment, and heat treatment was performed to induce defects into the sidewalls. Next, the acid-treated SWNT and the aggregation inhibitor PmPV were added to 10 mL of dichloroethane and subjected to ultrasonic treatment. Then, the dispersion solution was centrifuged, and the supernatant was dropped on the substrate. The substrate was washed and then heated to remove PmPV. A gold electrode was deposited on one half of this substrate, and the electrical characteristics of sGNR were measured by the PCI-AFM method (Fig. 2). In case of using p-methoxyphenol for unzipping SWNT, only by changing PmPV to it, we can obtain GNRs which is unzipped by p-methoxyphenol.

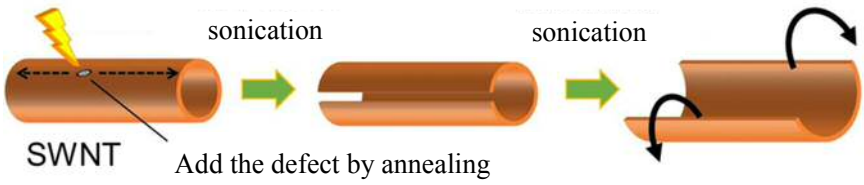

Fig. 1. Procedure to obtain GNRs by SWNT and DWNT.

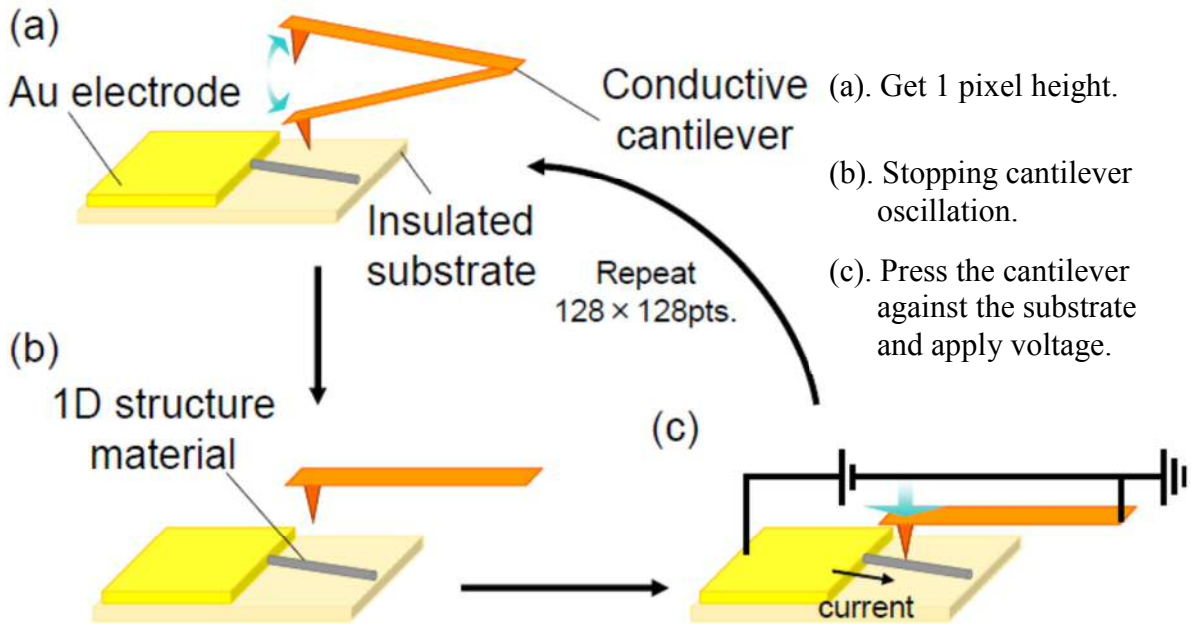

Fig. 2. The Pattern diagram of PCI-AFM method.

[Result and Discussion]

We could obtain GNRs by using PmPV and p-methoxyphenol. Next, the electric properties of each of the GNRs were measured by PCI-AFM method. First, an AFM image of the GNR to be measured was obtained (Fig. 3). Electric properties of isolated GNR made with PmPV showed rectification properties at all measured points. It is considered that this GNR has semiconductive property because we use metal-coated cantilever for PCI-AFM measurement. We will introduce the electric property of GNR made with p-methoxyphenol on the day.

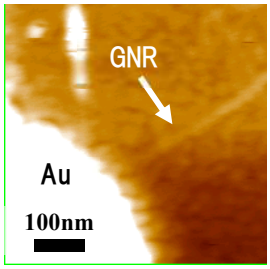

Fig. 3. AFM image of individual GNR appeared from Au electrode.

Refs:

[1] International Technology Roadmap for Semiconductors 2013. [2] H.Tanaka et al., Sci. Rep. **5**, 12341 (2015)
[3] Y. Otsuka et al., Appl. Phys. Lett **82**, 1944 (2003) [4] H. Tanaka et al., Adv. Mater. **18**, 1411 (2006).

Presentation session:
Presentation: Poster
Presenter name: Nisa Syakirah Kamal Azhar

Basic Characteristic of Fruit Battery Based Oil Palm Maturity Sensor

Norhisam Misron[1,2], Nisa Syakirah Kamal Azhar[1], Tashiro Kunihisa[3], Kaiko Minakata[3]

[1]Department of Electrical & Electronic, Faculty of Engineering, Universiti Putra Malaysia, 43400 UPM Serdang, Selangor, Malaysia
[2]Institute of Advanced Technology, Faculty of Engineering, Universiti Putra Malaysia, 43400 Serdang, Selangor, Malaysia
[23]Faculty of Engineering, Shinshu University, 4-17-1 Wakasato, Nagano, 380-8553, Japan

Email: [nsyakeerah@yahoo.com]

Abstract

This paper explains on fruit battery based which is used in this study to determine the ripeness of oil palm fruits from Fresh Fruit Bunches (FFB) to ensure better rate of oil extraction. Grading process is an important part in choosing quality fruits for good palm oil production which the grading process in the mills play an important role in fruit classification. Fruit battery is useful to determine the ripeness of the oil palm fruits during grading process in the mills. Zinc and Copper electrode are used in this study which oxidation and reduction chemical reaction happened in the electrolyte of the oil palm fruits. The methodology involved in this study contain several steps; samples collection from different type of oil palm fruit; identify the important specification; implementing the fruit battery and moisture content method, and analysis of the data collection. The ripeness of the oil palm fruits are the main part in this study in order to obtain high oil extraction rate from the best fruits of FFB. The result obtained from this study found that ripe fruits have lower average voltage and moisture content compared to unripe fruit. The grading process in the mills may take less time and reduce work load of the workers to do the grading classification of the fruits of FFB.

Keywords : Oil Palm, Ripeness, Fruit battery, Moisture Content

Introduction

Palm oil industry is one of the main largest production in Malaysia especially sustainable agriculture sector. Malaysia is the world's largest producer and exporter of palm oil with 50% share of world's palm oil production and 61% share of exports [1]. Oil extraction rate (OER) performance plays an important role in contribution to global oils production which has now declined below than 20 percent. Besides, the national OER in 2017 declined slightly by 2.3% to 19.72% from 20.18% in 2016 due to lower quality FFB processed by the mills [2]. Thus, high quality in choosing fruits of FFB during grading process in the mill is an important part need to be taken by MPOB. Research conducted by Federal Land Development Authority (FELDA) at mills shows the estimated oil content for ripe fruit is 60%, while under ripe is 40% and unripe is only 20% minus water and dirt [3]. According to MPOB, the determination to identify the ripeness of the fruits are at 95% of confidence level which indicates that fruit classification process is the most critical part. Therefore, any false or error happened during fruit classification might affect the estimation of oil content.

The objective of this study is to determine the ripeness of the oil palm fruits. The fruit battery method is implemented in this research with chart analysis. The parameters of the electrode such as depth and distance are chosen to determine the ripeness of the oil palm fruit. Thus, the analysis of the ripeness of fruitlet FFB are varied on the maturity of the fruitlet.

Performance of fruit battery based of oil palm maturity sensor

Fruit battery method is implemented in this research which uses chemical reaction between zinc and copper electrode. Figure 1 shows the schematic diagram of the fruit battery method tested on the fruit and actual view of fruit battery method conducted in this study. From figure (a), the zinc and copper electrodes are pricked through the surface of the fruit which have different in electrochemical series. The fruit that the electrode pricked through is called as an electrolyte which there is reduction and oxidation reaction happened. From the figure, as the zinc and copper electrode pricked through the surface of the fruit, the zinc loses electron while the copper accepts electron from the zinc due to high ionization tendency of zinc more than copper. As this chemical reaction happened, positive ion of hydrogen of moisture content of electrolyte will combine with the electron that accepted from the zinc which hydrogen gas is produced and small current is generated from the movement of the electrons. Thus, the fruit function as a battery.

Figure 2 shows the color chart of average load voltage against moisture content of 39 samples. From the data recorded, ripe fruits has lower generated voltage and lower moisture content compared to unripe fruits. The graph shows there is a linear increment of the graph from the ripe to unripe fruitlet.

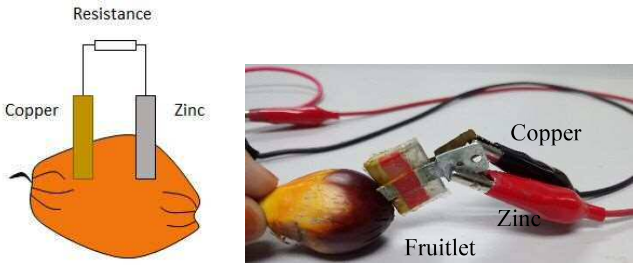

Figure 1 : (a) Schematic diagram of fruit battery, (b) Actual view of fruit battery method done in experiment

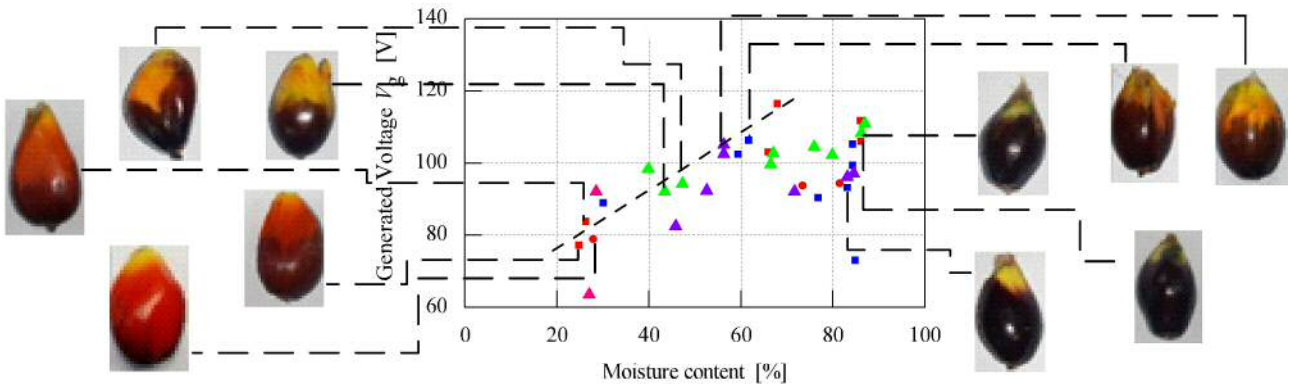

Figure 2 : Color chart of generated load voltage against moisture content

References

[1] Chang L. C.; Abdul Rahim A. S.; Zainon B., *An Economic Perspective of Oil Extraction Rate in the Oil Palm Industry of Malaysia*, MPOB 2003.

[2] MPOB, "Overview of Industry 2017", PALMOILIS Palm Oil Information Online Service, 2018.

[3] Mohamad F. S.; Manaf A. A.; Chuprat S., *Exploiting Suitable Color Model for Ripeness Identification*, 2012

Please choose: Poster
Presentation session: Material science
Presenter name: Takuya Kojima

Effect of drying conditions on photo polymerization of diacetylene thin films

Takuya Kojima, Yoshihide Mawatari, Masato Yamamura
Department of Applied Chemistry, Kyushu Institute of Technology, 1-1 Sensuicho, Tobata, Kitakyushu, Fukuoka, 804-8550, Japan
Email: yamamura@che.kyutech.jp

Keywords (5 words)
Thin film, orientation, polydiacetylene, drying, photo polymerization

[Introduction]

Polydiacetylene (PDA) is a representative organic semiconductor and is used for the fabrication of devices such as field effect transistors (FET) [1]. Ultra thin PDA films exhibit chromatic transitions from colorless monomer, through metastable blue phase, to stable red phase of polymer under ultraviolet (UV) irradiation [2].

The PDA thin films are often fabricated by coating and drying of thin solution film. Initially, diacetylene molecules are homogeneously dissolved in a solvent. The molecules then precipitate as the concentration exceeds a solubility limit during the solvent evaporation. Subsequent ultraviolet irradiation promotes photo-polymerization reactions, leading to form PDA solid films with a particular molecular orientation. It is of practical importance to fabricate uniform films with well-aligned PDA molecules along a transverse or thickness direction. Previous studies have shown how molecules orient by shear, and mechanical friction, usually referred to as rubbing [1]. However, it is not yet well understood how solvent drying assists the photo reactions and molecular orientations in the film. Indeed, most previous studies only focused on polymerization reactions in solid films after solvent evaporation completes. In this study, we aim at fabricating PDA thin films by using photo reactions in the presence of solvent, and investigating the effect of drying condition on morphologies and final properties of the films.

[Experiment]

Sample solutions were prepared by dissolving 0.2 wt% 10, 12 pentacosadienic acid (PCDA) in ethanol. The solution was stirred between 2 and 4 hours in a light-shaded tube at room temperature. The experimental equipment used is shown in Fig.1. The 1.25 mL solution was cast onto a glass substrate from a micropipette to form a 500 µm thick liquid film. The bottom surface of the substrate was continuously heated to maintain the temperature at 323 K. The mass loss of the sample during the solvent evaporation was measured using an electronic balance with an accuracy of 1 mg. To trigger photo-polymerization reactions, UV light of 365 nm in wavelength and 100 µW/cm^2 in intensity was irradiated at different drying times.

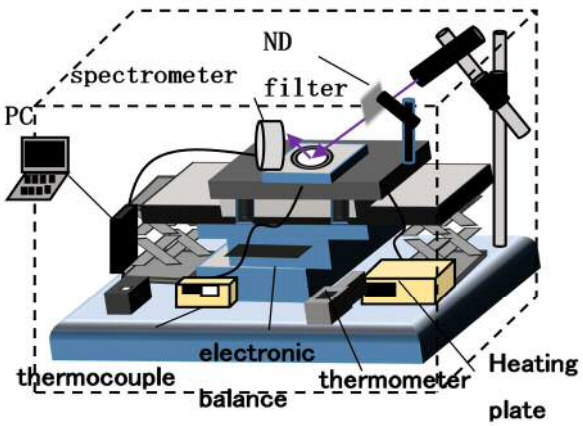

Fig.1 Experimental device

To monitor the photo-reactions and the chromatic transition in the film, the time evolutions in UV-VIS absorption spectra were simultaneously measured during the solvent drying for ~ 1h. The entire experimental apparatus was covered with a windproof dark curtain to minimize the effects of external disturbances on the mass measurements and the spectroscopy

[Result and Discussion]

Fig.2 shows the variations in absorbance at the wavelength of 645 nm with drying times. The absorbance was measured after the onset of UV irradiation. The absorbance was almost constant and slightly decreased with time when the ultraviolet irradiation was start at early drying stages of 0 and 30 min. On the other hand, the absorbance increased with increasing drying time when the UV light irradiation onsets at 40 min. Previous study has shown that the absorbance at 645 nm is associated with the characteristic peak of poly(-diacetylene), indicating that photo-polymerization reactions proceed in this drying condition. When we irradiate UV light at 50 min drying, the absorbance increases but its intensity is lower than the case of light irradiation at 40 min drying, showing lower conversion from PCDA (monomer) to PDA (polymer). These facts imply that we have an optimum drying time to enhance the photo polymerization reactions in the course of solvent evaporation. We need further studies to clarify how the solvents assist the polymerization reactions.

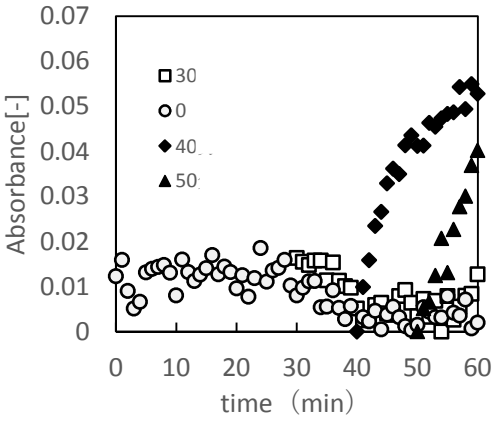

Fig.2 Variations in absorbance at 645 nm with drying time. The ultraviolet irradiation was start at different times of 0, 30, 40, and 50 min during solvent evaporation.

[Conclusion]

We fabricated poly(-diacetylene) solid films by evaporating ethanol from solution films containing 10, 12 pentacosadienic acid (PCDA), followed by UV irradiation to induce photo polymerization reactions. The absorbance spectroscopy revealed that highest absorbance intensity was observed when we irradiation UV light at 40 min drying, at which solvents still exist in liquid films, implying that we have an optimum drying time to enhance the photo polymerization reactions.

[References]

1) M. Brinkman et al, Macromolecular Rapid Communications 35 (2014), 9-26

2) A. Upcher et al, Langmuir 28 (2012) 4248-4258

Please choose: Poster
Presentation session: Material Science and Technology
Presenter name: Shinnosuke Hara

The Mechanism of Unzipping Double-Walled Carbon Nanotubes.

Shinnosuke Hara, Hirofumi Tanaka

Department of Human Intelligence Systems, Kyushu Institute of Technology, 2-4 Hibikino, Wakamatsu, Kitakyushu, 808-0196, Japan.
E-mail: tanaka@brain.kyutech.ac.jp

[Keywords] Graphene nanoribbons, Double-walled carbon nanotubes, Sonochemistry, Unzip, PmPV

[Introduction] Graphene nanoribbon (GNR) is a narrow strip of graphene which has exceptional properties and are being expected for various applications. Unzipping multi-walled carbon nanotube by sonochemical method[1] is scalable, which high quality GNR can be obtained. We have already succeeded to unzip double[2] and single-walled carbon nanotube[3] (DWNT and SWNT) to obtain GNR. However, there are still many problems in this method. For example, the cost of dispersant polymer PmPV(poly[(m-phenylenevinylene)-co-2.5-dioctoxy-p-phenylenevinylene]) is so high, it is still difficult to separate GNR and remaining CNT, the condition for stably obtaining GNR has not been established. the mechanism of unzipping DWNT is still unclear, and so on. We focused to know the mechanism of unzipping DWNT to solve these problems. Unzipping method as follows: DWNT was annealed at 500 □ for 3 h, then sonicated in 1,2-dichloroethane solution of PmPV. The original research paper explains the unzipping process as follows[1]: 1. In annealing process, oxygen reacts with pre-existing defects in nanotubes to form etch pits on the sidewalls. 2. In the solution-phase sonication step, sonochemistry and hot gas bubbles enlarge the pits and unzip the tubes. (Fig.1) However, a theoretical calculation predicted that partly unzipped nanotubes immediately recovered the tube structures by reversible reaction[4]. Explanation of original paper is not enough to know the unzipping mechanism. We assumed that dispersant polymer PmPV become radical and connect to a disconnected C-C bonding of DWNT by sonication occur irreversible unzip. Thus, we tried to unzip DWNT by using moieties of PmPV as unzip agent: p-methoxyphenole, trans-stilbene, 1,4-dimethoxybenzene, 1,4-dioctyloxybenzene(Fig.2).

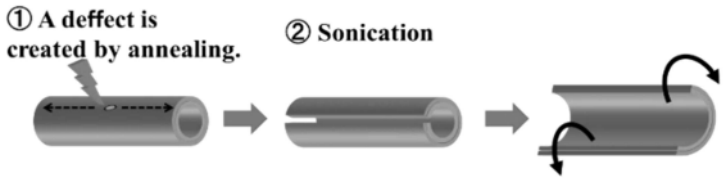

Fig. 1 Procedure to obtain GNR from SWNT and DWNT.

[Experiment] Unzipping procedure as follows: DWNT was annealed at 500 ˚C for 3h, then sonicated in 1,2-dichloroethane solution of these moieties instead of PmPV for 5 h. The solution was drop-casted on mica substrate and measured height of 200 materials on mica substrate by atomic force microscopy to compare the progress rate of unzipping.

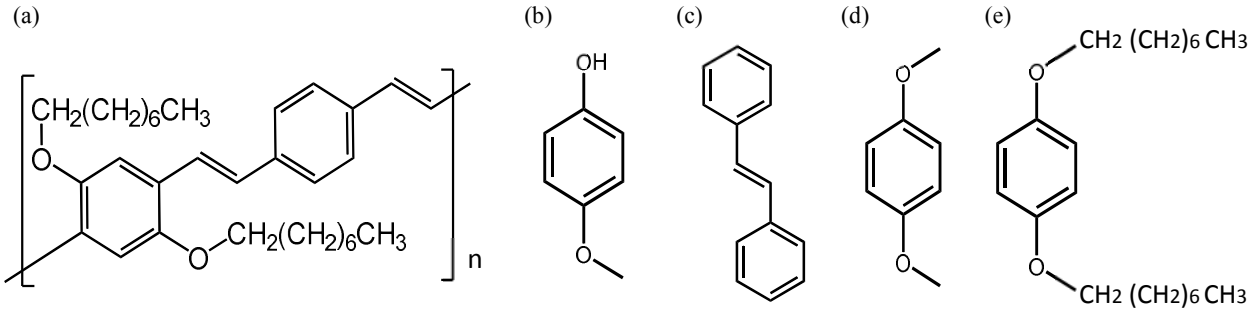

Fig.2 The structure of (a) PmPV, and moieties of PmPV: (b) p-methoxyphenol, (c) trans-stilbene, (d) 1.4-dimethoxybenzene, (e) 1,4-dioctyloxybenzene.

[Result and Discussion] We found GNR in all samples which fabricated by using each unzip agents. Therefore, all unzip agents were effective on unzipping, but the progress rate of unzipping DWNT was different from each agent. The magnitude of progress rate was as follows order: 1,4-dioctyloxybenzene, p-methoxyphenol, trans-stilbene, 1,4-dioctyloxybenzene. This difference was considered because of radical emissions from each agent moieties. 0

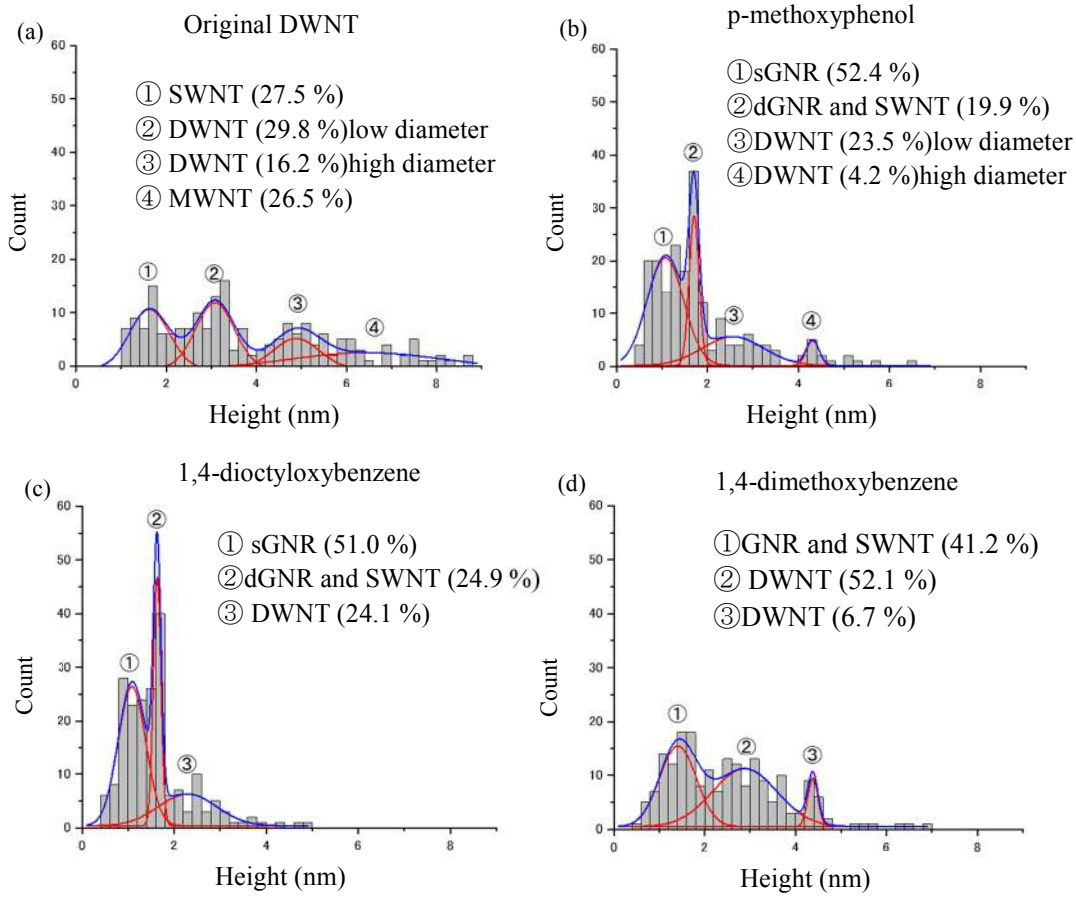

Fig.3 Height distribution of the materials on mica substrate. (a): Original DWNT, unzipped by (b):p-methoxyphenol, (c): 1,4-dioctyloxybenzene, (d): 1,4-dimethoxybenzene

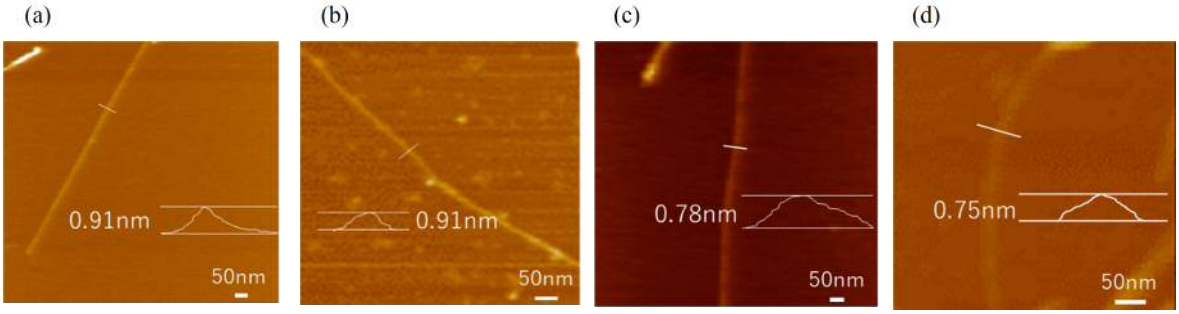

Fig.4 AFM image of GNR unzipped by (a):p-methoxyphenol, (b): trans-stilbene, (c): 1,4-dioctyloxybenzene, (d): 1,4-dimethoxybenzene

From these results, the mechanism of unzipping DWNT was estimated as follows: (1) the defect was cleated on side wall of DWNT by annealing, (2) C-C bonding of DWNT was craved by sonication, (3) The radical which generate from unzip agents connected to broken C-C bonding[5]. The obtained result in this work can greatly contribute to know the mechanism of the sonochemical unzipping SWNT and DWNT.

[1] L Jiao *et al.*, Nat. Nanotechnol. **5**, 321 (2010). [2] H. Tanaka *et al.*, Sci. Rep. **5**, 12341 (2015).[3] M. Fukumori *et al.,* Jpn. J. Appl. Phys. 56,06GG12 (2017). [4] C. Tang *et al.*, Phys. Rev. B **83**, 075410 (2011). [5] M. Fukumori, S. Hara et al., Jpn. J. Appl. Phys. 57, 03ED01 (2018)

Poster
Presentation session: Material Science and Technology
Presenter name: Arata Nakagawa

Research on Sponge/Carbon Nanotube-Based Flexible Tactile Sensor

Arata, Nakagawa[1], Takuya, Setoguchi[2], Iwao, Sasaki[2], Mohd, Hamidon[3], Hirofumi, Tanaka[1]

[1]Department of Human Intelligence Systems, Kyushu Institute of Technology, 2-4 Hibikino, Wakamatsu-ku, Kitakyushu-shi, Fukuoka, 808-0196, Japan
[2]Department of Biological Functions Engineering, Kyushu Institute of Technology, 2-4 Hibikino, Wakamatsu-ku, Kitakyushu-shi, Fukuoka, 808-0196, Japan
[3]Faculty of Engineering, University Putra Malaysia, 43400 UPM Serdang, Selangor, Malaysia

Email: tanaka@brain.kyutech.ac.jp

Keywords (5 words)
Tactile sensor, Harvesting Robot, Piezoresistive, Carbon nanotube, Composited material

[Introduction]

Tactile sensor is used for variable purposes presently. For the harvesting robots, soft sensor is required to avoid the damage of fruits or vegetables [1]. Also, sensitivity of sensor is necessary to identification the ripe of fruits or vegetables. Previously, we reported a piezoresistive tactile sensor fabricated by complex of carbon nanotube (CNT) and polydimethylsiloxane (PDMS) [1]. However, the flexibility and the sensitivity of the sensor were not sufficient. In the present work, sponge/CNT was utilized for the tactile sensor to make more flexible sensor. Furthermore, amount of CNT put into sponge was varied to improve the sensitivity.

[Experiment]

Two solutions of tetrahydrofuran (THF) with CNT were prepared. The solution at a concentration of 0.25 mg/mL was named as solution 1 and the other solution with a concentration of 0.5 mg/mL is named as solution 2. PDMS was put into each solution to promote immersing CNTs into sponges well with 1 h sonication. Then, the sponge and 9 mL of the curing agent were put into each solution and sonicated for 1 h more. The sponge/CNT was picked up from each solution and dried to evaporate the solvent [2]. Comb shape electrodes with 1 mm gap were printed on Si substrate by silver paste. Sponge/CNT used as a detection part was placed on the electrodes. Pressure was applied on the detection part by placing 24 g weights and placing 4.8 g weight increased up to 24 g. Then varying of resistance was measured by multimeter.

[Result and Discussion]

As shown Fig. 1, CNT was attached more to the sponge/CNT made from solution 2 than that made from solution 1. As shown in Fig. 2, resistance of sensor made from solution 2 (sensor 2) was more stable than that made from solution 1 (sensor 1). It was considered that the increase in CNT creates multiple conductive paths, and disconnecting a few path haven't influenced the overall resistance value. As shown in Fig. 3, sensor made from solution 2 was more sensitive than sensor form solution 1. It is proved that amount of CNTs are involved to the conduction in the sponge largely. Also, CNTs attached tend to concentrate on one side. Therefore, it was considered that the sensitivity of sensor was improved depending on increase the degree of contact between the substrate and the sensor. Resistance of sensor 1 varied up to 24 g, but don't varied in the low load region (0 g - 9.6 g). Resistance varying of the sensor 2 was saturated at 19.2 g of the weight. We succeeded to fabricate a tactile sensor with a flexible detection part using sponge. The sensitivity was improved by the amount of CNTs immersed into sponge.

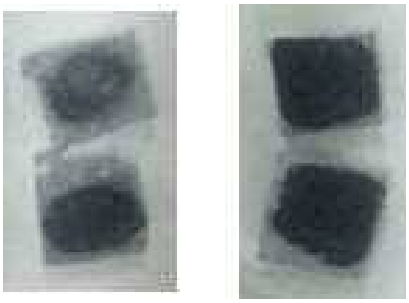

Fig. 1. Fabricated sponge/CNTs sensors. Left side shows the sponge/CNT made from the solution with concentration of 0.25mg/mL solution 1, right side shows that of 0.5mg/mL

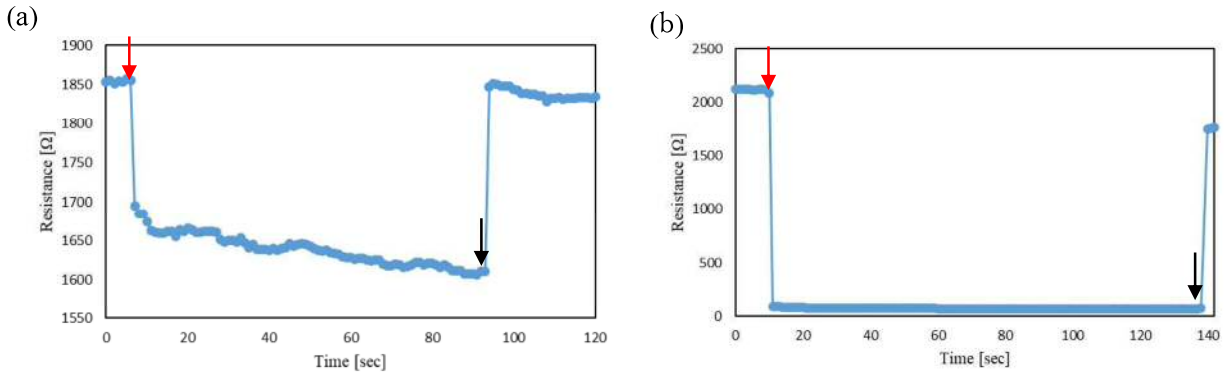

Fig. 2. Variation of resistance of sponge sensor against time. (a) shows resistance of sponge sensor made from the solution with concentration of 0.25mg/mL (solution **1**) and (b) shows that of 0.5mg/mL (solution **2**). Red arrows indicate the timing when weight is placed on the sensor. Black arrow indicates when removed.

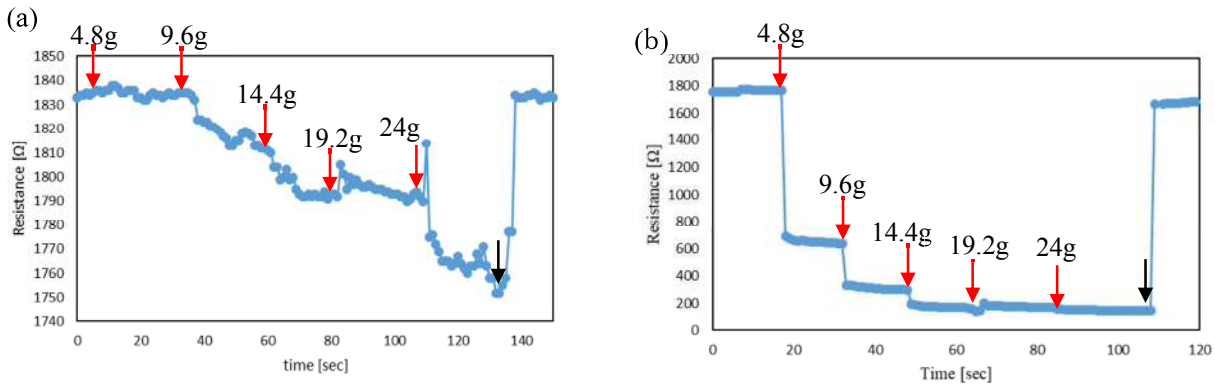

Fig. 3. Variation of resistance of sponge sensor against time. (a) shows resistance of sponge sensor made from the solution with concentration of 0.25mg/mL (solution **1**) and (b) shows that of 0.5mg/mL (solution **2**). Red arrows indicate the timing when weight is placed on the sensor. Black arrow indicates when removed.

References: [1] A. TermehYousefi *et al.*, Mater. Sci. Eng. C, 77, 1098-1103 (2017), [2] Zhaoyao Zhan *et al.*, ACS Appl. Mater. Interfaces, 9 (43), 37921–37928 (2017)

Please choose: Poster

Presentation session: Material Engineering and Science

Presenter name: Yusuke Nakao

Synthesis of Ag-Ag2S core-shell nanoparticles for non-linear conduction

Y.Nakao1), Hadiyawarman1),and H.Tanaka1)* 1)

Graduate School of Life Science and Systems Engineering, Kyushu Institute of Technology, Kitakyushu 808-0196, Japan

Email: *tanaka@brain.kyutech.ac.jp

1.INTRODUCTION

For the several decades, Von Neumann computers have downsized with higher performance advance. However, it reaches to the limit of downsizing due to tunneling effect of transistor or fabrication limit. To overcome such limitations, the system mimicking human brain information processing is expected to be applied. Atomic switch is one of the promising material to enable mimicking human brain device. S. K. Bose et al., reported that Au nanoparticles networks were made and works as logic gate at low temperature [1]. H. O. Sillin et al., reported the functionality of Ag-Ag_2S nanowires for logic circuit [2]. Neuromorphic devices were proposed due to high performance with significantly low power consumption. Purpose of the present work is to fabricate the nanoparticles for non-linear conduction behavior for utilizing to neuromorphic device in future. Ag-Ag2S core-shell nanoparticles were fabricated by following modified Brust-Schiffrin procedure1).

2.EXPERIMENT

Fabrication procedure with molar ratio of Ag/S = 0.25/1 is following; 370 g of allylmercaptane in 40 mL of toluene was mixed with 0.2 g of silver nitrate in 20 mL of deionized water. Then, 0.37 g of tetraoctylammonium bromide in 40 mL of toluene was added to the solution. The mixture was allowed to react for 30 mins at room temperature with magnetic stirring. The water phase was then removed from obtained solution. Sodium borohydride with 0.27 g in 15 g of deionized water was added to the solution and reacted at room temperature for 2 h with magnetic stirring. Then, the water phase was removed to obtain the nanoparticles. Since, narrow distribution of particles size is necessary to fabricate such non-linear devices, Molar ratio of Ag/S were varied with 0.25/1, 0.5/1, and 1/1 to control the size distribution of the particles for optimized non-linear conduction.

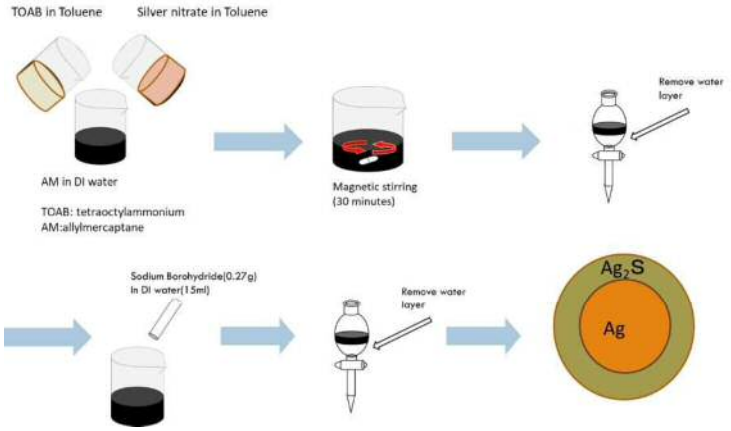

Fig1. Experimental procedure

3.RESULTS AND DISCUSSION

Figure1 shows XRD chart of the synthesized Ag-Ag2S with molar ratio 0.25:1 for Ag:S, respectively. The existence of Ag and Ag2S phase was proved by matching the experimental result with powder diffraction data of Ag and Ag_2S. Moreover, Sharp peaks indicates that the sample has high crystallinity.Figure2 shows TEM image of core-shell Ag-Ag_2S core-shell

nanoparticle. We can confirm the existence of Ag_2S surrounding Ag.

Mechanism of synthesis is following. At first, organic layer is formed above water layer mixed tetraoctylammonium and allylmercaptane Then, silver nitrate was added to water layer. Tetraoctylammonium works as a phase transit catalysis to move silver nitrate to organic layer. This procedure is used for making reaction happens in organic layer. Sodium borohydride was added to water layer, reducing agent to get core-shell nanoparticles.

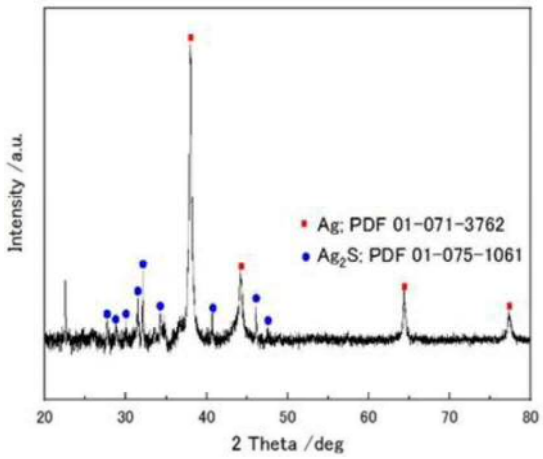

Fig. 2 XRD ~~pattern~~ chart of obtained Ag-Ag_2S core-shell nanoparticles with molar ratio of Ag/S=0.25/1

Reference : 1) C. Battocchio, C. Meneghini, I. Fratoddi, I. Venditti, M. V. Russo, G. Aquilanti, C. Maurizio, F. Bondino, R. Matassa, M. Rossi, S. Mobilio, and G. Polzonetti, J. Phys. Chem. C 116, 19571-19578 (2012).

Please choose: Poster
Presentation session: Material Science and technology
Presenter name: Takuya Setoguchi

Research on haptic sensor with nanocarbon composite material

Takuya Setoguchi[1], Arata Nakagawa[1], Iwao Sasaki[1,*], Mohd Nizar Hamidon[2], Hirofumi Tanaka[1,**]

[1] Graduate School of Life Science and Systems Engineering, Kyushu Institute of Technology,
2-4 Hibikino, Wakamatsu-ku, Kitakyushu-shi, Fukuoka, 808-0196, Japan
[2]Faculty of Engineering, University Putra Malaysia, 43400 UPM Serdang, Selangor, Malaysia

Email: *sasaki@life.kyutech.ac.jp, **tanaka@brain.kyutech.ac.jp

Keywords (5 words)
Harvesting robot, Piezoresistive, Carbon nanotubes, Polydimethylsiloxane

[Introduction]

In agricultural field, utilization of robots has been expected to eliminate recent constraint of manpower and the technology promotion is demanded. The harvesting robot currently being developed uses the camera to detect ripen fruits by color. To improve the discrimination rate, it is necessary to distinguish the ripeness by mechanical hardness using haptic sensors. Furthermore, machine learning using haptic sensor array (Fig. 1) can be applied to the robots to evaluate automatically the ripeness of fruits (Fig. 2). Since commercially available haptic sensors, however, are hard, it is problem that the fruits could be damaged by the sensors. To protect fruits from the damages, we fabricated a piezoresistive haptic sensor using a composite material of carbon nanotubes (CNTs) and polydimethylsiloxane (PDMS) [1]. There is, however, a problem that the sensitivity of the sensor's signal was not enough. In the present work, we modified the electrodes to improve the sensitivity of the sensors.

[Experiment]

Our haptic sensor consists of electrodes and a detection part. Electrodes were printed on a silicon substrate with silver paste and the paste was dried in an electric furnace at 125 ℃ for 20 min. Fig. 3 shows the fabrication procedure of a composite material of CNTs and PDMS (CNTs/PDMS) for use of a detection part of pressure. CNT and PDMS were mixed in tetrahydrofuran as a solvent. After evaporating the solvent, the obtained sample was thermally annealed. CNTs/PDMS composite material was formed to 10 mm × 10 mm × 1 mm to use as a detection part, then placed on electrodes. Pressure was applied on the detection part by placing weights and resistance of the sensor were measured by a muiltimeter.

[Result and Discussion]

Fig. 4 shows a fabricated haptic sensor. Fig. 5 shows the resistance of sensor plotted against the applied pressure. Resistance monotonically decreased as the applied pressure increased. In the sensor, CNTs in CNTs/PDMS composite material play the role of conductive paths. When no pressure is applied on the sensor, the number of conductive paths was small to make the resistance large. Once pressure was applied, the composite material is deformed and a new conductive path was formed to make resistance decreased. Also, since the resistance decreases in the small pressure up to 0.2 kPa, it can be seen that the sensor can detect very small pressure. Since small pressure can be detected, hardness of fruits can be evaluated without damaging fruits. Therefore, the sensor could be used for harvesting robot.

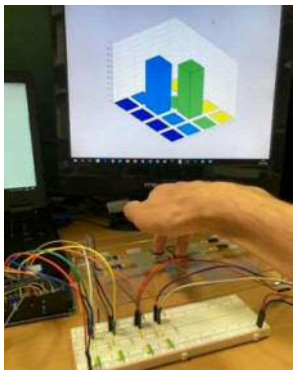

Fig. 1 Demonstration of haptic sensor array.

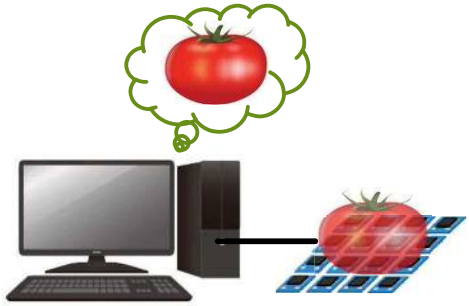

Fig. 2 Schematic image of evaluate the ripeness of fruits with machine learning.

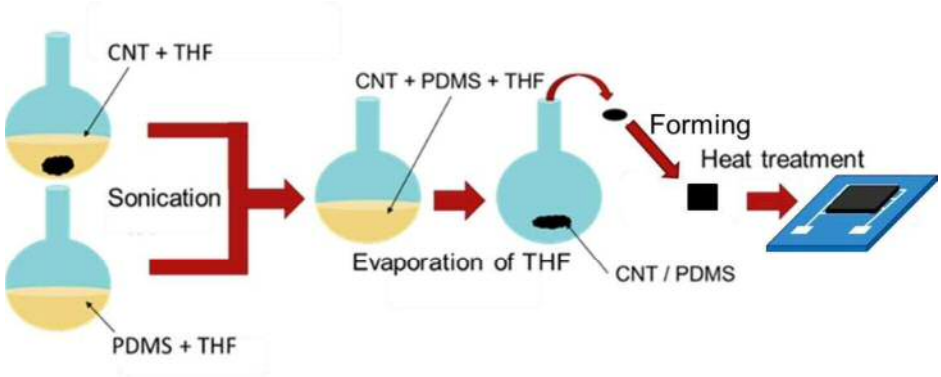

Fig. 3 Schematic illustration of the fabrication process of CNTs/PDMS composite material.

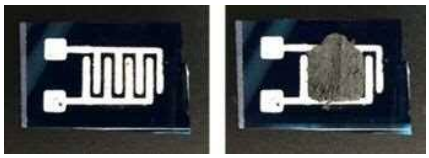

Fig. 4 The picture of the fabricated haptic sensor.

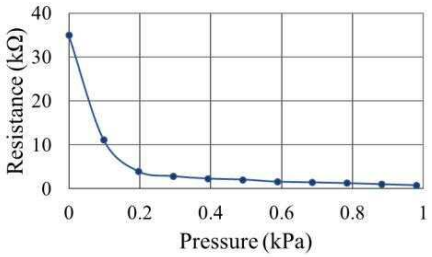

Fig. 5 Resistance-pressure curve of the sensor.

Reference : [1] A. TermehYousefi et al., Mater. Sci. Eng. C 77, 1098-1103 (2017),

Please choose: Poster
Presentation session: Neuroscience
Presenter name: Hirofumi Arai

Epileptic discharges recorded by multielectrode system in rat hippocampal slices

[Hirofumi Arai][1], [Itsuki Kageyama][1], [Kiyohisa Natsume][1]

[1]Department of human Intelligence Systems, Graduate School of Life Science and Systems Engineering, Kyushu Institute of Technology, 2-4 Hibikino Wakamatsu-ku, Kitakyushu, Fukuoka, 808-0196, Japan

Email: [arai.hirofumi545@mail.kyutech.jp, natume@brain.kyutech.ac.jp]

Keywords Hippocampus, Slices, Epileptic discharges, Multielectrode, Disinhibition

[Introduction]

Epileptic patients have the epileptic discharges in their brains. Population of neurons fires synchronously in the discharges. In rat hippocampal slices, the application of $GABA_A$ receptor antagonists induces the discharges [1]. In the present study, we have studied the spatiotemporal patterns of the epileptic discharges induced by the application of $GABA_A$ receptor antagonists in the hippocampal slices.

[Materials and Methods]

Rats were anaesthetized with isoflurane. The brains were removed and placed in ice-cold artificial cerebrospinal fluid (ACSF) of the following composition (in mM): 124 NaCl, 5 KCl, 1.25 NaH_2O_4, 2 $MgSO_4$, 26 $NaHCO_3$, 10 glucose, 2 $CaCl_2$. Transverse hippocampal slices in 410-450 μm thick were prepared using a tissue slicer (Micro Slicer Zero-1, Dosaka-EM Co., Japan). The slices were transferred to an interface recording chamber and incubated in ACSF bubbled with 95% O_2-5% CO_2 at 33.1 ± 0.1°C for at least 1 hour for the recovery. The slices were continuously perfused with ACSF at a flow rate of 1.5 ml/min on the preservation chamber. The slices were transferred from the chamber to the recording MED probe (MED-P530 or MED-P515A). The extra field potential was recorded using Alpha MED multielectrode system (Alpha MED Scientific Inc., Japan). The potentials were filtered with low-cut of 1Hz and high-cut of 1 kHz. The system sampled the signal with the sampling frequency of 20 kHz. The slices were continuously perfused with ACSF at a flow rate of 2.0 ml/min at 33.5 ± 1℃. $GABA_A$ receptor antagonists picrotoxin and SR95531 (Gabazine) (30 μM), AMPA receptor antagonist CNQX, and cell firing blocker TTX (1 μM) were applied to the slices. Using the extracellular field potentials recorded at 8X8 electrodes current source density (CSD) analysis was done. In the CSD analysis, current flow was calculated with the equation $-(\sigma_x \nabla^2_x \varphi + \sigma_y \nabla^2_y \varphi)$ [2]. Φ is the potentials, and σ_x, σ_y are the electrical conductivity along x and y axes. When the flow has the negative sign, it was called sink, and when it has the positive sign, it was called source.

[Result and Discussion]

When 30 μM PTX was applied to the slice with no spontaneous activity (Fig. 1B), the epileptic discharges were induced 30 minutes after the onset of the application (Fig. 1C). Then with the application of 10μM CNQX, the discharges were diminished 30 minutes after (n=3; Fig. 1D). From the CSD analysis, when the potential of epileptic discharges had the negative sign, the current at the recording site was sink, while the potential of epileptic discharges had the positive sign, the current at the recording site was source (Fig. 2B and C). The sink and source appeared rapidly as shown in Fig. 2D. PTX-induced epileptic discharges were diminished 25-35 minutes after the onset of the application of 1 μM tetrodotoxin (n = 3) (data not shown). These results suggest that the glutamatergic excitatory synapse and cell firing are necessary to induce the epileptic discharges. Fig. 1 shows the potential at the cell soma layer. The negative and positive potential indicate the sink and source currents, respectively. Thus, it is suggested that sink current can reflect the population spike, and the positive current can do the population excitatory synaptic potential (EPSP). Therefore, during the generation of the epileptic discharges, at first population spikes are induced, and then population EPSP's are induced.

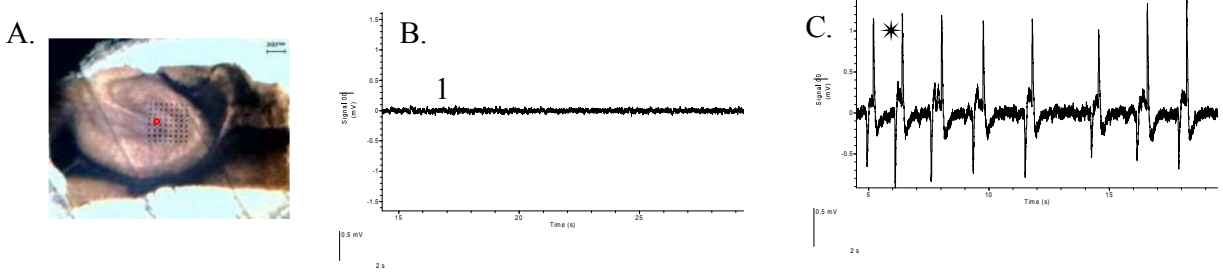

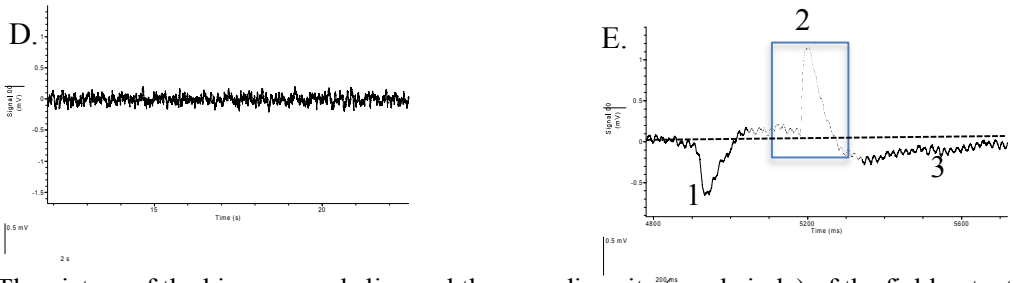

Fig. 1. A. The picture of the hippocampal slice and the recording site (a red circle) of the field potential in B-E. B. The potential before the application of PTX. C. The discharges 30 minutes after the application of 30 μM PTX. The recording site was in cell layer of dentate gyrus. D. No discharges 30 minutes after the application of 10 μM CNQX. X- and Y-axes indicate 3.25mV and 155 sec in B, 2.3 mV and 155 sec in C, 3.1 mV and 115 sec in D. E. Expanded signal at the asterisk in C. The horizontal broken line indicates 0 mV. X- and Y-axes indicate 2.3mV and 0.95 sec.

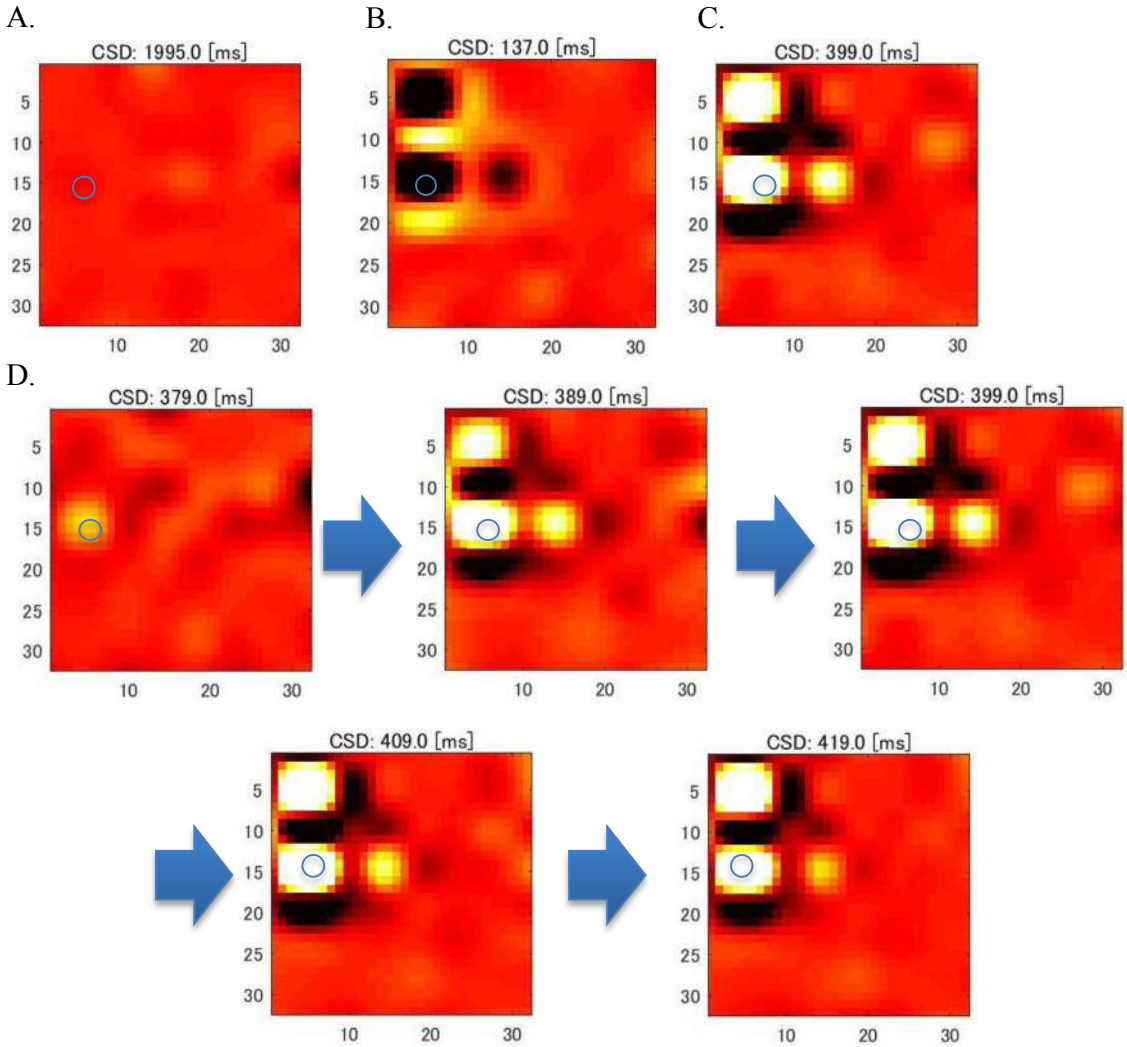

Fig. 2. The results of CSD analysis. Black and white color indicate the sink and source current, respectively. A. Heat map of the analysis at "1" in Fig. 1B. B. Heat map of CSD analysis at "1" in Fig. 1E. C. Heat map at "2" in Fig. 1E. D. Time course of the current flow at the blue rectangle in Fig. 1E. The figures are shown every 10 msec. The circles in all figures indicate the recording site of the field potential as shown in Fig. 1.

[References]

[1] A.S. Galanopoulou., Curr. Neuropharmacol. vol. 6(1), pp. 1-20 (2008). [2] K. Shimono, F. Brucher, R. Granger, G. Lynch, and M. Taketani., J. Neuroscience, vol. 20(22), pp. 8462-73 (2000).